Dissertation
submitted to the
Combined Faculties for the Natural Sciences and for Mathematics
of the Ruperto-Carola University of Heidelberg, Germany
for the degree of
Doctor of Natural Sciences

put forward by
Dipl.-Phys. Johannes Zielcke
born in Stuttgart
Date of oral examination: 17.06.2015

Observations of reactive bromine, iodine and chlorine species in the Arctic and Antarctic with Differential Optical Absorption Spectroscopy

Referees: Prof. Dr. Ulrich Platt
Prof. Dr. Bernd Jähne

Abstract
A unique feature of the polar troposphere is the strong activity of halogen photochemistry, in which reactive halogen species (RHS), such as BrO, IO and ClO, are responsible for ozone depletion, the oxidation of elemental mercury and dimethyl sulphide. The typical abundances, sources, as well as the release and recycling mechanisms of these halogen species are far from being completely understood.

Within this work, field observations were undertaken, in the Arctic (at Alert) and Antarctic (around Ross Island and in the Weddell Sea), using remote sensing and in-situ instruments based on Differential Optical Absorption Spectroscopy (DOAS) techniques such as MAX-DOAS, CE-DOAS and LP-DOAS. Chlorine monoxide was directly detected and quantified (up to 60 pptv, 20 pptv typical) in the Antarctic boundary layer for the first time, with IO and BrO being present simultaneously. The diurnal variation, correlating with insolation, point to the source being the oxidation of surface Cl^- by OH or O_3. In the Arctic, IO was observed for the first time on a regional scale and throughout the sunlit period during several years (2007 - 2014). The IO mixing ratios between 0 - 0.5 pptv are in agreement with an inorganic, oceanic source and resemble those at both Antarctic sites. The Antarctic IO mixing ratios are significantly lower than previous measurements at similar locations. IO was not detected (<1 pptv) originating from the snowpack nor within a penguin colony.

Zusammenfassung
Die polare Troposphäre ist durch die hohe photochemische Aktivität reaktiver Halogenverbindungen, wie BrO, IO und ClO gekennzeichnet, welche dort mit Frühlingsbeginn nach der Polarnacht auftritt und zu Ozonabbau, Quecksilberdeposition und Oxidation von Dimethylsulfid führt. Die Mengen, Quellen und Freisetzungs- sowie Regenerierungsmechanismen sind noch nicht vollständig verstanden.
In dieser Arbeit wurden Verfahren der Differentiellen Optischen Absorptionsspektroskopie (DOAS), wie MAX-DOAS, CE-DOAS und LP-DOAS angewandt, um Halogenverbindungen in der Arktis (bei Alert) und der Antarktis (um die Ross-Insel und im Weddell-Meer) zu messen. Chlormonoxid (ClO) wurde zum ersten Mal in der antarktischen Grenzschicht detektiert und quantifiziert (bis zu 60 pptv, typisch 20 pptv), bei gleichzeitiger Anwesenheit von BrO und IO. Der mit Sonneneinstrahlung korrelierende Tagesgang lässt auf eine Quelle durch Oxidation von gelöstem Cl^- durch OH oder O_3 schliessen. In der Arktis wurde zum ersten Mal IO auf regionaler Skala und über den gesamten Polartag mehrerer Jahre beobachtet (2007 - 2014). Die Mischungsverhältnisse zwischen 0 - 0.5 pptv lassen sich über eine ozeanische, inorganische Iodquelle erklären, und spiegeln die beiden Messungen in der Antarktis wider. Die Mischungsverhältnisse in der Antarktis sind signifikant niedriger als bei früheren Beobachtungen an ähnlichen Orten. IO konnte dort weder im Schneepack noch in einer Pinguinkolonie nachgewiesen werden (<1 pptv).

Contents

1 Introduction

The five elements called halogens are the ones in the seventh main group of the periodic table of elements, namely fluorine, chlorine, bromine, iodine and astatine. They are rarely found as free elements in nature, but in bound states due to their reactivity, which is amongst the highest of all elements. At macroscopic quantities, flourine for example reacts explosively with alkali metals and even forms molecules with otherwise inert noble gases such as krypton and xenon (Holleman, 1995). Several compounds containing halogen atoms also possess this high reactivity. Chlorine dioxide (OClO), for example, is a strong oxidant and used commercially as a bleaching agent in the production of paper, and also for the disinfection of drinking water.

In the atmosphere, the high reactivity of the halogens, while invisible to the naked eye, can also lead to large effects. For those effects, even tiny quantities of certain halogen compounds are sufficient, typically a few *parts per billion* (ppb, 10^{-9}), *parts per trillion* (ppt, 10^{-12}) or even less. This potentially large impact of these minute quantities is possible due to the existence of catalytic reaction cycles, in which the involved halogen compounds are recycled again and again. Thereby the same atom is participating in the same reaction scheme hundreds if not thousands of times. The compounds involved in those cycles are summarily referred to as reactive halogen species (RHS).

The first time the potential impact of RHS was noticed in the atmosphere was the discovery of the ozone hole in the Antarctic stratosphere. The majority of the involved ozone depleting substances, containing chlorine and bromine, were then identified to originate from anthropogenic chlorofluorocarbons (CFCs) (Molina and Rowland, 1974; Stolarski and Cicerone, 1974; Farman et al., 1985). This led to the international Montreal Protocol, phasing-out the use of CFCs.

In the 1980s, the first observations of a similar, but natural, phenomenon in the

lowest few hundreds of meters of the polar atmosphere were made (Oltmans and Komhyr, 1986; Bottenheim et al., 1986). It was found that after the end of the polar night, with the arrival of the first few rays of sunlight, ozone concentrations could suddenly drop from average levels to values close to zero for periods of days to weeks. Shortly thereafter, natural bromine compounds were found to be responsible for this loss of ozone (Barrie et al., 1988; Hausmann and Platt, 1994; Tuckermann et al., 1997).

Since then, three decades have passed and numerous field, laboratory and modeling studies have been undertaken to further the knowledge of all involved processes, such as the release into the atmosphere, possible reactions, sinks etc. It emerged that reactive halogen compounds in the air also play a role in the marine environment, at coastal sites and salt lakes, as well as in the emissions of volcanoes. While significant progress has been made, there are still major unknowns, especially in the polar areas, where field studies are challenging to undertake due to the adverse environmental conditions.

The scientific questions range from more elementary issues, such as typical abundances of certain compounds, to the more complex ones, such as the heterogeneous chemistry leading to the release of dissolved halides, or the gas phase interaction of several dozens of halogen compounds. For iodine and chlorine compounds for example, little is known about typical abundances, not to mention the sources or release processes. The interplay between different compounds containing the different halogens is also unclear.

The mentioned high reactivity and low abundance in the ppt range of RHS also poses a challenge to their measurement. Measurement methods offering reaction surfaces, e.g. sample tubes, inlets or other surfaces, to the substances which are to be sampled incur losses in the compounds of interest, which are challenging to quantify and calibrate. Fortunately optical, contact-less methods exist, such as the Differential Optical Absorption Spectroscopy (DOAS, e.g. Platt and Stutz, 2008), which allow the direct measurement of halogen oxides as well as other compounds.

The aim of this work was to improve the state of knowledge of the halogen activity in the polar troposphere, in terms of abundances, spatial distribution, as well as source and sink processes. In order to attain this aim, Cavity Enhanced-DOAS (CE-DOAS) instrumentation was built, for which a new calibration method was devised, and the Multi Axis-DOAS (MAX-DOAS) evaluation methodology was systematically analyzed and improved. This was subsequently applied during springtime field observations at three locations. Those were conducted in the high Canadian Arctic at Alert, as well as in the Antarctic around Ross Island at the New Zealand research station Scott Base, and finally aboard the German research vessel Polarstern during expedition ANT-XXIX/7 in the Weddell Sea. Each of those field observations provides new insights for the quantification and chemical behavior of several halogen compounds at the respective location. Even more importantly, the three studies combined provide new insights into the chemistry of reactive halogens at those locations as not seen before in previously

published research.

The layout of this work is the following: Beginning with the chapters 2 and 3, the foundations are laid for the following description of this work. In chapter 2, the two polar regions of this planet are described with a focus on the lower atmosphere. Afterwards, in chapter 3, the method used within this work, the Differential Optical Absorption Spectroscopy in its various applications for the measurement of halogen compounds is introduced. Then, the field measurements are described separately with their results and conclusions in the chapters 6 (Scott Base, Antarctica), 7 (Alert, Nunavut, Canada) and 8 (Polarstern cruise ANT-XXIX/7 in the Weddell Sea). The data analysis and discussion pertaining to the used measurement techniques or the inter-comparison between different techniques and mixing ratios are presented in the chapters of the individual field studies. The interpretation in regard to chemical and meteorological processes, on the other hand, is given in chapter 9, thereby combining the data from the field studies to directly compare the different settings side-to-side. This gives a clearer picture of the polar halogen chemistry in general and the similarities of the three studied sites. Finally, in chapter 10, the conclusions of this thesis are drawn and unresolved questions formulated for future research in this field.

Lastly, a few technical remarks need to be mentioned. All measurement errors in this work are given as 1-σ errors. All times and dates are given as UTC times, unless otherwise noted. The unit of the Slant Column Density (SCD) and Vertical Column Density (VCD), molecules per square centimeter, is abbreviated as molec cm^{-2} throughout this work.

2

Reactive halogen chemistry in the polar troposphere

This chapter introduces the details involved in the cycling of reactive halogen species in the polar troposphere. Its aim is to provide an overview of the current state of knowledge. First, the geographic setting is briefly introduced, before describing aspects which are critical for the phenomena studied in this work, which include the vertical structure of the atmosphere and properties of sea ice. Thereafter, the chemistry of reactive halogens in the atmosphere, their involvement with ozone and other substances is detailed. Halogens, the seventh main group in the period table of elements, in the following stands for bromine, iodine and chlorine. Fluorine compounds are chemically too stable to play a similar role in the atmosphere, and the amounts of astatine on Earth, less than one gram at any given time, are insignificant (Holleman, 1995).

2.1 The geographical setting

The Earth's two polar regions are surrounding its geographic poles, the Arctic in the north, and the Antarctic in the south. For both regions, there is no single delimiting outer boundary which is universally accepted. A common one for both, are the respective polar circles at approx. 66.6 ° latitude. For the Arctic, further commonly referenced boundaries are the 10 °C isotherm in July, or the treeline (illustrated in fig. 2.1). For the Antarctic (shown in fig. 2.2), areas south of 60 °S fall under the international Antarctic Treaty, which regulates scientific, political and economic activities in that area. Therefore it is also commonly taken as the boundary. For the purposes of this work, the differences between those definitions are not critical, as the phenomena studied depend more on the

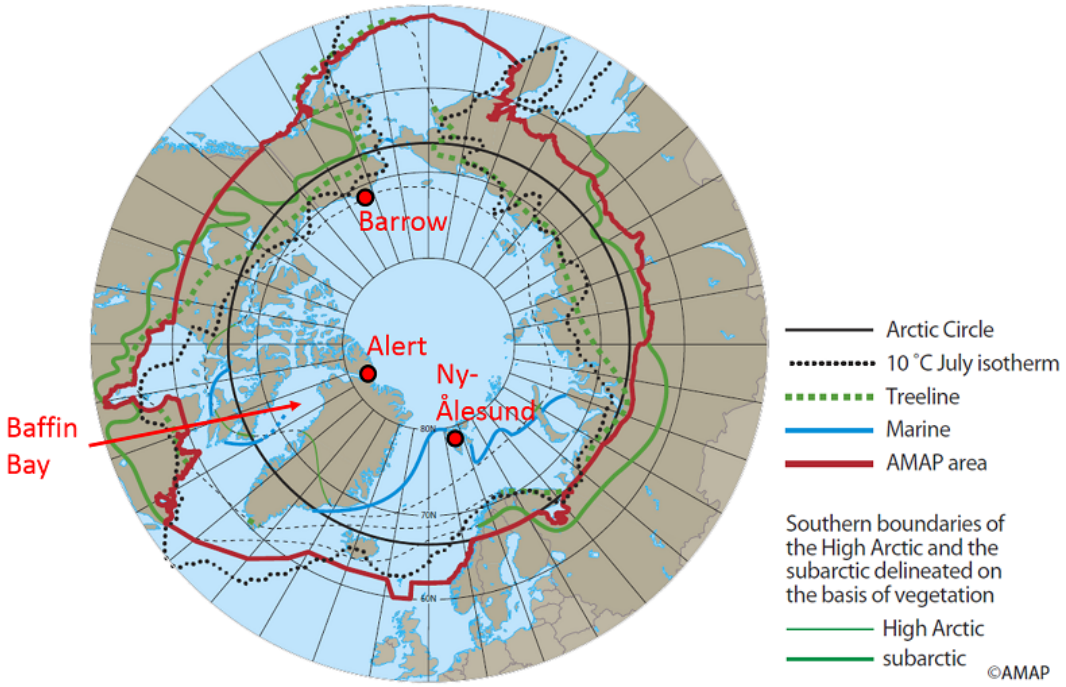

Figure 2.1.: A polar projection map of the Arctic, indicating locations which are referenced or studied within this work. Also shown are the different boundaries that are commonly taken to define the Arctic's limits. Map adapted from AMAP (2009).

presence of sea ice and polar air masses and their transport, which can occur even to mid-latitudes.

Geographically, the two polar regions are more or less opposites of each other. The Arctic is an ocean surrounded by continental land masses, whereas Antarctica is a continent surrounded by ocean. One result of this, are the different temperatures in both regions. In the Arctic, air temperatures are moderated by the warm, underlying ocean, which prevents the air from reaching the extremely cold temperatures of inland Antarctica, where the surrounding Antarctic Circumpolar Current (ACC) shields the continent from warmer waters, and enables the extremely low temperatures below -50 °C.

The continental interior of Antarctica receives extremely little precipitation, making it the driest continent on earth. This is however not the case for the sea ice zone around the continent, where more precipitation occurs. In the Arctic, precipitation is highly variable depending on the location, but generally drier in the Arctic Basin than in areas south of it.

While there are continental land masses in either hemisphere around the pole, apart from a few weeks in summer in certain parts of the Arctic and the Antarctic peninsula, the landscape and the surface exposed to the atmosphere is dominated by water in its many forms and their interplay. Those comprise the ocean, snow, sea ice, shelf ice, glaciers, icebergs, melt ponds, salt lakes just to name a few.

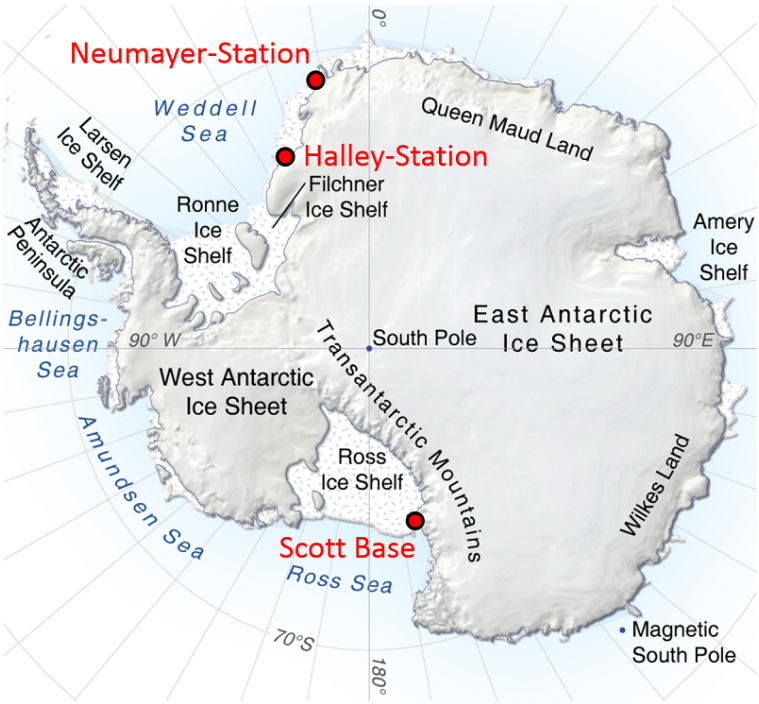

Figure 2.2.: A polar projection map of the Antarctic, indicating locations which are referenced or studied within this work. Map adapted from Hugo Ahlenius (UNEP/GRID-Arendal, `http://www.grida.no/graphicslib/detail/antarctica-topographic-map_8716`).

Due to their distance from the equator, both places experience a strong annual variation in insolation, with the phenomena of polar day, when the sun is always above the horizon, and its opposite, the polar night. This is an important aspect, in the following, for the chemistry described in this chapter, which, as will be seen, is strongly dependent on photolytic reactions. Yet, this phenomenon is also important for the remote-sensing methods described in chapter 3, as some of those are based on the analysis of atmospherically scattered sunlight, and therefore only work during daylight hours.

2.2 Polar sea ice

Sea ice is linked in several ways to the polar reactive halogen chemistry, therefore a brief overview of the most relevant properties is given below. Sea ice can be described as "a substrate, which after the initial freezing of sea water is profoundly modified by the interaction of physical, chemical and biological processes. Sea ice becomes a heterogeneous, semi-solid matrix in its simplest form resembling a sponge" (Thomas and Dieckmann, 2009). Generally one can discriminate between *first-year* or annual sea ice (FYI) and *multi-year* sea ice

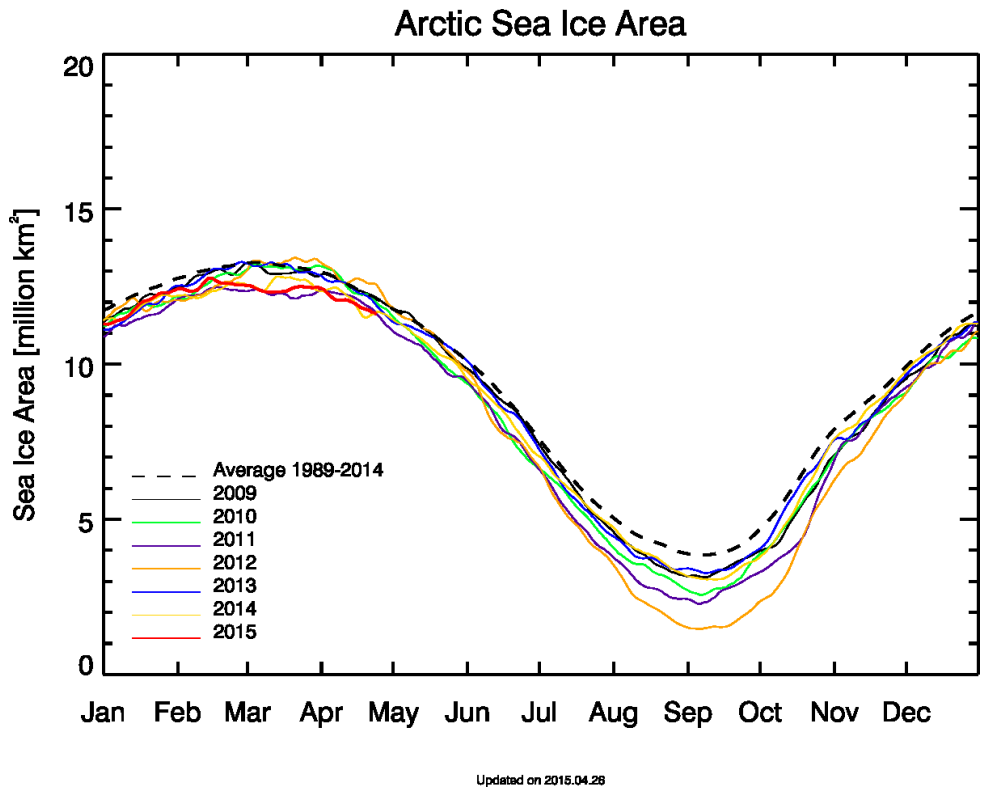

(a)

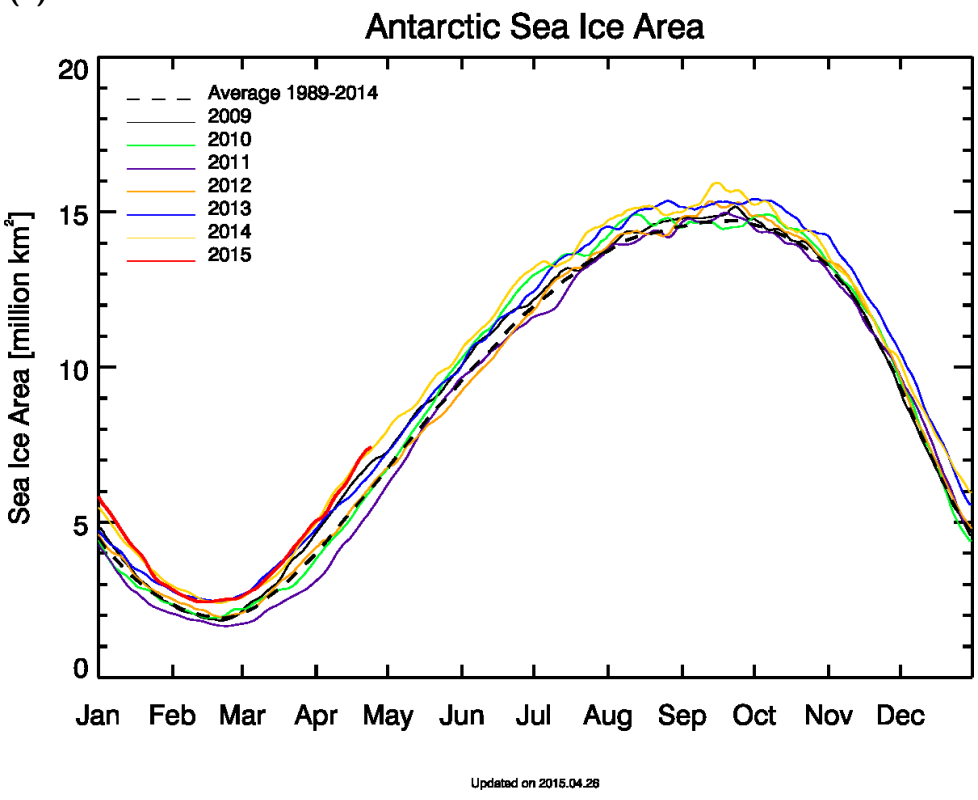

(b)

Figure 2.3.: The sea ice covered area in **(a)** the Arctic, and **(b)** the Antarctic, as seen by the Advanced Microwave Scanning Radiometer 2 (AMSR2) instrument aboard the GCOM-W satellite. Whereas the Arctic winter extent has been rather constant, the area covered during summer has decreased in the last few years. In contrast, in the Antarctic, the extent of the sea ice coverage has been relatively stable during the last years. Images provided by `http://www.iup.uni-bremen.de:8084/amsr2`.

(a) **(b)**

Figure 2.4.: **(a)** An example of first-year sea ice in the Weddell Sea (Antarctic). The ice is flat, without any rafting, and saltier than older ice. **(b)** Multi-year sea ice off the coast of Alert (Arctic). Due to the long-term effects of rafting, it is less even and has a lot of rubble on its surface.

(MYI). First-year ice is saltier and has a higher fraction of brine, multi-year ice is depleted in salts and brine and therefore denser, but can also contains larger air pockets. One can further differentiate between landfast ice, which is attached to land masses, and pack ice, which is drifting in the ocean.

The spatial extent of sea ice is oscillating annually, and lags approximately two months behind the solar irradiance (see fig. 2.3a and fig. 2.3b). In winter (boreal or austral), sea ice covers up to 7% of the Earth's surface (Thomas and Dieckmann, 2009), clearly indicating its global significance. Whereas in the Arctic the sea ice extent has been decreasing dramatically in the last few years with projections indicating an ice free summer during the next 30 years (fig. 2.3a, also Laxon et al., 2013; Overland and Wang, 2013), the situation is wholly different in Antarctica, where the extent has been highly stable.

Sea ice is commonly covered with snow. The mean snow depth is 0.2 m in both hemispheres. Spatially however, snow depth tends to be quite heterogeneous. In-between snow and ice, there is often a slush layer, due to seawater influx from underneath through so-called brine channels. The pH of the natural brine inside the sea ice has been measured to be in the range from 7.8 to 9.9 (Thomas and Dieckmann, 2009).

In terms of the characteristics of sea ice, there are several differences between North and South. While the absolute extent is similar in both regions, the ice is on average a lot thicker in the Arctic, with ca. 1.5 m compared to ca. 0.5 m in th Antarctic. In the Arctic, a large part of the ice is multi-year ice, in contrast the amount of multi-year ice in the Antarctic is marginal due to strong currents, ripping ice apart and transporting it to lower latitudes, where it melts. In the Antarctic, the ice's salinity is higher, where sea ice floes are also commonly flooded by sea water. This phenomenon is comparatively rare in the Arctic (Thomas and Dieckmann, 2009, and references therein).

Albedo

The albedo of the sea ice surface is important, for one, because it acts as a positive feedback loop on the melt process of the ice. The more melt ponds appear on the surface, the lower the albedo and therefore more radiation is absorbed. This is a major driver of the melting process in the Arctic. Additionally, the albedo is important for this work, as it alters the radiative transport in the atmosphere, critical for the inverse modeling of remote sensing observations. Figure 2.5, reproduced from Perovich (1998), gives values of the wavelength-averaged albedo for different states of the sea ice and snow surface. Depending on the state and inner structure of the ice and its overlying snow layer the albedo can vary considerably. It further varies considerably for different wavelengths.

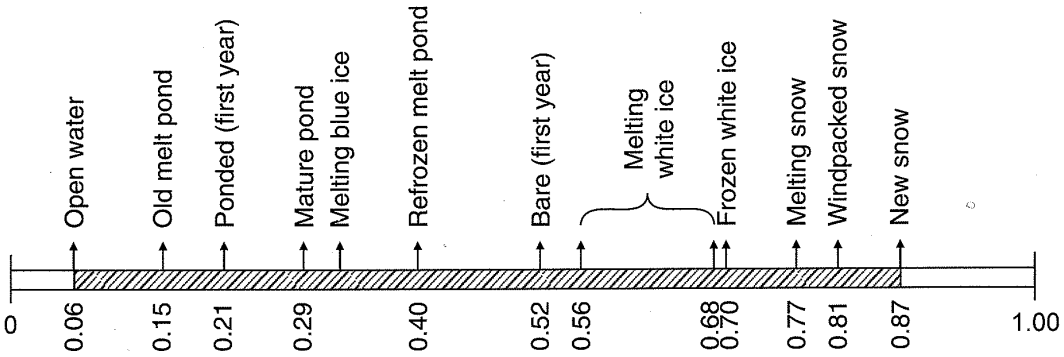

Figure 2.5.: The wavelength-averaged albedo for various surface states of sea ice and snow. Depending on the inner structure and degree of weathering of snow and ice, values can vary considerably. Reproduced from Perovich (1998).

Algae

Algae are known to be able to release iodine into the atmosphere and therefore of interest here, as will be detailed later in section 2.5.3. The bottom of sea ice is a habitat for ice algae. During the polar day, the lowermost few centimeters of the ice are often populated with ice algae, where they receive both sunlight from above as well as nutrients from below. On flooded ice, algae also grow on top in the slush layer between ice and snow. In mid-latitude coastal settings, algae were observed to be able to emit reactive iodine into the atmosphere when under stress, due to e.g. exposure to direct sunlight or air (e.g. Dixneuf et al., 2009). This is one reason why ice algae have been considered as a possible source for iodine in the Antarctic atmosphere. It was also shown that they can emit significant amounts of halocarbons (Sturges et al., 1992).

2.3 Peculiarities of the lower polar atmosphere

Compared to mid-latitudes, the polar atmosphere features several peculiarities. The polar atmosphere is characterized by low amounts of volatile organic compounds (VOCs) and very low aerosol loads, and therefore a low number of cloud condensation nuclei (CCN), due to the general lack of vegetation and pollution. An exception to this are episodes of *Arctic Haze*, in which pollutants from North America and Eurasia, stemming e.g. from industrial emissions or forest fires, are transported to the Arctic. They remain there for extended periods of time during winter and spring, due to the slow removal in the dark, cold and stable environment. In contrast, this does not happen in Antarctica due to the lack of local pollution sources in the region (Shaw, 1995). Penguins, however, can contribute to significant amounts of VOCs on a local scale. Such VOCs are formic and acetic acid, ammonia, acetaldehyde, acetone and also formaldehyde (Legrand et al., 2012).

2.4 Vertical structure of the polar troposphere

The troposphere is typically subdivided into two entities, the *planetary boundary layer* (PBL), i.e. the part that is directly in contact with the surface, and the *free troposphere* (FT) above, which is not. Stull (1988) defines the boundary layer as "that part of the atmosphere that is directly influenced by the presence of the earth's surface, and responds to surface forcing with a time scale of an hour or less". This direct influence is due to turbulent mixing caused by convection, wind and surface roughness, and the potential temperature profile.

The PBL can broadly be distinguished as being either stable, or convective. The polar boundary layer is often characterized by strong temperature inversions, which lead to a very stable stratification. This happens because of efficient radiative cooling of the ground, and thus of the air directly above the surface, due to a high albedo, the lack of insulation and a large long-wave emissivity.

The vertical extent of the PBL is typically several hundred meters in polar areas, but can be as low as a few tens or meters or as high as over 1 km. For the chemistry of trace gases released into the boundary layer, the PBL height can be an important aspect, as it determines the reaction volume available and changes of its height can lead to changes in concentrations. This is important in the nonlinear processes described later, such as the ozone destruction by bromine radicals (in section 2.5.2). Often, the boundary layer height is deduced from the potential temperature profile, because temperature gradients are comparatively easy to measure. This is a good proxy for mixing in mid-latitudes where insolation has a strong diurnal variation, in polar areas those variations may at times be comparatively small compared to katabatic forcings or the convection over polynyas (Anderson and Neff, 2008).

2.5 Polar tropospheric ozone, reactive halogens and their (photo-)chemistry

A unique feature of the polar atmosphere is the strong natural activity of halogen chemistry, which starts every year in polar spring with the first few rays of sunlight. Contrary to other climate zones, the polar environment is not only conducive to source halogen compounds from the ocean, transport them towards the surface and into the atmosphere, then activate them to become highly reactive radicals, but it also facilitates their regeneration, while not having strong enough sink mechanisms to suppress this.

Since the 1980s, when the effects and the significance became clear, a lot of follow-up research has been conducted on these processes - field measurements, laboratory and chamber experiments, satellite observations as well as chemical and meteorological modeling. As a result, several extensive review publications exist such as Barrie and Platt (1997), Platt and Hönninger (2003), Simpson et al. (2007b), Abbatt et al. (2012), Saiz-Lopez and von Glasow (2012), and most recently, Simpson et al. (2015). In this section the processes and observations most relevant to this work will be introduced.

2.5.1 Ozone

In the troposphere, ozone (O_3) is a short lived trace gas, which is produced by precursor gases and sunlight. It is globally prevalent at mixing ratios of ~30 ppb in the undisturbed southern hemisphere, and ~40 ppb in the northern hemisphere. Ozone acts as an important greenhouse gas, and while shielding the terrestrial surface from energetic UV radiation in the stratosphere, at the surface, it can also negatively affect human health and vegetation at higher concentrations (IPCC, 2013).

In the early 1980s, people first started to notice a strong ozone variability during spring in the Arctic at Barrow (Oltmans, 1981; Oltmans and Komhyr, 1986) and at Alert (Bottenheim et al., 1986; Barrie et al., 1988). It was found that in polar regions, with the end of the winter darkness, and more and more incident solar radiation, there were periods in which ozone in the boundary layer could become practically completely depleted (< 1 ppbv). These periods are therefore called *Ozone Depletion Events* (ODEs, Oltmans et al., 1989) if ozone is completely depleted, otherwise partial ODEs if ozone destruction is incomplete. The occurrence of ODEs was found to be primarily over the frozen ocean. They can last several days and be spread over large areas (Jones et al., 2013). During those events, when amounts of ozone are low and, as was also found, levels of reactive halogen oxides are elevated, those latter compounds become the major oxidants in the atmosphere. They have a different reactivity compared to the hydroxyl radical (OH) and ozone, and therefore different effects on several substances.

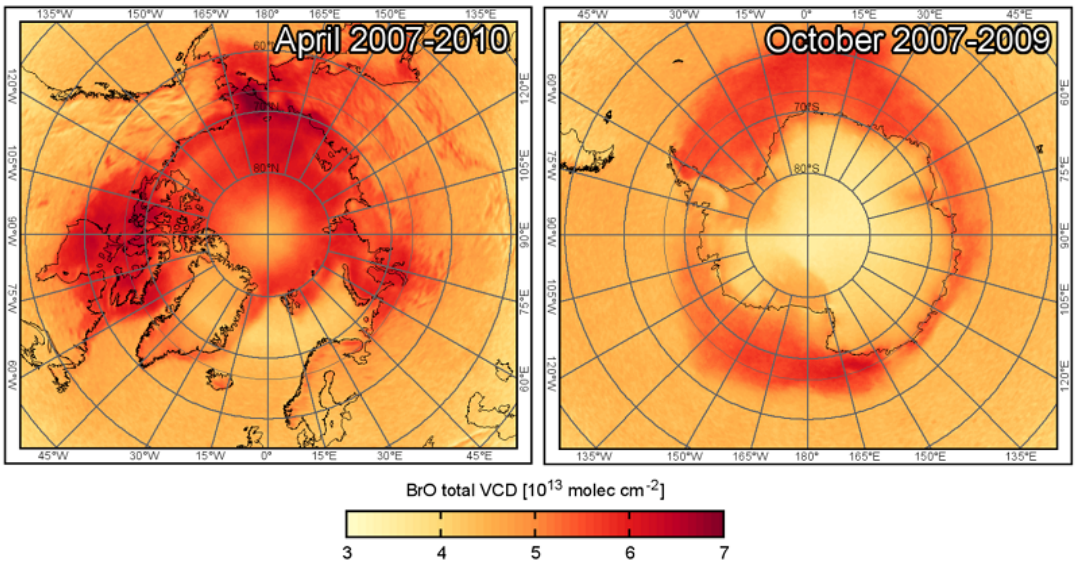

Figure 2.6.: The monthly means of the total BrO vertical column density in April over the Arctic (left) and in October over the Antarctic (right). In the Antartic, the bromine activation is closely correlated with the extent of the sea ice. In the Arctic, the Canadian archipelago shows a strong activation. Graphs adapted from Sihler (2012).

2.5.2 Bromine

Bromine has early on been implicated in these ODEs, due to observations of a concurrent excess of filterable bromine (Berg et al., 1983; Sturges, 1990) and observations of an anti-correlation between this filterable bromine and ozone levels (Barrie et al., 1988). Then, bromine monoxide (BrO) was identified to play a central role in these events by LP-DOAS measurements (Hausmann and Platt, 1994; Tuckermann et al., 1997). Later on, BrO was also identified in satellite data, giving a more precise idea of the large areas affected by this phenomenon, and also implicating a relationship with sea ice (Wagner and Platt, 1998; Schönhardt et al., 2008; Pöhler et al., 2010; Schönhardt et al., 2012; Sihler, 2012). An example of those maps is shown in fig. 2.6. Surface concentrations of BrO typically range from values around zero to maxima around 45 pptv during ODEs (Simpson et al., 2007b; Pöhler et al., 2010; Liao et al., 2011). Lower levels, up to 5 pptv, of BrO have even been observed on the middle of the Greenland ice cap, at Summit (Stutz et al., 2011). The majority of reactive bromine however is thought to be active close to the ground (Zeng et al., 2003), but layers of bromine higher up in the troposphere (so called *elevated layers*) have also been found (Hönninger et al., 2004b; Wagner et al., 2007; Friess et al., 2011). Furthermore, BrO has been observed in the free troposphere, assumed to be lifted to this altitude by large open leads in the sea ice and the ensuing strong convection, which is due to the large temperature difference between sea water and the surrounding atmosphere (McElroy et al., 1999). While fundamentally a strictly polar phenomenon on this scale, the transport of bromine from the Arctic to

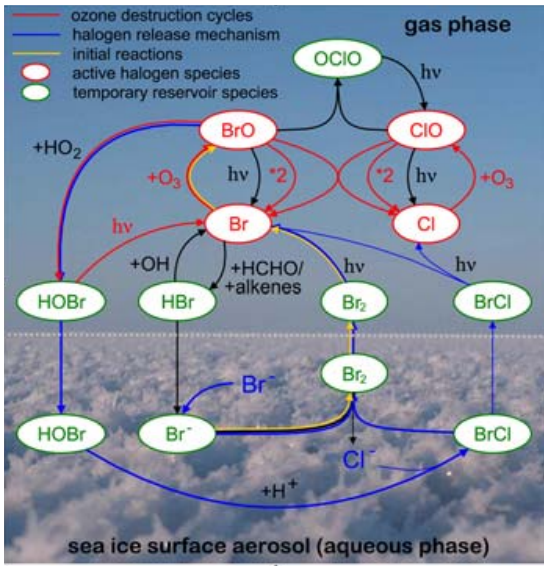

Figure 2.7.: Schematic of the reactions involved in the bromine explosion mechanism as well as inter-halogen reactions between bromine and chlorine. A detailed description is given in the text. Figure adapted from Pöhler et al. (2010).

lower latitudes, so called *spill outs*, to places as far south as the Azores islands have also been observed (Hollwedel et al., 2004; Watanabe et al., 2005; Lampel, 2014).

Of the three halogens of interest in this work, bromine is the one most researched and best understood so far (Simpson et al., 2007b). The reaction mechanism involving bromine, which leads to ozone loss is rather well understood and described below.

Reaction mechanism: Ozone destruction by bromine explosion

In the gas phase, Br can react with ozone to form BrO (Rattigan et al., 1995)

$$\mathrm{Br} + \mathrm{O_3} \longrightarrow \mathrm{BrO} + \mathrm{O_2} \tag{R1}$$

which can be quickly reversed by photolysis

$$\mathrm{BrO} \xrightarrow{h\nu} \mathrm{Br} + \mathrm{O} \tag{R2}$$

$$\mathrm{O} + \mathrm{O_2} \longrightarrow \mathrm{O_3} \tag{R3}$$

with the oxygen atom reacting back to ozone with molecular oxygen. Due to this photolysis, individual BrO molecules have a lifetime on the order of 2 minutes around noon in polar spring, but around 99% immediately get recycled back to BrO by R1 (Simpson et al., 2007b). Therefore this is a null cycle in terms of

ozone destruction. BrO can however also react with other BrO molecules:

$$\begin{aligned} \mathrm{BrO + BrO} &\longrightarrow \mathrm{2\,Br + O_2} && (85\%) && \text{(R4)} \\ &\longrightarrow \mathrm{Br_2 + O_2} && (15\%) && \text{(R5)} \\ &\longrightarrow \mathrm{OBrO + Br} && (?\%) && \text{(R6)} \end{aligned}$$

in effect destroying ozone. The branch R4 is approx. 5.6 times more likely than the branch R5 (Atkinson et al., 2007), whereas the last branch seems possible but negligible (Butkovskaya et al., 1983; Papayannis et al., 1999). The BrO self-reaction is comparatively slow, cross reactions, such as BrO + ClO and BrO + IO are an order of magnitude faster (refer to tab. 2.1, Solomon et al., 1994; Le Bras and Platt, 1995). BrO can also react with HO_2:

$$\mathrm{BrO + HO_2 \longrightarrow HOBr + O_2} \qquad \text{(R7)}$$

The formation of HOBr is important, as it leads to the release and activation of dissolved bromide into the gas phase, which is possible in an acidic environment (Ammann et al., 2013) via:

$$\mathrm{HOBr_{(g)} + Br^-_{(l)} + H^+_{(l)} \xrightarrow{multiphase} Br_{2(g)} + H_2O_{(l)}} \qquad \text{(R8)}$$

During the daytime Br_2 is photolysed rapidly to form Br, which can start the cycle again, with the amount of gas phase Br/BrO getting (nearly) doubled after each iteration.

This cycle can also been written summarily as:

$$\mathrm{BrO_{(g)} + HOBr_{(g)} + Br^-_{(l)} + H^+_{(l)} + HO_{2(g)} + 2\,O_{3(g)} \longrightarrow 2\,BrO_{(g)} + H_2O_{(l)} + 3\,O_{2(g)}} \qquad \text{(R9)}$$

Due to this doubling of reactive bromine in the gas phase with each cycle, and thus the exponential increase of gas phase bromine, the reaction mechanism has been dubbed the *bromine explosion* (Platt and Janssen, 1995; Platt and Lehrer, 1997; Wennberg, 1999). It is illustrated schematically in figure 2.7. The bromine explosion has since been found to occur also over salt lakes, such as the Dead Sea (Hebestreit et al., 1999) or Salar de Uyuni (Hönninger et al., 2004a), and in degassing plumes of volcanoes worldwide (Bobrowski et al., 2003).

Figure 2.8.: Frost flowers in Alert, Nunavut, Canada. They usually grow in cold, calm conditions on fresh, thin sea ice and have high salinities, but, sometimes as seen here, also on refreezing melt ponds.

Higher bromine oxides

For bromine, the creation of higher oxides such as OBrO (R6), through oxidation of BrO by ozone

$$\mathrm{BrO} + \mathrm{O_3} \longrightarrow \mathrm{OBrO} + \mathrm{O_2} \tag{R10}$$

is unimportant, according to Chipperfield et al. (1998). During daylight, OBrO is thought to be rapidly photolysed back to BrO (Vetter, 2008) resulting in a null cycle for ozone destruction. Importantly, it has not been been detected in the troposphere so far, and it is unclear whether OBrO has ever been identified in the stratosphere (Renard et al., 1998; Erle et al., 2000).

Prerequisites for bromine activation

For the above described reaction mechanism to take place, several prerequisites have to be met, which will be mentioned in the following.

Obviously **bromide** is needed, which is ultimately sourced from the ocean. The idea is that, through the freezing process of sea water, the remaining liquid brine is enriched in halide concentrations through fractionation processes (Koop et al., 2000). The salts contained therein, either through upward migration, or the transport of frost flower particles, then get transported onto snow. Another possibility would be the transport of salts onto the surface via sea spray (Domine et al., 2004). Biogenic halocarbons, which are known to be present in sea ice and frost flowers (Granfors et al., 2013), are not thought to be a sufficiently strong source of bromine to explain the observed reactive bromine levels during ODEs (Simpson et al., 2007b).

Some sort of **reaction surface** is necessary as well to support the involved heterogeneous reactions. Possible surfaces for those reactions, the recycling and the release, are sea ice, surface snow, blowing snow, frost flowers or aerosols.

For the release of bromine by reaction R8, an **acidic environment** is necessary, as the reaction exhibits a strong pH dependence and consumes protons (Fickert et al., 1999; Sander et al., 2006). Sea water, with a buffered pH around 8, is already alkaline enough to stop the reaction, brine in sea ice is even more alkaline. For surfaces exposed to the cold air, the freezing process can be conducive to create an acidic environment. At sufficiently low temperature calcium carbonate is precipitated, and carbonate and bicarbonate are responsible for the buffering capacity of the involved surfaces (Koop et al., 2000; Sander et al., 2006; Morin et al., 2008; Hara et al., 2012). Frost flowers, pictured in fig. 2.8, are not thought to be as important anymore as was assumed previously due to their high salinity (Kalnajs and Avallone, 2006; Simpson et al., 2005, 2007a; Piot and von Glasow, 2008). They may serve as a source for bromine, as they are fragile and easily blown away by wind, but due to their alkaline bulk pH, their importance in activation processes is discounted (Kalnajs and Avallone, 2006). Instead, **surface snow** is given a more important role nowadays (Yang et al., 2010; Pratt et al., 2013). As reaction surface it is exposed to the cold air, well shielded from the warm and basic ocean, has a large surface area and little bulk. Indeed, in chamber and field studies, under the right conditions, snow surfaces have been shown to be able to release reactive bromine into the air (Foster et al., 2001; Spicer et al., 2002; Pratt et al., 2013). Once released, it can then be spread and mixed into the atmosphere. One possible mechanism for that would be wind pumping or snow drift (Yang et al., 2010).

Ozone is obviously necessary as well, for the constant recycling of photolytically lost BrO (R1, e.g. Rattigan et al., 1995; Fleischmann et al., 2004). If ozone levels are completely diminished, the bromine explosion stops.

Sea ice was, as mentioned above, already early on suspected to play an important role. Currently, it appears that it is crucial that air masses have had contact with first-year sea ice, and multi-year sea ice seems to be not sufficient (Wagner et al., 2001; Friess et al., 2004; Simpson et al., 2007a).

The **molecular ratio of bromide to chloride** at the source surface has also been implicated in attempts to explain the bromine explosion. The causality, though, between the bromine activation and the molecular ratio is unclear. It can probably be both, a prerequisite, as well as an indication that some bromine release has occurred. A molecular ratio comparable or higher than that of sea salt aerosol ($\approx 1:600\,mol/mol$, Simpson et al., 2005) appears to be necessary in order to start the bromine explosion (Adams et al., 2002; Pratt et al., 2013). Bromide-to-sodium ratios, enhanced compared to sea water, were detected in frost flowers, in field studies by Simpson et al. (2005), but also in snow samples, where the ratios were found to be enhanced by over an order of magnitude. After ODEs, measured Br/Cl ratios were lower than sea salt aerosol values, which is seen as a sign that the surface has been depleted in bromide (Simpson et al., 2005).

Most depletion events happen close to the surface, which speaks against a major role of **aerosols** as the primary source (Zeng et al., 2003), although lifted

layers of reactive halogens have also been observed (Hönninger et al., 2004b; Wagner et al., 2007; Friess et al., 2011). A certain amount of aerosol particles seems to be necessary, though, in any case for two reasons. Firstly, the reaction mechanism above relies on fast multiphase reactions to drive and sustain the necessary gas phase amounts of bromine, e.g. by reaction R8. To facilitate those reactions, some sort of reaction surface is necessary. In order to sustain bromine activity over several hours, aerosol surfaces appear to be necessary in order to recycle BrO (Fan and Jacob, 1992). They are also found to be bromine enriched during events (Lehrer et al., 1997). The second reason is the aerosol's function as a transportation vehicle for bromine atoms from sea spray, wind blown frost flowers, as well as drifting and blowing snow. Especially to explain the observations of BrO higher up in the boundary layer, and in the free troposphere, aerosols are necessary as reaction surfaces.

Another requirement, established from field observations, seem to be **low temperatures**, preferably below -20 °C (Tarasick and Bottenheim, 2002; Pöhler et al., 2010). While similar bromine chemistry has been observed at warm, tropical, and even hot temperatures, at volcanoes and salt lakes, in polar areas, maximum BrO mixing ratios are highly correlated to low air temperatures. This might be due to a multitude of temperature dependent processes, such as the above mentioned fractionation and salt precipitation from brine and surfaces, or the formation of new sea ice.

Besides cold temperatures, other meteorological parameters seem to be critical as well. **Stable conditions** such as a stable boundary layer, characterized by low wind speeds and clear sky conditions seem to be favored, which create a sort of sealed reaction chamber (Wagner et al., 2001; Friess et al., 2004; Jones et al., 2006; Jacobi et al., 2010; Peterson et al., 2015). Those conditions are rather common in polar regions (Anderson and Neff, 2008). Nonetheless, depletion events have also been observed during storms with blowing snow (Friess et al., 2011).

Finally, even if all of the above mentioned requirements are met, there can still be periods without indications for ODEs or bromine explosion events. Therefore, it appears that some sort of **trigger** is necessary to ignite the reaction cycle. What constitutes a possible trigger, however, remains unclear. It is speculated that a certain amount of **seed BrO**, e.g. from photolytically decomposed halocarbons, could be such a trigger (Simpson et al., 2007b).

The end of activation episodes

The end of ODEs is not very well understood so far. Meteorology, especially strong vertical atmospheric mixing, such as the passing of fronts has been associated with the ending of ODEs. The reason is that this leads to the mixing of the depleted air with O_3 rich air to recover ozone levels, as chemical ozone production is generally not quick enough due to the low NO_x levels (Lehrer et al., 2004; Simpson et al., 2007b). Bromine deposited onto the snow can however be rapidly re-released into the atmosphere (Pratt et al., 2013). Therefore it is necessary to be deposited into deeper snow layers or the open (unfrozen) ocean to be removed for longer periods.

Interaction with NO_x chemistry

The interplay between halogen and NO_x chemistry is not fully understood yet. On the one hand, NO_2 can act as a sink for halogen oxides, e.g. by forming bromine nitrate

$$BrO + NO_2 \longrightarrow BrONO_2 \tag{R11}$$

because $BrONO_2$ is comparatively stable, and can subsequentially be taken up by surfaces. On the other hand, NO_x can also drive the bromine explosion by (e.g. Cao et al., 2014)

$$BrONO_2 + H_2O \longrightarrow HOBr + HNO_3 \tag{R12}$$

Also, higher NO_x levels could lead to a more acidified reaction surface, and therefore accelerate the bromine chemistry (e.g. Pratt et al., 2013; Custard et al., 2015). It is furthermore known, that the interstitial air in the snow pack is photochemically highly active (Grannas et al., 2007) and illuminated by the sun, NO_x is emitted from the snow pack (Honrath et al., 1999).

Enhancement of Mercury deposition

The current levels of mercury in the Arctic are mainly due to its long range transport from industrial sites at lower latitudes (predominantly coal burning) via the atmosphere, rivers and also via the ocean. This long range transport is possible due to the long residence time of Gaseous Elemental Mercury (GEM) of around 1 year, leading to practically homogeneous concentrations throughout the hemispheres, with slightly higher levels in the northern hemisphere (Schroeder and Munthe, 1998). Eventually, mercury gets oxidized, leading to residence half-lifes of less than 1 day (Lindberg et al., 2007), due to subsequent deposition. Once on the surface, it can be incorporated into biota and accumulate through the food chain, especially in fish, which are prone to this. This is the reason, why a large number of Inuit people, due to their traditional, fish-based diet, have blood mercury levels significantly above guidelines from the World Health Organization (WHO).

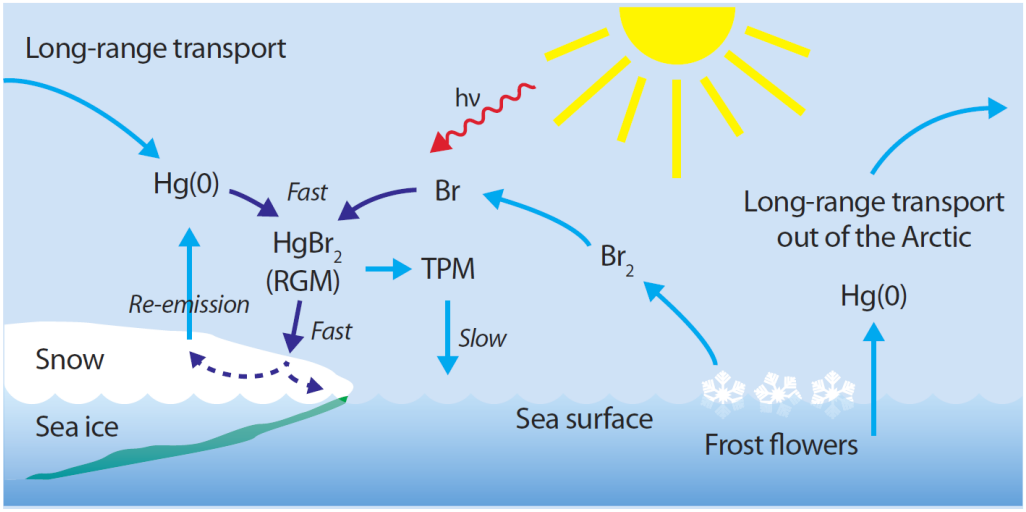

Figure 2.9.: Sketch of the assumed reason of the enhanced mercury deposition in polar regions: Elemental mercury, Hg(0) is brought into the region by long-range transport from mid-latitude industrial sites. Bromine atoms, stemming from the sea ice, then react with Hg(0) to form $HgBr_2$, a species of Reactive Gaseous Mercury (RGM), which in contrast to Hg(0) is easily and rapidly deposited onto snow and ice. Graph reproduced from AMAP (2011).

The relevance to this work is that the mercury cycle is connected to the halogens, because bromine compounds have an effect on the deposition of mercury. Bromine radicals can react with GEM to form $HgBr_2$ via several possible intermediate steps, which is a form of Reactive Gaseous Mercury (RGM):

$$\mathrm{Hg} + 2\,\mathrm{Br} \longrightarrow \mathrm{HgBr_2} \qquad \text{(R13)}$$

RGM is a lot more reactive and lends itself to wet and dry deposition onto land masses and the ocean. If sufficient bromine is available, it leads to so-called *Atmospheric Mercury Depletion Events* (AMDEs), in which the air can be completely depleted of GEM, which is deposited onto snow and ice surfaces (Schroeder et al., 1998; Lu et al., 2001; AMAP, 2011, and references therein). Iodine could also play a similar role to bromine if present at sufficiently high concentrations. The reaction of chlorine with mercury is thought to be too slow to be relevant at atmospheric concentrations (Skov et al., 2004).

Altered oxidation of dimethyl sulfide

Dimethyl sulfide (DMS) is naturally emitted by planktonic algae in the ocean. Typical concentrations of DMS in the Arctic troposphere are up to 300 ppt during the algae summer bloom, but only a few ppt during the dark winter months (Park et al., 2013). The oxidation of DMS in the atmosphere leads to sulphate aerosol formation. It is the most important source of cloud condensation nuclei (CCN) over the ocean. As the amount of CCNs available has an effect on cloud albedo, it was proposed that this forms a biological regulation (negative feedback loop) of climate via the reduction of incident radiation and thus a reduction in DMS production (Charlson et al., 1987).

The fate of DMS in the atmosphere, however, can be twofold. At higher ambient temperatures, or by the reaction with NO_3 radicals, DMS, via several multi-stage reaction pathways mostly ends up as SO_2. SO_2 is indeed a precursor for new particle formation. If, however, halogen radicals such as BrO are present, a reaction pathway to form dimethyl sulfoxide (DMSO)

$$\mathrm{DMS} + \mathrm{BrO} \longrightarrow \mathrm{DMSO} + \mathrm{Br} \tag{R14}$$

is enabled. Br can then be recycled into BrO by reacting with ozone (reaction R1). This reaction is an important sink for DMS, but not for ozone, because ozone concentrations are typically a factor of 1000 larger than those of DMS (Nakano et al., 2001). If IO would be present at similar concentrations as BrO, its reaction with DMS could be equally important (Nakano et al., 2003). The reaction with of DMS with ClO though, is thought to be significantly slower (Barnes et al., 2006).

DMSO then reacts further, to form methylsulfinic acid (MSIA) and later methylsulfonic acid (MSA). Those compounds, MSIA and MSA, are more likely to be taken up by already existing aerosol, and are thus not available to produce new CCN which could whiten clouds and raise the albedo (von Glasow and Crutzen, 2004; Barnes et al., 2006).

2.5.3 Iodine

After bromine, iodine is the second best studied of the three halogen elements of interest in this work. This is because iodine monoxide (IO) destroys ozone more effectively than BrO on a per molecule basis. Due to its usually lower concentrations compared to BrO, the impact of IO alone is thought to be weaker. If both IO as well as BrO are present simultaneously however, the combined ozone destruction rate can be drastically enhanced compared to BrO alone (Solomon et al., 1994; Calvert and Lindberg, 2004; Mahajan et al., 2010). This is because inter-halogen reactions allow a quicker recycling of monoxides to the atomic form (Gilles et al., 1997). Estimates are, for example, that 1 pptv IO can enhance the ozone destruction rate through the cross reaction with BrO by

around 20% at BrO levels of 14 pptv (Sander et al., 1997).

Prevalence of reactive iodine in the Antarctic

In the boundary layer, IO has been found to be present in a variety of settings globally, including mid-latitude coastal areas (e.g. Alicke et al., 1999) and the tropical open ocean (e.g. Großmann et al., 2013). In polar regions, reactive iodine chemistry has been connected mainly with Antarctica and less with the Arctic in the past.

At Neumayer station in Antarctica, Friess et al. (2001) first detected IO in zenith-sky DOAS measurements, and concluded from radiative transfer calculations that the bulk of it is located in the troposphere. Saiz-Lopez et al. (2007) conducted LP-DOAS measurements at Halley Station and detected very high IO mixing ratios whenever the sun was higher than 92 ° with average values around 5 pptv in spring and a maximum of 20 pptv. The presence of IO over Antarctica was also observed from space. Schönhardt et al. (2008, 2012) mapped IO using the SCIAMACHY instrument. Their maps, one of which is reproduced in fig. 2.10, appear to show two "hot spot" regions, the Weddell Sea area and the Ross Sea area with their respective ice shelfs, but IO is also found inland over the continent. Later on, Friess et al. (2010) deduced from measurements of light scattered on the snow pack, that enormous mixing ratios of iodine must be present in the interstitial air pockets, on the order of several ppbv. Finally, Atkinson et al. (2012) conducted MAX-DOAS measurements on a cruise in the Weddell Sea in late summer and obtained vertical column densities (VCDs, explained later in section 3.4.4) between 1.5 and 3 $\cdot 10^{12}$ molec cm^{-2}, comparable

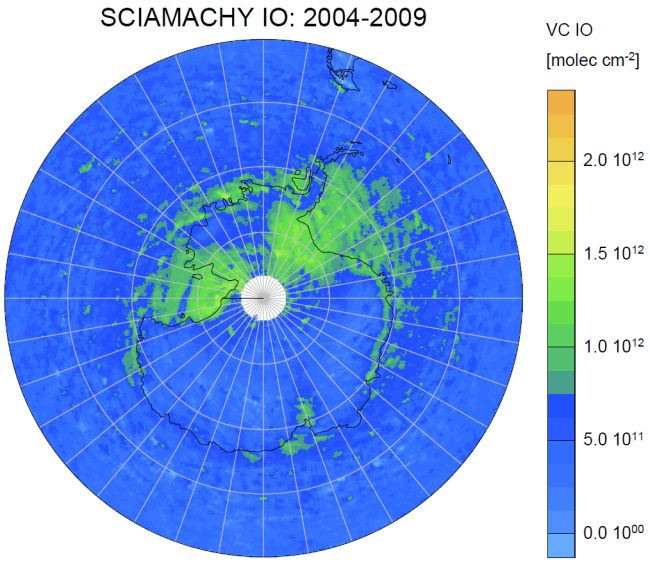

Figure 2.10.: Southern hemispheric IO data from the SCIAMACHY instrument averaged from 2004 to 2009 (Reproduced from Schönhardt et al., 2012). The two regions around the Weddell Sea and Ross Sea exhibit the highest vertical column densities.

to VCDs of satellite data, albeit on the high side.

Prevalence of reactive iodine in the Arctic

In the Arctic in comparison, far fewer measurements of IO have been undertaken so far. Sturges and Barrie (1988) and Barrie and Barrie (1990) determined total iodine content in aerosol at Alert at around 1 ng m^{-3} and annual maxima in spring and a smaller one in autumn. Tuckermann et al. (1997) conducted LP-DOAS measurements in Ny-Ålesund (Svalbard, 79 °N), during April and May in two consecutive years, but did not observe any IO with detection limits (DL) of 2.5 pptv (1995) and 0.9 pptv (1996). Wittrock et al. (2000) detected IO in the stratosphere at sub-pptv levels over Ny-Ålesund and found "some indications for tropospheric amounts of IO" in zenith-sky DOAS observations, but without conclusive evidence for tropospheric IO. Other LP-DOAS measurements on the sea ice in the Amundsen Gulf (Canada, 71 °N), undertaken by Pöhler et al. (2010) during March and early April did not reveal any IO at DLs between 0.3 pptv and 2.5 pptv. Studies by Mahajan et al. (2010) in the Canadian sub-Arctic however, found IO episodically on a local scale with mixing ratios of up to 3.4 pptv, attributed to the local emission of iodocarbons at open water polynyas.

Sources

It is known that biogenic iodocarbons such as CH_3I, CH_2I_2 and many more, are emitted from the ocean into the atmosphere and several have been found to be present in the polar atmosphere, even in areas far removed from the ocean (Reifenhäuser and Heumann, 1992; Heumann, 1993; Granfors et al., 2013). This is due to their long photolytic lifetimes, which typically range from days to weeks and allow their transport into areas distant from the source.

The main source of iodine in the marine environment, however, is currently thought to be due to the emission of molecular iodine (I_2) by inorganic processes (Carpenter et al., 2013; Lampel, 2014). I_2 photolyses rapidly, thereby initiating iodine radical chemistry. It is also known that certain types of algae can emit I_2, when placed under natural, but stressful conditions, e.g. exposure to air and sunlight (Dixneuf et al., 2009).

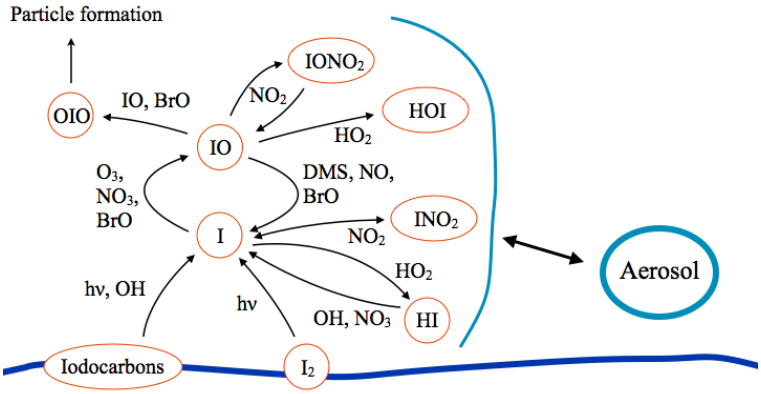

Figure 2.11.: A highly simplified scheme of the reactive iodine chemistry in the marine boundary layer.

Chemistry

In principle, iodine can undergo similar reaction cycles as bromine, but something alike the bromine explosion has not been observed yet. There are several possible reactions cycles though, which lead to ozone loss. At low IO concentrations, the dominant one is supposedly

$$\mathrm{IO} + \mathrm{HO_2} \longrightarrow \mathrm{HOI} + \mathrm{O_2} \tag{R15}$$

$$\mathrm{HOI} \xrightarrow{h\nu} \mathrm{I} + \mathrm{OH} \tag{R16}$$

$$\mathrm{I} + \mathrm{O_3} \longrightarrow \mathrm{IO} + \mathrm{O_2} \tag{R17}$$

as suggested by Chameides and Davis (1980).

At higher concentrations, the self-reaction dominates, which is fast compared to the ones of bromine, chlorine and also compared to inter-halogen reactions (refer to table 2.1, Harwood et al., 1997). For the self-reaction, four branches are possible:

$$\mathrm{IO} + \mathrm{IO} \longrightarrow \mathrm{OIO} + \mathrm{I} \quad (38\%) \tag{R18}$$

$$\longrightarrow \mathrm{I_2} + \mathrm{O_2} \tag{R19}$$

$$\longrightarrow 2\,\mathrm{I} + \mathrm{O_2} \tag{R20}$$

$$\longrightarrow \mathrm{IOIO} \tag{R21}$$

At least channels R19 and R20 can lead to catalytic ozone destruction. The other two depend on the products of the destruction of OIO. IOIO is unstable and presumed to quickly end up as I + OIO (Kaltsoyannis and Plane, 2008), though IO + IO seems to be viable as well. OIO can also be produced by the

cross-reaction with BrO:

$$\mathrm{IO + BrO \longrightarrow Products} \qquad (100\%) \qquad \text{(R22)}$$
$$\mathrm{\longrightarrow OIO + Br} \qquad (80\%) \qquad \text{(R23)}$$

During daytime, OIO is assumed to have a short photolytic lifetime of the order of seconds (ref. tab. 2.2), though this is not clearly established. The partitioning of the two product channels of the photolysis

$$\mathrm{OIO \xrightarrow{h\nu} I + O_2} \qquad \text{(R24)}$$
$$\mathrm{\xrightarrow{h\nu} IO + O(^3P)} \qquad \text{(R25)}$$

is still under debate and different publications indicate very different outcomes (Ingham et al., 2000; Ashworth et al., 2002; Tucceri et al., 2006; Saiz-Lopez et al., 2012). Depending on which channel is dominating or the relative percentage of its likelihood, the OIO producing channels of the IO self-reaction or the cross-reaction between IO and BrO, for example, either lead to ozone-destruction or not. If the I yielding channel would be the major one, the OIO formation through the IO self-reaction should be import as an ozone depleting cycle (Vogt et al., 1999).

OIO may also be playing a role in the formation of new particles due to polymerization via the possible intermediates I_2O_4 and I_2O_5 (O'Dowd and Hoffmann, 2005). The mechanisms involved, however, as well as the reaction rate coefficients, are still poorly understood (Saiz-Lopez et al., 2012).

Iodine in meteorites and rocks in Antarctica

A curious finding, backing the presence of iodine in the Antarctic atmosphere, is that meteorites discovered on the Antarctic ice sheet were found to show an overabundance of iodine compared to meteorites of the same class found elsewhere on Earth. This was assumed to be a consequence of local atmospheric contamination and weathering. Hence, normal rocks from Antarctica were analyzed as well, in which a decreasing iodine concentration with depth from the rock surface was found. In the course of those studies, the authors further analyzed Antarctic aerosol and snow samples and found iodine-to-chlorine ratios in snow up to 186 times higher than in sea water (Heumann et al., 1987). In a subsequent study Heumann et al. (1990) also found an iodine concentration gradient in Antarctic meteorites from high values at the surface to low values in the interior confirming the atmospheric weathering hypothesis. They attributed this phenomenon to the long range transport of methyl iodide, which has been detected both, at coastal sites as well as in the interior of the continent, its subsequent photolysis and finally reaction with the rock and meteorite surfaces (Reifenhäuser and Heumann, 1992; Rasmussen et al., 1982; Heumann, 1993).

2.5.4 Chlorine

Of the three halogens of interest, the role of chlorine is easily the least understood so far. One reason for this is that, in comparison to BrO and IO, the absorption cross section of chlorine monoxide (ClO) is deeper in the ultraviolet range where most of the sunlight is absorbed by the stratospheric ozone layer. Therefore, so far, it is not as easily accessible to passive scattered sunlight measurements from the ground or from space. Chlorine dioxide however, OClO, has absorption bands in the visible wavelength range and is therefore more easily accessible to spectroscopic measurements, but its speciation depends on certain circumstances (described below) and it rapidly photolyses during the daylight hours (ref. tab. 2.2). As a result, only very few studies have succeeded to directly measure reactive chlorine species in the polar troposphere (Saiz-Lopez and von Glasow, 2012). There are other indications for the involvement of chlorine, e.g. due to loss rates and loss patterns of hydrocarbons (Kieser et al., 1993; Jobson et al., 1994).

Currently, reactive chlorine is thought to be of minor importance in ozone loss in the troposphere, which is in contrast to the ozone destruction cycles in the stratosphere. There, it is of prime importance, where ozone losses are dominated by the ClO self-reaction, forming Cl_2O_2, as well as halogen cross-reactions (Yung et al., 1980; McElroy et al., 1999).

Prevalence of reactive chlorine in the polar troposphere

Tuckermann et al. (1997) conducted LP-DOAS observations in 1995 and 1996 in Ny-Ålesund (Svalbard) and found indications for chlorine. The individual ClO measurements were mostly below the DLs of 20 pptv (1995) and 9 pptv (1996). Averaging the results gave mean values only slightly under the DLs during ODEs. OClO was always under the DL of 1.3 pptv. Perner et al. (1999) determined ClO_x (Cl, ClO, OClO) mixing ratios in spring of less than 2 pptv by utilizing Chemical Amplification (CA). The presence of low levels of ClO_x was however also noticed in the absence of ODEs and BrO. Keil and Shepson (2006) studied the involvement of chlorine by measuring gas phase Br/Cl atom ratios in halogenated VOCs during partially ozone depleted conditions. Those ratios ranged from 80 to 990. Buys et al. (2013), using Chemical Ionization Mass Spectrometry (CIMS), determined nighttime BrCl mixing ratios in coastal Antarctica of up to 6 pptv, showing the involvement of chlorine in Antarctic tropospheric chemistry. Finally, Liao et al. (2014) observed Cl_2 levels of up to 400 pptv at Barrow in the Arctic. The maximum daytime amounts were proportional to ozone levels, indicating the need for both sunlight as well as ozone for the production of Cl_2. They estimated that at those amounts chlorine is overtaking OH as the major sink for atmospheric methane.

In a different setting, at the Great Salt Lake (USA), Stutz et al. (2002) measured ClO in conjunction with BrO by LP-DOAS. The observed ClO mixing

ratios ranged up to 15 pptv. This finding might apply in some form to polar regions, as the ultimate halogen source, sea salt, is likely to be similar. Also in a different setting, though in the marine environment, on the eastern coast of the USA, Spicer et al. (1998) observed dozens of pptv, up to 150 pptv, of Cl_2 during the night in air masses from the ocean.

Sources

The release processes of reactive chlorine are not completely understood so far. Chamber studies have shown that sea salt particles release Cl_2 into the gas phase under the presence of ozone and sunlight (Oum et al., 1998). The proposed mechanism for this release is the oxidation of Cl^- in the aqueous phase by OH, which, in turn, is produced by the photolysis of ozone, which leads to the chlorine equivalent of reaction R8 (Keene et al., 1993). Lately, in further chamber studies, a release under similar conditions has also been shown from artificial snow samples doped with NaCl (Wren et al., 2013).

Chemistry

A chlorine explosion, analogously to the bromine explosion, has not been observed under natural circumstances (in chamber studies though, Buxmann, 2012) and is thought to be hampered by several reasons. Probably the most important, is that the reaction of chlorine with hydrocarbons, especially the relatively abundant methane (≈1.8 ppmv, IPCC, 2013), is fast (ref. tab. 2.1):

$$\mathrm{Cl + RH \longrightarrow HCl + R} \tag{R26}$$

The likelihood of chlorine atoms to react with methane molecules is around 50% in the troposphere (Simpson et al., 2007b). Another reason is that several analogous reactions, e.g. as R8, are significantly slower for chlorine than for bromine, making it questionable whether efficient ozone depleting cycles only involving chlorine exist at all in the troposphere. Both the oxidation of ClO by ozone

$$\mathrm{ClO + O_3 \longrightarrow OClO + O_2} \tag{R27}$$

as well as the ClO self-reaction are slow (tab. 2.1, Birks et al., 1977; Wongdontri-Stuper et al., 1979). Photolysis of ClO is also only a minor sink for individual molecules (Langhoff et al., 1977).

In comparison, the cross-reaction with BrO with three possible reaction pathways

$$\begin{aligned} \mathrm{ClO + BrO} &\longrightarrow \mathrm{OClO + Br} \quad (49\%) && \text{(R28)} \\ &\longrightarrow \mathrm{ClOO + Br} \quad (44\%) && \text{(R29)} \\ &\longrightarrow \mathrm{BrCl + O_2} \quad (7\%) && \text{(R30)} \end{aligned}$$

is three orders of magnitudes faster at equal concentrations. R28 is the most probable branch, forming OClO (Sander and Friedl, 1989; Atkinson et al., 2007; Sander et al., 2011). The cross-reaction with IO is similarly fast at equal concentrations:

$$\begin{aligned} \mathrm{ClO + IO} &\longrightarrow \mathrm{OClO + I} && (55\%) && \text{(R31)} \\ &\longrightarrow \mathrm{Cl + I + O_2} && (25\%) && \text{(R32)} \\ &\longrightarrow \mathrm{ICl + O_2} && (20\%) && \text{(R33)} \end{aligned}$$

As OClO is realistically only formed by inter-halogen reactions, it can be taken as an indicator for inter-halogen chemistry, as illustrated in fig. 2.7. As mentioned above, OClO is spectroscopically easier to measure than ClO, and is thus used as a proxy for reactive chlorine chemistry (e.g. Sessler et al., 1995). On the other hand, OClO only has a lifetime of the order of seconds under daylight conditions (tab. 2.2).

In inter-halogen reactions, chlorine can act as a boost for the bromine-driven ozone depletion, through the opening of several ozone destroying reaction pathways in addition to the slower BrO self-reaction and R7. Furthermore chlorine chemistry can produce HO_2, which is necessary for the speciation of HOBr (R7), through the oxidation of methane and VOCs. Another role for chlorine involvement could be the activation of bromine chemistry via BrCl release from surfaces (Platt et al., 2004).

Reaction	**k (T=298K)** $[\frac{\mathbf{cm^3}}{\mathbf{molec\,s}}]$	**Reference**
IO + IO → Products	$9.9 \cdot 10^{-11}$	Atkinson et al. (2007)
IO + BrO → Products	$8.3 \cdot 10^{-11}$	Atkinson et al. (2007)
IO + ClO → Products	$1.2 \cdot 10^{-11}$	Atkinson et al. (2007)
BrO + ClO → Products	$1.15 \cdot 10^{-11}$	Turnipseed et al. (1991)
BrO + BrO → Products	$2.76 \cdot 10^{-12}$	Bedjanian et al. (1998)
ClO + ClO → Products	$1.64 \cdot 10^{-14}$	Nickolaisen et al. (1994)
$Cl + O_3 \rightarrow ClO + O_2$	$1.2 \cdot 10^{-11}$	Atkinson et al. (2007)
$Cl + CH_4 \rightarrow HCl + CH_3$	$1.07 \cdot 10^{-13}$	Bryukov et al. (2002)
$BrO + O_3 \rightarrow$ Products	$< 2 \cdot 10^{-17}$	Atkinson et al. (2007)
$ClO + O_3 \rightarrow$ Products	$< 1.6 \cdot 10^{-17}$	Atkinson et al. (2007)

Table 2.1.: Reaction rate coefficients k for selected reactions mentioned in the text. On top the reactions involving only the halogen monoxides are listed, ordered by their k value, below, other reactions of interest in this work are given.

Compound	**J** $[\mathbf{s^{-1}}]$	SZA [°]	**Reference**
I_2	0.15	0	Saiz-Lopez et al. (2004)
Br_2	0.034	0	Saiz-Lopez et al. (2004)
Cl_2	0.0022	0	Saiz-Lopez et al. (2004)
OClO	0.076	-	Birks et al. (1977)
OIO	0.4	≈16.5	Saiz-Lopez et al. (2012)

Table 2.2.: Photolysis frequencies J for several compounds of interest within this work. The solar zenith angle (SZA) for which the value was calculated is indicated as well as the literature reference. The dependency on the SZA is smaller for molecules absorbing in the visible wavelength range, e.g. I_2, compared to those that absorb in the ultraviolet, e.g. OClO.

3

Remote sensing and in-situ measurement methods

In order to observe and quantify the concentrations or mixing ratios of the above mentioned halogen compounds in the natural environment, a method is needed that fulfills several requirements. Due to the commonly very low mixing ratios in the parts per trillion (ppt) range, a high sensitivity is needed. Additionally, a high degree of specificity is needed to be able to distinguish between the multitude of different compounds involved, which are constituted by only a few select elements. Another important issue is the extremely high reactivity of some of the involved substances, posing significant problems when trying to pipe measurement air through any sort of tubing or if surfaces are involved in the measurement process.

Differential Optical Absorption Spectroscopy (DOAS) is utilized in this thesis, which is molecule/absorber-specific and contactless by principle and can have a high degree of sensitivity. In this chapter, starting with the fundamentals of absorption spectroscopy, the DOAS principle is introduced. Afterwards, the different methods utilizing DOAS which have been used in this work are described with their respective peculiarities. An exhaustive treatment of DOAS and its many applications can be found in Platt and Stutz (2008). Parts of this chapter are reproduced from Zielcke (2010).

3.1 Absorption spectroscopy

Absorption spectroscopy is the concept of determining the absorption of electromagnetic radiation caused by a test substance as a function of wavelength or frequency, and thereby gaining insight into the composition or volume of the test substance. All materials absorb in some part of the electromagnetic spectrum. So if light of a known spectral intensity traverses an absorber, the emerging spectral absorption structures can be used to specify and quantify the substances involved.

If light with an initial intensity $I_0(\lambda)$ passes i absorbers with absorption cross-sections $\sigma_i(\lambda, p, T)$, which are distributed over a length L with concentrations $c_i(l)$, the remaining intensity $I(\lambda)$ is given by the Beer-Lambert equation:

$$I(\lambda) = I_0(\lambda) \cdot \exp\left(-\int_0^L \sum_i (\sigma_i(\lambda, p, T) \cdot c_i(l))\, dl\right) \tag{3.1}$$

The absorption structures σ_i can depend on ambient pressure p and temperature T, which in the ultraviolet and visible wavelength range is only a small effect compared to the infrared region.

In optics, the negative exponent in equation 3.1 is called the optical density $\tau(\lambda)$:

$$\tau(\lambda) = -ln\left(\frac{I(\lambda)}{I_0(\lambda)}\right) \tag{3.2}$$

For atmospheric studies equation 3.1 is not directly applicable, as it doesn't account for scattering. There are two dominant types of scattering processes in the atmosphere, Rayleigh and Mie scattering, both elastic, with inelastic scattering being much weaker. Rayleigh scattering is caused by particles small compared to the wavelength of the incident light. In the atmosphere, those scatterers are air molecules and small aerosols. Mie scattering on the other hand is due to particles of a size comparable to the wavelength of the light involved, which in the atmosphere is usually due to aerosols.

Including scattering, equation 3.1 becomes:

$$I(\lambda) = I_0(\lambda) \cdot exp\left(-\int_0^L \sum_i (\sigma_i(\lambda, p, T) \cdot c_i(l)) + \epsilon_R(\lambda, l) + \epsilon_M(\lambda, l)\, dl\right) \tag{3.3}$$

ϵ_R and ϵ_M are the coefficients for Rayleigh and Mie scattering. ϵ_R is proportional to λ^{-4} and ϵ_M is approximately proportional to $\lambda^{-1.3}$ in the atmosphere. Both of them are broadband scattering processes (van de Hulst, 1957).

If applied in this manner however, several problems emerge. For one, acquiring the initial intensity $I_0(\lambda)$ theoretically means measuring outside of the atmosphere, i.e. in space. Secondly, the distinction between different simultaneously occurring broadband absorption features, namely from scattering and broadband absorption of multiple absorbers, is nearly impossible. Differential Optical Absorption

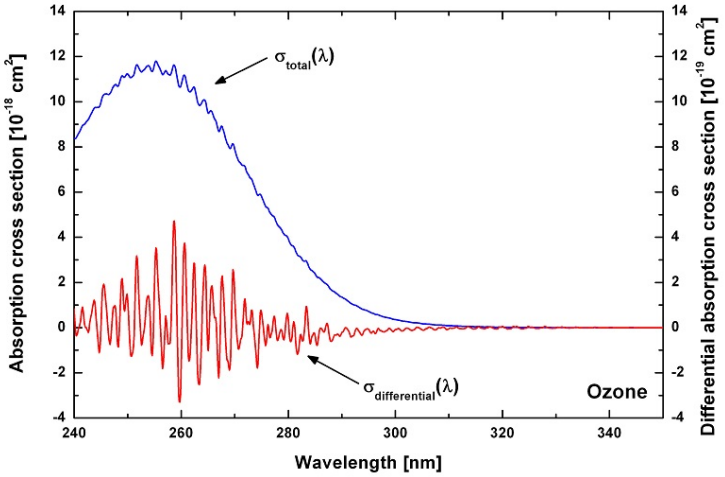

Figure 3.1.: The ozone absorption cross section in the UV range in blue, and, after the application of a high-pass filter, its narrowband parts in red. Note the different scale for each part. Reproduced from Zielcke (2010).

Spectroscopy (DOAS), introduced by Platt et al. (1979) is a technique which solves these issues.

3.2 Differential Optical Absorption Spectroscopy

The underlying idea of differential absorption spectroscopy is to separate all unspecific spectral broadband features from narrowband absorption structures, that are characteristic to individual species of molecules. These narrowband structures can be due to electronic, rotational and vibrational excitations of molecules of a particular species. As the absorption cross sections depend on the structure and binding of a type of molecule, they are highly individual, therefore it is possible to measure and differentiate between several of them simultaneously in the same wavelength range.

The cross sections $\sigma(\lambda)$ of each absorber can be split into two parts (fig. 3.2), its broadband part $\sigma_B(\lambda)$ and its differential part $\sigma'(\lambda)$:

$$\sigma(\lambda) = \sigma_B(\lambda) + \sigma'(\lambda) \tag{3.4}$$

Figure 3.2 shows the example of the ozone cross section being split into both parts. With this, equation 3.3 can be written as:

$$\begin{aligned} I(\lambda) = I_0(\lambda) \cdot \exp\left(- \int_0^L \sum_i \left(\sigma_{B,i}(\lambda) \cdot c_i(l)\right) + \epsilon_R(\lambda, l) + \epsilon_M(\lambda, l)\, dl \right) \\ \cdot \exp\left(- \int_0^L \sum_i \left(\sigma'_i(\lambda) \cdot c_i(l)\right)\, dl \right) \end{aligned} \tag{3.5}$$

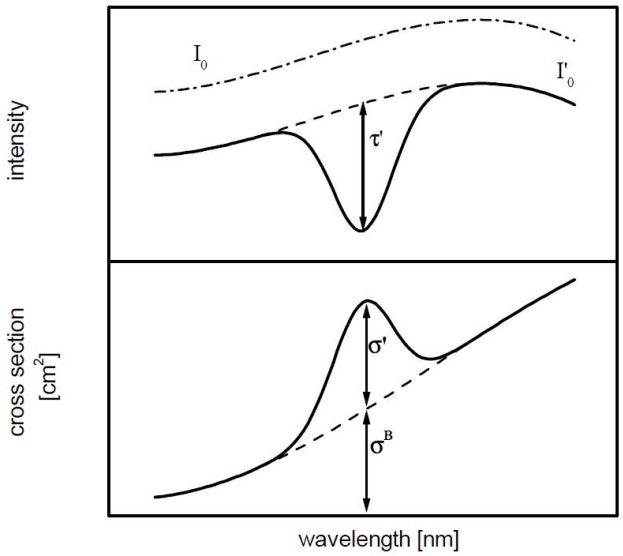

Figure 3.2.: A sketch of the basic DOAS principle. Absorption cross sections are split into broadband parts (I'_0 and σ_B) and narrowband parts (τ' and σ'). Adapted from Platt and Stutz (2008).

The first two factors vary only weakly as a function of wavelength in sufficiently small intervals. Combining them into $I_{B,0}(\lambda)$ yields:

$$I(\lambda) = I_{B,0}(\lambda) \cdot \exp\left(-\int_0^L \sum_i (\sigma'_i(\lambda) \cdot c_i(l))\ dl\right) \tag{3.6}$$

With this we can define the differential optical density:

$$\tau'(\lambda) = -\ln\left(\frac{I(\lambda)}{I_{B,0}(\lambda)}\right) = \int_0^L \sum_i (\sigma'_i(\lambda) \cdot c_i(l))\ dl \tag{3.7}$$

$I_0(\lambda)$ and $I(\lambda)$ can be acquired through measurements, with which the next section deals, and $I_{B,0}(\lambda)$ is numerically approximated. This allows the determination of the sort and amount of different trace gases through their differential absorption cross sections $\sigma'_i(\lambda)$. The quantity gained it the slant column density (SCD) S, which is the concentration of an individual absorber integrated along the light path and the result of a DOAS retrieval:

$$S_i = \frac{\tau'_i}{\sigma'_i} = \int_0^L c_i(l)\ dl \tag{3.8}$$

As absorption path lengths L are typically on the scale of kilometers, usually only a mean concentration is acquired. Furthermore, L has to be inferred by some other means, which is detailed in the descriptions of the specific varieties of DOAS.

3.3 The measurement process

When acquiring spectra, these not only contain the desired signals caused by the atmosphere, but they are also influenced by the instrument, particularly the spectrometer. Figure 3.3 shows the basic measurement principle of all DOAS measurements. Photons from a light source pass the atmosphere and are collimated onto the entrance slit of a spectrometer. Depending on the wavelength of the photons, they are imaged by the grating onto different parts of the sensor. Due to the finite optical and spectral resolution of the spectrometer, the resolution of the spectra is degraded. Mathematically this can be described by the convolution of the incoming light $I_0(\lambda)$ with the instrument function $H(\lambda)$:

$$I_0^*(\lambda) = I_0(\lambda) * H(\lambda) = \int I_0(\lambda') \cdot H(\lambda - \lambda')\, d\lambda' \tag{3.9}$$

$I_0^*(\lambda)$ denotes the light falling onto the imaging sensor. As the often used charge-coupled device (CCD) sensors have a finite pixel size, the measured spectra are also discretized:

$$I_0^+(x) = \int_{\lambda(x)}^{\lambda(x+1)} I_0^*(\lambda')\, d\lambda' \tag{3.10}$$

x enumerates the pixels of the CCD array, typical sizes of which are 1024 and 2048 pixels. $\lambda(x)$ is the spectrometers wavelength-to-pixel mapping, which is an almost linear function, and usually it is approximated by a polynomial of degree 2 or 3:

$$\lambda(x) = \sum_{i=0}^{n=(2,3)} a_i \cdot x^i \tag{3.11}$$

The signal coming out of the spectrometer $S(x)$ has two more components added compared to $I_0^+(x)$, namely electronic offset $O(x)$ and dark current $D(x)$. Therefore the final acquired signal $S(x)$ is:

$$S(x) = I_0^+(x) + O(x) + D(x) \tag{3.12}$$

The offset signal is artificially added onto the signal to shift voltage levels into a defined, positive range necessary for the A/D converter of the read-out electronics. It is therefore proportional to the number of acquired scans and can thus be corrected by subtracting a scan-weighted offset spectrum, which is acquired dark at the shortest possible integration time. The dark current signal stems from thermal excitations of electrons in the CCD. The signal is thus proportional to the Boltzmann factor $e^{-\Delta E/kT}$ and the integration time of spectra. It can therefore be corrected by subtracting a time-weighted dark spectrum, which is acquired at the longest possible integration time typically. Both of these effects are temperature-dependent, the spectrometers are therefore usually temperature-stabilized to avoid a drift in those signals. In the following, $I(x)$ or $I(\lambda)$ will always denote spectra, which are already corrected for offset

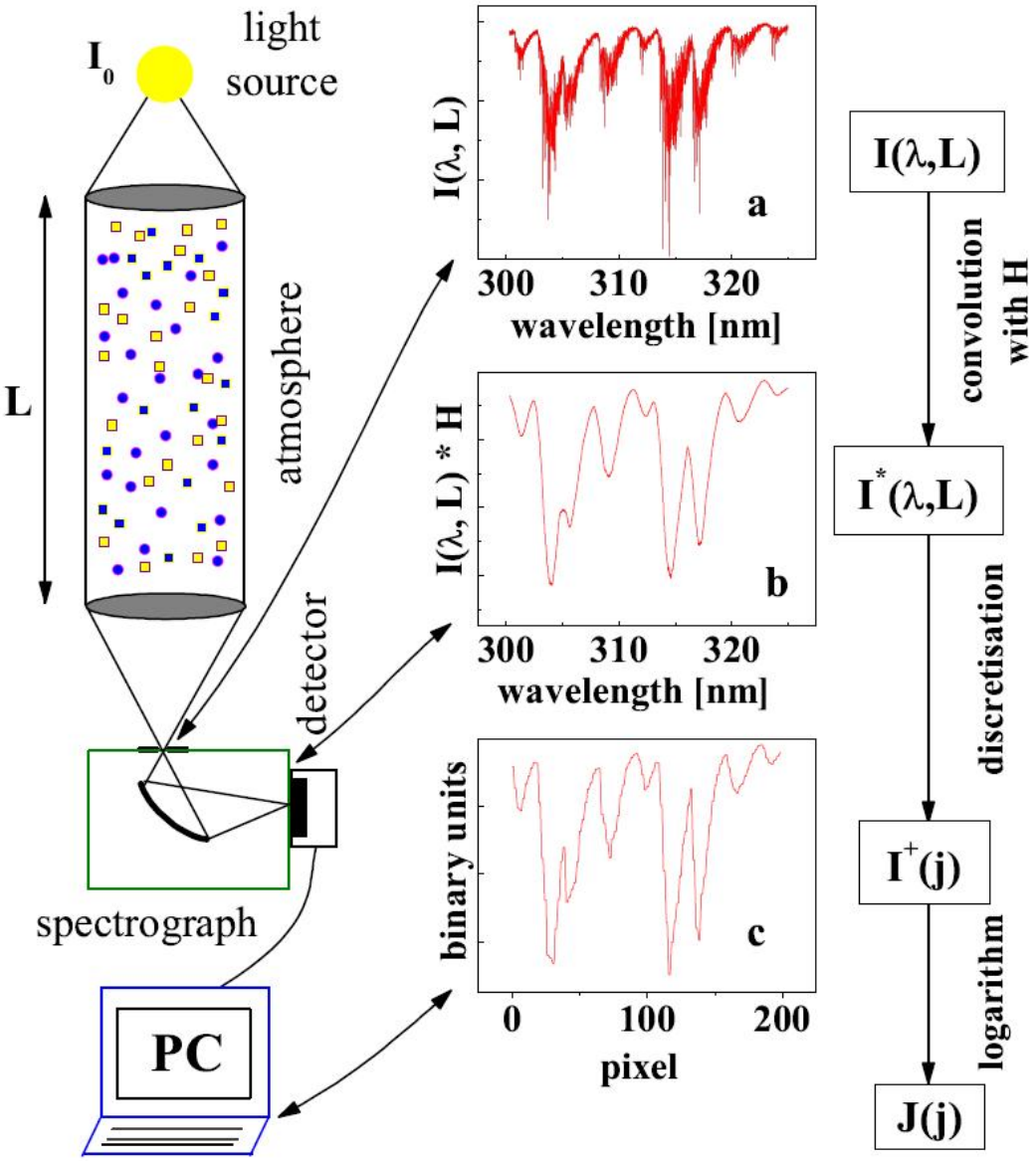

Figure 3.3.: The DOAS measurement process (adapted from Stutz and Platt, 1996). Light of spectral intensity I_0 passes an absorber, in this case formaldehyde, and is focused into a spectrometer. There the spectrum is convoluted with the instrument function H. The acquisition of the spectrum with an imaging sensor then causes a discretization into pixels on the detector array and counts for the spectral intensity.

and dark current.

3.3.1 Evaluation procedure

With the corrected spectra, the differential optical density as given by equation 3.7 can be computed. For this, $I_{B,0}$ needs to be derived from the measured I_0, i.e. the reference spectra with broadband absorption or scattering features removed. From equation 3.6 follows:

$$ln(I_{B,0}(\lambda)) = ln(I_0(\lambda)) - \left(\int_0^L \sum_i (\sigma_{B,i}(\lambda) \cdot c_i(l)) + \epsilon_R(\lambda, l) + \epsilon_M(\lambda, l)\, dl \right) \tag{3.13}$$

The second term on the right hand side is unknown, yet it is a function varying slowly with wavelength. Platt et al. (1979) suggested approximating this term with a polynomial $P(\lambda)$. The degree of this polynomial has to be chosen according to the size of the wavelength region in question and the number of absorbers present. With this, equation 3.5 can be rewritten:

$$\tau(\lambda) = -ln\left(\frac{I(\lambda)}{I_0(\lambda)}\right) = P(\lambda) + \left(\int_0^L \sum_i (\sigma_i'(\lambda) \cdot c_i(l))\ dl \right) \tag{3.14}$$

Assuming that the absorption cross sections do not depend on the light path, they can be pulled out of the integral, and also inserting the definition of the SCD leads to:

$$\tau(\lambda) = P(\lambda) + \sum_i (\sigma_i'(\lambda) \cdot S_i) \tag{3.15}$$

This defines the model function $F(\lambda)$

$$F(\lambda) = P(\lambda) + \sum_i (\sigma_i'(\lambda) \cdot S_i) \tag{3.16}$$

which will be fitted to the measured optical density. To do so, it is necessary to adjust the resolution of cross sections $\sigma_i(\lambda)$. The cross sections are commonly measured in laboratory experiments and the spectrometers used to measure those reference cross sections typically have a very high resolution compared to the spectrometers used in this thesis (FWHM resolution of 0.4 nm - 0.8 nm) and for DOAS measurements in general. To adapt the resolution of these spectra, they are convoluted with the instrument function $H(\lambda)$:

$$\sigma_i^*(\lambda) = \sigma_i(\lambda) * H(\lambda) = \int \sigma_i(\lambda') \cdot H(\lambda - \lambda')\, d\lambda' \tag{3.17}$$

Finally, a combination of linear least-squares fit and Levenberg-Marquardt fit

(Levenberg, 1944; Marquardt, 1963) is used to minimize χ^2, given by:

$$\chi^2 = \sum_{x_i=x_1}^{x_2} \left(\tau(x_i) - F(x_i)\right)^2 \tag{3.18}$$

with x_1 and x_2 denoting the beginning and the end of the fit range. The coefficients of the polynomial and the desired SCDs of the absorber species are parameters of the fitting procedure. Additionally, a slight shift and squeeze of the reference cross sections is often allowed to accommodate for calibration errors and temperature shifts.

The fit thus retrieves the SCDs. However even a perfect fit, that is, a fit in which all structures caused by absorbers and by scattering are removed, has a χ^2 greater than zero, as noise (photon noise, detector noise, offset noise) is always present. To assess the quality of a fit, apart from the single numerical value of χ^2, its residual R can be scrutinized, which is given by:

$$R(\lambda) = \tau(\lambda) - F(\lambda) \tag{3.19}$$

It should contain only noise and no distinct artefacts. Sometimes this is not possible, due to a temperature drift of the spectrometer, an instrument function which varies strongly with detector position, artefacts in reference cross spectra or unknown absorbers.

The DOAS evaluations in this work were all done using the software *DOASIS* by Kraus (2005), which can handle both data acquisition as well as most computations necessary for the data evaluation, such as offset and dark current correction, wavelength calibration, convolution, DOAS fitting, calculation of Ring spectra (see next section) etc. It also features a JScript scripting interface for the automation of acquisition and evaluation and the implementation of new features.

3.3.2 Definition of the detection limit

In DOAS, the detection limit describes the smallest SCD of an absorber which can still be positively identified in a measurement. It can be derived by two means.

The more conservative approach is to analyze the residual of the DOAS fit. If there were any absorbers present, which were not included in the fit, having a higher optical density than the noise, they should appear in the residual. If their optical density is smaller than the noise, they are below the detection limit. Therefore as an estimate, differential optical densities have to be larger than noise. One can take the RMS of the residual of the fit Δ twice and divide it by the largest absorption structures present in the fit interval:

$$S_{i,DL} = \frac{2 \cdot \Delta}{\sigma_i} \tag{3.20}$$

The other method is based on the fit error stemming from the minimization of χ^2. Assuming the distribution of the fit error is Gaussian, then there is a probability of 68% of the true SCD to be in the $1\,\sigma$-interval and a probability of 95.5% to be in the $2\,\sigma$-interval. Typically the $2\,\sigma$-interval is taken as the necessary level of confidence and if it is located above zero, it can be said that the absorber was positively identified. In this thesis, the second method is chosen for reasons of automation, unless otherwise noted. Fit errors were also adjusted after Stutz and Platt (1996) if necessary.

3.4 Scattered sunlight DOAS

The numerous applications of the DOAS method can be roughly divided into two categories: active and passive. Active methods have their own, artificial light source such as Xenon arc lamps or LEDs, passive methods use direct or scattered sunlight, moonlight (Zielcke, 2010) or even starlight (Fussen et al., 2006). In the following sections, the variations of DOAS used within this thesis, namely scattered sunlight DOAS, Long-Path DOAS and Cavity-Enhanced DOAS are described.

Scattered sunlight DOAS utilizes photons from the sun, scattered in the atmosphere, to gain information about the air constituents as well as their spatial distribution. It is viable in the ultraviolet and visible wavelength range as light in this wavelength range is effectively scattered by air molecules and aerosols.

3.4.1 Elastic scattering

As mentioned above, scattering processes in the atmosphere can broadly be divided into two categories, elastic scattering and inelastic scattering. Elastic scattering happens on air molecules (Rayleigh scattering) and on aerosols (Mie scattering), whereas inelastic scattering is mainly due to Raman scattering on nitrogen and oxygen molecules. By far the largest part of the scattered photons are scattered elastically which is described by Mie theory.

Rayleigh scattering

Rayleigh scattering can be thought of as the emission of a Hertzian dipole stimulated by the incoming light. It occurs on scatterers significantly smaller than the wavelength of the scattered light and with that assumption can be described by the approximation of Mie theory. In the atmosphere, Rayleigh scattering mainly takes place on N_2 and O_2 molecules (Roedel and Wagner, 2011).

The scattering cross section σ_R can be approximated as

$$\sigma_R = \frac{8 \cdot \pi^3 \cdot (\epsilon - 1)^2}{3 \cdot \lambda^4 \cdot n_{air}^2} \tag{3.21}$$

with the dielectric permittivity ϵ and the number density of air n. It therefore has a strong wavelength dependency ($\propto \lambda^{-4}$), which is the reason why the sky is blue.

Its phase function Φ_R for unpolarized incident light is given by

$$\Phi_R(\theta) = \frac{3}{4}(1 + \cos^2(\theta)) \tag{3.22}$$

which is a relatively weak angular dependency compared to Mie scattering (Roedel and Wagner, 2011).

Mie scattering

Mie scattering occurs when the size of the scatterer is not negligible in comparison to the wavelength of the incoming light. It can be thought of as the result of the addition of coherently exited elementary scattering centers on a particle (Mie, 1908), leading to interference patterns and enhanced forward scattering. In Mie theory an analytical expression for the scattering intensity or phase function cannot be derived. However, for size-averaged, macroscopic phase functions, several parametrizations exist. Due to its simplicity, the one most often used is the Henyey-Greenstein parametrization given by:

$$\Phi_{HG}(\theta) = \frac{1 - g^2}{4\pi(1 + g^2 - 2g\cos(\theta))^{3/2}} \tag{3.23}$$

Only one parameter is necessary, the asymmetry parameter $g = \langle\cos(\theta)\rangle$, which is the averaged cosine of the scattering function (Henyey and Greenstein, 1941). It can vary between pure isotropic scattering ($g = 0$) and complete forward scattering ($g = 1$), but common values in the atmosphere range from 0.65 for aerosol particles and 0.85 for water clouds (Roedel and Wagner, 2011).

The wavelength dependency of Mie scattering depends on the size distribution of the scatterers and is proportional to $\lambda^{-\alpha}$ with $\alpha \approx 1.3$, which is why clouds appear white.

3.4.2 Inelastic scattering

If light passes the atmosphere, it not only gets scattered elastically by Rayleigh and Mie scattering, but also, to a minor degree inelastically by Raman scattering. The photon can either give energy to the molecule (Stokes lines) or take up energy from the molecule (Anti-Stokes lines). Of all the photons scattered in the atmosphere, only around 2% - 4% are scattered inelastically (Roedel and Wagner, 2011). In contrast to the Rayleigh scattering phase function, Raman scattering is practically isotropic (Roedel and Wagner, 2011).

Rotational Raman Scattering and the Ring effect

In the atmosphere this leads to an effect, termed the *Ring effect*, first described by Grainger and Ring (1962), which is due to the redistribution of energy along the electromagnetic spectrum (Chance and Spurr, 1997). If absorption bands are present in a spectrum, there is less light available in these bands, compared to adjacent parts of the spectrum, to be scattered out of them into different energy levels, than is scattered into them. So they are filled up to a certain degree. The absorptions mostly affected by this are the solar Fraunhofer lines, as these can have quite high optical densities.

While the total amount of light that is scattered in this fashion is fairly small (changes in optical depth are on the order of a few percent), it nonetheless causes structures huge compared to the absorption by trace gases. If it is not corrected accurately, the residual usually contains remaining Ring structures, which can severely hamper the detection of trace gases. To account for this effect, a so called Ring spectrum is calculated from the Fraunhofer reference spectrum and included in the fitting procedure.

During atmospheric conditions dominated by multiple scattering, i.e. in clouds and high aerosol loads, the wavelength dependency of this Ring spectrum can change. To account for this, a second Ring spectrum with a different wavelength dependency, usually scaled with λ^4, is often included in the fitting routine (Wagner et al., 2009).

Vibrational Raman Scattering

A much weaker inelastic scattering mechanism is Vibrational Raman scattering (VRS) on air molecules, mainly on N_2, which contributes around 0.04% of the total light intensity (Lampel, 2014) and is therefore a hindrance for the further reduction of detection limits. Similarly to the Ring effect, correction spectra for the scattering on N_2 and O_2 can be calculated and included in the fit process (Lampel et al., 2015).

3.4.3 Macrophysical optical properties of aerosol

Two further quantities are introduced here which are needed later in this work. They pertain to the macrophysical description of the optical properties of aerosol.

As mentioned above, aerosol particles can scatter light, but they can also absorb light. The *single scattering albedo* (SSA) ω is a measure of the relationship between extinction due to scattering ϵ_s and the total extinction $\epsilon_M = \epsilon_s + \epsilon_a$

$$\omega(\lambda) = \frac{\epsilon_s(\lambda)}{\epsilon_s(\lambda) + \epsilon_a(\lambda)} \tag{3.24}$$

with ϵ_a being the extinction due to absorption. The SSA can therefore range from 0 (complete absorption of radiation) to 1 (complete scattering). For average atmospheric distributions, typical values are between 0.8 and 1.0 (Takemura et al., 2002).

Another relevant quantity is the wavelength dependency of the aerosol extinction. It can be parametrized by

$$\epsilon_M(\lambda) = \epsilon(\lambda_0) \cdot \left(\frac{\lambda}{\lambda_0}\right)^{-\alpha} \tag{3.25}$$

with some reference extinction $\epsilon(\lambda_0)$ at λ_0, and α which is called the *Ångström exponent*. α is inversely proportional to the size distribution of the aerosol. Its possible values range from 0 to 4, typically between 1 and 1.5, and an average around 1.3 (Ångström, 1929).

3.4.4 Multi Axis-DOAS (MAX-DOAS)

In Multi Axis-DOAS, spectra are collected of scattered sunlight with a telescope at several different elevation angles. A typical sequence for ground based measurements would be 1 °, 2 °, 5 °, 10 °, 20 ° and 90 ° (zenith). The principle is illustrated in figure 3.4. The acquired spectra of the lower angles are then typically evaluated against the zenith spectrum, which yields differential SCDs (dSCDs), relative to the respective zenith spectrum. The light paths for the different elevation angles have different lengths in the lower atmosphere, and approximately the same stratospheric exposure. Therefore, combining the measurements at different angles, information about the vertical distribution of absorbers can be gained. As the light path of spectra collected at lower angles is usually longer in the atmospheric layers at instrument altitude, there is also a higher sensitivity for those layers.

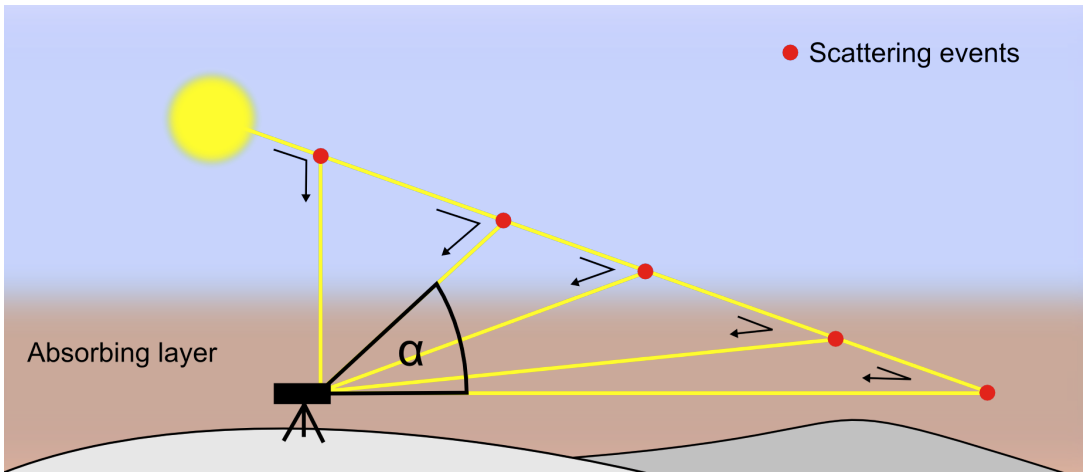

Figure 3.4.: The principle of MAX-DOAS measurements: Scattered sunlight is collected by a telescope from different telescope elevation angles α. While the radiative transfer is highly simplified in this diagram, it can be seen that the relative light path length contribution in the absorbing layer is different for different elevation angles. This allows to gain vertical profile information from these measurements.

Vertical column density and Air mass factor

The dependence of the SCDs on the light path and therefore viewing geometry makes direct comparisons of SCDs at different angles problematic. Here another quantity is useful, the vertical column density (VCD) V, which is the integral of the concentration c of some substance from the surface to the top of the atmosphere:

$$V = \int_0^\infty c(z)dz \tag{3.26}$$

This gives rise to the concept of the Air mass factor (AMF) A, which is the quotient of the SCD S and the VCD V:

$$A = \frac{S}{V} \tag{3.27}$$

The AMF is therefore a measure of the exposure of the measured SCDs to the atmospheric concentrations and therefore sensitivity. Radiative transfer modeling also allows to calculate AMFs, which allows the conversion of SCDs to VCDs.

3.4.5 Retrieving vertical profile information through inversion

The VCD is only a single quantity which does not give any information about the vertical distribution of the substance. As mentioned above however, there is information about the vertical distribution of absorbers in MAX-DOAS measurements due to the different elevation angles. Depending on clouds and aerosols and the viewing geometry, retrieving this information from the measurements can become complex. As there are typically 5 data points per measurement sequence and usually a much higher number of altitude levels at which concentrations are desired, this problem is inherently under-determined. Nonetheless it lends itself well to the application of inverse methods. In this section, the principle of inverse methods as used in this work is presented, for an extensive overview of the subject refer to Rodgers (2000).

Theory

If x denotes the state of the atmosphere (state vector, e.g. concentrations at different altitudes) and y the ensemble of measurements (measurement vector, e.g. SCDs at different elevation angles). Then the measurement function or forward function F, simulating the measurement process, is a mapping from state space to measurement space:

$$y = F(x) \tag{3.28}$$

F is typically not only varying as a function of x but also of additional parameters b ($F_b(x)$), which are taken to be constant and are not varied during the inversion. In order to derive the current state x given the measurements y, the inverse of the above is needed:

$$x = F^{-1}(y) \tag{3.29}$$

The measurement vector has an error vector ϵ associated with it, containing the measurement error for each measurement, or more generally, an error covariance matrix $\mathbf{S}_\epsilon$. As mentioned above, the inversion problem is under-determined, therefore additional information is necessary in order to obtain a meaningful solution. One way to do so is to include an *a priori profile* x_a together with an assumed covariance matrix $\mathbf{S}_a$ for the a priori profile. The a priori profile should contain any information that is known or assumed about the true state x and its error should reflect the uncertainty in that knowledge.

The inversion is done using the cost function

$$\chi^2 = (F(x) - y)^T \mathbf{S}_\epsilon^{-1} (F(x) - y) + (x - x_a)^T \mathbf{S}_a^{-1} (x - x_a) \tag{3.30}$$

and the retrieved state is then acquired by the minimization of it, i.e.

$$\nabla_x \chi^2(\hat{x}) \stackrel{!}{=} 0 \tag{3.31}$$

For linear problems, i.e. if F is linear in x, F can be expressed as:

$$F(x) = \mathbf{K}x \tag{3.32}$$

and the solution can be found analytically. In atmospheric inversion theory, $\mathbf{K}$ are called the *weighting functions*, as they demonstrate the change in measurement signal for given changes in atmospheric state. If the problem is non-linear, F can be piece-wisely linearized and the problem solved iteratively using the Gauss-Newton or Levenberg-Marquardt method. More generally then, $\mathbf{K}$ are thus defined by:

$$\mathbf{K} = \frac{\partial \mathbf{F}}{\partial x} \tag{3.33}$$

The other sensitivity determining quantity is how the inversion result is varying as a function of measurement signal. This quantity is called the *gain function* $\mathbf{G}$ for which also an analytic expression can be derived (Rodgers, 2000):

$$\mathbf{G} = \frac{\partial \hat{x}}{\partial y} = (\mathbf{S}_a^{-1} + \mathbf{K}^T \mathbf{S}_\epsilon^{-1} \mathbf{K})^{-1} \mathbf{K}^T \mathbf{S}_\epsilon^{-1} \tag{3.34}$$

Combined, the weighting function and the gain function give rise to the *averaging kernels* (AK) $\mathbf{A}$, which denote the sensitivity of the inversion of the retrieved state $\hat{x}$ for the true state x of the atmosphere:

$$\mathbf{A} = \mathbf{G}\mathbf{K} = \frac{\partial \hat{x}}{\partial x} = (\mathbf{S}_a^{-1} + \mathbf{K}^T \mathbf{S}_\epsilon^{-1} \mathbf{K})^{-1} \mathbf{K}^T \mathbf{S}_\epsilon^{-1} \mathbf{K} \tag{3.35}$$

An ideal measurement method would have $\mathbf{A} = \mathbf{I}_n$, i.e. the retrieved state is exactly equal to the true state.

With the quantities introduced here, the result of the inversion $\hat{x}$ can be written as:

$$\hat{x} = x_a + \mathbf{A}(x - x_a) + \mathbf{G}\epsilon \tag{3.36}$$

Errors and information content

There are several ways to assess the quality of the result of the inversion. The most basic method is to analyze the resulting χ^2, if the algorithm has converged at all or the chosen parameters don't allow a further reduction. As another convergence indicator, the modeled SCDs can be compared to the measured SCDs. The total error on the resulting state $\hat{x}$ is made up of the noise error of the measurement, which propagates into the result via

$$\mathbf{S}_m = \mathbf{G}\mathbf{S}_\epsilon \mathbf{G}^T \tag{3.37}$$

with $\mathbf{S}_m$ being the covariance matrix of the resulting state and secondly the smoothing error. The smoothing error is due to the limited spatial, that is vertical, resolution and therefore in this work is not taken as an error on inverted

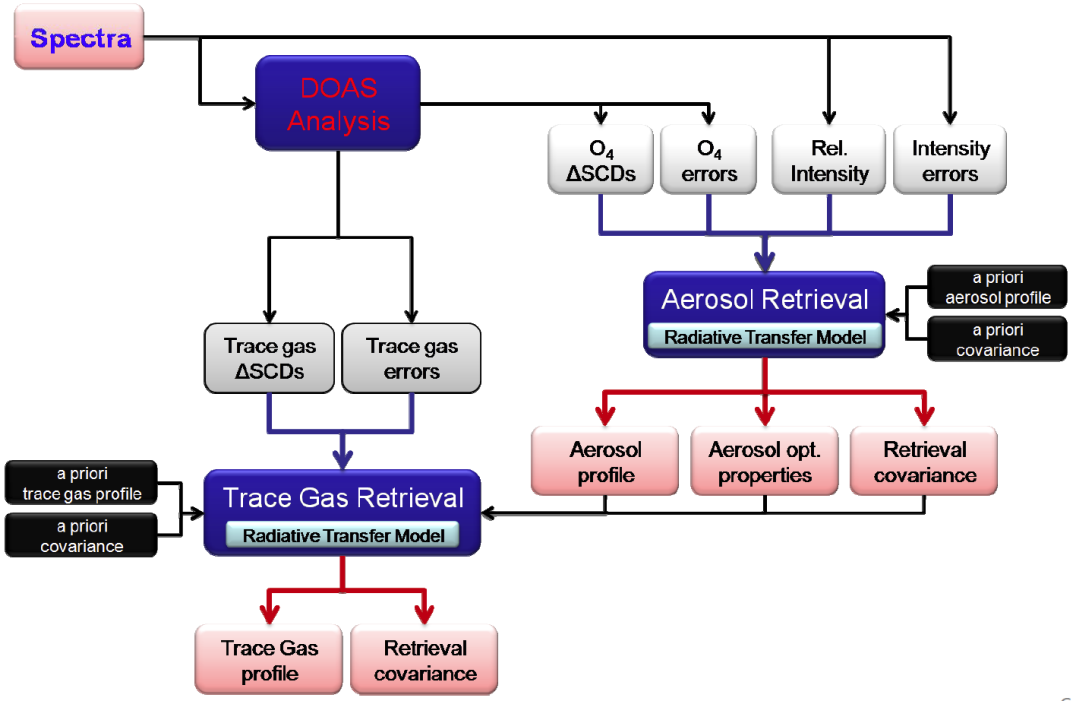

Figure 3.5.: Sketch showing the data flow in the two-stage *HEIPRO* retrieval. First O_4 SCDs are input into the aerosol inversion, the resulting aerosol extinction and trace gas SCDs are then input into the actual trace gas inversion. Figure adapted from Yilmaz (2012).

concentrations. Instead the vertical resolution is stated, as suggested by Rodgers (2000) and von Clarmann (2014).

There are also several indicators based on the concept of information content of the inversion result. The one most commonly used is *degrees of freedom for signal* d_s. It indicates the amount of degrees of freedom which originate from the measurement and inversion procedure. If the measurement data is highly redundant or the inversion parameters are flawed, then it decreases. Mathematically it is also easy to compute:

$$d_s = tr(\mathbf{A}) \tag{3.38}$$

The opposite is *degrees of freedom for noise* d_n. Together they add up as $d_s + d_n = \mathbf{I}_m$, with m being the rank of the problem.

Practical implementation

As forward models, radiative transfer models such as *SCIATRAN* (Rozanov et al., 2002, 2005) or *McArtim* (Deutschmann et al., 2011) can be used. In this thesis, *SCIATRAN 2* is always used as the forward model. The *HEIPRO* inversion implementation of Yilmaz (2012) is further used in this work. It is based on a two step approach, which is pictured in figure 3.5.

First, SCDs of the oxygen collision complex O_4, derived from the DOAS analysis, are fed into the aerosol inversion, together with applicable vertical pressure and temperature profiles and a suitable aerosol a priori profile. The measured O_4 SCDs depend on the vertical profile of O_4, which is proportional to the square of the atmospheric oxygen profile, and aerosol optical properties, which are the varied parameters. As radiative transfer in the atmosphere depends on the wavelength of interest, usually SCDs of O_4 absorption bands near the trace gas absorption of interest are used.

The resulting aerosol extinction profile is then input together with trace gas SCDs and a trace gas a priori profile into the trace gas inversion, which then yields the trace gas profile.

3.5 Long Path-DOAS (LP-DOAS)

Long Path-DOAS is an active DOAS method using Xenon arc lamps or LEDs as light source and a (geometrically) long light path through the atmosphere, which is usually located close to the ground. As depicted in figure 3.6, the light from the light source is coupled into a telescope with a fiber bundle, then sent through the atmosphere to a reflector, then back to the telescope and coupled

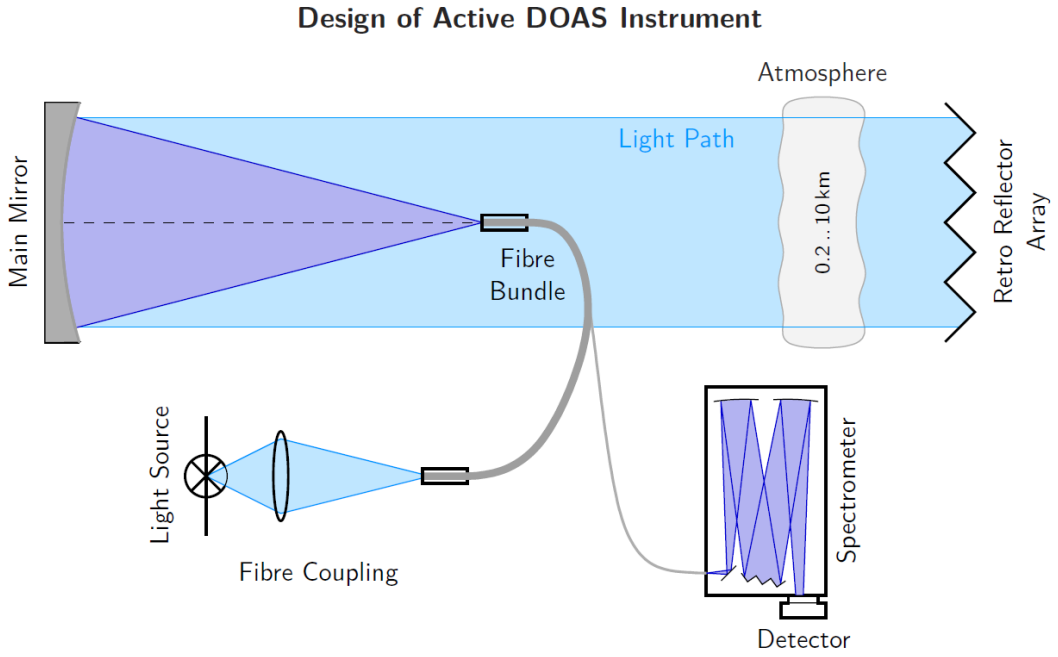

Figure 3.6.: Sketch of a Long Path-DOAS measurement: The light generated by a light source, e.g. a Xenon arc lamp or LED, is coupled into the telescope, via an optical fiber, and from there traverses the atmosphere to the retro reflector, where it is sent back to the telescope and then coupled back into the fiber and finally analyzed by the spectrometer. Image adapted from Sihler (2007).

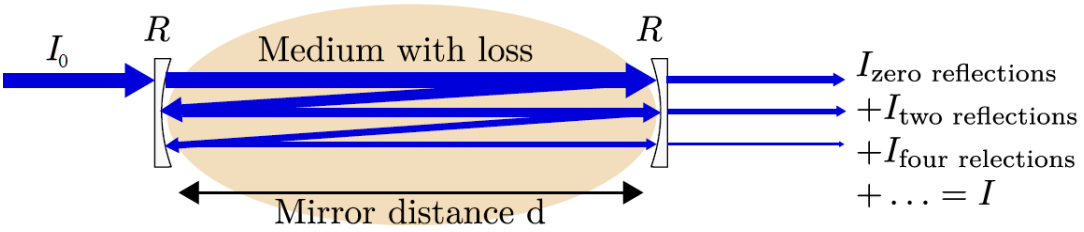

Figure 3.7.: Illustration of the principle of Cavity Enhanced-DOAS (CE-DOAS). The path length through a medium with absorbers of interest is lengthened by two highly reflective mirrors forming a cavity. The light enters the cavity through one mirror and passes the absorber numerous times, every time a small part of the light is coupled out of the cavity. The resulting overlay of all parts transmitted is then analyzed. Image adapted from Horbanski (2010).

out again via the fiber bundle into the spectrometer, where it is analyzed finally (e.g. Merten, 2008).

Advantages of LP-DOAS are the ability to measure day and night, to utilize a wide spectral range, including regions without any significant solar irradiation such as the deep UV. The light path is also clearly defined in terms of location as well as length. A disadvantage is, as the obtained concentrations are averages over the typically several km long light path, smaller concentration gradients can not be resolved.

3.6 Cavity Enhanced-DOAS (CE-DOAS)

Cavity Enhanced-DOAS is an in-situ absorption spectroscopy method (Platt et al., 2009). High sensitivity, that is, a long absorption light path, is achieved by folding the light path with highly reflective mirrors. Usually a cell consisting of two dielectric mirrors with a separation between one and two meters is used as illustrated in figure 3.7. LEDs (Kern et al., 2006; Sihler et al., 2009) are a good light source for this application, because they have an emission peak which often has the same wavelength FWHM as the reflectivity curve of the mirrors. As the mirrors are almost completely transmitting outside their reflective range, the light at other wavelengths would otherwise be completely transmitted into the spectrometer entrance optics and could cause stray light.

The CE-DOAS instruments can be either closed-path or open-path resonators. Closed-path ones have their absorption cell inside a tube shielded from the environment and sample air is usually pumped through aerosol filters and then into the cell. This has the advantage that the mirrors of the resonator are protected against dust etc. and works well for substances like NO_2. For highly reactive compounds such as IO however, the involved surface losses at the inlet and the measurement cell are significant and difficult to quantify accurately under changing environmental conditions. Therefore, instruments to measure substances such as IO are built as open-path ones, where the beam between the

two mirrors directly traverses the air mass to be probed.

3.6.1 Intensity and optical density

Due to the nature of the resonator, the light exiting the cavity and analyzed by the spectrometer is a superposition of all transmitted parts. It therefore has contributions from each pair of reflections (Fiedler, 2005):

$$\begin{aligned} I &= I_0 \cdot T_{mirror}^2 \cdot T_{gas} \\ &\quad + I_0 \cdot T_{mirror}^2 \cdot R_{mirror}^2 \cdot T_{gas}^3 \\ &\quad + ... \\ &\quad + I_0 \cdot T_{mirror}^2 \cdot R_{mirror}^{2n} \cdot T_{gas}^{2n+1} \\ &\quad + ... \\ &= I_0 \cdot T_{mirror}^2 \cdot T_{gas} \sum_{n=0}^{\infty} R_{mirror}^{2n} \cdot T_{gas}^{2n} \end{aligned} \tag{3.39}$$

with the intensity of the light source I_0, the mirror transmission T_{mirror} and the transmission of the absorber T_{gas}. As $R_{mirror} \cdot T_{gas} < 1$ this series converges.

The light path length inside the cavity depends on the mirror reflectivity R, and, if absorbers or scatterers are present, their extinction. This effect has to be considered to determine accurate concentrations and for spectroscopic reasons as well, as it modulated present absorption structures.

On the assumption that R is close to 1 and the absorption within the resonator is small, an effective optical depth D_{eff} was derived by Platt et al. (2009). The advantage of D_{eff} is that it corrects the extinction dependency and therefore can be treated evaluation-wise as if the length of the light path was not depending on absorption. It is given by

$$D_{eff} = e^{D_{CE}} - 1 = \frac{I_0}{I} - 1 \tag{3.40}$$

with $D_{CE} = \ln(\frac{I}{I_0})$ being the conventional optical density.

3.6.2 Path length calibration

In CE-DOAS, the effective path length is usually a function with a strong wavelength dependency and has to be determined experimentally. Several methods exist for calibrating CE-DOAS instruments, each with their respective advantages and disadvantages. The ones applied within this work are introduced here.

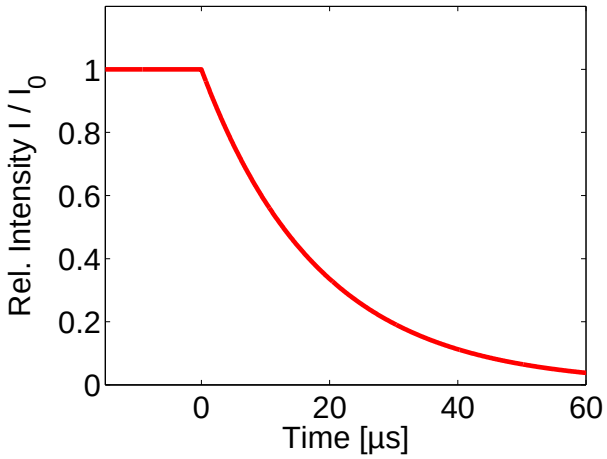

Figure 3.8.: Illustration of the light intensity exiting an optical resonator decaying after the light source is switched off at t = 0 for a light path length of L = 5500 m relative to the light intensity before.

Different Rayleigh scatterers: Air vs. Helium

One method which can be employed, first described by Washenfelder et al. (2008), is using two gases with different Rayleigh scattering extinction coefficients. The larger the difference in the extinction coefficients, the more accurate the final calibration curve. While one could use normal air at different pressure levels, technically the easiest is to use air and another gas at ambient pressure. Helium is a practical choice, its Rayleigh scattering cross section differs by two orders of magnitude from the one of air. According to Horbanski (2010), the path length curve is then given by

$$L(\lambda) = \frac{\frac{I_{Air}(\lambda)}{I_{Helium}(\lambda)} - 1}{\epsilon_{Helium}(\lambda) - \epsilon_{Air}(\lambda)} \tag{3.41}$$

with the extinction coefficients for helium ϵ_{Helium} and air ϵ_{Air} and the respective measured intensities I_{Helium} and I_{Air}. This method gives L for the whole wavelength range. Drawbacks are that it critically relies on the stability of the light source and of the optical setup during the calibration time, as absolute light intensities are directly compared. Typical calibration durations are on the order of tens of minutes and there is the potential for systematic offsets due to incomplete flushing of the resonator with helium or air.

Ring-down time

A further way to derive the path length of the optical resonator is to measure so-called *ring-downs*, the decay curves of the light intensity exiting the resonator after shutting off the light source (O'Keefe and Deacon, 1988). An example is

illustrated in figure 3.8. The intensity I decays as a function of time t as:

$$I(t, \lambda) = I(t_0, \lambda) \cdot \exp\Big(- \frac{c \cdot t}{L(\lambda)} \Big) \tag{3.42}$$

with c being the speed of light. Measuring the decay curve and fitting a model function to it directly gives the mean path length.

Due to the weak intensity of the decay curve the light cannot be measured with the instrument's spectrometer, but has to be acquired using for example a photomultiplier tube (PMT) with an appropriate amplifier. A plain PMT however is not wavelength discriminating and therefore only wavelength-averaged path length curves can be recorded this way. L usually is highly wavelength-dependent and a method to determine it wavelength-resolved using ring-downs is presented in section 4.1.1.

Advantages are that the stability of the light source I_0 is not as important on a scale of minutes, but on the duration of averaged ring-downs, i.e. tens of seconds. Also, no compressed gas cylinders are necessary, which are difficult to transport in polar regions due to safety regulations.

Calibration gas

For measurements of trace gases such as NO_2, the calibration can be performed by flushing the resonator with a gas of a known concentration. This is a common method for in-situ measurement instruments for atmospheric trace gases such as NO_2 or O_3. The path length can then be derived from the column density $S_{measured}$ and the concentration c_{calib} simply by

$$L = \frac{S_{measured}}{c_{calib}} \tag{3.43}$$

This does not directly provide the wavelength dependency of the path length, which is necessary e.g. to evaluate other trace gases in that spectral region. The dependency can be retrieved by minimization though under certain circumstances as described in the following.

NO_2 absorption fitting

The qualitative shape of the path length curve can also be retrieved when a strong, suitable, and preferably only one, absorber is present in the light path. This is because its absorption cross section gets modulated by the path length curve, which can be exploited. If the absorber furthermore has absorption structures over the whole covered wavelength range, as is the case for NO_2 in the visible region, then by minimization $a \cdot L(\lambda)$ with some scaling factor a can be determined. An example of this is shown in figure 3.9.

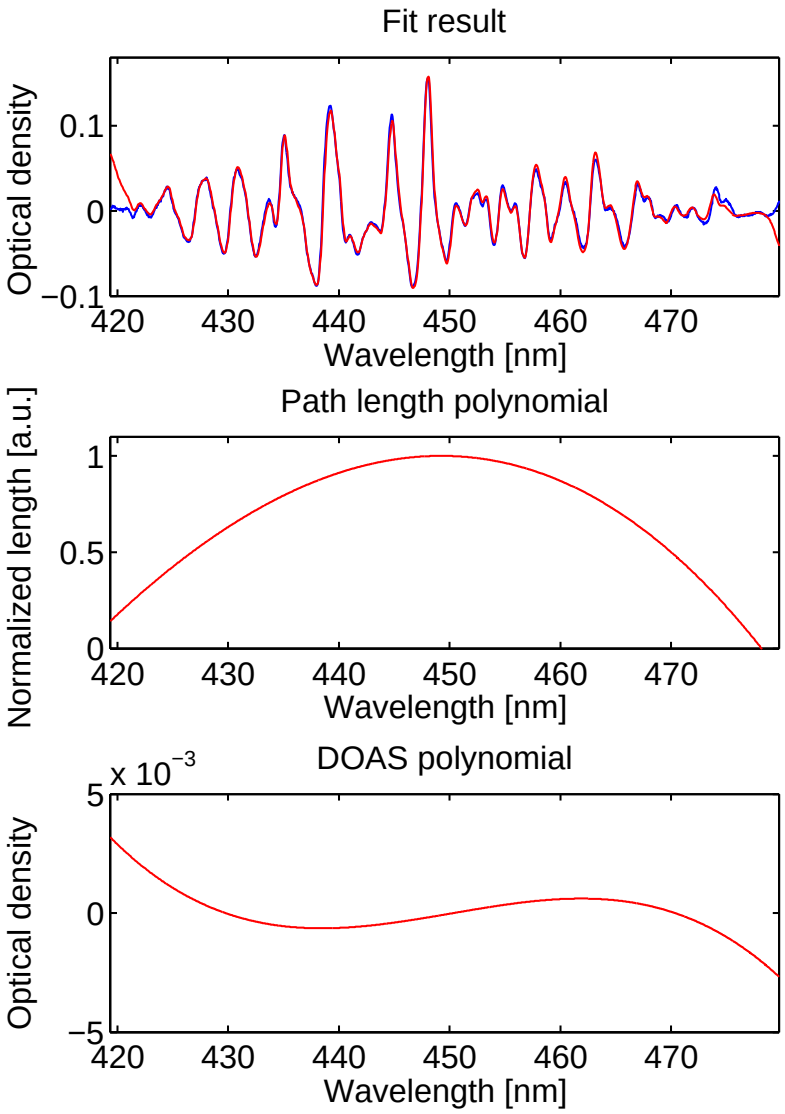

Figure 3.9.: Example of the retrieval of the shape of the path length curve by exploiting the NO_2 absorption, done by minimizing the DOAS cost function, where the path length polynomial coefficients (here 7th order) are also varied. The resulting curve is shown in the middle, on the bottom the DOAS polynomial.

4

DOAS instrumentation

In this chapter the spectroscopic measurement instruments used in the field studies at Scott Base (chapter 6) and on RV Polarstern (chapter 8) are described. This includes the Antarctic IO CE-DOAS, the Amundsen LP-DOAS and a mobile MAX-DOAS instrument.

4.1 Antarctic IO CE-DOAS instrument

To investigate possible local sources of IO, an open-path CE-DOAS instrument was desired. Previously, a device had been built and tried at Neumayer station in Antarctica in 2011 but revealed a multitude of problems which had to be addressed for successful future measurements (Martin Horbanski, Udo Frieß, personal communication, 2012). Therefore the existing instrument was extensively modified. Apart from the resonator mirrors, the embedded PC and the two cases, all major parts were replaced. Used commercial components are listed in table 4.1, other components were custom-made. The objective was that the instrument would be capable of operating down to -40 °C and above, and be able to retain the optical alignment during, often bumpy, transportation in the field by e.g. track vehicles and snowmobiles.

The general layout of the instrument is as shown schematically in figure 4.4. The core of the device is formed by two dielectric mirrors (1 inch diameter) with a reflectivity of 99.98% at 445 nm, where IO shows several absorption bands and absorption path lengths of 4 km to 6 km can be achieved under field conditions. A picture of the actual device is shown in figure 4.1. It consists of two polycarbonate boxes, each containing one mirror side of the resonator, which are mounted on a 2 m long aluminum rail. For transportation purposes, the rail is cut into two 1 m long parts, which are connected by a screw to a cubic

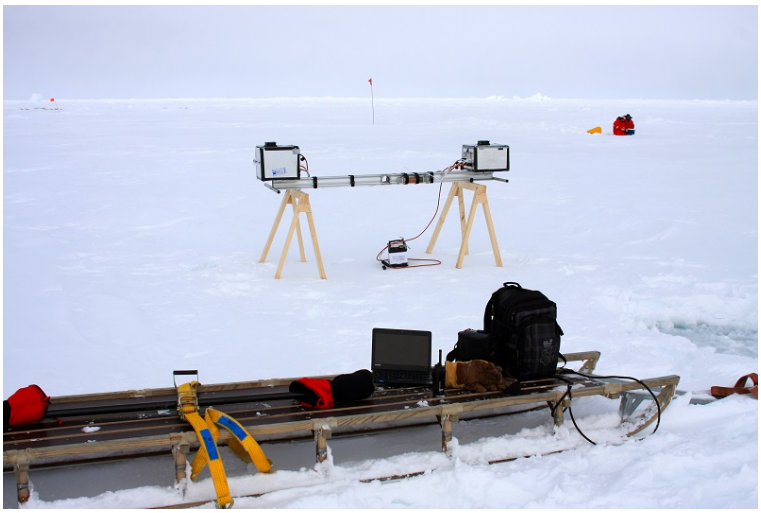

Figure 4.1.: Picture of the CE-DOAS instrument, as used during the field work, on wooden stands. It consists of two boxes, each housing one side of the resonator, linked by an aluminum rail. Here, the device is powered by a gel lead-acid battery and controlled wirelessly by a laptop computer.

mount. At both ends of the rail, handlebars can be attached to facilitate the transportation in the field. Between the rail mount and the optic plate inside each box, a 40 mm thick spacer made from polyoxymethylene (POM) was placed. POM has a high degree of stiffness but a very low heat conductivity compared to metals. The distance between the two resonator mirrors is 190 cm, less than the 200 cm focal length of the mirrors and therefore in the stable resonator regime (Horbanski, 2010). The actual open path in the atmosphere between the two boxes is 162 cm long. The interior of both boxes is insulated and the inner air temperature is stabilized by Peltier elements in the top covers.

Light from the LED (peak wavelength 440 nm) is coupled into the resonator by a lens with 25 mm focal length and out of it via a 75 mm focal length lens into a 1 m long 400 μm fused silica mono fiber. The fiber is connected to the spectrometer which is an Avantes AvaSpec with 75 mm focal length, a 100 μm entrance slit, f/number of 7.1, 16 bit ADC and a spectral resolution (FWHM) of 0.53 nm at 445 nm.

The resonator mirror sockets mounted on the inner rail are mechanically decoupled from the outer outlets by a gap of approximately 5 mm which is closed airtight with PTFE foil. The outlets on both sides have an indentation to allow a purge tube to be mounted in-between, isolating the light path from the surrounding atmosphere. This is needed to acquire path length calibrations, the reference spectra and during periods with inclement weather. Two light and stiff carbon fiber tubes are used to avoid bending and shading the light path. In the middle, they slide into each other, with the thinner one having an outer diameter of 32 mm, which equals the inner diameter of the thicker one. Near the center of the purge tube, a small hole is placed to allow the purge air or helium to vent.

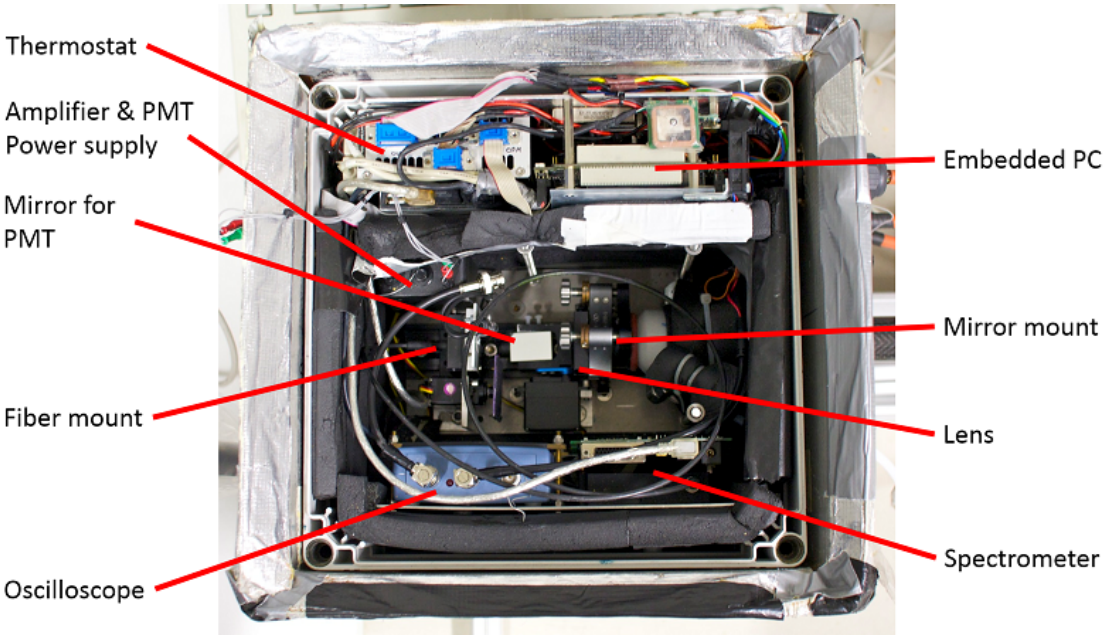

Figure 4.2.: View into the spectrometer box from above with the light path to the right. The module containing the PMT and amplifier is sitting above the mirror mount when mounted, here it is removed to allow a view underneath.

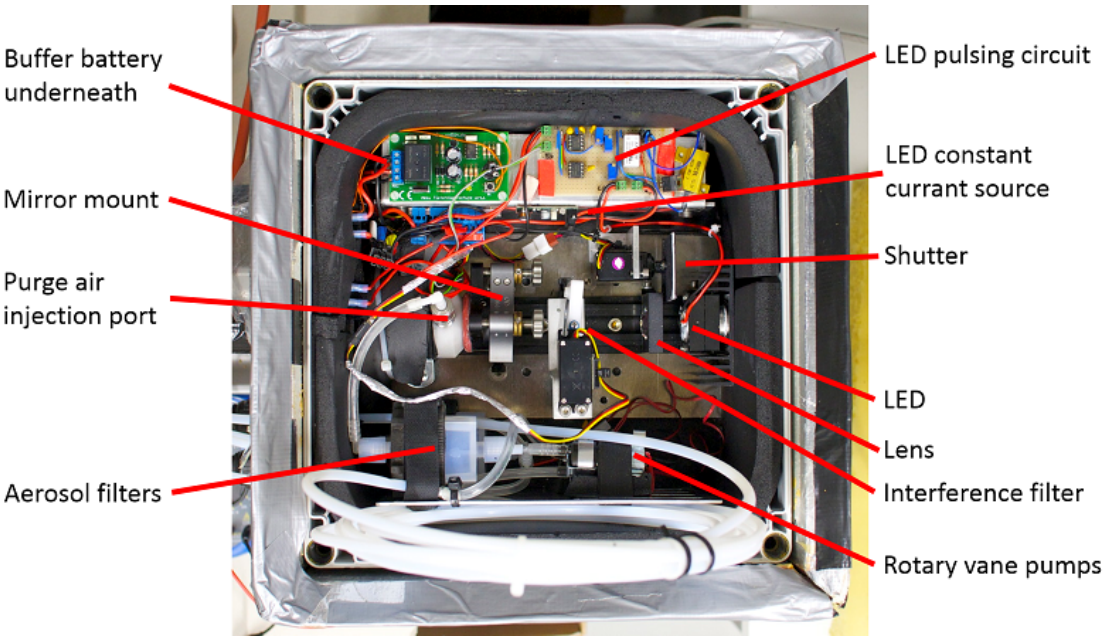

Figure 4.3.: View into the LED box from above with the light path to the left. At the bottom, a loop of several meters of tubing can be seen, used to warm up air before purging the mirrors.

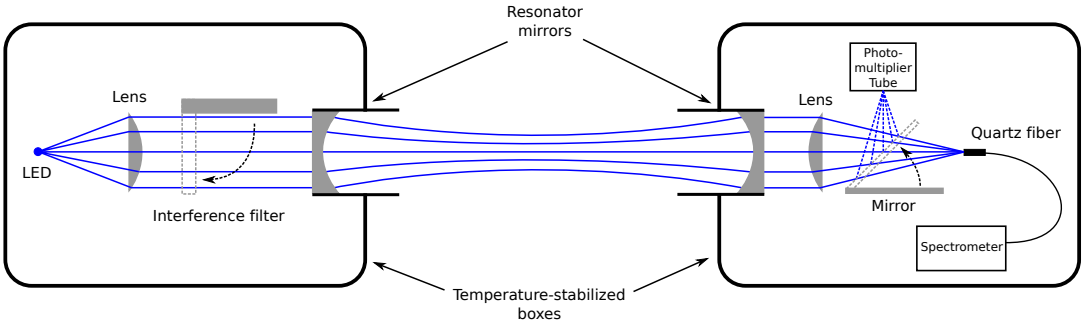

Figure 4.4.: Schematic drawing of the CE-DOAS setup consisting of two boxes, each containing one resonator mirror, which are mounted on an optical rail. The atmosphere in between the two boxes is probed. One side contains the light source and the interference filter for ring-down calibrations, the other box the spectrometer, and a photomultiplier tube also for the path length calibration.

The resonator mirrors are constantly flushed with purge air to avoid particles from snow or dust from settling onto the mirror surfaces. For this, two rotary vane pumps, one for each resonator side, suck air through a drying cartridge containing silica gel and PTFE aerosol filters at $3.6\,\mathrm{l\,min^{-1}}$. To be able to inject helium into the purge tube for path length calibrations, a bypass connection is routed out of the case. The pumps have a lifetime of at least 3000 hours (GD Thomas, personal communication, 2013) and are rated for -30 °C. The cold air led the membranes of earlier used membrane pumps to become brittle and rupture. PTFE tubing is used for the purge and helium flow as PTFE is still flexible at low temperatures.

The external wiring was changed to silicone sheathed cables, which are still flexible at extremely low temperatures (-50 °C and less). Further features are a 2.3 Ah lead acid buffer battery to be able to switch power supplies during operation, a GPS receiver for accurate position data and time, a wireless transmitter for connectivity with laptop computers to avoid the use of cables. For purposes of wavelength calibration, a krypton lamp is mounted next to the fiber and a diffuser plate can be driven in front of the fiber to reflect the light into the fiber. This diffuser plate is also used to record dark spectra. The LED can be darkened with a shutter, which is used to record background spectra.

4.1.1 Wavelength-resolved ring-down calibration system

In addition to the possibility to conduct path length calibrations with helium, a wavelength-resolved ring-down calibration system was developed and implemented. The system is based on the one described by Anthofer (2013), which is not wavelength-resolved and pictures schematically in figure 4.4.

For this, a wavelength discriminating element is needed in the setup. A simple, yet sufficient method is to exploit the angular dependence of the transmission curve of an interference filter (see Pollack, 1966). Two filters were tested and

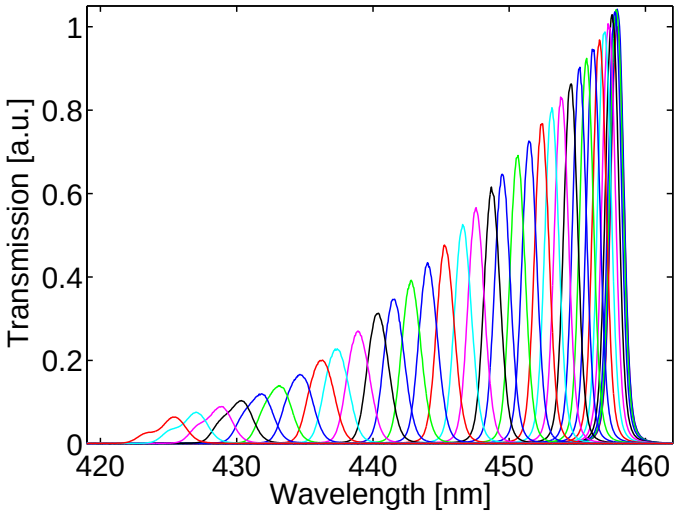

Figure 4.5.: The measured transmission of the interference filter with nominal center wavelength at 457.9 nm under different angles of incident light. Transmission curves are shown for tilt angles from 0 ° (orthogonal) to 35 ° in steps of 1 °. Graph reproduced from Zielcke et al. (2013).

used, both from the same product line with a nominal spectral transmission curve width of 1.0 nm (FWHM) and 50 mm diameter. One with a center wavelength of 441.6 nm and a transmission of 35%, the other one with a center wavelength of 457.9 nm and a transmission of 40%. Figure 4.5 shows the measured transmission spectra of the 457.9 nm filter depending on the angle of the incident light. The further the filter is tilted, the lower the transmitted center wavelength. However, the transmission peak is broadened at the same time and the transmission is reduced as well.

To record ring-down curves, a mirror has to be driven into the light path, reflecting the light exiting the resonator onto a photomultiplier tube (PMT). The PMT is attached to an amplifier, which is connected to a small USB oscilloscope. The oscilloscope is read out by the embedded PC. The amplifier is a replica of the three-stage design by Anthofer (2013), of which only the first two stages are necessary to use, providing a gain on the order of 10^7. The maximum sensitivity of the utilized PMT is at 400 nm. A BG25 band pass filter is placed directly in front of the PMT to block off light with wavelengths higher than 470 nm. The LED can be switched to a pulsed mode, in which it is turned on and off with a frequency of 8.7 kHz.

A LabVIEW interface provided by Martin Horbanski (personal communication, 2012) is used to control the tilt angle of the filter, record data from the oscilloscope, average data, fit the model function and write out the results.

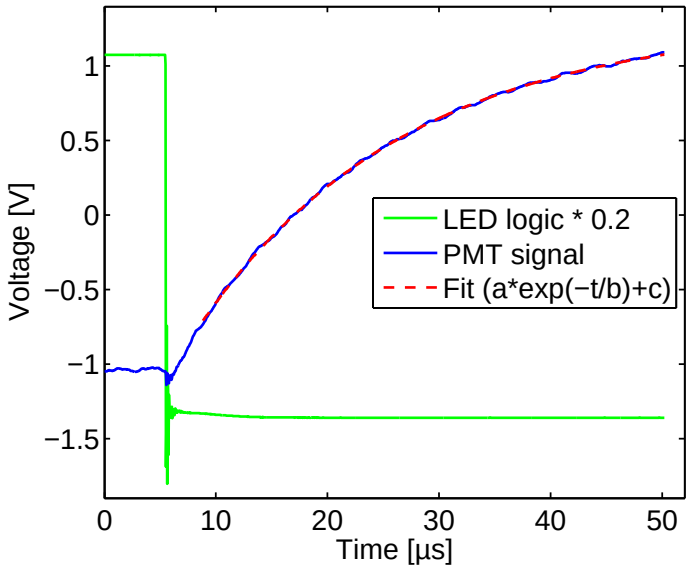

Figure 4.6.: Example of a recorded ring-down curve and the corresponding model fit, indicating a path length of 5607 m. In green the logic signal to the LED driver is shown (high: LED on), in blue the signal at the PMT amplifier output. Time 0 is the time when the oscilloscope starts the recording (pre-triggered).

Calibration routine

The path length calibration using this method is done as follows. For a select number of wavelength windows at which ring-down signals are to be taken, the interference filter is driven by its servo to the desired positions and spectra are acquired. This yields a mapping of servo position to transmitted center wavelength. Then, the LED is switched to pulsed operation and, for all the selected servo positions, ring-down signals are recorded, of which 1000 are averaged. Usually, 3 sets are taken for each position in order to determine their standard deviation as measure of precision. The wavelength calibration of the spectrometer is done using krypton emission lines of which there are several in the region of interest. Finally, combining the path lengths gotten from fitting the model function to the signals with the servo position to wavelength mapping from the spectra, followed by fitting a polynomial (3rd or 4th order) to the data points, the wavelength-resolved calibration curve is derived. An example of a recorded ring-down curve, and the exponential function fit to it, is shown in figure 4.6.

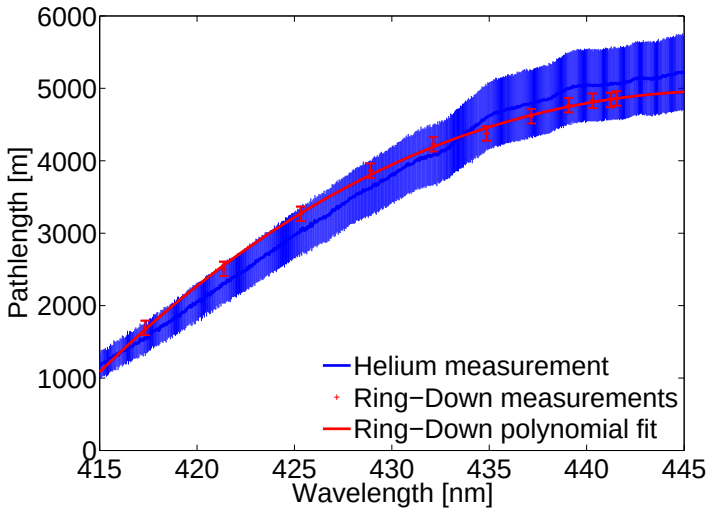

Figure 4.7.: A comparison of path length curves derived from the helium (in blue) and the ring-down methods. The individual ring-down measurements are shown in red with their standard deviation (3 samples per point), along with a 3rd order polynomial fit (red line). Errors of the helium calibration are estimated based on intensity fluctuations of the LED.

Comparison with helium method

A comparison of the results of this new technique and the other, more established one using helium is shown in figure 4.7. Both methods agree within the errors which are rather large, especially for helium. The errors given for the ring-down measurement are the standard deviation from 3 individual measurements and therefore only reflect statistical errors not systematic ones. The errors of the helium calibration were estimated from the fluctuation of the intensity of the LED and therefore also neglect systematic errors such as incomplete flushing of the purge tube with air or helium. Until now, the errors in the path length dominate the CE-DOAS measurement errors, therefore more work is needed in this area. In this thesis however, the accuracy turned out to be sufficient as will be evident in the result chapters.

This method has several important advantages over the helium method. For one, no pressurized gas cylinders with calibration gases are needed. As those cylinders are categorized as hazardous goods, apart from the weight, the transport into remote areas is often problematic. The method is also independent on the absolute light intensity during calibration runs, leading to much more robust and reproducible calibrations. Lastly, this method needs less time and can be easily automated. For all those reasons this method was the main calibration method used in this work.

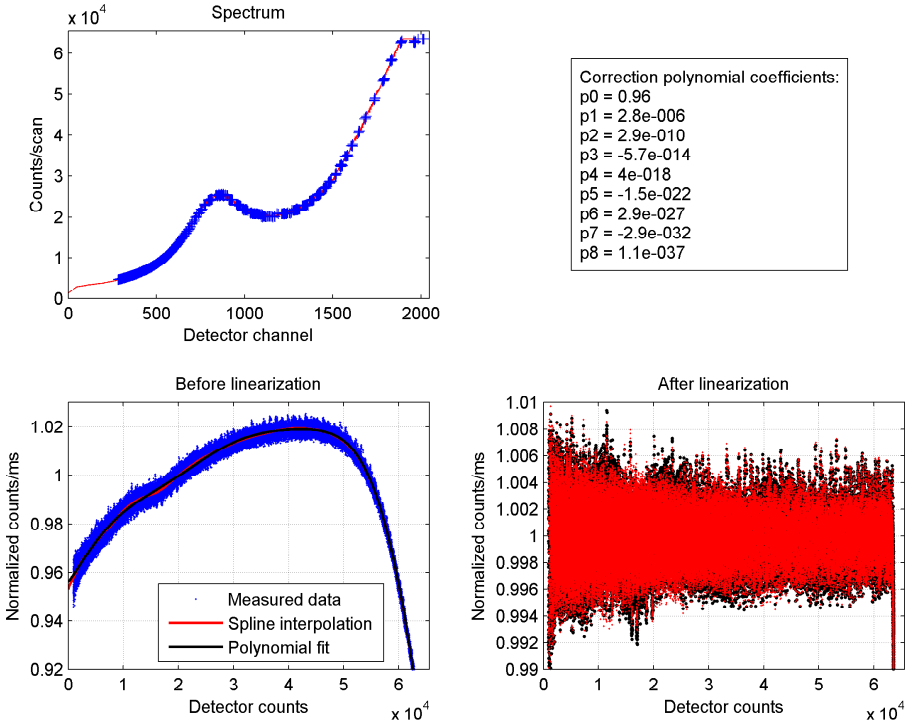

Figure 4.8.: Graph showing the result output of the determination of the non-linearity correction curve. Upper left: An exemplary spectrum showing the spectrometer channels included in the analysis as blue crosses. Lower left: The detection efficiency of the detector as a function of counts measured. At high exposure levels the efficiency drops significantly. Also shown are the polynomial and spline correction functions. Lower center: The same plot after applying the correction functions.

4.1.2 Spectrometer linearity

The linearity of the response of the spectrometer counts to the incoming light intensity was assessed using a measurement and evaluation routine provided by Martin Horbanski (personal communication, 2013). The linearity is especially critical for helium calibrations, as ratios of absolute intensities are compared in this method. As the LED in the instrument is temperature-stabilized and deemed stable enough, this test is simply done by recording spectra at different integration times and comparing that to a linear relationship. This was done for four consecutive runs to average over possible instabilities of the light source or optical setup. 500 spectra were acquired and averaged for integration times from 5 ms to 100 ms in steps of 1 ms.

The results of the analysis are shown in figure 4.8. The analysis also yields a correction polynomial and spline function. Due to the dip at around 18000 counts, an eighth order polynomial was necessary to find a correction function for the whole count range. This polynomial was then always applied to spectra before further evaluation in this work.

Figure 4.9.: The telescope of the LP-DOAS system. Photo courtesy of Denis Pöhler.

4.2 Amundsen LP-DOAS instrument

The LP-DOAS instrument used within this work had previously already been used, amongst other places, in polar environments in the Amundsen Gulf (Canada) and in Barrow (Alaska, USA) and has therefore already been extensively described in Pöhler et al. (2010) and Liao et al. (2011).

The system is set up as already shown in figure 3.6. The telescope consists of a spherical mirror with 150 cm focal length and 30 cm diameter on an azimuthal mount. The mirror is shielded by a 1 m long tube, which is flushed with purge air to prevent snow, dust etc. from depositing on the mirror. Two stepper motors drive the two axis of the mount.

Light is coupled in and out of the telescope through the use of a Y-shaped fiber optic bundle consisting of seven individual 200 μm fibers. The common end is mounted near the focal point of the telescope, the one central fiber is connected to the spectrometer and the six outer fibers are attached to a 800 μm mono fiber which leads to the light source. The distance of the fiber from the mirror near the focal point can be adjusted by a stepper motor. A diffuser plate can be driven into the light path in front of the telescope end of the fiber in order to record spectra of the lamp (so-called *optical shortcut*).

As light source, xenon arc lamps such as the 500 W PLI Hanovia HSAX5002 or the 75 W Osram XBO (non OFR) are coupled into the fiber using a single fused silica lens. The housing containing the lamps and the coupling also includes a motorized filter wheel, with which optical filters can be driven into the light path. Filters manufactured by Schott (all 2 mm thick) were used with the 75 W lamps,

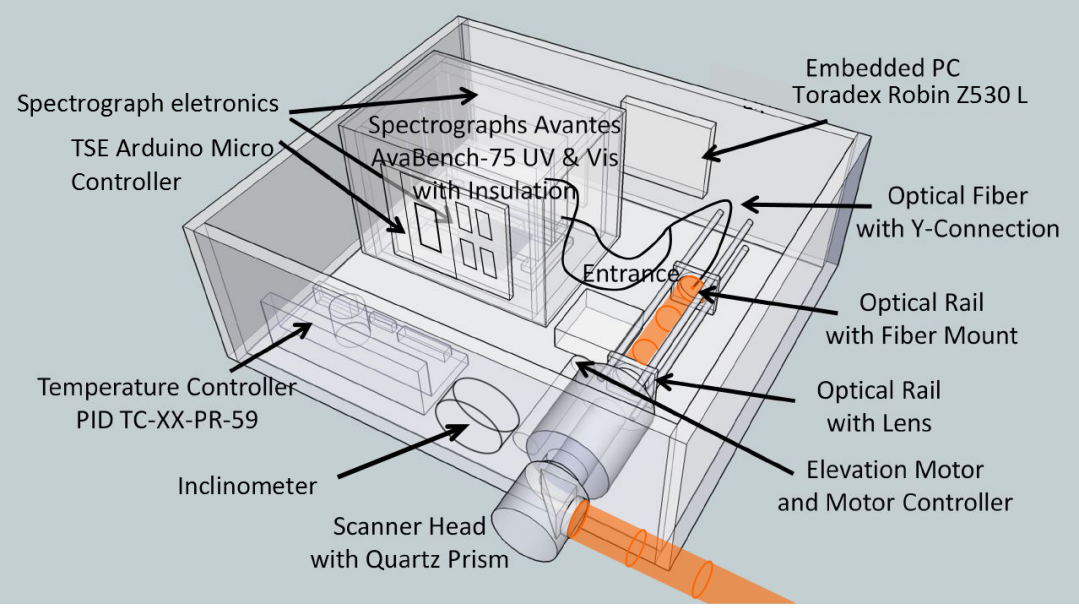

Figure 4.10.: Sketch drawing of the mobile MAX-DOAS instrument used in this work. Adapted from Nasse (2014).

a UG5 filter for wavelengths below 370 nm, a BG25 for the blue wavelength range (370 nm - 460 nm), a BG42 for 450 nm to 600 nm and a OG590 for higher wavelengths. For the 500 W PLI lamp, no filters were used as due to the strong light intensity and their strong local absorption thermal fractures of the filters occured within seconds. The lamp housing also features a shutter in front of the fiber coupling to block off the lamp, in order to be able to record background spectra with the telescope, i.e. spectra of the light entering the telescope due to scattering on the surface or air and not from the dedicated light source.

As spectrometer, an Acton 300i was used, which has a focal length of 300 mm and an f/number of 3.1. Its grating has a groove density of 600 mm^{-1} and a 300 nm blaze wavelength. With that a resolution of 0.50 nm is achieved. The grating turret is motorized, therefore the mapped wavelength interval can be adjusted by the software. The spectra are recorded by a 2048 by 512 pixel, back-illuminated CCD camera from Roper Scientific (Spec-10:2KBUV) in the full vertical binning mode.

The used retro reflector arrays consisted of 12 to 50 individual elements with a diameter of 63.5 mm each, depending on the length of the light path. They are pictured in figure 6.4 and in figure 8.6b.

4.3 Mobile MAX-DOAS instrument

The compact MAX-DOAS instrument was used before by Holla (2013) at the Dead Sea Basin, and is described and characterized in detail in that work. Here a

brief overview is given. A sketch drawing is shown in figure 4.10. The instrument features two spectrometers, an Avantes AvaSpec ULS2048x64 in the UV range from 295 nm to 450 nm and a ULS2048L-U2 in the VIS region from 430 nm to 565 nm. The optical resolution of the spectrometers is around 0.6 ° depending on the exact wavelength. The field-of-view of the telescope was determined to be 0.27 ° for the UV spectrometer and 0.32 ° for the VIS spectrometer (Holla, 2013). Both spectrometers are encased with insulation material and temperature stabilized by a Peltier element. Light is collected by a scanner containing a fused silica prism, and then reflected onto a lens (f = 100 mm) which focuses the light into an optical fiber bundle consisting of 7 individual 100 μm fibers. One single fiber is connected to the VIS spectrometer, the remaining 6 are used for the UV spectrometer. The elevation angle of the scanner is corrected for instrumental tilt by a capacitive inclinometer, with the precision of the correction estimated to be 0.5 ° at least (Nasse, 2014).

Some modifications were necessary to adapt it to the polar environment. Insulation was added inside the case and also attached to the outside of the housing. After major problems with the embedded PC (Lippert CRR-LX800) during the field work at Scott Base (chapter 6), the PC was changed to a newer one with more computing power (Toradex Robin Z530L) which proved to be stable during the measurements on RV Polarstern (chapter 8).

Part	**Model**
Spectrometer	Avantes AvaSpec ULS2048L-U2 (S/N 1104119U1)
Resonator mirrors	Advanced Thin Films R~99.98%, Run V6-176, A9-A12
LED	CREE XLamp XR-E bin D316 royal blue
Constant currant source (LED)	A1W HKO-KL50-1000
Housing	Ernsto Cubo O (OPCP303018T)
Outer rail	LINOS X95 system
Inner rails	OWIS 40 mm rail system
Mirror mounts	Newport gimbal mounts (U100-G2K)
Embedded PC	Lippert CRR-LX800 1GB RAM
Thermostat	OsTech PSx1
Rotary vane pumps	GD Thomas G12/02 EB
Servos	Hitec HS-5496MH
Servo controller	Micro Maestro (6 channel)
USB oscilloscope	PicoScope 2204
Photomultiplier tube (PMT)	Hamamatsu H6780-01
Interference filter	LOT Oriel 442FS02-50 & 458FS02-50
GPS	Navilock NL-402U
Relais card	Mattronik INDUSB5

Table 4.1.: List of manufacturers and model types of commercially available components used in the CE-DOAS instrument.

5

MAX-DOAS inversion sensitivity studies

For the inversion of the MAX-DOAS measurement data in this work, as mentioned in section 3.4.5, the HEIPRO implementation (Yilmaz, 2012) was used. While this implementation had been applied in previous studies (e.g. Holla, 2013; Lampel, 2014; Nasse, 2014), so far no (published) systematic studies of this algorithm or comparable ones for MAX-DOAS have been shown.

Therefore, in order to assess the validity and information content of retrieved vertical aerosol and trace gas profiles derived from ground-based MAX-DOAS measurements and its inversion algorithm, sensitivity studies were conducted. These were undertaken using simulated measurement data from synthetic profiles, with the fundamental advantage of simulated data being that the outcome of the retrieval algorithm can be directly compared to the true synthetic atmospheric state, which is unknown during real measurements. The general idea of the study in this chapter is pictured in figure 5.1.

From these studies, the influence of certain inversion parameters can be investigated. This not only allows to identify those parameters, whose values influence the resulting inversion results the most, but also makes it possible to optimize several of them.

Parameters, about which no information can be gained from the use of synthetic profiles are e.g. the absolute scaling of the O_4 absorption cross section, possible instrumental offsets of the elevation and azimuth angles and aerosol optical properties such as the single scattering albedo or the asymmetry parameter. Also errors in the radiative transfer model cancel out, as the measurements are simulated with the very forward model the inversion algorithm is based on (SCIATRAN 2, Rozanov et al., 2005).

These studies were conducted for both the aerosol inversion and the trace gas inversion at the example of BrO. The latter, however, is also applicable to

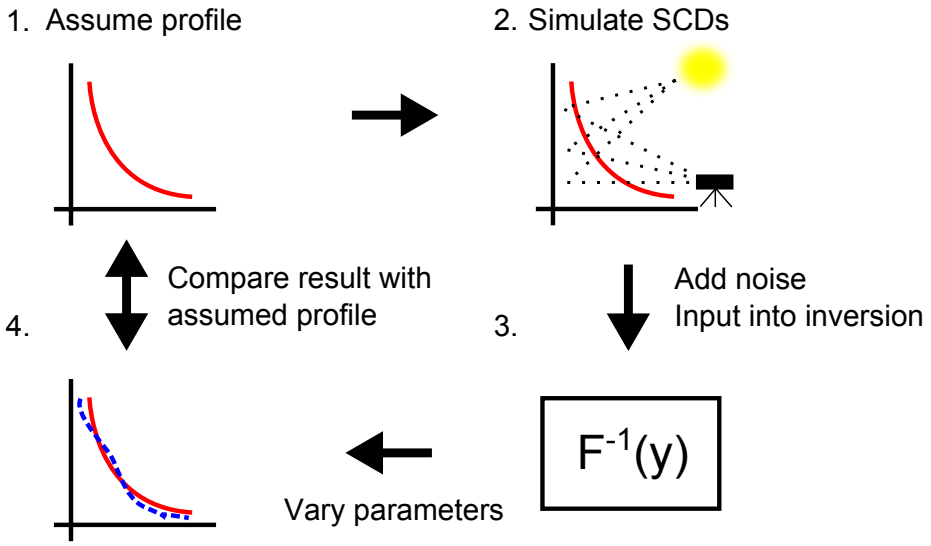

Figure 5.1.: Sketch of the basic idea behind the conducted sensitivity studies. Different profile shapes are assumed. For these, SCDs are simulated for a typical ground-based measurement geometry. Random noise within the bounds of typical measurement error was added to them before they were input into the inversion algorithm. Different parameters can then be varied and optimized to achieve a good reproduction of the known original profile, which was assumed at the beginning.

other absorbers with similar properties in terms of vertical distribution and the measurement signal-to-noise ratio. In the following, the sensitivity studies for the inversion of the aerosol extinction will be presented first, afterwards the ones for the trace gas inversion. At the end of the chapter a summary is given.

5.1 Aerosol inversion

In order to check the reproduction of the true atmospheric state by the measurement technique and the influence of certain inversion parameters, the outcome was analyzed on simulated measurement data for four synthetic scenarios. These, while simplified still realistic and shown in figure 5.2, are (1) a layer with a low mixing scale height of 0.2 km, (2) a layer with a higher mixing scale height of 0.7 km, (3) an elevated layer close to the ground at 0.5 km and (4) an elevated layer higher above ground at 1 km.

The parameters that were varied include different a priori profile settings (surface extinction, scale height, error), aerosol optical properties (single scattering albedo, asymmetry parameter), offsets of the telescope's elevation and azimuth angles, variation of the ground albedo, the cross section scaling, variations in temperature and pressure profiles and whether to recalculate the weighting functions for each and every iteration step or only once.

For this, SCDs were simulated for a given measurement geometry, then, random white noise within the error bounds of typical measurement situations within

this work was added to the SCDs. Afterwards the inversion was performed on those SCDs, with the assumed errors, and one parameter at a time was varied.

This was done for three different extinctions ("cases") for each of the four scenarios. In case 1 (C1), the largest extinction is approximately $0.05\,\mathrm{km}^{-1}$, in case 2 (C2) $4.0\,\mathrm{km}^{-1}$ and in case 3 (C3) $20.0\,\mathrm{km}^{-1}$.

5.1.1 Assumptions

The assumed measurement geometry is based on the situation of the instrument located at Alert (see chapter 7) and is as follows. The instrument is at 50 m altitude with a northerly viewing direction of 10 ° and a field-of-view of 0.4 °. The solar zenith angle is 60 °, the solar azimuth angle is 190 °. The sequence of elevation angles is 1 °, 2 °, 5 °, 10 °, 20 ° and 90 °. The errors of the simulated SCDs were taken from a typical clear day situation at Alert during May 2013 and were around $3 \cdot 10^{41}$ molec^2 cm^{-5}.

While these assumptions are based on the situation of the instrument at Alert, the conditions in chapters 6 and 8 are highly similar, and the studies here are therefore applicable to those situations as well.

5.1.2 Inversion settings

The basic settings used for the inversion are listed in table 5.1. Apart from the one parameter that was varied in each run, these were taken for each and every run. The names of the parameters in the table reflects their names as used in the HEIPRO configuration file. Table 5.2 gives an explanation for each parameter and their values. Exemplary averaging kernels are pictured in fig. 5.3.

5.1.3 Results

In the following, the results of the studies are presented. They are grouped first after the varied parameter into sections, after the different cases, i.e. aerosol extinction (low, medium, high) onto different pages, and further, on each page, into four figures for the four utilized synthetic profiles.

In the figures, the assumed, true profile is always shown as a dashed red line and the used a priori profile as a dashed black line. The other lines represent the different outcomes of the inversion.

In the legend of each figure, for each of the resulting inverted profiles, three numbers are given. First, the value set for the parameter that was varied in this specific run. These values are given in the way they were input into the HEIPRO inversion, which is described in table 5.2. The next number is the resulting χ^2 between the measured (i.e. simulated) and the modeled SCDs of the inversion. And lastly the degrees of freedom for signal d_s is given, as a measure of the information drawn from the measured SCDs into the result. Studies of further parameters not presented here can be found in the appendix (A.1).

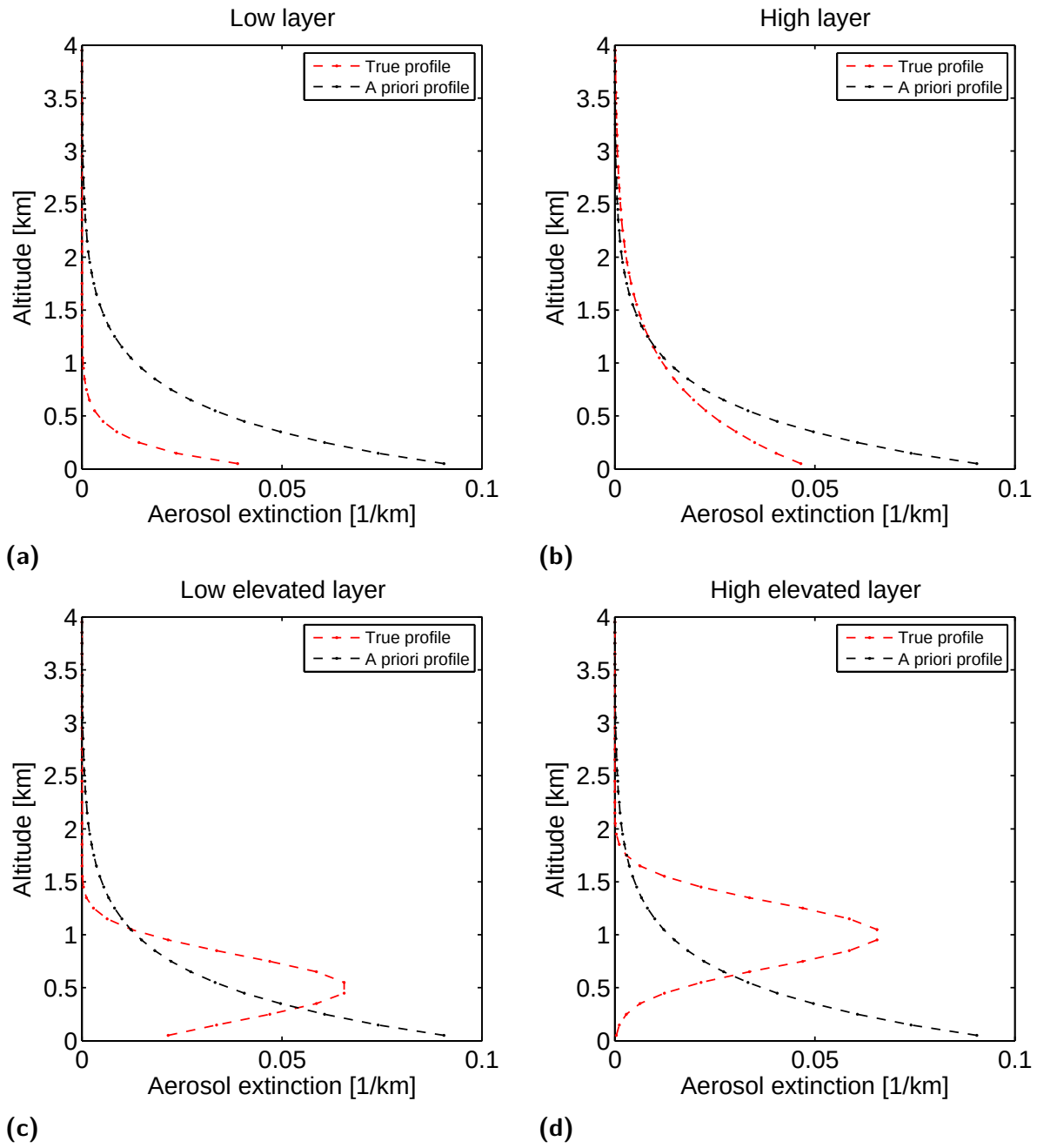

Figure 5.2.: The four synthetic vertical aerosol extinction profiles, shown in red, that were used to simulate SCDs, onto which noise was added, and then fed into the inversion algorithm. The four profiles are based on cases that would be desirable to distinguish in measurements. **(a)** A layer very close to the ground, common during e.g. blowing snow events **(b)** A layer with a larger scale height **(c)** A low cloud-like layer **(d)** A cloud-like layer further up.

Parameter	Value	Parameter	Value
A priori profile error	500%	Only variance	false
Albedo at 360 nm	0.8	Parameter 1	0.2 km^{-1}
Ångström exponent	1.36	Parameter 2	0.4 km
Asymmetry at 360 nm	0.72	Number of runs	2
Correlation length	0.5 km	Safe state	true
Fix weighting function	true	Scale O_4 SCD error	1.0
Iteration steps per run	8	SSA at 360 nm	0.95
MPI latitude	85 °N	XS (O_4) scale	1.0

Table 5.1.: The base settings used for the inversion of the aerosol extinction vertical profiles. The parameter names are given as used in the HEIPRO algorithm. An explanation of their meaning and values is given in table 5.2.

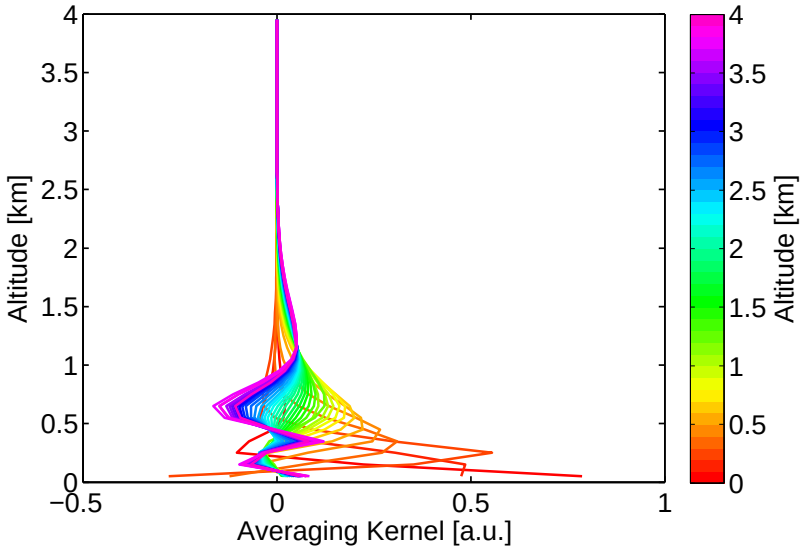

Figure 5.3.: Typical aerosol extinction averaging kernels (AKs) for a 100 m height resolution grid with inversion settings as listed in table 5.1. Ideally, the individual AKs would peak at their respective altitude which is indicated by the color bar.

		Page ref.	
Parameter	**Value given as**	**Aer.**	**BrO**
Fix weighting function	Boolean, recalculate WF for each iteration step	75	310
Runs	Number of inversion runs for one data set	304	318
Iteration steps	Number of max. iteration steps in one run	307	320
Elevation angle	Offset on the angle, given in degrees	96	122
Azimuth angle	Offset on the angle, given in degrees	99	124
Parameter 1	A priori profile surface extinction (km^{-1}) or mixing ratio (ppm)	78	114
Parameter 2	A priori profile scale height in km	81	116
A priori error	Relative as percentage of the a priori profile value	84	118
Scale SCD/O_4 error	Factor with which to multiply the error	286	316
XS scale	Factor with which to multiply the O_4 cross section	105	n/a
MPI latitude	Given in degrees latitude, e.g. 65n equals 65 °N	102	322
Correlation length	The correlation between different altitudes of the a priori profile, given in km	289	312
Albedo	Ground albedo, 0 - 1	87	120
Ångström exponent	Value of the exponent, with relative error	-	-
Asymmetry at 360 nm	Value of the asymmetry parameter, with relative error	90	-
SSA at 360 nm	Value of the single scattering albedo, with relative error	93	-
Safe state	Transform measurements into a safe state	298	-
Only variance	Use only variance or also covariance (the magnitude of which is set by the correlation length)	295	314
Use retrieved aerosol	Boolean, assume a pure Rayleigh atmosphere	n/a	126

Table 5.2.: List of the meaning and possible values of the parameters which are used in the HEIPRO algorithm and in the result plots. The page number of the first case figure for each studied parameter is also listed for the aerosol and trace gas (BrO) inversion for reference.

Fix weighting function

This option determines whether the weighting functions **K** are calculated for each iteration step of the inversion or only once at the beginning of one run. As they depend on the current aerosol extinction, i.e. the inversion result, they should always be recalculated. This, however, is extremely resource-consuming. Therefore, as stated above, two consecutive runs were conducted for each data set, where the weighting functions are updated after the first run as an approximation. The results are shown in figs. 5.4 (C1), 5.5 (C2) and 5.6 (C3). The chosen approach seems to be a valid approximation. In cases C1 and C2, the difference is minor, in C3 it is larger, however, with either of the two options, the inversion is deviating strongly from the true profile.

A priori profile parametrization: Surface aerosol extinction

Two values parametrize the a priori profile which decreases exponentially with altitude. The first a priori parameter sets the aerosol extinction at the surface. The second one sets the profile's scale height in km.

In this first test, the a priori surface extinction is varied from $0.05\,\mathrm{km}^{-1}$ to $1.0\,\mathrm{km}^{-1}$ in different steps. The output is pictured in figs. 5.7 (C1), 5.8 (C2) and 5.9 (C3). While values larger than $0.5\,\mathrm{km}^{-1}$ work for cases 2 and 3, at low extinctions they lead to strong artifacts. Smaller values around $0.2\,\mathrm{km}^{-1}$ have no issues in cases 1 and 2 and also work partly in case 3 (profiles a and d). Therefore this value was chosen.

A priori profile parametrization: Scale height

Here, the scale height of the exponential a priori profile is varied from 0.1 km to 1 km in steps of 0.1 or 0.2 km. The results are presented in figs. 5.10 (C1), 5.11 (C2) and 5.12 (C3). All of the elevated layers and some of the other profiles show, that if the scale height is too small (0.1 km - 0.2 km), the algorithm forces the observed aerosol to lower altitudes. This can be nicely seen e.g. in figure 5.10d. A very large scale height on the other hand, can lead to artifacts at higher altitudes where the measurement sensitivity is close to zero.

A priori profile parametrization: Profile error

In these runs, the assumed relative error of the a priori profile is varied from 50% to 1000%. The results are shown in figs. 5.13 (C1), 5.14 (C2) and 5.15 (C3). The error on the assumed a priori profile controls how much information from the measurements precipitates into the inversion result. This is also evident in the simulations - the larger the a priori error, the larger the resulting degrees of freedom for signal d_s.

The problem with very large errors is the resulting overfitting of the measurements which often leads to oscillations in the shape of the profile or runaway iterations as can be seen in case 3. Therefore, the error value has to be a compromise which depends on the signal-to-noise ratio of the measurements. For most applications, values from 200% to 500% are in a suitable range.

Albedo

In this test, the surface albedo is deviated from the simulated albedo of 0.8 from 0.1 to 0.95. The results are pictured in figs. 5.16 (C1), 5.17 (C2) and 5.18 (C3). The resulting effect can be large compared to that of most other parameters. Deviations on the order of a factor of 2, or even 3 are possible, especially in scenarios with low aerosol levels (see C1). With increasing aerosol loads, the radiative transfer is more and more determined by those and the effect becomes progressively smaller.

Aerosol optical properties: Asymmetry parameter

Here the Henyey-Greenstein asymmetry parameter is varied from the simulated one (0.72) within realistic bounds (0.60 - 0.84, e.g. Roedel and Wagner, 2011). The outcomes are presented in figs. 5.19 (C1), 5.20 (C2) and 5.21 (C3). The deviations from the true state are pronounced. The higher the aerosol extinction, the higher the possible deviation. In C1 the span between different resulting profiles is approximately a factor of 2, in C3 however already a factor of 5.

Aerosol optical properties: Single scattering albedo

In the test of the influence of the aerosol's single scattering albedo (SSA) at 360 nm, its value is varied from the simulated state of 0.95 in a range between 0.85 and 0.99, representative for typical atmospheric aerosols (e.g. Takemura et al., 2002). The findings of the runs are shown in figs. 5.22 (C1), 5.23 (C2) and 5.24 (C3). The difference in the resulting profiles is comparatively minor among all three cases no matter the amount of aerosol or its vertical distribution.

Telescope alignment: Elevation angle

In the algorithm an offset for the telescope's elevation angle can be entered. To study the effect of a skewed instrumental alignment, different angles from -1 ° to +1 ° from the real geometry were input into the inversion while the SCDs were simulated without any offset. Negative angles indicate that the telescope is looking further towards the zenith than assumed, positive angles that the light path is closer to the ground. The output is pictured in figs. 5.25 (C1), 5.26 (C2) and 5.27 (C3). It is apparent that the knowledge of the telescope elevation is crucial, especially in the case C1. Even an offset of 0.5 ° can lead to large qualitative and quantitative deviations from the true state. At higher extinctions this is less pronounced (except in fig. 5.27b), due to the nonlinearity of the aerosol inversion.

Telescope alignment: Azimuth angle

Here the instrument's azimuth angles are modified from the true state, from -20 ° to +20 °, values which are unrealistically large for most ground-based instruments, unless they are mounted onto a quickly moving and rotating platform, e.g. a ship or airplane. Positive angles indicate a viewing direction off the assumed axis in a counterclockwise manner. The results are given in figs. 5.28 (C1), 5.29 (C2) and 5.30 (C3). The difference in the resulting profiles is very small in all cases and for all profile shapes.

Atmospheric pressure and temperature profiles

The algorithm includes monthly averaged pressure and temperature profiles for different latitudes in steps of 10 ° from +90 ° to -90 °. As a proxy for deviations from these averaged profiles and other variations, two other ones were tried from neighboring latitudes. The results are shown in figs. 5.31 (C1), 5.32 (C2) and 5.33 (C3). The overall effect is very small. The larger the aerosol extinction however, the smaller the effect.

O_4 cross section scaling

Several recent studies have been claiming that the scaling of the magnitude of the O_4 laboratory cross sections is wrong by a factor on the order of 1.25 (e.g. Clémer et al., 2010). While this per se is not possible to test with the method described here, the results of an over correction can be studied, where a correction factor is applied but not necessary. Therefore the assumed scaling was varied from 0.75 to 1.5, while the SCDs where simulated with the normal scaling (1.0). The results are pictured in figs. 5.34 (C1), 5.35 (C2) and 5.36 (C3). The deviations of the outputs from the true profile can be very large for values higher than 1.0 and can lead to pathological, recurring structures (ghost clouds) in the results no matter what measurement data is input. If a scaling of

0.75 is used, the algorithm does not see any aerosol in case 1 and underestimates the aerosol extinction in cases 2 and 3.

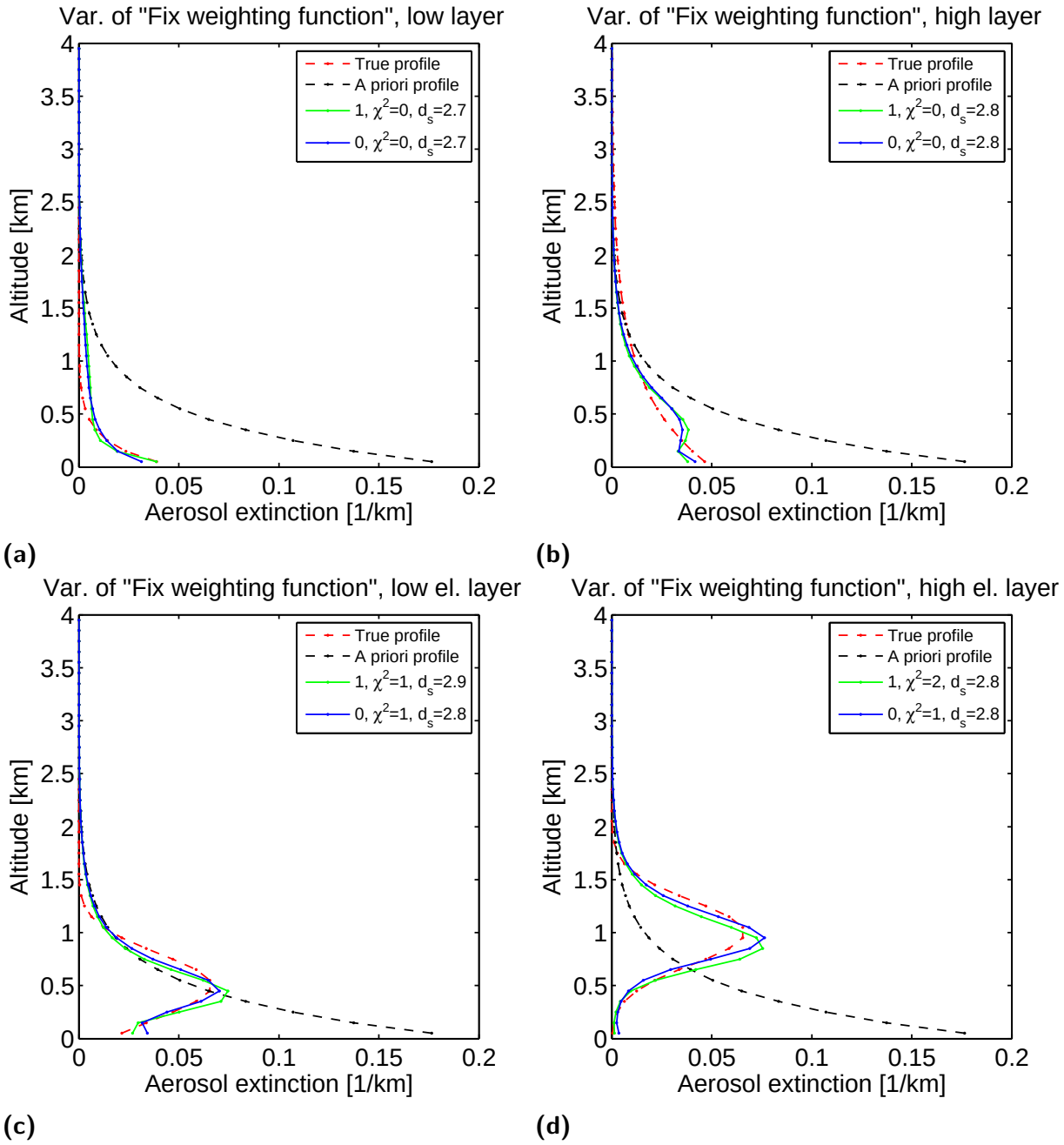

Figure 5.4.: Case 1 - Low aerosol extinction scenarios: Analysis of the effect of the recalculation of the weighting functions with every single iteration step. Two settings are possible: True (1) and false (0). For details of the method see section 5.1. The true profiles are the ones shown in fig. 5.2.

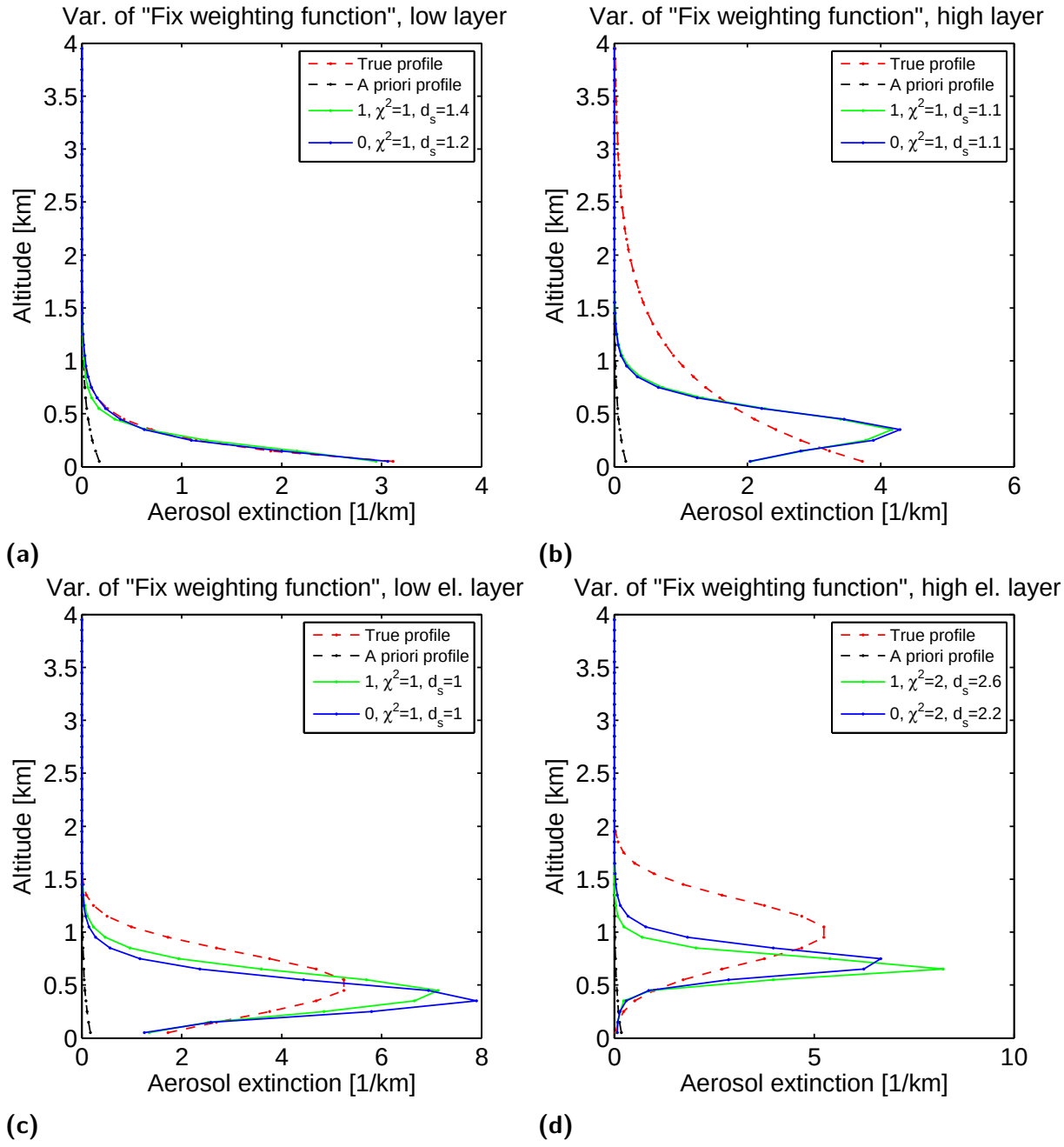

Figure 5.5.: Case 2 - Medium aerosol extinction scenarios: Analysis of the effect of the recalculation of the weighting functions with every single iteration step. Two settings are possible: True (1) and false (0). For details of the method see section 5.1.

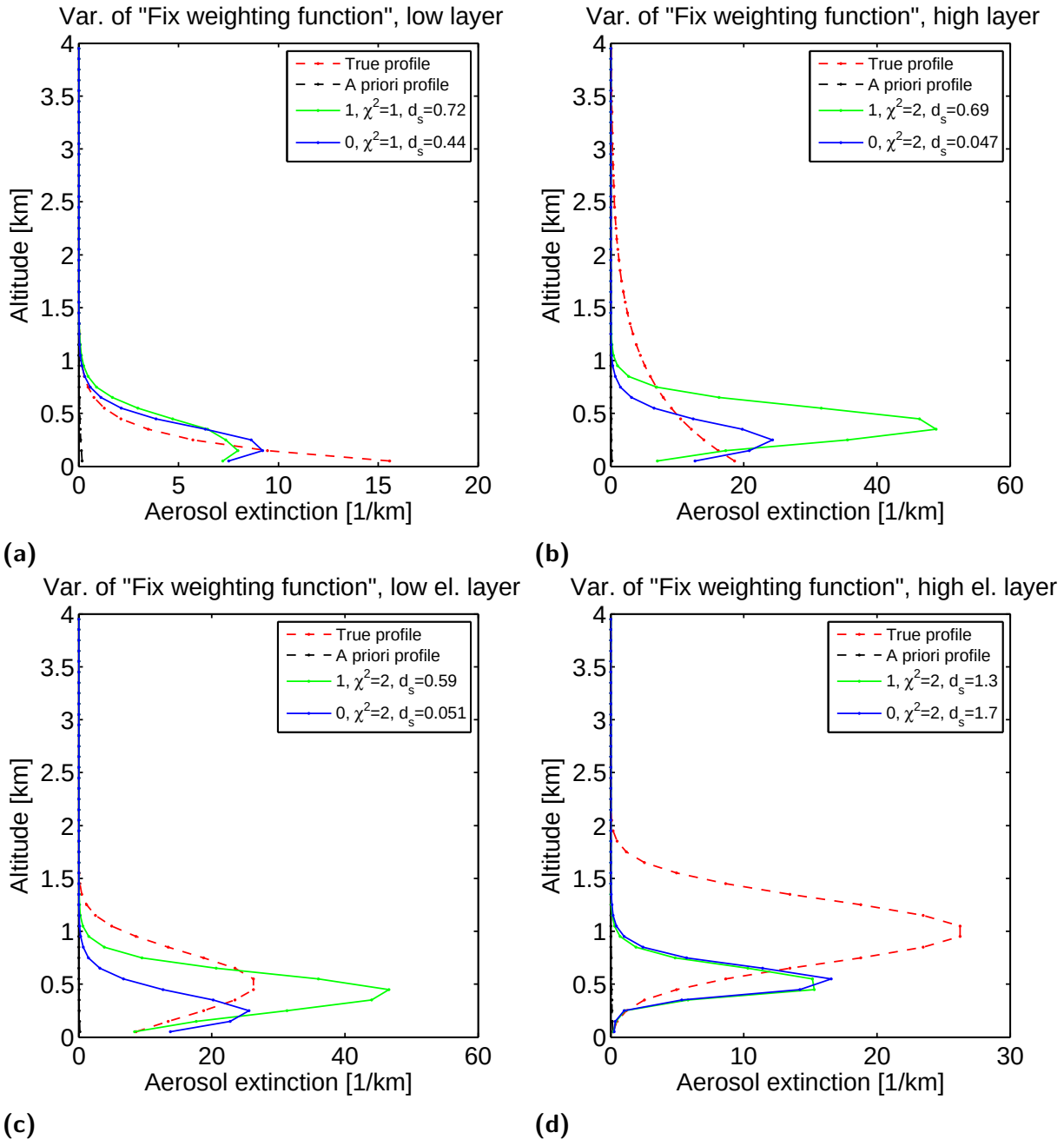

Figure 5.6.: Case 3 - High aerosol extinction scenarios: Analysis of the effect of the recalculation of the weighting functions with every single iteration step. Two settings are possible: True (1) and false (0). For details of the method see section 5.1.

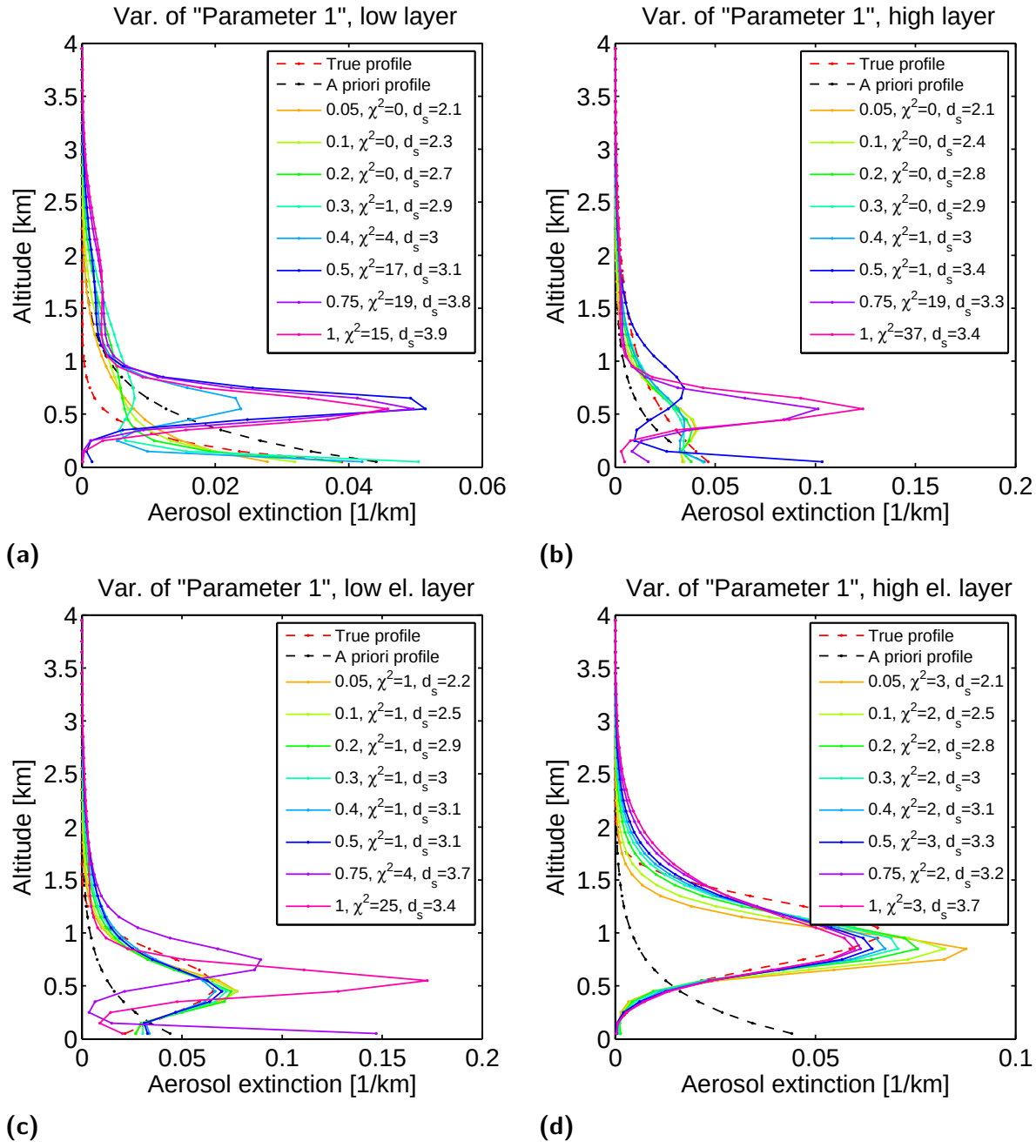

Figure 5.7.: Case 1 - Low aerosol extinction scenarios: Analysis of the effect of the used a priori profile surface aerosol extinction between $0.05\,\mathrm{km}^{-1}$ and $1.00\,\mathrm{km}^{-1}$. The indicated a priori profile is the one used in the first run, with $0.05\,\mathrm{km}^{-1}$ at the surface. For details of the method see section 5.1.

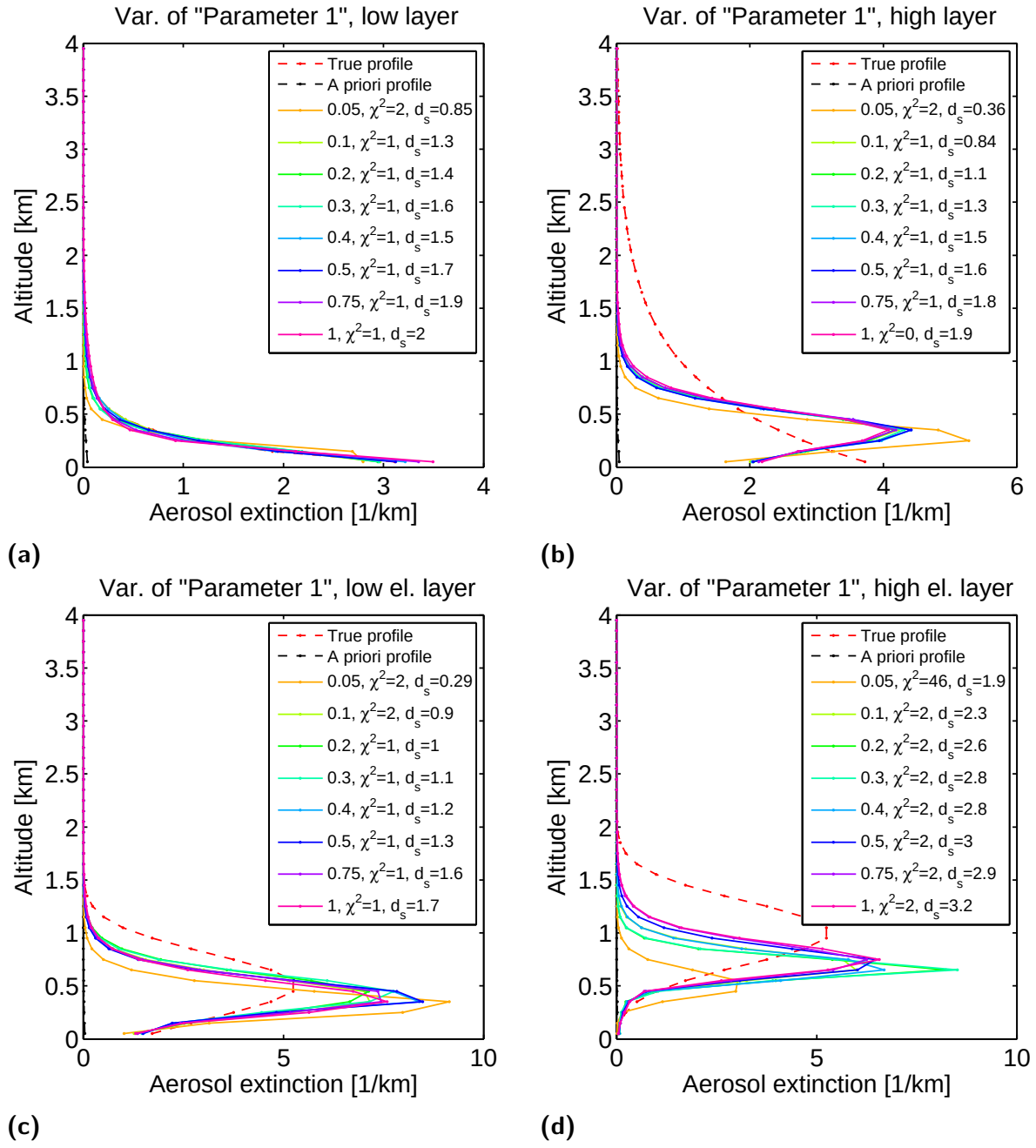

Figure 5.8.: Case 2 - Medium aerosol extinction scenarios: Analysis of the effect of the used a priori profile surface aerosol extinction between $0.05\,\mathrm{km}^{-1}$ and $1.00\,\mathrm{km}^{-1}$. The indicated a priori profile is the one used in the first run, with $0.05\,\mathrm{km}^{-1}$ at the surface. For details of the method see section 5.1.

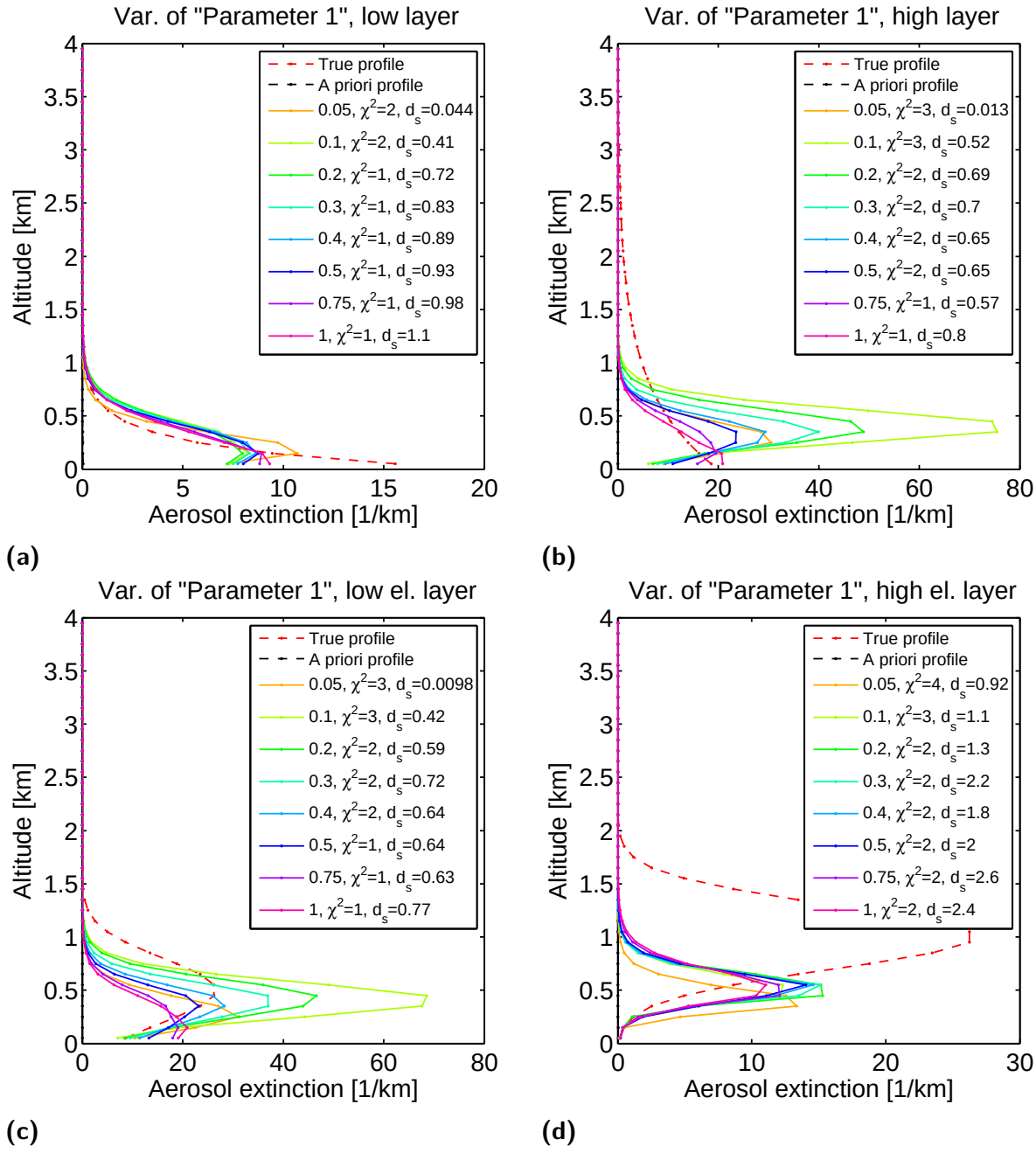

Figure 5.9.: Case 3 - High aerosol extinction scenarios: Analysis of the effect of the used a priori profile surface aerosol extinction between $0.05\,\mathrm{km}^{-1}$ and $1.00\,\mathrm{km}^{-1}$. The indicated a priori profile is the one used in the first run, with $0.05\,\mathrm{km}^{-1}$ at the surface. For details of the method see section 5.1.

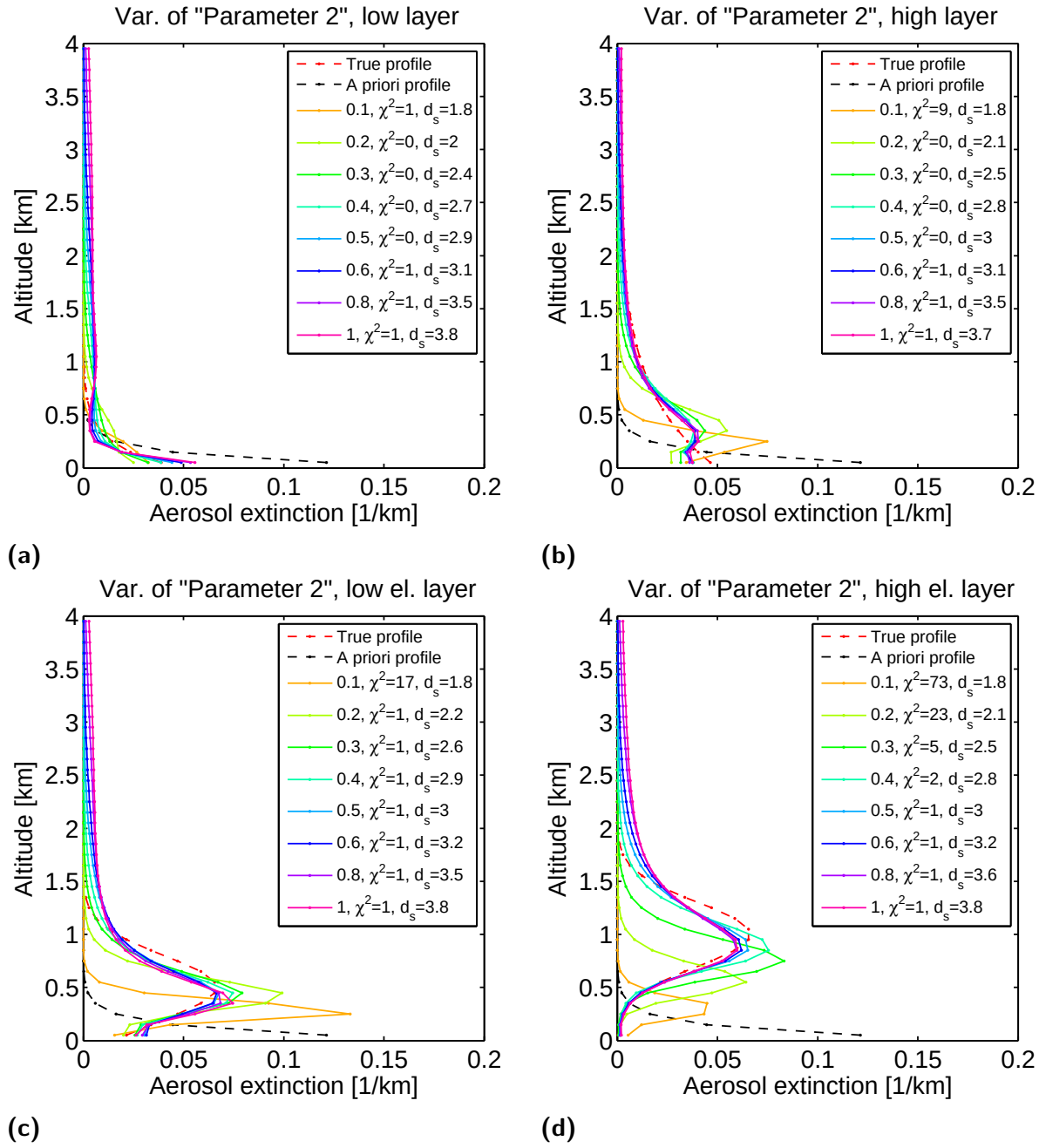

Figure 5.10.: Case 1 - Low aerosol extinction scenarios: Analysis of the effect of the scale height of the used a priori profile being varied between 0.1 km and 1.0 km. The shown a priori profile is the one used in the first run, with a height of 0.1 km. The scale height is indicated in km. For details of the method see section 5.1.

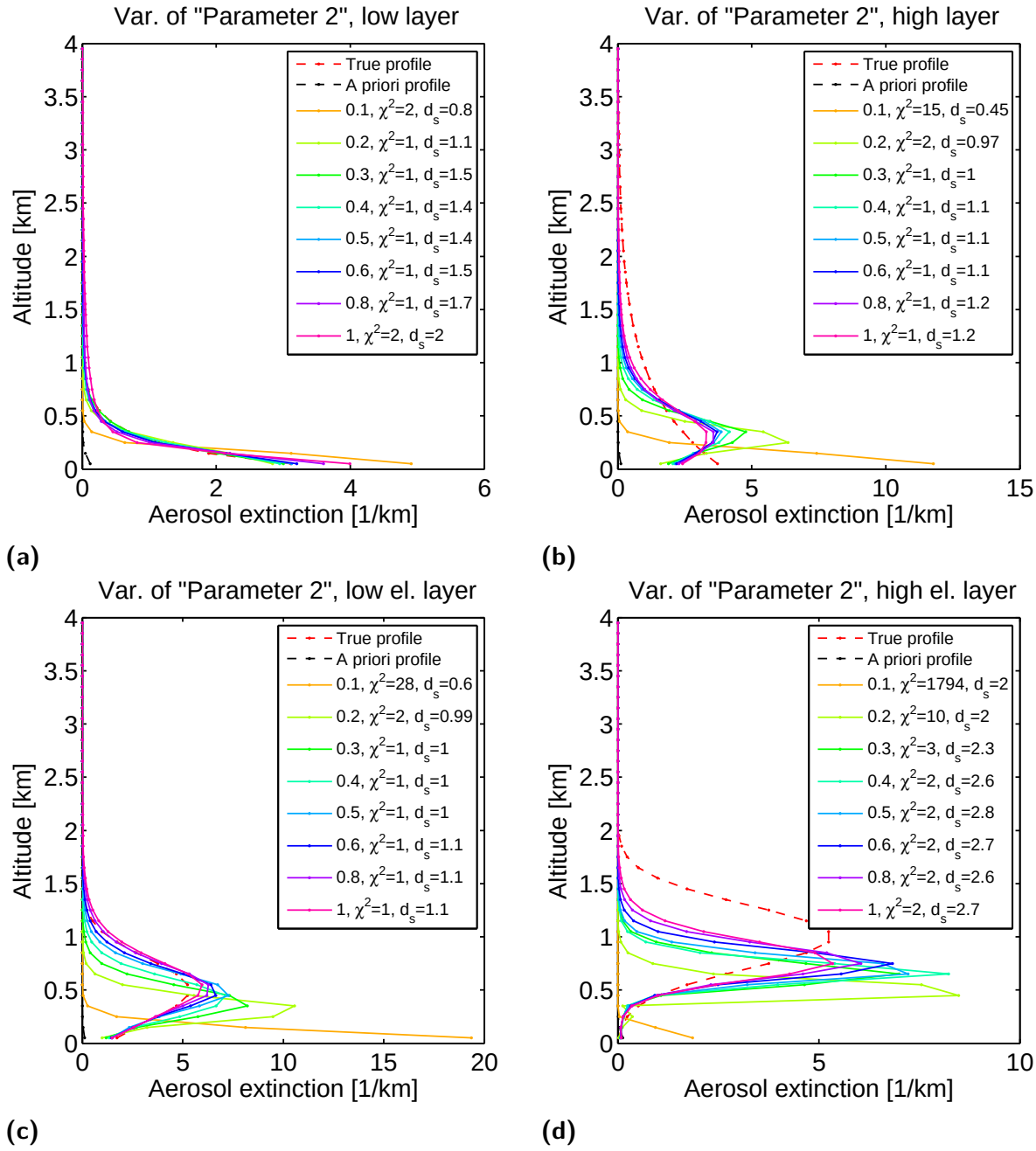

Figure 5.11.: Case 2 - Medium aerosol extinction scenarios: Analysis of the effect of the scale height of the used a priori profile being varied between 0.1 km and 1.0 km. The shown a priori profile is the one used in the first run, with a height of 0.1 km. The scale height is indicated in km. For details of the method see section 5.1.

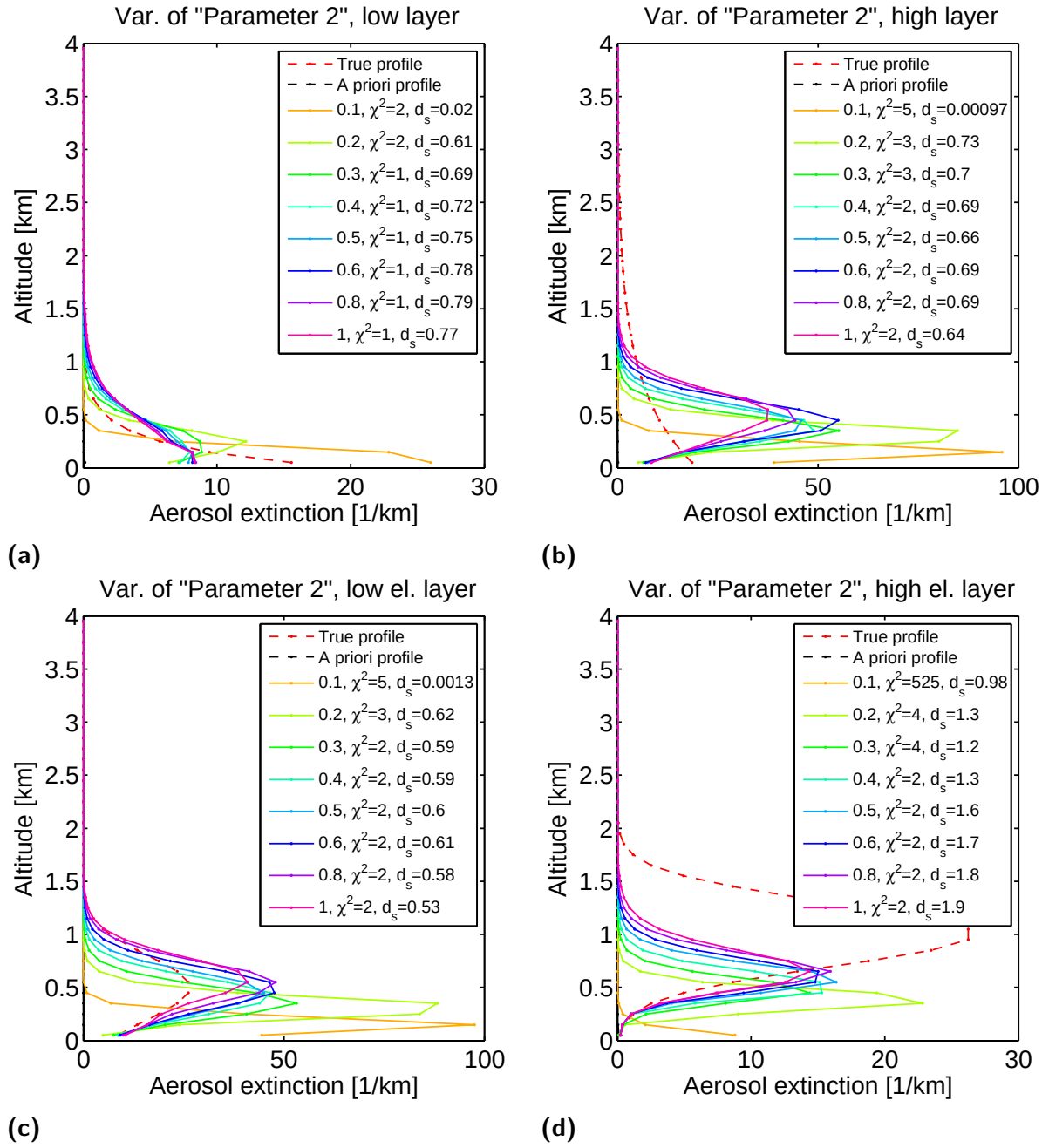

Figure 5.12.: Case 3 - High aerosol extinction scenarios: Analysis of the effect of the scale height of the used a priori profile being varied between 0.1 km and 1.0 km. The shown a priori profile is the one used in the first run, with a height of 0.1 km. The scale height is indicated in km. For details of the method see section 5.1.

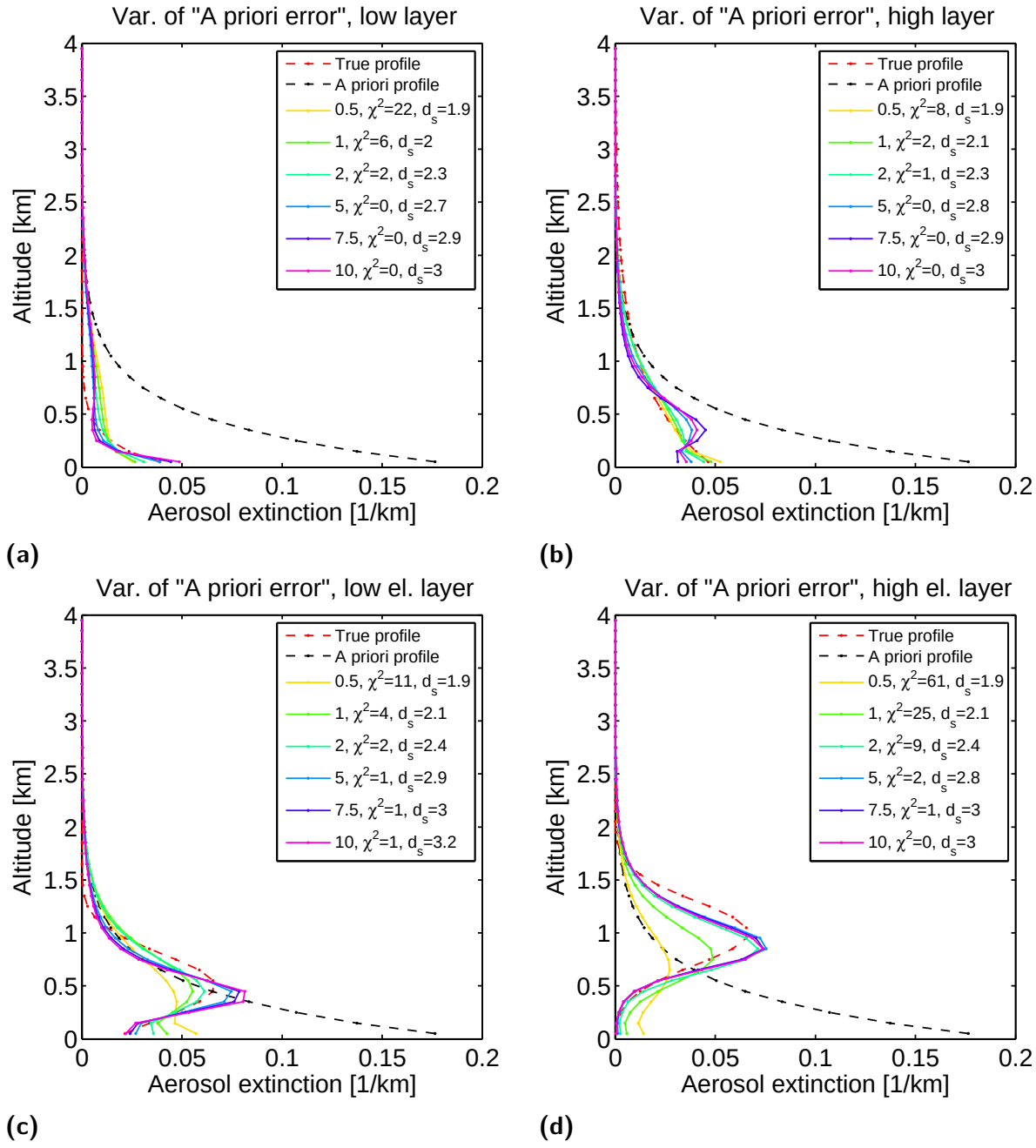

Figure 5.13.: Case 1 - Low aerosol extinction scenarios: Analysis of the effect of different values taken as the relative error for the a priori profile, from 50% (given as 0.5) to 1000% (given as 10). For details of the method see section 5.1.

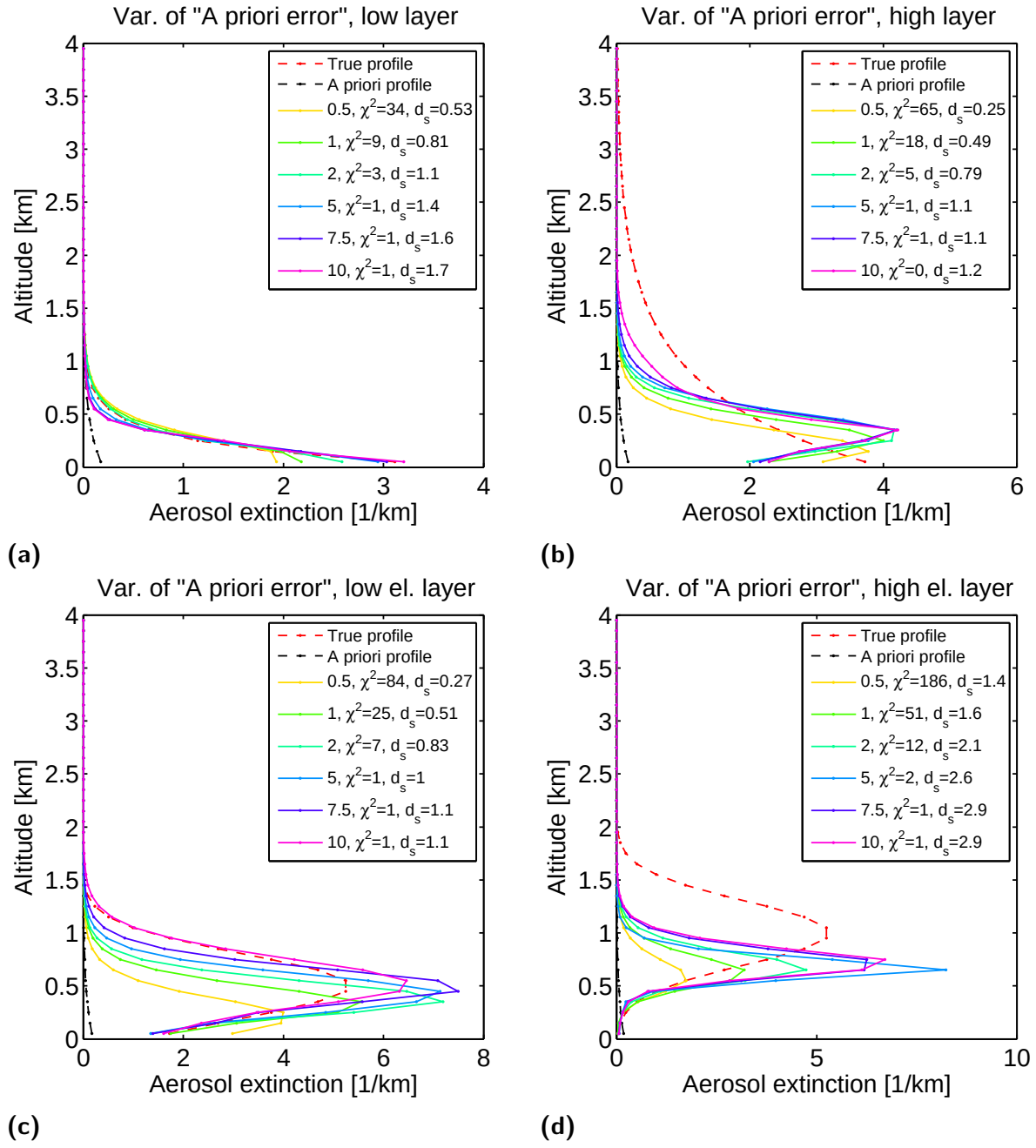

Figure 5.14.: Case 2 - Medium aerosol extinction scenarios: Analysis of the effect of different values taken as the relative error for the a priori profile, from 50% (given as 0.5) to 1000% (given as 10). For details of the method see section 5.1.

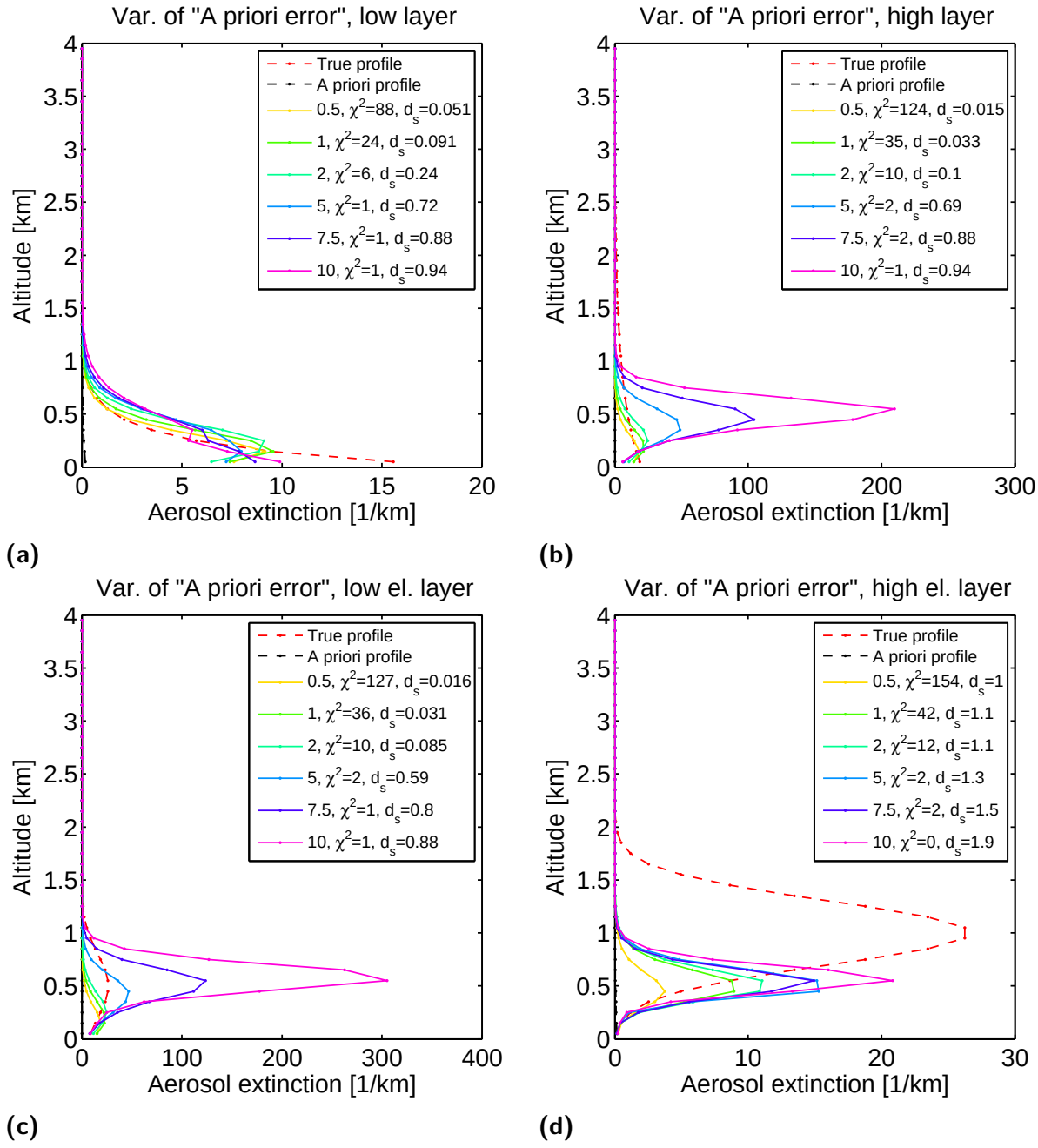

Figure 5.15.: Case 3 - High aerosol extinction scenarios: Analysis of the effect of different values taken as the relative error for the a priori profile, from 50% (given as 0.5) to 1000% (given as 10). For details of the method see section 5.1.

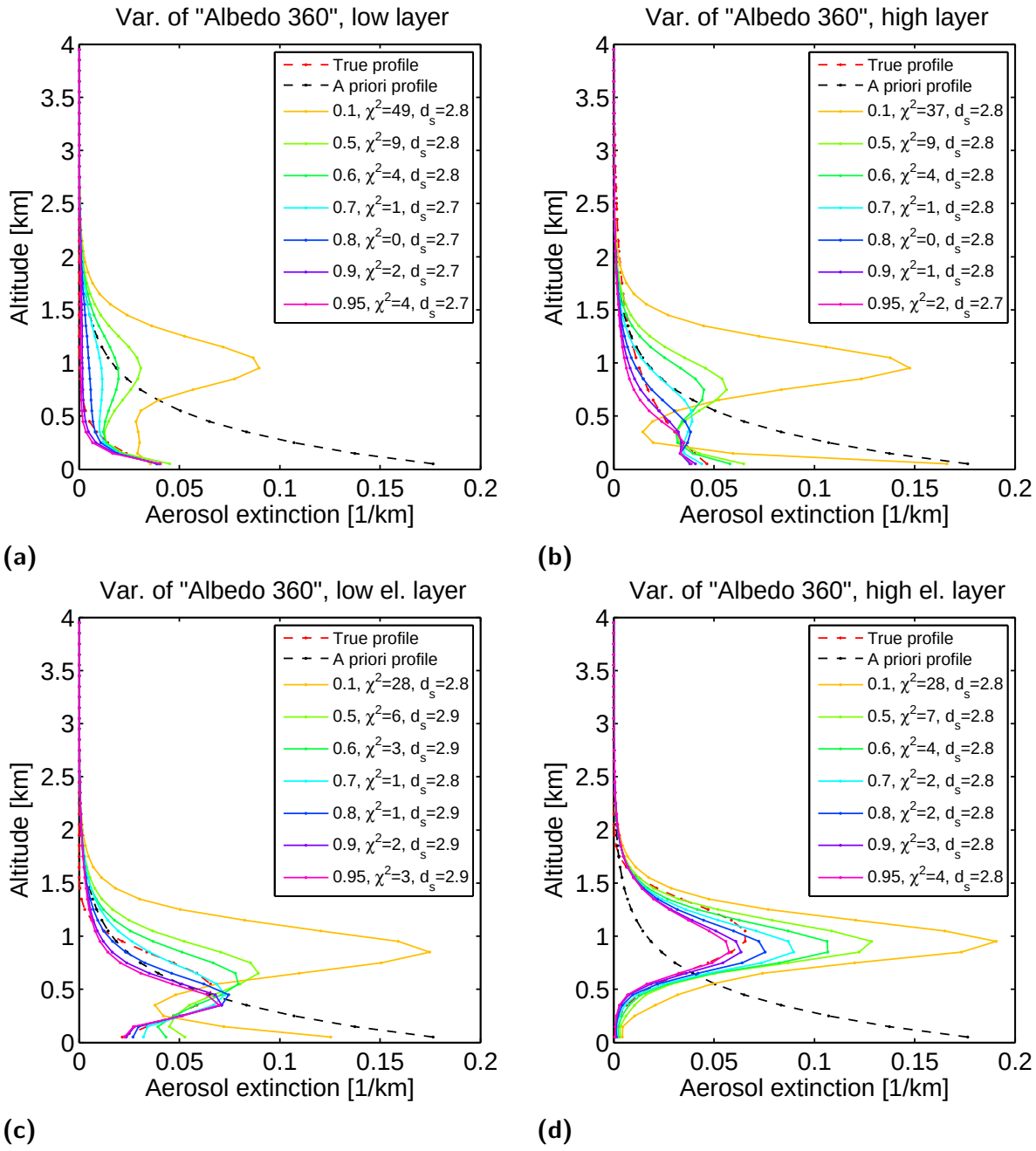

Figure 5.16.: Case 1 - Low aerosol extinction scenarios: Analysis of the effect of the assumed albedo for values from 0.1 to 0.95, with the true albedo being 0.8. For details of the method see section 5.1.

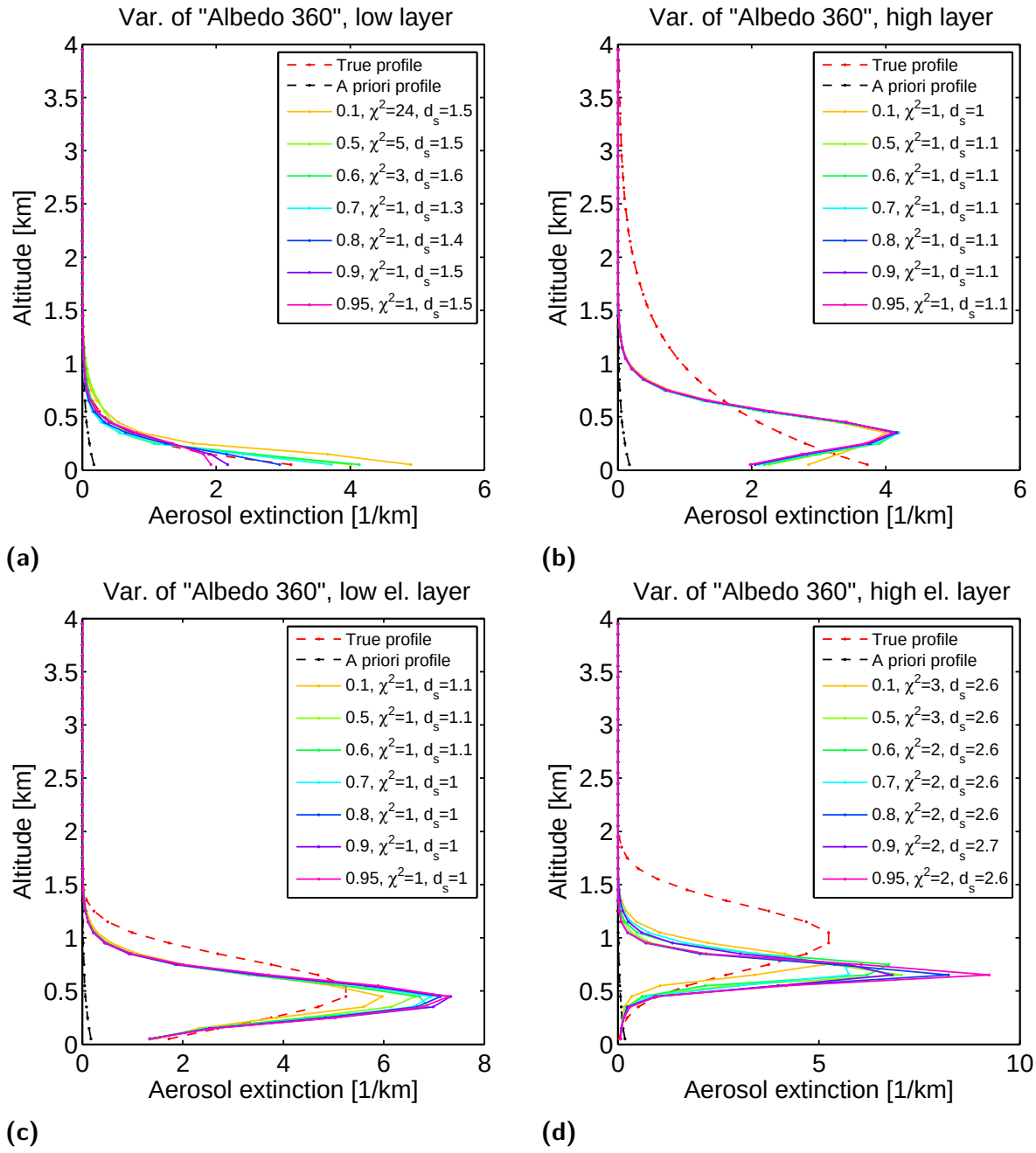

Figure 5.17.: Case 2 - Medium aerosol extinction scenarios: Analysis of the effect of the assumed albedo for values from 0.1 to 0.95, with the true albedo being 0.8. For details of the method see section 5.1.

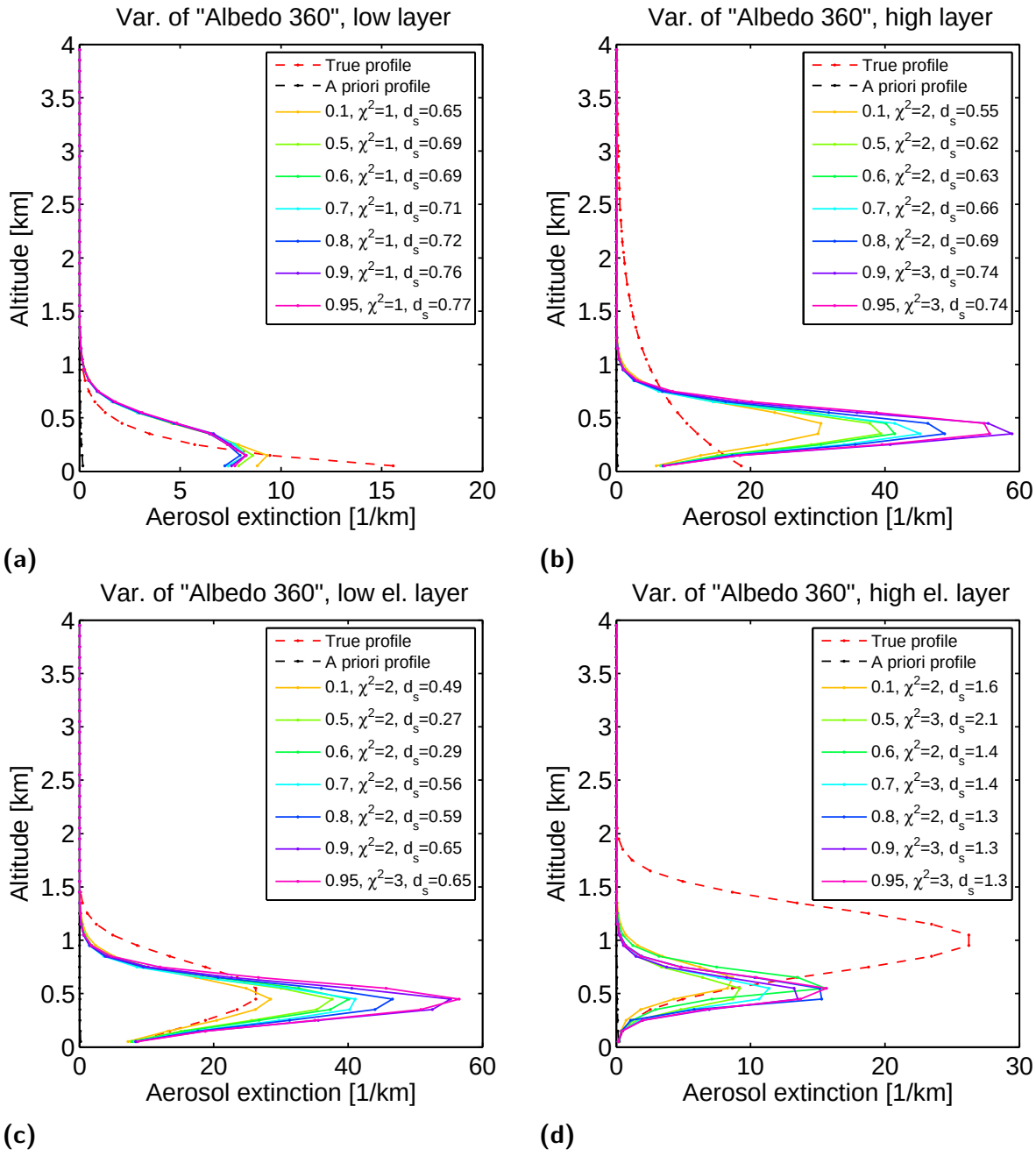

Figure 5.18.: Case 3 - High aerosol extinction scenarios: Analysis of the effect of the assumed albedo for values from 0.1 to 0.95, with the true albedo being 0.8. For details of the method see section 5.1.

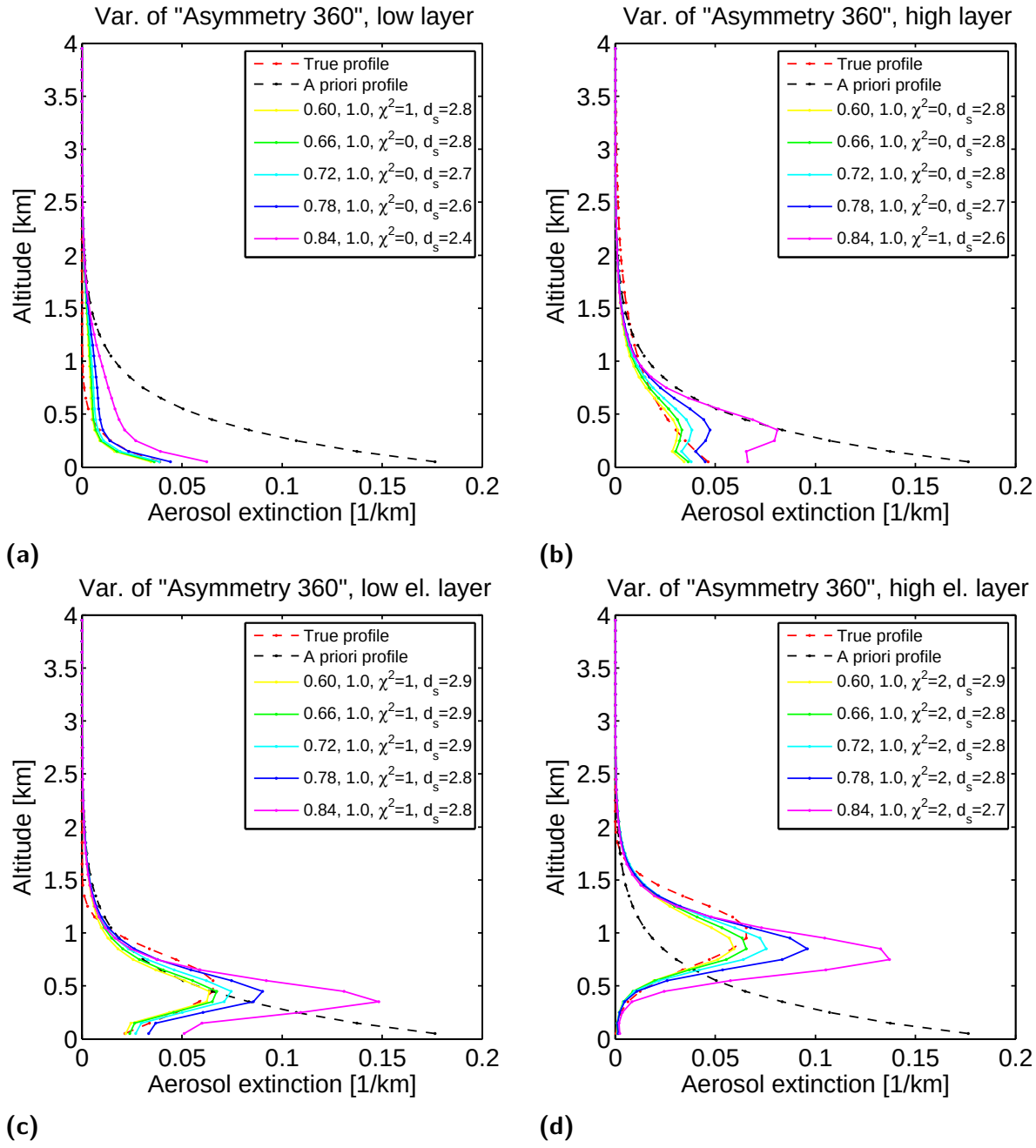

Figure 5.19.: Case 1 - Low aerosol extinction scenarios: Analysis of the effect of using a different Henyey-Greenstein asymmetry parameter instead of the true value of 0.72 within a realistic span from 0.60 to 0.84. For details of the method see section 5.1.

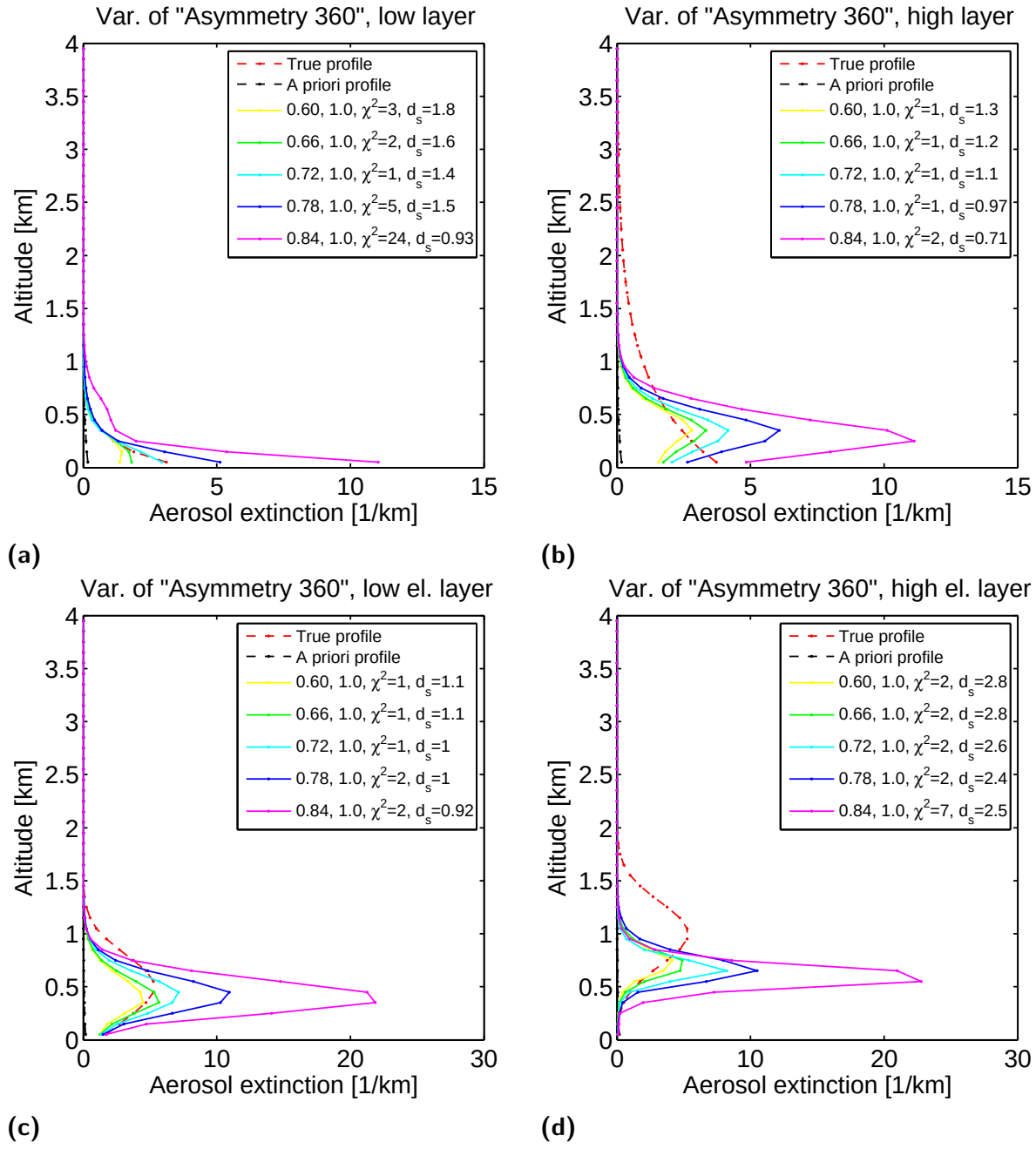

Figure 5.20.: Case 2 - Medium aerosol extinction scenarios: Analysis of the effect of using a different Henyey-Greenstein asymmetry parameter instead of the true value of 0.72 within a realistic span from 0.60 to 0.84. For details of the method see section 5.1.

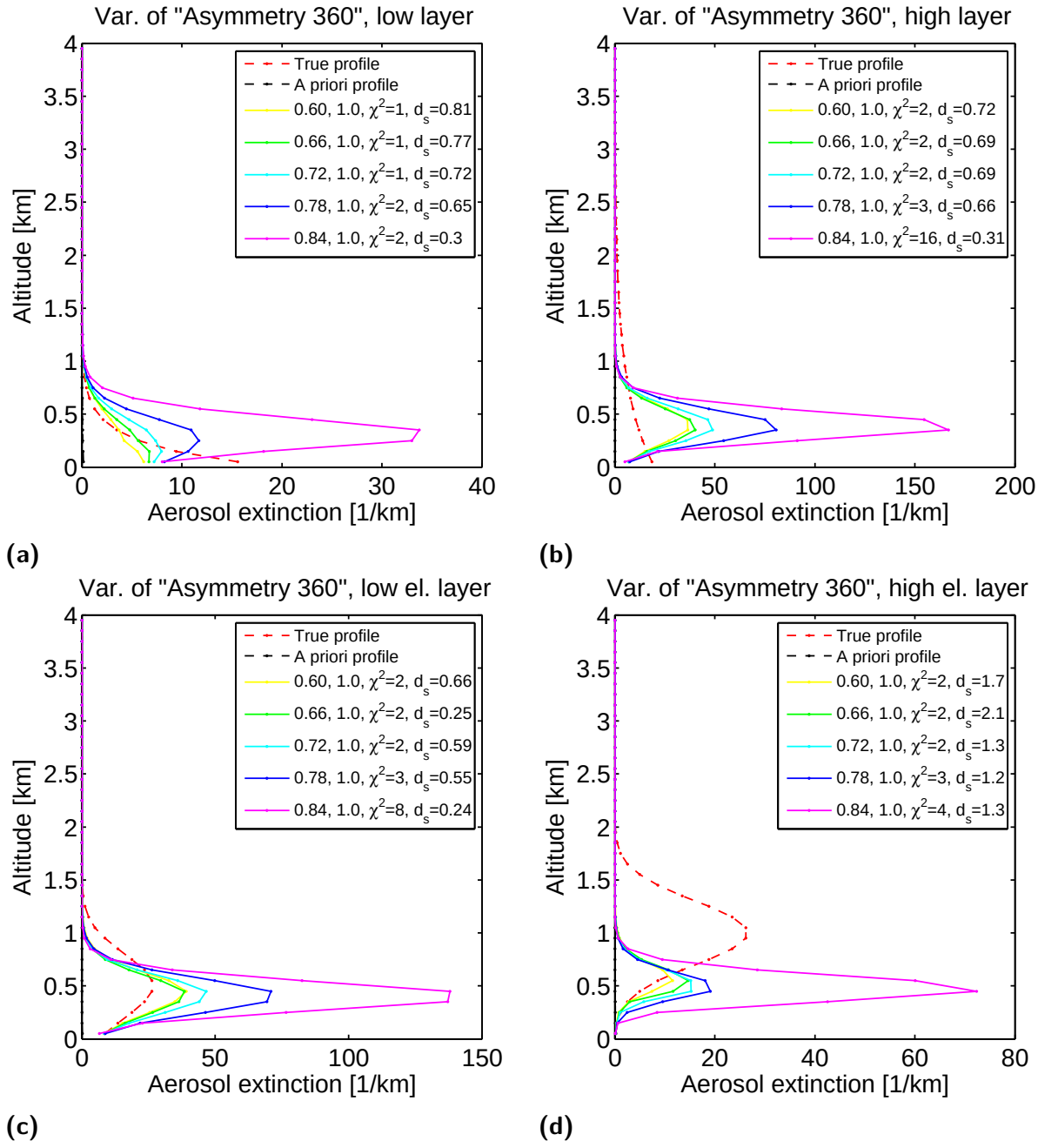

Figure 5.21.: Case 3 - High aerosol extinction scenarios: Analysis of the effect of using a different Henyey-Greenstein asymmetry parameter instead of the true value of 0.72 within a realistic span from 0.60 to 0.84. For details of the method see section 5.1.

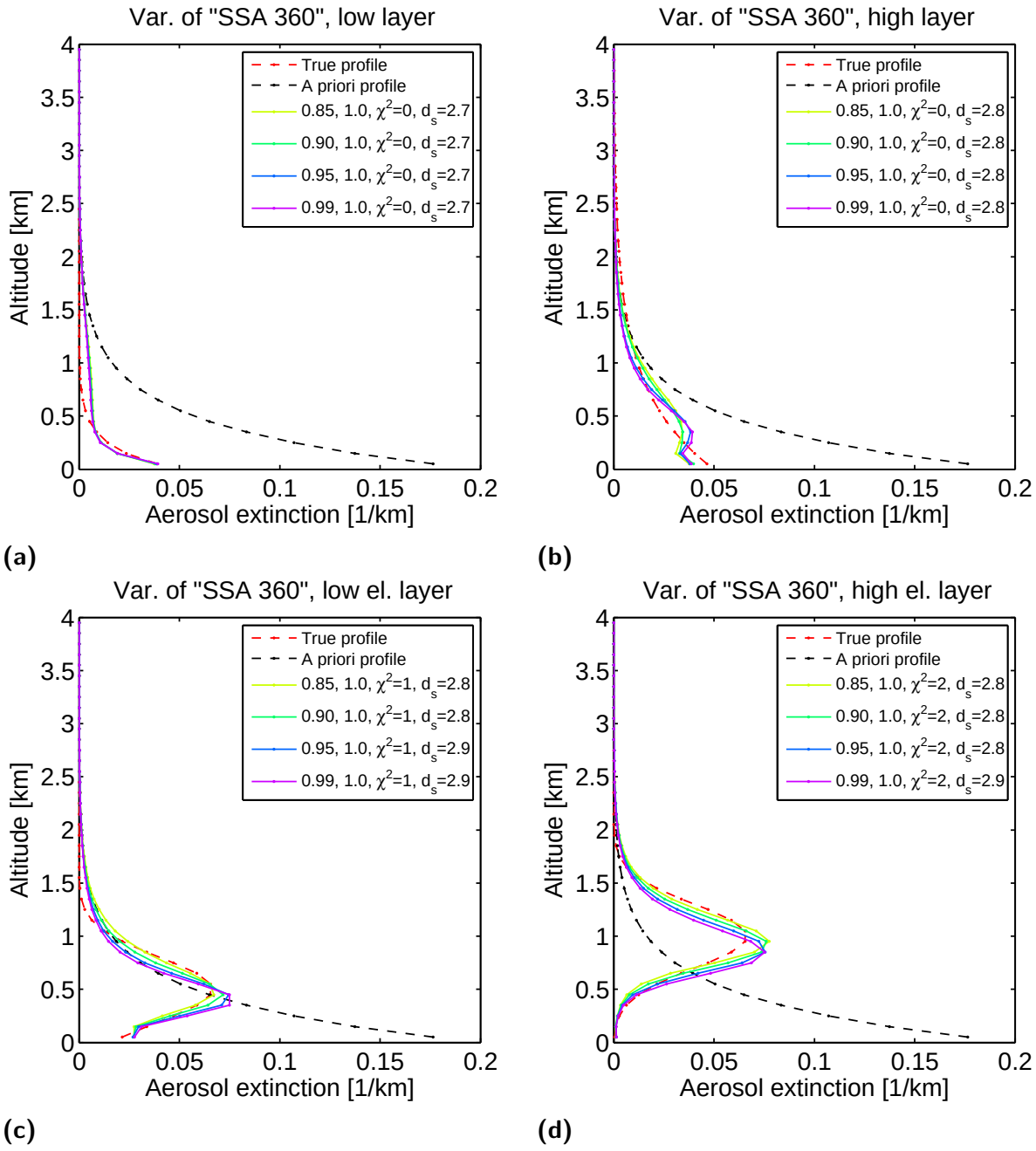

Figure 5.22.: Case 1 - Low aerosol extinction scenarios: Analysis of the effect of using a different aerosol single scattering albedo instead of the true value of 0.95. For details of the method see section 5.1.

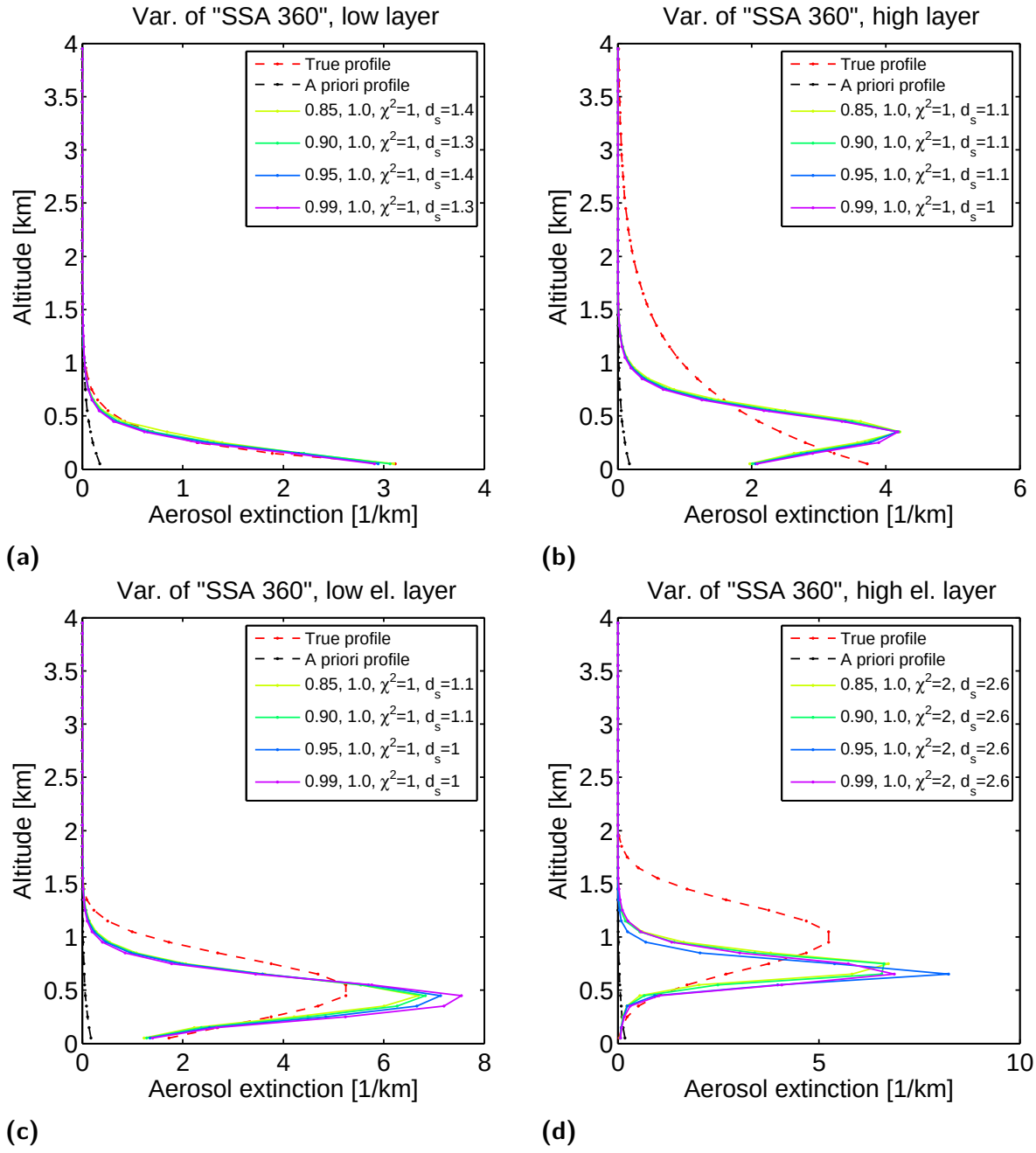

Figure 5.23.: Case 2 - Medium aerosol extinction scenarios: Analysis of the effect of using a different aerosol single scattering albedo instead of the true value of 0.95. For details of the method see section 5.1.

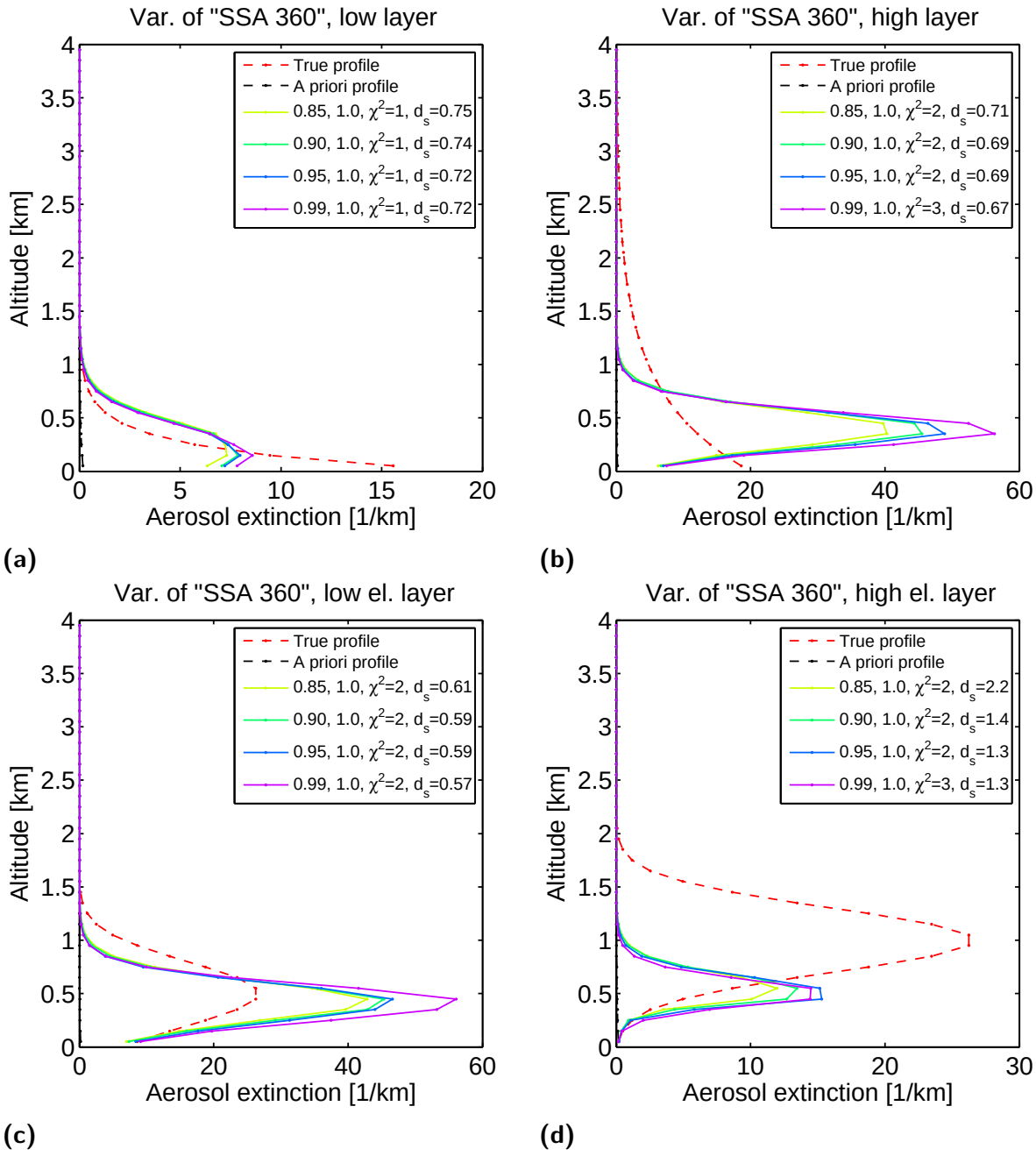

Figure 5.24.: Case 3 - High aerosol extinction scenarios: Analysis of the effect of using a different aerosol single scattering albedo instead of the true value of 0.95. For details of the method see section 5.1.

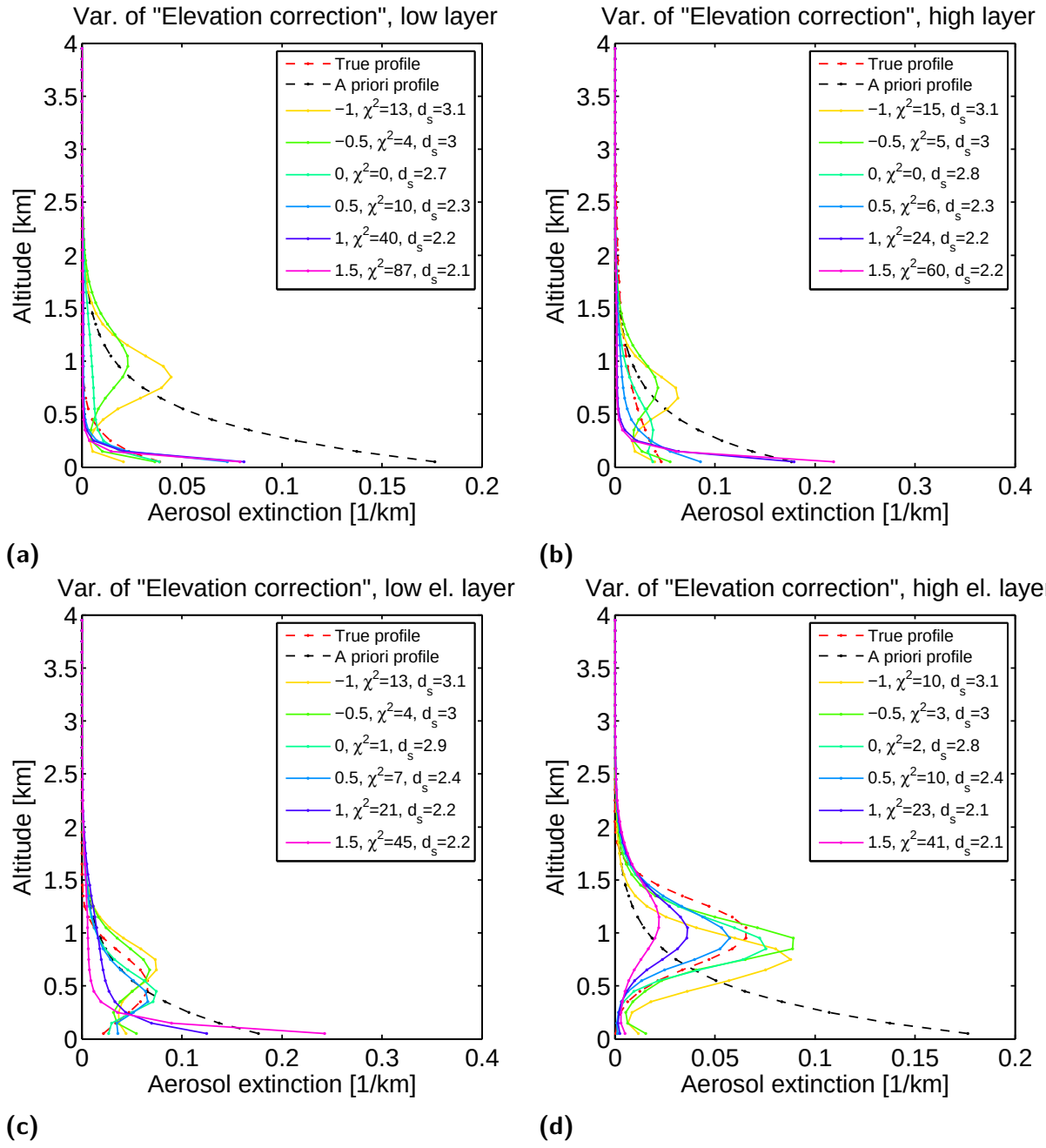

Figure 5.25.: Case 1 - Low aerosol extinction scenarios: Analysis of the effect of an instrumental offset, from -1 ° to +1.5 °, in the elevation angle of the viewing direction of the telescope. Positive angles indicate the instrument is looking lower than assumed. For details of the method see section 5.1.

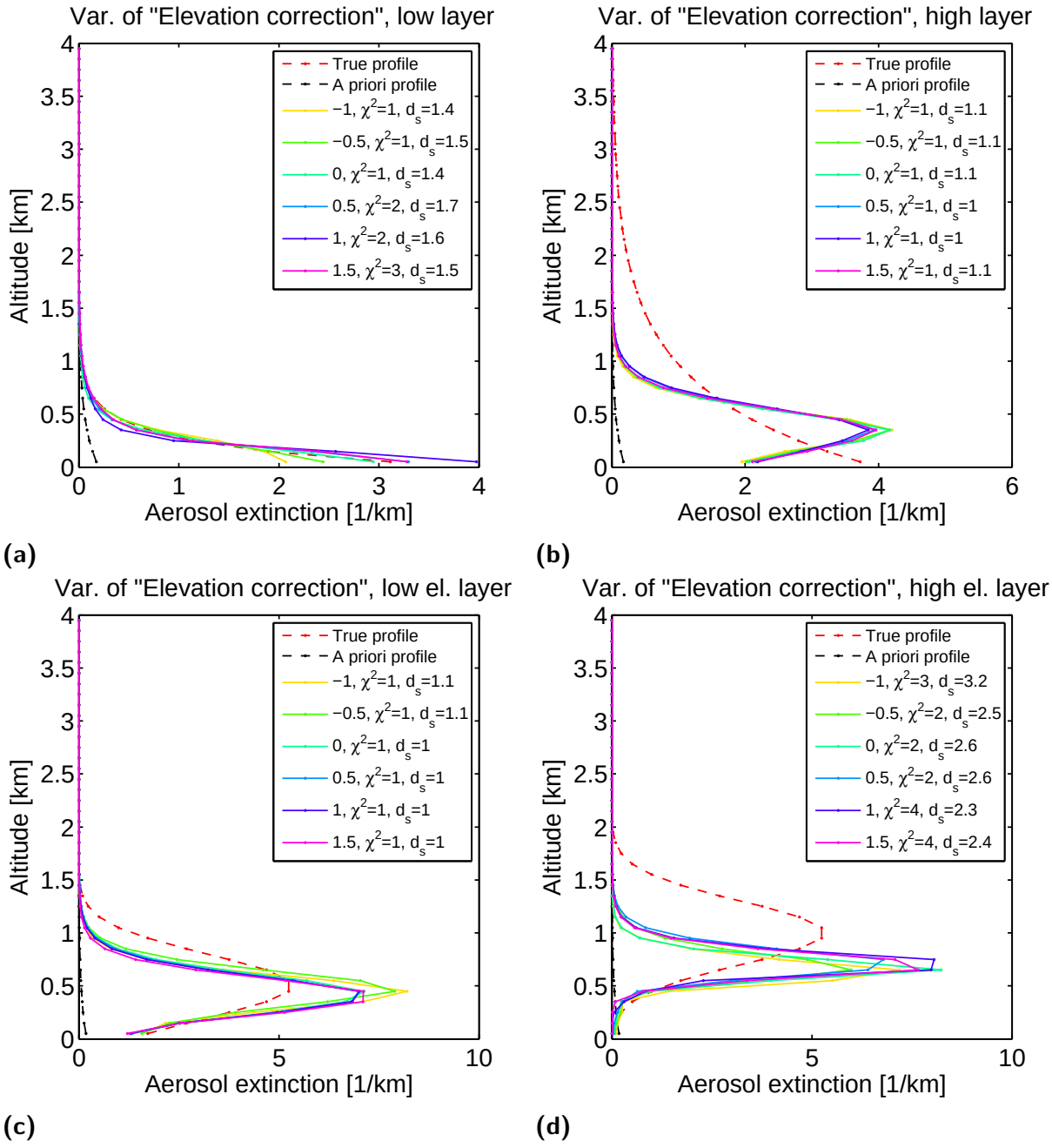

Figure 5.26.: Case 2 - Medium aerosol extinction scenarios: Analysis of the effect of an instrumental offset, from -1 ° to +1.5 °, in the elevation angle of the viewing direction of the telescope. Positive angles indicate the instrument is looking lower than assumed. For details of the method see section 5.1.

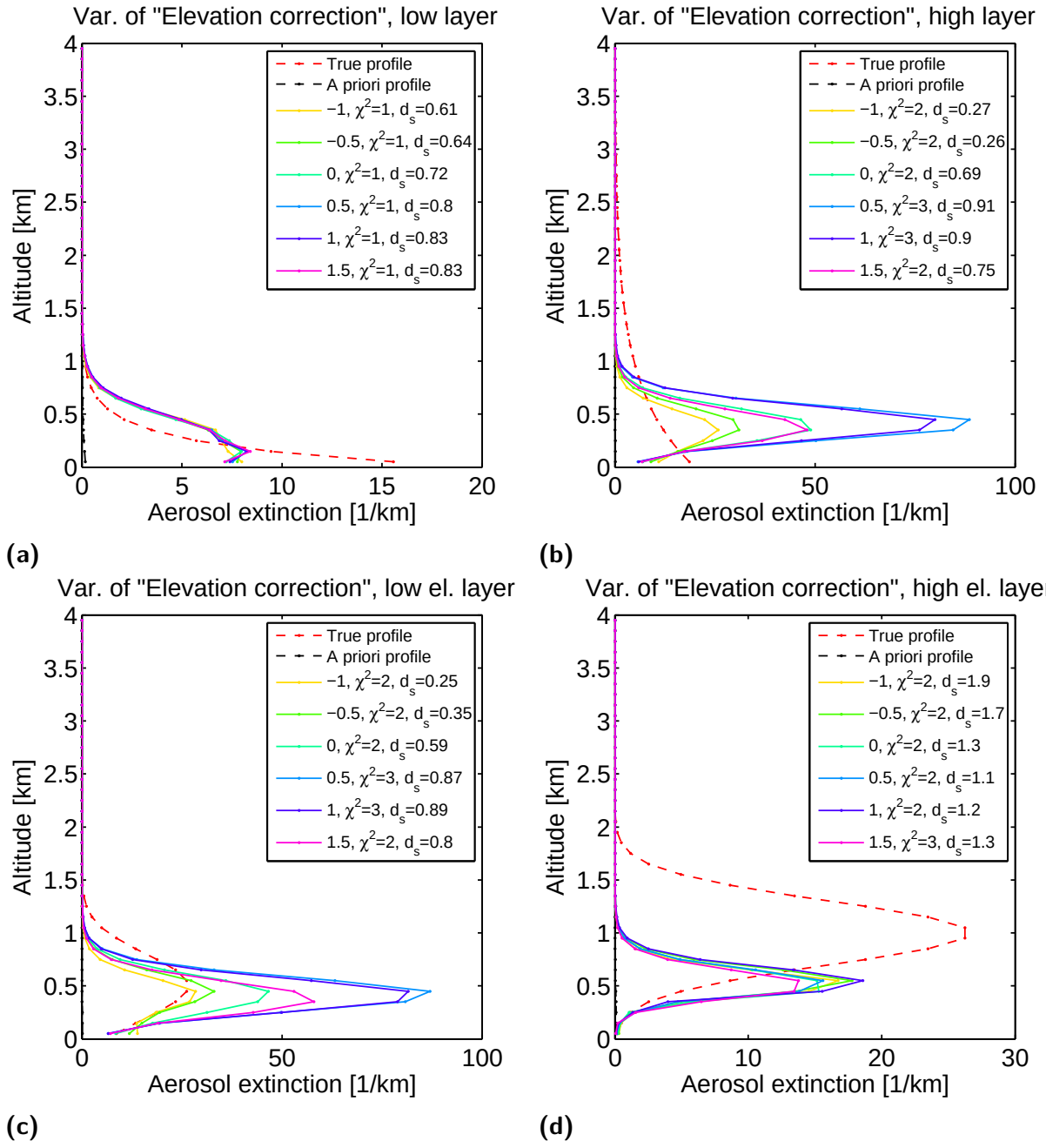

Figure 5.27.: Case 3 - High aerosol extinction scenarios: Analysis of the effect of an instrumental offset, from -1 ° to +1.5 °, in the elevation angle of the viewing direction of the telescope. Positive angles indicate the instrument is looking lower than assumed. For details of the method see section 5.1.

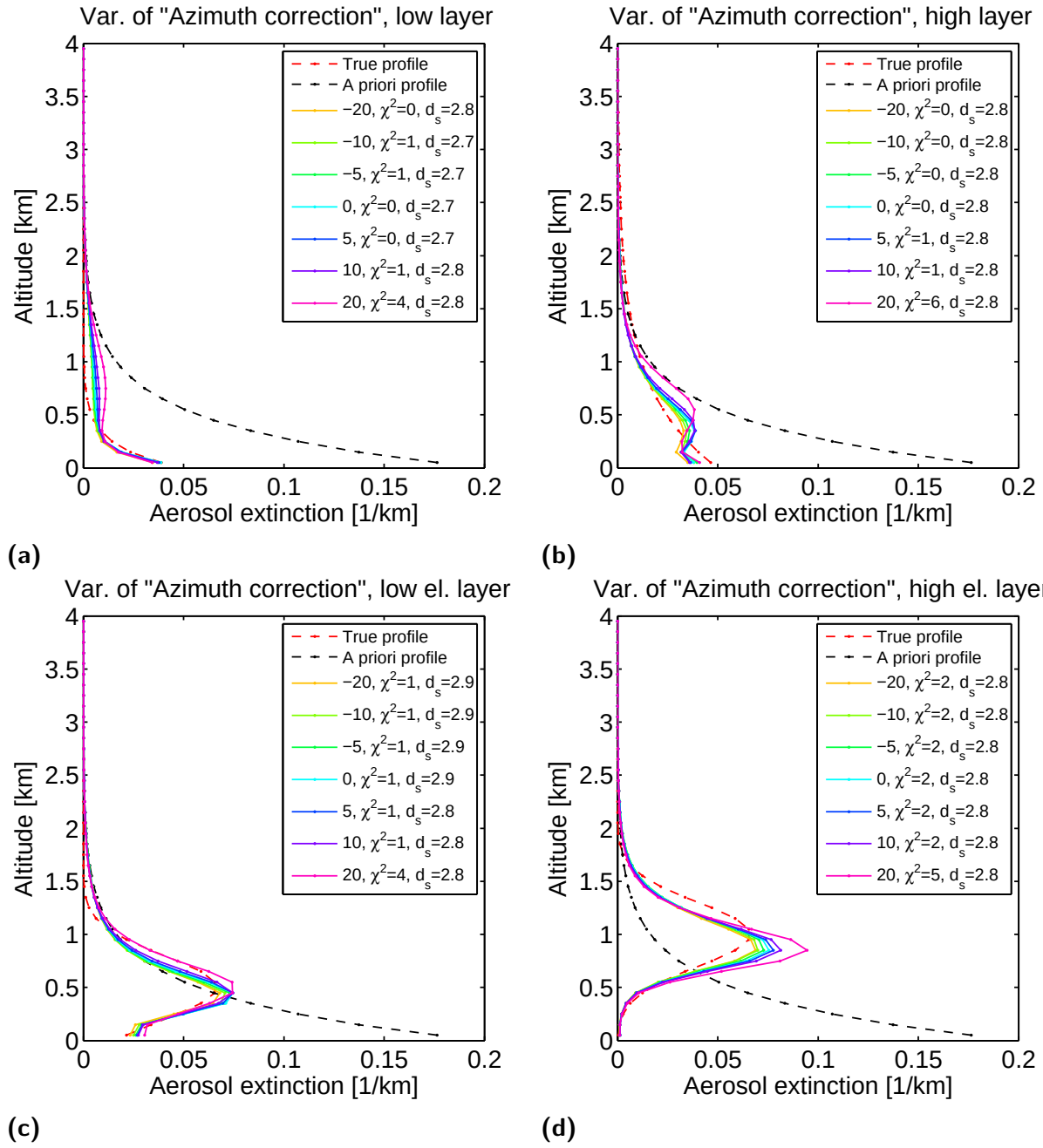

Figure 5.28.: Case 1 - Low aerosol extinction scenarios: Analysis of the effect of an instrumental offset, from -20 ° to +20 °, in the azimuth angle of the viewing direction of the telescope. Positive angles indicate the instrument is looking further left than assumed. For details of the method see section 5.1.

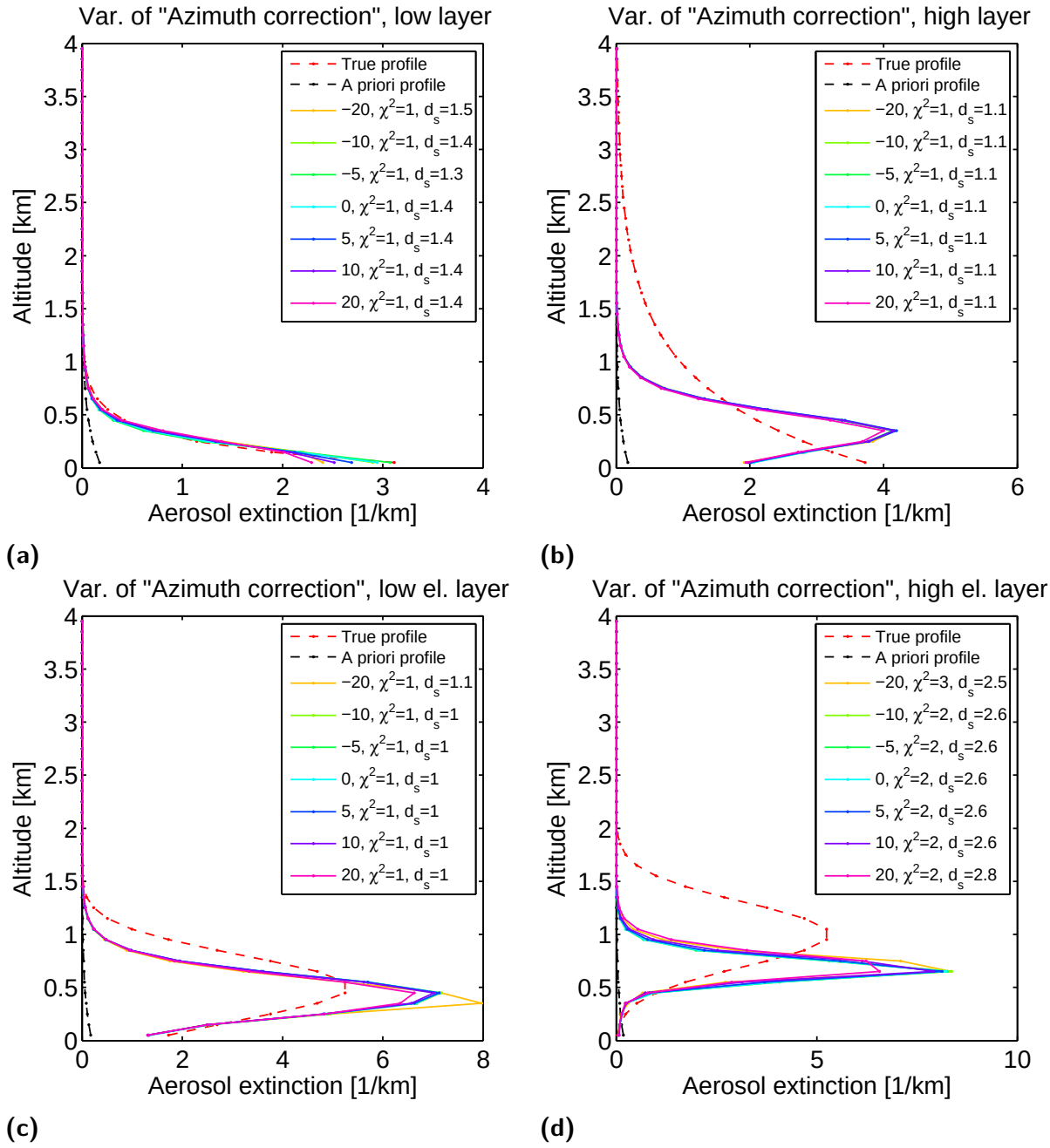

Figure 5.29.: Case 2 - Medium aerosol extinction scenarios: Analysis of the effect of an instrumental offset, from -20 ° to +20 °, in the azimuth angle of the viewing direction of the telescope. Positive angles indicate the instrument is looking further left than assumed. For details of the method see section 5.1.

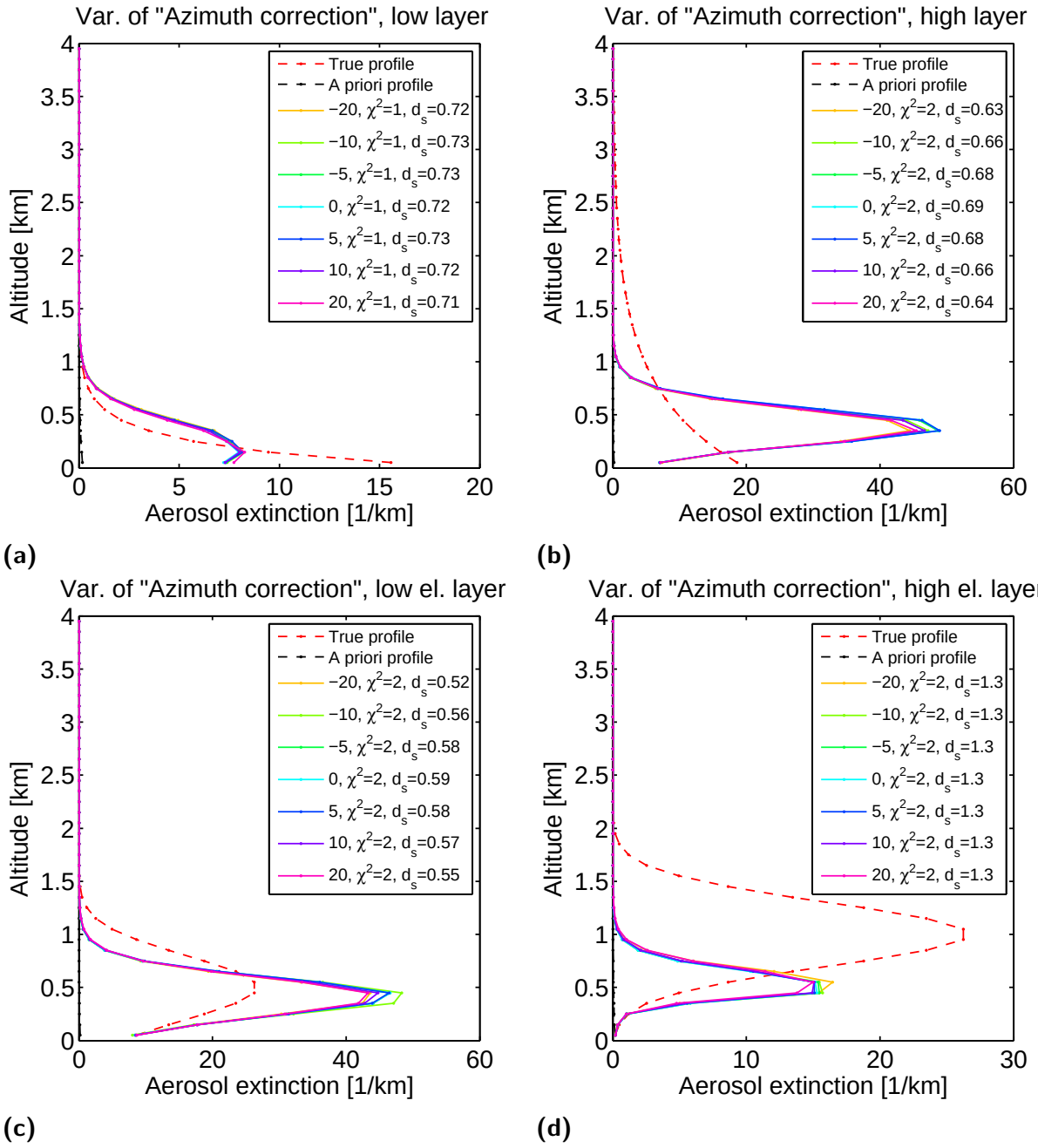

Figure 5.30.: Case 3 - High aerosol extinction scenarios: Analysis of the effect of an instrumental offset, from -20 ° to +20 °, in the azimuth angle of the viewing direction of the telescope. Positive angles indicate the instrument is looking further left than assumed. For details of the method see section 5.1.

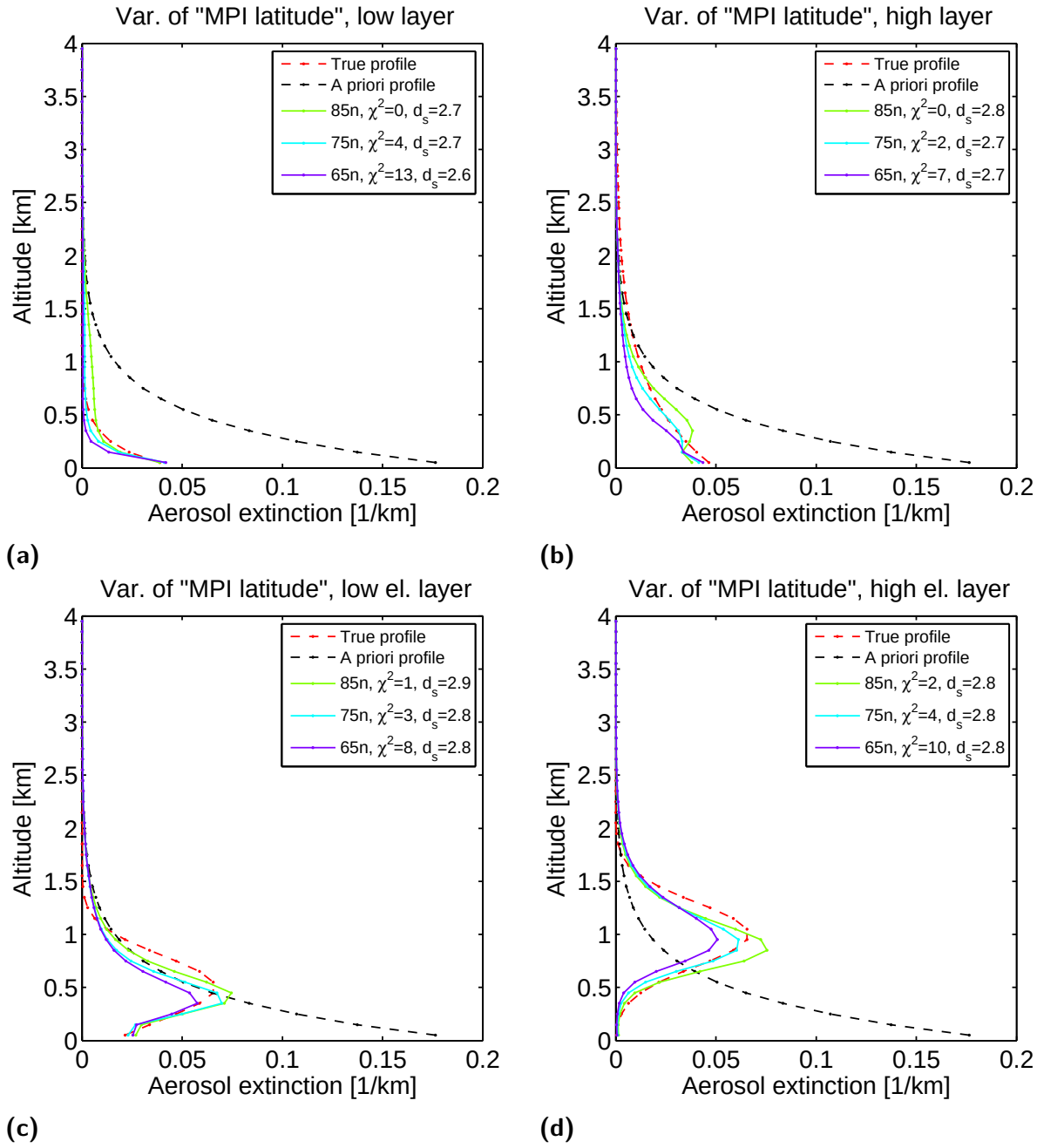

Figure 5.31.: Case 1 - Low aerosol extinction scenarios: Analysis of the effect of using different atmospheric temperature and pressure profiles included in the algorithm for 65 °N, 75 °N and 85 °N (true state). The provided profiles are monthly averages and given in steps of 10 ° latitude. For details of the method see section 5.1.

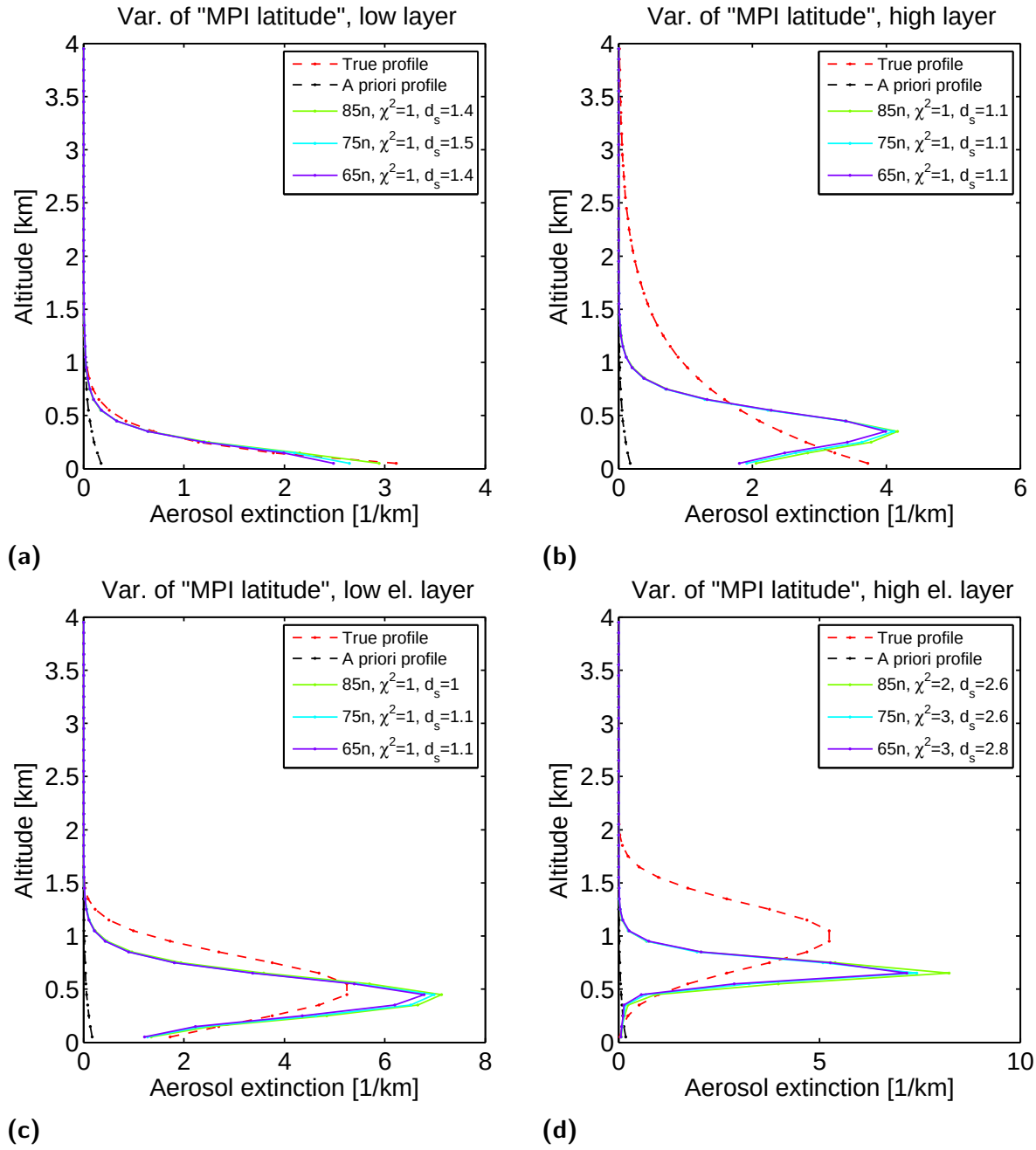

Figure 5.32.: Case 2 - Medium aerosol extinction scenarios: Analysis of the effect of using different atmospheric temperature and pressure profiles included in the algorithm for 65 °N, 75 °N and 85 °N (true state). The provided profiles are monthly averages and given in steps of 10 ° latitude. For details of the method see section 5.1.

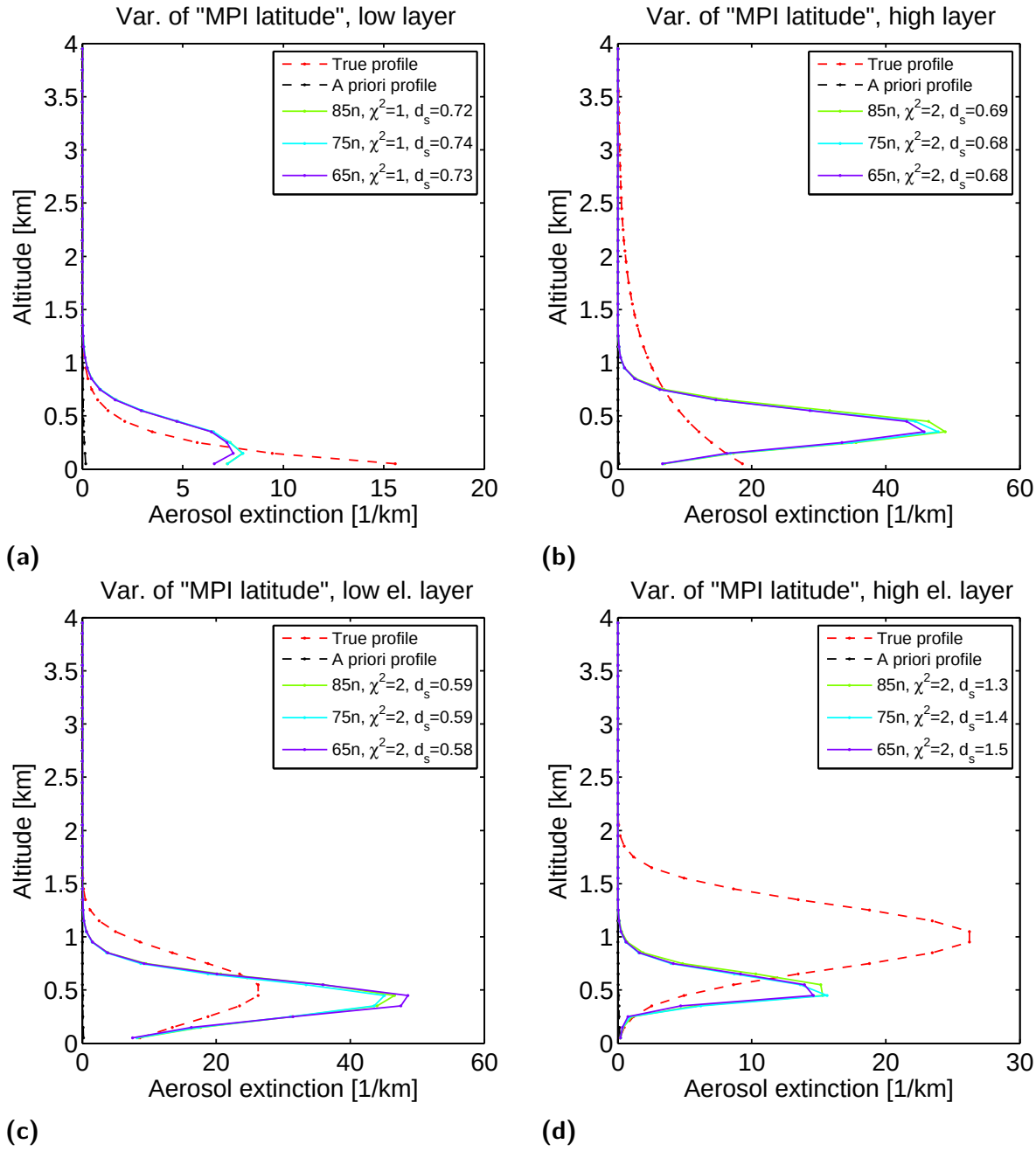

Figure 5.33.: Case 3 - High aerosol extinction scenarios: Analysis of the effect of using different atmospheric temperature and pressure profiles included in the algorithm for 65 °N, 75 °N and 85 °N (true state). The provided profiles are monthly averages and given in steps of 10 ° latitude. For details of the method see section 5.1.

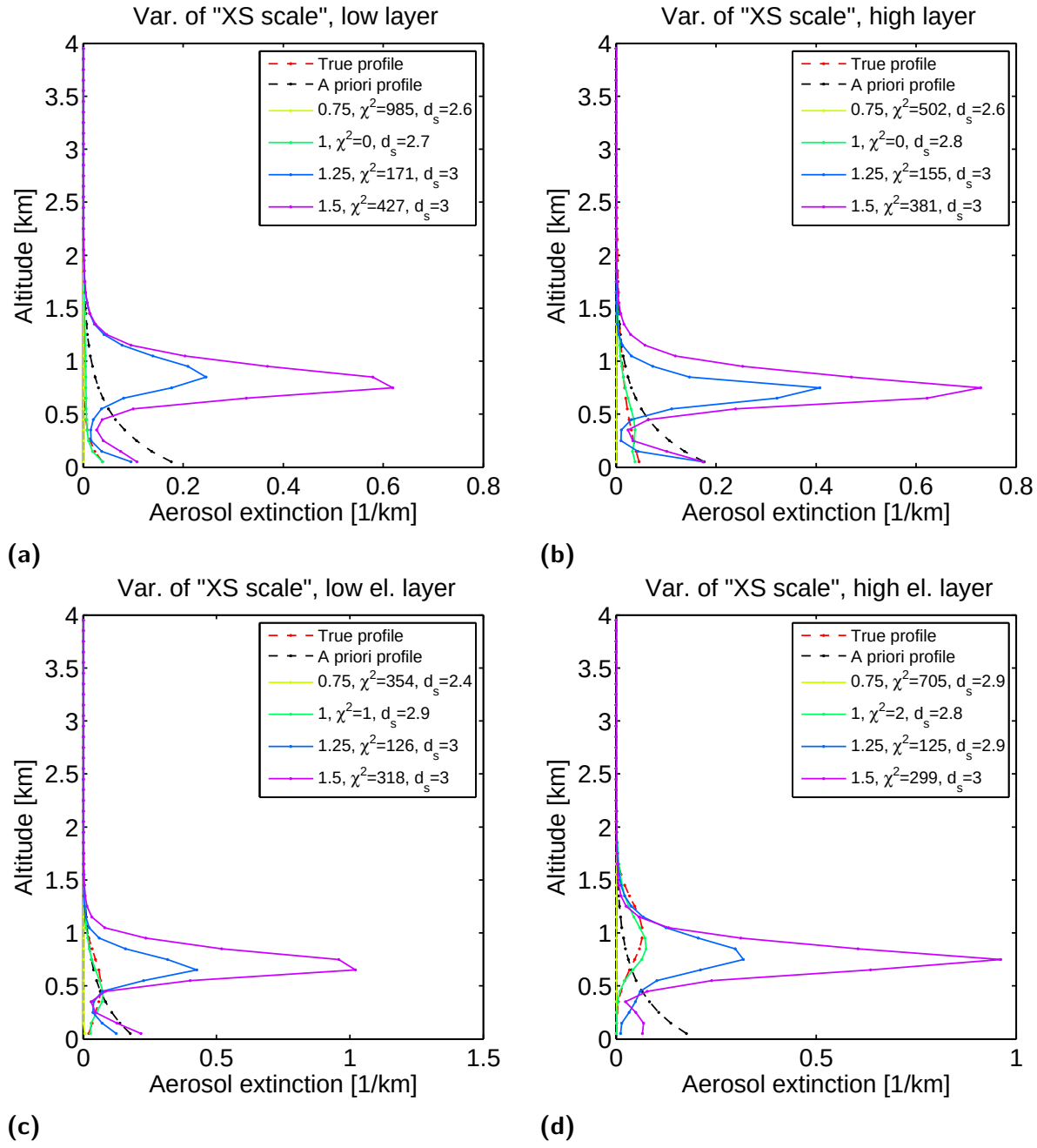

Figure 5.34.: Case 1 - Low aerosol extinction scenarios: Analysis of the effect of a factorial deviation in the scaling of the O_4 absorption cross section, between 0.75 to 1.5, different from the true value of 1.0. For details of the method see section 5.1.

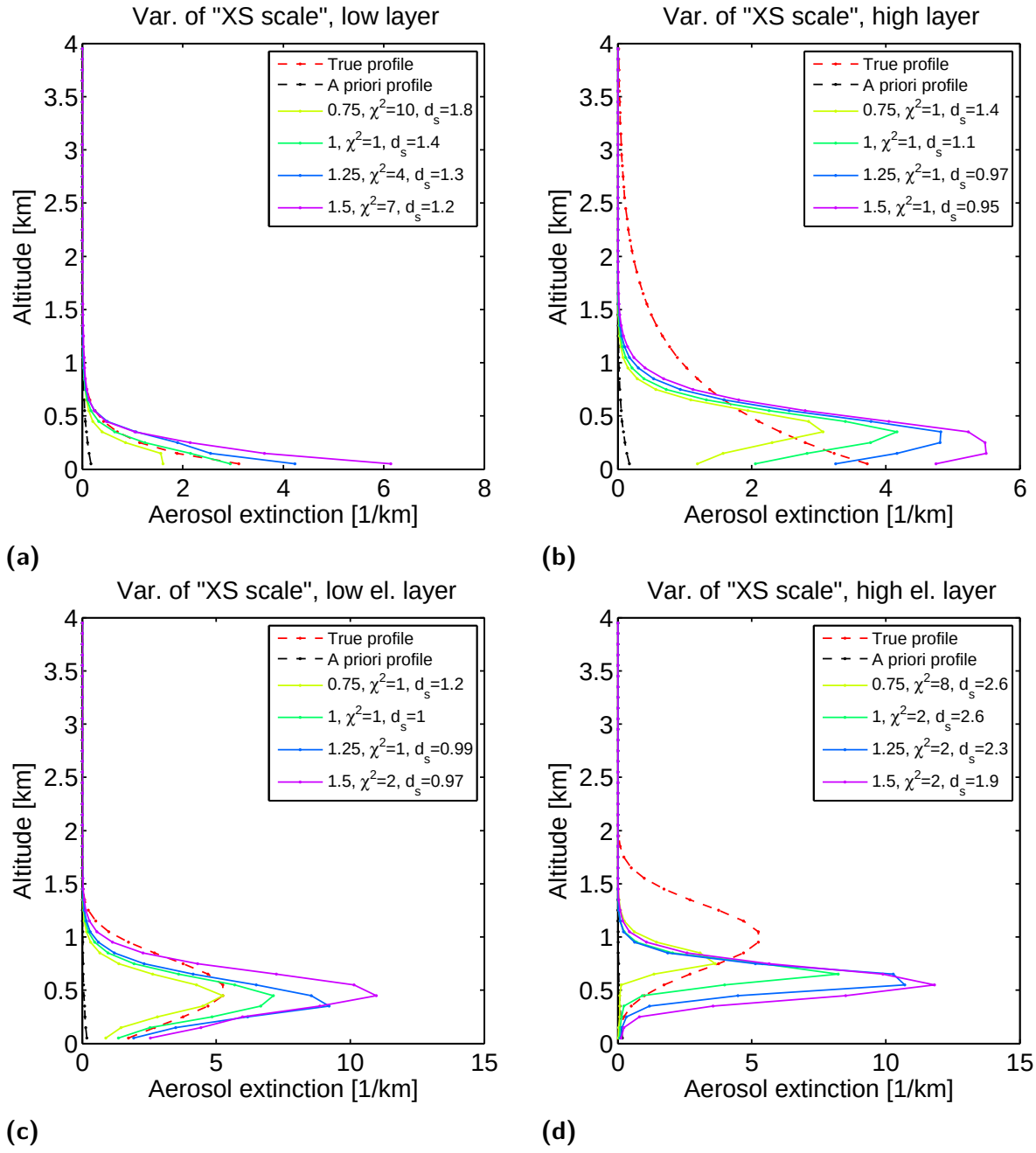

Figure 5.35.: Case 2 - Medium aerosol extinction scenarios: Analysis of the effect of a factorial deviation in the scaling of the O_4 absorption cross section, between 0.75 to 1.5, different from the true value of 1.0. For details of the method see section 5.1.

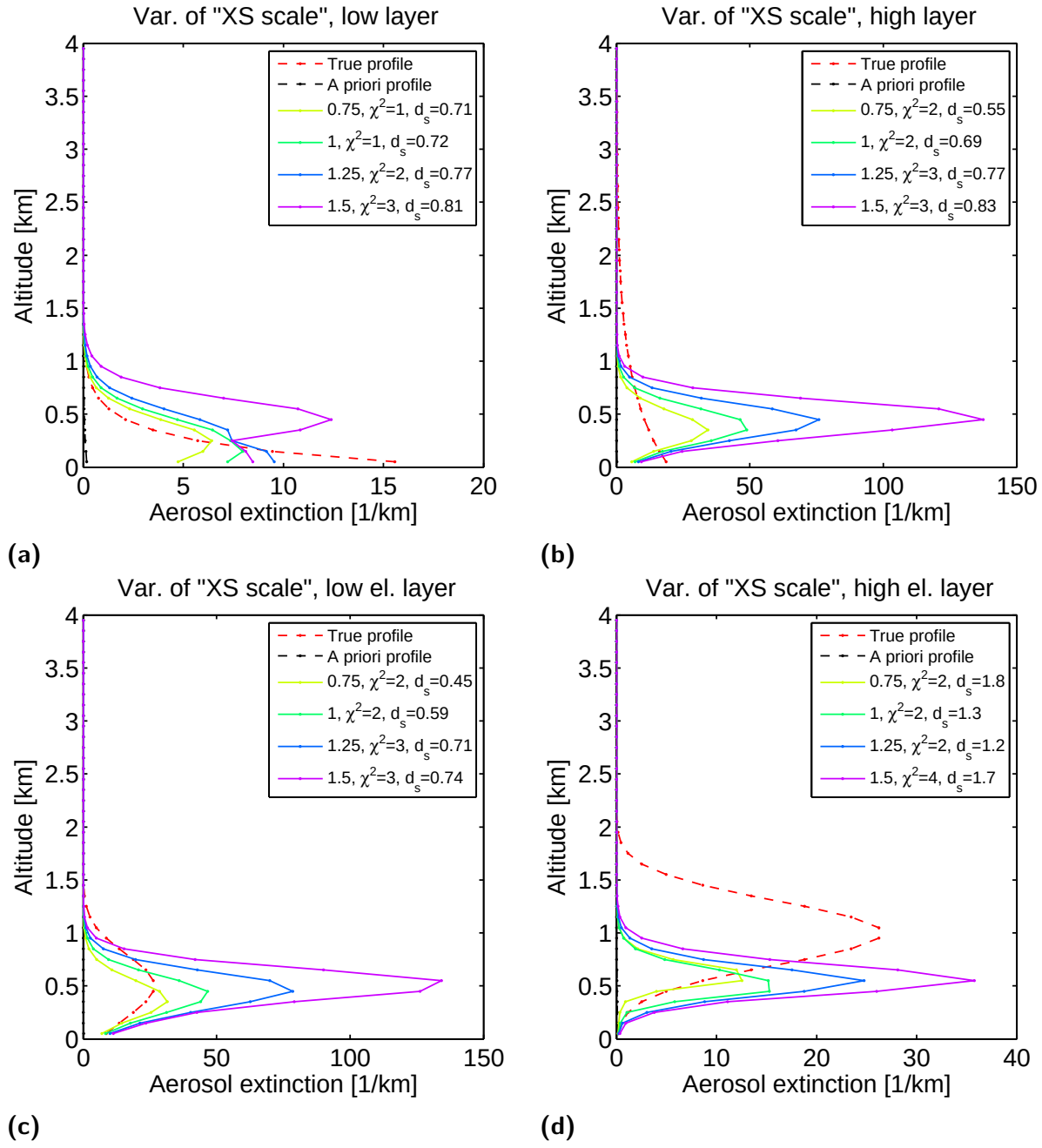

Figure 5.36.: Case 3 - High aerosol extinction scenarios: Analysis of the effect of a factorial deviation in the scaling of the O_4 absorption cross section, between 0.75 to 1.5, different from the true value of 1.0. For details of the method see section 5.1.

5.2 Trace gas inversion at the example of BrO

Similarly to the sensitivity studies for the aerosol inversion, studies for the inversion of trace gas SCDs were done. These were undertaken for the case of BrO, however are also applicable to other trace gas measurements with similar signal-to-noise ratios and assumed vertical distributions.

As done for the aerosol sensitivity studies, for the BrO studies, also four different synthetic profiles were tested. SCDs were simulated for each of them, noise was added within the margins of typical measurement errors, and lastly the data was fed into the inversion algorithm.

The four profiles were also chosen similarly as for the aerosol tests as those also comprise the most interesting cases which are desirable to be distinguishable in trace gas measurements. Therefore they are (1) a layer with a low mixing scale height of 0.2 km, (2) a layer with a higher mixing scale height of 0.7 km, (3) an elevated layer close to the ground at 0.5 km and (4) an elevated layer higher above ground at 1.0 km. They are pictured in fig. 5.37.

This was further done for two different levels of mixing ratios ("cases") for each of the four scenarios. In case 1 (C1), the highest mixing ratios are around 30 pptv and in case 2 (C2), they are around 5 pptv, both values which are commonly found in polar environments in spring.

5.2.1 Assumptions

The measurement geometry for the BrO sensitivity studies is the same as for the aerosol inversions described in section 5.1.1. The assumed errors for the simulated BrO SCDs were taken from data of the instrument in Alert from a typical clear day in March 2013, and are around $6 \cdot 10^{12}$ molec cm^{-2}. Aerosol was assumed to be present with an exponentially decreasing profile with a surface extinction of 0.1 km^{-1} and a scale height of 0.2 km.

5.2.2 Inversion settings

The standard settings used for the BrO inversion are listed in table 5.3. As for the aerosol inversion, apart from one parameter varied in each run, these were taken for each and every evaluation. The names of the parameters in the table reflects their names as used in the HEIPRO configuration file, a description of those is given in table 5.2. An example of the averaging kernels for these settings is given in figure 5.38.

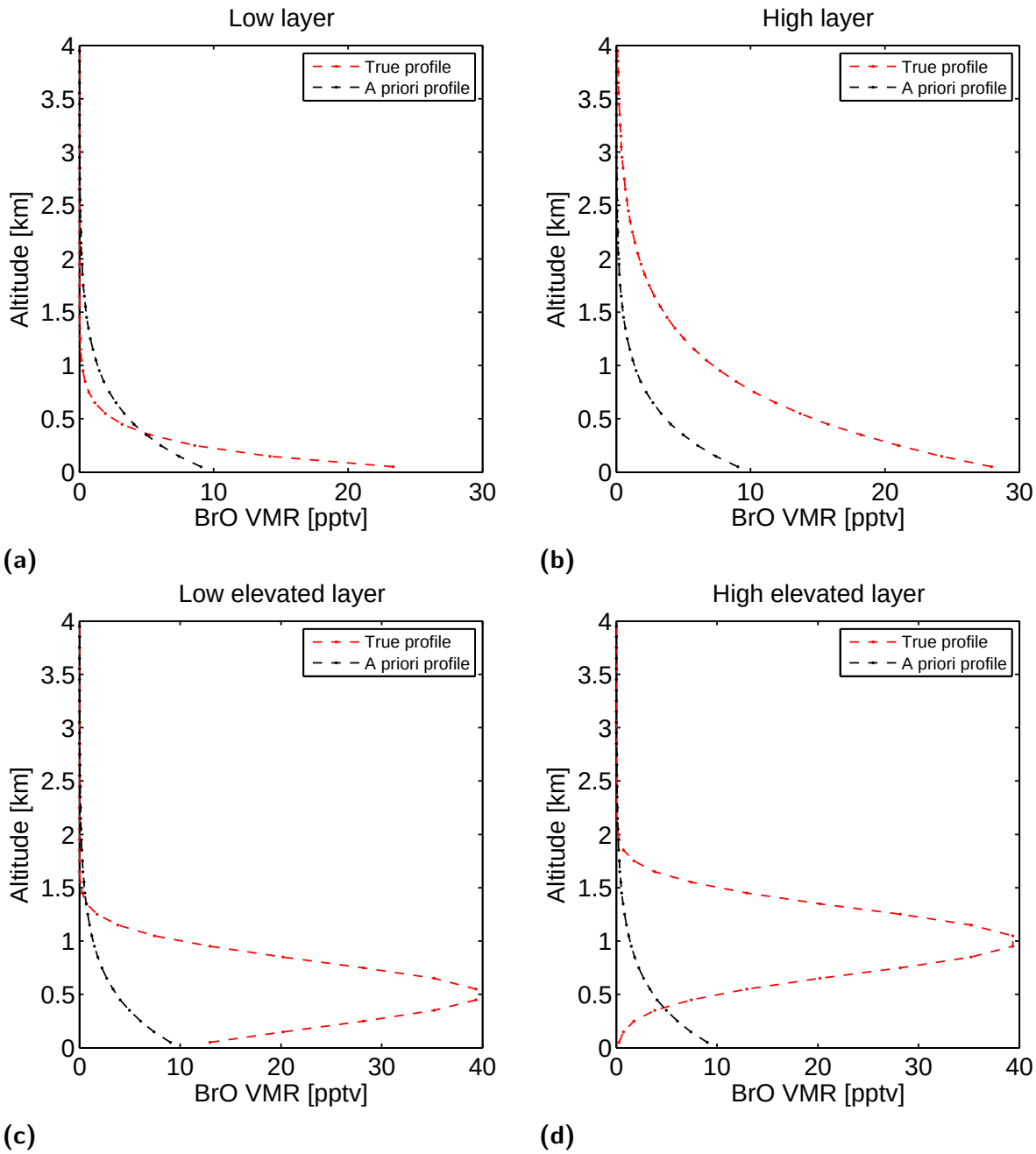

Figure 5.37.: The four synthetic BrO vertical profiles that were used to simulate SCDs, which were then fed into the inversion algorithm. The four profiles are based on cases that would be desirable to distinguish in measurements. **(a)** A layer very close to the ground, expected when having a strong surface source **(b)** A layer with a higher scale height **(c)** A lower elevated layer **(d)** A higher elevated layer.

Parameter	**Value**	**Parameter**	**Value**
A priori profile error	500%	Only variance	false
Albedo at 360 nm	0.8	Parameter 1	20 pptv
Number of runs	1	Parameter 2	0.5 km
Correlation length	0.5 km	Safe state	true
Fix weighting function	false	Scale SCD error	1.0
Iteration steps per run	15	MPI latitude	85 °N

Table 5.3.: The settings used for the inversion of the vertical profiles of the BrO mixing ratio. The parameter names are given as used in the HEIPRO algorithm. An explanation of their meaning and values is given in table 5.2.

Two step process

Since the trace gas inversion is a two step process, with the algorithm to retrieve the aerosol extinction first and then thereon the inversion of trace gas SCDs, and with some parameters being necessary in both stages, there is a possibility of an enhanced contribution of those. Errors in the telescope's elevation and azimuth angles for example will lead to erroneous aerosol profiles, which are then input into the trace gas inversion, again with the same erroneous geometry, thereby contributing twice into the result. Those parameters affecting both stages therefore, were also varied simultaneously during both stages. Other parameters, only affecting the trace gas inversion were also only varied there. A list referencing which one was altered in which way is listed in table 5.4.

5.2.3 Results

The following results of the examinations of the complete trace gas inversion algorithm are presented in the same manner as for the aerosol extinction inversion shown above and described in section 5.1.3, i.e. one page for each case and parameter containing the four profiles. Further studies of parameters not presented here can be found in the appendix (A.2).

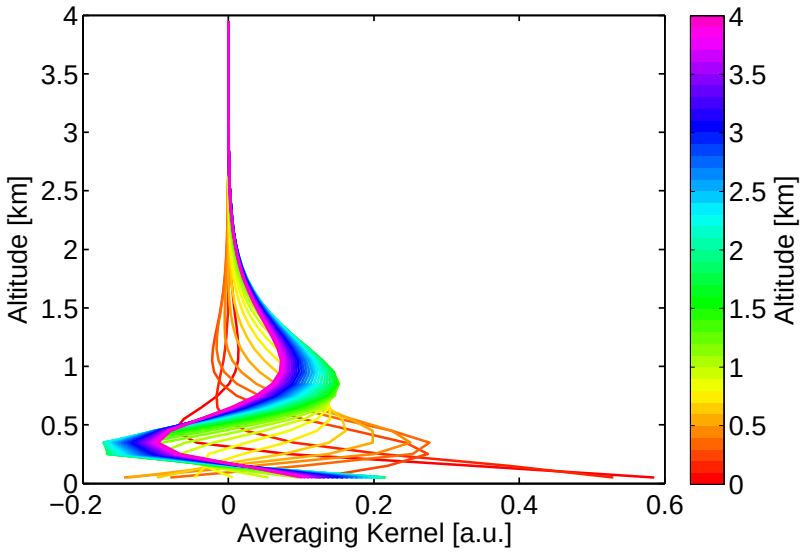

Figure 5.38.: Typical averaging kernels (AKs) for the BrO inversion with a 100 m height resolution grid and settings as given in table 5.3. Ideally the individual AKs would peak at their respective altitude which is indicated by the color bar.

Parameter varied for inversion of	
Aerosol & trace gas	**Only trace gas**
Elevation angle	Parameter 1
Azimuth angle	Parameter 2
Albedo	A priori error
Scale SCD error	Use retrieved aerosol
Only variance	Fix weighting function
Correlation	Runs
MPI latitude	Iteration steps

Table 5.4.: A list of the parameters, the influence of which was examined showing if they were altered in both stages of the inversion algorithm or only during the second, trace gas part.

A priori profile parametrization: Surface mixing ratio

Here also two values parametrize the a priori profile which decreases exponentially with altitude. The first one sets the mixing ratio at the surface, while the second one sets the profile's scale height in km.

In this first test, the surface mixing ratio of the used a priori profile is varied between 5 ppt and 50 ppt. The results are shown in figs. 5.39 (C1) and 5.40 (C2). Overall, the choice of the VMR is less important than for the aerosol inversion, and the general reproduction of the input profiles is good in both cases. Especially in the case of low mixing ratios, differences are insignificant.

A priori profile parametrization: Scale height

Here the scale height of the a priori profile is varied from 0.1 km to 1 km. The output is presented in figs. 5.41 (C1) and 5.42 (C2). In figure 5.42d the same effect as for the aerosol inversion can be nicely seen, where a low scale height a priori profile pulls the observed mixing ratios to lower altitudes. Similarly, a too large scale height profile has at 2 km and above still the same values as the a priori as the measurement is not sensitive at those altitudes.

A priori profile parametrization: Profile error

In this test the assumed error on the a priori profile is varied between 50% and 1000%. Figs. 5.43 (C1) and 5.44 (C2) show the results. Higher values for the error lead to more information from the measurement reaching the outcome and therefore a higher number of degrees of freedom for signal d_s. On the other hand, too large values lead to overfitting and with that oscillations in the profile shape as can be seen in figure 5.43b.

Albedo

The ground albedo was deviated from the true (simulated) state of 0.8 in a range from 0.1 to 0.95. Figures 5.45 (C1) and 5.46 (C2) show the outcome. It is evident that compared to the aerosol inversion, the albedo has a much smaller effect in all cases.

Telescope alignment: Elevation angle

To study the effect of a skewed instrumental alignment, offsets between -1 ° and +1 ° from the real elevation angle of the telescope were studied. Negative angles indicate that the telescope is looking higher than assumed, positive angles that the light path is lower. The resulting profiles are shown in figs. 5.47 (C1) and 5.48 (C2). It is apparent that accurate knowledge of the telescope elevation is critical, much more so than in the case of the aerosol inversion and especially at higher mixing ratios (C1). Angular offsets of the order of 0.5 ° can already cause significant differences of several hundred percent, including resulting profile shapes completely different from the true state.

Telescope alignment: Azimuth angle

The other axis, the instruments azimuth angle, was also modified from -20 ° to +20 °of the true state, again very large deviations for most ground-based settings. Positive angles indicate a viewing direction off the assumed axis in a counterclockwise manner. The results are depicted in figs. 5.49 (C1) and 5.50 (C2). Even more so than for the aerosol inversion, the deviations are negligible in all cases and for all profile shapes.

Use retrieved aerosol

This parameter determines whether the aerosol profile determined by the inversion of O_4 SCDs is used or whether simply a pure Rayleigh atmosphere is assumed and the aerosol profile discarded. This allows to study the effect on the radiative transfer of aerosols. The output is shown in figs. 5.51 (C1) and 5.52 (C2). The difference observed here is small. In terms of the shape of the resulting profile, the run utilizing the aerosol data closer resembles the true states. And while the aerosol load is also comparatively small, it is representative for the measurement conditions faced within this work. As the total difference of using the aerosol data or not is small, this indicates that the errors on the aerosol inversion are negligible as well in those circumstances.

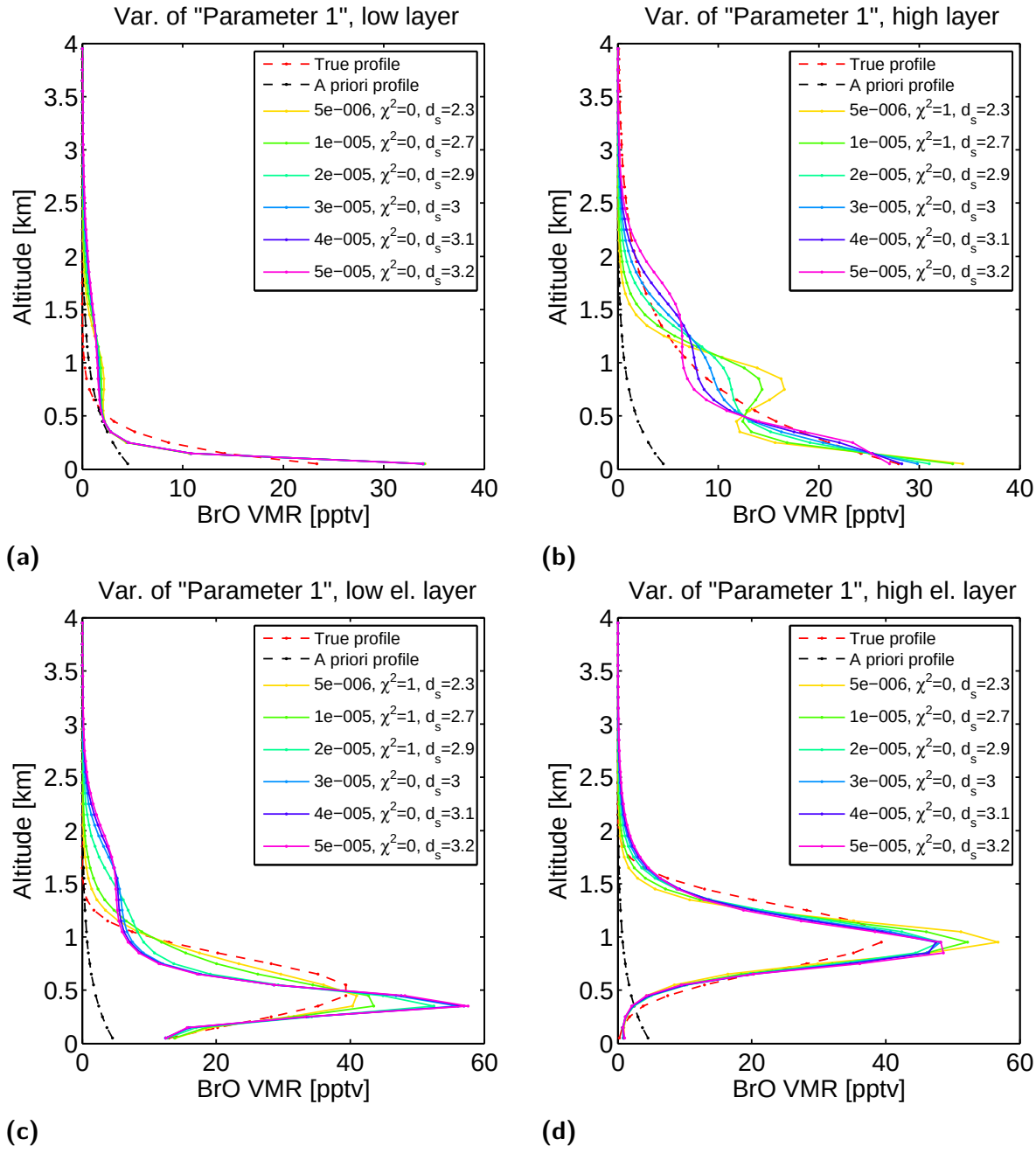

Figure 5.39.: Case 1 - High BrO mixing ratios: Analysis of the effect of the used a priori profile surface mixing ratio. The indicated a priori profile is the one used during the first run, with 5 ppt at the surface. Mixing ratios are indicated in ppm. For details of the method see section 5.2.

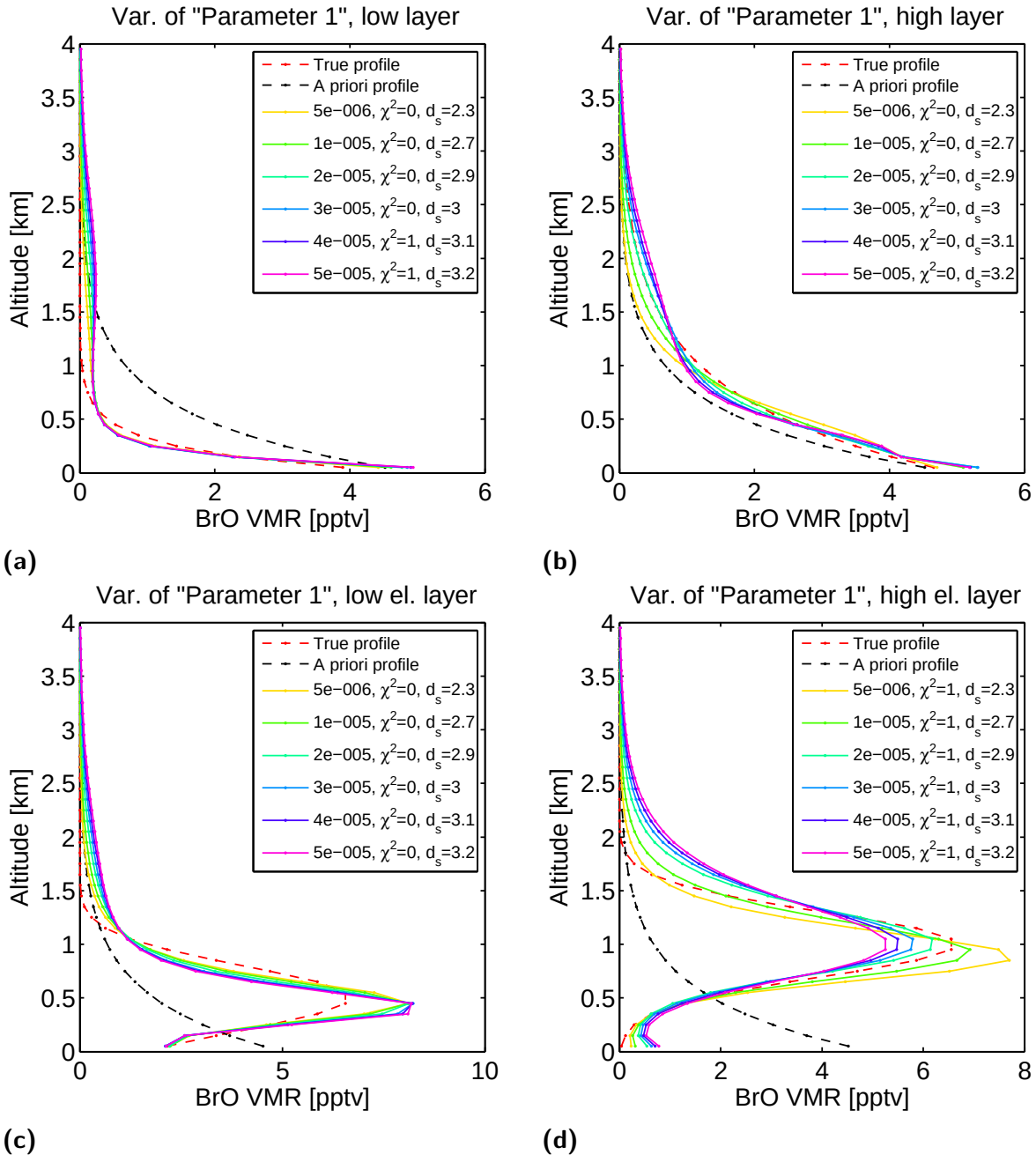

Figure 5.40.: Case 2 - Low BrO mixing ratios: Analysis of the effect of the used a priori profile surface mixing ratio. The indicated a priori profile is the one used during the first run, with 5 ppt at the surface. Mixing ratios are indicated in ppm. For details of the method see section 5.2.

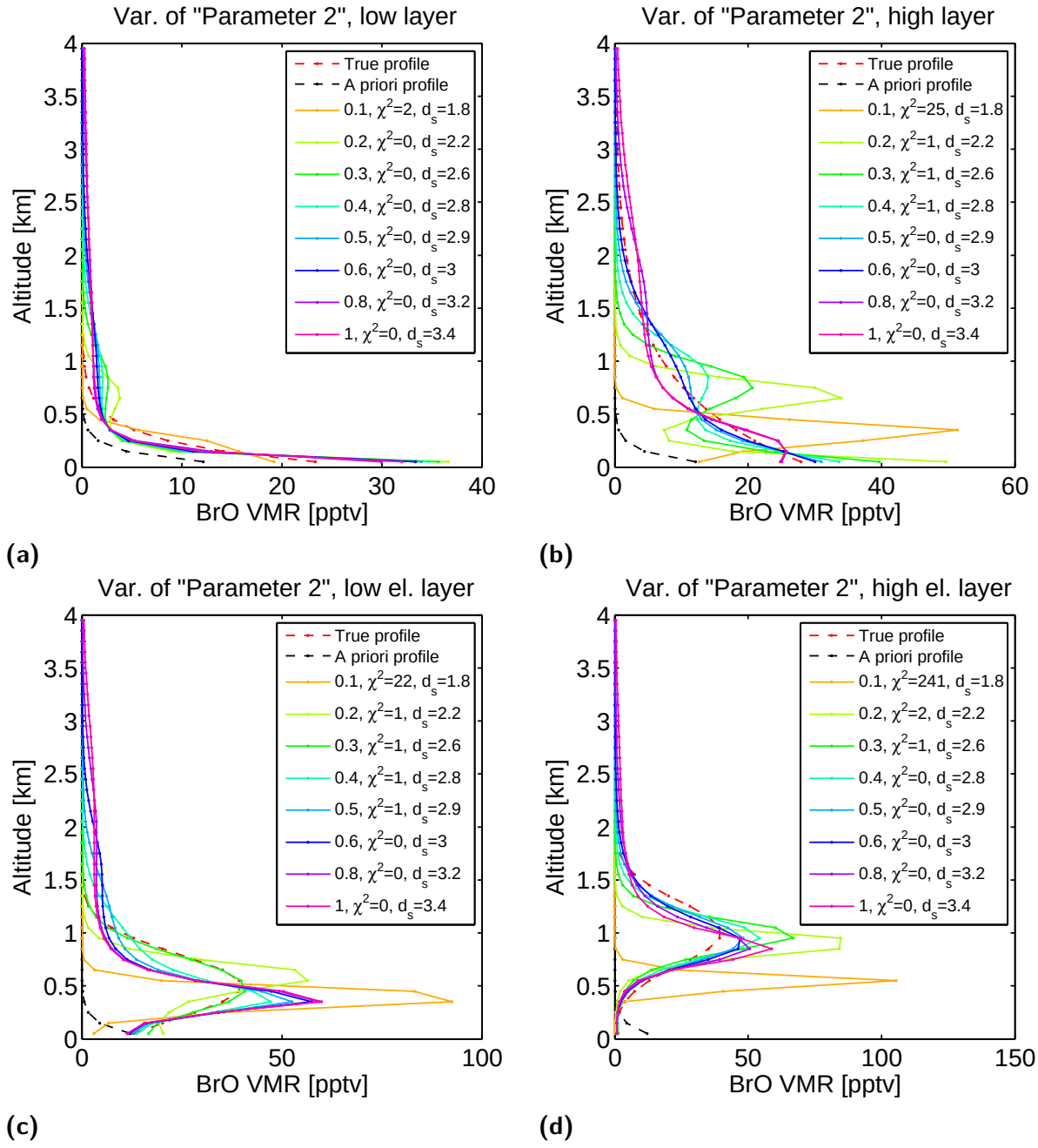

Figure 5.41.: Case 1 - High BrO mixing ratios: Analysis of the effect of the scale height of the used a priori profile. The shown a priori profile is the one used during the first run, with a height of 0.1 km. The scale height is indicated in km. For details of the method see section 5.2.

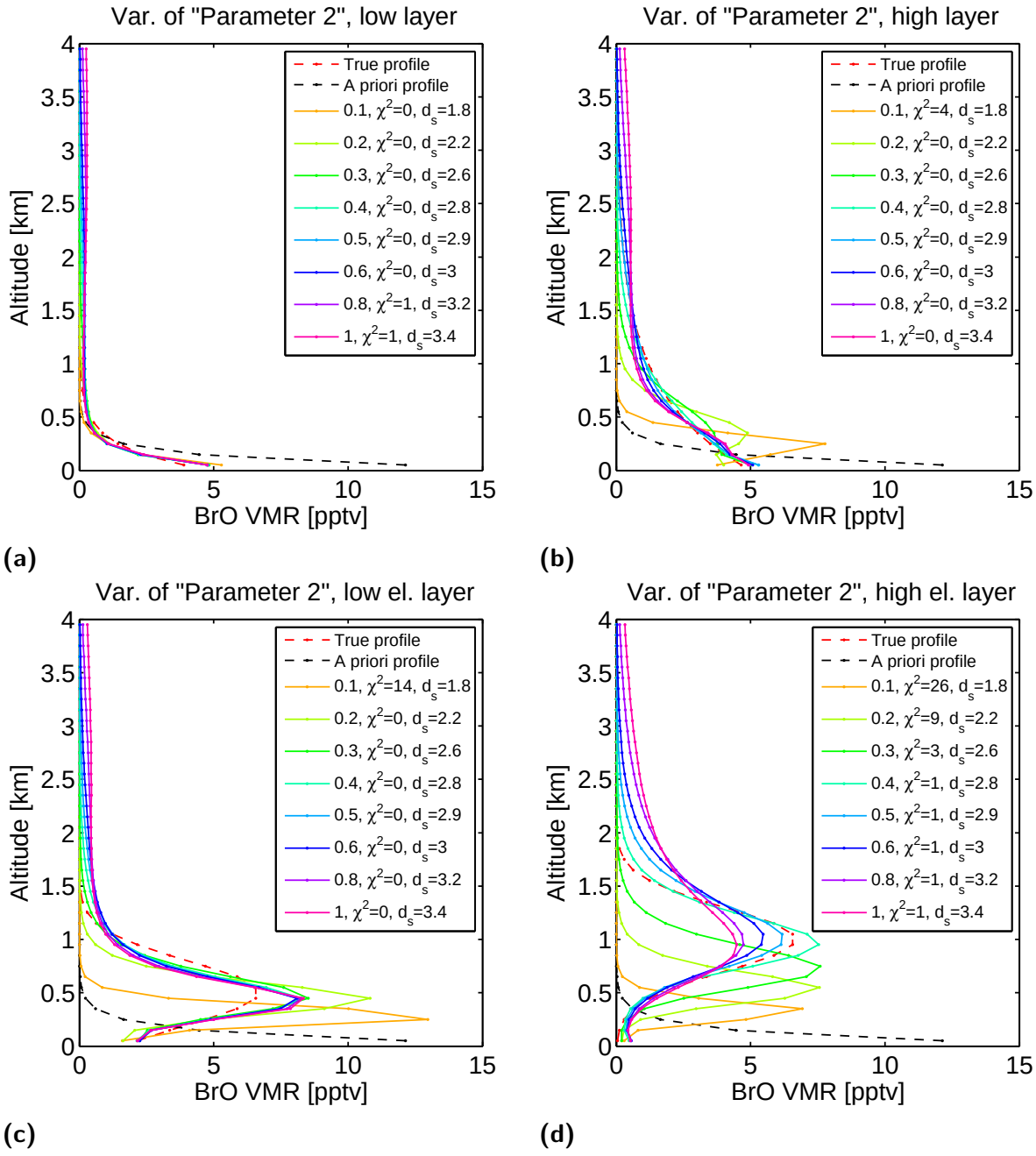

Figure 5.42.: Case 2 - Low BrO mixing ratios: Analysis of the effect of the scale height of the used a priori profile. The shown a priori profile is the one used during the first run, with a height of 0.1 km. The scale height is indicated in km. For details of the method see section 5.2.

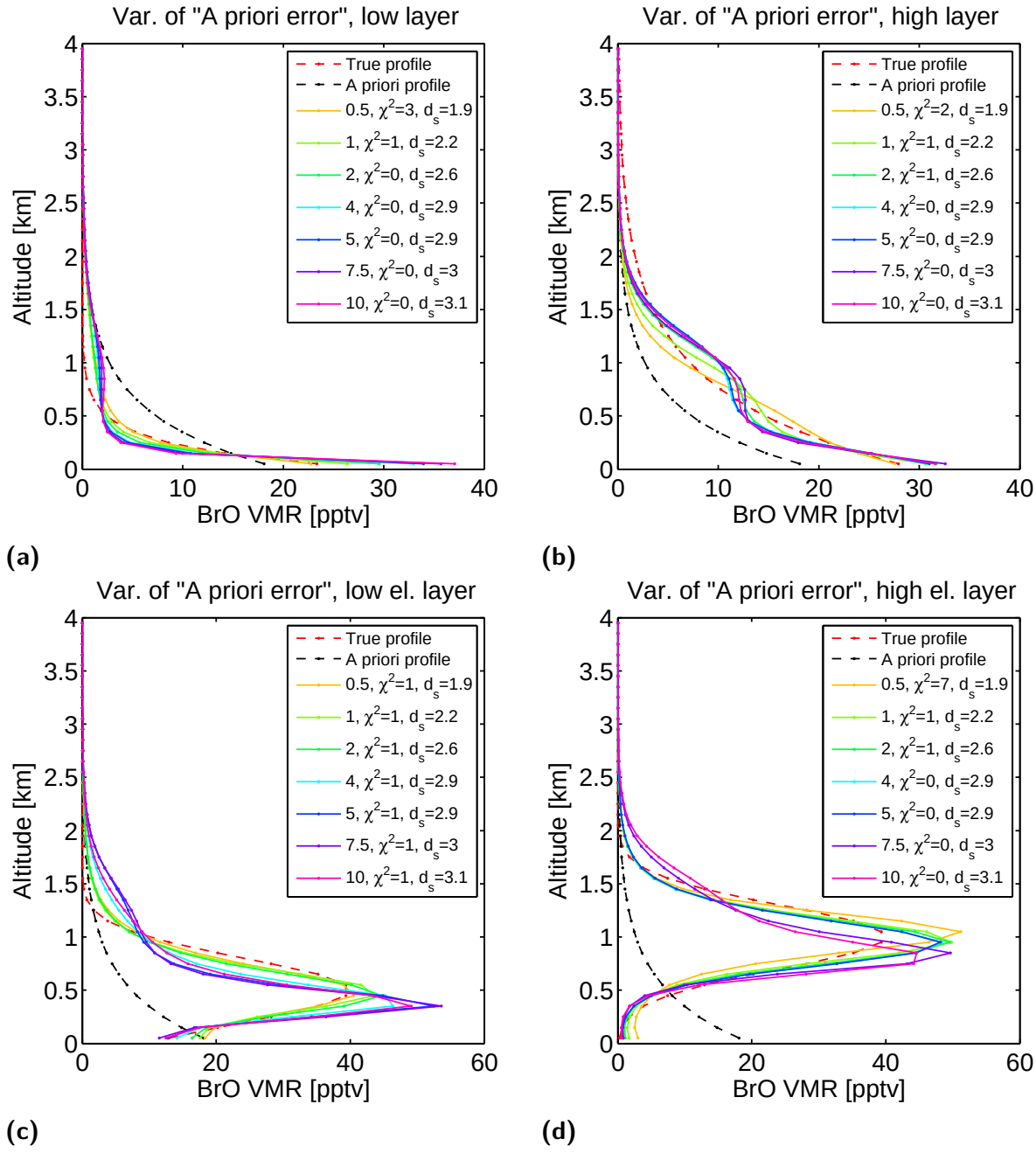

Figure 5.43.: Case 1 - High BrO mixing ratios: Analysis of the effect of different assumed relative errors for the a priori profile between 50% (given as 0.5) and 1000% (given as 10). For details of the method see section 5.2.

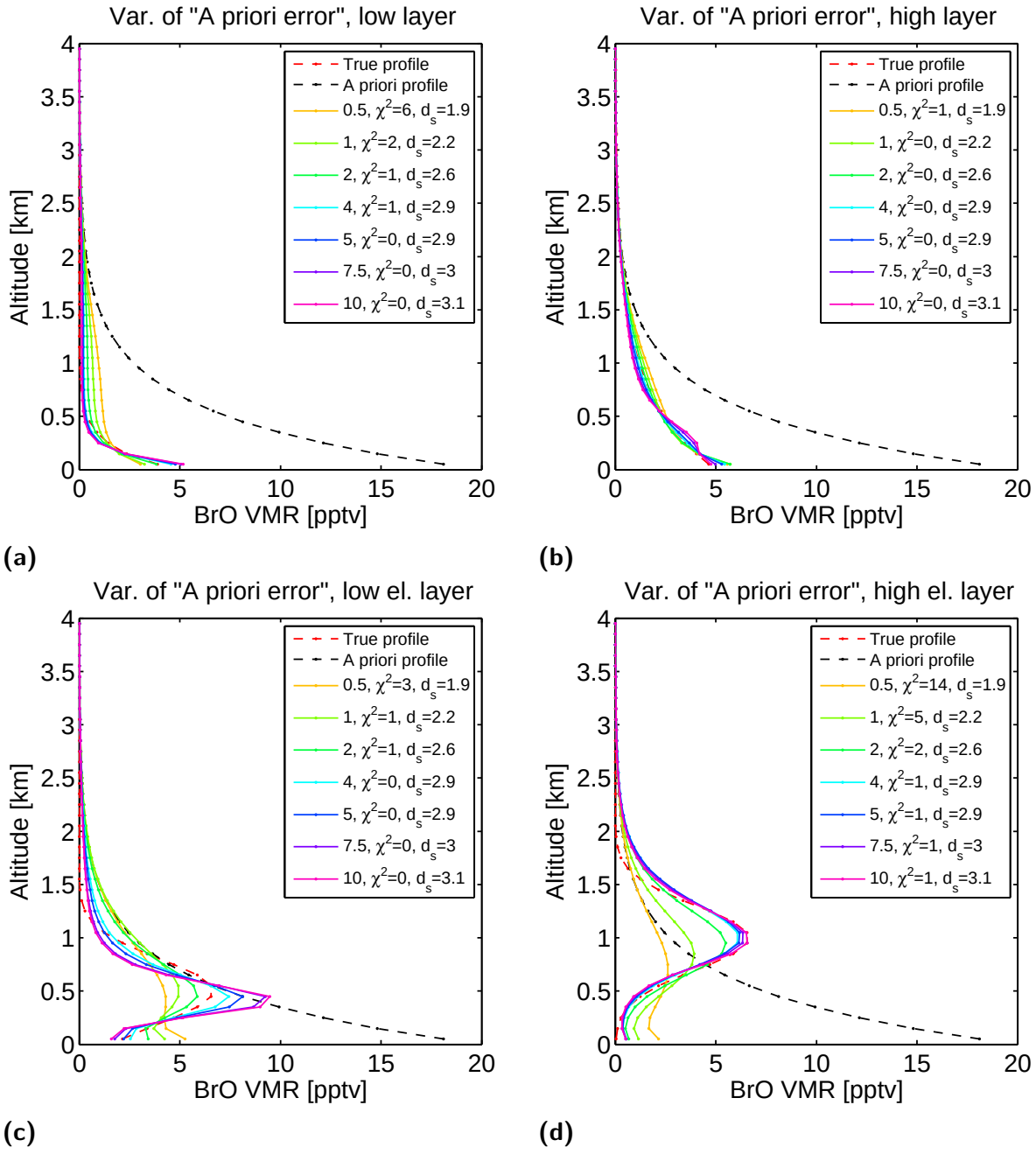

Figure 5.44.: Case 2 - Low BrO mixing ratios: Analysis of the effect of different assumed relative errors for the a priori profile between 50% (given as 0.5) and 1000% (given as 10). For details of the method see section 5.2.

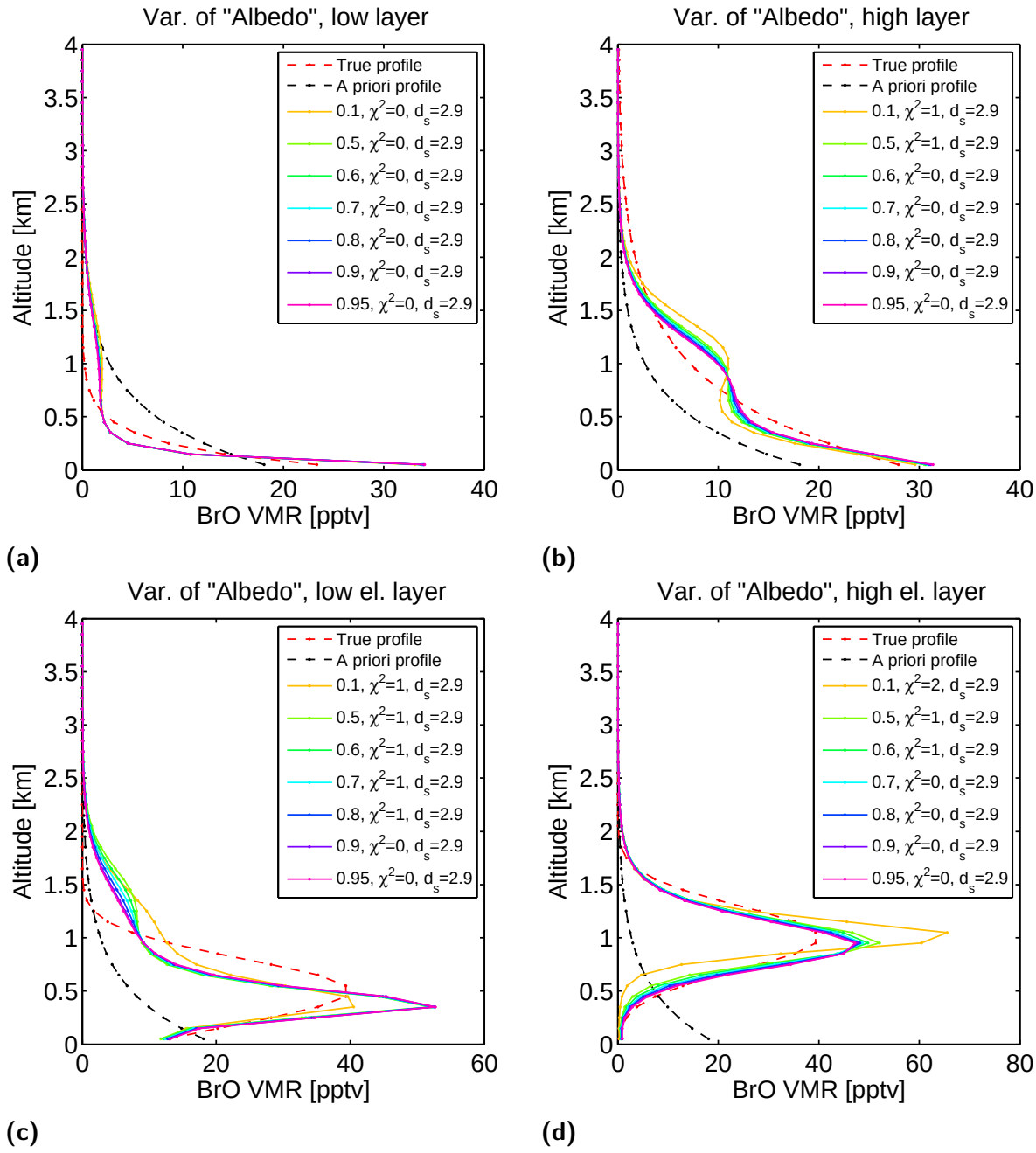

Figure 5.45.: Case 1 - High BrO mixing ratios: Analysis of the effect of the assumed albedo for values from 0.1 to 0.95, with the true, simulated albedo being 0.8. For details of the method see section 5.2.

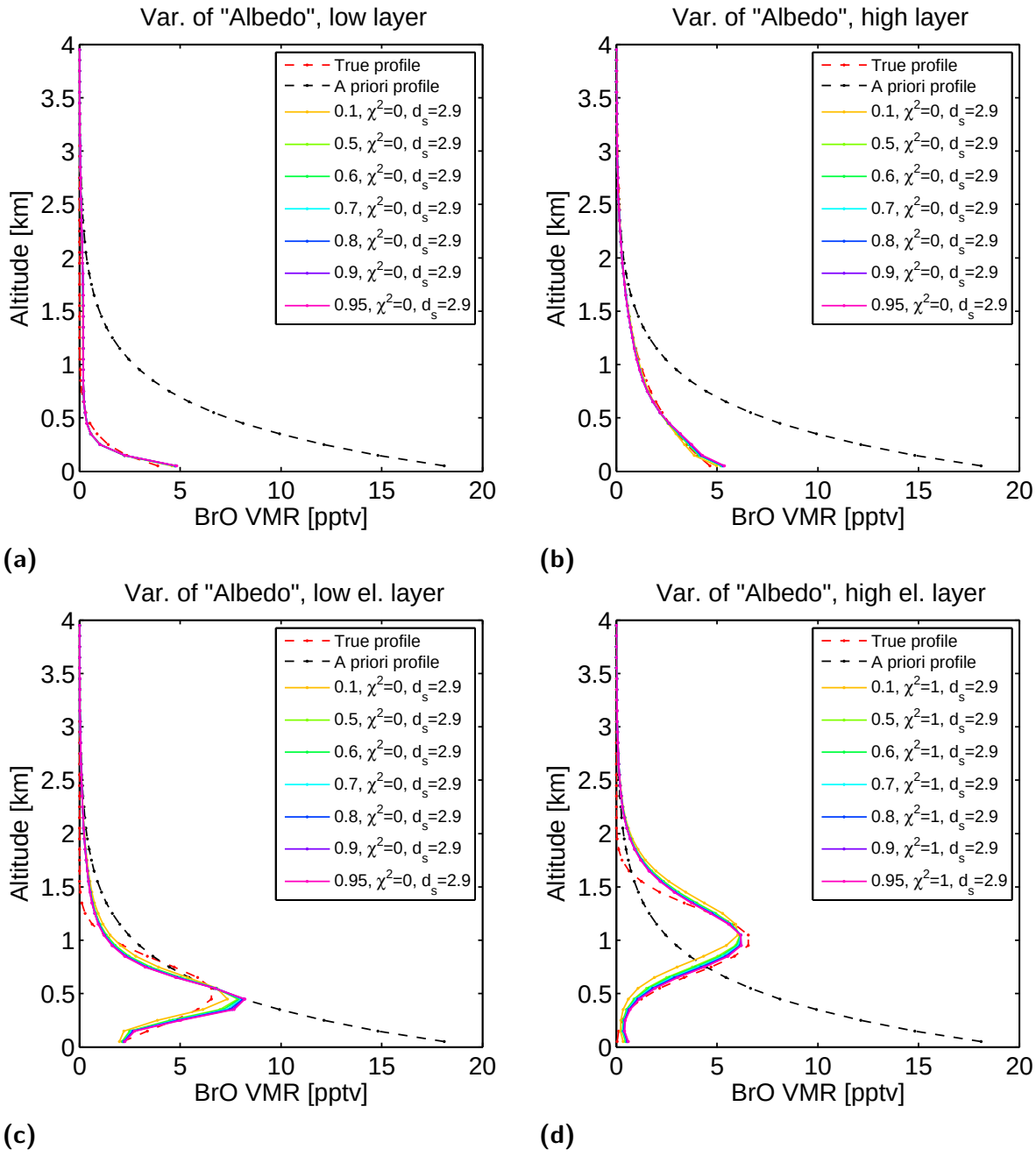

Figure 5.46.: Case 2 - Low BrO mixing ratios: Analysis of the effect of the assumed albedo for values from 0.1 to 0.95, with the true, simulated albedo being 0.8. For details of the method see section 5.2.

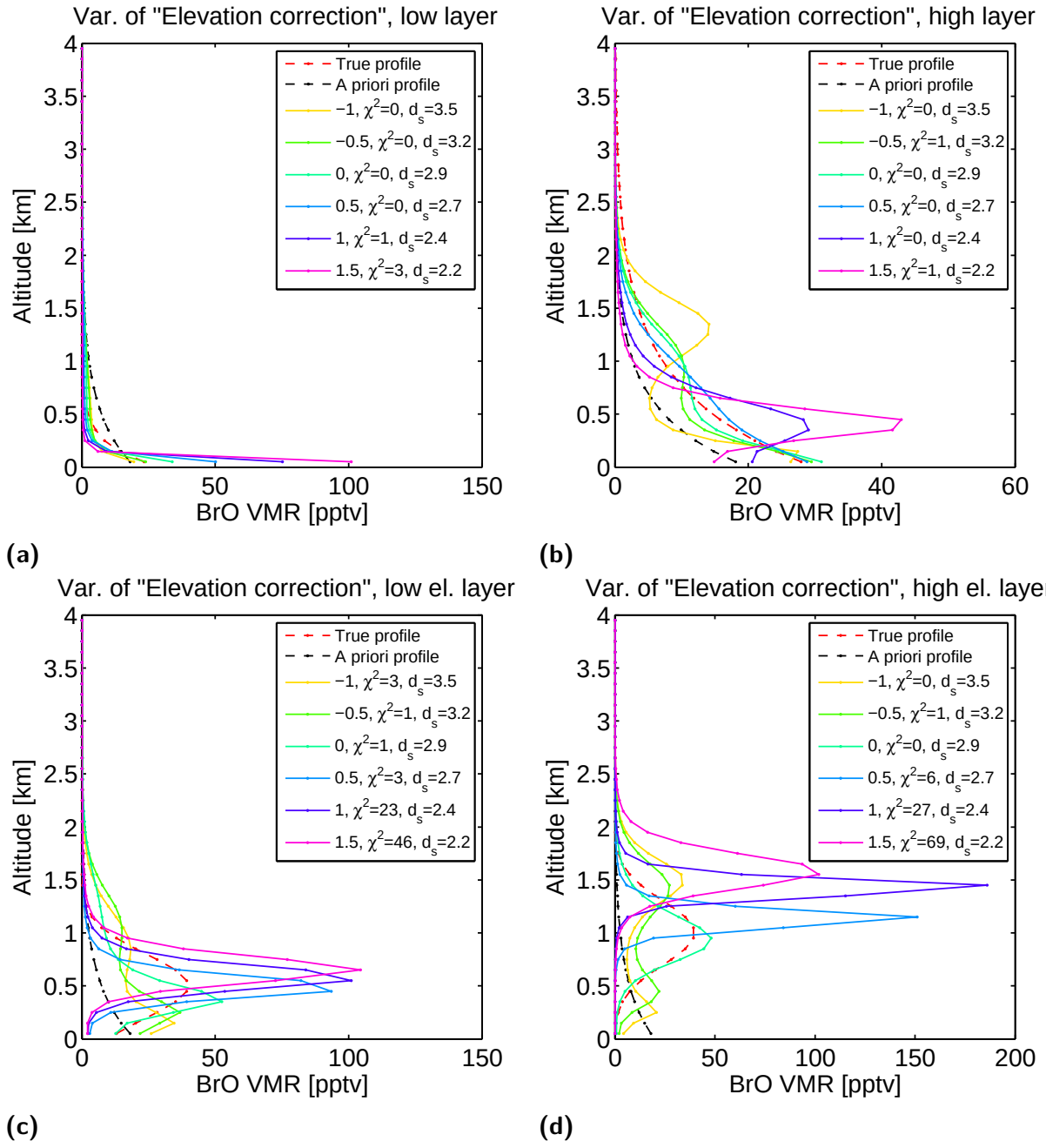

Figure 5.47.: Case 1 - High BrO mixing ratios: Analysis of the effect of an offset, between -1 ° and +1.5 °, in the elevation angle of the viewing direction of the telescope. Positive angles indicate the instrument is looking lower than assumed. For details of the method see section 5.2.

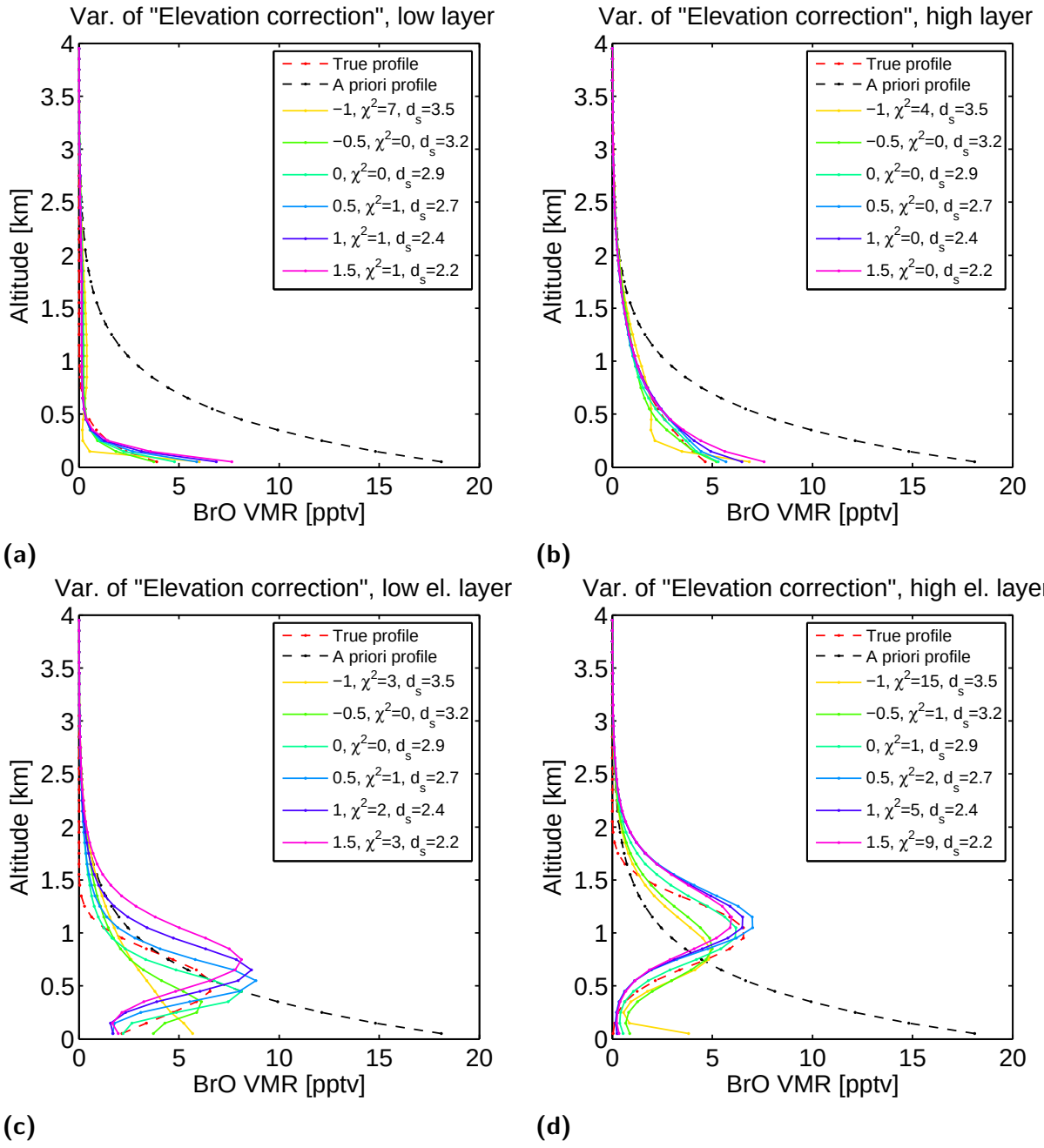

Figure 5.48.: Case 2 - Low BrO mixing ratios: Analysis of the effect of an offset, between -1 ° and +1.5 °, in the elevation angle of the viewing direction of the telescope. Positive angles indicate the instrument is looking lower than assumed. For details of the method see section 5.2.

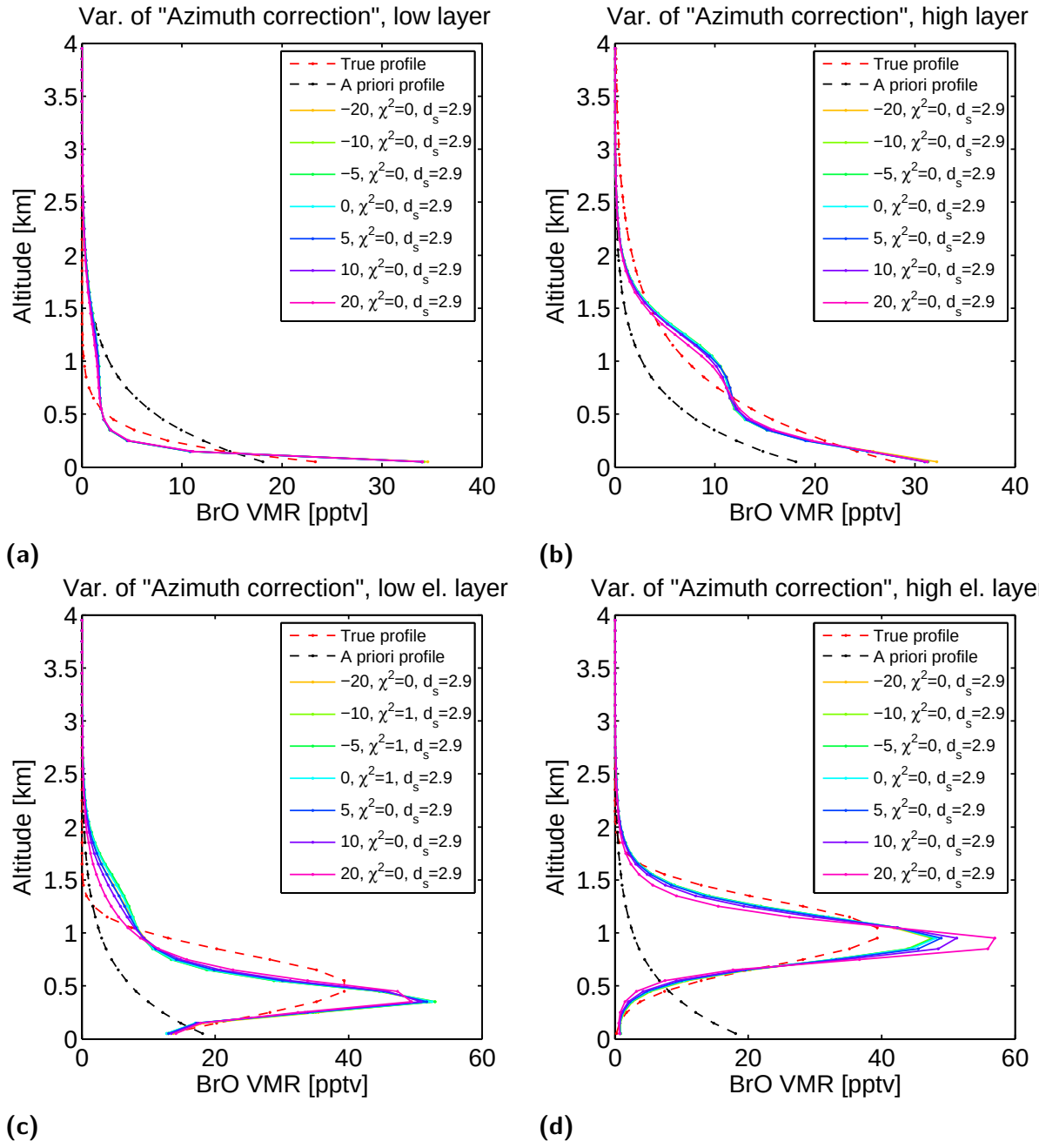

Figure 5.49.: Case 1 - High BrO mixing ratios: Analysis of the effect of an offset, between -20 ° and +20 °, in the azimuth angle of the viewing direction of the telescope. Positive angles indicate the instrument is looking further left than assumed. For details of the method see section 5.2.

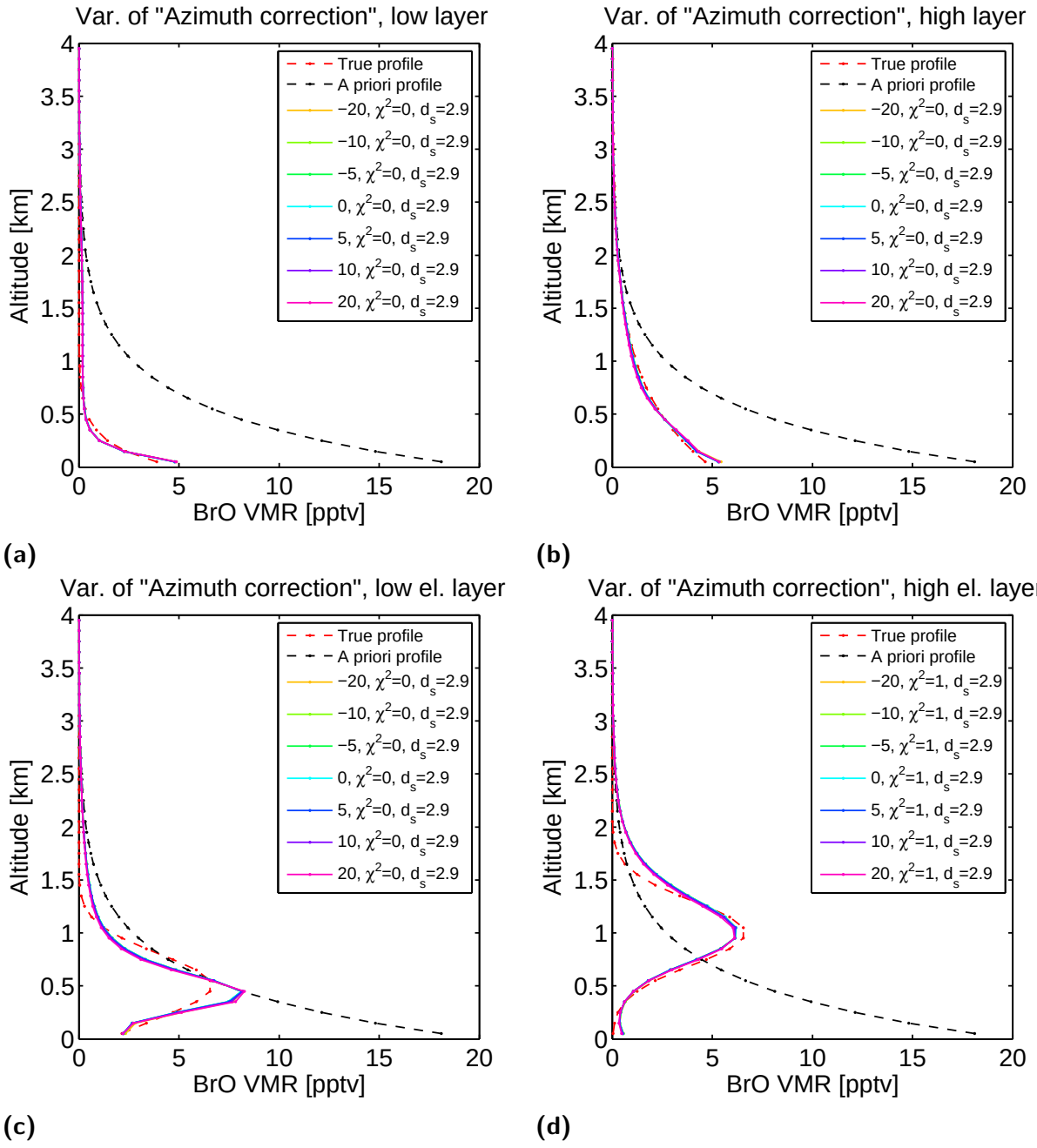

Figure 5.50.: Case 2 - Low BrO mixing ratios: Analysis of the effect of an offset, between -20 ° and +20 °, in the azimuth angle of the viewing direction of the telescope. Positive angles indicate the instrument is looking further left than assumed. For details of the method see section 5.2.

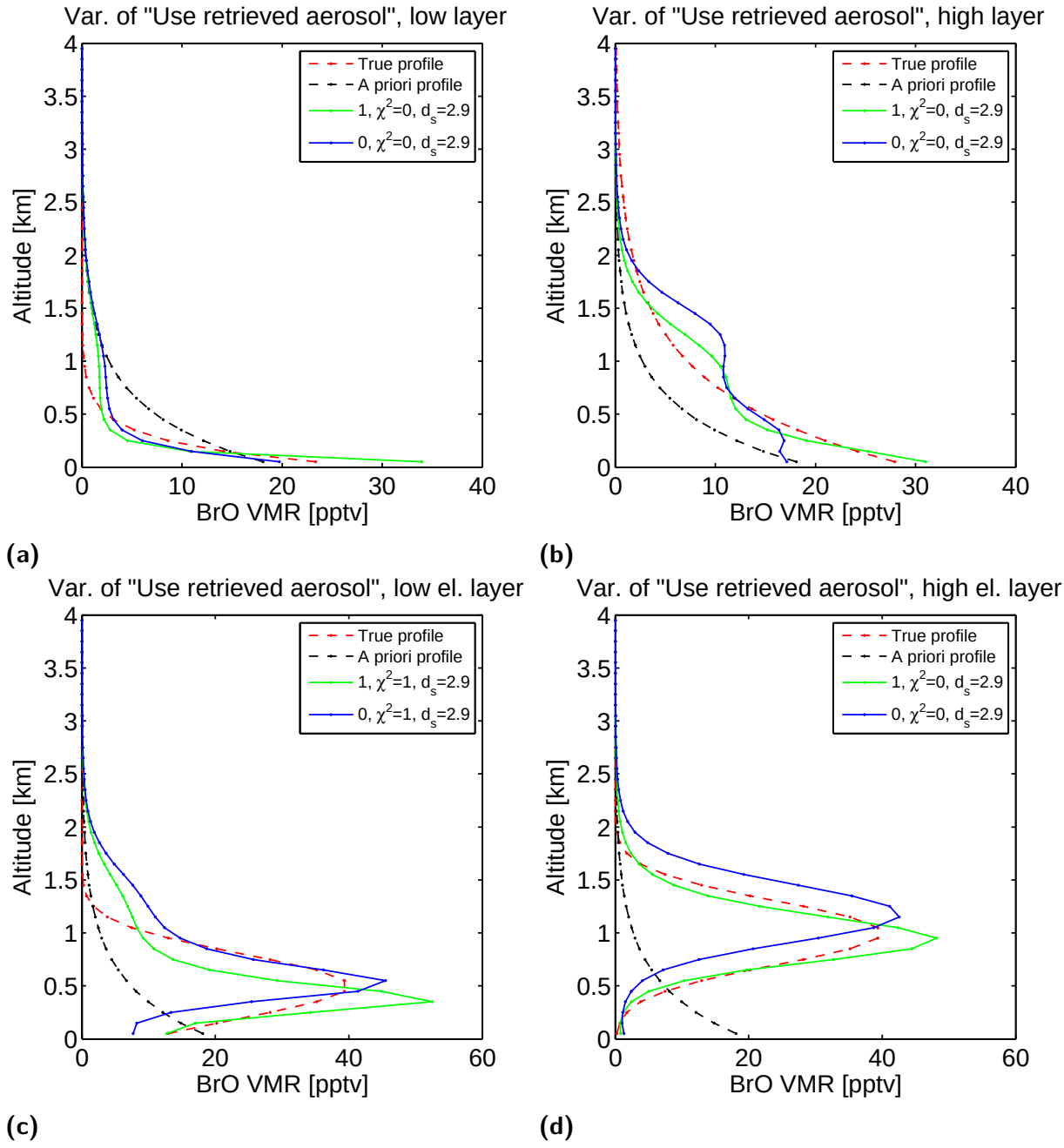

Figure 5.51.: Case 1 - High BrO mixing ratios: Analysis of the effect of whether to use the retrieved aerosol profile (indicated by 1), or not (indicated by 0) and instead assume a pure, aerosol free atmosphere. For details of the method see section 5.2.

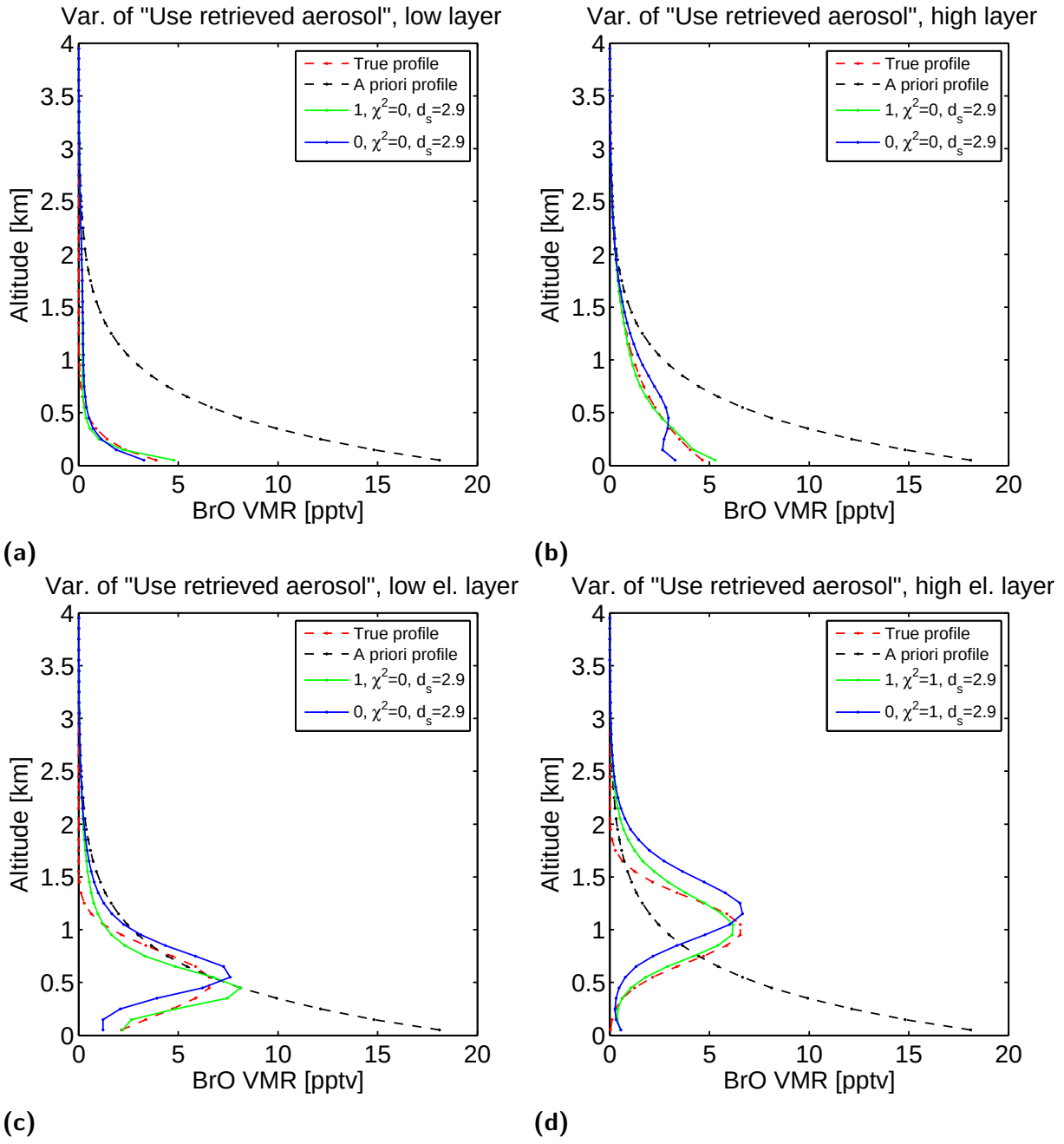

Figure 5.52.: Case 2 - Low BrO mixing ratios: Analysis of the effect of whether to use the retrieved aerosol profile (indicated by 1), or not (indicated by 0) and instead assume a pure, aerosol free atmosphere. For details of the method see section 5.2.

5.3 Discussion and conclusions

A systematic study of the sensitivity of ground-based MAX-DOAS measurements and the utilized inversion algorithm HEIPRO has been conducted. For both the sole aerosol inversion as well as the trace gas inversion combined with an aerosol inversion, four synthetic profile shapes were tested with different extinctions and mixing ratios which were of interest to be distinguishable in field measurements in this work.

Generally it can be stated, by using a suitable measurement setup and inversion parameters, a remarkably high degree of reproduction of the true states is possible when several parameters, which are mentioned below, are known with a realistically achievable accuracy. The four different input synthetic profiles can be clearly distinguished with the technique.

The encountered deviations can be roughly categorized into two classes. First, the ones which cause deviations on the order of a few dozen, or even only a few, percent. And secondly, the ones which cause deviations on the order of a factor of 2 or more. Another additional classification can be done depending on whether those effects are more of less only quantitative, i.e. the resulting profile is scaled by some factor, or if it is also qualitative, i.e. the profile shape is skewed. From the results of this chapter, this classification is given in table 5.5, where the inversion parameters are grouped by their influence of the result in terms of the kind and amount of impact they have for the aerosol inversion. The same for the trace gas inversion is given in table 5.6.

5.3.1 Aerosol

Beginning with the aerosol inversion, in terms of general reproduction of the true vertical profiles (states), at low aerosol loads a very good agreement can be attained (case 1). At medium aerosol loads (case 2), still, for the profile shapes a and c a very good reproduction is possible, while profiles b and d are not reproduced well. At high aerosol loads (case 3), the amount of information present in the measurements drops severely ($d_s < 1$). Profile shape b appears to be almost pathologic as the algorithm does not have any information left of the state of the atmosphere on top of the lowest several hundred meters of aerosol with the resulting multiple scattering.

The inversion settings used in this study were optimized for the low aerosol case, as it is by far the predominant one in the MAX-DOAS measurements in this work (chapters 6, 7 and 8). Fortunately, case b is also not very likely to occur at high aerosol extinction in polar regions due to the usually low boundary layer height (e.g. Anderson and Neff, 2008). In other environments, a better reproduction of those cases might be possible using different a priori profile settings, but this has to be further studied.

At low aerosol extinctions, the surface albedo is important. Of the parameters

	Influence mainly quantitative	Influence also qualitative
Strong	Albedo	Elevation angle
	Asymmetry parameter	O_4 cross section scaling
	-	A priori properties
	-	Weighting function recalculation
Weak	Azimuth angle	-
	MPI latitude	-
	Single scattering albedo	-

Table 5.5.: Classification of the results of the sensitivity studies from this chapter for the aerosol inversion. The parameters are sorted by their kind of influence, whether they mainly have a quantitative influence, i.e. scale the profile shape, or whether their influence is also strongly qualitative, i.e. modify the shape of the retrieved profiles. Furthermore they are grouped by the magnitude of their impact on the result, whether it is weak (variation between the results on the order of 10% - 20%) or strong (results vary more than 100%).

describing the aerosol optical properties, the Henyey-Greenstein asymmetry parameter is the most critical. The single scattering albedo (SSA) on the other hand is only of minor importance.

A possible scaling factor in the magnitude of the O_4 cross section would also have a large effect on the result. How accurate the scaling is, however, has to be determined from measurements. Different pressure and temperature profiles also have a relatively minor effect.

5.3.2 Trace gas

The reproduction of the true state in the resulting profiles for the linear inversion of the trace gas measurements is even better than for the nonlinear aerosol application for both cases and all four profile shapes. This is of course when assuming ideal conditions and a suitable measurement setup and inversion parameters. Different than for the aerosol inversion, profile shape b does not pose the same problem to the technique as the averaging kernels, i.e. the measurement sensitivity at higher altitudes, do not depend on the amount of trace gas at the surface.

Also due to the linearity of the problem, the choice of the a priori profile is not as important compared to the aerosol inversion within reasonable bounds. At low aerosol loads, in this study a surface extinction of $0.1\,\mathrm{km}^{-1}$, the induced changes in radiative transfer and thus the use of the aerosol inversion itself is also a comparatively minor effect.

	Influence mainly quantitative	Influence also qualitative
Strong	-	Elevation angle
	-	A priori properties
Weak	Azimuth angle	Use retrieved aerosol
	Albedo	-

Table 5.6.: Classification of the results of the sensitivity studies for the trace gas (BrO) inversion. The parameters are sorted by their kind of influence, whether they mainly have a quantitative influence, i.e. scale the profile shape, or whether their influence is also strongly qualitative, i.e. modify the shape of the retrieved profiles. Furthermore they are grouped by the magnitude of their impact on the result, whether it is weak (variation between the results on the order of 10% - 20%) or strong (results vary more than 100%).

5.3.3 Common issues

A common issue for both measurements and inversions is the necessity to accurately know the elevation angles of a measurement sequence, where offsets cause drastic deviations both in terms of magnitude as well as shape of the profile. An unknown offset of $0.5\,^{\circ}$ can be enough to completely distort the retrieved profiles from the true state. For the azimuth angle on the other hand, even larger offsets only show a minor effect in the results.

Furthermore, the properties of the a priori profile are important in both inversion stages and have to be determined from the measurement setting. It is evident that the error on the a priori profile has to be chosen in way that maximizes the extraction of information from the measurements while preventing overfitting and the accompanying oscillations. The scale height has to be high enough to avoid the dragging down of higher layers into lower boxes.

5.3.4 Concluding remarks

Due to the generally good reproduction of the simulated profile shapes and no possibilities of further improvements, the parameter values given in table 5.1 for the aerosol inversion and 5.3 for the trace gas inversion are used in this work and can be given as a recommendation for future studies under similar conditions.

Finally, it can be stated that it is evident from these studies that fine-tuning the weaker parameters is of little use unless all of the high impact ones have been accurately determined.

6

Field studies at Scott Base, Antarctica

In 2012, a measurement campaign was undertaken, based at the New Zealand station Scott Base in cooperation with the National Institute of Water and Atmospheric Research (NIWA) of New Zealand. The station is situated on Ross Island in Antarctica at 78 °S (see figure 6.1) and the campaign lasted throughout austral spring, from end of August until end of November.

Logistically, Scott Base and neighboring McMurdo Station, are the only locations in Antarctica accessible during the winter and spring period and therefore fortunate locations to study the springtime phenomenon of reactive halogen chemistry. Another criterion for the Ross Sea area was, that it is one of the two regions in Antarctica where elevated VCDs of IO were observed from space.

Compared to locations in the Arctic, only few previous studies had been undertaken in Antarctica to investigate the reactive halogen chemistry occurring in austral spring. The whole campaign had several objectives, the major one however, was to investigate the sources of iodine monoxide. As mentioned in section 2.5.3, previous measurements by Saiz-Lopez et al. (2007) at Halley Station found IO mixing ratios of up to 20 pptv, with a yearly average of 8 pptv. Furthermore, Friess et al. (2010) concluded from measurements of light scattered on the snow at Neumayer Station and radiative transfer calculations, that IO of the order of several ppbv should be present in the interstitial air of the uppermost layers of snow pack.

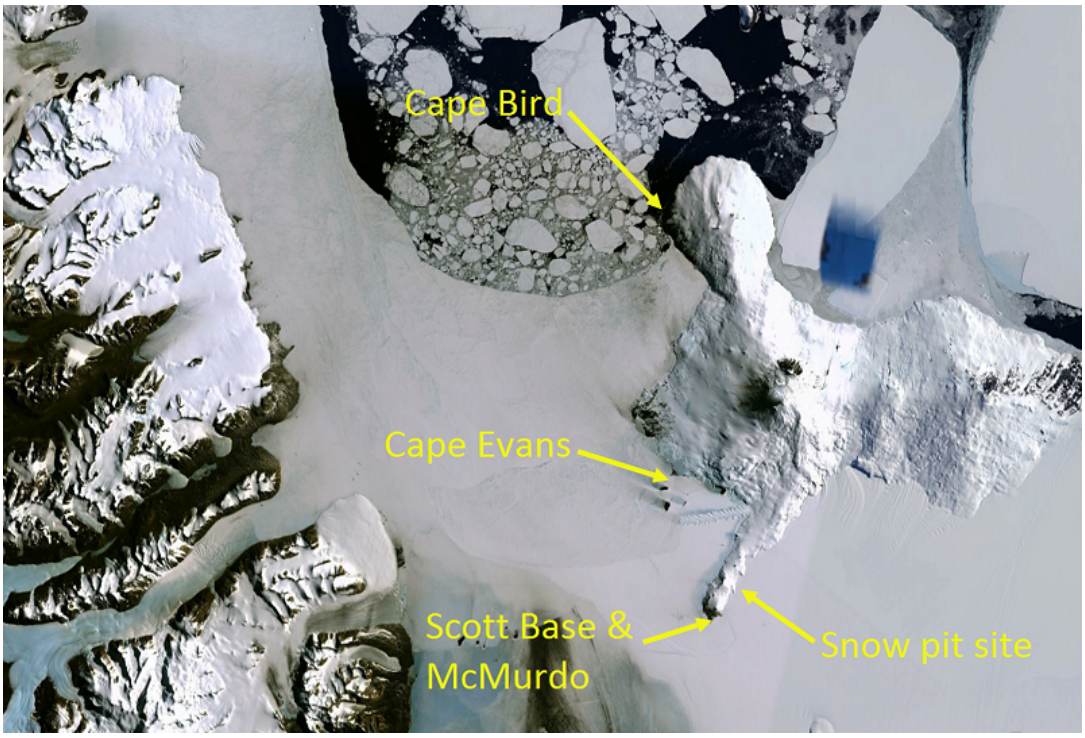

Figure 6.1.: A satellite image of the McMurdo Sound region. Scott Base and McMurdo Station are located at the southernmost tip of volcanic Ross Island. To the south, the McMurdo ice shelf begins. On the other side of the sound (left), the Transantarctic Mountains are rising. Cape Bird, Cape Evans and the snow pit site are indicated as places where measurements were also undertaken. Map data: Google, U.S. Geological Survey.

6.1 Location and description of the campaign

Several DOAS instruments were brought to the field, in order to combine the different kinds of information they offer. Those were:

- An LP-DOAS instrument, in order to observe a multitude of species, day and night, and reliably pin down mixing ratios at the surface, due to the well known light path.

- The CE-DOAS instrument described in 4.1, with the ability to conduct point-like measurements, to probe locations deemed to be possible sources of IO. Due to the expected concentrations of the order of several pptv, a detection limit of 1 pptv for IO under optimal conditions was deemed to be sufficient, which the instrument fulfilled.

- Lastly, a small, mobile MAX-DOAS instrument was deployed, in order to gain information about vertical distributions, but also to take advantage of the very long absorption light paths in scattered light measurements, and the ensuing small detection limit in terms of mixing ratios.

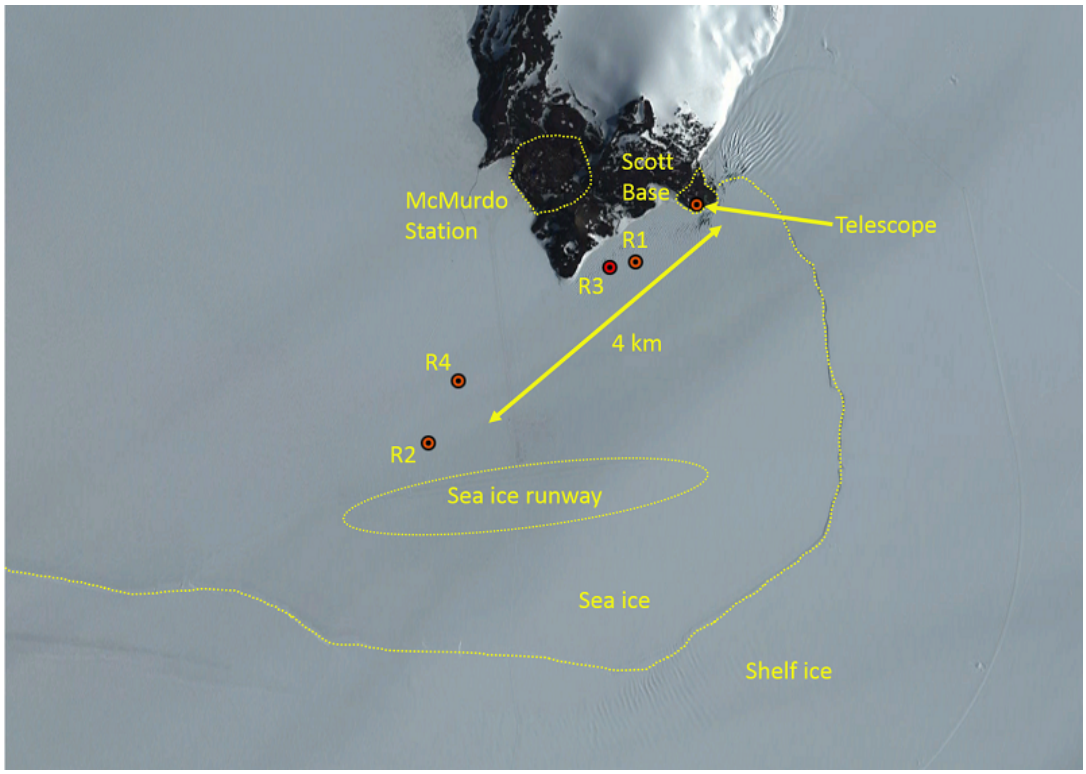

Figure 6.2.: Map showing the setup of the LP-DOAS at the southern tip of Ross Island, where Scott Base and McMurdo are situated. The telescope was located at Scott Base, the two retro reflectors on sea ice. The first two locations, R1 and R2, were changed after two weeks to new ones, R3 and R4, to sample air less influenced by the air field. Map data: Google, DigitalGlobe.

The field work was based at Scott Base, where the LP-DOAS telescope was also located. The mobile measurements with the CE-DOAS and MAX-DOAS instruments were done at several different locations around Scott Base and Ross Island. Meteorological data measured at Scott Base and at Arrival Heights was kindly provided by NIWA. The first day, when the sun was coming above the horizon, was the 18th August. The 22nd of October was the last day, when the sun set below the horizon. The times and dates are indicated as UTC times as in the rest of this work, which is 12 hours behind the local New Zealand time.

6.1.1 LP-DOAS measurements

The layout of the LP-DOAS light paths is mapped in figure 6.2. The LP-DOAS telescope was set up below a station building (Hatherton Lab) and shielded by a polar tarp, pictured in fig. 6.3. Two light paths were set up, for which two retro reflector arrays were deployed. One was located closer to the station, to be able to measure during periods with fog or snow drift, the other one further away (pictured in figure 6.4b), for lower detection limits. Furthermore, two light paths give some spatial resolution.

Figure 6.3.: The LP-DOAS telescope was located inside the blue polar tarp, in order to shield it from strong winds and thereby reduce vibrations and jitter, but also to prevent snow from accumulating on top. Photo courtesy of Tim Hay.

Initially, the two reflector arrays were set up at the positions R1 (short, distance 1.14 km) and R2 (long, distance 4.86 km). They were moved to two new locations at R3 (short, distance 1.46 km) and R4 (long, distance 4.01 km) on the 14th September, to have less exposure to the significant pollution coming from the sea ice runway. Another problem were the frequent mirages, which occurred over the sea ice and led to problems with the alignment of the telescope onto the reflectors. To alleviate this, the size and the number of individual retro reflectors at R4 was increased. The retro reflector arrays used for R1/R3 and R2/R4 are shown in fig. 6.4.

For most of the time of the campaign, a 75 W xenon arc lamp (Osram XBO, not ozone-free) was used as the light source. During the last two weeks, a 500 W arc lamp (PLI Hanovia HSAX5002) was used, which has a much higher luminous density, as well as higher operating temperature and pressure, which leads to broader, less interfering, spectral structures of xenon. The primary reason the lamp was used however, was to have more light intensity, and thus a lower limit of detection in the deeper UV region around 300 nm, where the absorption bands of ClO are located.

The measurement procedure during the campaign was as follows. Spectra were acquired alternatingly on both light paths. For each light path, spectra were recorded at four different wavelength intervals by turning the grating inside the spectrometer. The intervals were chosen to cover regions, where the relevant species of interest show absorption bands. They were chosen to be 271 nm - 355 nm, 362 nm - 443 nm, 493 nm - 572 nm and 604 nm - 680 nm. For each of those, 25 spectra with a saturation of 70% were recorded, with a maximum duration of 1 s per spectrum. Typical exposure times for one spectrum were between 6 ms and 500 ms depending on wavelength range, visibility conditions

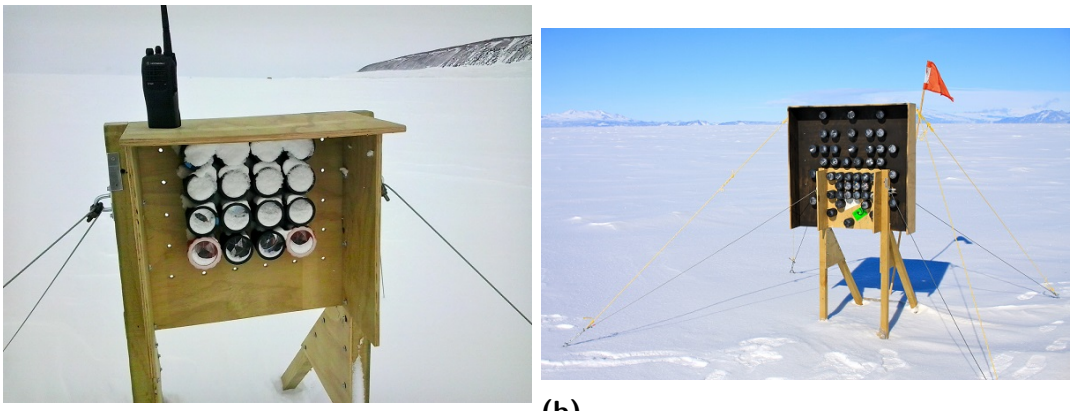

(a) **(b)**

Figure 6.4.: **(a)** The array used for the short light path at R1 and R3, covered with snow. **(b)** The retro reflector array used for the longer of the two LP-DOAS light paths at R2 and R4. The reflector was enlarged with the darkened, wooden extension to cope with the frequent mirages above the sea ice.

and the used arc lamp.

6.1.2 CE-DOAS measurements

All of the CE-DOAS measurements were conducted in the following way. The instrument was set up and typically left for an hour, to reach a thermal equilibrium while the purge tube was still mounted. When ready, a path length calibration using the wavelength-resolved ring-down method (refer to section 4.1.1) was done, followed by the acquisition of several I_0 spectra. Afterwards, the acquisition of measurement spectra was started and the purge tube removed. Usually, by the time the instrument could be reached again after a couple of days, the light path was clogged up with snow and the resonator mirrors contaminated with snow or salt. Therefore the evaluations were all done against the I_0 spectra that were taken at the beginning of each measurement series.

6.1.3 MAX-DOAS measurements

The mobile MAX-DOAS instrument was deployed in a similar fashion to the CE-DOAS instrument, i.e. placed at several different locations, for a couple of days each, and then moved to a different location. Often, the instrument was located next to the CE-DOAS instrument on top of the yellow trailer (e.g. fig. 6.19). Twice, the instrument was placed on the wooden balcony, visible in picture 6.3, 1 m above the LP-DOAS telescope, looking towards the same direction, for an inter-comparison of the different DOAS techniques. Unfortunately, the instrument had several technical issues during the campaign, which occasionally resulted in the measurement computer to crash and therefore a lot of downtime.

Species	**Fit range [nm]**	**Accounted absorbers**	**Co-added sequences**
BrO, O_3 HCHO, HONO	315.6 - 350.7	BrO, O_3, NO_2, HONO HCHO, O_4	4
IO, NO_2	407.6 - 438.9	IO, NO_2, H_2O	32 (IO) 4 (NO_2)
ClO	294.0 - 313.3	ClO, O_3, NO_2, HCHO BrO, SO_2, DeltaSC	8
OClO	327.6 - 348.7	OClO, BrO, O_3, NO_2 HONO, HCHO, O_4	32
OBrO	531.4 - 567.2	OBrO, NO_2, H_2O	32
OIO, I_2	543.0 - 567.2	OIO, I_2, NO_2, H_2O	32

Table 6.1.: LP-DOAS evaluation: The six fit intervals used, with the absorbers included in the procedure, as well as the number of averaged measurement sequences. All fit scenarios contain an optical shortcut spectrum and a background spectrum. The used DOAS polynomial was always of 3rd order.

One measurement sequence consisted in acquiring spectra for the angles of 1 °, 2 °, 5 °, 10 °, 20 ° and 90 °, with a duration of 1 minute for each angle.

6.2 Spectral evaluation and inversion of SCDs

6.2.1 LP-DOAS evaluation

The recorded spectra from the LP-DOAS were averaged over a certain number of measurement sequences for a higher signal-to-noise ratio. The optical density was calculated by dividing atmospheric and optical shortcut spectra, after their respective background spectra had been subtracted. The optical densities were then high-pass filtered, before the fit was applied to them in a number of wavelength intervals. The applied fit scenarios for the compounds of interest, BrO, O_3, HCHO, HONO, IO, NO_2, ClO, OClO, OBrO, OIO and I_2, are listed in table 6.1 with the respective wavelength intervals, the number of measurement sequences that were averaged, as well as all absorbers considered in each scenario. Two exemplary fits are given in figure 6.5 for IO and in figure 6.6 for ClO, showing the presence of both compounds.

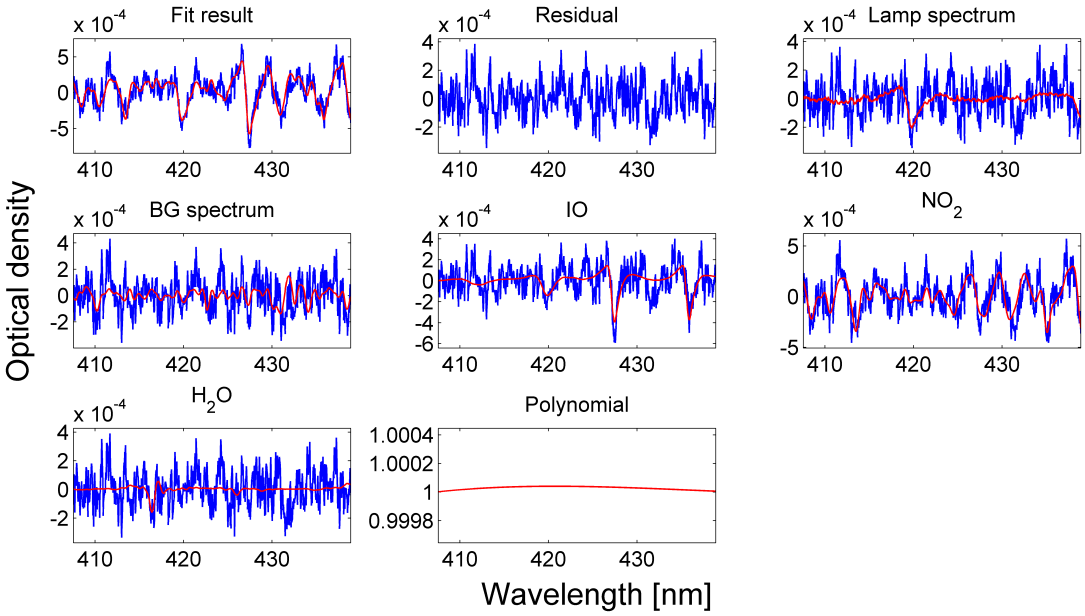

Figure 6.5.: IO: LP-DOAS fit result of 32 co-added sequences from the 26th November on R4. The absorption of IO is visible. The retrieved mixing ratios are: IO (0.83 ± 0.1) pptv, NO_2 (101.7 ± 7.0) pptv and H_2O (3377 ± 1390) ppmv.

6.2.2 CE-DOAS evaluation

The CE-DOAS evaluation was done separately for each measurement series, using the corresponding path length curve and the I_0 spectra, which were recorded before the start of each series. As many I_0 spectra as available were averaged. The DOAS fit was done combining two fit ranges, which were 424.65 nm - 430.30 nm and 437.15 nm - 457.70 nm. The region in-between was excluded due to strong spectral structures. These structures probably emerged due to a combination of detector nonlinearity, and a strong variation of wind speeds, and therefore measured light intensity, with a significantly higher frequency than the spectral acquisition. Included in the fit process were reference spectra for IO, NO_2, H_2O, O_4 and glyoxal. Figure 6.7 shows the fit residual RMS and IO detection limit depending on the number of co-added spectra, for a data set from the field, with favorable measurement conditions such as low wind speeds (Cape Bird, see below in section 6.3.2). The further attainable decrease in RMS, or detection limit, after averaging around 10^6 spectra is insignificant, therefore this number of co-added spectra was chosen for the evaluations. An exemplary fit is shown in figure 6.22 and discussed below.

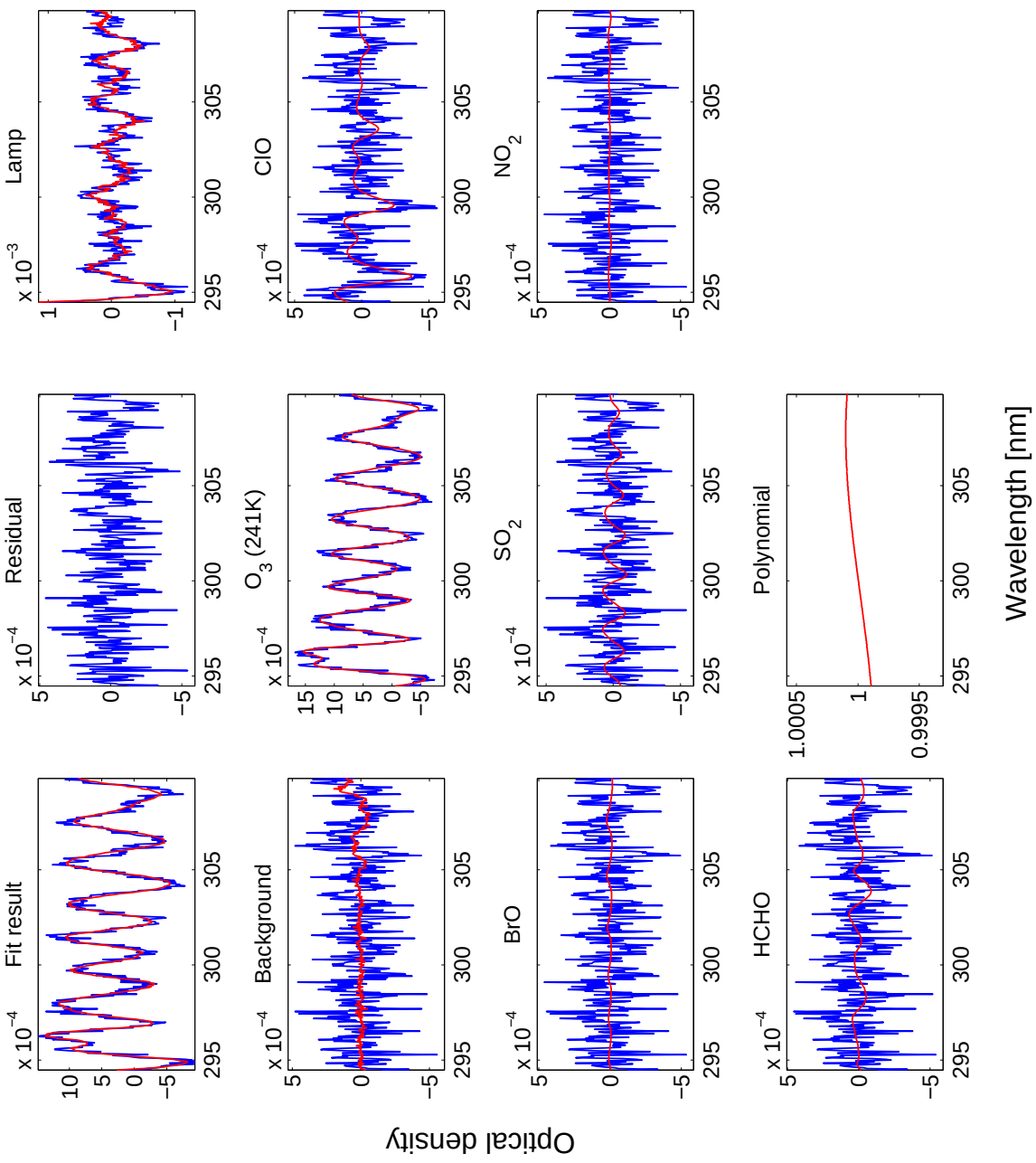

Figure 6.6.: ClO: LP-DOAS fit result of 4 co-added sequences from the 22nd November on R3. The absorption of chlorine monoxide is clearly visible. The retrieved mixing ratios are: ClO (41.9 ± 6.8) pptv, O_3 (17.8 ± 0.6) ppbv, BrO (1.1 ± 1.4) pptv, NO_2 (161 ± 362) pptv, SO_2 (50.1 ± 14.6) pptv and HCHO (306.3 ± 158.8) pptv.

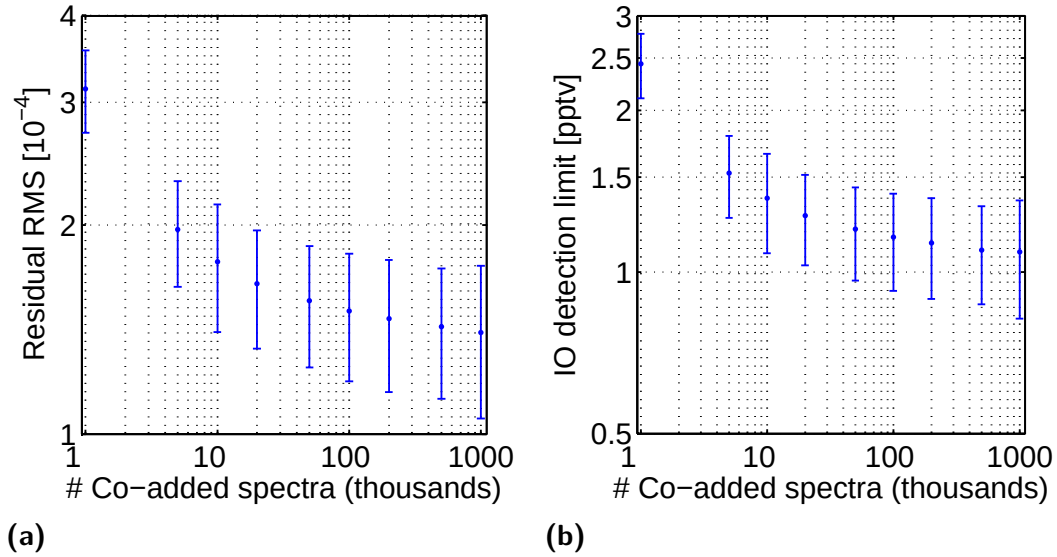

Figure 6.7.: CE-DOAS: Log-log graphs showing the increase in fit quality with the increase of spectral averaging, as quantified by **(a)** the residual RMS, and **(b)** the resulting instrumental detection limits for IO. The error bars indicate the standard deviation. The analysis was done for the field measurements at Cape Bird (section 6.3.2).

6.2.3 MAX-DOAS evaluation

The MAX-DOAS spectra were subjected to three DOAS evaluations, for BrO, IO and O_4. Before, the spectra were averaged over 8 measurement sequences, or less, if beginning and end of the averaging interval would be more than two hours apart. The evaluation was always done relative to the current 90 ° (zenith) spectrum. The wavelength ranges used, as well as the included absorbers for each of the three intervals are listed in table 6.2. An exemplary fit showing the presence of IO is given in figure 6.8.

Species	**Fit range [nm]**	**Accounted absorbers**
BrO	332.5 - 353.0	BrO, O_3, NO_2, HCHO, O_4
IO	413.5 - 440.5	IO, NO_2, H_2O, O_3, VRS N_2, VRS O_2
O_4	365.7 - 398.0	O_4, NO_2, O_3, HCHO

Table 6.2.: MAX-DOAS evaluation: The three fit intervals and the absorbers included in the fitting procedure. All fit scenarios contained a Ring spectrum, a Ring spectrum multiplied with λ^4, and an inverse spectrum to correct for spectrometer stray light. The used DOAS polynomial was always of 5th order.

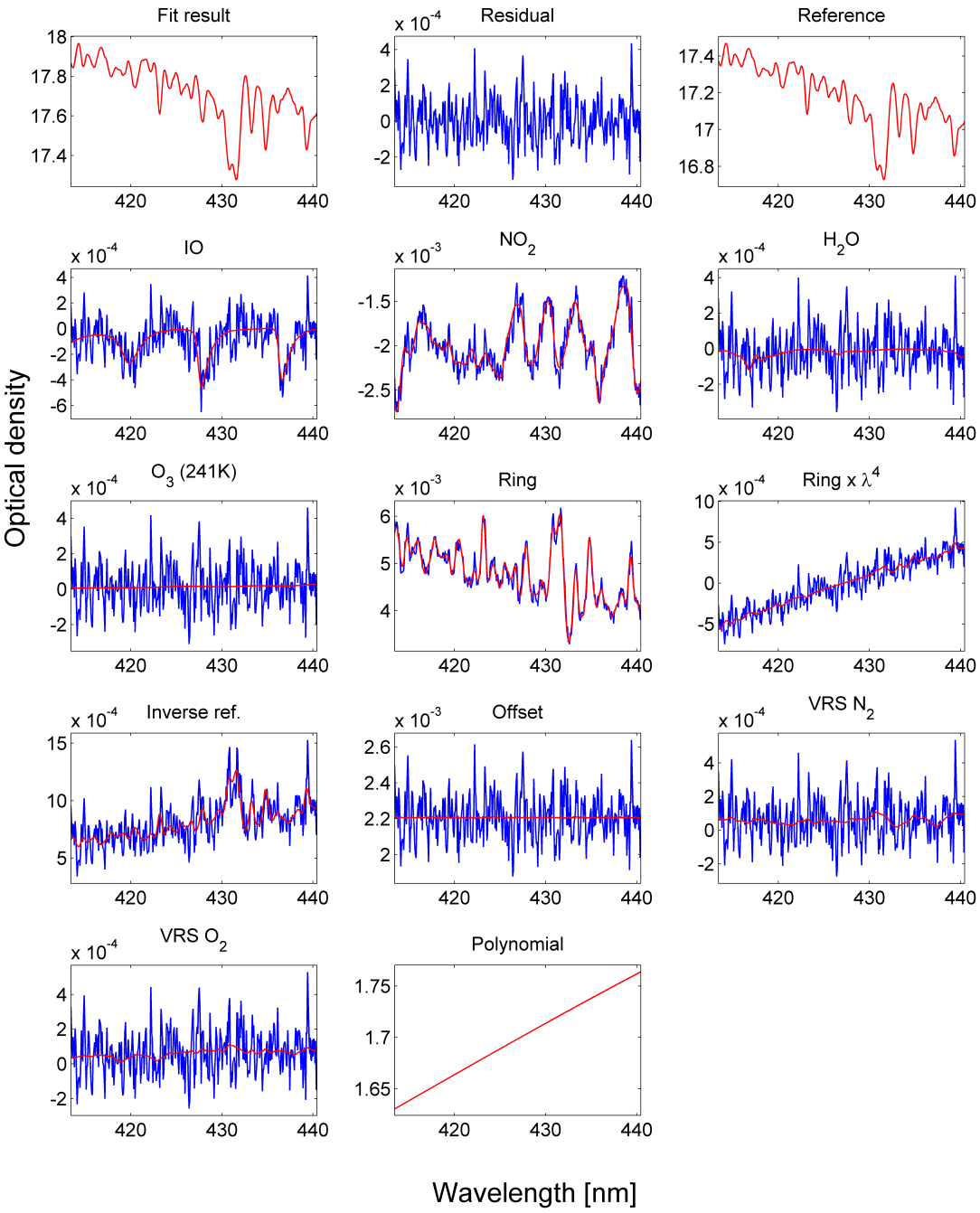

Figure 6.8.: MAX-DOAS IO fit result of 8 co-added 2° elevation angle sequences from the 26th November. The absorption of iodine monoxide is visible. Retrieved column densities are: IO $(1.62 \pm 0.26) \cdot 10^{13}$ molec cm^{-2}, NO_2 $(3.68 \pm 0.18) \cdot 10^{15}$ molec cm^{-2}, H_2O $(3.1 \pm 3.0) \cdot 10^{22}$ molec cm^{-2}, O_3 $(0.2 \pm 2.6) \cdot 10^{18}$ molec cm^{-2}.

Elevation angle offset

The evaluation results of the MAX-DOAS instrument indicated a problem with the elevation angle. The retrieved O_4 SCDs for the elevation angle of 1 ° turned out to be as small as those obtained for negative angles such as -2 °, indicating that the light path was similarly short. This was most likely because the instrument was looking onto the ground due to an offset in the calibration of the elevation angle. As this was systematically the case for all measurement series during the field study, a random variation or error in the elevation angle is unlikely. The 2 ° O_4 SCDs were undoubtedly the highest on clear days, this angle was therefore clearly above the horizon. Taking the instruments field-of-view ($\alpha = 0.3\,°$) into account, the 1 ° angle must have been completely below the horizon (minimum offset of $1\,° + \alpha/2 = 1.15\,°$), while the 2 ° angle must have been completely above the horizon (maximum offset of $2\,° - \alpha/2 = 1.85\,°$). The magnitude of this offset was therefore estimated to be -1.5 °, the center between the two bounds.

Inversion of SCDs

The determined O_4, BrO and IO SCDs were used to compute vertical mixing ratio profiles as detailed in section 3.4.5. For the inversions, only the SCDs from positive elevation angles were used. The settings for the aerosol inversion were chosen as described in section 5.1.2, with the exception of a lower a priori profile error of 300% and the pressure and temperature profiles were taken for 75 ° S.

The settings for the trace gas inversions were also similar to the ones detailed in section 5.2.2. Differences were, the for the BrO inversion, an a priori profile with 5 ppt BrO at the surface and a scale height of 0.5 km and 300% error was used. For IO, an a priori profile with 0.3 ppt at the surface and a scale height of 1.0 km and also 300% error was taken. No inversion was done for NO_2, because, due to its inhomogeneous distribution as apparent from the CE-DOAS and LP-DOAS results, the prerequisite of horizontal homogeneity was not fulfilled.

6.3 Results

6.3.1 LP-DOAS: Mixing ratios of BrO, O_3, IO, NO_2 and ClO

The time series of the mixing ratios derived from the LP-DOAS are shown in the following pages. They are given for BrO, O_3, IO and NO_2. For the last two weeks, they also include ClO, when its evaluation was possible due to the usage of the PLI lamp. The scale of the NO_2 mixing ratios is logarithmic due to their high variability. Compounds which were not observed by the LP-DOAS above the detection limit during the entire campaign are OClO, OBrO, OIO, I_2 and HONO. Their respective typical detection limits for both light paths are listed in table 6.3.

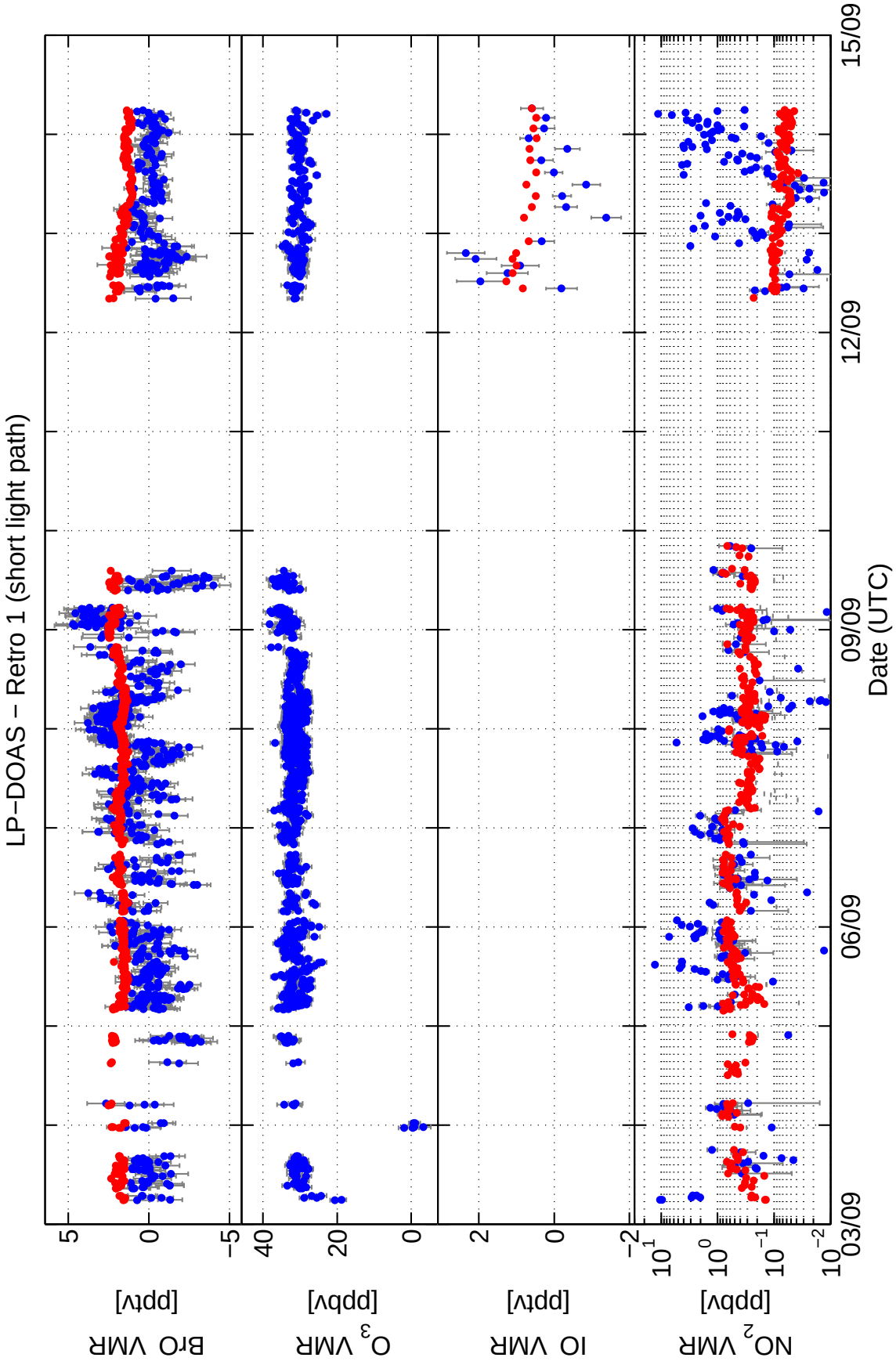

Figure 6.9.: LP-DOAS: Time series of the volume mixing ratios of BrO, O_3, IO and NO_2 derived from the data of the light path to the retro reflector R1. Blue points denote measured mixing ratios, red points the respective detection limit.

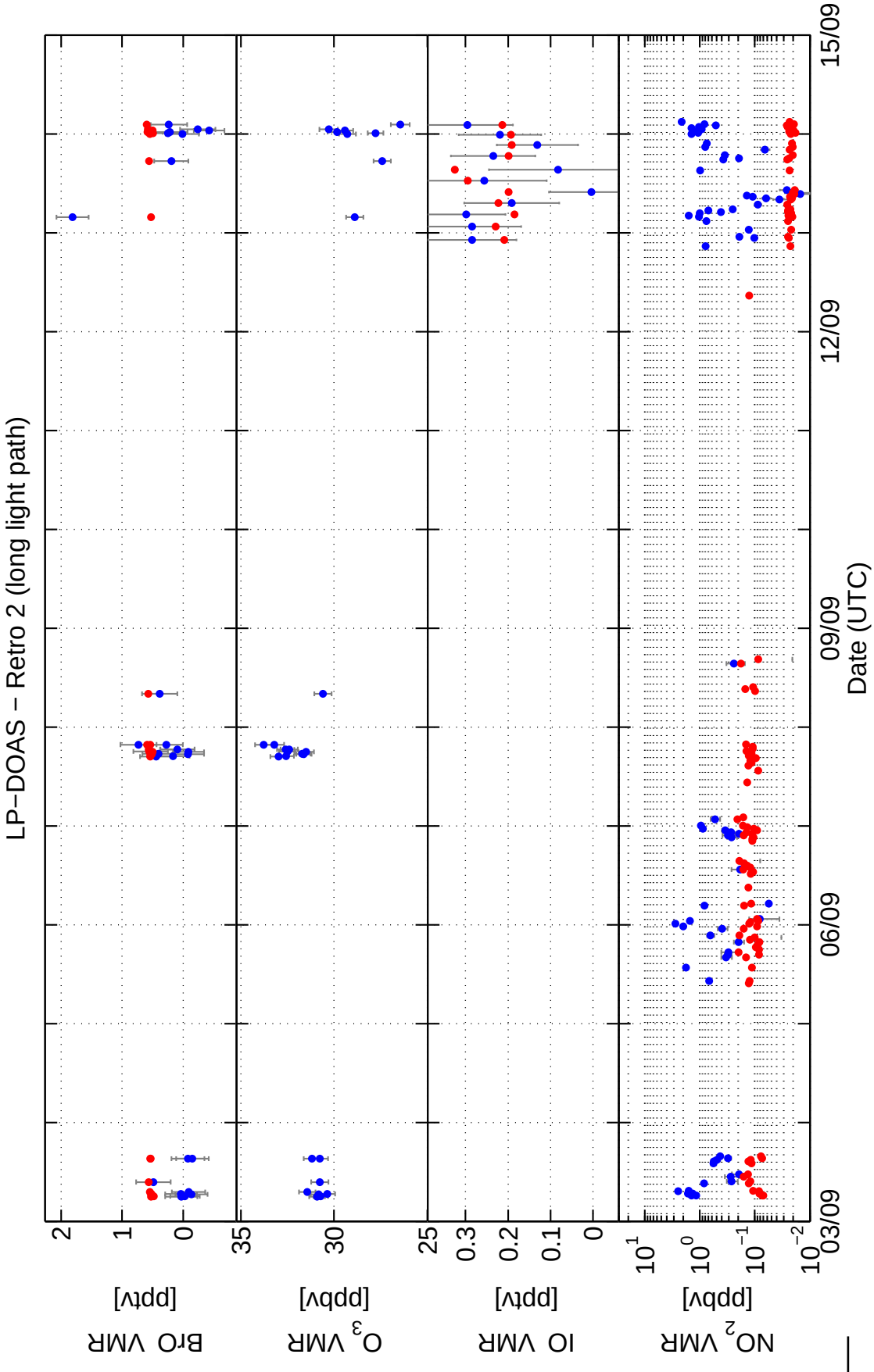

Figure 6.10.: LP-DOAS: Time series of the volume mixing ratios of BrO, O_3, IO and NO_2 derived from the data of the light path to the retro reflector R2. Blue points denote measured mixing ratios, red points the respective detection limit.

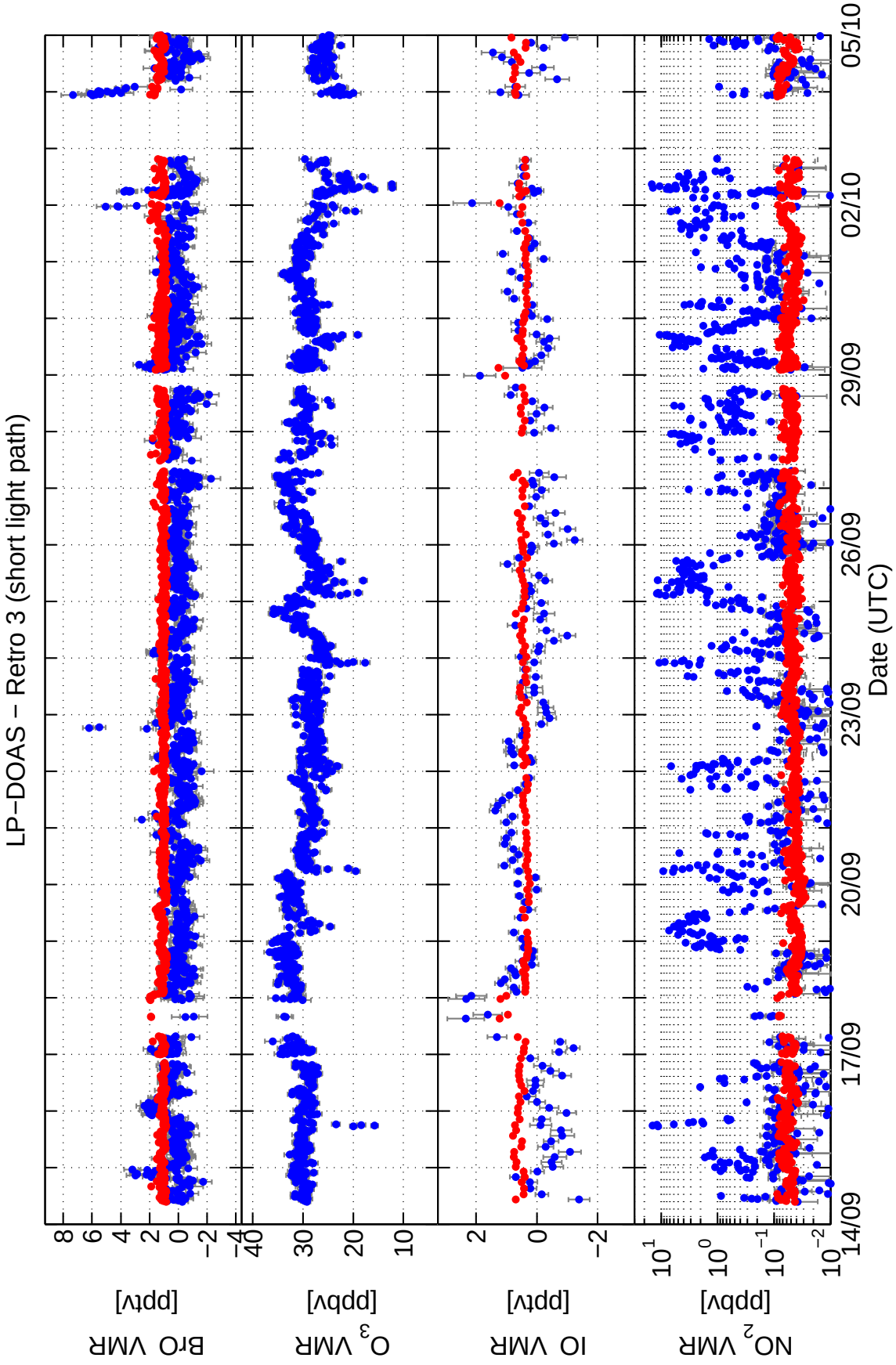

Figure 6.11.: LP-DOAS: Time series of the volume mixing ratios of BrO, O_3, IO and NO_2 derived from the data of the light path to the retro reflector R3. Blue points denote measured mixing ratios, red points the respective detection limit.

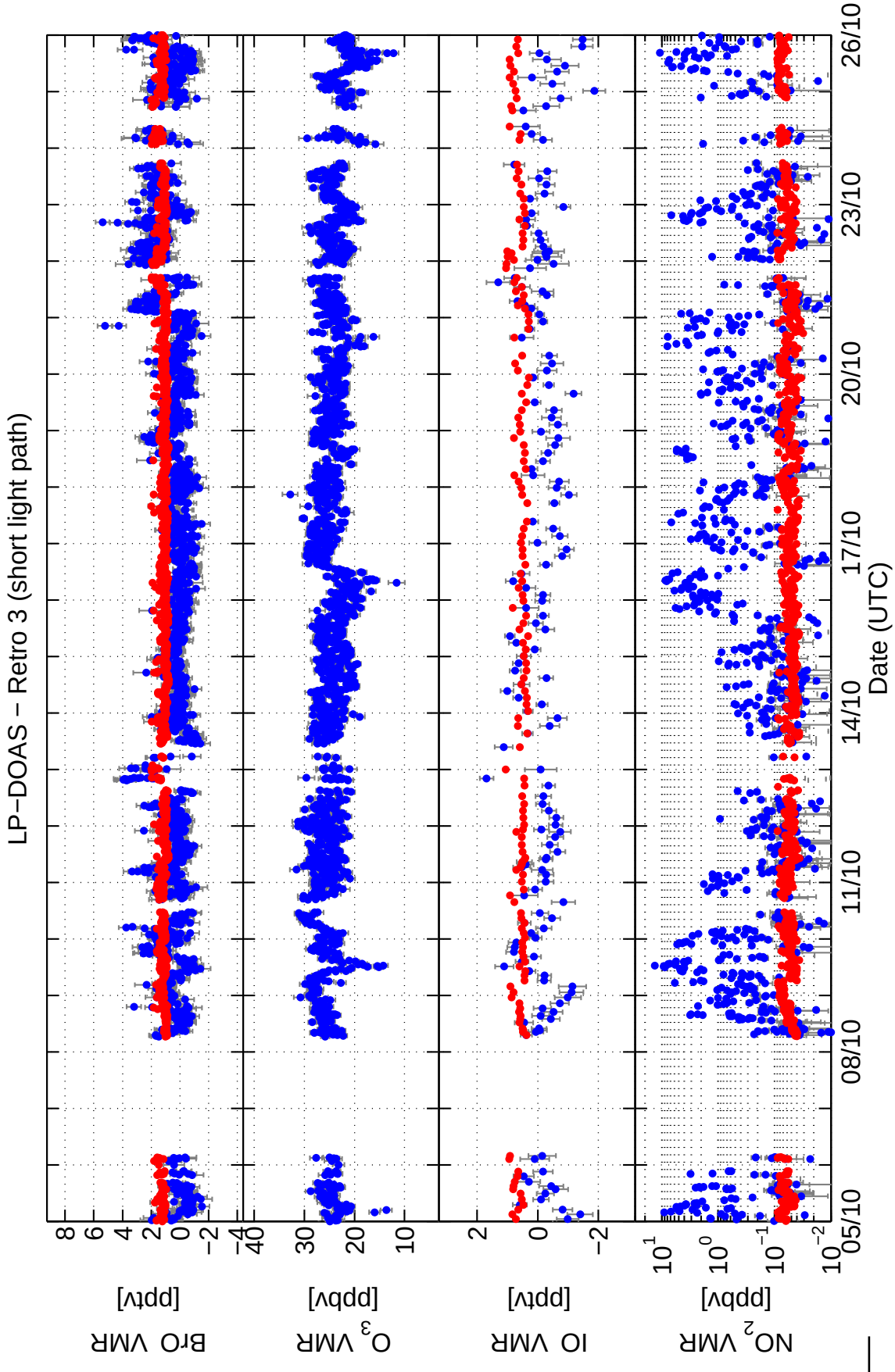

Figure 6.12.: LP-DOAS: Time series of the volume mixing ratios of BrO, O_3, IO and NO_2 derived from the data of the light path to the retro reflector R3. Blue points denote measured mixing ratios, red points the respective detection limit.

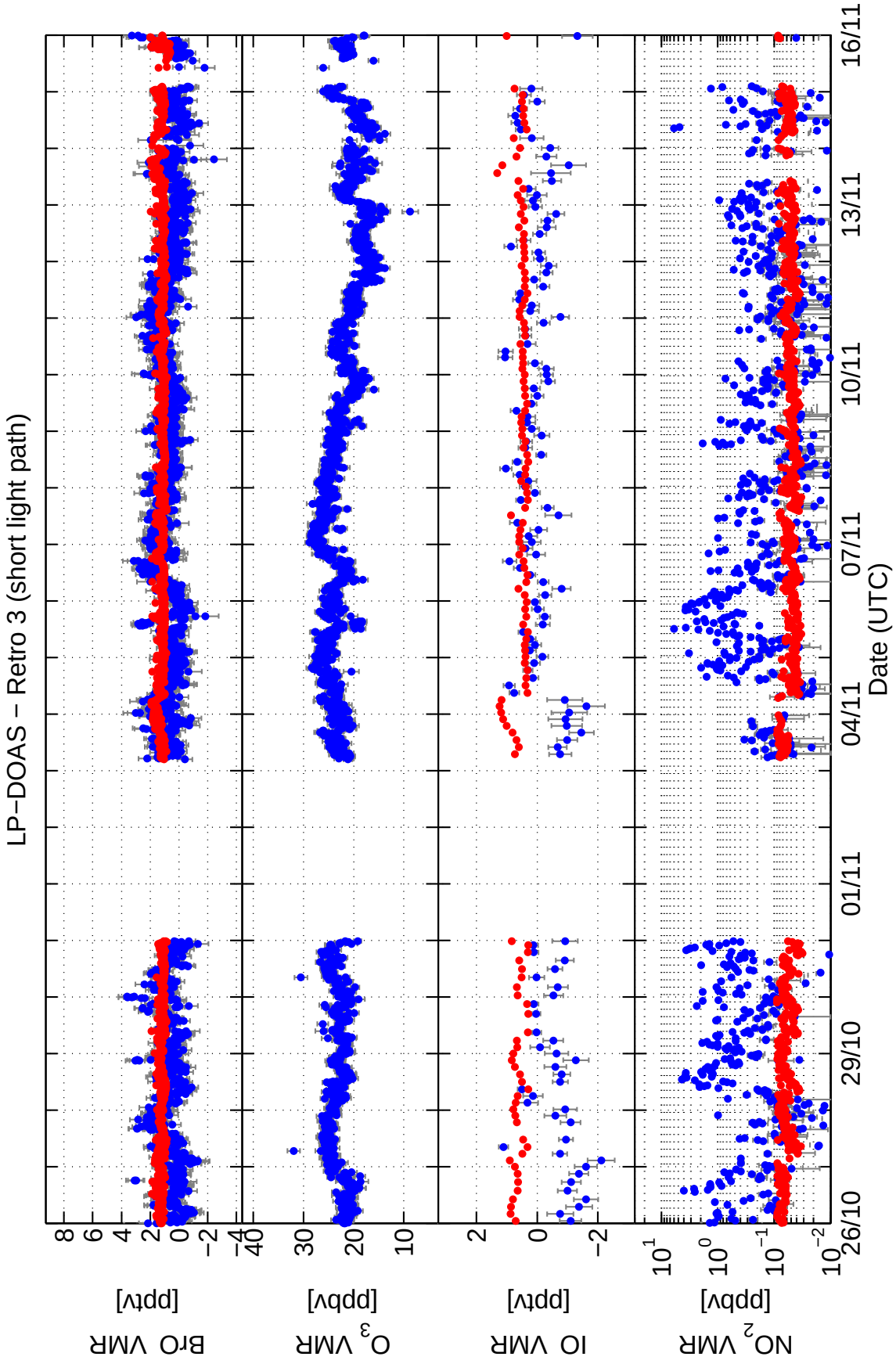

Figure 6.13.: LP-DOAS: Time series of the volume mixing ratios of BrO, O_3, IO and NO_2 derived from the data of the light path to the retro reflector R3. Blue points denote measured mixing ratios, red points the respective detection limit.

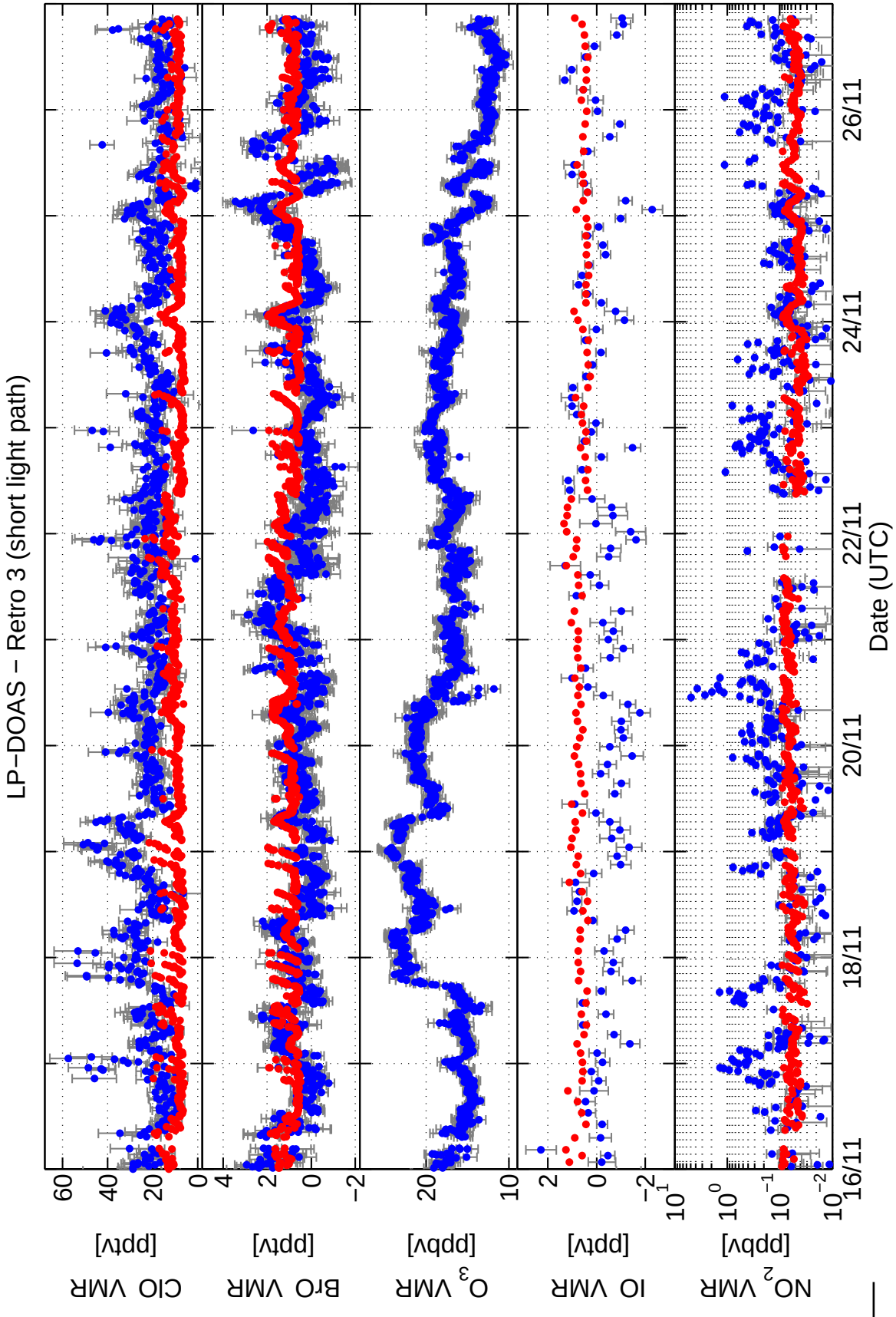

Figure 6.14.: LP-DOAS: Time series of the volume mixing ratios of ClO, BrO, O_3, IO and NO_2 derived from the data of the light path to the retro reflector R3. Blue points denote measured mixing ratios, red points the respective detection limit.

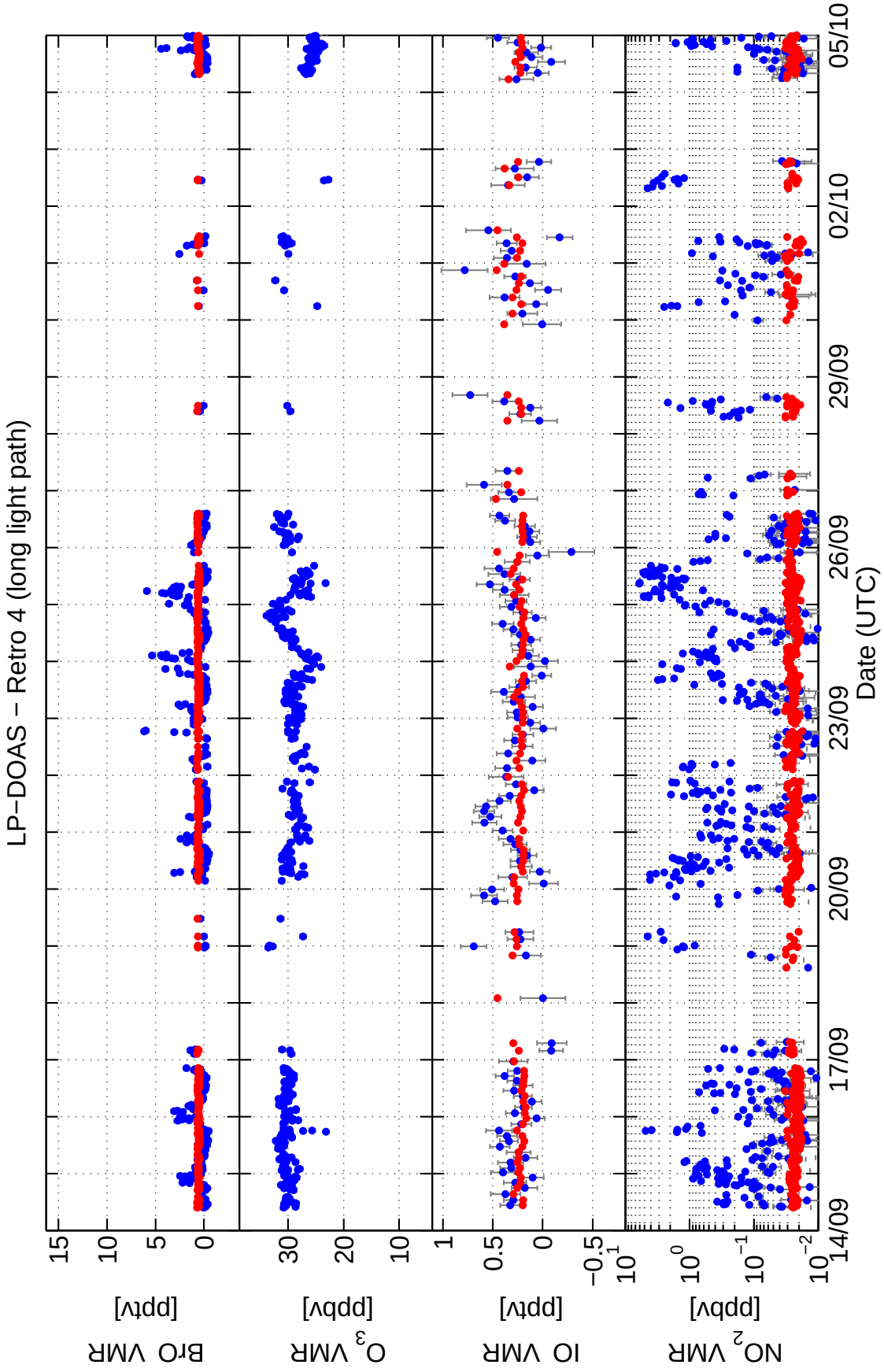

Figure 6.15.: LP-DOAS: Time series of the volume mixing ratios of BrO, O_3, IO and NO_2 derived from the data of the light path to the retro reflector R4. Blue points denote measured mixing ratios, red points the respective detection limit.

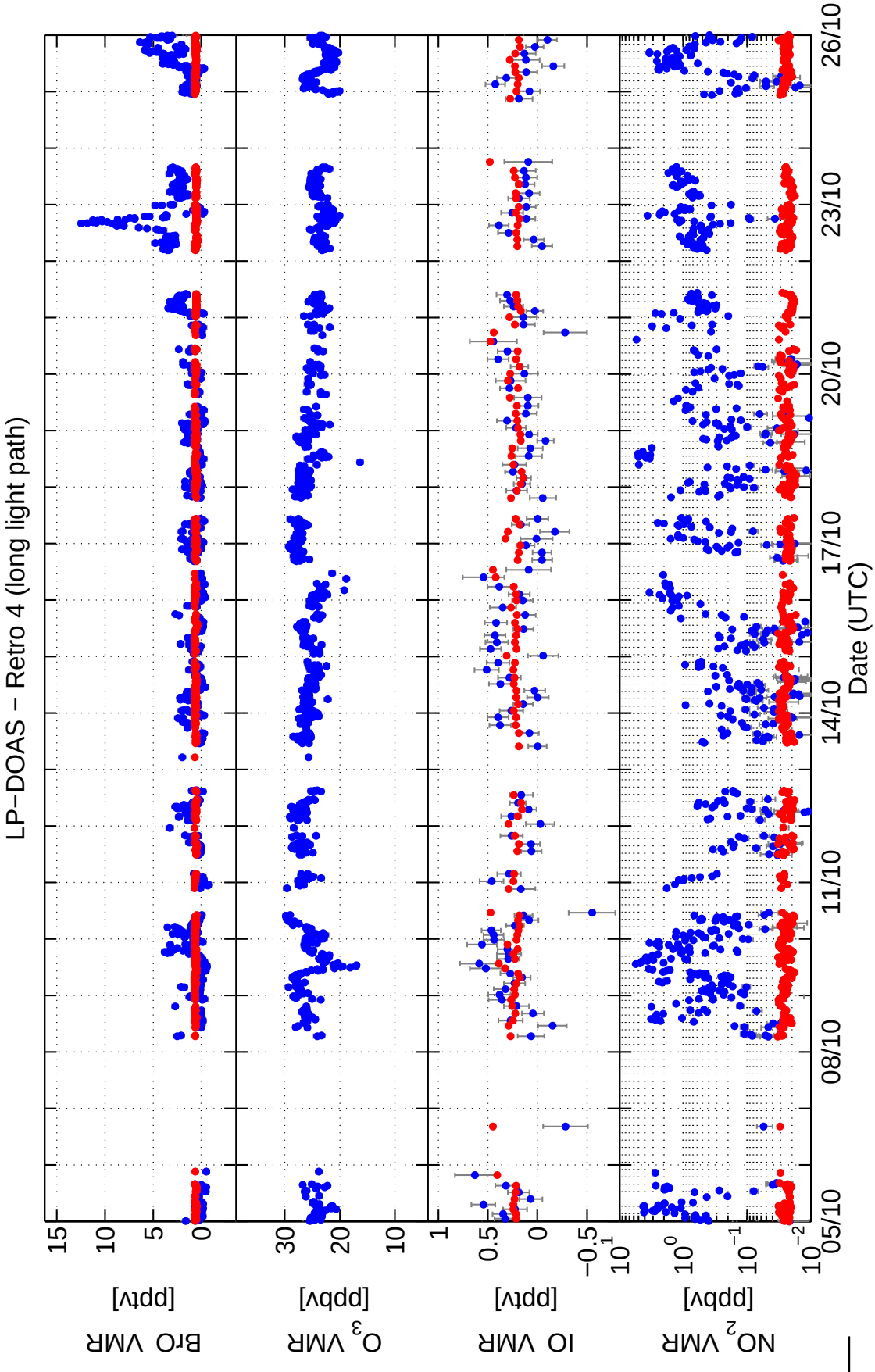

Figure 6.16.: LP-DOAS: Time series of the volume mixing ratios of BrO, O_3, IO and NO_2 derived from the data of the light path to the retro reflector R4. Blue points denote measured mixing ratios, red points the respective detection limit.

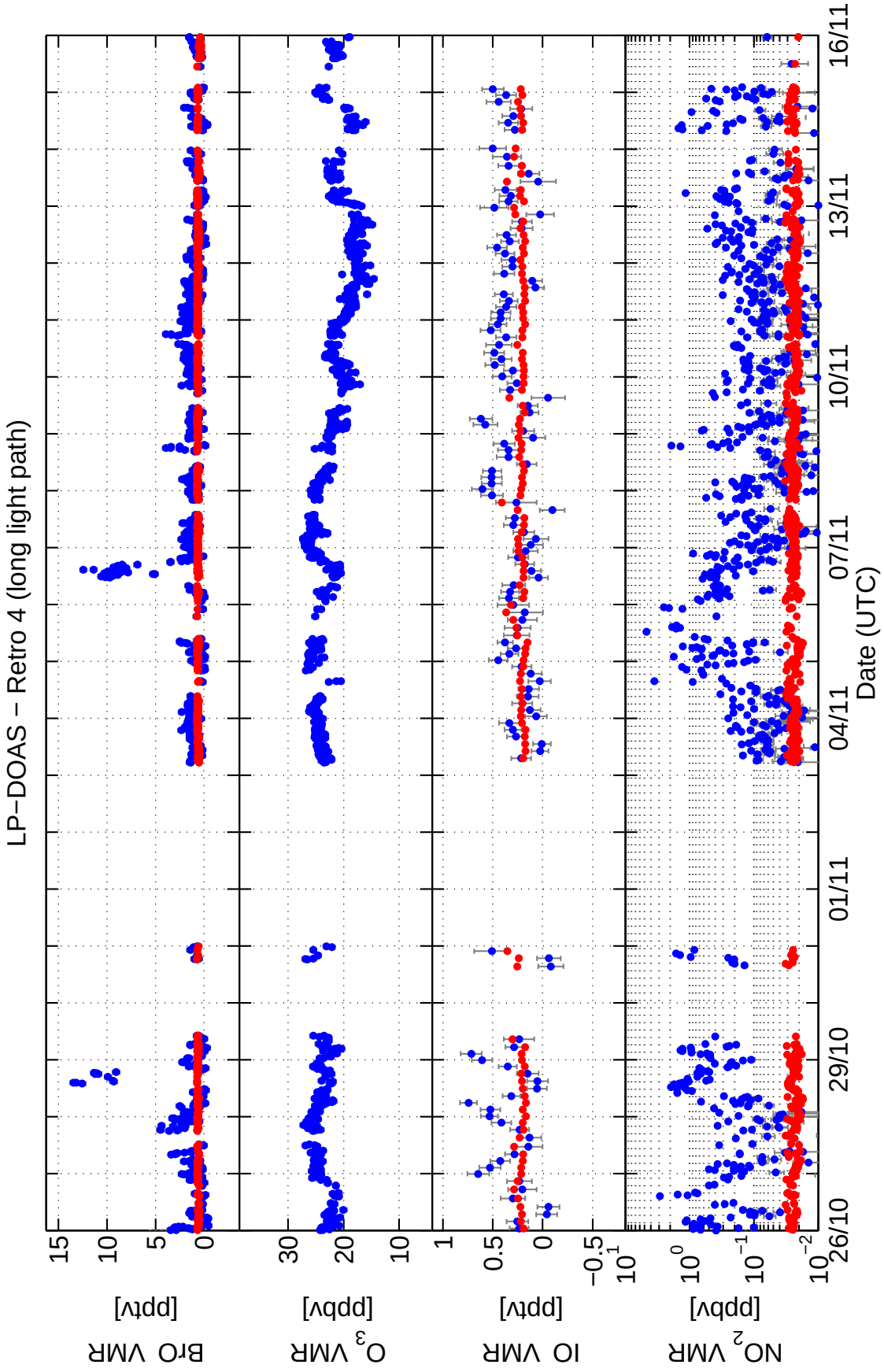

Figure 6.17.: LP-DOAS: Time series of the volume mixing ratios of BrO, O_3, IO and NO_2 derived from the data of the light path to the retro reflector R4. Blue points denote measured mixing ratios, red points the respective detection limit.

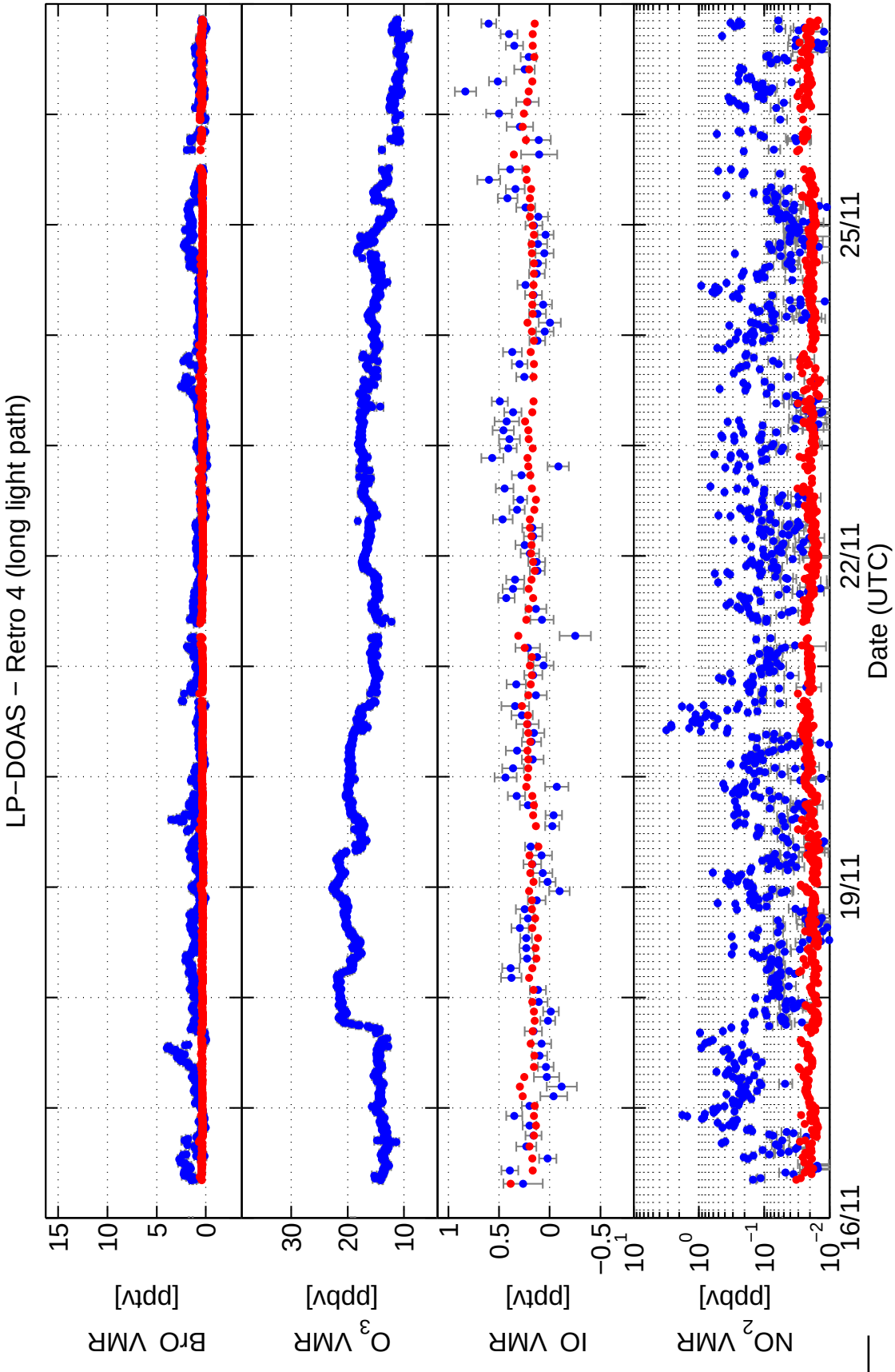

Figure 6.18.: LP-DOAS: Time series of the volume mixing ratios of BrO, O_3, IO and NO_2 derived from the data of the light path to the retro reflector R4. Blue points denote measured mixing ratios, red points the respective detection limit.

	Typical detection limit [pptv]	
Compound	**Long light path**	**Short light path**
OClO	0.7	1.5
OBrO	0.7	1.9
OIO	0.8	2.0
I_2	5	15
HONO	50	100

Table 6.3.: LP-DOAS: Detection limits for compounds for which a DOAS analysis was conducted on the data, but which could not be detected during the entire campaign, given for both light path lengths.

The first two weeks, when measurements were conducted on light paths R1 and R2, are given in figures 6.9 (R1) and 6.10 (R2). The measurements afterwards on R3 and R4 are split into several plots due to their duration. They are given in figs. 6.11 - 6.14 for R3 and figs. 6.15 - 6.18 for R4. Gaps in the time series are due to inclement weather, storms, strong snow drift, or strong mirages, when the reflectors were not visible anymore from the station. No downtime occurred due to instrumental problems.

Evident from the ozone time series is the complete lack of ODEs, with the possible exception of an hour around noon on the 4th September, when due to stormy conditions only few observations were possible. Throughout the campaign there is variability in the mixing ratios, however, what is most apparent is a steady decline from the beginning with approx. 30 ppbv towards the end of November, when mixing ratios are only around 10 ppbv. This is the normal annual trend with higher mixing ratios during winter and lower ones in summer in polar regions (e.g. Oltmans and Levy, 1994).

The 4th September is also the first day where BrO was above the instrument's detection limit. During the campaign, BrO mixing ratios were mostly below 6-7 pptv. Only during three short time periods did the mixing ratios exceed 10 pptv, namely on the 23rd October, the 29th October and the 7th September. Ozone levels dropped only slightly (2-3 ppbv) during those periods.

For most of the campaign, pollution from the air field and station buildings is visible, as indicated by high NO_2 mixing ratios regularly above 5 ppbv for both light paths. The values only occasionally dropped below the detection limit of ~25 pptv on the long light path.

The first day when IO exceeds the detection limit is the 13th September. Thereafter, on the long light path, it was observed almost every single day, with mixing ratios between the detection limit and 1 pptv. On the short light path, mixing ratios of a few, single points are higher, at around 2 pptv, but errors are

Figure 6.19.: The CE-DOAS instrument at Cape Evans. Power was supplied by six lead acid batteries located inside the yellow trailer and the two solar panels visible on its side.

also higher.

ClO was also observed during the last ten days on the short light path (fig. 6.14). The mixing ratios were between 20 pptv and 50 pptv during this period. Before this period, with the other light source, the detection limit was typically around 100 pptv and no ClO was observed above this threshold.

6.3.2 CE-DOAS: Upper limits on local IO mixing ratios

In order to examine potential sources of IO, such as the sea ice, the shelf ice or penguins, the CE-DOAS instrument was brought to several different sites. This was feasible due to the instrument being mobile and not integrating over large distances, thereby possibly resolving local inhomogeneities. Three types of measurement sites are presented here, which, as mentioned, had been suspected to be possible sources of IO, namely the sea ice (both close to the station and further afield), the snow pack on shelf ice and penguin colonies. Additional time series are included in the appendix at A.4, when the instrument was being tested, conditions were too adverse or the pollution due to NO_2 was too strong. IO was not detected in any of the measurements, NO_2 was often present and glyoxal was possibly identified twice.

Cape Evans

Due to being distanced (ca. 25 km) from the station buildings at Scott Base and McMurdo and the accompanying pollution, while still being accessible by track vehicles, more measurements were done at Cape Evans than at other sites. As operational schedules did not allow for frequent visits to this spot, the instrument was usually placed there and left for a couple of days, after which the light path was always clogged up with snow. Picture 6.19 shows the instrument at Cape Evans, being powered by solar panels and six lead acid batteries stored in the yellow trailer.

The time series of IO and NO_2 are shown in figures 6.20a, 6.20b and 6.21. NO_2 levels are low except for a few events stemming from local pollution as other groups were also working in the area with snowmobiles and gasoline-powered generators. During the last time at Cape Evans (fig. 6.21), some snow came onto the mirrors after 24 hours and left residue, mainly salt, on their surface, thereby shortening the effective light path and ramping up errors and DLs. Glyoxal is around the detection limit and also above it several times. The fit best showing the absorption features, i.e. highest glyoxal signal-to-noise, before the mirrors got completely contaminated, is pictured in figure 6.22.

Snow pit experiment

As mentioned in section 2.5.3, there were indications that enormous amounts of reactive iodine could be located in the interstitial air of the snow pack on shelf ice. In order to test whether any iodine would come out of the snow pack, an experiment was done in which the instrument was successively lowered down from the usual stands into a pit dug into the snow above the shelf ice. Care was taken not to contaminate the site, therefore digging was only done standing down-wind of the pit. The location was several km away from station buildings and the wind was coming from the south, i.e. the ice shelf during the whole time of the experiment. The dimensions of the pit were a depth of 0.5 m, a length of 2.4 m and a width of 0.4 m, barely larger than the dimensions of the instrument.

There were four stages of the experiment: (1) The instrument was standing next to the pit on stands. (2) The instrument was placed directly onto the snow, next to the pit. (3) The instrument was lowered into the pit. (4) The pit was covered with transparent PTFE foil, to allow a possible buildup of higher iodine concentrations while not inhibiting photochemistry (pictured in figure 6.23).

The mixing ratios during this experiment are shown in figure 6.24, and the four mentioned periods are marked in green. The IO mixing ratio fluctuates throughout, but is never above the detection limit. Interestingly on the other hand, a significant increase in NO_2 levels can be seen. As already mentioned in section 2.5.2, it is known that snow, especially in Antarctica, is emitting NO_2 under the influence of solar irradiation. In this instance, it also shows that the chamber study principally worked.

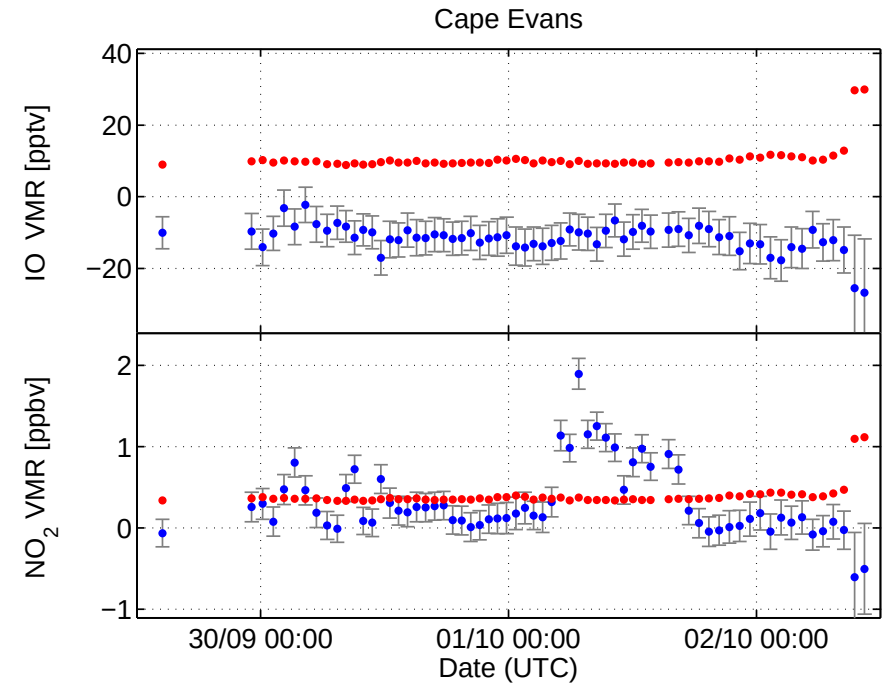

(a)

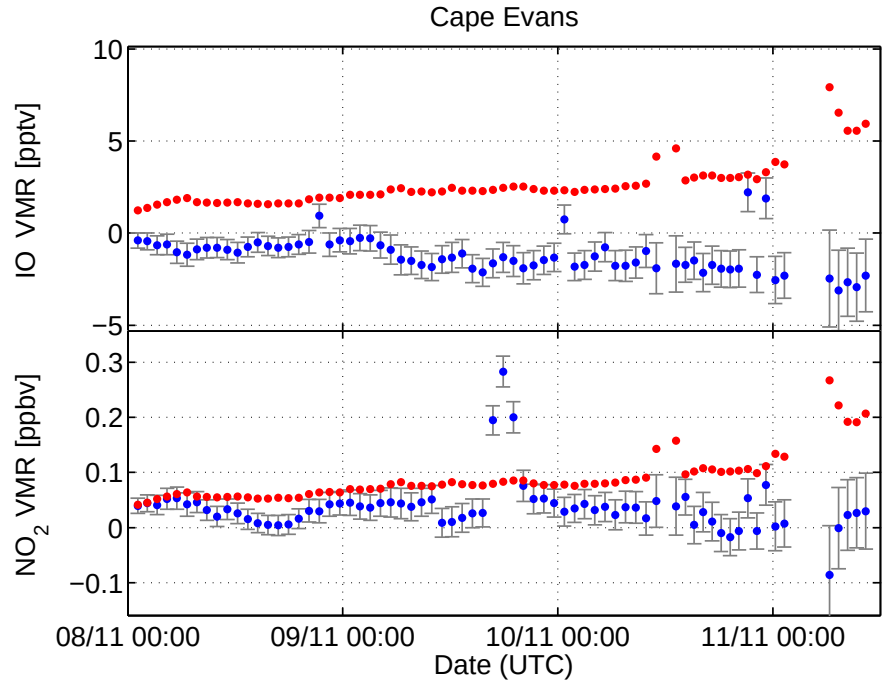

(b)

Figure 6.20.: CE-DOAS: Derived mixing ratios for IO and NO_2 of the measurements at Cape Evans. IO is never above the detection limit. Measurement data is shown in blue, the calculated detection limits in red.

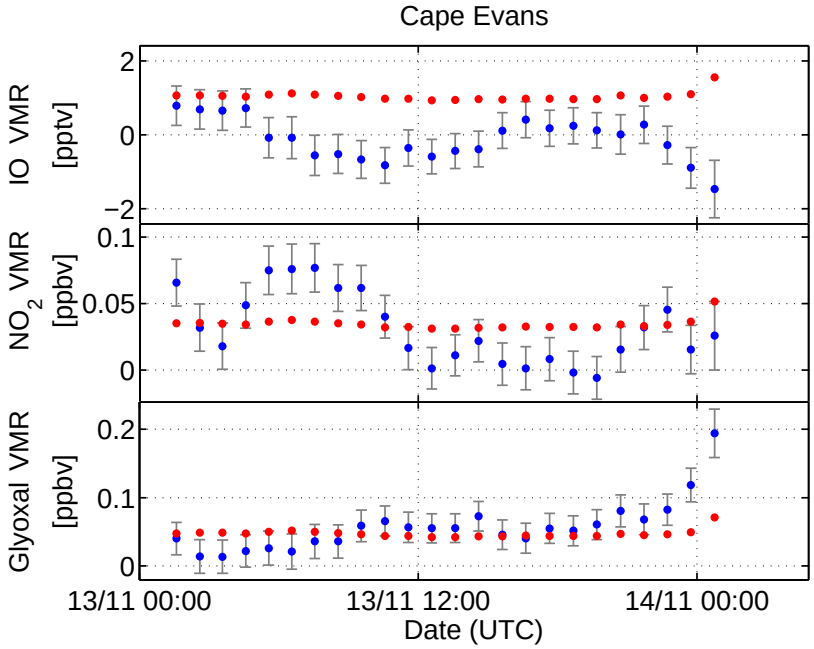

Figure 6.21.: CE-DOAS: Derived mixing ratios for IO, NO_2 and glyoxal of the measurements at Cape Evans. IO is never above the detection limit, however glyoxal mixing ratios rise towards the end at local noon. After one day the light path drastically decreased due to snow on the mirror surface and increased DLs to tenfold levels. Measurement data is shown in blue, the calculated detection limits in red.

Penguin rookery

Due to the penguin diet, which consists only of sea foods such as fish and krill (e.g. Emison, 1968; Ainley, 2002), which in turn feed on iodine-accumulating algae (Fogelqvist and Tanhua, 1995), one hypothesis was that they or their excrements are possibly involved in the release of reactive iodine. In order to assess this, the instrument was brought to a major Adélie rookery located at Cape Bird at the northern end of Ross Island, where also a small hut is located. The time there fell into the beginning of the mating season (late October). A very strong stench of animals was present. During the two days time, there was almost no wind. The penguins breed there, because parts of the coastline at this location consist of black volcanic rock and sand, which are not covered with snow. These black spots therefore warm up remarkably during the day.

The instrument was placed at two locations. On the first day the instrument was located close to the shore (approx. 20 m inland), where only a few dozen penguins were roaming around, to get data less influenced by the birds in relation to the coast and also to check how the animals would respond to the instrument. Due to their complete lack of interest in the device (mating season), the next day, the instrument was placed close to several groups of penguins inside the main rookery at the northern beach.

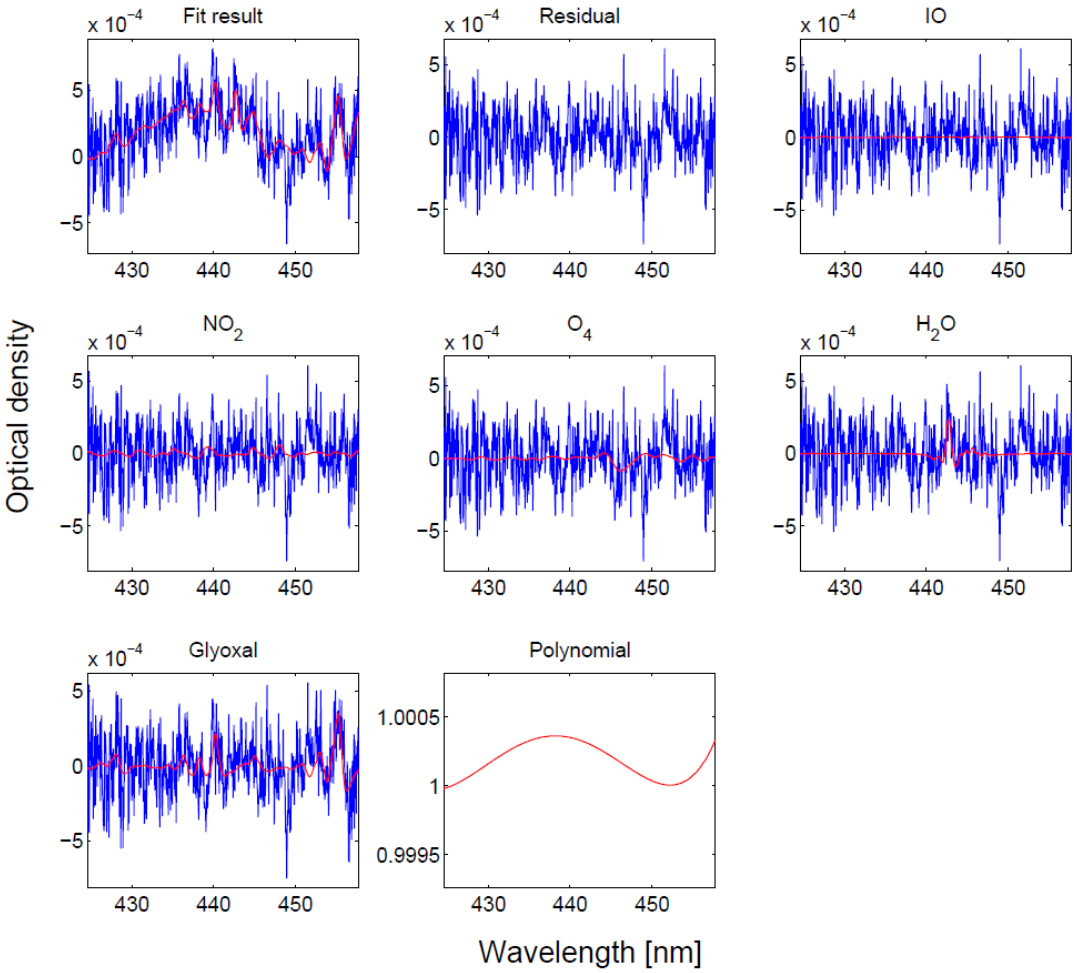

Figure 6.22.: A sample evaluation of the CE-DOAS instrument at Cape Evans, showing the absorption of glyoxal (Time series shown in fig. 6.21). Retrieved mixing ratios are: IO (0.01 ± 0.80) pptv, NO_2 (25.8 ± 25.9) pptv, H_2O (808 ± 418) ppmv and glyoxal (193.8 ± 35.4) pptv. O_4 is well below the detection limit.

The mixing ratios are shown in figure 6.26. IO stayed clearly below the detection limit during the entire time. The first day also marks the period with the lowest detection limits achieved during this campaign, due to the windless conditions. NO_2 is present however, and glyoxal is close to the detection limit and slightly above as well. Emissions of VOCs are known to occur at penguin rookeries (Legrand et al., 2012), therefore the presence of glyoxal there is not unlikely. The coast, however, with large areas of cracked sea ice and the open ocean were also close and could also be possible sources and has to be assessed in future studies.

Figure 6.23.: Part of the snow pit experiment: The instrument was placed inside a hole dug into the snow on the ice shelf and covered with PTFE foil to inhibit the exchange of air but still allow sunlight to enter the chamber.

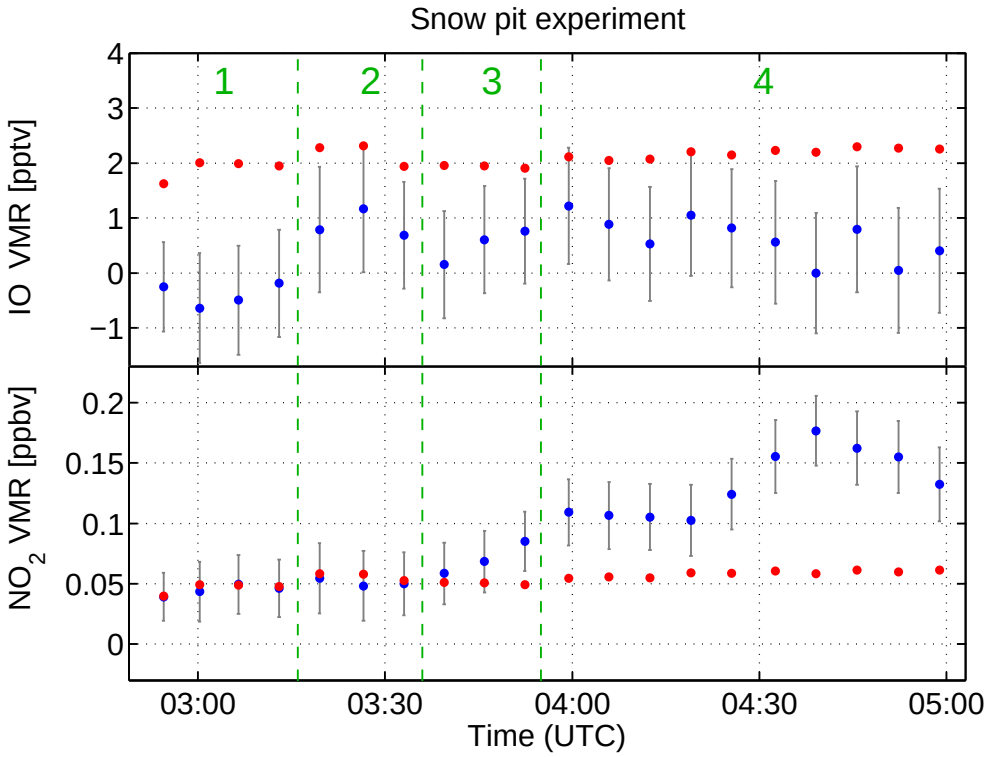

Figure 6.24.: CE-DOAS: IO and NO_2 mixing ratios during the shelf ice experiment. Measurement data is shown in blue, the calculated detection limits in red. The numbers 1-4 mark the four different set-ups: (1) The instrument was on stands on the snow. (2) The instrument was lying directly on the snow surface. (3) The instrument was placed inside the snow pit. (4) The snow pit was covered with PTFE foil.

Figure 6.25.: The CE-DOAS instrument (left foreground) at the Adélie penguin rookery at Cape Bird on the second day. In the background the coastline and further away the open ocean is visible.

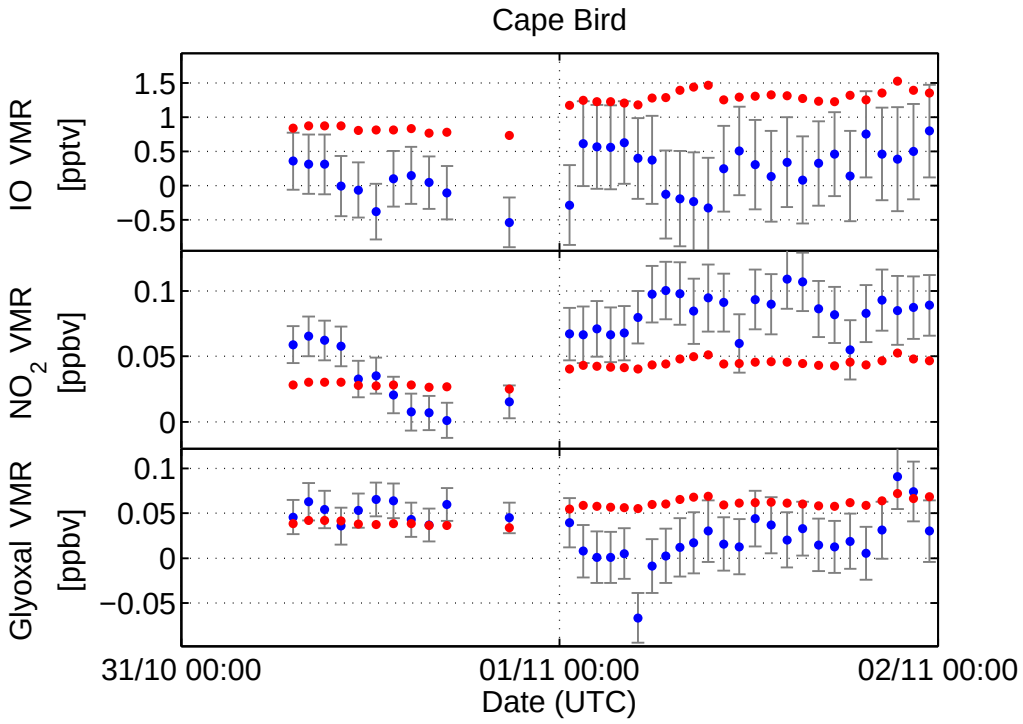

Figure 6.26.: CE-DOAS: Derived mixing ratios of the measurements at the Adélie penguin rookery located at the northern end of Ross Island, Cape Bird. During the first day, the instrument was located in the area of a few penguins, the second day the instrument was placed inside a large rookery (see above). Measurement data is shown in blue, the calculated detection limits in red.

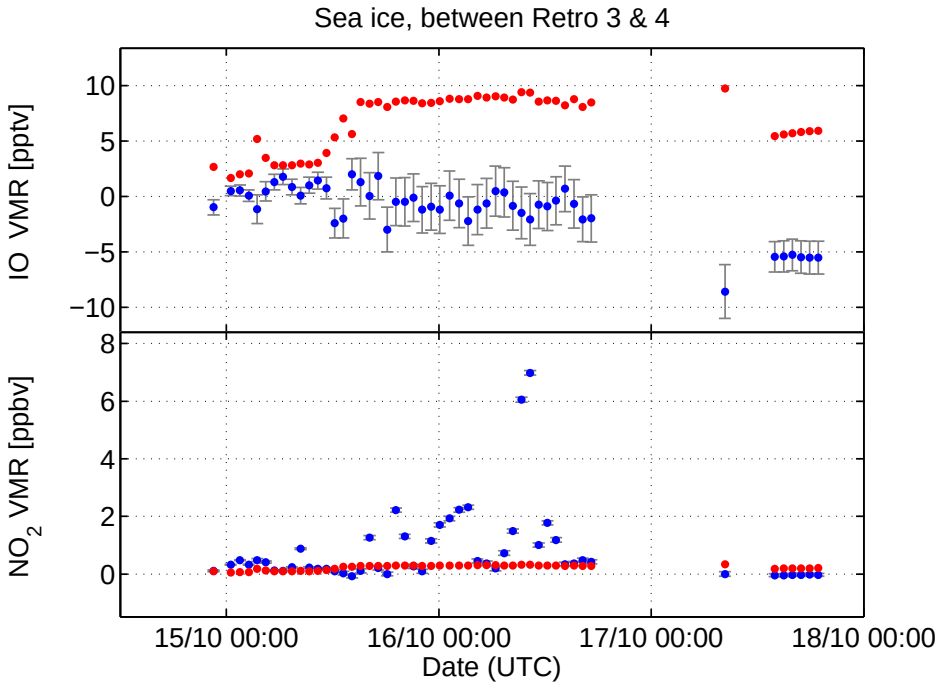

Figure 6.27.: CE-DOAS mixing ratios for IO and NO_2 for the instrument location between R3 and R4. Being located not far from one of the air fields, local pollution can be seen in elevated NO_2 levels. Measurement data is shown in blue, the calculated detection limits in red.

Sea ice: Along the LP-DOAS light path

Twice the instrument was placed along the light path of the LP-DOAS. The LP-DOAS only gives average mixing ratios over the several kilometer long light path, this was done to see whether there are any local inhomogeneities. The results are shown in fig. 6.27 for a position midway between both R3 and R4, and in fig. 6.28, when the instrument was placed directly next to R3. IO was not observed at both locations, however the measurements confirmed the high local NO_2 pollution seen by the LP-DOAS.

6.3.3 MAX-DOAS: SCDs and vertical profiles of BrO and IO

For the mobile MAX-DOAS instrument, results are presented from Square Frame Hut, where the CE-DOAS snow pit experiment was done, the two times the instrument was next to the LP-DOAS telescope as well as when the instrument was taken to Cape Bird together with the CE-DOAS. In the following, the determined SCDs will be presented, followed by the results from the inversion, the vertical profiles of aerosol extinction and BrO and IO mixing ratios.

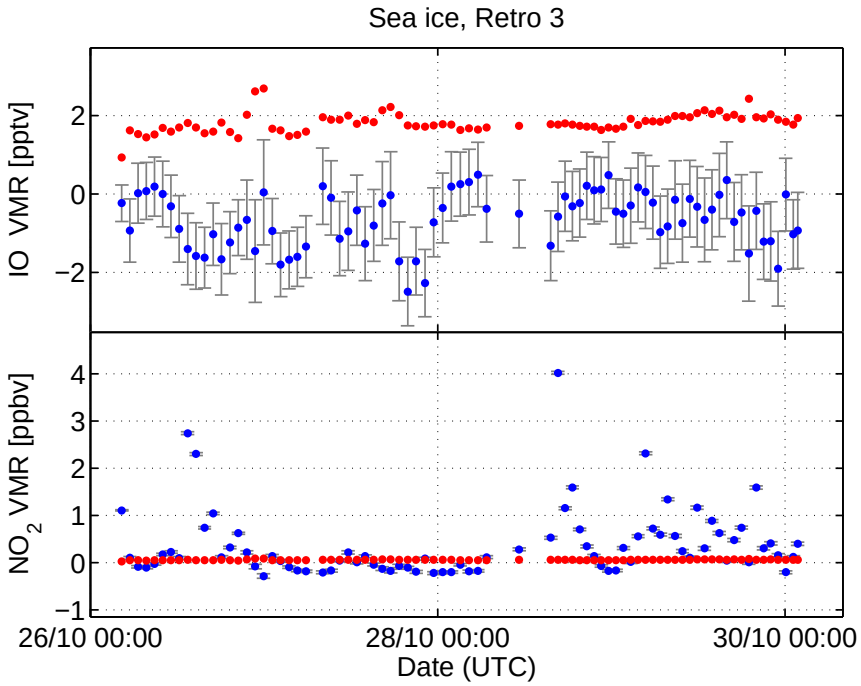

Figure 6.28.: CE-DOAS mixing ratios for IO and NO_2 for the instrument location directly next to R3. Being located close to Scott Base and McMurdo stations, strong local pollution can be seen. Measurement data is shown in blue, the calculated detection limits in red.

Slant column densities

The SCDs for *Square Frame Hut* are shown in figure 6.29, together with the detection limit for the SCDs of the 2° elevation angle. For clarity, the DL for other angles are not shown. Usually, the ones for the 2° are the highest, compared to the other angles, therefore if SCDs of the other angles are above those, they can be considered to be above their respective DL as well. For neither BrO nor IO, SCDs are significantly above the detection limit for more than a few scans during this period. Therefore the data from Square Frame Hut was also not input into the inversion.

Afterwards, the instrument was placed next to the LP-DOAS for several days (*Balcony 1*). The SCDs are shown in figure 6.30. BrO and IO are above the detection limit several times, and a clear separation of different elevation angles can be seen for BrO. Elevated NO_2 SCDs are also apparent.

Then the instrument was taken to *Cape Bird*. The SCDs for the three days of measurements are given in figure 6.31. Both BrO and IO are above the DL at times. The instrument was left there for a total of ten days, with the hope of a higher exposure to clean and halogen-rich air masses closer to the sea ice, but unfortunately crashed only shortly after leaving the measurement site.

Towards the end of the campaign, the instrument was again placed next to the LP-DOAS telescope for another inter-comparison (*Balcony 2*). The SCDs of this period are given in figure 6.32 with BrO as well as IO above the DL several times. For IO, only in this dataset a clear angular separation can be seen.

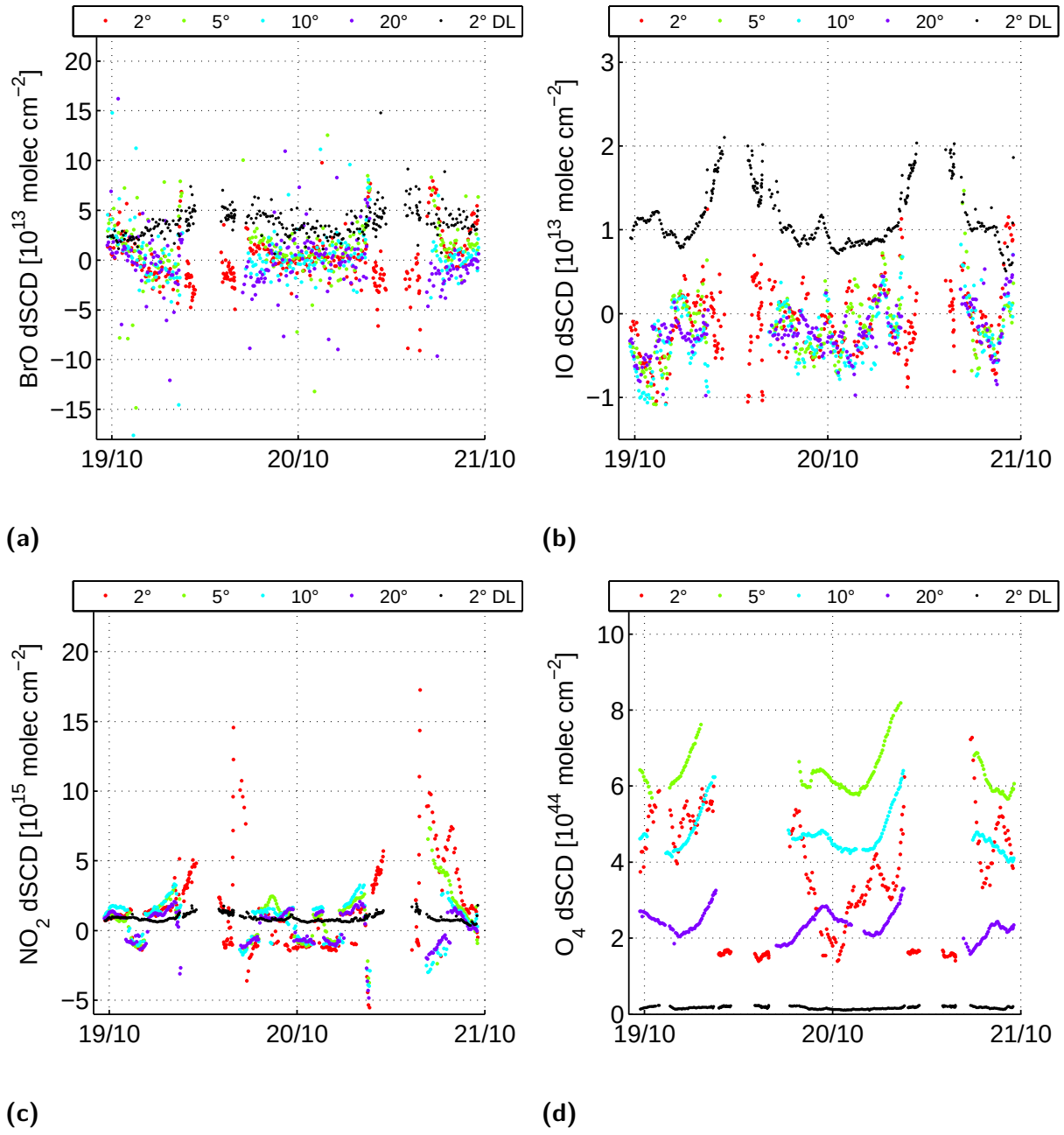

Figure 6.29.: MAX-DOAS slant column densities from *Square Frame Hut* for **(a)** BrO **(b)** IO **(c)** $\mathrm{NO_2}$ **(d)** $\mathrm{O_4}$. The SCDs are color-coded depending on their respective elevation angle. Furthermore the detection limit of the 2 ° elevation angle is indicated.

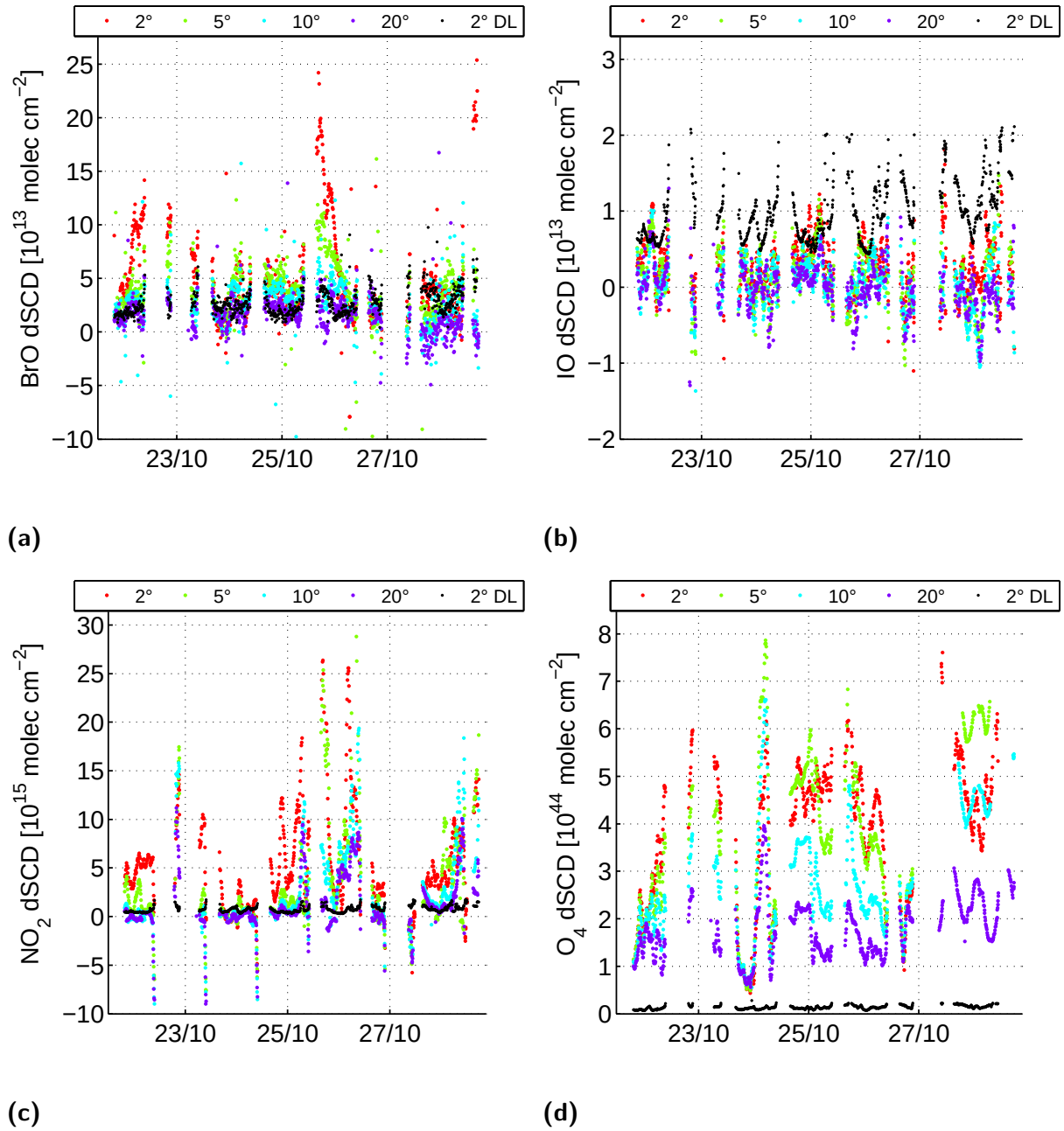

Figure 6.30.: MAX-DOAS slant column densities from *Balcony 1* for **(a)** BrO **(b)** IO **(c)** $\mathrm{NO_2}$ **(d)** $\mathrm{O_4}$. The SCDs are color-coded depending on their respective elevation angle. The SCDs are color-coded depending on their respective elevation angle. Furthermore the detection limit of the 2 ° elevation angle is indicated.

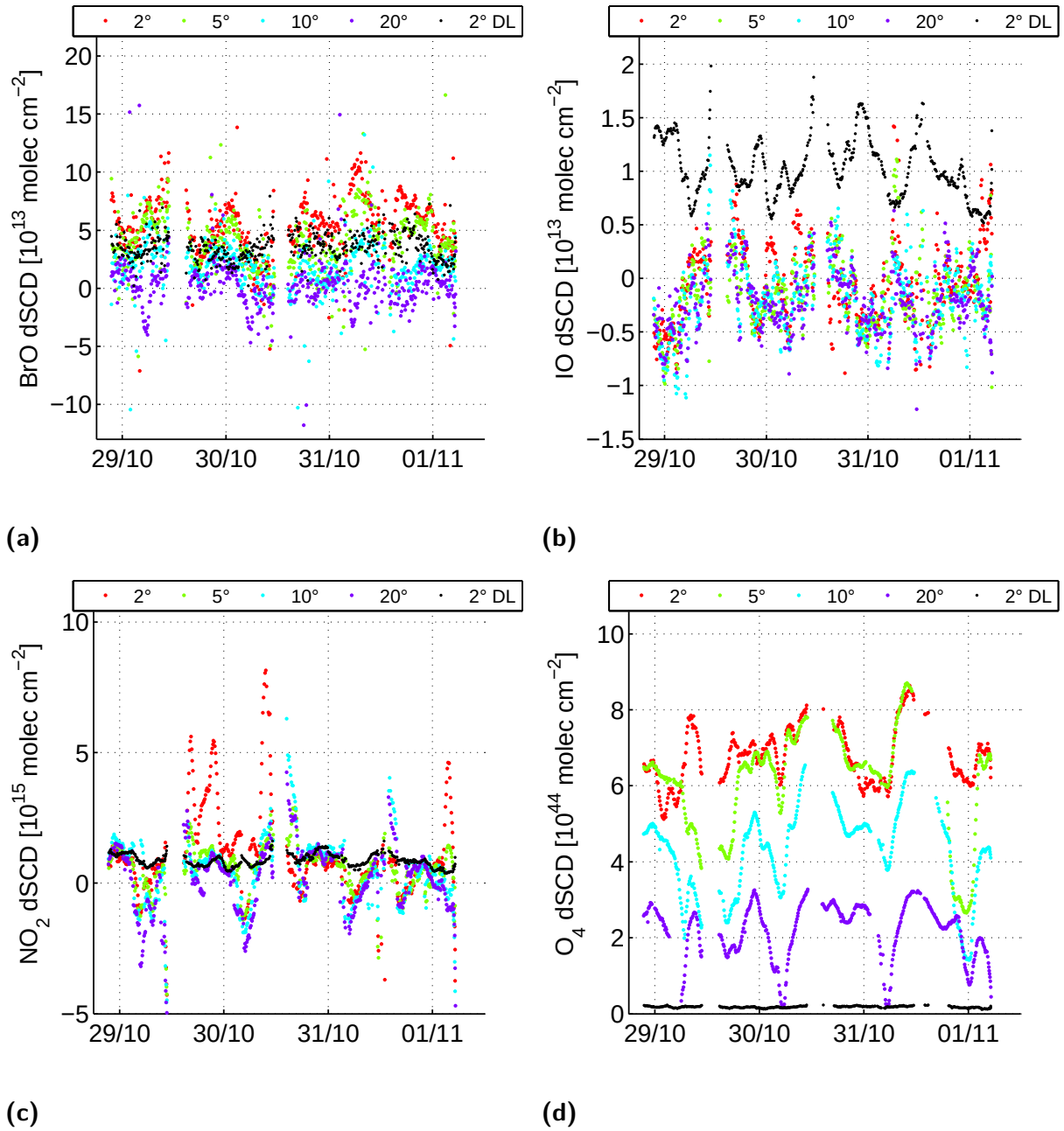

Figure 6.31.: MAX-DOAS slant column densities from *Cape Bird* for **(a)** BrO **(b)** IO **(c)** $\mathrm{NO_2}$ **(d)** $\mathrm{O_4}$. The SCDs are color-coded depending on their respective elevation angle. The SCDs are color-coded depending on their respective elevation angle. Furthermore the detection limit of the 2 ° elevation angle is indicated.

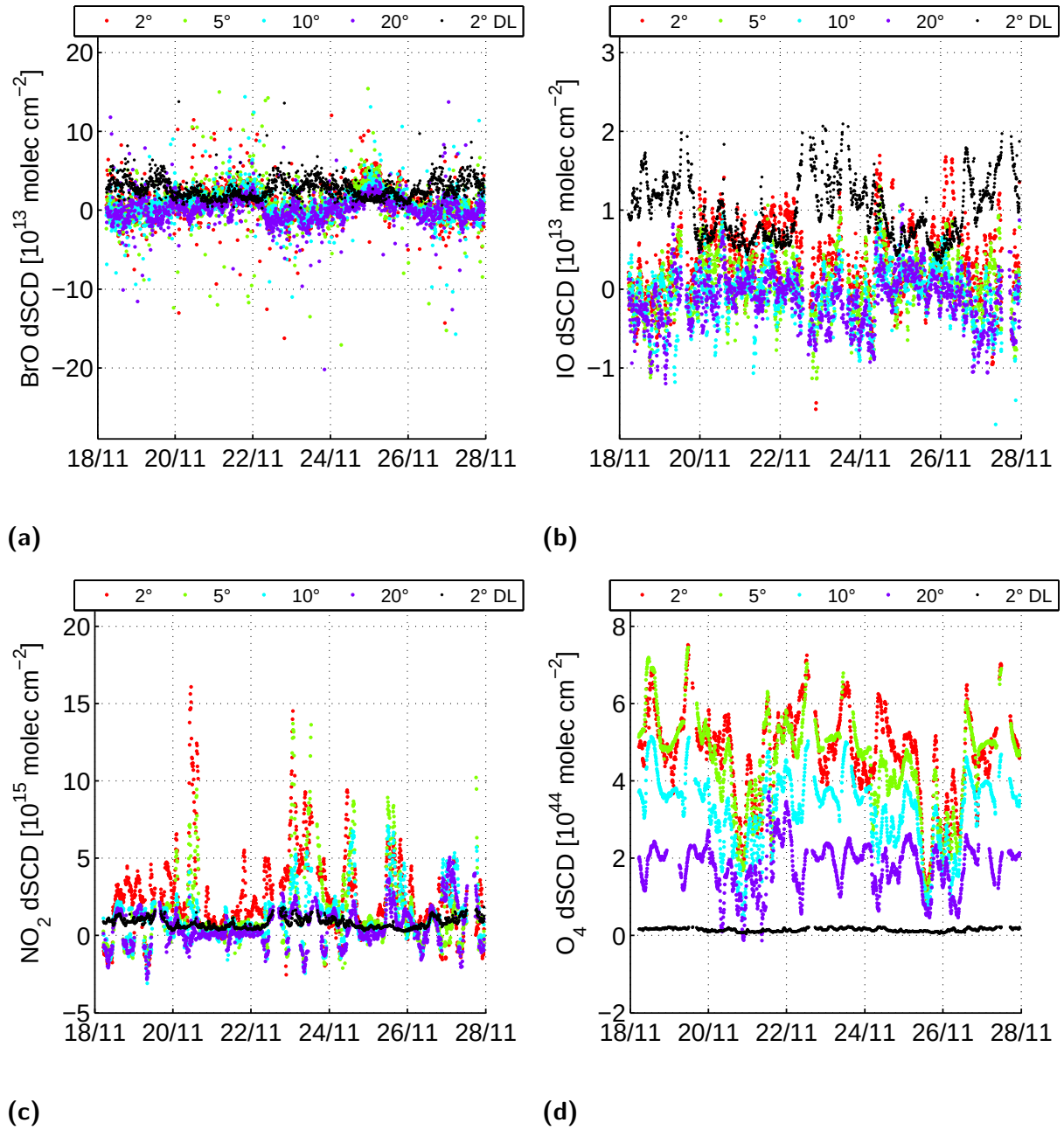

Figure 6.32.: MAX-DOAS slant column densities from *Balcony 2* for **(a)** BrO **(b)** IO **(c)** $\mathrm{NO_2}$ **(d)** $\mathrm{O_4}$. The SCDs are color-coded depending on their respective elevation angle. The SCDs are color-coded depending on their respective elevation angle. Furthermore the detection limit of the 2 ° elevation angle is indicated.

Site	Lat. (°S)	Long. (°E)	Snow depth	pH
Next to R4	77.87207	166.62979	top 10 mm	6.02
Next to CE-DOAS	77.86848	166.65080	top 5 mm	5.98
Close to the US road	77.86571	166.66757	top 5 mm	6.00
Between R3 and R4	77.86237	166.68767	top 5 mm	6.10
Behind R3 towards R4	77.85874	166.70850	top 5 mm	5.57
Between telescope and R3	77.85580	166.72578	top 5 mm	5.58
Between telescope and R3	77.85346	166.74098	top 5 mm	5.65
Snow pit exp. (CE-DOAS)	77.86237	166.68767	top 5 mm	5.05
Snow pit exp. (CE-DOAS)	77.85874	166.70850	3 cm to 4 cm	4.80
Snow pit exp. (CE-DOAS)	77.85580	166.72578	20 cm	4.95
Snow pit exp. (CE-DOAS)	77.85346	166.74098	bottom (47 cm)	5.00

Table 6.4.: Results of the measurements of the bulk pH of snow samples. The location where the sample was taken is given, as well as the depth below the snow surface, where the snow was taken from. For details about the measurement procedure refer to section 6.3.4.

Inverted vertical profiles

The inversion results of the three locations and time periods, *Balcony 1*, *Cape Bird* and *Balcony 2* are given in figures 6.33, 6.34 and 6.35. In terms of the aerosol extinction, in all three cases, significant extinction was mostly seen at an altitude of 1 km. On the 23rd October, higher ($2\,km^{-1}$ - $3\,km^{-1}$) extinctions were also seen at the surface. Those correlate well with clouds and fog that were present during this time, which is analyzed in section 6.4.2.

The results for the trace gases need to be interpreted with caution. As seen above at the IO and BrO SCD results, in most cases only the SCDs of the lowest elevation angle exceeds the detection limit. A detailed discussion is given in the analysis below. The situation for BrO and IO appears surprisingly similar to the case of aerosol, in that the highest mixing ratios are also located at around 1 km altitude. BrO reaches mixing ratios of up to 20 pptv and IO up to 1.1 pptv, values which have not been observed on the ground. An inter-comparison of the retrieved surface mixing ratios with the ones seen by the LP-DOAS is given below in section 6.4.3.

6.3.4 Snow pH measurements

In addition to the spectroscopic measurements, analyses of the bulk pH of snow samples were conducted as well, as the pH of surfaces plays an important role for the involved heterogeneous chemistry, as stated in section 2.5.2. The samples were taken close to the retro reflectors, in-between them and also during the CE-DOAS snow pit experiment (see section 6.3.2) at several different depths inside the snow pit. All samples were taken using a polycarbonate shovel and placed in polyethylene bags. They were brought back to the station, melted inside their closed bags, thereafter the pH of the melt water was determined using a commercial pH meter (Gresinger GPH 014). All samples were analyzed back-to-back. The instrument was calibrated using provided pH calibration standards at pH 4 and pH 7. According to the manufacturer, the device has an accuracy of 0.1 pH after said calibration.

The determined pH values are given in table 6.4 for each location and snow depth. The snow bulk was acidic at all sampled location. The samples that were taken above sea ice, i.e. all except the snow pit samples, had a pH around 6. The snow pit was dug into snow on the ice shelf, possibly older snow, and had a lower pH of around 5. Those values are comparable to previously published measurements in this region (DeFelice, 1998). While the bulk pH does not necessarily indicate the pH of the quasi-liquid layer at the surface of ice crystals and snow flakes where the reactions take place, if the bulk is acidified, then the surface layer should be acidic as well. Therefore, the pH of the snow should be conducive to the release and recycling of reactive halogens.

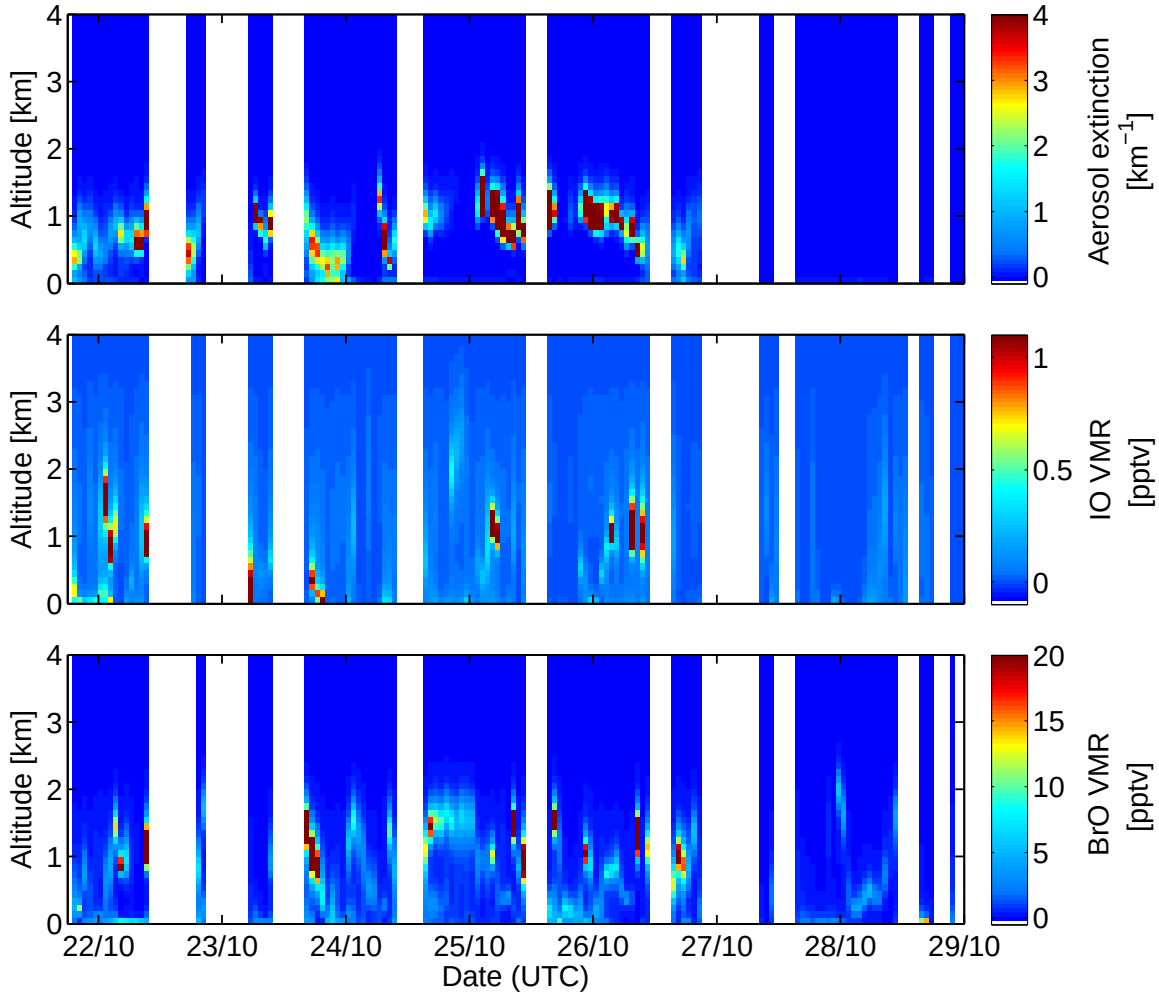

Figure 6.33.: *Balcony 1*: Vertical profiles of aerosol extinction and IO and BrO mixing ratios derived from the MAX-DOAS measurements. The BrO and IO profiles indicate a presence of those at an altitude around 1 km, where also clouds are often present. The plausibility of the aerosol profiles is discussed in section 6.4.2 and a comparison of the surface values is given in section 6.4.3. As discussed in the text, the SCDs are close to the DL and/or below, therefore the higher layers could also be due to inversion artefacts.

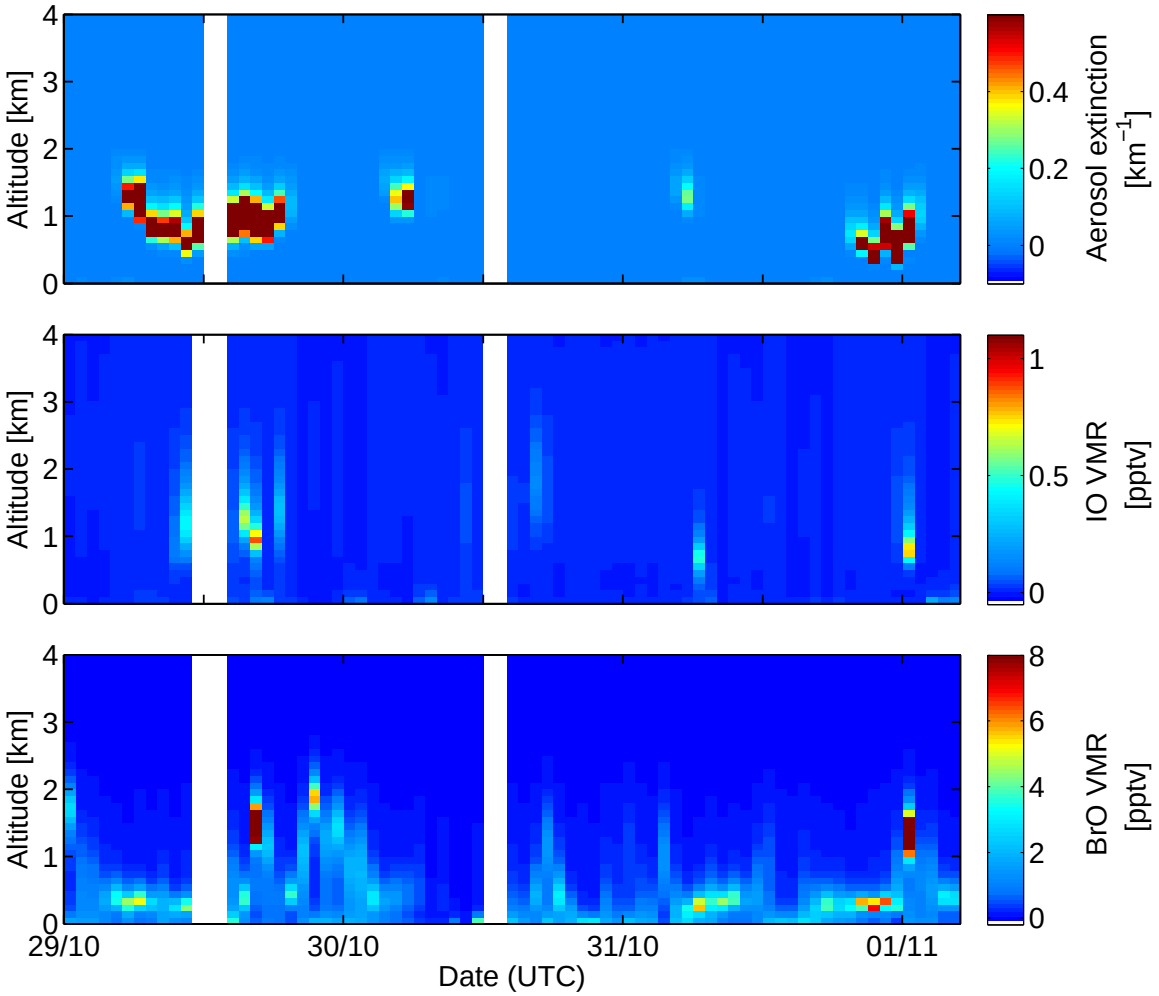

Figure 6.34.: *Cape Bird*: Vertical profiles of aerosol extinction and IO and BrO mixing ratios derived from the MAX-DOAS measurements. The BrO and IO profiles indicate a presence of those at an altitude around 1 km, where also clouds are often present. The plausibility of the aerosol profiles is discussed in section 6.4.2 and a comparison of the surface values is given in section 6.4.3. As discussed in the text, the SCDs are close to the DL and/or below, therefore the higher layers could also be due to inversion artefacts.

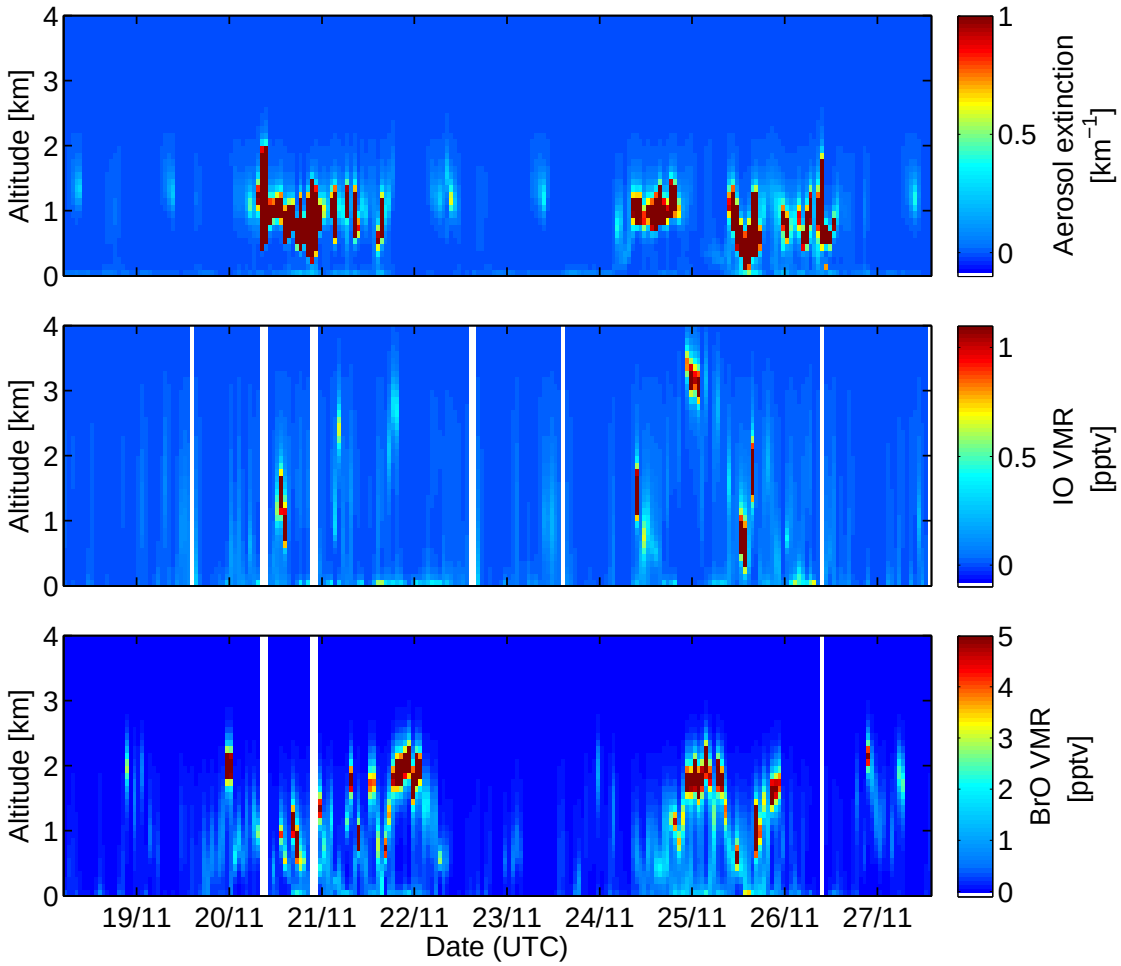

Figure 6.35.: *Balcony 2*: Vertical profiles of aerosol extinction and IO and BrO mixing ratios derived from the MAX-DOAS measurements. The BrO and IO profiles indicate a presence of those at an altitude around 1 km, where also clouds are often present. The plausibility of the aerosol profiles is discussed in section 6.4.2 and a comparison of the surface values is given in section 6.4.3. As discussed in the text, the SCDs are close to the DL and/or below, therefore the higher layers could also be due to inversion artefacts.

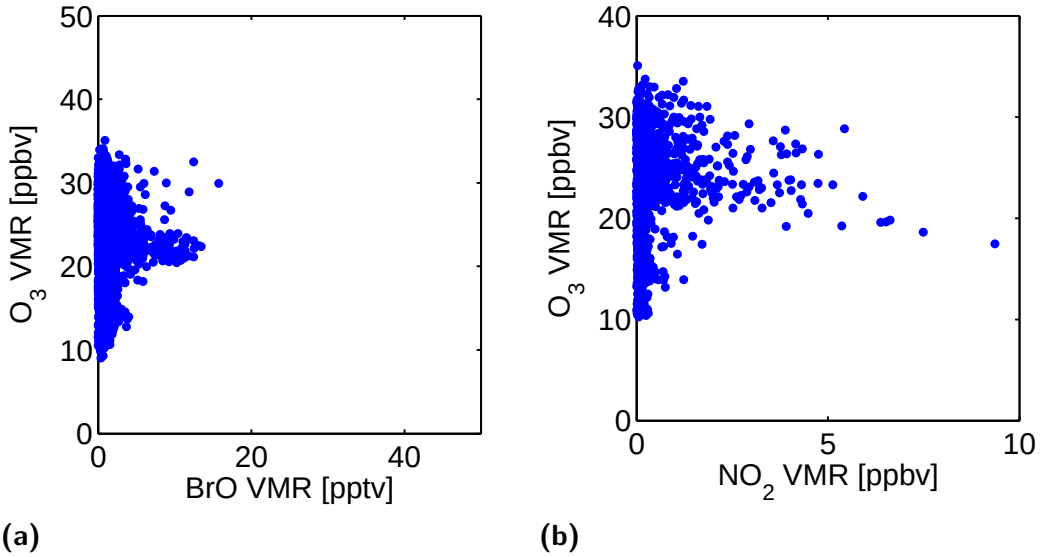

Figure 6.36.: LP-DOAS: Scatter plot of mixing ratios for the entire dataset on R4 for **(a)** BrO with O_3 and **(b)** NO_2 with O_3.

6.4 Analysis

An analysis of the results described above is given in this section for the aspects of measurement techniques, as well as issues only pertaining to this location, such as the local pollution. An analysis of the observed halogen chemistry is given in chapter 9 side-to-side with the results of the other two field sites.

6.4.1 LP-DOAS

Anthropogenic pollution

Pollution due to human activities was a major problem during this field study, as seen in the NO_2 mixing ratios observed with all instruments. This indicates that those sampled air masses were also not representative for the pristine Antarctic boundary layer.

In figure 6.36, scatter plots for O_3 with BrO and NO_2 mixing ratios are displayed. It is evident that in the case of NO_2, a stronger trend towards lower ozone mixing ratios is apparent than in the case of BrO. For BrO there does not seem to be any clear trend during the few observed events with mixing ratios above 5 pptv. At least parts of the ozone depletion therefore seem to correlate better with an increase in NO_2 mixing ratios. The degree of decrease due to NO_x, an approximate 10 ppbv of ozone, resulting in an increase of approx. 10 ppbv of NO_2, further suggests that most of this is due to the oxidation of NO. Likely sources of the NO are the combustion engines of the vehicles (construction vehicles, fork lifts, snowmobiles etc.) and air craft operating in this area.

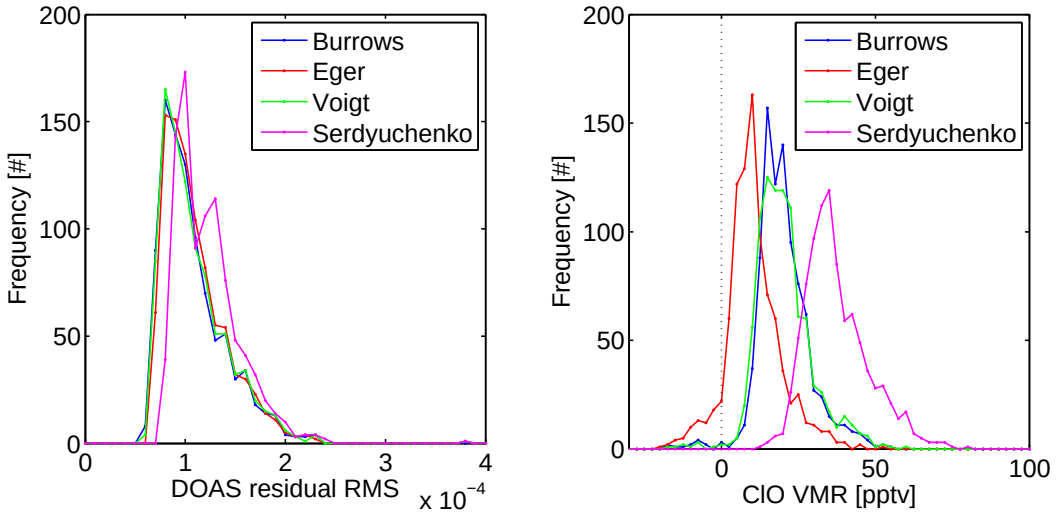

Figure 6.37.: The dependence of the LP-DOAS ClO evaluation on the specific O_3 absorption cross section used. **(a)** Histogram of the achieved fit residual RMS. **(a)** Histogram of the retrieved ClO mixing ratios. The cross sections by Burrows et al. (1999) and Voigt et al. (2001) yield very similar results, the latter was therefore chosen for the final evaluation.

ClO: Influence of ozone absorption cross sections on DOAS retrieval

The measurement of ClO by LP-DOAS is challenging for two reasons, namely a low light intensity, as at those wavelengths more light of the light source gets scattered out of the light path, in comparison to higher wavelengths, and secondly the strong ozone absorption bands. The issue of light intensity was addressed, as mentioned above, by the use of a much brighter light source than during the rest of the campaign. The strong absorption of ozone has to be corrected with an accurate laboratory absorption cross section, otherwise residual structures will influence the fit to the point where ClO absorption bands are masked. At lower wavelengths than the range used in this work, 294.0 nm - 313.3 nm, where ClO features its largest differential absorption structures, the absorption of oxygen is too strong and hinders a ClO retrieval. This is because to date, precise enough laboratory absorption cross sections are not available. Additionally, even less light is available. Lastly, a multitude of hydrocarbons have absorption bands in this region. For all those reasons, a wavelength interval slightly higher than the one with the largest absorption structures of ClO was chosen.

To investigate possible spectral interferences between ClO and ozone absorption structures, the entire evaluation was done four times, each time with a different ozone absorption cross section. The tested ones are the ones recorded by Burrows et al. (1999), Eger (2014), Voigt et al. (2001) and Serdyuchenko et al. (2014). Frequency distributions of the resulting residual RMS values are shown in figure 6.37a. No large difference is apparent between the four, the residual is a bit

higher though when using the one by Serdyuchenko et al. (2014). The frequency distribution of the retrieved ClO values, depending on the used ozone absorption cross section, is displayed in figure 6.37b. Depending on which one is used, values vary by about a factor of 2, especially the one provided by Serdyuchenko et al. (2014) leads to significantly higher values. The one by Eger (2014), measured with the same spectrometer as used here, though with a different grating and higher resolution, and therefore also convoluted with the instrument function before the analysis, leads to smaller values. Remarkably though, the cross sections by Burrows et al. (1999) and Voigt et al. (2001), recorded by different means and instruments lead to almost identical ClO values. Due to this agreement, the cross section by Voigt et al. (2001) was used for the final analysis, which has a slightly better resolution than the one by Burrows et al. (1999). In any case, no matter which O_3 cross section is used, several ClO values are always significantly higher than the detection limit of typically 10 pptv, the time series is also unchanged in its variation, except for a shift of all mixing ratios to higher or lower values.

6.4.2 MAX-DOAS vertical profiles

The aerosol extinction profiles derived from the MAX-DOAS allow a simple qualitative comparison, for various visibility conditions, with images taken with an automated camera located in the building where the LP-DOAS system was placed. In all three instances of which measurements were presented in section 6.3.3, the instrument often sees the highest aerosol extinctions at around 1 km altitude. This corresponds well to clouds which were present at those times as well as their altitude. For four points in time, images are shown in fig. 6.38 together with the concurrent, retrieved aerosol extinction profile. Under clear conditions White Island is visible, which reaches a maximum altitude of 701 m and is 30 km away. On the 23rd October (22:17) the MAX-DOAS data shows an extinction of 2.5 km^{-1} at the surface, in picture 6.38a apart from the station building little else is visible. On the 20th November (11:33) the extinction is at 3 km^{-1} at 1 km altitude and cloud cover is visible on the corresponding image (6.38b). On the 22nd November (17:35) the retrieved extinction is below 0.01 km^{-1} everywhere, clear sky conditions, as also evident on image 6.38c. On the 24th November (09:26) the aerosol extinction profiles show the lower base of the layer at around 800 m altitude, on the camera image (6.38d) clouds can be seen only slightly above White Island.

This qualitatively confirms the results of the aerosol inversion. For the shape of the retrieved BrO and IO vertical profiles such an analysis is not possible. A possible issue for those, is that the aerosol inversion is based on the O_4 SCDs, which are almost always dozens if not hundreds of times above the detection limit and have errors of the order of 1%. This is not the case for BrO or IO, where errors are a lot higher, relative ones between 10% and 50% for lower angles, and the SCDs of higher angles are all under the detection limit, where most of the

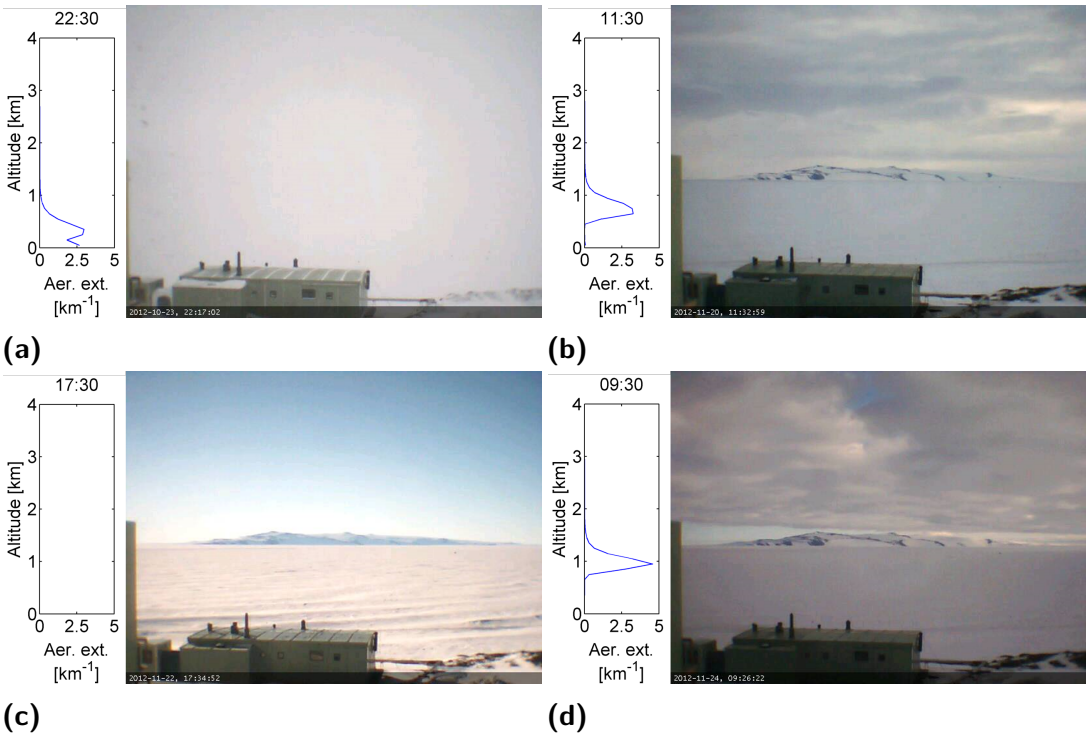

Figure 6.38.: Images for different weather conditions from the Hatherton Lab, the building where the LP-DOAS was located, towards White Island, roughly 60 ° counterclockwise from the LP-DOAS and MAX-DOAS light paths. The concurrent, retrieved aerosol extinction profiles are shown next to the image. **(a)** Storm, 23rd October 22:17 **(b)** Cloud cover, 20th November 11:33 **(c)** Clear sky, 22nd November 17:35 **(d)** Cloud cover, 24th November 09:26.

information about higher layers derives from. What can be done is a comparison of the surface mixing ratios from the inversion and LP-DOAS results which is given in the next section. It would not be entirely unrealistic to have elevated layers of halogens at this location. On the other side of the McMurdo Sound of Scott Base, the Transantarctic Mountains are rising followed by the high-altitude plateau (>2 km) of inland Antarctica (compare fig. 6.1). The katabatic flow of air from those altitudes brings cold, continental air masses down to sea level. Halogen-rich air masses would be expected to come from the comparatively warmer sea ice-covered ocean to the north. Those air masses therefore should get undercut by the katabatic flow and lifted towards higher altitudes. This can however not be concluded from the measurements presented here, as due to the low signal-to-noise ratios the resulting mixing ratios at those altitudes could also be inversion artifacts. Thus, this point needs to be researched in future studies.

6.4.3 Comparison of surface mixing ratios: MAX-DOAS vs. LP-DOAS

The two situations, when the MAX-DOAS was placed next to the LP-DOAS, allow for a direct inter-comparison of the resulting surface mixing ratios. An exact match is not to be expected. Although the instruments are looking into the same direction, they sample different air masses. The light path of the LP-DOAS is closer to the ground and looking slightly downward, whereas the lowest angle of the MAX-DOAS is 1 ° and therefore higher. Also the LP-DOAS is only sampling the first 4 km away from the telescope, whereas the MAX-DOAS, depending on the wavelength range, has an average light path of several times that distance, from 10 km to 25 km under aerosol free conditions (Roedel and Wagner, 2011).

For the MAX-DOAS, the mixing ratios of the lowermost box (0 m - 100 m) were taken. For the LP-DOAS, the data from the longer light path towards R4 is used in all cases. The comparisons were done for IO and BrO, both of which were above the detection limit of both instruments several times during those periods.

The first period is shown in figure 6.39, together with meteorological data from Scott Base, which was provided by NIWA. During the first two days, there is only sparse data for both instruments and little simultaneous data due to the weather conditions. For the last four days, starting at the 25th, for BrO both methods yield very similar results. For IO the difference is larger, with the LP-DOAS seeing something resembling a strong diurnal variation during the last two and a half days, and the MAX-DOAS seeing little to no IO.

During the second comparison period, shown in figure 6.40, BrO levels are lower, while IO levels are of a similar magnitude. At times, a remarkable match of the mixing ratios for both instruments is evident for BrO and IO (21st, 22nd and 25th, 26th November). For BrO higher wind speeds seemingly lead to a better match, which should be the case, due to the better mixing achieved then. However, during the beginning of this comparison period, as well as later on the 23rd, the LP-DOAS sees significant amounts of BrO and IO when the MAX-DOAS values are close to zero.

The slightly better match of BrO compared to IO could be due to the different effective length of the light path of the MAX-DOAS, which for the IO wavelength range is roughly twice as long as for the BrO range during aerosol free conditions.

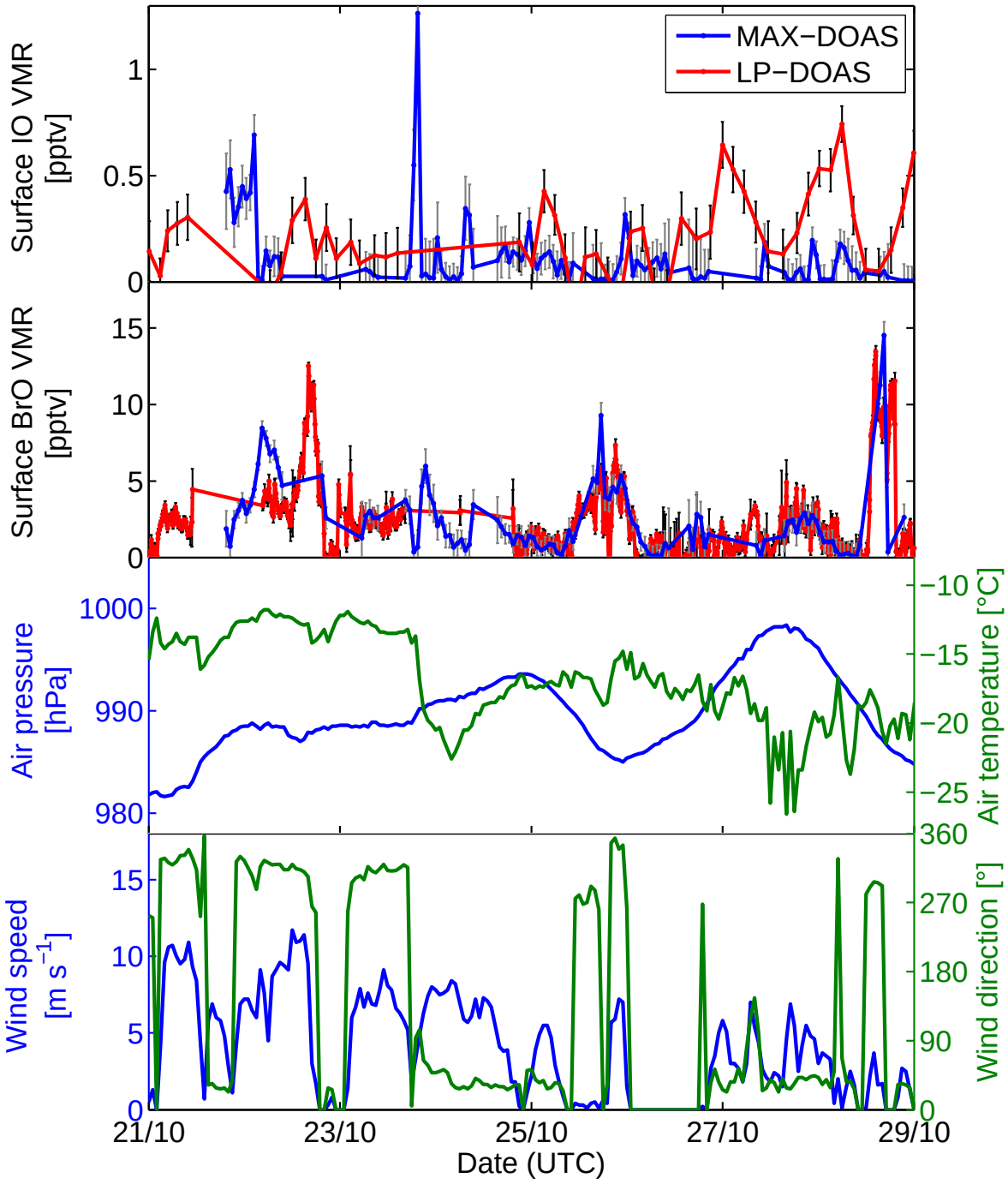

Figure 6.39.: First comparison (*Balcony 1*) of IO and BrO mixing ratios from LP-DOAS measurements on R4 and the lowest box (0 m - 100 m) of the MAX-DOAS vertical profile inversions shown on top. Below air pressure, temperature, wind speed and direction at Scott Base. The meteorology data was provided by NIWA.

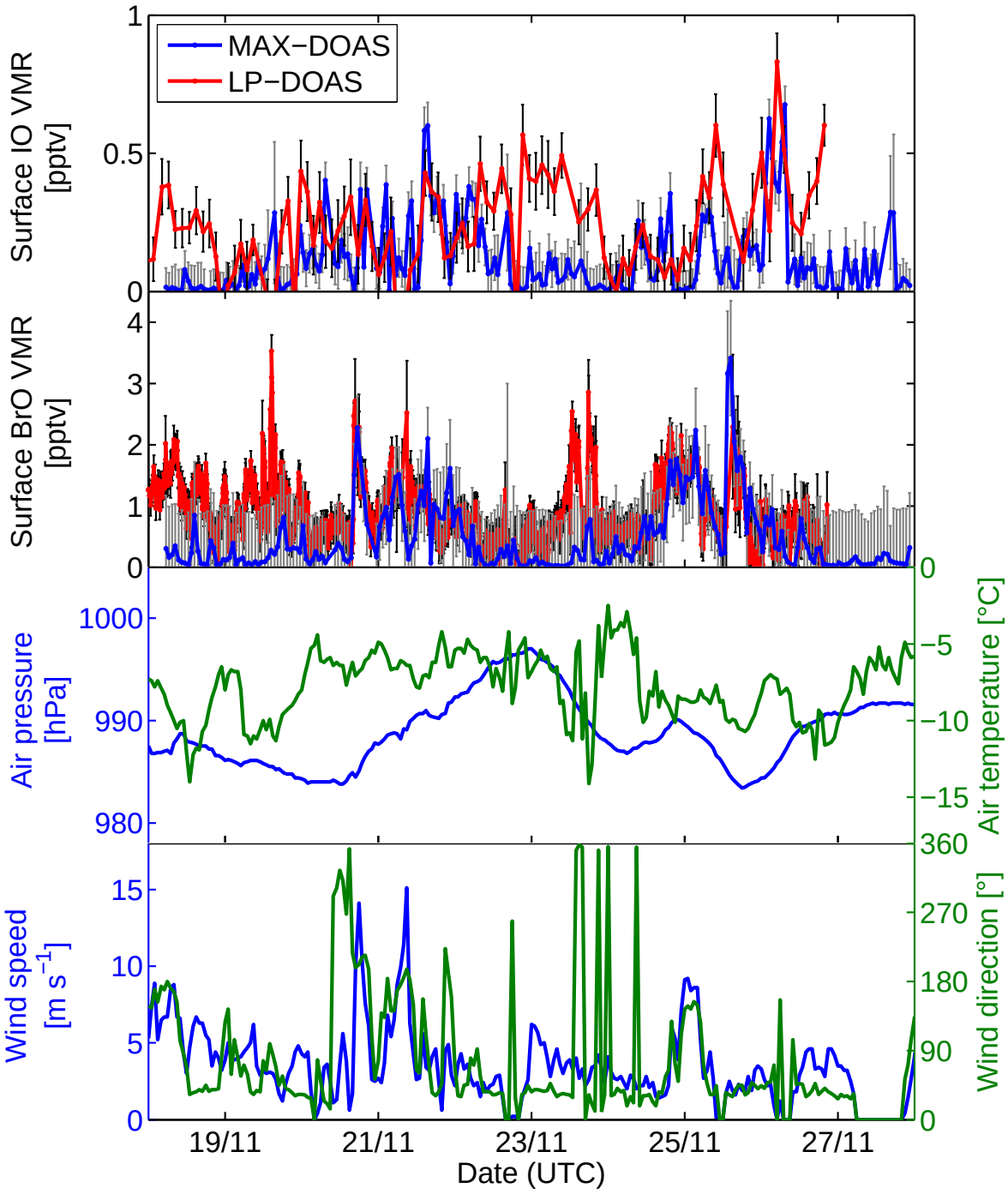

Figure 6.40.: Second comparison (*Balcony 2*) of IO and BrO mixing ratios from LP-DOAS measurements on R4 and the lowest box (0 m - 100 m) of the MAX-DOAS vertical profile inversions shown on top. Below air pressure, temperature, wind speed and direction at Scott Base. The meteorology data was provided by NIWA.

6.5 Concluding remarks

The results of the campaign were unexpected in several ways. The lack of even a single ODE during a three month period in austral spring was surprising, likewise the low BrO mixing ratios. Even more surprising was, that due to previous studies, IO was expected to be present at mixing ratios of the order of at least several pptv with the measurements of all three instruments indicating mixing ratios most often in the range of 0 to 0.5 pptv.

Although the detection limit of the CE-DOAS finally turned out to be too high for the average mixing ratios as seen be the LP-DOAS and MAX-DOAS, the CE-DOAS measurements nonetheless provide insight into the homogeneity of the distribution of IO. They discredit the idea of strong local sources from the sea ice, shelf ice, snow or penguin colonies with the resulting strong gradients, and point to a more homogeneous distribution. In the snow pit experiment with the CE-DOAS instrument, IO also was not observed, which resembles similar measurements at Neumayer Station by Udo Frieß (unpublished results, personal communication, 2012). A noticeable increase in NO_2 concentration however could be detected as expected due to emission from the sunlight snow pack (e.g. Honrath et al., 1999).

ClO was observed for the first time in the Antarctic boundary layer with a strong diurnal cycle, with maxima around noon and minima around midnight. Furthermore, that at least under favorable, well-mixed meteorological conditions, MAX-DOAS inversion results are comparable with LP-DOAS results even at the scale of a few ppt, or less in the case of IO, adds a lot of confidence to the technique. This is especially helpful for measurements for which no inter-comparison with over devices is or was possible for whatever reasons, such as the data from Alert presented in the next chapter.

7

Field studies of iodine monoxide in the high Arctic at Alert

Figure 7.1.: View of Alert from Mount Pullen. The station and air field are located on the right. The GAW laboratory is visible on the plateau in the left part of the picture.

Alert, a Canadian military outpost in the high Arctic at 82.5 °N, is the place where bromine-catalyzed ozone depletion was first observed by Barrie et al. (1988). Since then, numerous field studies in relation to the tropospheric halogen chemistry have been undertaken at this location.

In springtime, Alert is in a region of higher bromine activation, as observed from space (Sihler, 2012), and numerous halogen field observations have been undertaken there, making it a good location for longterm studies. In 2007, a

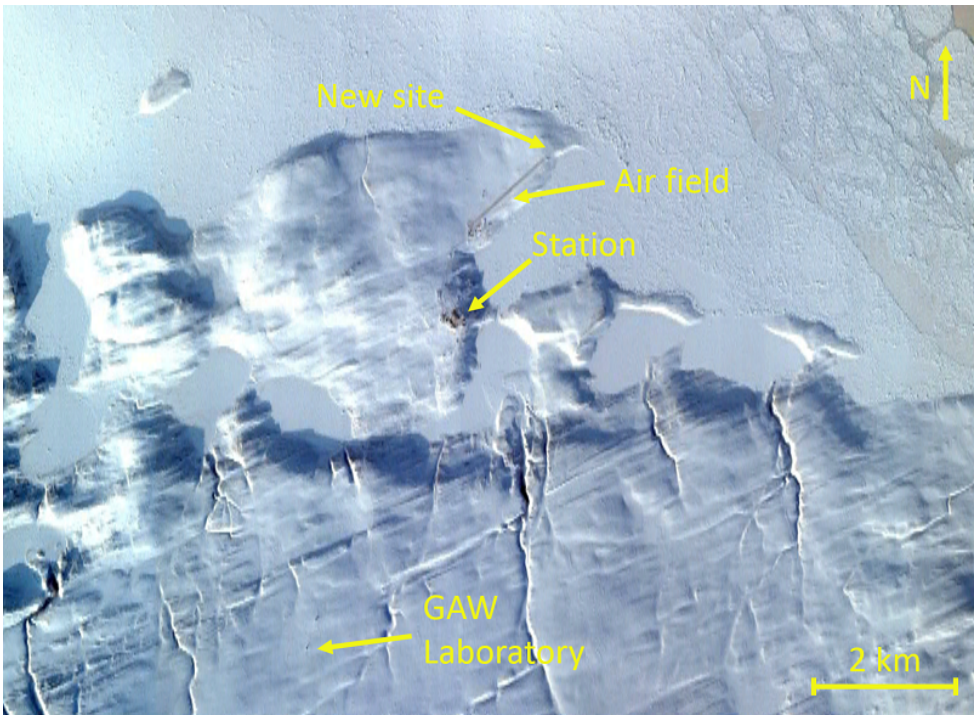

Figure 7.2.: Map of the area around Alert. The station and the air field are indicated. The MAX-DOAS instrument was formerly located at the GAW laboratory on the plateau in the south but was moved to the new site in 2013. The Arctic Ocean is located to the north. Map data: Google, DigitalGlobe, NASA.

MAX-DOAS instrument was permanently installed by Helmschmidt (2008) at the Global Atmospheric Watch (GAW) laboratory at Alert. The data set is currently spanning the years from 2007 to 2014, with the exception of 2010 where no data is available. In 2013, the instrument was moved from its previous position at the GAW laboratory (pictured in 7.3a), located around 8 km from the shore line, closer to the coast and the sea ice, in order to get more exposure to the sources of the reactive halogens.

7.1 The Alert MAX-DOAS instrument

The MAX-DOAS instrument is described and characterized in detail in Helmschmidt (2008), therefore only a brief description is given here.

The instrument consists of two parts, one is the scanner (pictured in fig. 7.3b), the other the spectrometer, a temperature-stabilized OceanOptics QE65000, together with the controller electronics (pictured in 7.3c). The latter are located inside the laboratory for shelter from the harsh climate, while the scanner (field-of-view of 0.4 °) is located outside on a metal tower. The altitude of the scanner was 5 m above ground and 190 m above sea level until the end of 2012. The azimuth of the scan direction was 340 °. Now the instrument is ~3 m above

ground and ~5 m above sea level and the azimuth is 10 °.

In order to be able to measure both BrO and IO with the single spectrometer, a compromise had to be made in terms of the wavelength range covered. The range was therefore set to 340 nm - 456 nm, covering three large absorption bands of BrO and all major ones of IO (see figure 7.5).

No major instrumental modifications have taken place since its inception. Minor repairs were done at the end of 2011, when the heating controller of the spectrometer and a power converter broke down and were replaced with similar models.

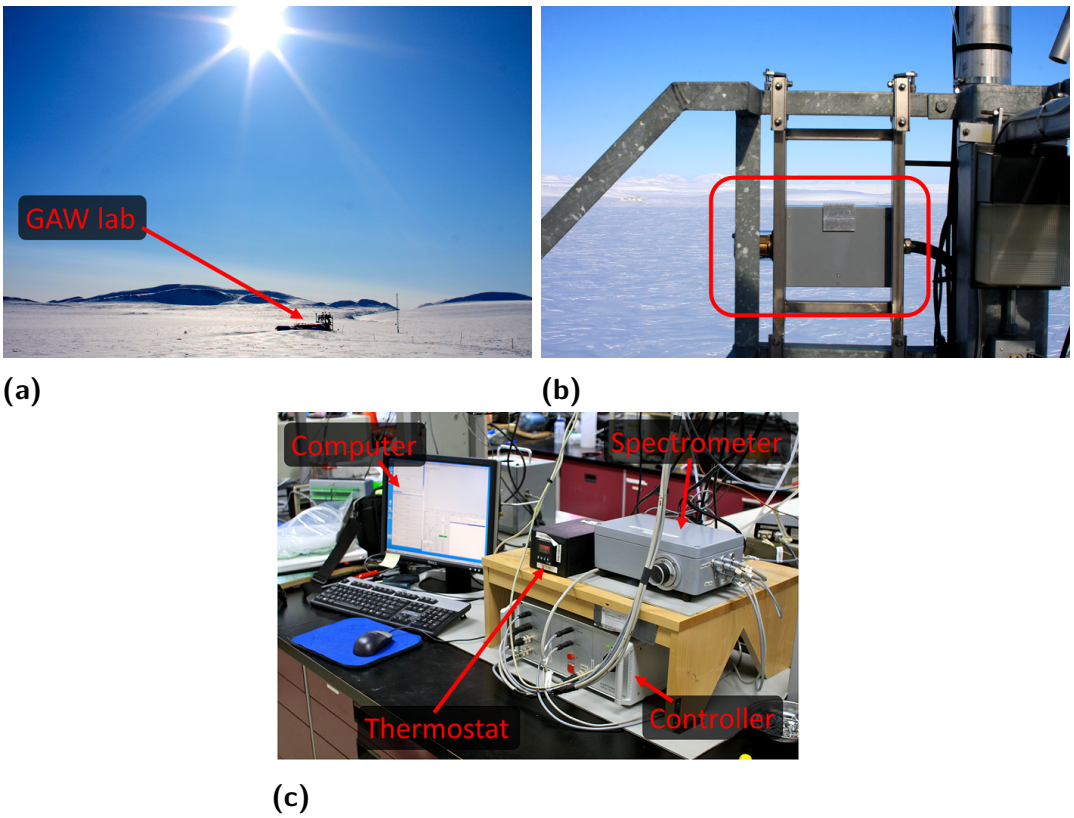

Figure 7.3.: Images of the location of the instrument from 2007 until 2013. **(a)** The GAW laboratory with its metal instrument platform. **(b)** The scanner (circled in red) mounted on the rail of the platform. **(c)** The spectrometer and controlling electronics inside the lab building.

(a)

(b)

(c)

(d)

(e)

(f)

Figure 7.4.: Images from the new location of the instrument (since 2013), closer to the sea ice. Photos provided by Stoyka Netcheva (Environment Canada).

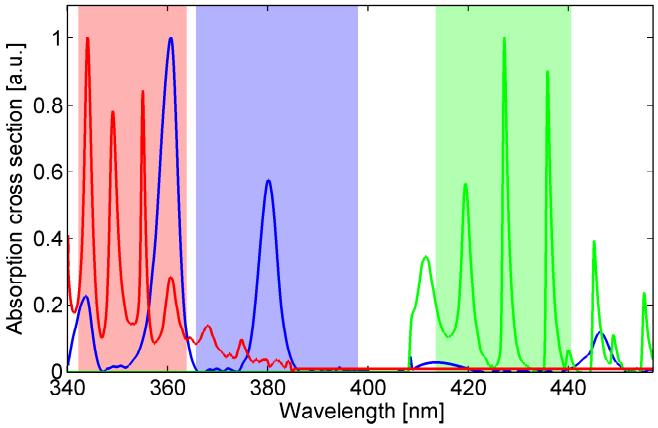

Figure 7.5.: The fit ranges used for the three fits performed on the Alert spectra. Convoluted absorption cross sections are shown for BrO (red), O_4 (blue) and IO (green) with the respective fit ranges for their retrieval (shaded areas).

7.1.1 Measurement program

The measurement program of the instrument consists of two parts. For SZAs smaller than 88 °, considered to be daytime, the instrument performs a MAX-DOAS measurement sequence. During twilight, for SZAs greater than 88 °, up to 97 °, the instrument performs zenith-sky measurements to allow the investigation of stratospheric processes, which are not part of this thesis.

The standard MAX-DOAS sequence consists of the angles 90 °, 20 °, 10 °, 5 °, 2 °, 1 °, -2 ° and -20 °. The last three were only added in May 2012, to increase sensitivity for the lowermost layer (1 °) and perform measurements of the light reflected off the snow (negative angles). Depending on the SZA, spectra are integrated for 2 minutes (up to an SZA of 80 °), 5 minutes (up to an SZA of 85 °) and 10 minutes (for SZAs up to 92 °). During those time periods, as many spectra as possible are acquired with a saturation of 70% (60% in the mornings for SZAs greater than 80 °) and co-added. Dark spectra and mercury emission line spectra are taken manually by the local operator roughly once every week.

7.1.2 DOAS evaluation

As the instrument was usually taken down during the winter period and reinstalled the following spring, the alignment of the optical fiber at the spectrometer changed every time and with that the wavelength calibration and resolution. The spectra were therefore evaluated on a yearly basis. For each year of the series, 2007 - 2009 and 2011 - 2014, one dark current, one offset and one mercury emission line spectrum was chosen and used for the evaluation of the whole year as measurement conditions were stable throughout all years. The numbers of those chosen spectra are listed in the appendix in table A.2 for reference.

For each year a wavelength calibration was performed by fitting a high res-

Species	Fit range [nm]	Accounted absorbers
BrO	342.25 - 363.90	BrO, O_3, NO_2, HCHO, O_4, Hot pixel (channel 76)
IO	413.50 - 440.50	IO, NO_2, H_2O, O_3, VRS N_2, VRS O_2
O_4	365.75 - 398.00	O_4, NO_2, O_3, HCHO

Table 7.1.: Fit intervals and absorbers included in the fitting procedure of the MAX-DOAS evaluation. All fit scenarios contained a Ring spectrum, a Ring spectrum multiplied with λ^4 and an inverse spectrum to correct for spectrometer stray light. The used DOAS polynomial was always of 4th order.

olution solar spectrum (Chance and Kurucz, 2010) against a well exposed summertime measurement spectrum. The calibration derived from this, together with the instrument response of the 404.66 nm mercury emission line was taken to convolute the laboratory cross sections. To improve the signal-to-noise ratio, multiple measurement spectra of the same elevation angle were co-added. The spectral averaging was set to a maximum of 8 sequences, less if the time between the beginning of the first spectrum to the end of the last was more than two hours. The individual measurement spectra were corrected for offset and dark current.

On those averaged spectra three DOAS fits were performed for the three absorbers of interest BrO, O_4 and IO. The chosen wavelength ranges were 342.25 nm to 363.90 nm for BrO, 365.75 nm to 398.00 nm for O_4 and 413.50 nm to 440.50 nm for IO (see figure 7.5). The DOAS fits include the current zenith reference spectrum, Ring spectra derived from it, a DOAS polynomial, the absorber of interest as well as other absorbers present in this wavelength range. The complete list of references included in the fits is listed in table 7.1. The used laboratory absorption cross sections are the same throughout this work and given in table A.1. Results with a fit residual RMS value worse than 10^{-3} were discarded as they are not useful for the analysis here, and fortunately also rather infrequent. An exception are the negative angles, which all resulted in large RMS values and strongly structured residual spectra, which is most likely due to an inhomogeneous illumination of the instruments field-of-view caused by the snow and ice crystals.

An exemplary BrO fit is shown in figure 7.6, with the absorption of BrO visible. Another fit example, clearly showing the presence of IO, is given in figure 7.7.

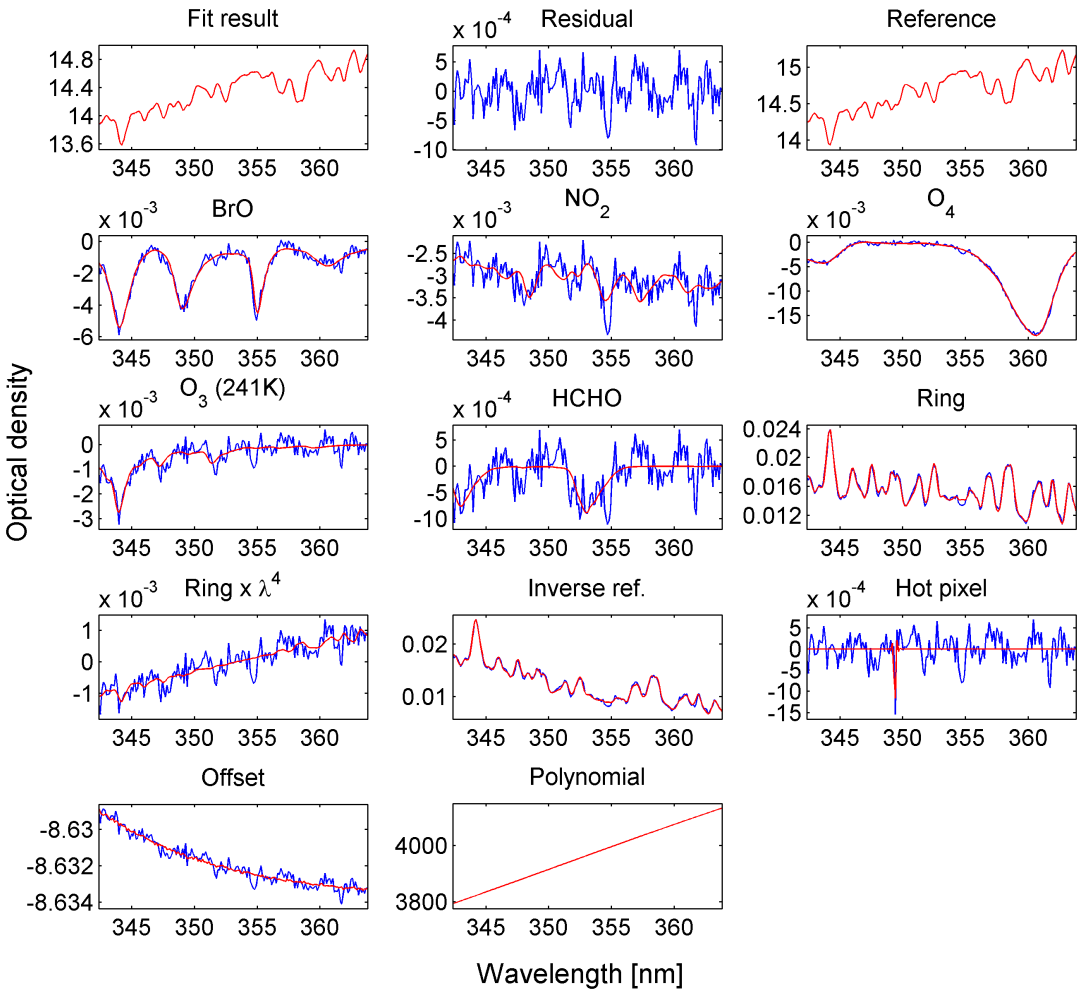

Figure 7.6.: BrO: DOAS fit result of 8 co-added 1 ° elevation angle sequences from 20th March 2012. The absorption of bromine monoxide is clearly visible. Retrieved column densities are: BrO $(5.73 \pm 0.32) \cdot 10^{14}$ molec cm^{-2}, O_3 $(2.4 \pm 0.6) \cdot 10^{18}$ molec cm^{-2}, NO_2 $(6.6 \pm 2.0) \cdot 10^{15}$ molec cm^{-2}, O_4 $(4.55 \pm 0.08) \cdot 10^{43}$ molec^2 cm^{-5}, HCHO $(3.6 \pm 1.0) \cdot 10^{16}$ molec cm^{-2}.

7.1.3 Inversion of trace gas SCDs

Inversions of the measured SCDs, as described in section 3.4.5, were done for the trace gases BrO, IO and NO_2 (SCDs used from the IO fit), in addition to the aerosol inversion. The settings for the aerosol inversion were taken as discussed in chapter 5 and listed summarily in table 5.1. Likewise, the settings for the BrO inversion were the ones already given and discussed in table 5.3. For IO, the only difference to the BrO settings is the different a priori profile that was used, with a surface mixing ratio of 0.3 pptv, a scale height of 1.0 km and a 400% relative error. For NO_2, an a priori profile with a mixing ratios of 500 pptv at the surface, a scale height of 0.5 km and a relative error of 500% was used.

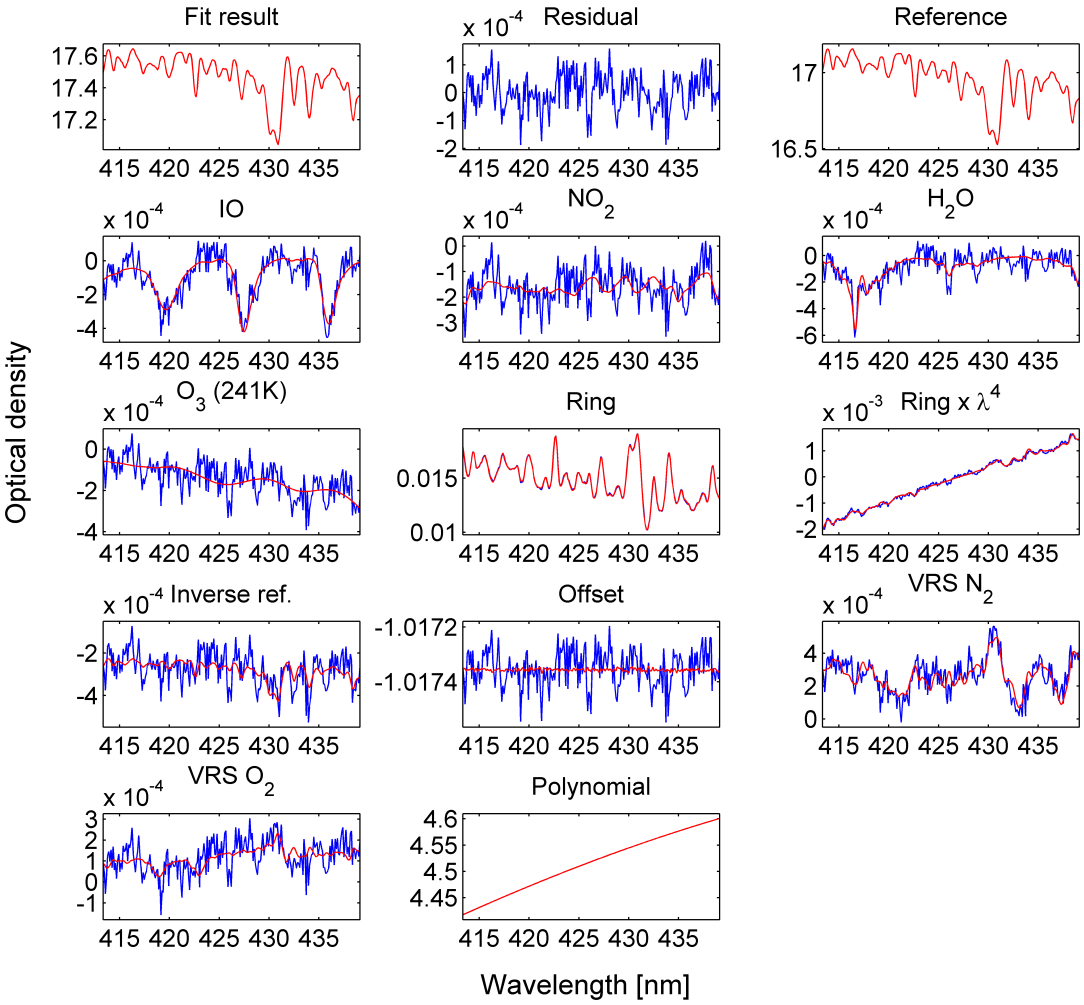

Figure 7.7.: IO: DOAS fit result of 8 co-added 1° elevation angle spectra from 30th May 2013. The absorption of iodine monoxide is clearly visible. Retrieved column densities are: IO $(1.66 \pm 0.16) \cdot 10^{13}$ molec cm^{-2}, NO_2 $(3.7 \pm 1.6) \cdot 10^{14}$ molec cm^{-2}, H_2O $(1.35 \pm 0.20) \cdot 10^{23}$ molec cm^{-2}, O_3 $(2.0 \pm 1.4) \cdot 10^{18}$ molec cm^{-2}.

7.2 Results

7.2.1 Time series of BrO and IO SCDs

This section presents the time series of bromine monoxide and iodine monoxide. As mentioned above, the data quality is rather inhomogeneous between the different years, in terms of spectral resolution, signal-to-noise ratio and instrument uptime. The spectral quality, resolution and light throughput, were highest in 2012, 2013 and 2014 and also consistent over those years. During 2009, the spectra are still usable for the analysis here. In 2007 and 2008, the fiber coupling was apparently adjusted several times during spring until a usable configuration was reached. For most of these adjustment periods, either no mercury emission

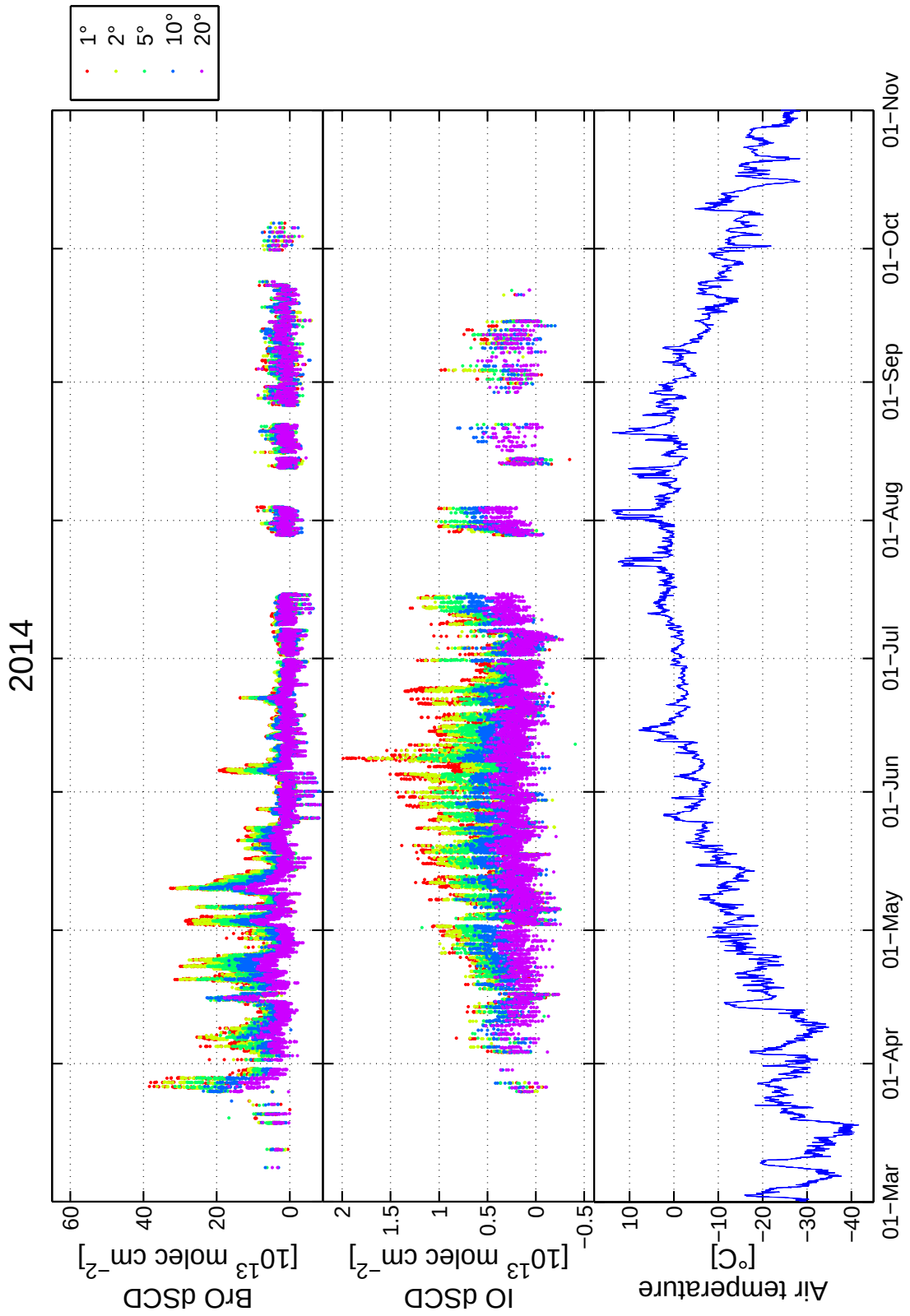

Figure 7.8.: 2014: The derived BrO and IO column densities of the Alert MAX-DOAS measurements. The elevation angle is color-coded and values are selected to have a DOAS fit residual RMS of less than $5 \cdot 10^{-4}$ for BrO and $1 \cdot 10^{-4}$ for IO. Also shown is the local air temperature to give an impression of the yearly seasonal variation. The meteorological data was provided by Environment Canada.

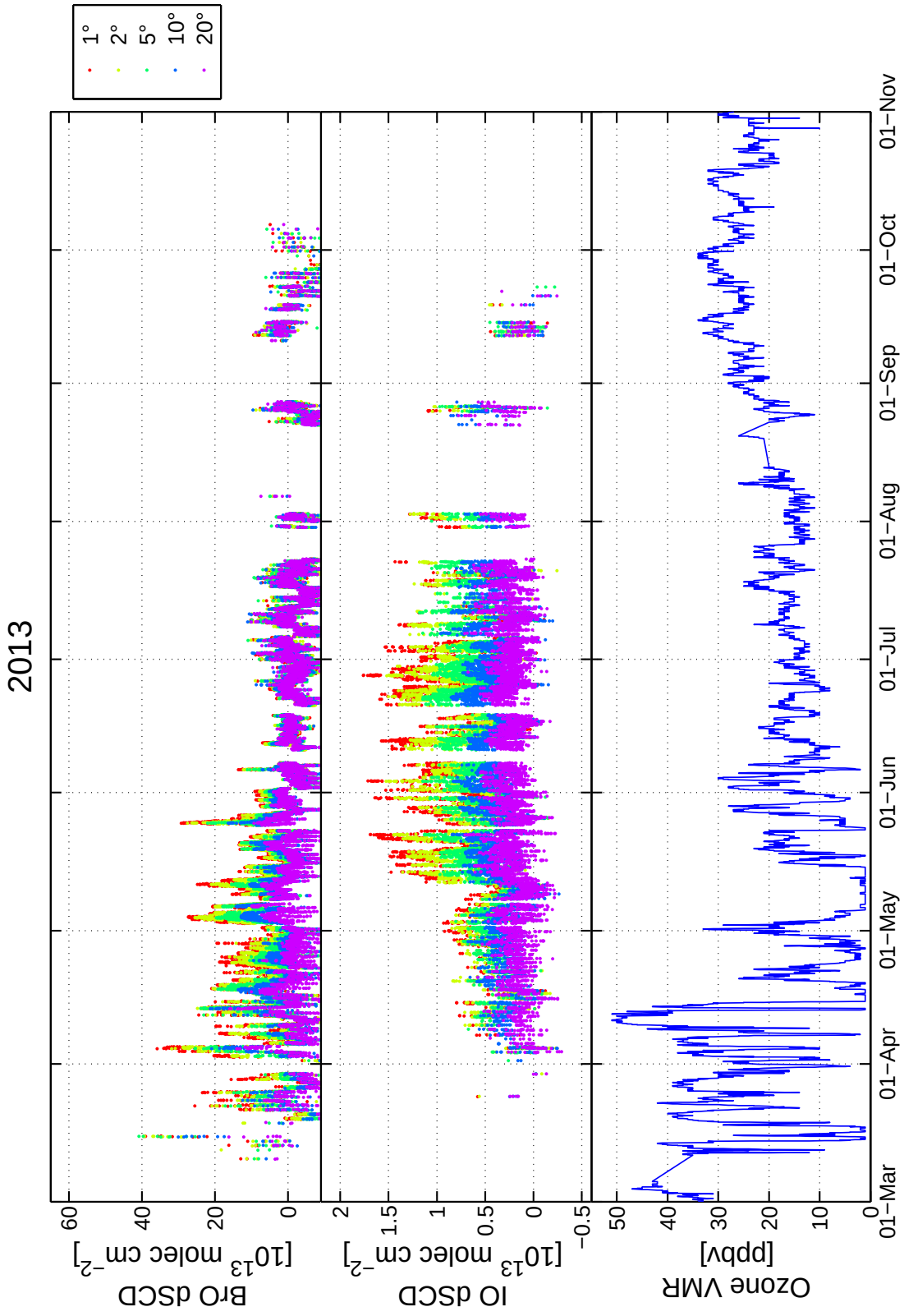

Figure 7.9.: 2013: The derived BrO and IO column densities of the Alert MAX-DOAS measurements. The elevation angle is color-coded and values are selected to have a DOAS fit residual RMS of less than $5 \cdot 10^{-4}$ for BrO and $1 \cdot 10^{-4}$ for IO. Also shown are the local surface ozone mixing ratios, which were provided by Environment Canada.

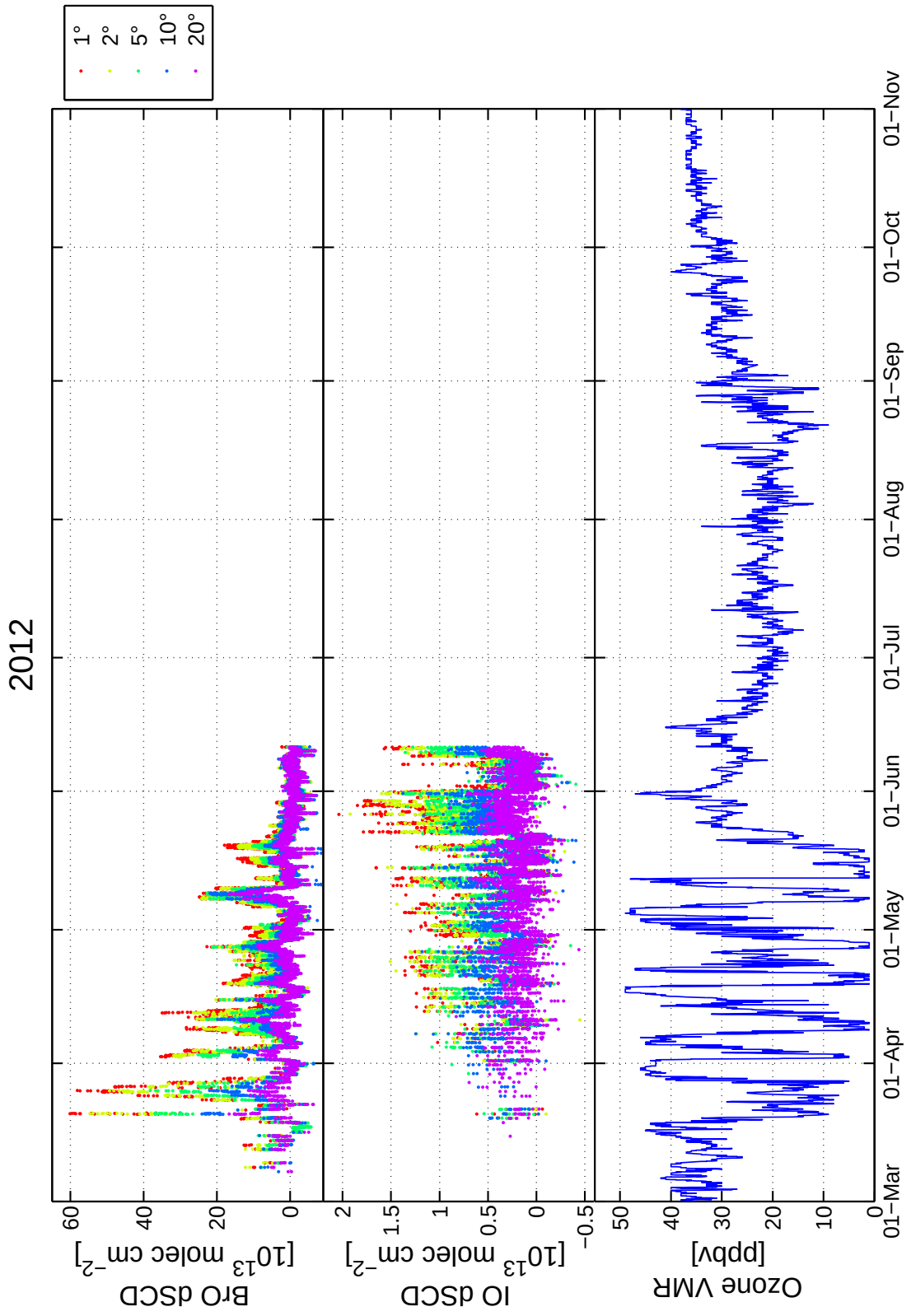

Figure 7.10.: 2012: The derived BrO and IO column densities of the Alert MAX-DOAS measurements. The elevation angle is color-coded and values are selected to have a DOAS fit residual RMS of less than $5 \cdot 10^{-4}$ for BrO and $1 \cdot 10^{-4}$ for IO. Also shown are the local surface ozone mixing ratios, which were provided by Environment Canada.

line spectra are available or the resolution is extremely low, on the order of several nanometers, and useless for the evaluation of trace gases. In 2011, the spectral quality is especially low, with very little light throughput over the entire measurement period.

In terms of instrument uptime, only during the years 2009, 2013 and 2014 was the instrument running for most of the sunlit time of the year. In 2007 and 2008, the instrument was operating mainly during summer, whereas in 2011 and 2012 the instrument was shut down after spring for unknown reasons.

The data, that is available and has sufficient quality, is shown in figures 7.8 for 2014, 7.9 for 2013, 7.10 for 2012 and in the appendix in figures A.48 for 2011, A.49 for 2009, A.50 for 2008 and A.51 for 2007. The ozone mixing ratios are also shown for the years 2007 till 2013, for 2014 no processed ozone data was available as of now, the air temperature is shown in this case to give a sense of the typical yearly seasonal cycle. The in-situ surface ozone data, as well as the weather data used in the following was provided by Environment Canada with a time resolution of one hour.

7.2.2 Bromine monoxide and ozone

Polar sunrise, i.e. a noontime SZA smaller than 90 °, is around the 27th February in Alert. For the years of 2009, 2012 to 2014 and possibly 2007, events of higher than average BrO SCDs can be seen in the time series. The periods with elevated BrO SCDs start at the beginning of the sunlit period until the beginning of June in the data from 2009 and 2012 - 2014. During those periods, ozone mixing ratios are highly volatile and ODEs occur frequently. In 2012 and 2013, for which both ozone as well as BrO SCDs are available for March, the first ODEs are accompanied by elevated BrO SCDs. Afterwards, from July onwards, average ozone mixing ratios continue to decline until summer, sometimes until August, when they begin to recover.

7.2.3 Detection of iodine monoxide

One unexpected finding was the presence of iodine monoxide absorption features in the spectra. As mentioned, a sample fit result is given in figure 7.7, with the IO absorption clearly visible. The retrieved SCD of $(1.66 \pm 0.08) \cdot 10^{13}$ molec cm^{-2} is also significantly above the detection limit of $0.32 \cdot 10^{13}$ molec cm^{-2} in this case.

In fact, IO could be positively identified in spectra from five years (2008, 2009, 2012 - 2014). In the two other years, 2007 and 2011, the data quality is not sufficient to be able to detect the amounts present.

As can be seen in the data from the years 2009, 2013 and 2014, IO is seemingly almost always present from spring to autumn. The observed column densities are highest during summer (May - August). This could be due to the highest concentrations of IO, the best visibility conditions and therefore longest average

light paths, or a combination of both. This is resolved by the inversions presented below. During springtime, the SCDs are lower, as they are during autumn, at least during the years with measurements in that season. There are however large gaps in the time series during autumn and major events could have been missed.

7.2.4 Time series of BrO, IO, O_3 and NO_2 mixing ratios

The results from the inversion allow the separation of the effects of variations in concentrations and variations in visibility conditions. The resulting retrieved surface mixing ratios for BrO, IO and NO_2 together with the ozone surface mixing ratios are given exemplary for the year 2014 in figure 7.11. The times series of the other years are given in the appendix in figures A.52 for 2013, A.53 for 2012, A.55 for 2009, A.56 for 2008 and A.57 for 2007. The data were filtered to have at least 1.0 degree of freedom for signal (refer to section 3.4.5).

The yearly cycles for BrO and IO show a highly similar behavior as the SCDs and will not be further studied on a daily or weekly basis, but by monthly means and histograms in the following, due to the size of the dataset. One point to be noted, is that the NO_2 levels indicate that the new location of the instrument since 2013 has a lot less exposure to the pollution from the station buildings.

7.3 Analysis

The extensive dataset spanning seven years lends itself to the investigation by statistical approaches. Aspects of interest are for example whether concentrations or yearly cycles have changed over the last few years, especially as this part of the Arctic has experienced significantly warmer periods lately compared to two or three decades ago (e.g. Miller et al., 2013). The aspects of inter-halogen chemistry and diurnal cycles, as well as the influence of meteorology and aerosols on halogen speciation, is discussed in combination with the other two field studies in chapter 9 in order to directly compare those.

7.3.1 Histograms

IO is measured with unprecedented accuracy in this study at Alert and simultaneously it is also the first long-term observation, demanding a closer look of its typical amounts and yearly cycles, especially in contrast to BrO, which is comparatively well studied in the Arctic generally and at Alert in particular.

Frequency distributions of the annual BrO surface mixing ratios are given in figure 7.12 for the seven years. The event-like manner of atmospheric BrO is evident in that, for most of the year mixing ratios are close to zero, which is also the most common value. The higher the mixing ratios, the less likely they are to occur.

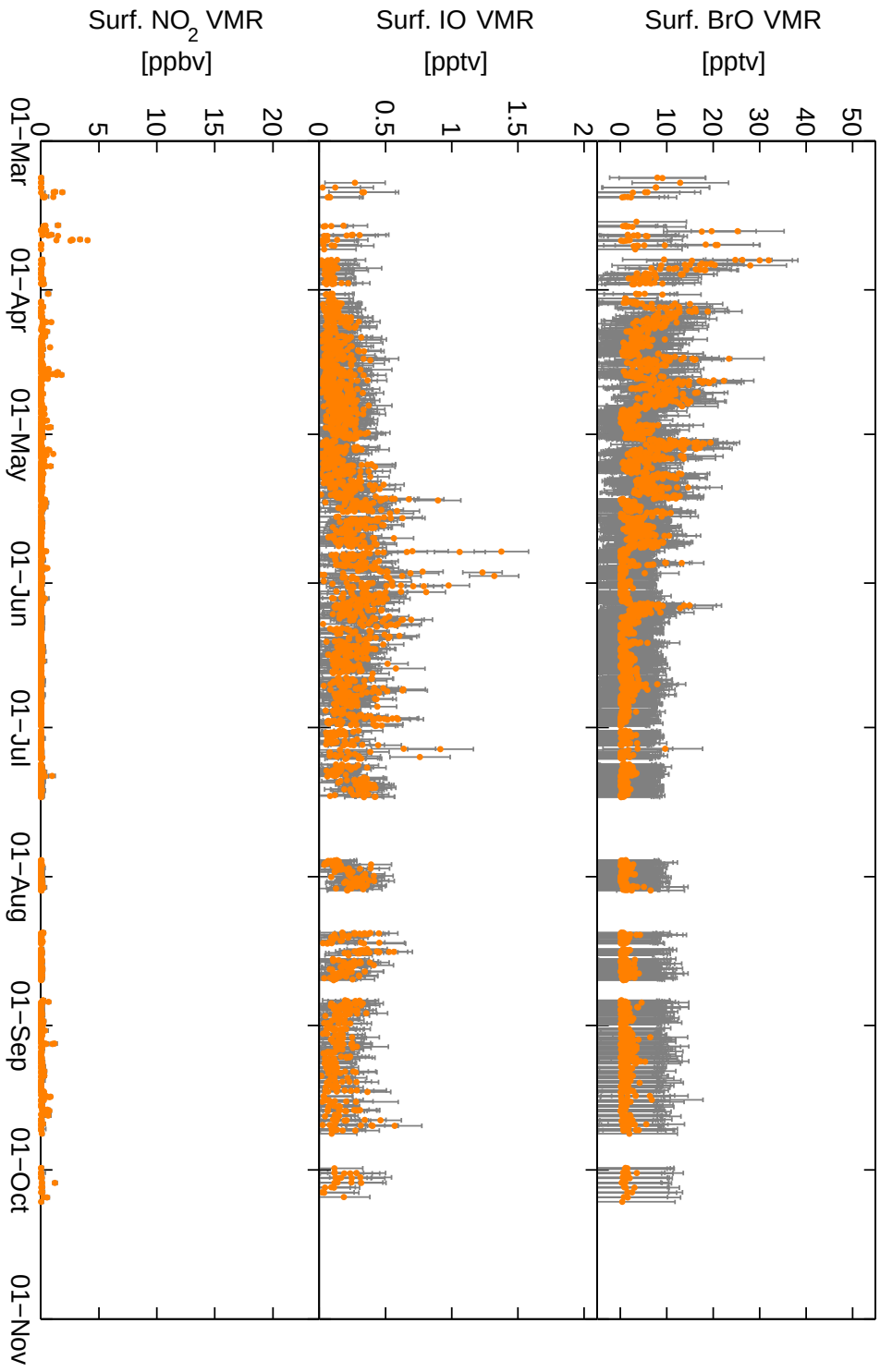

Figure 7.11.: 2014: Time series of retrieved surface mixing ratios of BrO, IO and NO_2. The results are filtered to have at least 1 degree of freedom for signal.

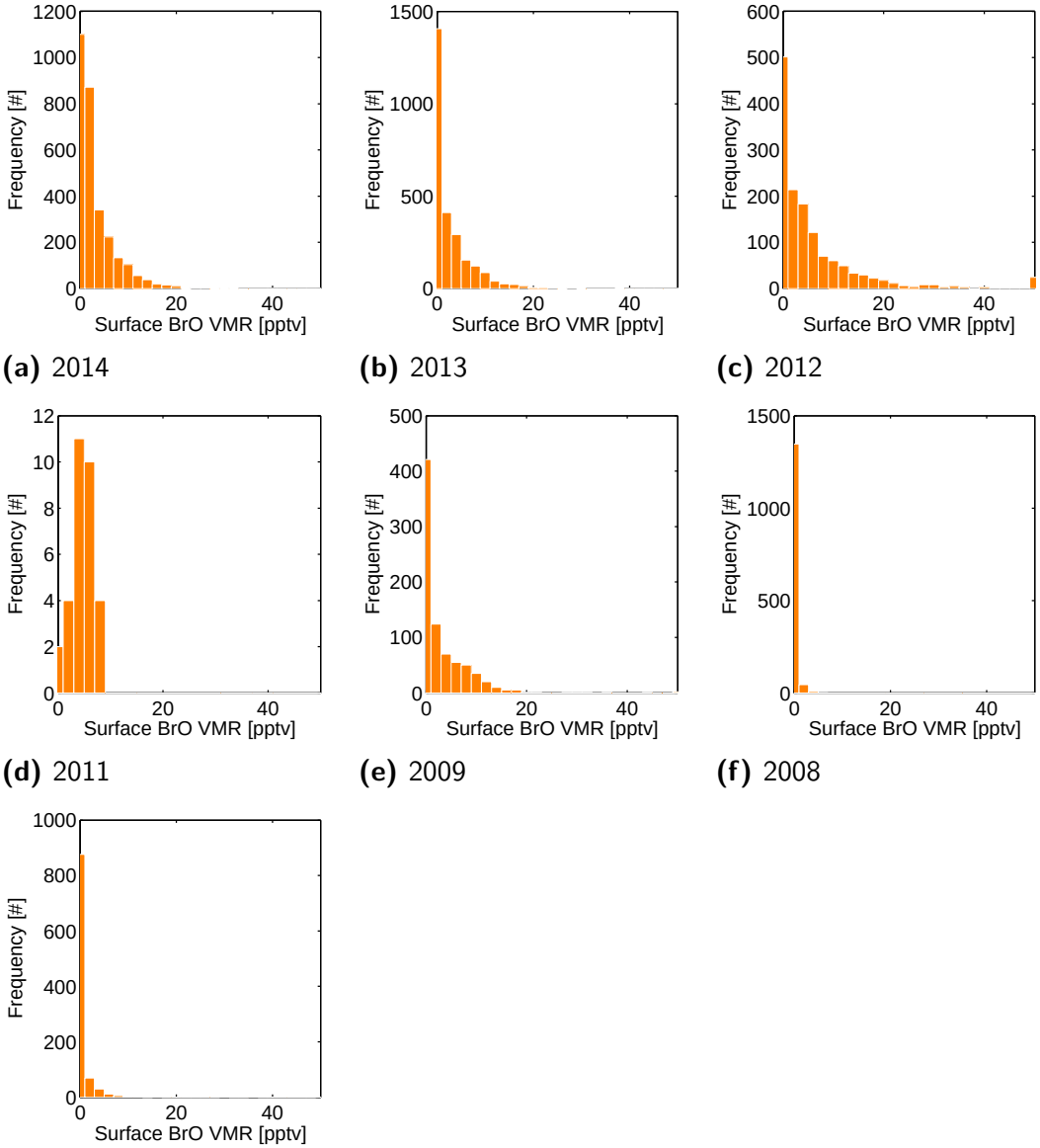

Figure 7.12.: Frequency distributions of the retrieved surface mixing ratios (0 m - 100 m box) of BrO for the years 2007 - 2014. The bin size is 2 pptv. The years with the most complete data during the springtime are 2014, 2013 and 2012, which all show similar distributions.

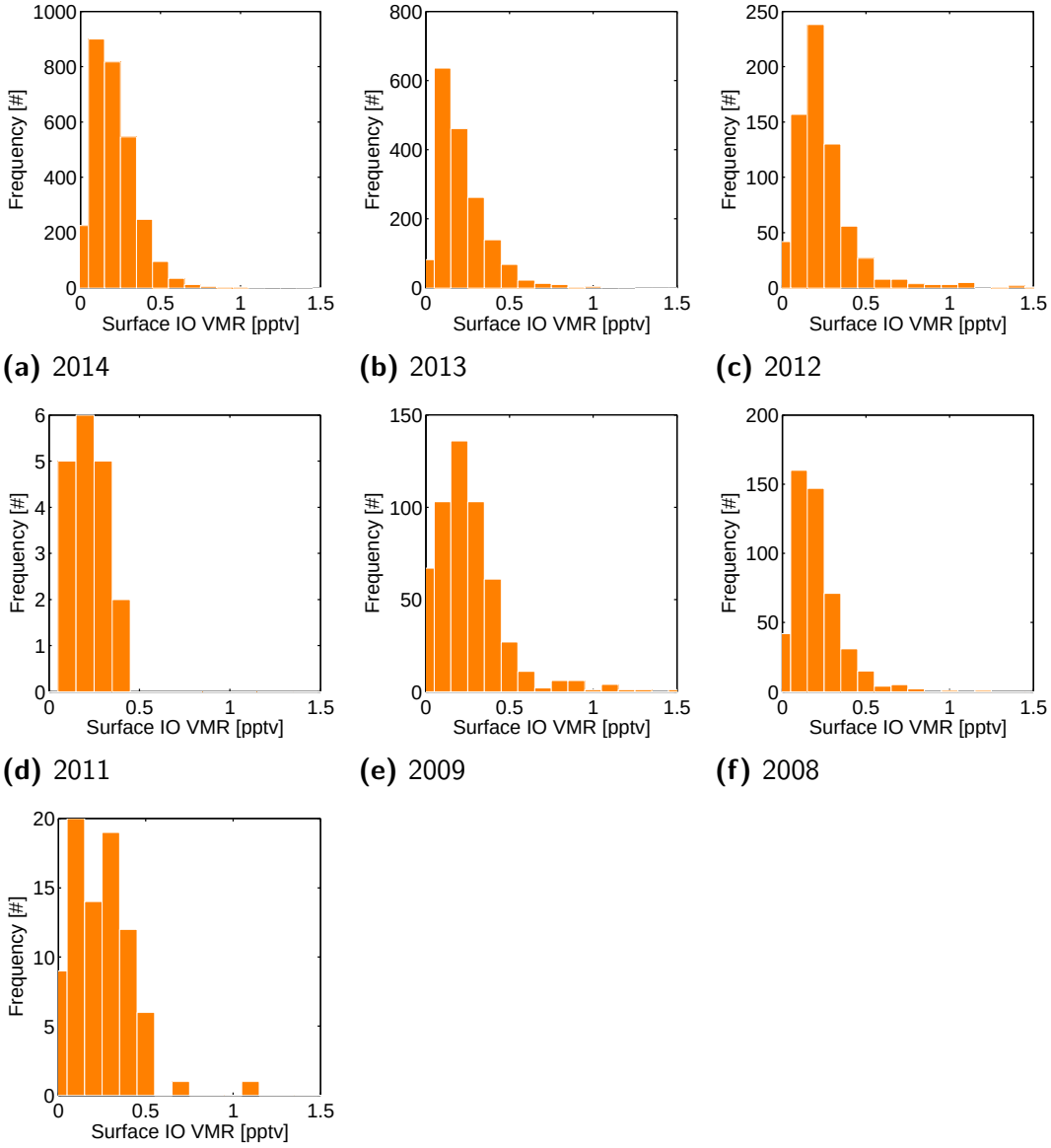

Figure 7.13.: Frequency distributions of the retrieved surface mixing ratios (0 m - 100 m box) of IO for the years 2007 - 2014. The bin size is 0.1 pptv. The years with the overall most complete data are 2014 and 2013. The difference between all distributions though is small, being predominantly in the range from 0.0 pptv to 0.5 pptv.

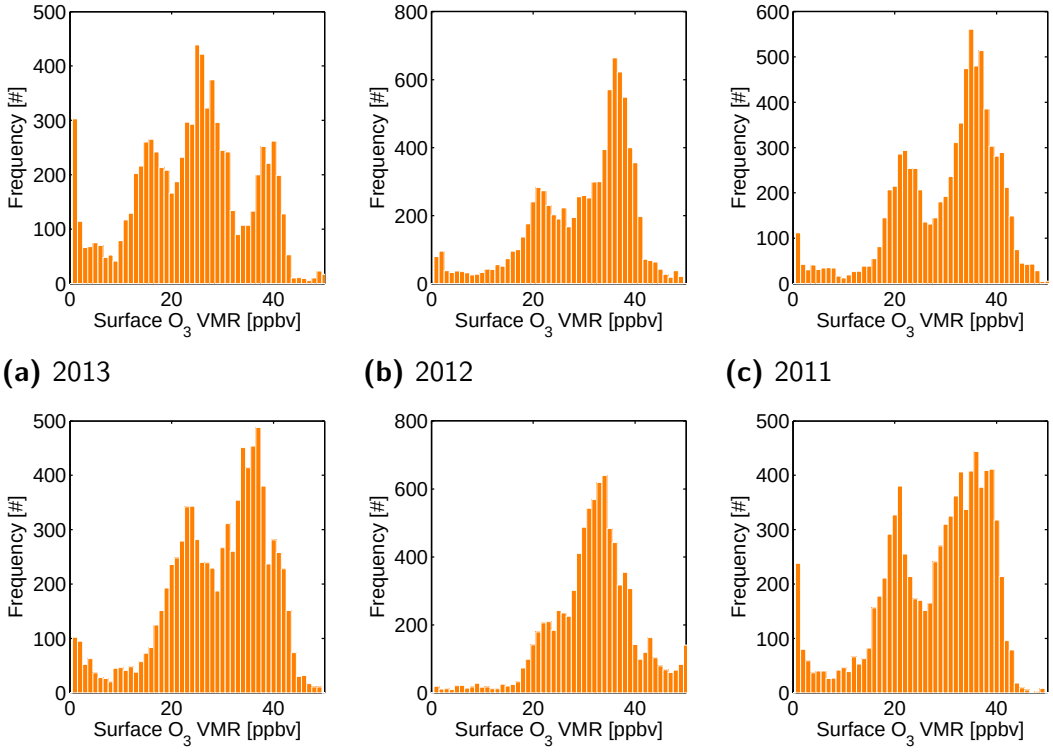

Figure 7.14.: Frequency distributions of the ozone mixing ratios for the years 2007 - 2013. The bin size is 1 ppbv. The ozone data was provided by Environment Canada.

This is not the case for IO. At least during the sunlit period where passive measurements are possible, IO is present most of the time. This can be seen in the frequency distributions shown in figure 7.13. The mixing ratios are between 0 and 0.5 pptv mostly, and occasionally between 0.5 and 1 pptv. The most common values are 0.1 or 0.2 pptv during those seven years.

Further histograms are given for ozone mixing ratios in figure 7.14 for the years with ozone data. Interestingly, in contrast to the halogen distributions, which are unimodal, the one of ozone is multimodal with 2 or 3 modes. The highest mode are the wintertime levels unperturbed by photochemistry. The low end of mixing ratios is the springtime ODE regime. Then, depending on the year, one (2007, 2009, 2011, 2012) or two (2013) modes are in between, marking the regimes of photochemistry and halogen effects.

7.3.2 Monthly mean surface mixing ratios of BrO, IO, O_3 and NO_2

Monthly means are useful to better infer the seasonal changes in halogen amounts over the years. They are given for BrO, IO, O_3 and NO_2 exemplary for the year 2013 in figure 7.15. Furthermore they are also given for each of the four compounds for the entire measurement period. For BrO, means are shown in figure 7.16 with the respective standard error of the means. For the years with the most complete springtime data, that is 2012, 2013 and 2014, it is evident, that during March, April and May average concentrations are highest and thereafter rapidly decline. Towards fall a small increase in BrO can be seen in 2008, 2009, 2013 and 2014. Due to the episodicity of the appearance of BrO and the downtime of the instrument also being rather episodic, a sampling bias cannot be excluded, which could possibly explain the different derived yearly cycles. For example, why average May levels are low in 2009, but not in other years. However, the data for the years 2012, 2013 and 2014, where the time series are at least almost complete for April, May and June, and the second half of March, a variation on the order of a factor of 2 can also be seen between different years, especially in May.

The monthly means of IO show, in comparison to BrO, a more similar cycle throughout the years, as pictured in figure 7.17. The annual maximum of around 0.4 pptv is in May and June. Another secondary maximum is possibly in September or October. The lowest values are reached in March, with an average of around 0.1 pptv.

For ozone, the means are given in figure 7.18. Starting from wintertime mixing ratios of 30 - 40 ppbv, they decline until May when the minimum is reached in most years with an average as low as 8 ppbv. Afterwards, the mixing ratios rise during summer and autumn, and in October reach the level of March again. In the years 2008, 2011 and 2012, the minimum was reached later however, and in summer the average mixing ratios reach a plateau and only start to recover in September.

7.3.3 Monthly mean vertical profiles and VCDs of IO

In addition to the surface mixing ratios, monthly means were furthermore calculated for the vertical mixing ratio profiles (fig. 7.20a), and of the retrieved VCDs of IO (fig. 7.20b) as a comparison with satellite data and their detection limits (see below, in section 7.4.2). Because the MAX-DOAS sensitivity drops quickly at altitudes higher than 2 km (compare section 5.2.2), the retrieved VCD is not the total column, but the column for this sensitive altitude range (also compare section 5.2.2). The profiles are also given for this height.

The derived VCDs of IO are in the range of 0.6 - 1.6 molec cm^{-2} and their seasonal variation is correlated with that of the monthly surface mixing ratios (ref. fig. 7.17a), with one exception. The second peak, seen in the surface mixing ratios in autumn, is absent or less pronounced in the vertical columns. This

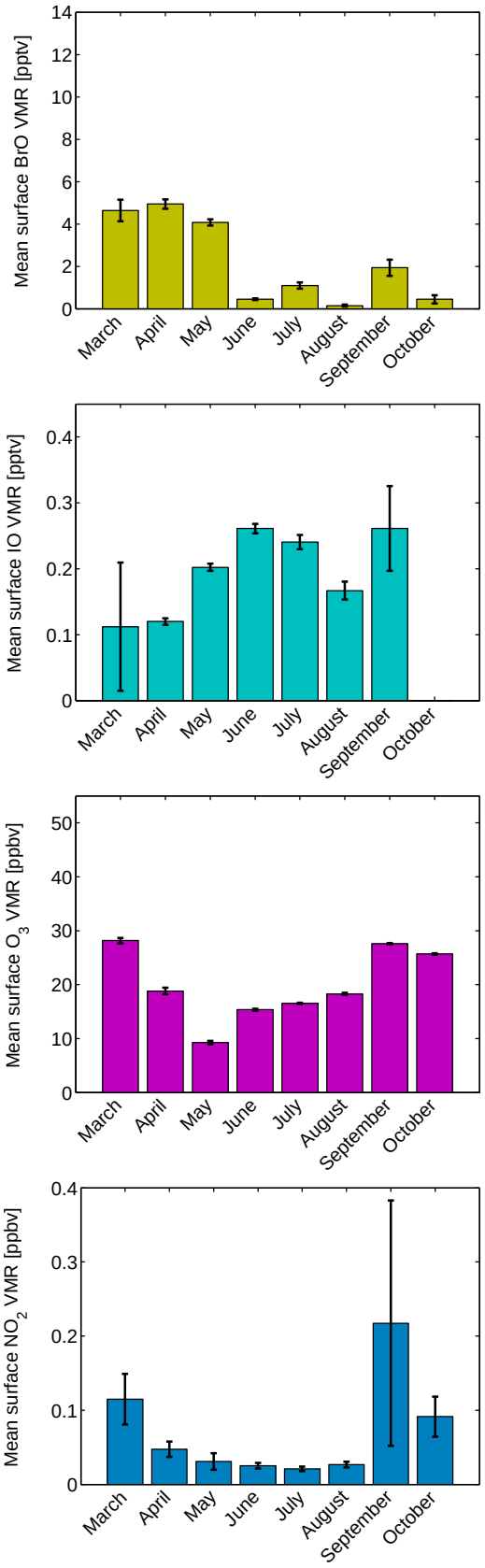

Figure 7.15.: Monthly means of the surface mixing ratios in Alert for **(a)** BrO, **(b)** IO, **(c)** O_3 and **(d)** NO_2. Error bars indicate the standard errors of the means.

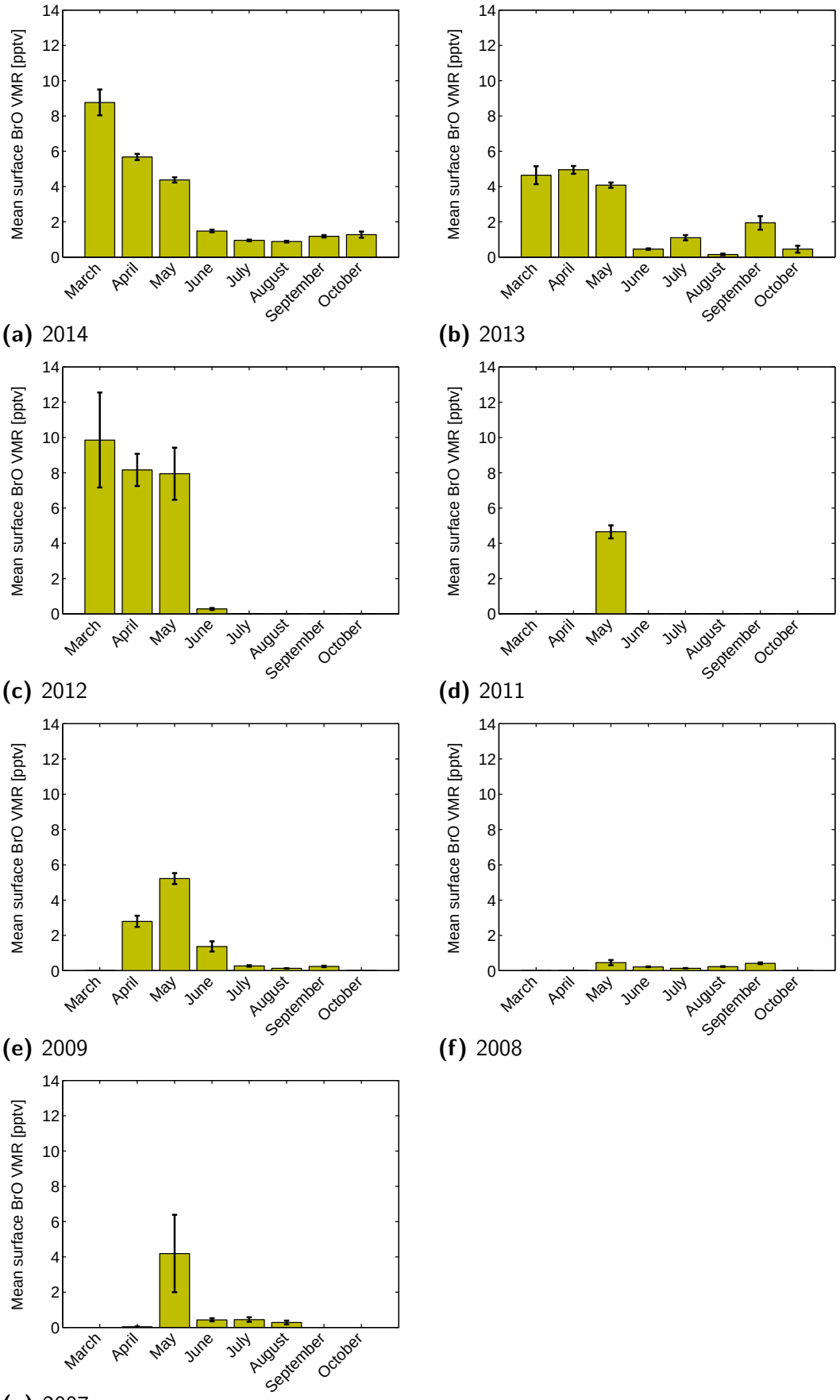

Figure 7.16.: Monthly means of the BrO surface mixing ratios in Alert for the years 2007 - 2014. Error bars indicate the standard errors of the means. Only the years 2013 and 2014 have a largely complete time series.

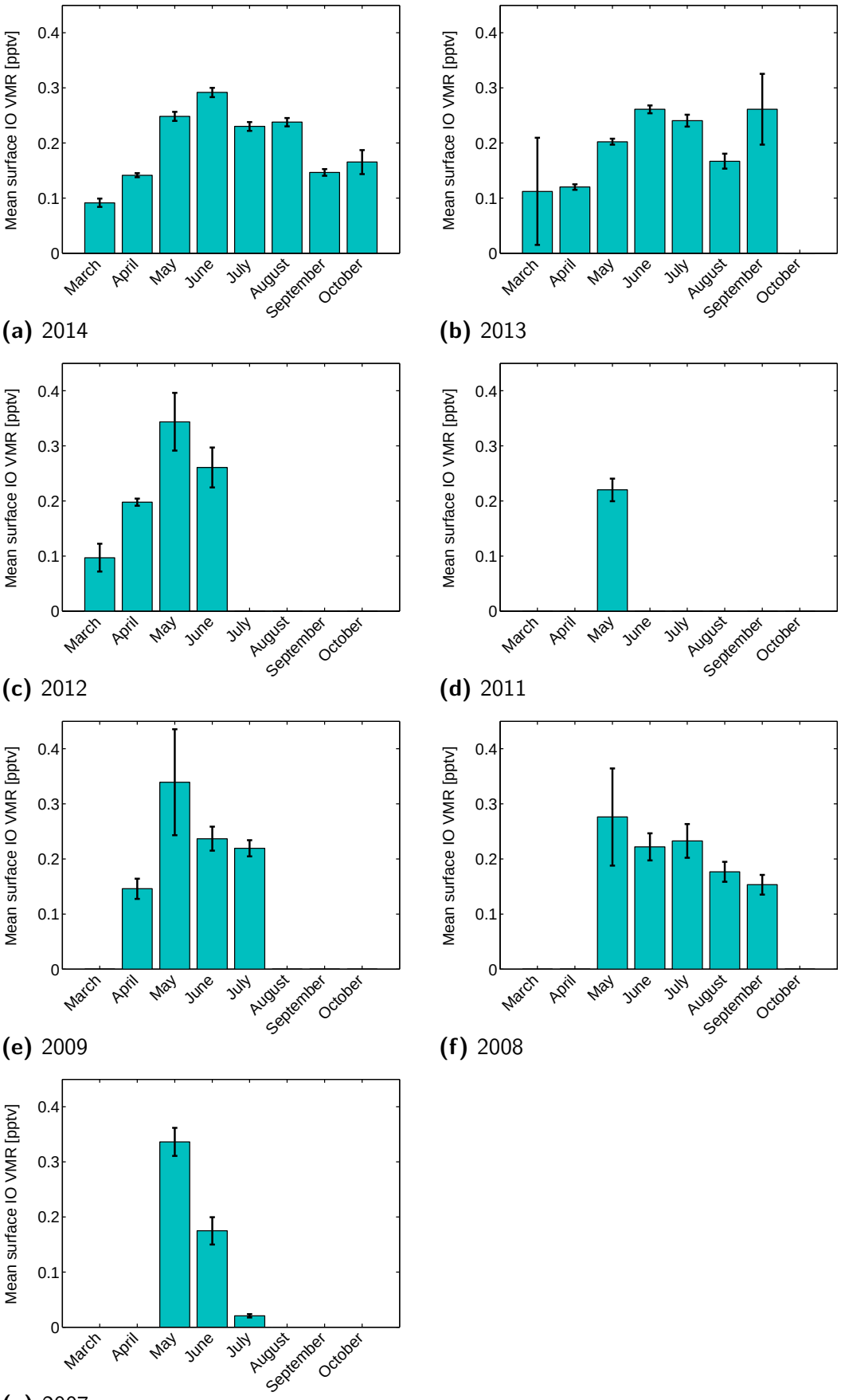

(a) 2014 **(b)** 2013

(c) 2012 **(d)** 2011

(e) 2009 **(f)** 2008

(g) 2007

Figure 7.17.: Monthly means of the IO surface mixing ratios in Alert for the years 2007 - 2014. Error bars indicate the standard errors of the means. Only the years 2013 and 2014 have a largely complete time series.

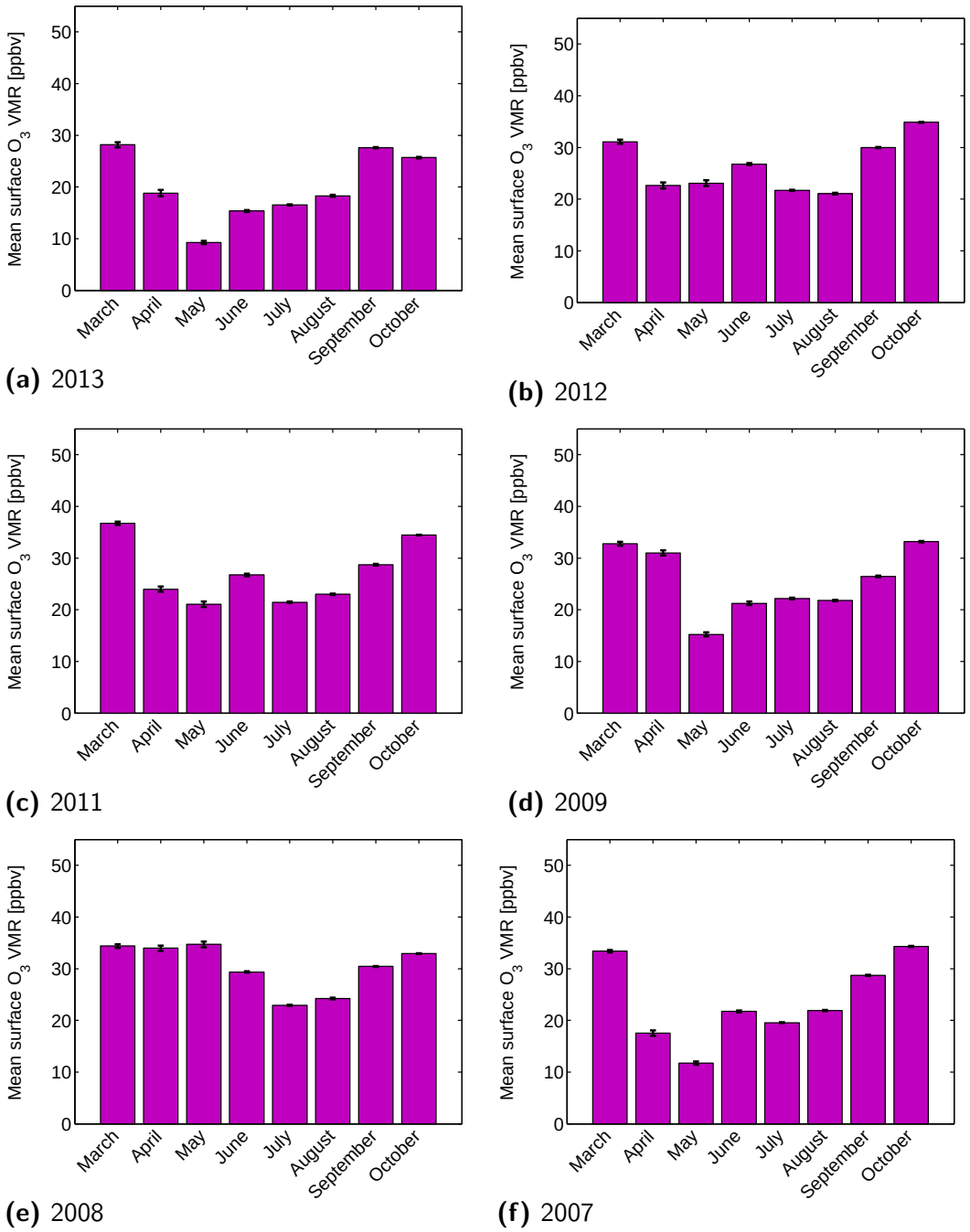

Figure 7.18.: Monthly means of the ozone surface mixing ratios in Alert for the years 2007 - 2014. Error bars indicate the standard errors of the means.

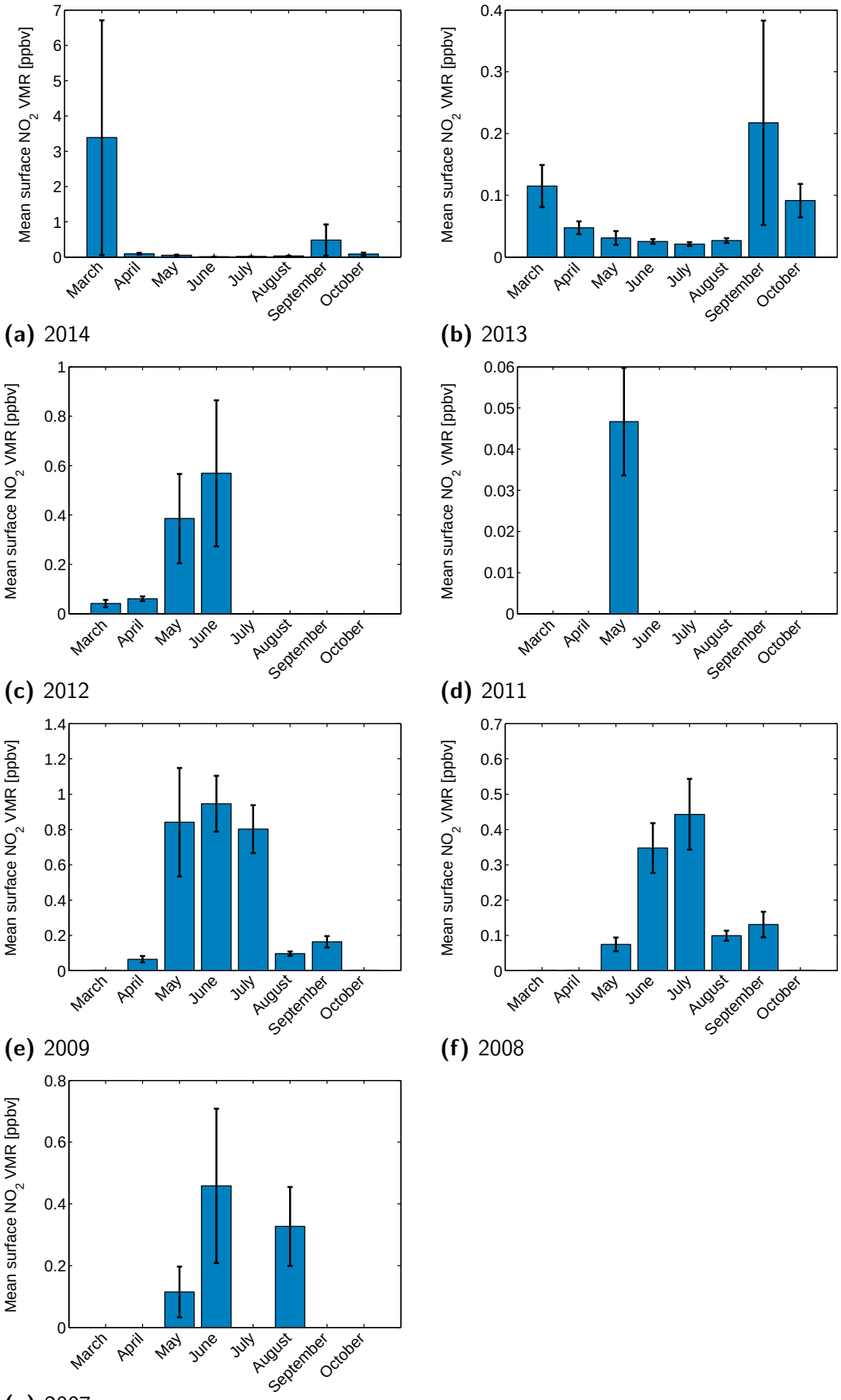

Figure 7.19.: Monthly means of the NO_2 surface mixing ratios in Alert for the years 2007 - 2014. Error bars indicate the standard errors of the means. Only the years 2013 and 2014 have a largely complete time series.

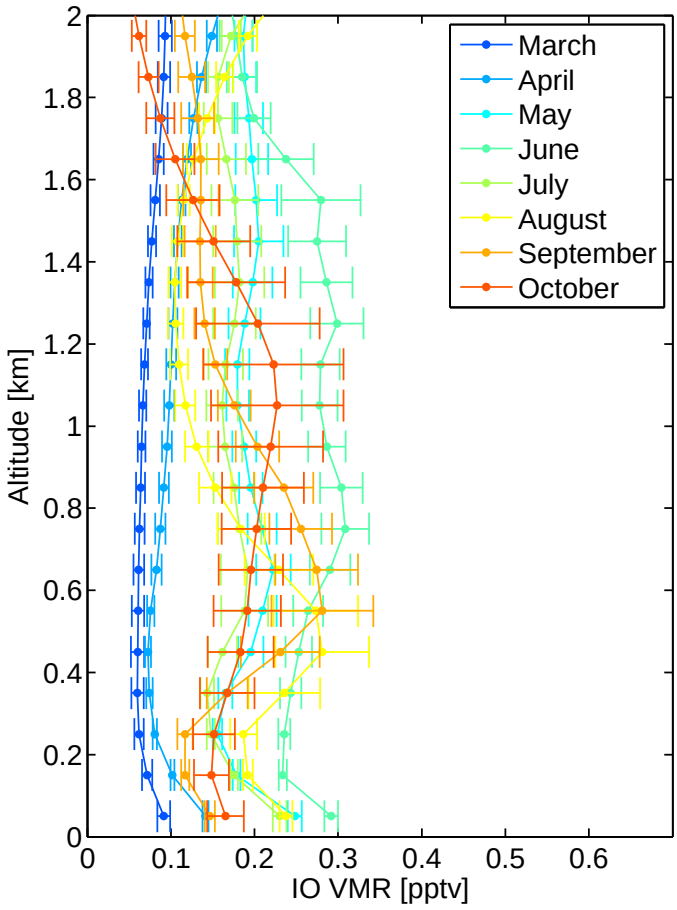

(a)

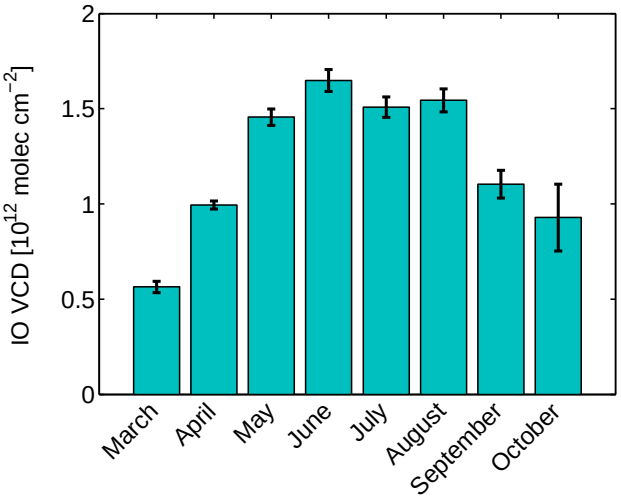

(b)

Figure 7.20.: **(a)** Monthly-averaged vertical profiles of IO for 2014, showing a largely homogeneous distribution of IO in the lowermost 2 km of the atmosphere, to which the instrument is sensitive. **(b)** The monthly mean Vertical Column Densities (VCDs) of IO for 2014. The error bars in both graphs indicate the standard errors of the means.

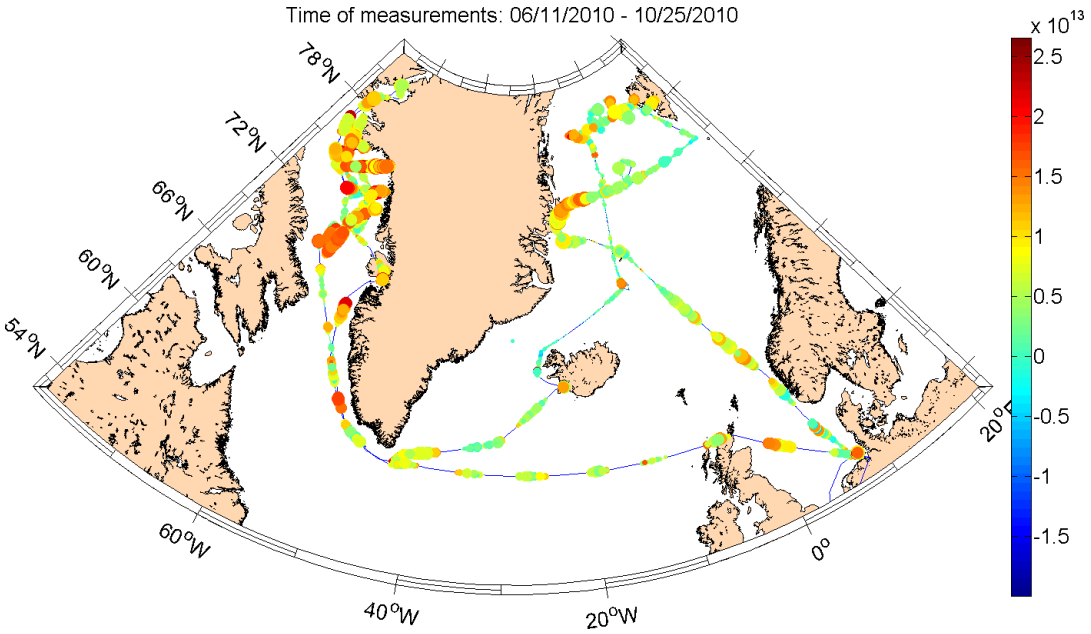

Figure 7.21.: Iodine monoxide MAX-DOAS SCDs of the 3 ° elevation angle, measured during R/V Polarstern cruise ARK-XXV. The color indicates the IO column density, whereas the size of the dots corresponds to the O_4 column density as a proxy for visibility conditions. Enhanced SCDs can be seen in Baffin Bay, but also east of Greenland and at its southern tip. Image provided by Johannes Lampel (personal communication, 2014).

could be due to a lower boundary layer height in autumn, pressing the vertical column into a shallower layer and therefore resulting in higher mixing ratios. However errors are also large for the values of October, therefore this difference is not significant.

7.4 Comparative measurements

The absorption of iodine monoxide in the Alert spectra is clearly visible and some retrieved values are more than 10 sigma above the detection limit. It was also shown that the presence of IO is observable during several years. Nonetheless, this could be due to some persistent local cause only affecting Alert. Therefore additional studies are presented here, in order to back up this finding, and to infer more about the regional distribution of IO and to show that this is not a local effect.

7.4.1 R/V Polarstern expedition ARK-XXV

In 2010, from June to October, the research vessel R/V Polarstern was on expedition ARK-XXV in the Greenland Sea and in Baffin Bay. The ship features a permanently installed MAX-DOAS instrument, which is described briefly in

section 8.2.1, and in detail in Lampel (2010, 2014). The map, showing the fully evaluated data (IO SCDs) from this cruise was provided by Johannes Lampel (personal communication, 2014). The settings of the measurement and DOAS evaluation were comparable with the ones described in section 7.1.2 for Alert, and are also described in Lampel (2014).

The IO SCDs of the 3 ° elevation angle are shown as color-coded points on a map depicting Greenland and the surrounding seas in figure 7.21. The size of the dots corresponds to the O_4 column density as a proxy for visibility. Elevated levels of IO with up to $2 \cdot 10^{13}$ molec cm^{-2} can be seen in most parts of Baffin Bay, but also east of Greenland in the Greenland Sea and Fram Straight, and almost as far south as the southern tip of Greenland. It also appears that the higher IO column densities usually correspond to conditions with better visibility. The column densities of IO are significant (above the detection limit) and comparable in absolute value to the ones seen in Alert. This independently confirms the presence of IO in the Arctic.

7.4.2 GOME-2 case study

A further study was conducted in collaboration with Holger Sihler (Max-Planck-Institute for Chemistry, Mainz, Germany) to assess the possibility of detecting and retrieving IO column densities in the Arctic from satellite instruments.

One of the reasons why the study of IO in the Arctic had been neglected so far, was amongst others, that previously published satellite data did not indicate the presence of IO in high northern latitudes, compared to the Antarctic with higher column densities (Schönhardt et al., 2008, 2012).

As iodine monoxide was now known to be clearly present in significant quantities from ground-based measurements, and also over a wider region, it should therefore also be detectable in satellite data, at least after adequate spectral averaging.

Methodology

For this first case study the GOME-2a instrument aboard the MetOp-A satellite was chosen due to existing infrastructure and supposedly spectral stability, necessary for averaging spectra to increase the signal-to-noise ratio. Spectra were averaged both temporally and spatially in order to get a sufficient signal-to-noise ratio.

For spatial averaging, two geographical sectors were defined, one measurement sector and one reference sector, and all spectra which were recorded within the chosen sectors during a specified time period were co-added. The approach to utilize a reference sector, as opposed to the also available direct sunlight spectra, was chosen to correct for influences of the stratosphere, changes in solar azimuth angle and other effects such as differences in albedo. The location of the sectors is shown in figure 7.22, with the measurement sector being located over Baffin

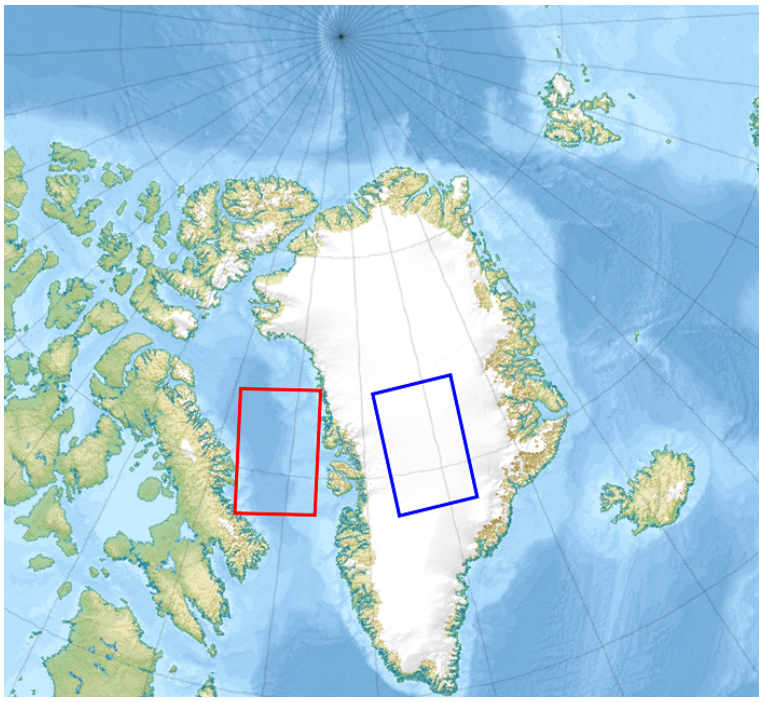

Figure 7.22.: Map showing the location of the measurement sector (red square) and reference sector (blue square), which were used for spatial averaging of the GOME-2a data. All spectra that were located within the respective sector were co-added for the DOAS analysis.

Bay and the reference sector over the Greenland ice sheet. Both sectors have the same geographical latitude, similar albedo and it appeared unlikely that they have the same column density of IO, especially due to the high altitude of central Greenland (Holger Sihler, personal communication, 2014).

To assess the possibility of temporal averaging, several different time intervals were defined. These were each orbit separately, a duration of one day, three days, eight days and an entire month. The whole analysis was conducted for data from May 2008, as IO could be seen in Alert peaking in May usually, and the measurement quality of the satellite was better in 2008 than in other years (Holger Sihler, personal communication, 2014).

The DOAS analysis was conducted similarly as for the Alert data, as described in section 7.1.2. In contrast to the Alert evaluation, only two absorption bands of IO were included in the fit range from 414.8 nm to 430.1 nm, due to the strong influence of vibrational Raman scattering and the strong NO_2 absorption at higher wavelengths.

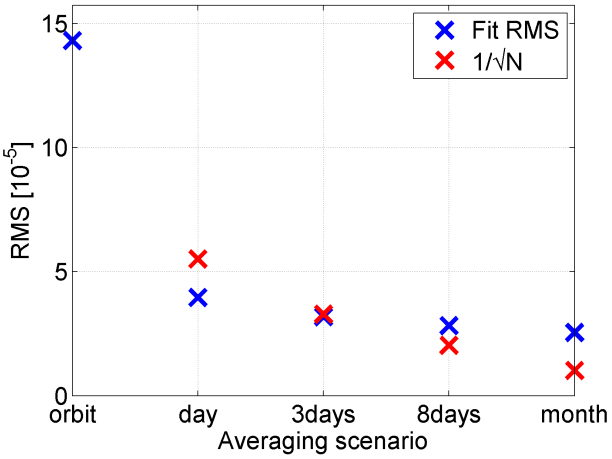

Figure 7.23.: GOME-2a: The DOAS fit residual RMS as a function of the averaging scenario for GOME-2a spectra from May 2008. Also shown is the theoretically expected curve, proportional to $1/\sqrt{\mathrm{N}}$, with N being the number of averaged spectra.

Results

In figure 7.23 the dependence of the average DOAS fit RMS is shown for the different averaging scenarios. Also shown are calculated values for the theoretical RMS from the RMS of the average single orbit and assuming all co-added spectra contribute the same amount of signal, and that the RMS is therefore proportional to $1/\sqrt{N}$. It can be seen, that the fit RMS is decreasing with the number of co-added spectra and roughly in line with the theoretical expectation. Averaging 8 days of data yields a resulting residual RMS of around $2.5 \cdot 10^{-5}$, resulting in an IO detection limit of around $1 \cdot 10^{12}$ molec cm^{-2}. The values, which are expected, from the results of the ground-based MAX-DOAS observations on the other hand, are a factor of 2-5 higher.

A successful DOAS fit of the second 8 day period (9th to 16th) of May 2008 is shown in figure 7.24. The absorption of iodine monoxide is visible and the derived column density, $(5.12 \pm 1.30) \cdot 10^{12}$ molec cm^{-2}, is almost above the $4\,\sigma$-confidence level of detection.

Conclusions of the case study

This case study has shown that, in principle, the data from the GOME-2a instrument can be used to derive iodine monoxide column densities in the Arctic, given sufficient spatial and temporal averaging of spectra. Iodine monoxide has been detected in data from May 2008, a time of the year, when it is also present in Alert. The retrieved VCDs (fig. 7.20b) in Alert are on the order of $1.5 \cdot 10^{12}$ molec cm^{-2}. For the satellite, assuming an average SZA of 70 °, this would correspond to a geometrical AMF of around 4, and therefore an expected column of around $6.0 \cdot 10^{12}$ molec cm^{-2}, which compares very well with

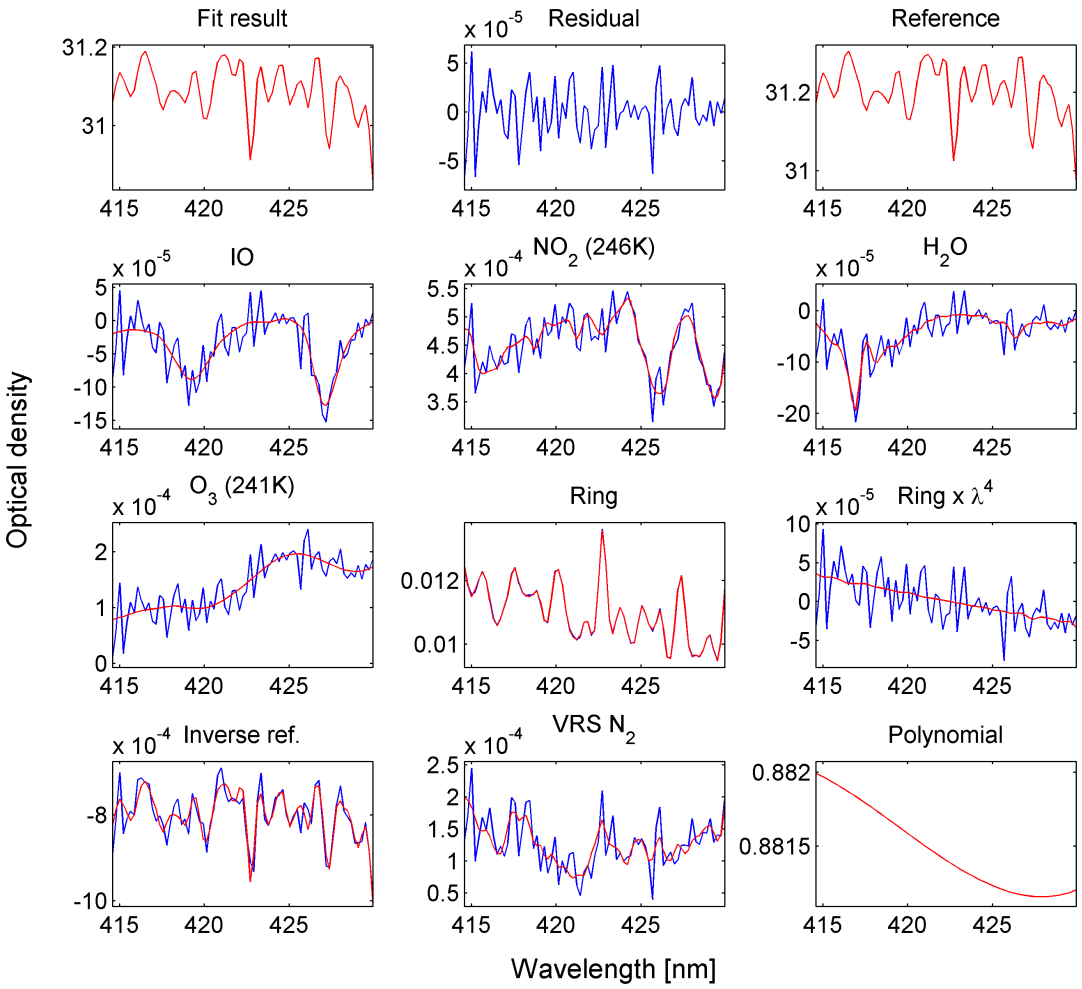

Figure 7.24.: GOME-2a: DOAS fit result of the spectrum averaged over all orbits over the measurement sector during the second 8 day period (9th to 16th) in May 2008, with a fit RMS of $2.6 \cdot 10^{-5}$. The retrieved column densities are: IO $(5.12 \pm 1.30) \cdot 10^{12}$ molec cm^{-2}, NO_2 $(-8.7 \pm 1.8) \cdot 10^{14}$ molec cm^{-2}, H_2O $(4.8 \pm 1.8) \cdot 10^{22}$ molec cm^{-2}, O_3 $(-2.7 \pm 2.6) \cdot 10^{18}$ molec cm^{-2}.

the column actually derived here, of $(5.12 \pm 1.30) \cdot 10^{12}$ molec cm^{-2}. This match suggests, that the IO is also located in layers close to the ground, where both instruments are sensitive, i.e. mostly below 2 km. Furthermore, this supports the hypothesis that iodine monoxide is indeed wide spread in the Arctic, and that existing data could be used for further studies of its distribution.

In order to extend this first case study towards a full map of IO in the Arctic, or possibly the entire globe, a multitude of other tests and algorithm development has to take place, which is outside the scope of this work. Points that would need to be addressed are e.g. the choice of suitable reference sectors, as well as the size of those sectors, the dependence on solar zenith angle differences between measurement and reference sectors, and also the spectral influence of vibrational Raman scattering on air molecules.

7.5 Concluding remarks

Iodine monoxide has been observed and quantified in the boundary layer of the high Arctic for the first time for a period spanning several years. The temporal as well as the spatial extent of the presence of IO is significantly larger than previously assumed (Mahajan et al., 2010; Saiz-Lopez et al., 2012). As mentioned above, the mean IO VCD derived from our measurements is of the order of $1.5 \cdot 10^{12}$ molec cm^{-2}. In comparison, Schönhardt et al. (2008, 2012) give a detection limit around $1.7 \cdot 10^{12}$ molec cm^{-2} for their IO VCD evaluations of global satellite data for single measurements. Therefore, it is not surprising that the amounts of IO observed here have not been seen before from space. During summer, the low albedo of the dark Arctic Ocean may have been a further hindrance compared to the snow surface of Antarctica. In Alert at least, IO appears to persist throughout most of the polar day with average mixing ratios of around 0.2 pptv. The measurements from R/V Polarstern further show a spatial extent of at least a regional level in the Arctic around Greenland in Baffin Bay and the Fram Strait. The amounts of IO observed in this study are also not in disagreement with any previously published upper limits. The observed annual cycle of BrO mixing ratios is as expected, with a maximum in spring and low values for the remainder of the year.

8

Field studies during R/V Polarstern expedition ANT-XXIX/7 in the Weddell Sea

In addition to the measurements at Scott Base (chapter 6), further field studies were undertaken in the Weddell Sea during austral spring 2013. They were conducted aboard the German research ice breaker R/V Polarstern, which is normally operating in the Arctic at this time of the year. In 2013 however, it spent the austral winter and spring in the Weddell Sea (expedition ANT-XXIX) for studies of a wide range of ecosystem processes in this part of the Southern Ocean. This presented a fortunate opportunity to study the springtime halogen chemistry in this region, otherwise unaccessible during this time.

The 7th leg of the expedition ANT-XXIX, named *Winter Sea Ice Study on Key Species* (WISKY), from Punta Arenas in Chile to Cape Town in South Africa, lasted two months, from the 14th August to the 16th October. The cruise track is mapped in figure 8.1. One of the main goals of the campaign was the study of krill, and the connected food webs, during winter. Other research was done on sea ice properties, chemistry in the water column and atmospheric observations. The latter consisted of mercury speciation measurements in the air, but also in snow and sea water, in addition to the halogen oxide studies presented in this work and in Nasse (2014) and further ozone measurements. Originally, the plan was to undertake three transects of the sea ice edge, each time entering the *Marginal Ice Zone* (MIZ), followed by a ten day long *ice station* and then heading back to the open ocean. During those ice stations a makeshift field camp was to be erected. Those were therefore also deemed suitable for LP-DOAS and CE-DOAS measurements in addition to continuous MAX-DOAS

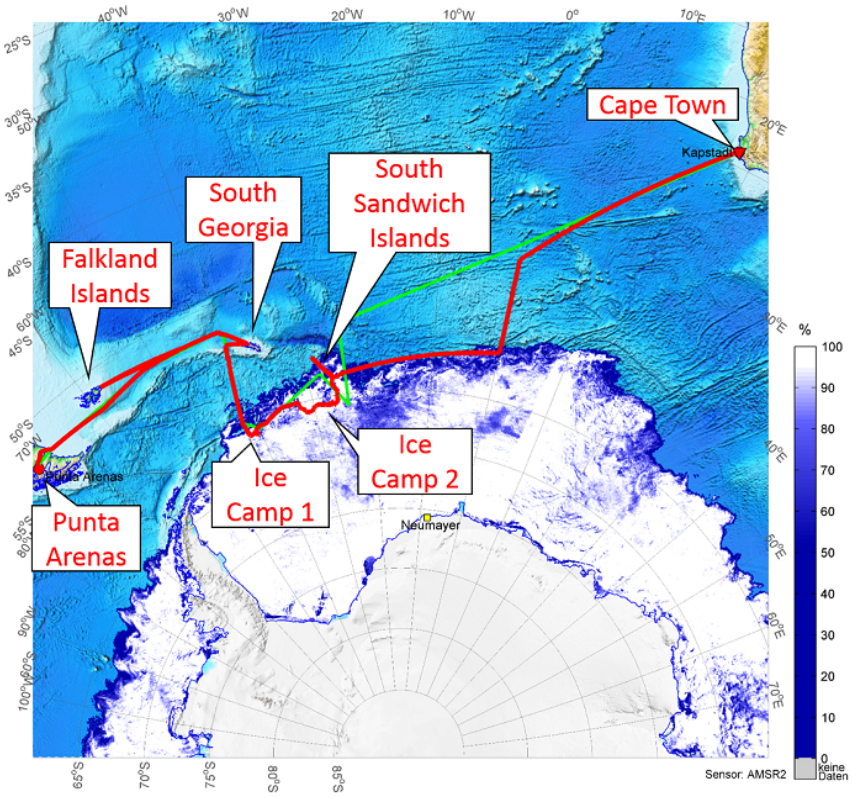

Figure 8.1.: The planned (in green) and the actual (in red) cruise track of leg 7 (14.08.2013 to 16.10.2013) of R/V Polarstern expedition ANT-XXIX from Punta Arenas (Chile) to Cape Town (South Africa). The sea ice concentration is also indicated. The map was provided by the Alfred Wegener Institute (AWI).

observations and airborne MAX-DOAS studies. In the end, only two shorter ice stations were done. Additional details of the expedition can be found in the cruise report, edited by Meyer and Auerswald (2014).

8.1 Environmental conditions during the cruise

The cruise took place during austral spring in the Southern Ocean. During this time, the weather in this region is characterized by low pressure systems circling around the Antarctic continent in a clockwise manner over the sea ice zone, and high pressure systems on the continent itself. The transport of air masses to the ship's location therefore was determined by the position of the nearest lows (see fig. 8.2). Due to the clockwise atmospheric circulation around southern hemispheric lows, those west of the ship led to northerly winds and warmer air, while those east of it led to colder, polar air. The presence of the lows also led to cloudy conditions for most of the cruise with only a handful days with blue sky conditions.

The sea ice concentration during the cruise is indicated in fig. 8.1. The ice

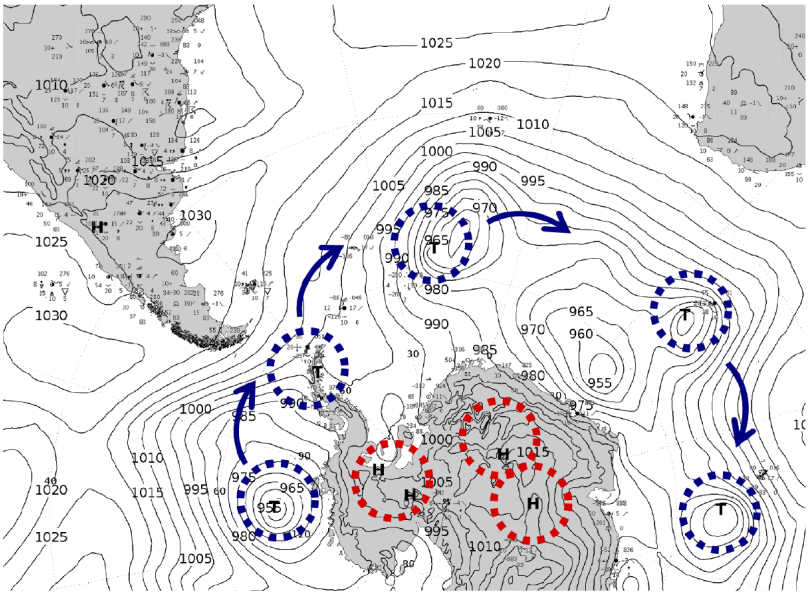

Figure 8.2.: Model data from ECMWF for the 16th September 2013, showing the pressure highs and lows in the region of the cruise. Typically, six or seven lows circle the Antarctic continent in the sea ice zone in a clockwise manner. Adapted from Nasse (2014, and references therein).

conditions were inhomogeneous, ranging from patchy nilas and pancake ice, along the edge of the MIZ, to more consolidated extents of thicker first-year ice at the two ice camp locations. Exemplary images are shown in fig. 8.3.

8.2 Measurements during the cruise

As mentioned, a suite of measurements was undertaken during the winter fiel study. Measurements conducted by the Heidelberg group were continuous MAX-DOAS and surface ozone measurements. Furthermore, airborne MAX-DOAS measurements were undertaken using the ship's two helicopters, which are described in Nasse (2014). During the two ice camps, LP-DOAS and CE-DOAS measurements were conducted.

Most of the instruments utilized during this field study have already been described above, or elsewhere previously, in which case only a brief description is given here. The CE-DOAS, LP-DOAS and mobile MAX-DOAS instruments were the ones that were used before during the Scott Base field study described in chapters 4 and 6. The evaluation of the data was also conducted in the same manner, therefore is not explained again here (see section 6.2.1 for the LP-DOAS and section 6.2.2 for the CE-DOAS evaluation).

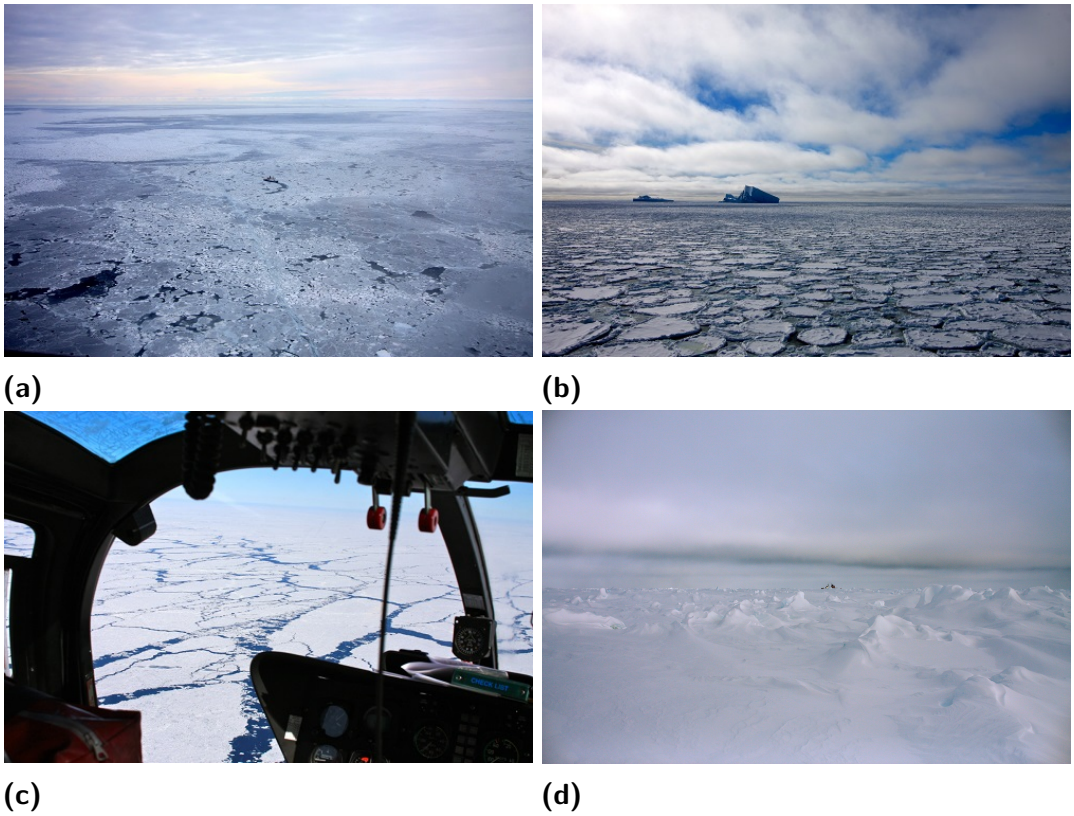

Figure 8.3.: The different sea ice conditions which were encountered during the cruise in the Marginal Ice Zone (MIZ) ranged from **(a)** nilas and **(b)** pancake ice to **(c)** thin, broken up platelet ice and **(d)** more consolidated ice floes.

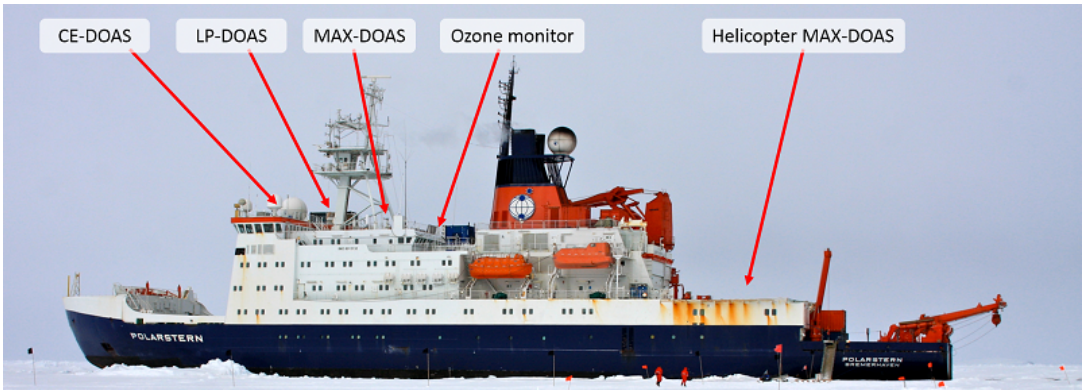

Figure 8.4.: R/V Polarstern as seen from portside during the second ice station. The location of the utilized instruments on the campaign is indicated. The CE-DOAS was placed on the signal's deck, where also the telescope of the LP-DOAS was erected. The scanner of the MAX-DOAS is portside on the deck behind the bridge, the inlet for the ozone monitor was also on that deck starbord. Furthermore the helicopter deck is indicated.

(a) **(b)**

Figure 8.5.: **(a)** The scanner (circled in red) of the permanently installed MAX-DOAS on Polarstern is looking towards port and located on the deck behind the bridge **(b)** The unit in the laboratory below housing the spectrometers, electronics and computer. Picture adapted from Lampel (2010).

8.2.1 Ship MAX-DOAS setup

The permanently installed MAX-DOAS instrument has been operating in its current configuration since 2009 and is described and characterized in detail in Lampel (2010, 2014). The scanner is conceptually similar to the one in Alert and has a vertical field-of-view of 0.7 °. It is located portside behind the bridge and also looking straight towards port (see figs. 8.4, 8.5). The set elevation angle sequence is 1 °, 3 °, 5 °, 10 °, 20 °, 40 ° and 90 ° and those angles are corrected for the roll movement of the ship using a capacitive tilt meter. Two temperature-stabilized spectrometers cover the wavelength ranges of 277 nm - 415 nm (UV) and 390 nm - 633 nm (VIS) with FWHM spectral resolutions of 0.67 nm (UV) and 0.90 nm (VIS). Together with the controlling computer they are located inside the observation deck. For each elevation angle, spectra are collected for 2 minutes.

8.2.2 LP-DOAS setup

The Long-Path DOAS measurements were intended to be carried out during the two ice camps, as it was deemed possible to bring out the retro reflector array onto the ice then. The telescope was erected on the signal's deck inside a tent to shield it from the wind, while the spectrometer and controller electronics were located in the radar and antenna room behind the bridge. The retro reflector array was constructed from wood and made to be foldable, to be able to transport it by helicopter out onto the ice floes, where it was anchored into the ice using four ice screws. The whole setup is pictured in figure 8.6.

(a)

(b)

(c)

Figure 8.6.: The Long Path-DOAS setup aboard R/V Polarstern: **(a)** The spectrometer, xenon arc lamp and computer were located in the antenna room behind the bridge. **(b)** The retro reflector array on the sea ice. **(c)** The telescope was erected on the signals deck, next to the main mast and below the crow's nest.

Species	Fit range [nm]	Accounted absorbers
BrO	331.90 - 357.45	BrO, O_3, NO_2, HCHO, O_4
IO	413.50 - 440.50	IO, NO_2, H_2O, O_3, VRS N_2, VRS O_2
O_4	365.75 - 398.00	O_4, NO_2, O_3, HCHO

Table 8.1.: MAX-DOAS evaluation: Fit intervals and absorbers included in the fitting procedure. All fit scenarios contained a Ring spectrum, a Ring spectrum multiplied with λ^4, and an inverse spectrum to correct for spectrometer stray light as well as specific corrections for electronic problems of the read-out electronics. The used DOAS polynomial was always of 4th order.

8.2.3 Surface ozone measurement

The measurements of surface ozone mixing ratios were done using a commercial ozone monitor (Horiba APOA-350E) equipped with a custom-made Arduino-based data logger. The sample line inlet was located starboard stern on the signal's deck (see fig. 8.4) and inside an upside-down funnel to avoid snow or rain entering the sampling line. This inlet was checked at least once every day to ensure it did not clog up with snow or ice.

8.3 Spectral evaluation and inversion of SCDs

As mentioned above, the CE-DOAS evaluation was done as for the measurements at Scott Base, described in section 6.2.2. For the LP-DOAS the data evaluation was done as described in section 6.2.1 with one modification. Due to problems with the light path alignment on the moving ship, spectra were not averaged, as they usually went from being severely over-saturated to underexposed within a couple of minutes.

8.3.1 MAX-DOAS evaluation

The evaluation of the spectra from the permanent MAX-DOAS was done as for the evaluation in Alert (see 7.1.2). Spectra were averaged over 8 sequences as long as the beginning and the end were less than 2 hours apart from each other. Three fits, for BrO, IO and O_4, were applied to the spectra. The wavelength ranges and all included absorbers are detailed in table 8.1. The measurement sequences were always evaluated relative to the current zenith (90 °) spectrum.

Inversion of trace gas SCDs

The determined O_4, BrO and IO SCDs were used to compute vertical mixing ratio profiles as detailed in section 3.4.5. The settings for the aerosol inversion were chosen as already described in section 5.1.2, with the exception of a lower a priori profile error of 300% and the pressure and temperature profiles were taken for 65 ° S. The current instrumental azimuth angle was calculated from the current heading of the ship which was provided by the ship's navigation system. The settings for the trace gas inversions were also chosen as the ones detailed in section 5.2.2. One difference for the BrO inversion is the a priori profile error set to 300%. For IO, the settings were taken as for the instrument in Alert (refer to section 7.1.3).

8.4 Results

In the following, the results of the observations made with the different instruments are presented, starting with the BrO, IO and ozone mixing ratios (sec. 8.4.1), followed by the CE-DOAS (sec. 8.4.2) and LP-DOAS (sec. 8.4.3) studies during the ice stations.

8.4.1 Continuous MAX-DOAS measurements and ozone

The surface mixing ratios of BrO and IO which are derived from the inversion are shown together with the surface ozone mixing ratios in figure 8.7. Three time periods with strong ozone depletions can be distinguished. The first was from the 28th August to the 5th September. The second one starts on the 9th September to the 19th September, and the last one was from the 24th September to the 2nd October. During each of those three ODE periods, the mixing ratios of BrO are enhanced with values over 40 pptv and reaching a maximum of (50.2 ± 3.0) pptv on the 29th August. The IO mixing ratios during the whole cruise were between 0.0 pptv and 0.7 pptv with the exception of two days, the 28th August and the 22nd September, when they increased to around 1.2 pptv.

8.4.2 CE-DOAS measurements

The CE-DOAS instrument was operated twice. Due to the high wind speeds and frequent snowfall as well as blowing snow, the instrument did not achieve the detection limits, which it reached at Scott Base (section 6.3.2). Another issue was that the snow contaminated the mirrors of the instrument almost immediately after the removal of the purge tube, making open-path CE-DOAS measurements almost impossible.

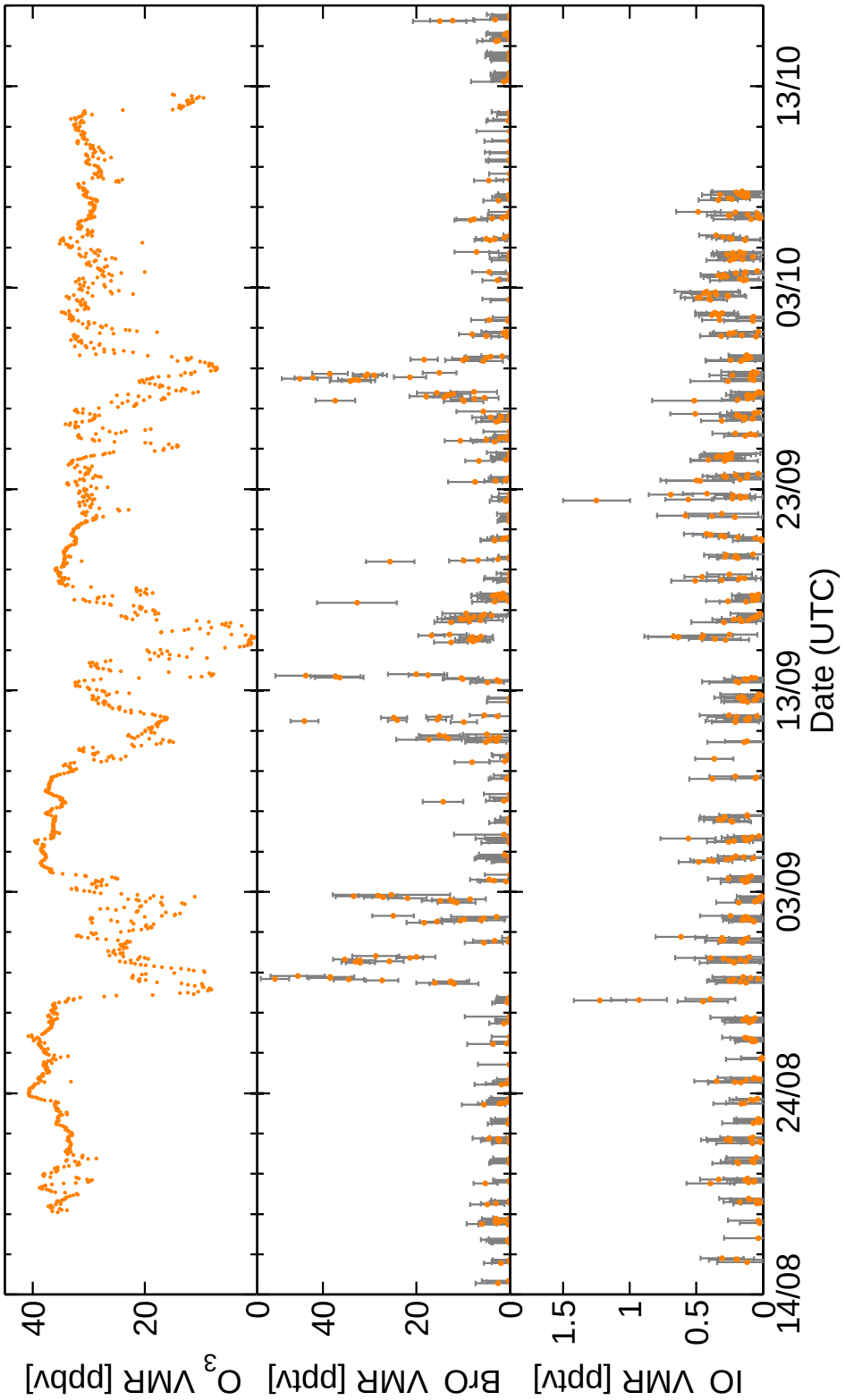

Figure 8.7.: Time series of mixing ratios of O_3, BrO and IO during ANT-XXIX/7. The BrO and IO mixing ratios were determined through inverse methods applied on the MAX-DOAS data and are the results of the lowest box (0 m - 100 m). Three periods with ODEs and enhanced BrO levels can be distinguished.

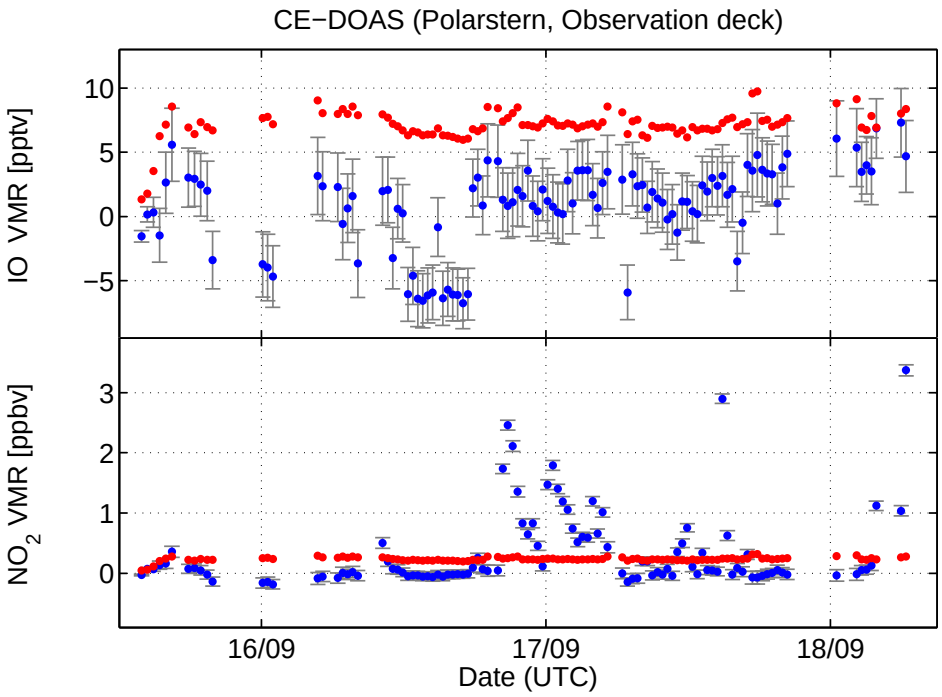

Figure 8.8.: CE-DOAS: Determined mixing ratios of the measurements on top of the observation deck. Measurement data is shown in blue, the calculated detection limits in red. The detection limits deteriorated rapidly after the removal of the purge tube due to strong winds and blowing snow.

Measurements on the observation deck

The first measurement was undertaken on top of the signals deck. The determined mixing ratios of IO and NO_2 are shown in figure 8.8. IO was not detected during this period. As soon as the purge tube was removed, the mirrors got more and more contaminated due to blowing snow and the IO detection limit rapidly deteriorated to 5 pptv and worse, hindering meaning measurements.

Measurements on the sea ice

The second measurement was undertaken during Ice Camp 2 outside the ship on the sea ice in the assigned clean sector (see figure 8.9). The instrument was placed on its stands for most of the time. During the first hour though, it was lying directly on the sea ice surface, where the overlying snow and parts of the slush were removed. to check whether those deeper layers could release iodine. The determined mixing ratios for this time period are given in figure 8.10 and again, IO was not detected.

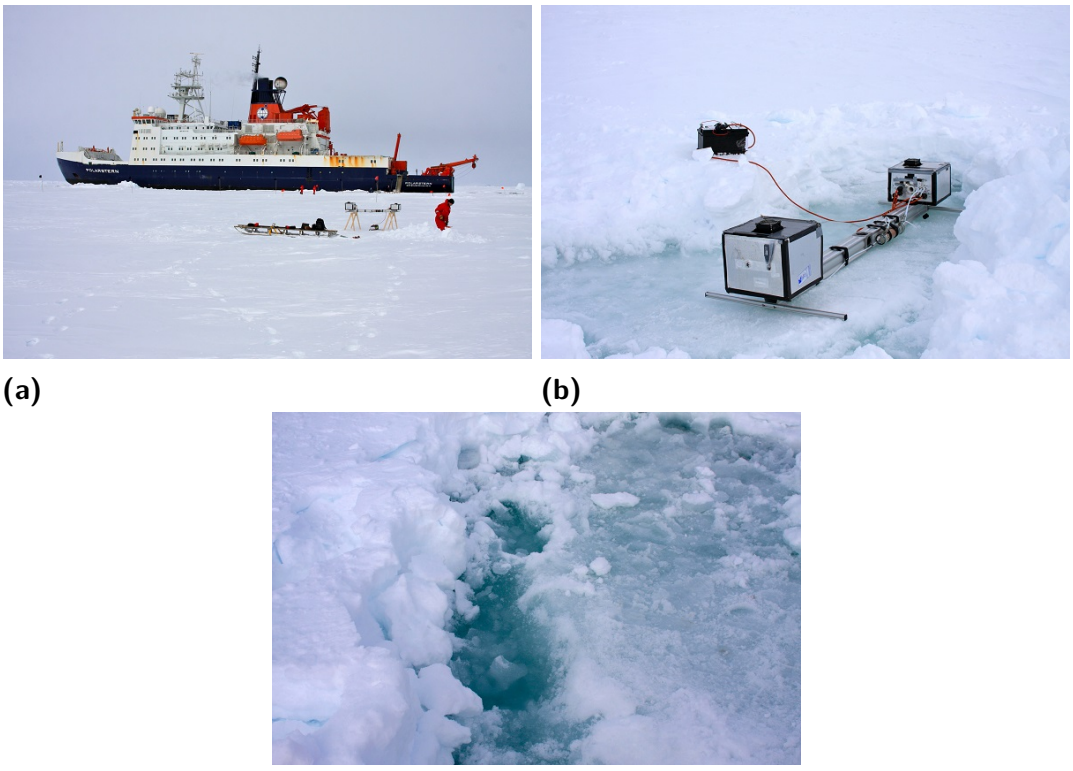

Figure 8.9.: **(a)** The CE-DOAS instrument on the sea ice during Ice Camp 2. **(b)** After removing the surface snow, the instrument was also placed onto the underlying slush layer. **(c)** Close up of the slush layer.

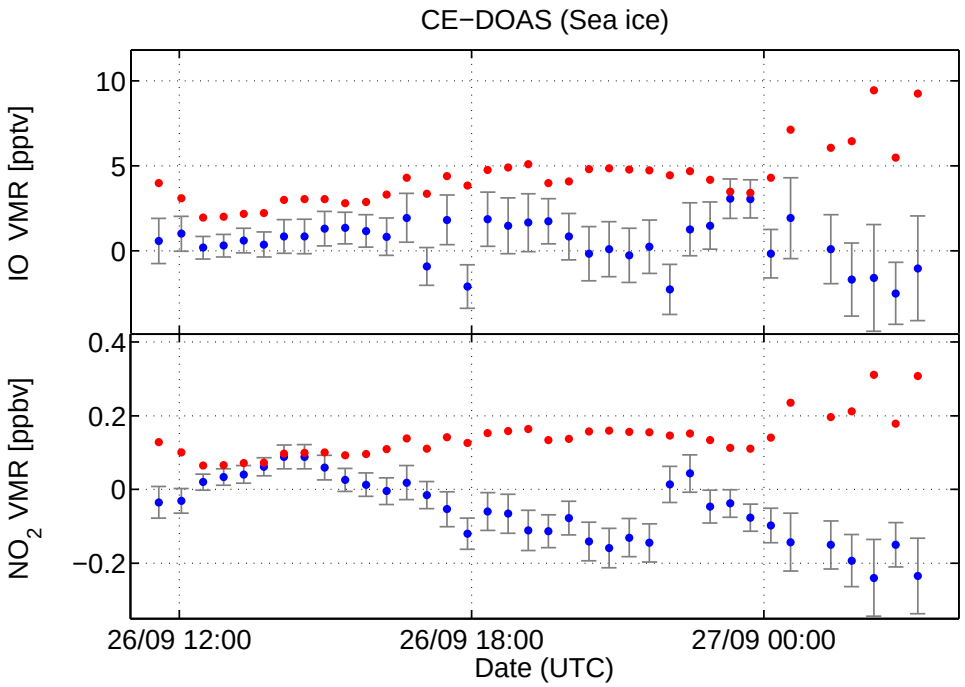

Figure 8.10.: CE-DOAS: Determined mixing ratios of the measurements on the sea ice surface. The measurement data is shown in blue, the calculated detection limits in red. IO was not detected at this location.

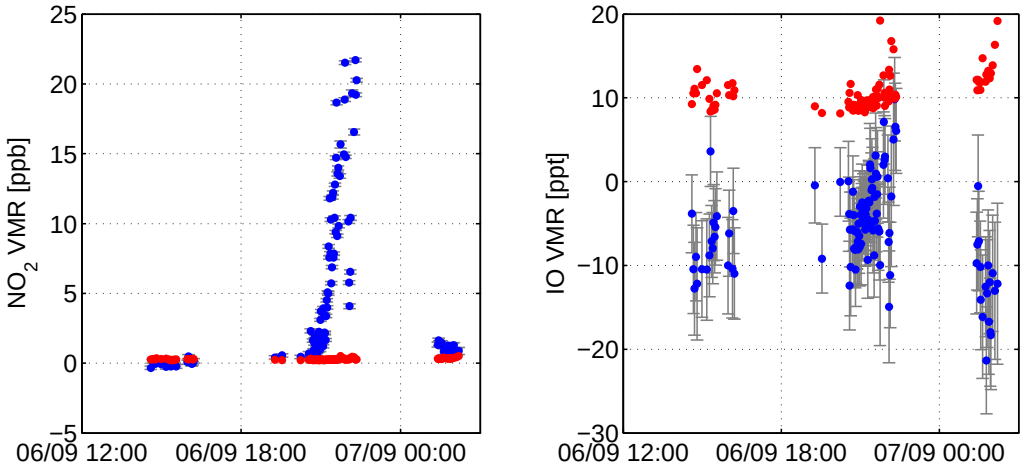

(a) **(b)**

Figure 8.11.: LP-DOAS: Determined mixing ratios of the measurements during Ice Camp 1 from the 6th to the 8th September for **(a)** NO_2 and **(b)** IO. As can be seen in the NO_2 data, the measurements were severely influenced by the ship's exhaust plume on the second day. IO was not detected during Ice Camp 1.

8.4.3 LP-DOAS measurements

Ice Camp 1

At the beginning of the first ice camp, the retro reflector array was brought out onto the ice on the opposite site of the ice floe at a distance of 4.5 km. Due to a mechanical failure of the electric motor controlling the horizontal movement of the telescope, measurements could not be undertaken for several days until the motor could be replaced with a modified similar one. During this time, an iceberg hit the ice floe close to the reflectors position. The reflector therefore had be brought back to the ship before the ice floe would break apart completely and losing the reflector for good. Once the telescope was repaired, the reflector was brought out again by snowmobile, this time close to the ice camp tents at a distance of 500 m as it was unclear how long the ship would stay at this ice floe. Afterwards, the ship was not as stable in the water any more and the light beam, most of the time, was not hitting the reflector. The automatic reflector search routine of the telescope failed, as the changes in position of the ship were too rapid and too large. Therefore the position had to be manually set most of the time. During the night, this was not possible however as the reflector, once lost, could not be seen anymore. as the light source, only a blue LED was used in order to measure IO and due to problems with the location of the xenon arc lamp.

The results of NO_2 and IO of the measurements that were conducted are shown in figure 8.11. As can be clearly seen at the high NO_2 levels, most of the

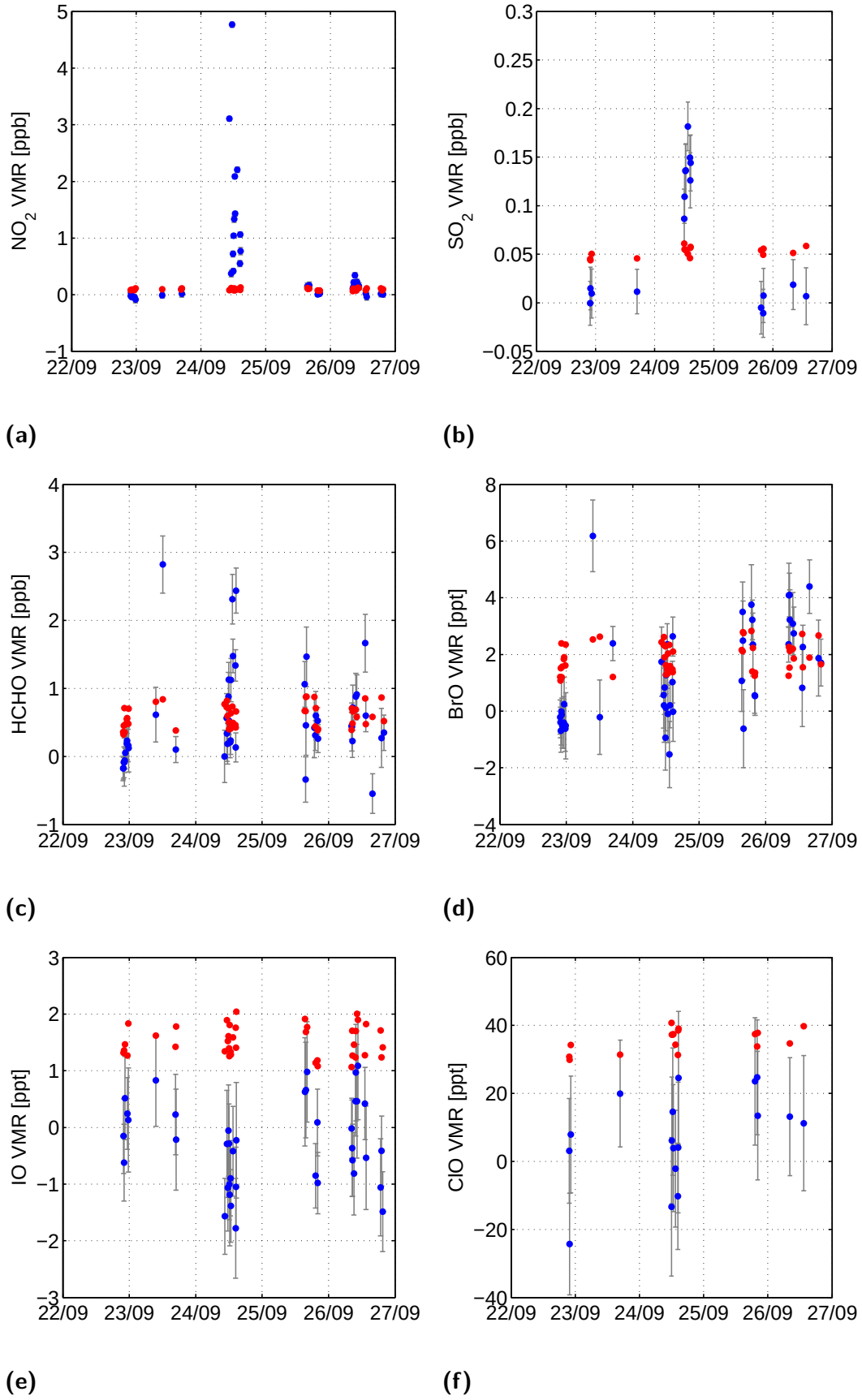

Figure 8.12.: LP-DOAS: Determined mixing ratios of the measurements during Ice Camp 2 from the 23rd to the 27th September for **(a)** NO_2, **(b)** SO_2, **(c)** HCHO, **(d)** BrO, **(e)** IO and **(f)** ClO. As can be seen in the NO_2 and SO_2 data, the measurements were severely influenced by the ship's exhaust plume on the 24th. Of all the halogen compounds, only BrO could be observed above the detection limit.

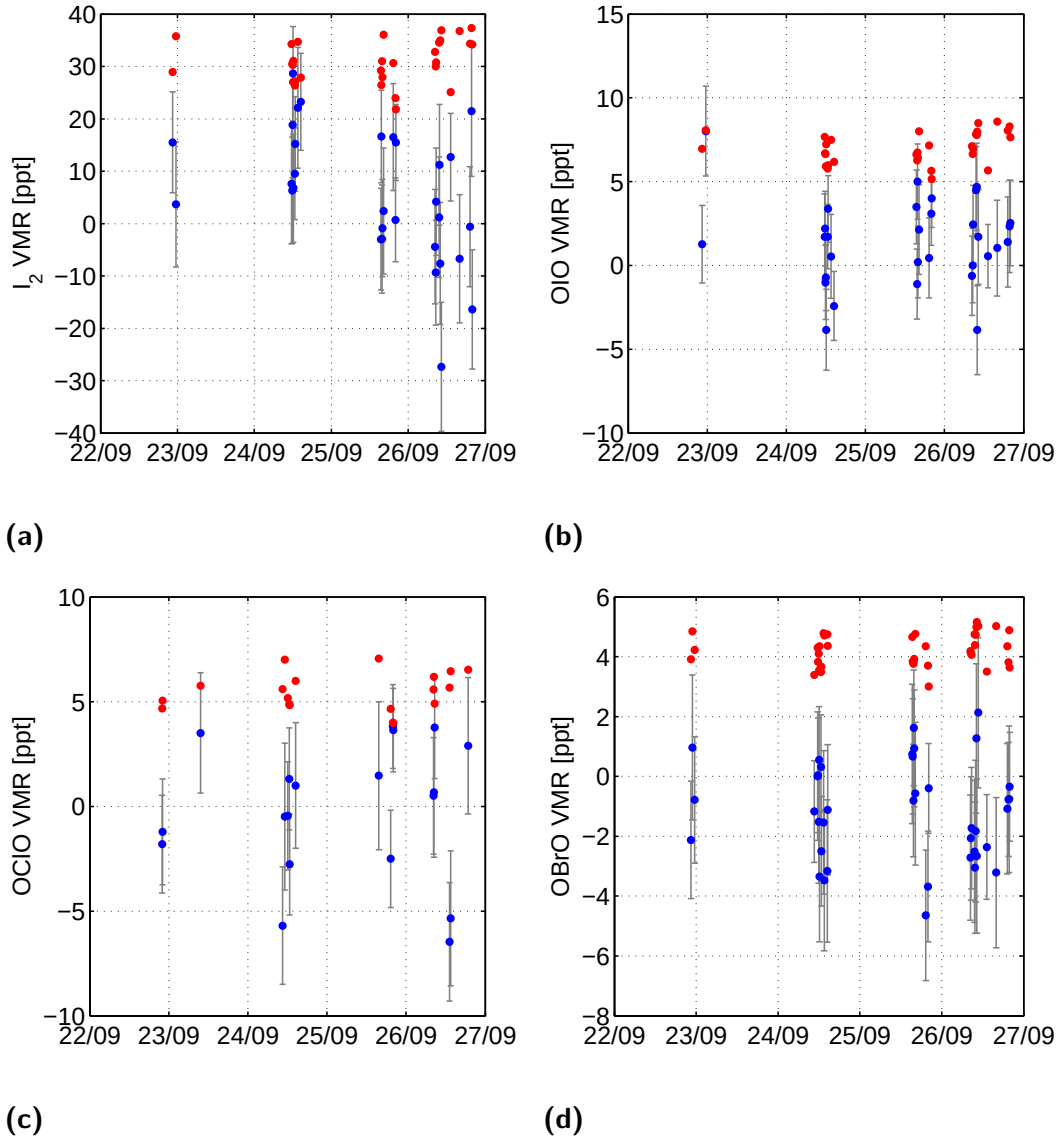

Figure 8.13.: *Continuation of figure 8.12.* LP-DOAS: Determined mixing ratios of the measurements during Ice Camp 2 from the 23rd to the 27th September for **(a)** I_2, **(b)** OIO, **(c)** OClO and **(d)** OBrO. None of them was observed during Ice Camp 2.

data was strongly influenced by the ship's exhaust plume. The IO mixing ratios scatter around zero with an amplitude of 20 pptv and are below the detection limit.

Ice Camp 2

During Ice Camp 2 the reflector was brought out onto the middle of the ice floe at a distance of 1850 m. As light source, a 75 W Osram XBO was used. Unfortunately, the same problem regarding the stability of the ship due to the deployment of fishing nets also occured here. In addition to that, the visibility was periodically severely limited due to fog.

The results from the 23rd September to the 27th September are given in figures 8.12 and 8.13. As can be seen from the mixing ratios of NO_2, SO_2 and HCHO, the sampled air masses were unfortunately heavily influenced by the ship's emissions on the 24th September, the day with the most acquired spectra. During the whole measurement period, only BrO could be positively detected of all of the halogen compounds. The mean detection limits, rather high compared to the measurements at Scott Base due to the short light path, were 1.5 pptv for IO, 35.6 pptv for ClO, 1.9 pptv for BrO, 5.5 pptv for OClO, 7.1 pptv for OIO, 31.1 pptv for I_2 and 4.2 pptv for OBrO. Of all the halogen compounds only BrO was observed above the detection limit in several spectra.

8.5 Analysis

The above described measurements indicate very low IO mixing ratios, highly similar to the observations at Scott Base (chapter 6) and also at Alert (chapter 7). A detailed analysis of the observed halogen chemistry and the amounts of halogen compounds, or the lack thereof, is given in combination with the other field observations in the next chapter (ch. 9) as the results closely resemble each other in terms of chemical behavior and abundances.

8.5.1 Origin of halogen containing air masses

As mentioned in section 8.1, the transport of air masses was determined by the presence and locations of the low pressure systems. In order to analyze what air masses were also containing the observed halogen species, wind rose diagrams, showing the frequency distribution of mixing ratios as a function of the wind direction, are given in figure 8.14. The most common wind directions were south-westerly and also north-westerly. It can be seen that the air masses with the highest BrO mixing ratios mainly have come from the south-westerly quadrant. Air masses from other, northerly and easterly mostly ice free areas show low to insignificant BrO values. As the high BrO values were found mostly in the sea ice zone, this indicates an origin from the sea ice covered Weddell Sea, which was located to the south-west for most of the cruise. This supports the findings that air masses with sea ice contact are likely to contain activated bromine compounds as explained in section 2.5.2. For air masses containing IO in contrast, this can not be stated. The determined IO mixing ratios correlate less

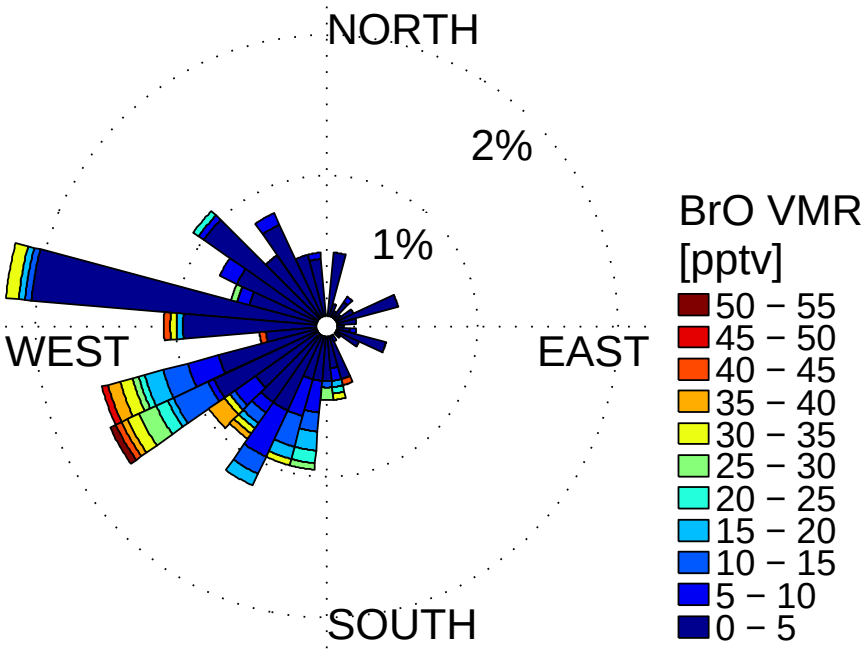

(a)

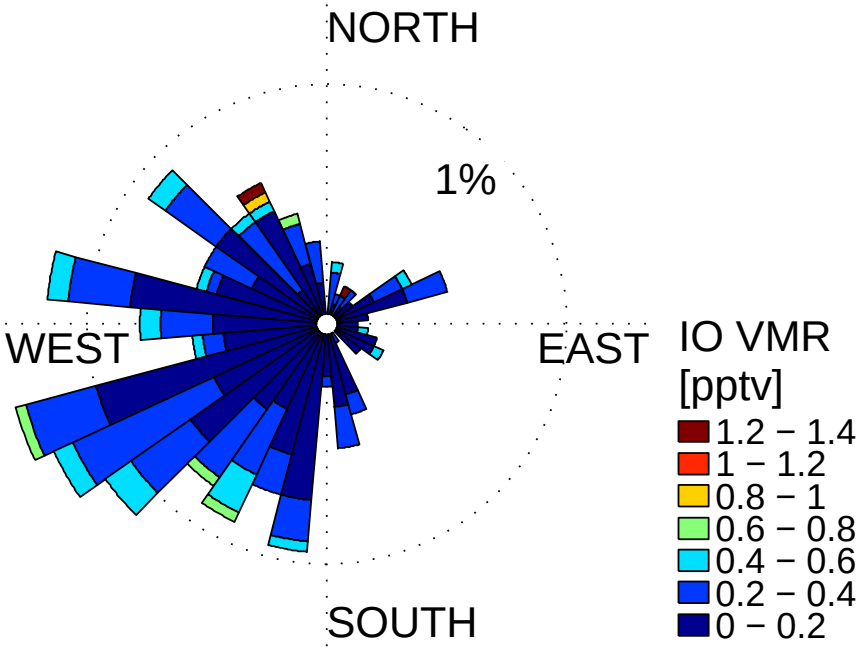

(b)

Figure 8.14.: Wind rose diagrams for the observed mixing ratios of **(a)** BrO and **(b)** IO during the cruise. The main wind directions were from the south-west, for those winds the highest BrO mixing ratios were observed as well. For IO there is no clear correlation with wind direction.

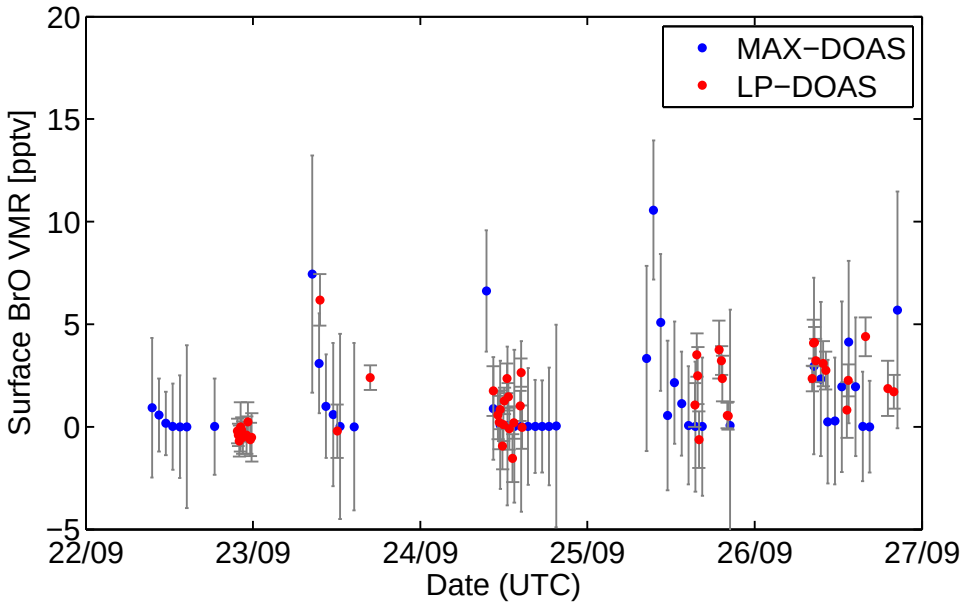

Figure 8.15.: Comparison of BrO mixing ratios from LP-DOAS measurements and the lowest grid box (surface, 0 - 100 m) of the MAX-DOAS vertical profile inversions.

with any specific wind direction and a similar intensity distribution can be seen for most directions except for the anyway rare south-easterly directions. This implies either local sources or sources evenly spread around the measurement location, e.g. the ocean and is discussed below in section 9.6.

8.5.2 Comparison of surface mixing ratios: MAX-DOAS vs. LP-DOAS

A comparison of retrieved mixing ratios from MAX-DOAS and LP-DOAS measurements, similar to the one described in section 6.4.3 for the Scott Base data, was done. Due to the sparsity of the LP-DOAS data, there is only little overlap in time with the MAX-DOAS data. The results of both instruments are given in fig. 8.15. Due to the large errors of both datasets, the mixing ratio, if present simultaneously, generally agree with each other. Only on the 26th September, the LP-DOAS once sees higher BrO levels than the MAX-DOAS device. As already mentioned in section 6.4.3, the instruments sample along light paths with different lengths and therefore see different air masses and this can possibly be explained by spatial inhomogeneities. Overall, a more thorough inter-comparison as done for the Scott Base data was hampered by the challenging conditions, which led to sparse measurements.

8.6 Concluding remarks

The difficult circumstances due to the altered actual cruise track compared to the planned one, as well as the always moving ship and the inclement weather unfortunately hindered longer measurements of the LP-DOAS and CE-DOAS instruments. The detection limits for the measurements which were finally undertaken in the field are also significantly worse, on average between 5 and 10 times, than the observations with the same instruments at Scott Base under more favorable conditions. The data from those two devices therefore only indicates upper limits for the presence of several halogen species in those regions of the Weddell Sea.

Nonetheless, the MAX-DOAS and surface ozone observations provide new insight into the chemical processes in the Weddell Sea during springtime. The observed BrO mixing ratios up to (50.2 ± 3.0) pptv are amongst the highest ones observed until now in the Antarctic. Wagner et al. (2007), also aboard R/V Polarstern, tentatively observed similarly high mixing ratios, depending on the assumptions made for its vertical distribution. Apart thereof, the previously reported maximum is only 13 pptv in the Antarctic (Buys et al., 2013; Simpson et al., 2015). This indicates that the highest BrO mixing ratios in the sea ice zone of the Antarctic are in fact very similar to the highest ones observed in the Arctic around 45 pptv (e.g. chapter 7, Pöhler et al., 2010; Simpson et al., 2015) and that the previously reported difference is likely due to a sampling bias, as the stations on the Antarctic continent where most of the previous observations were done, due to the above mentioned weather patterns, are less exposed to air masses from the sea ice zone, compared to those in the Arctic.

The observed IO mixing ratios are similar to the ones seen at Scott Base in the Ross Sea region, with the bulk of the measurements between 0.0 pptv and 0.7 pptv and thereby significantly smaller than the measurements by Saiz-Lopez et al. (2007) on the order of 8 pptv at Halley Station or the mixing ratio estimates of Schönhardt et al. (2008, 2012) and Atkinson et al. (2012) of several pptv. In the next chapter an inter-comparison between the two Antarctic sites studied in this work, and the measurements in the Arctic at Alert is given.

9 Synthesis

This chapter investigates the scientific questions thrown up at the beginning, in chapter 2, with the results of the field measurements, presented in the previous three chapters. Its aim is to answer the question of what can be learned for polar halogen chemistry from the observations made within this work.

The first addressed point is the typical abundance of halogen oxides in polar environments, as determined at the three studied sites (sec. 9.1). Afterwards, the average diurnal cycles of a multitude of species are analyzed, leading to constraints for the sources of reactive halogens and showing the interaction between the different compounds (sec. 9.2). Then, the connection of gas phase halogen oxides with aerosols is analyzed (sec. 9.5) and the question of the effects of meteorology, e.g. temperature and wind speed on observed mixing ratios (sec. 9.7). Lastly, the influence of NO_2 is presented (sec. 9.8). In each of those segments, a topic of special interest is the comparison between the Arctic and the Antarctic as the measurements in both regions within this work allow a direct comparison between them.

9.1 Abundances of halogen oxides in polar regions

The bulk of previous studies shows a discrepancy of the mixing ratios of BrO and IO between the two hemispheres. In the Arctic, BrO has regularly been observed with maxima of 40 pptv - 45 pptv (Pöhler et al., 2010). In the Antarctic sea ice zone, Wagner et al. (2007) tentatively observed mixing ratios around 50 pptv as well, depending on which assumptions are made for the vertical distribution. The highest definitive values for the Antarctic are significantly lower, at only 13 pptv (Buys et al., 2013; Simpson et al., 2015). The opposite is the case for IO with a previously reported maximum of 20 pptv in the Antarctic and 3 pptv

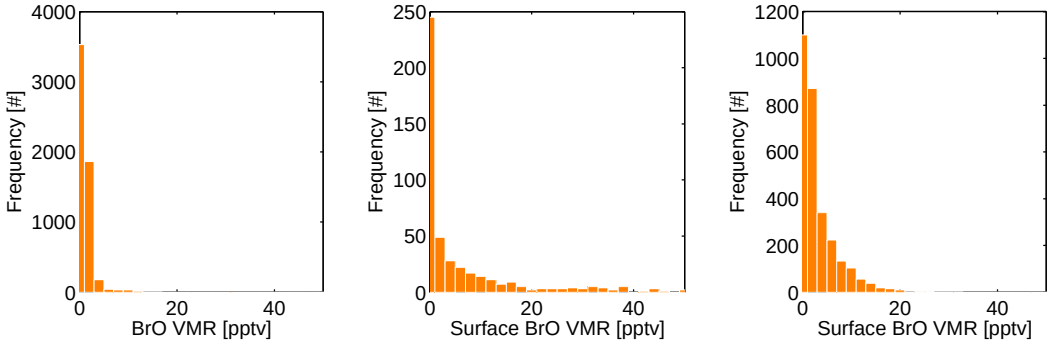

(a) Scott Base **(b)** Polarstern ANT-XXIX/7 **(c)** Alert 2014

Figure 9.1.: BrO: Frequency distributions for the three measurement locations of this work. **(a)** Scott Base, LP-DOAS **(b)** Polarstern expedition ANT-XXIX/7, MAX-DOAS **(c)** Alert, MAX-DOAS.

in the sub-Arctic (Saiz-Lopez et al., 2007; Mahajan et al., 2010; Simpson et al., 2015).

9.1.1 Bromine monoxide

Figure 9.1 shows the frequency distributions of the BrO mixing ratios observed at the three sites during the entire measurement periods for the two campaigns and for one year at Alert. The levels observed during expedition ANT-XXIX/7 were amongst the highest seen so far in the Antarctic (Wagner et al., 2007; Simpson et al., 2015, also chapter 8). There is however little difference between the measurements there and the Alert data, suggesting a stronger similarity between the two polar regions than previously assumed. The higher the mixing ratios, the less common they are until around 20 pptv. Higher mixing ratios are increasingly rare.

Scott Base, however, stands out with significantly lower levels of BrO. This could be due to the local pollution or the particular local topography as discussed in section 6.4. The local BrO MAX-DOAS profiles indicate higher mixing ratios at higher altitudes, which could be artifacts of the inversion procedure, but could also be due to the lifting of warmer halogen-rich marine air masses above colder catabatic air flows from the continent as discussed in section 6.4.2.

9.1.2 Iodine monoxide

Both the Ross Sea region and the Weddell Sea region have frequently been labeled as iodine "hot spots" in the past (Atkinson et al., 2012; Saiz-Lopez et al., 2012, and references therein). The measurements within this work do not confirm this and give a different picture for the studied locations. The frequency distributions of IO mixing ratios are given in figure 9.2 as for BrO above. Both in terms of averages, as well as frequency distributions, there is no significant difference between the studied sites in the Ross Sea region (Scott Base), the Weddell Sea (ANT-XXIX/7) and the measurements in the Arctic at Alert. In all cases, mixing ratios are mostly in the range of 0.0 pptv and 0.5 pptv. Ratios between 0.5 pptv and 1.0 pptv occur, but are rare. The most frequent mixing ratios are 0.1 pptv - 0.2 pptv.

The enormous levels of IO in the range of 3 pptv - 20 pptv (Saiz-Lopez et al., 2012, and references therein) could not be observed anywhere with any of the instruments. These levels were observed in the southern parts of the Weddell Sea, whereas expedition ANT-XXIX/7 was at the northern edge thereof. Perhaps peculiar local effects are playing a role in the southern region. For the study of Atkinson et al. (2012), another explanation would be the assumptions made for the vertical distribution of IO. They assumed that the entire IO VCD, which was estimated by assuming a geometrical light path, is located within a very shallow layer of only 200 m. This leads to mixing ratios of ca. 4 pptv. MAX-DOAS measurements are however also sensitive to higher layers of 1 km - 2 km, depending on the circumstances (see chapter 5). Homogeneously mixed into that height, this would lead to 5 - 10 times smaller mixing ratios, which would be of the order of the ratios observed in this work.

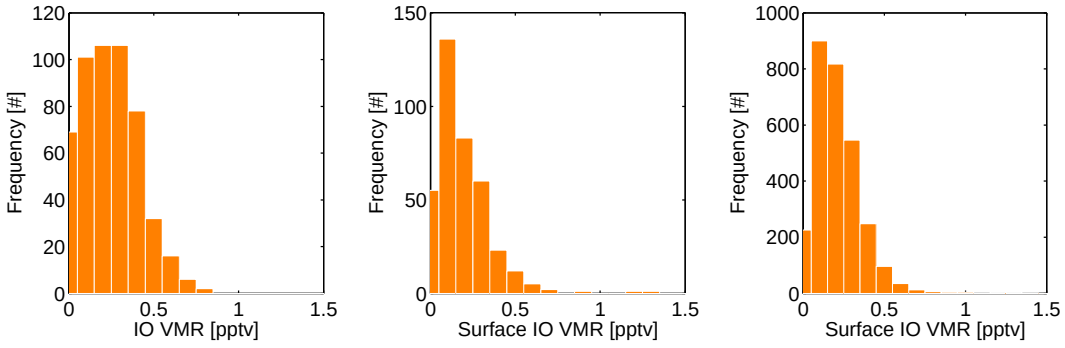

(a) Scott Base **(b)** Polarstern ANT-XXIX/7 **(c)** Alert 2014

Figure 9.2.: IO: Frequency distributions for the three measurement locations of this work. **(a)** Scott Base, LP-DOAS **(b)** Polarstern expedition ANT-XXIX/7, MAX-DOAS **(c)** Alert, MAX-DOAS.

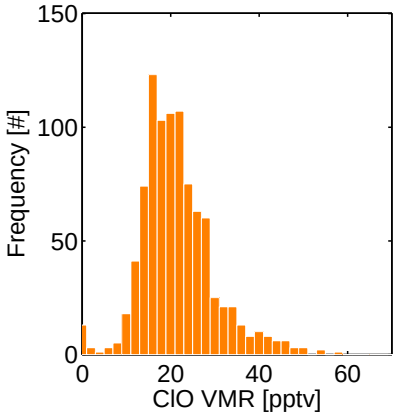

Figure 9.3.: ClO: Frequency distribution for the LP-DOAS measurements at Scott Base.

9.1.3 Chlorine monoxide

The ClO observations described in chapter 6 in this work are the first observations of ClO in the Antarctic PBL. However they lasted only 10 days, therefore is is difficult to assess how representative the observations during this period are for the spring season, even more so for the entire year. Still, a frequency distribution of the mixing ratios is given in figure 9.3. They span the range from 0 pptv to almost 60 pptv with ratios around 20 pptv the most common.

9.2 Average diurnal cycles

The analysis of diurnal cycles is useful to see the interplay of several photochemically active compounds over the day and determine constraints on the release and sink processes of certain species. Here, diurnal cycles averaged over longer time spans are analyzed as these give a clear view of the processes involved during the *average polar day*. Averaging shrinks the distortions by effects such as temperature, the presence of clouds and the transport of air masses. For the longer time series, daytime lengths vary drastically in polar spring from polar night to polar day, thus the local time is not a good indicator for the diurnal change in insolation. Instead of the time, the solar zenith angle (SZA) is used in those cases with 5 ° bins, which is further segregated for the morning and afternoon. For purposes of illustration, the SZA values in the morning are taken as negative values and the ones in the afternoon as positive SZAs.

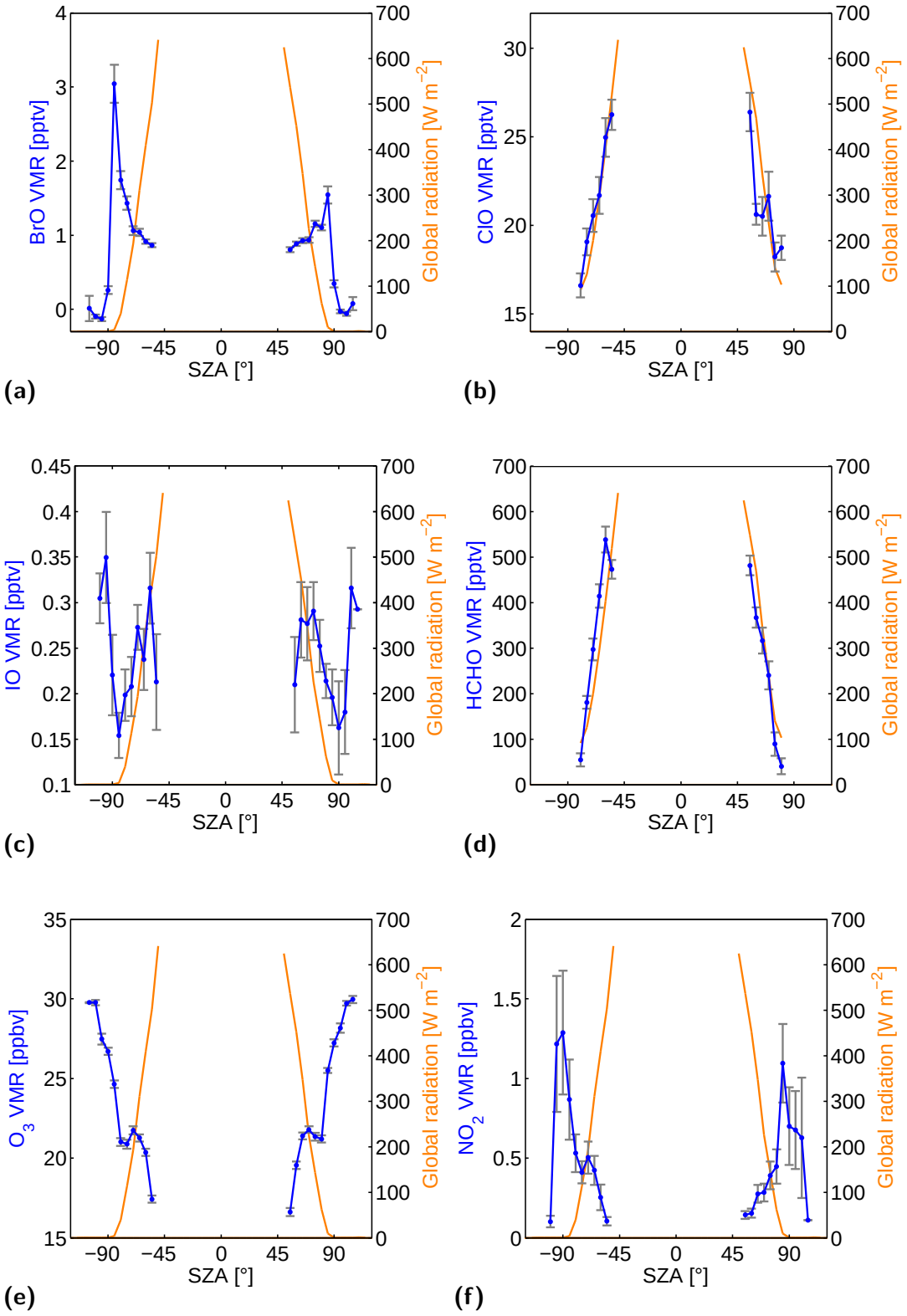

Figure 9.4.: Scott Base LP-DOAS: Observed mixing ratios averaged for 5 ° SZA bins for the entire field study (ClO and HCHO only after 16 November) for **(a)** BrO **(b)** ClO **(c)** IO **(d)** HCHO **(e)** O_3 and **(f)** NO_2. Error bars indicate the standard error of the means, negative SZA values the morning, positive ones the afternoon.

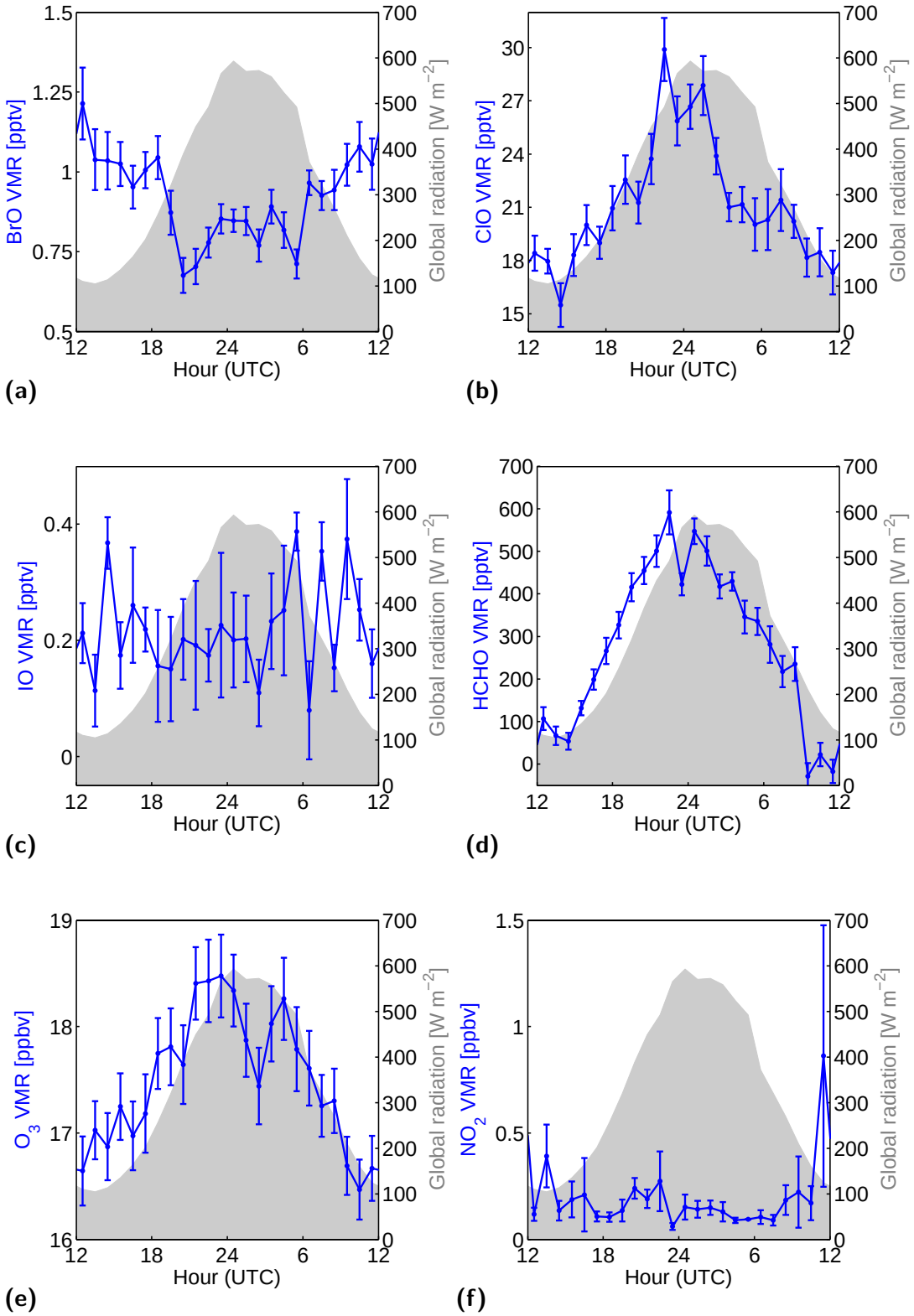

Figure 9.5.: Scott Base LP-DOAS: Diurnal cycles averaged hourly and for the time period from the 16th to the 27th November for **(a)** BrO **(b)** ClO **(c)** IO **(d)** HCHO **(e)** O_3 and **(f)** NO_2. Error bars indicate the standard error of the means.

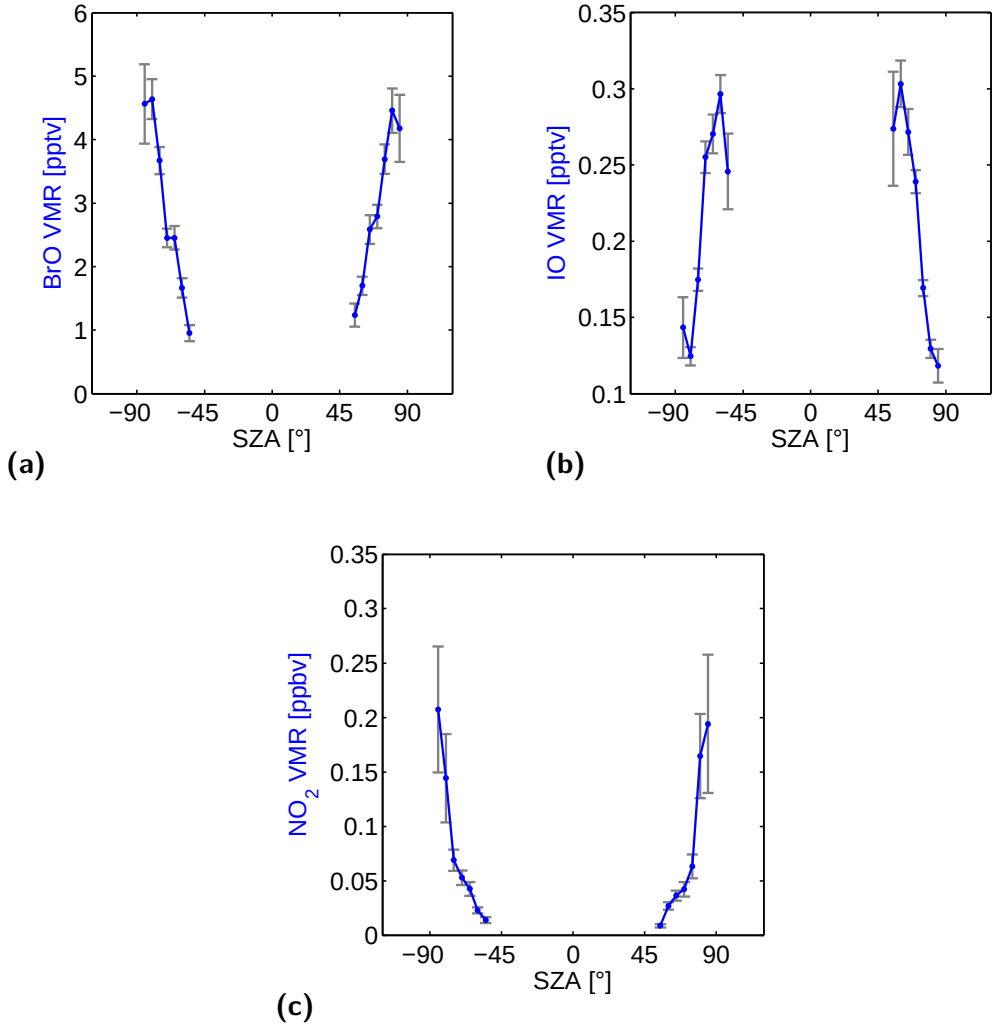

Figure 9.6.: Alert 2014: Observed mixing ratios averaged for 5 ° SZA bins for the year 2014 for **(a)** BrO, **(b)** IO and **(c)** NO_2. Error bars indicate the standard error of the means, negative SZA values the morning, positive ones the afternoon.

9.2.1 Scott Base

The LP-DOAS time series from Scott Base lends itself to such an analysis, as is spans almost the whole twilight period from polar night to polar day. Additionally, measurements were possible during the night and twilight period, and ClO was only observed at this location. The cycles were calculated for the whole duration of the campaign for the compounds BrO, IO, O_3 and NO_2. For those, as well as for ClO and HCHO, they were further calculated for the period from 16th - 27th November, when due to the used light source the observation of ClO and HCHO was possible. The results with the respective standard errors of the means are given in fig. 9.4. The measured global radiation, also averaged over the duration of the campaign, is also shown. They are also given in fig. 9.5 for the period of the 16th - 27th November as a function of daytime.

BrO

BrO shows a cycle which has in similar form already been observed in previous studies in polar regions (e.g. Pöhler et al., 2010; Buys et al., 2013), but also in tropical upwelling settings (Tschritter, 2013). Directly at sunrise, BrO mixing ratios rapidly rise until 85 ° SZA, when they reach a maximum of 3 pptv in this case. Afterwards BrO declines towards lower angles. Shortly before sunset, another smaller maximum is reached at 1.5 pptv. With that behavior, BrO is the only observed species with a significant asymmetry between morning and evening concentrations. No significant concentrations are present at SZAs higher than 90 °.

This diurnal cycle can be explained by the immediate source of BrO, Br radicals, that are formed by the photolysis of Br_2. Therefore, no BrO is seen in the dark period. The noontime drop in mixing ratios can be explained by one sink for BrO, which is the reaction with HO_2 forming HOBr. HO_2 can be produced via OH and therefore ozone photolysis, the diurnal variation of which has a sharper noontime peak than the photolysis of Br_2 (von Glasow et al., 2002; Pöhler et al., 2010, and references therein). This results in higher BrO mixing ratios in the morning and evening compared to noon. At low ozone concentrations or at low humidity, OH production might not be sufficient for this. There are however also several other potential sources of HO_2 such as HCHO, H_2O_2 or Cl, which are all interconnected. For example, HCHO can form HO_2 by

$$\mathrm{HCHO} + \mathrm{h}\nu \longrightarrow \mathrm{H_2} + \mathrm{CO} \tag{R34}$$

$$\mathrm{H_2} + 2\,\mathrm{O_2} + \mathrm{h}\nu \longrightarrow 2\,\mathrm{HO_2} \tag{R35}$$

Other possibilities are

$$\mathrm{HCHO} + \mathrm{OH} + \mathrm{O_2} \longrightarrow \mathrm{HO_2} + \mathrm{CO} + \mathrm{H_2O} \tag{R36}$$

$$\mathrm{HCHO} + \mathrm{Br} + \mathrm{O_2} \longrightarrow \mathrm{HBr} + \mathrm{CO} + \mathrm{HO_2} \tag{R37}$$

H_2O_2 can produce HO_2

$$H_2O_2 + h\nu \longrightarrow 2\,OH \quad \text{(R38)}$$
$$H_2O_2 + OH \longrightarrow HO_2 + H_2O \quad \text{(R39)}$$
$$H_2O_2 + Cl \longrightarrow HCl + HO_2 \quad \text{(R40)}$$
$$OH + CO + O_2 \longrightarrow CO_2 + HO_2 \quad \text{(R41)}$$

HO_2 in turn also recycles H_2O_2 by

$$2\,HO_2 \longrightarrow H_2O_2 + O_2 \quad \text{(R42)}$$

Another source of both HO_2 and HCHO is atomic chlorine via its reaction with methane, with one possible pathway being

$$Cl + CH_4 + O_2 \longrightarrow HCl + CH_3O_2 \quad \text{(R43)}$$
$$Cl + O_3 \longrightarrow ClO + O_2 \quad \text{(R44)}$$
$$ClO + CH_3O_2 + O_2 \longrightarrow Cl + HCHO + HO_2 \quad \text{(R45)}$$
$$Cl + HCHO + O_2 \longrightarrow HCl + CO + HO_2 \quad \text{(R46)}$$

Another sink for HO_2, besides the reaction with BrO, IO or ClO, is

$$HO_2 + CH_3O_2 \longrightarrow CH_3OOH + O_2 \quad \text{(R47)}$$
$$Cl + CH_3OOH \longrightarrow HCl + CH_3O_2 \quad \text{(R48)}$$

This cycle is also a sink for the chlorine radicals.

The above listed pathways therefore produce HO_2 when HCHO or Cl are present, which both are in the observations shown. HCHO as well as ClO further show a strong diurnal cycle with a (pre-) noontime peak (see below) explaining the simultaneous drop in BrO mixing ratios. Due to the strong interconnectedness between those compounds via the mentioned reactions above, kinetic modeling is necessary in future studies to identify the relevant processes involved.

IO

Interestingly, IO is observed at SZAs above 90 °, up to 100 °, and has its highest average mixing ratios actually at this time, when the sun is still below the horizon (Average global radiation levels are given as 0.1 - 0.4 $W\,m^{-2}$, the accuracy of those measurements at those low light levels is however questionable). Around sunrise (SZA of 85 °) and sunset (SZA of 90 °), IO reached its minimum values, simultaneously with the maxima of BrO. During the daytime, further maxima are reached at 60 - 70 ° SZA. At still lower SZA, IO mixing ratios decline again.

This can be explained by the rapid photolysis of I_2 (Saiz-Lopez et al., 2004), leading to the high values even before sunrise. Afterwards, when BrO is present,

the fast cross reaction BrO + IO possibly drags down steady-state IO mixing ratios to lower values. As BrO mixing ratios decrease towards local noon, the IO concentrations rise again only to fall off at around noon, possibly due to photolysis or the cross reaction with ClO, the mixing ratios of which peak at noon. There are also other sinks, such as the ones mentioned above for BrO via HO_2.

The simultaneous observation of IO and BrO allows to estimate the OIO production. Assuming a steady-state, where OIO is produced by BrO + IO, and lost only by photolysis, i.e.

$$\frac{d[OIO]}{dt} = k_{R22} \times [IO] \times [BrO] - [OIO] \times J_{OIO} \stackrel{!}{=} 0 \tag{9.1}$$

allows to estimate its mixing ratios by

$$[OIO] = \frac{k_{R22} \times [IO] \times [BrO]}{J_{OIO}} \tag{9.2}$$

The OIO concentrations therefore strongly depends on J_{OIO}, which is not well known, and a value of $0.003\,s^{-1}$ is assumed here. This magnitude is estimated using the value given by Saiz-Lopez et al. (2012), and the approximately 150 times smaller insolation in this work than for the value in the literature. Using the concentrations at 85 ° SZA, when BrO peaks, of 3 pptv BrO and 0.15 pptv IO, leads to a steady-state estimate of only 0.03 pptv OIO at this SZA. The IO self-reaction (R18) in contrast, would yield even less, only 0.0002 pptv OIO at the same time. Even before sunrise however, when the highest average IO mixing ratios of 0.35 pptv IO were observed, the IO self-reaction should lead to steady-state OIO mixing ratios of only 0.09 pptv, assuming an insolation of just $0.1\,\mathrm{W\,m^{-2}}$. It is therefore no surprise that it was never observed during the field study with a typical detection limit of 0.8 pptv.

ClO

ClO displays yet a different diurnal cycle compared to BrO and IO. Its mixing ratio increases with increasing solar irradiation to values about 50% higher at noon (~30 pptv) compared to "midnight" (~20 pptv) and the mixing ratios never reach values around zero. In fact, the maximum occurs slighty before the highest solar irradiation is reached, similarly to the case of HCHO.

Several laboratory reaction chamber studies have been undertaken previously to investigate release factors. Oum et al. (1998) showed that sea salt particles when subjected to ozone and light release molecular chlorine. They proposed that the release is due to the oxidation of liquid phase Cl^- by OH. Wren et al. (2013) studied the release of Cl_2 directly from artificial snow doped with NaCl and NaBr in chamber studies. They also only found significant release of molecular chlorine when ozone was present and the sample was illuminated as well.

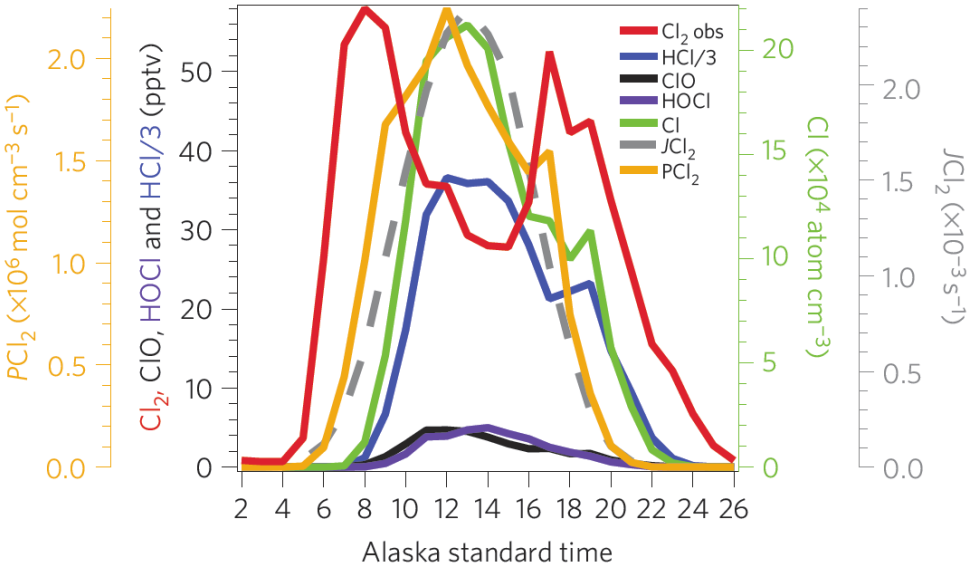

Figure 9.7.: Graph reproduced from Liao et al. (2014): The modeled diurnal variation of several chlorine species, constrained to measured Cl_2 mixing ratios at Barrow, Alaska, USA.

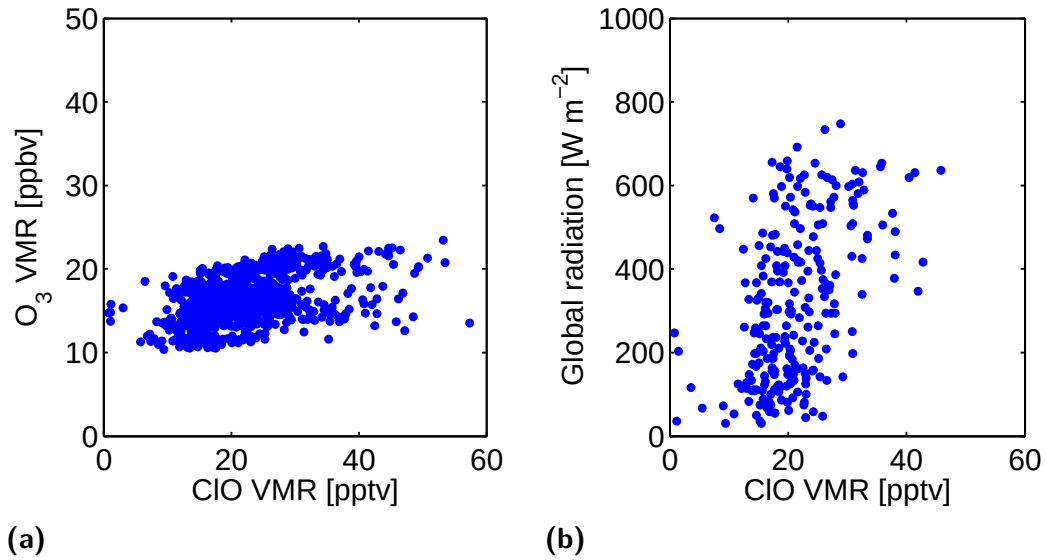

Figure 9.8.: LP-DOAS: Scatter plots of the ClO mixing ratio and **(a)** ozone mixing ratios and **(b)** the incident global radiation.

A scatter plot between ClO and ozone mixing ratios is displayed in figure 9.8a. At higher ozone mixing ratios, slightly higher ClO levels seem to be possible. Another scatter plot, between ClO VMRs and incident global radiation is given in figure 9.8b. There is a weak tendency at higher radiation towards higher mixing ratios but also towards a larger variability.

The observed diurnal cycle of ClO in this work could be explained by the release mechanism by oxidation of Cl^- by OH. Due to this release process, chlorine does not, as a result, offer an additional sink for atmospheric methane, which is usually removed the its oxidation by OH. For each released Cl_2 molecule however, also one OH radical is consumed. Typically, one of the resulting Cl radicals then reacts with ozone, the other with methane, which only compensates the OH radical, which is now missing for the methane oxidation due to the Cl_2 release. This should also holds at low ozone mixing ratios, as less chlorine is released then. The magnitude of the methane sink should therefore not change in first order. What does change however, is the isotopic composition of atmospheric methane due to the large fractionation effect of chlorine (Platt et al., 2004).

Interestingly, in comparison with BrO and IO, ClO does not exhibit a significant noontime dip in mixing ratios. The rate constant of its reaction with HO_2 is however also more than a magnitude slower ($k_{ClO+HO_2} = 6.9 \cdot 10^{-12} \frac{cm^3}{molec\,s}$ vs. $k_{BrO+HO_2} = 2.4 \cdot 10^{-11} \frac{cm^3}{molec\,s}$, Atkinson et al., 2007). Additionally, the photolysis of ClO is not a significant sink, as its absorption cross section peaks below 300 nm, where most light gets absorbed by the stratospheric ozone layer (Langhoff et al., 1977).

In the Arctic, as mentioned in section 2.5.4, Liao et al. (2014) found very high Cl_2 mixing ratios of up to 400 pptv. The authors of that study also modeled the resulting diurnal cycle of ClO and other chlorine species, the graph of which is reproduced in figure 9.7. At noontime mixing ratios of ~30 pptv of Cl_2, their model predicts ClO levels of only ~5 pptv. Interestingly, the model also predicts a peak in ClO mixing ratios slightly before the peak of the incident solar radiation. This is seemingly caused by the higher production rate PCl_2 of Cl_2 and a buildup of mixing ratios in the morning.

The observed lack of chlorine dioxide (OClO)

With both BrO and ClO present, OClO is formed by reaction R28, which has been proposed as a proxy for chlorine activation (e.g. Sessler et al., 1995). The primary formation of OClO is also due to the BrO + ClO reaction, as the direct oxidation of ClO by ozone is too slow (refer to 2.5.4). Its loss in the atmosphere is mainly caused by photolysis, because of its short photolytic lifetime on the order of 10 seconds Birks et al. (1977). With this, the concentration for the period when ClO was observed can be estimated by assuming a steady-state:

$$\frac{d[OClO]}{dt} = k_{R28} \times [ClO] \times [BrO] - [OClO] \times J_{OClO} \stackrel{!}{=} 0 \qquad (9.3)$$

which leads to

$$[OClO] = \frac{k_{R28} \times [ClO] \times [BrO]}{J_{OClO}} \tag{9.4}$$

For J_{OClO}, a value of $0.076\,s^{-1}$ is used (Birks et al., 1977). With 40 pptv of ClO and 2 pptv of BrO, the highest combination of both in the measurements, this would lead to a steady-state OClO mixing ratio of 0.15 pptv. This is well below the typical detection limit of 0.7 pptv on the long light path and 1.5 pptv on the short one (compare table 6.3).

OClO was also not observed during the earlier, darker months (August, September) of the campaign above the mentioned detection limits. This could be explained by the release mechanism of Cl_2 as mentioned above, and therefore the formation of ClO, which needs substantial amounts of solar irradiation. This furthermore suggests that other chlorine release mechanisms, e.g. due to hypobromous acid (HOBr), are not important at this location.

HCHO

Formaldehyde shows a similar cycle as ClO, with highest concentrations slightly before local noon. A rough empirical relationship can be given for the observed period as 1 pptv of additional HCHO for every $1\,W\,m^{-2}$ of additional incident radiation. HCHO is a product of the oxidation of methane by the hydroxyl radical or by the chlorine radical. As mentioned above, the formation of the hydroxyl radical has a noontime maximum. The ClO diurnal cycle also peaks around noontime as seen in the measurements. This therefore mostly explains the noontime peak of HCHO.

NO_2

The NO_2 cycle also shows an expected behavior. During the dark periods, mixing ratios are low at ca. 100 pptv. After sunrise they increase, most likely because the nighttime reservoir species NO_3 gets photolytically destroyed. The higher the sun afterwards, the lower the NO_2 concentrations. Several processes are possibly involved in this. One is the photolysis of NO_2 towards NO and therefore a lower steady-state ratio of $[NO_2]/[NO]$ (called Leighton ratio). Another process is the reaction of NO_2 with the halogen oxides to halogen nitrates, which can possibly result in the deposition of NO_2 into aerosols and surfaces (Holla, 2013). The NO_2 data was not filtered for single local pollution events, but those should occur mainly during the daytime as human activities are most frequent then. The snowpack source of NO_x furthermore is dependent on insolation and strongest at local noon (Honrath et al., 1999; Grannas et al., 2007). In order to accurately distinguish those processes, modeling of the sources, sinks and chemical reactions is inevitable.

O_3

The decrease of ozone from 30 ppbv during the dark periods to 16 ppbv at the smallest SZAs displays more the typical yearly cycle with higher values during winter and lower ones in summer (e.g. Oltmans and Levy, 1994), than an actual diurnal variation.

9.2.2 Alert

The diurnal cycles at Alert, determined for all measurements during the year 2014, give a highly similar picture, as can be seen in fig. 9.6. Global radiation data is not shown, as it was not available for Alert. Furthermore, due to the nature of the MAX-DOAS measurements, the sampled SZA range is smaller, as the sun has to be above the horizon for sufficient light. In the range that is sampled, the cycles of BrO, IO and NO_2 all show the same behavior as at Scott Base. For BrO, the maxima are reached at SZAs slightly larger than 90 ° and decrease towards lower angles. IO shows an increase towards lower angles until 60 ° and a decrease at even lower angles. The cycle of NO_2 is similar as well, although the average mixing ratios at Alert are significantly lower.

9.3 What destroys ozone during ODEs?

In section 2.5, many possible reaction cycles have been listed which can lead to the depletion of atmospheric ozone. In order to assess the result of persistent low levels of the halogens on long-term ozone, modeling is needed. However, an estimation can be made for stronger ozone depletion, such as during ODE, by scatter plots of ozone and the different halogen oxides. The highest values of a significantly ozone depleting substance should then anti-correlate with ozone. Of course many other factors also control ozone mixing ratios, e.g. meteorology, seasonal variability, transport of air masses.

This is displayed in fig. 9.9 for all three measurement locations and the oxides BrO, IO and ClO. Of all seven graphs, only in two instances can a behavior as described above be seen, both times for BrO, namely on Polarstern and at Alert. In those cases, higher BrO mixing ratios generally correspond to lower ozone levels. The picture for IO is largely indifferent. On Polarstern the bulk of points for higher iodine concentrations are actually at higher ozone, which could indicate a property of its release mechanism as discussed later. In the case of ClO, as written above, ozone is necessary for its release, which can be seen in slightly higher ClO mixing ratios at increasing ozone levels.

9.4 Inter-halogen comparison

The diurnal cycles of the three halogen oxides, BrO, IO and ClO, have shown that they are mostly present in different regimes of incident solar radiation. That inter-halogen reactions most likely also play a role is seen best in the daily minima of IO in the morning and evening, when BrO peaks. Another way to study the interplay between the halogen oxides is to plot their mixing ratios against each other. This is done in fig. 9.10 for the three possible pairings, along with color-coded ozone mixing ratios. In all three graphs, a triangular shape of the outer points can be seen. This is probably caused by the fast reactions in-between them, which reduce the steady-state mixing ratios of the different halogen oxides when more than one type is present (see section 2.5). At lower ozone mixing ratios, IO seems to reach its highest values at Scott Base. This is the opposite for ClO, which needs ozone for its release as discussed above.

9.5 The role of aerosols

In the description of halogen chemistry in chapter 2, the dependence of the bromine explosion mechanism on heterogeneous reactions was explained, which naturally needs reaction surfaces to take place. Aerosols can offer such a reaction surface in the atmosphere. Furthermore, depending on their composition, they can also be a potential source of reactive halogens or act as a sink for them.

9.5.1 Aerosols as a halogen source or sink

During the field studies at the three different locations in this work, the current aerosol composition was neither determined in the course of this work nor by collaborators. At Alert, a site where some of the earliest studies of polar halogen chemistry were conducted before, however, aerosol composition had been analyzed in the years between 1980 and 1986 by Sturges and Barrie (1988) and Barrie and Barrie (1990). They determined annual cycles of bromide (Br^-) as well as total iodine content in aerosol. Assuming that the annual halogen chemistry has not changed dramatically since the early 1980s at Alert, those data offer a comparison between the gas phase halogen oxide mixing ratios as determined in this work, and aerosol concentrations. This is given in fig. 9.11 with the monthly means of the 2014 data and the monthly-averaged results from Barrie and Barrie (1990).

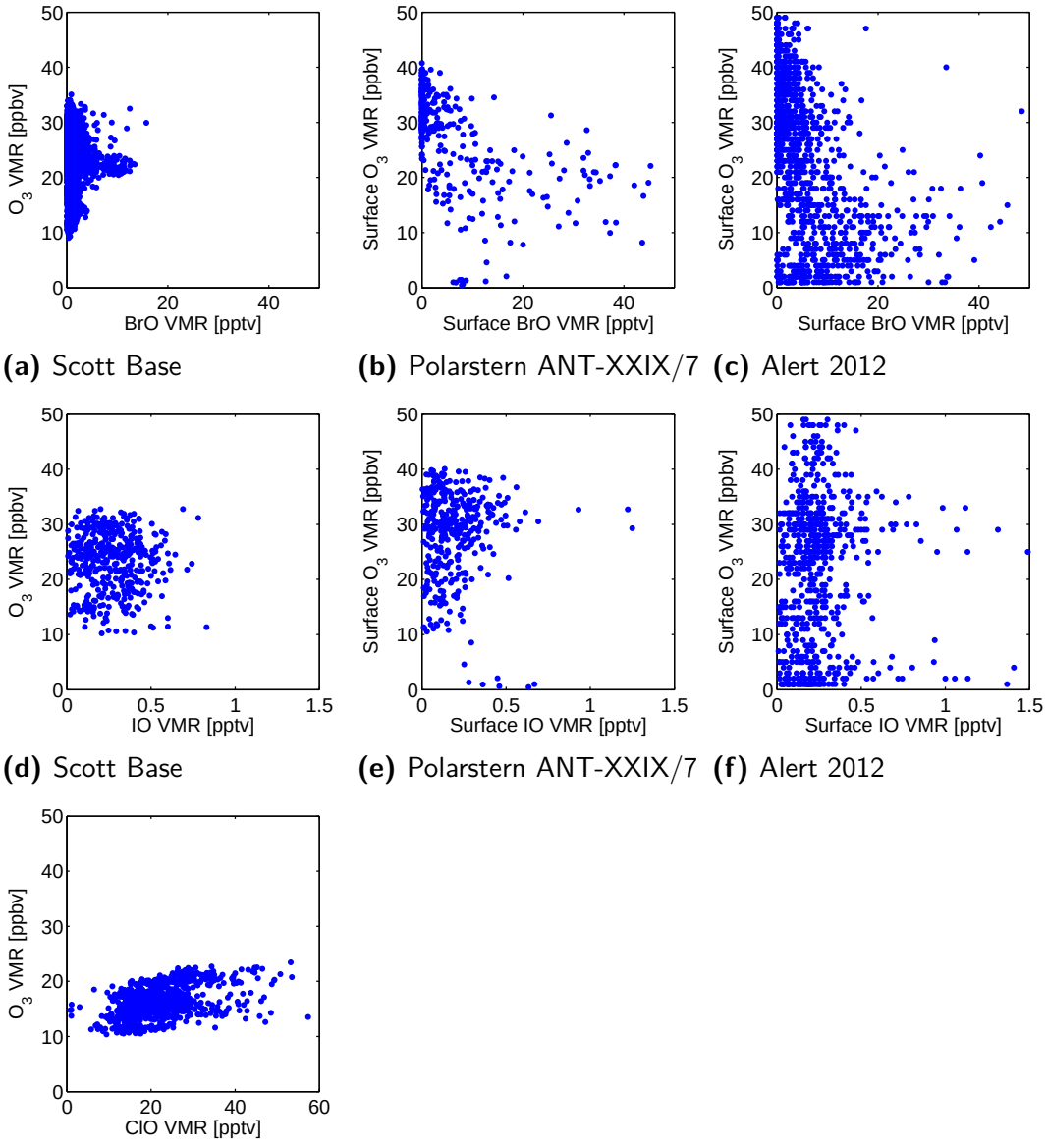

(a) Scott Base **(b)** Polarstern ANT-XXIX/7 **(c)** Alert 2012

(d) Scott Base **(e)** Polarstern ANT-XXIX/7 **(f)** Alert 2012

(g) Scott Base

Figure 9.9.: BrO vs. O_3 mixing ratios: Scatter plots of 1-hour averages for the three measurement locations of this work. **(a)** Scott Base, LP-DOAS **(b)** Polarstern expedition ANT-XXIX/7, MAX-DOAS **(c)** Alert, MAX-DOAS.

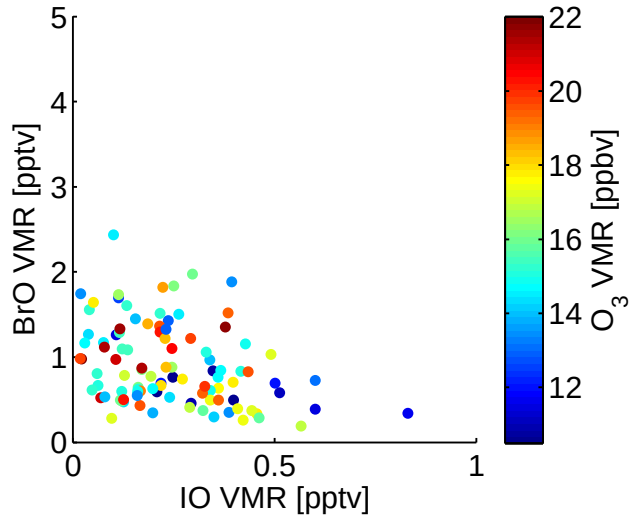

(a)

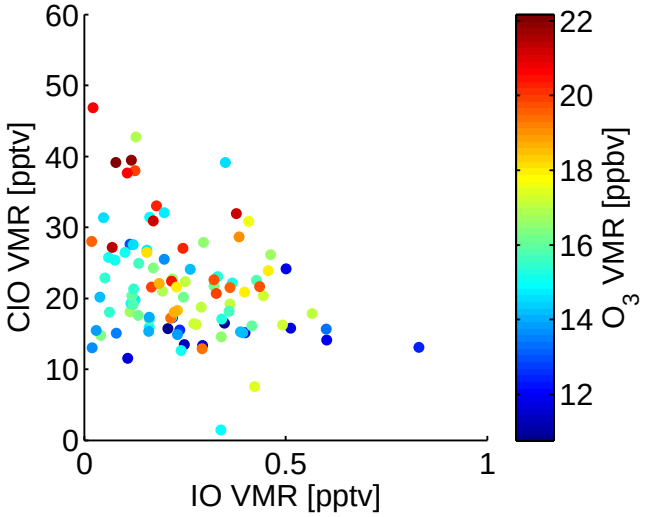

(b)

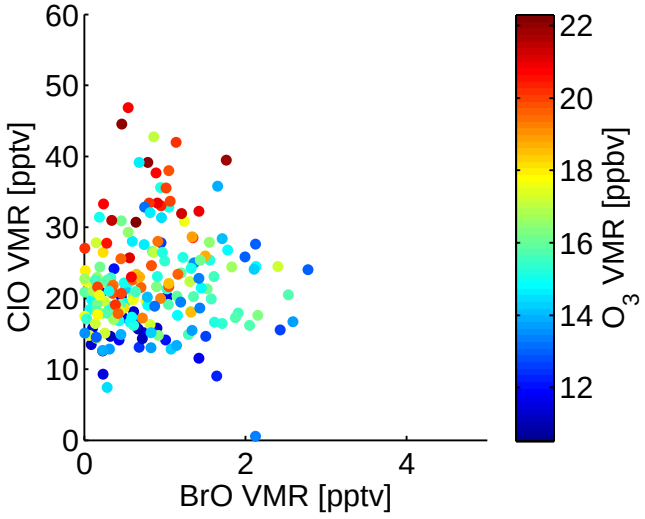

(c)

Figure 9.10.: Scott Base LP-DOAS: Scatter plots of 1-hour averages of the mixing ratios of **(a)** BrO and IO, **(b)** IO and ClO and **(c)** BrO and ClO during the last ten days (16th - 27th November). The ozone mixing ratio is color-coded.

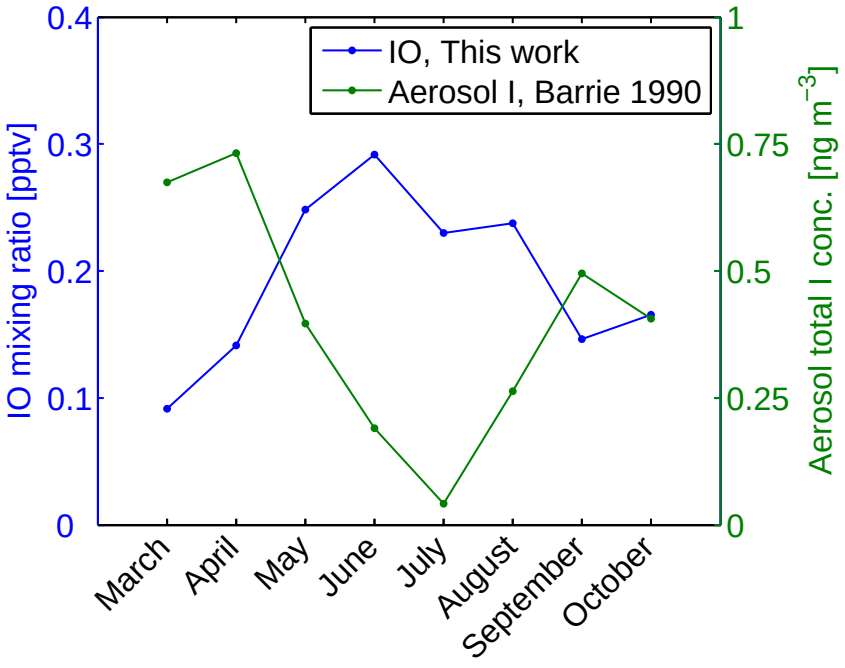

(a)

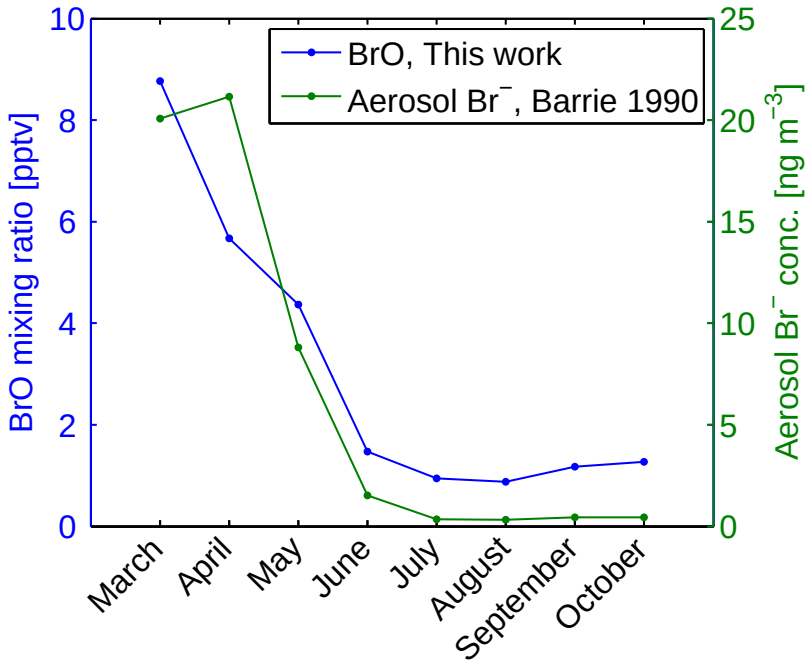

(b)

Figure 9.11.: Alert: **(a)** Comparison of the monthly mean IO mixing ratios of 2014 (from fig. 7.17a) and the total iodine content of aerosol as determined by Barrie and Barrie (1990). **(b)** Comparison of the monthly mean BrO mixing ratios of 2014 (from fig. 7.16a) and the Br^- content of aerosol as determined by Barrie and Barrie (1990).

Iodine

The analysis by Barrie and Barrie (1990), of the total iodine content, found annual iodine concentrations to have a marked yearly cycle with two maxima. One maximum occurs in early spring (April) at up to $0.73\,\mathrm{ng\,m^{-3}}$ total iodine, the equivalent of 0.12 pptv in the gas phase at 263 K and 1013 hPa. The other maximum is in early autumn (August and September, up to $0.50\,\mathrm{ng\,m^{-3}}$, equivalent to 0.08 pptv). The annual minimum occurs in summer during June and July with $0.04\,\mathrm{ng\,m^{-3}}$, equivalent to 0.007 pptv.

The gas phase IO mixing ratios, as determined in this work, are higher in summer than in spring, with a possible second maximum in October. The difference between the highest and the lowest mixing ratios is 0.20 pptv for the gas phase, but only an equivalent of 0.12 pptv for the aerosol content. A release of the entire iodine in aerosols into the gas phase, during summer, therefore can not fully explain the increase in summer time gas phase IO mixing ratios. Additional sources are necessary, yet the aerosol content could be part of the source of reactive gas phase iodine.

The low summer-time total iodine values could be due to several reasons. One possibility is simply that less aerosols are present, which was not determined in the study by Barrie and Barrie (1990). Another possibility would be the release of the iodine into the gas phase. One possible pathway for this could be due to molecular chlorine via

$$2\,I^- + Cl_2 \longrightarrow I_2 + 2\,Cl^- \qquad \text{(R49)}$$

For this Cl_2 is needed, but the studies by Liao et al. (2014), as mentioned above, recently found large concentrations thereof at Barrow, which might apply in similar form to Alert. The Cl_2 mixing ratios were furthermore found to be proportional to the incident radiation, which could also explain the observed decrease in iodine aerosol values in summer compared to spring and autumn. Other possible release processes, such as the direct ozonisation of I^- should correlate with ozone levels, and should therefore show the opposite annual trend in aerosol iodine levels, with a minimum in winter at high ozone and a maximum in summer at low ozone. As this is not the case, the importance of this latter process can probably be discounted.

Bromine

In the case of bromine, the annual cycle for BrO and aerosol Br^- content, shown in fig. 9.11b, shows a correlating behavior in contrast to the anti-correlation as seen in the case of iodine. The levels for both, gas phase and aerosol values, peak in March and April and decline thereafter until June/July, when they reach a plateau. At that point, aerosol Br^- content is close to zero at around $0.4\,\mathrm{ng\,m^{-3}}$, equivalent to 0.11 pptv in the gas phase. The highest aerosol content in April corresponds to 5.7 pptv, very similar in magnitude to the actual gas phase mixing ratios. The BrO mixing ratios around 1 pptv after June have only been observed

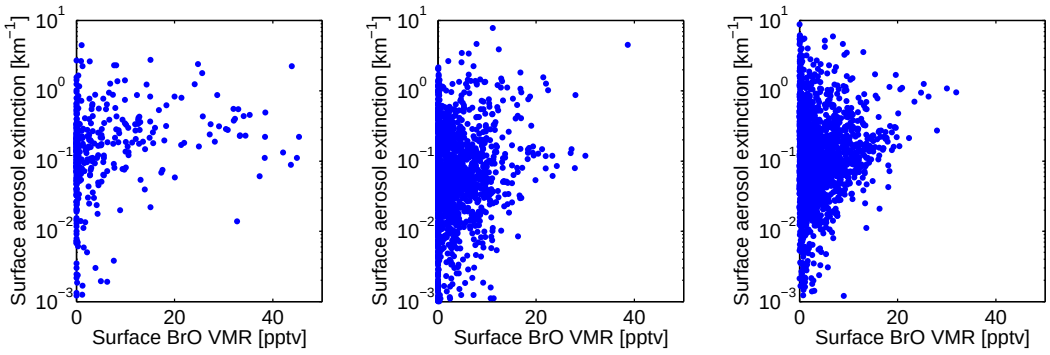

(a) Polarstern ANT-XXIX/7 **(b)** Alert 2013 **(c)** Alert 2014

Figure 9.12.: BrO mixing ratio vs. aerosol extinction as a crude proxy for aerosol amount/surface area: Scatter plots of 1-hour averages for the MAX-DOAS measurements during **(a)** Polarstern expedition ANT-XXIX/7 **(b)** Alert 2013 **(c)** Alert 2014.

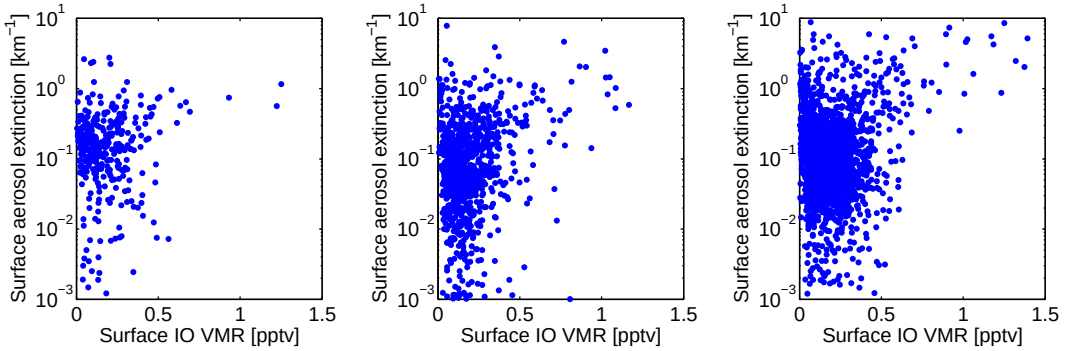

(a) Polarstern ANT-XXIX/7 **(b)** Alert 2013 **(c)** Alert 2014

Figure 9.13.: IO mixing ratio vs. aerosol extinction as a crude proxy for aerosol amount/surface area: Scatter plots of 1-hour averages for the MAX-DOAS measurements during **(a)** Polarstern expedition ANT-XXIX/7 **(b)** Alert 2013 **(c)** Alert 2014.

in 2014 in Alert and could be a special, non-representative case for other years (see fig. 7.16). As in the case of iodine, the Br^- content in aerosol can not explain the amounts of BrO in the gas phase. The concurrent trend in BrO and Br^-, in contrast, suggests a common source and sink, as well as a continuous exchange between both.

9.5.2 Aerosols as a reaction surface

As with the aerosol composition, the aerosol concentration was not measured in this work. The only parameter available to quantify the aerosol reaction surface, is the retrieved aerosol extinction from MAX-DOAS measurements, which offers a crude estimate for the surface area of aerosol. Comparisons between the aerosol extinction and BrO and IO mixing ratios were done for the data from Polarstern and Alert. Those are given in fig. 9.12 for BrO and in fig. 9.13 for IO.

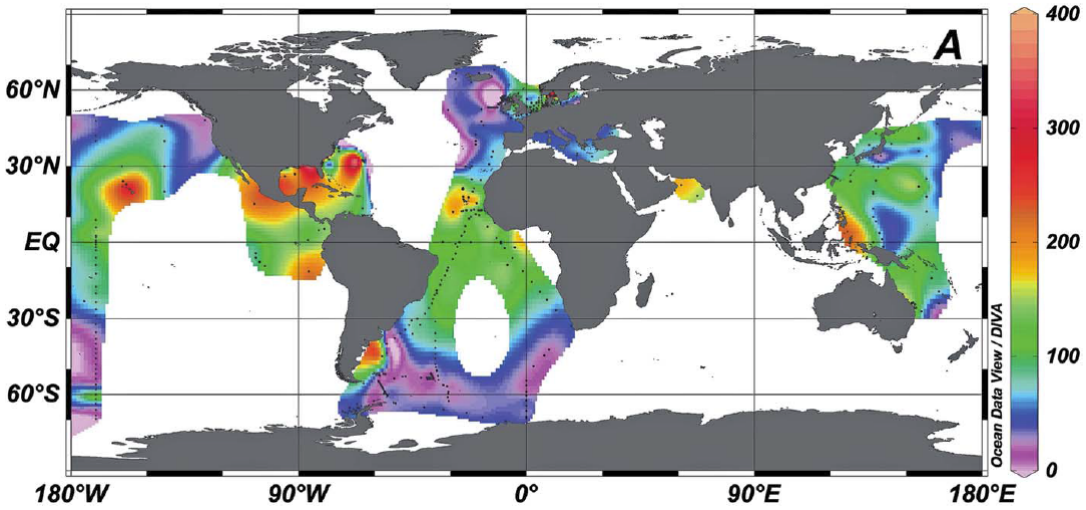

Figure 9.14.: Reproduced from Chance et al. (2014): Global sea surface iodide concentration given in $\mathrm{nM\,l^{-1}}$. The concentration in polar seas is several times smaller than in tropical seas.

Bromine

For BrO, the highest mixing ratios are seen in the range between $10^{-2}\,\mathrm{km^{-1}}$ to $5\,\mathrm{km^{-1}}$, but mostly between $0.1\,\mathrm{km^{-1}}$ and $1\,\mathrm{km^{-1}}$. Especially at extinctions smaller than $10^{-2}\,\mathrm{km^{-1}}$, BrO mixing ratios seem to decrease with decreasing extinction, possibly indicating a reaction limiting parameter with insufficient surface area available for the heterogeneous reactions. At Alert, the bulk of the values further seems to decrease at extinctions above $0.1\,\mathrm{km^{-1}}$, this time possibly indicating too much available aerosol surface, which can also act as a sink for gas phase bromine.

Iodine

The behavior of iodine is similar but not identical to bromine. In this case, the highest mixing ratios are observed at extinctions in the range from $0.1\,\mathrm{km^{-1}}$ to $10\,\mathrm{km^{-1}}$. A visible trend is that the smaller the extinctions get, the smaller the IO mixing ratios are. In contrast to bromine, there does not appear to be a decrease in mixing ratios at high extinctions above $1\,\mathrm{km^{-1}}$, instead those high extinctions appear to be conducive to higher IO mixing ratios. Aerosols therefore seem to have less of a sink function for iodine.

9.6 The source of iodine

As mentioned in section 2.5.3, the precursor species of IO are still not completely identified. In principle though, three possibilities are likely:

- The photo-degradation of biogenic, inorganic species, i.e. I_2, HOI, etc.

- The degradation of biogenic iodocarbons such as CH_3I, CH_2I_2, etc.
- The oxidation of iodide by strong oxidants like HOBr, i.e. iodine release being a by-product of the bromine explosion

The results from the measurements in this thesis show that, at least for the studied locations, the spatial distribution of IO is rather homogeneous. This does not support the idea of strong localized sources, but instead supports spatially extended sources. One potential source could be the ocean, even though underneath the sea ice through brine channels. Another possibility would be ice algae, which inhabit large areas.

The work of Carpenter et al. (2013) shows that, at least in tropical conditions, the first possibility to be the strongest contributor to the atmospheric IO budget, being responsible for around 75% of the total reactive iodine release. The mechanism involved was found to be almost linearly dependent on the atmospheric ozone mixing ratio, and also on the water iodide concentration. The release mechanism proposed in that work is the following:

$$I^- + H^+ + O_3 \longrightarrow HOI + O_2 \quad \text{(R50)}$$

$$HOI + I^- + H^+ \longrightarrow I_2 + H_2O \quad \text{(R51)}$$

The molecular iodine, once in the atmosphere then gets photolyzed and forms IO with ozone.

Previous studies of IO in tropical waters, with an I^- concentration of around $200\,\mathrm{nM\,l^{-1}}$, have reported atmospheric mixing ratios of about 1 pptv (Lampel, 2014). Therefore, an estimate can be made assuming the linear relationship on ozone and ocean iodide concentration to hold. Further assuming similar ozone mixing ratios, and an I^- concentration of $50\,\mathrm{nM\,l^{-1}}$ for polar waters (see fig. 9.14, Chance et al., 2014), a quarter of tropical levels, the corresponding iodine and IO mixing ratios should also be around a quarter of the 1 pptv, that is 0.25 pptv. This value compares well with the most frequently observed surface IO mixing ratios of 0.2 pptv to 0.3 pptv determined in this work, as shown in fig. 9.2. It appears therefore, that to explain the observed IO mixing ratios, both at Alert as well as in the Antarctic at Scott Base and during expedition ANT-XXIX/7, the above mentioned release process could be sufficient, and moreover predicts the measured mixing ratios. This mechanism would also explain the observed, highly similar mixing ratios in the Arctic and the Antarctic, as oceanic iodide concentrations are similar.

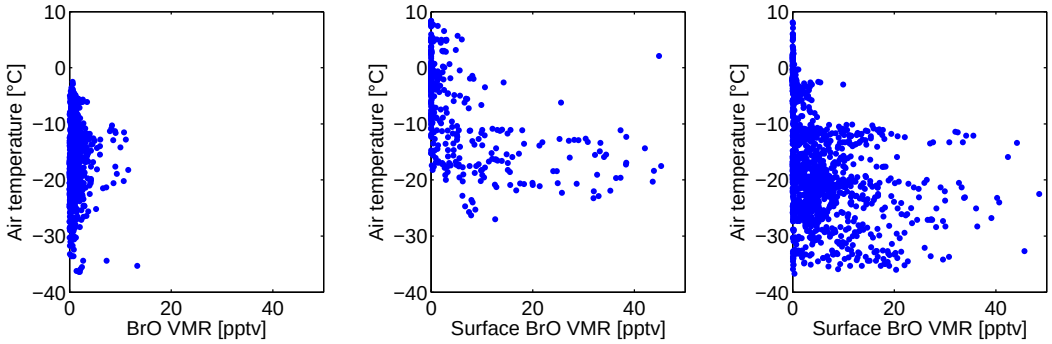

(a) Scott Base **(b)** Polarstern ANT-XXIX/7 **(c)** Alert 2012

Figure 9.15.: BrO mixing ratio vs. air temperature: Scatter plots of 1-hour averages for the three measurement locations of this work. **(a)** Scott Base, LP-DOAS **(b)** Polarstern expedition ANT-XXIX/7, MAX-DOAS **(c)** Alert, MAX-DOAS.

9.7 The influence of meteorology

Meteorological parameters are known to play a role in several of the processes responsible for the release and activation of reactive halogen species, as mentioned in section 2.5. Those parameters include temperature and wind speed, and their impact as observed during the measurements in this work is discussed in the following.

9.7.1 Temperature

BrO

An empirical temperature dependency has previously been mostly implicated in the activation of bromine chemistry. Pöhler et al. (2010) found a roughly linear increase of the highest observed BrO mixing ratios for the range between -15 °C and -24 °C. The lower the temperatures in this range, the higher the BrO mixing ratios. Such a straightforward relationship is not visible in all of the three datasets presented here. The correlation between those is given in fig. 9.15.

During expedition ANT-XXIX/7 and at Alert, temperatures below -10 °C seem to be favorable for enhanced BrO mixing ratios. Except for two data points, only below -10 °C do the BrO mixing ratios exceed 20 pptv. At lower temperatures, there is no obvious temperature dependency, and it seems, if the threshold of -10 °C is met, other factors are at play, and temperature is not a limiting factor for BrO levels.

At Scott Base, as discussed in chapter 6, only smaller BrO mixing ratios have been observed. However, also in this case do the higher measured mixing ratios only occur at temperatures below -10 °C.

These results are overall similar to the findings of Pöhler et al. (2010), in that a certain minimum temperature is necessary for bromine activation. The threshold

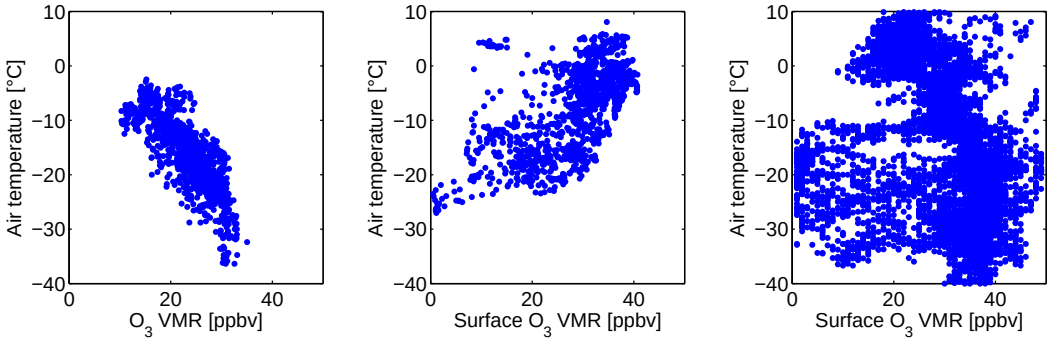

(a) Scott Base **(b)** Polarstern ANT-XXIX/7 **(c)** Alert 2012

Figure 9.16.: O_3 vs. air temperature: Scatter plots of 1-hour averages for the three measurement locations studied within this work. **(a)** Scott Base, LP-DOAS **(b)** Polarstern expedition ANT-XXIX/7, MAX-DOAS **(c)** Alert, MAX-DOAS.

observed in this work is slightly higher at -10 °C compared to the -15 °C, as seen in the previous study, and a strong linear increase in highest concentrations is not clearly visible.

Ozone

The observed ozone mixing ratios show a stronger correlation with air temperature than BrO. Those are shown in fig. 9.16. For the measurements at Scott Base and on Polarstern they show an almost linear relationship. Whereas at Scott Base the mixing ratios are higher at lower temperatures, they are lower at lower temperatures on Polarstern. This can be explained by the origin of the sampled air masses. At Scott Base, the air coming from the sea ice covered areas, is coming from the north of the station, and it is warmer and depleted in ozone, most likely due to previously occurring bromine chemistry. During the cruise ANT-XXIX/7 at the northern edges of the sea ice zone, the air masses from the colder, southern areas were over sea ice in their past, and therefore depleted in ozone. Both those observations support the results of Simpson et al. (2007a), which showed that sea ice contact is a predictor of bromine levels and therefore ozone depletion. The data set from Alert spans a whole year including the periods where no ozone depletion events happen, e.g. in summer or in dark winter. Strongly ozone depleted air is seen at temperatures between -10 °C and -35 °C, but not at warmer temperatures, further supporting the findings that there is a threshold for bromine activation and the accompanying ozone depletion.

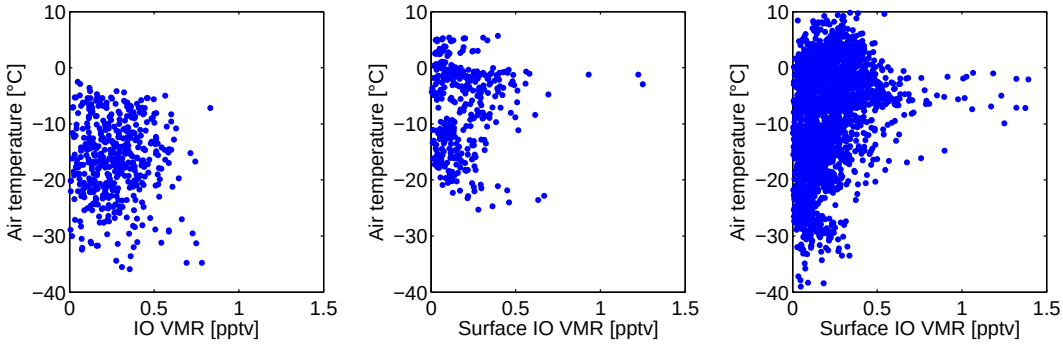

(a) Scott Base **(b)** Polarstern ANT-XXIX/7 **(c)** Alert 2014

Figure 9.17.: IO mixing ratio vs. air temperature: Scatter plots of 1-hour averages for the three measurement locations of this work. **(a)** Scott Base, LP-DOAS **(b)** Polarstern expedition ANT-XXIX/7, MAX-DOAS **(c)** Alert, MAX-DOAS.

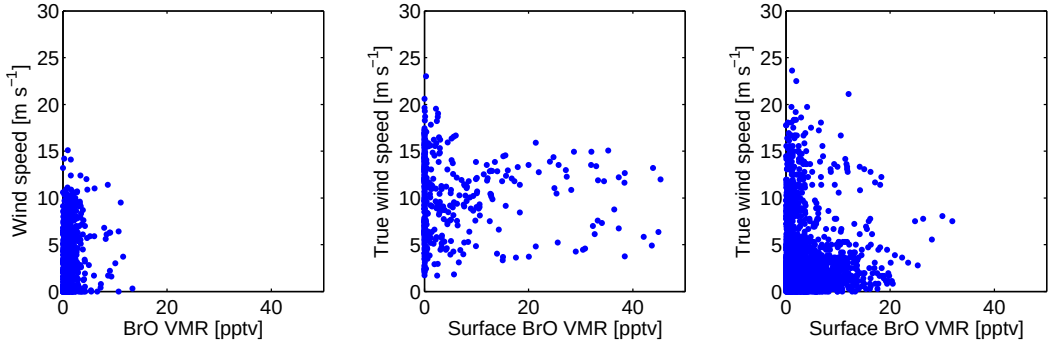

(a) Scott Base **(b)** Polarstern ANT-XXIX/7 **(c)** Alert 2014

Figure 9.18.: BrO mixing ratio vs. wind speed: Scatter plots of 1-hour averages for the three measurement locations of this work. **(a)** Scott Base, LP-DOAS **(b)** Polarstern expedition ANT-XXIX/7, MAX-DOAS **(c)** Alert, MAX-DOAS.

IO

In contrast to the case of BrO formation, for the speciation of IO, so far, no clear temperature dependencies have been published.

At Scott Base, IO mixing ratios seem to be independent of the air temperature. On Polarstern and at Alert, the highest ratios show an almost linear increase up to 0 °C. The few occasions with mixing ratios higher than 0.7 pptv also occur close to that point, between -10 °C and 0 °C. At higher temperatures than 0 °C, the IO mixing ratios appear to decrease again, at least for Alert.

9.7.2 Wind speed

As mentioned in section 2.5.2, most observations of BrO seem to have found higher amounts of BrO during stable meteorological conditions including low

wind speeds (Simpson et al., 2007b, and references therein). Exceptions to this, however, have also been observed, as Friess et al. (2011) found the highest values during conditions of blowing snow, the argument being that the bromine could be better released into the air when the snow was blowing over the surface.

In order to analyze this, scatter plots of 1h-averages of the BrO mixing ratios against the wind speed are given in fig. 9.18 for the three measurement locations. As can be seen, the behavior is different for the different locations. At Scott Base, BrO mixing ratios are largely unaffected by the wind. During Polarstern ANT-XXIX/7, there were no periods without wind, therefore it is difficult to exclude possibly even higher ratios during windless conditions. The mixing ratios, however, seem to be unaffected by wind speeds up to $15\,\mathrm{m\,s^{-1}}$.

At Alert, the BrO mixing ratios generally seem to be higher the lower the wind speeds, thereby following the majority of previous measurements. The highest mixing ratios are however observed at $7\,\mathrm{m\,s^{-1}}$ - $8\,\mathrm{m\,s^{-1}}$. Therefore both scenarios previously described in the literature were observed in this work as well.

9.8 The role of $\mathrm{NO_x}$

Due to its content of nitrates, the snowpack is known to feature an active $\mathrm{NO_x}$ chemistry in its interstitial air, which possibly also aids the release of reactive halogens (e.g. Grannas et al., 2007; Custard et al., 2015). On the other hand, higher concentrations of $\mathrm{NO_2}$ can act as a sink for reactive halogen species via the formation of halogen nitrates (via reaction R11 and its equivalents for IO and ClO). The halogen nitrates can possibly facilitate the deposition of the halogens into surface layers or aerosols. Therefore, lower levels of halogen oxides would be expected at higher $\mathrm{NO_2}$ levels. This has been observed, e.g., at Barrow (Alaska, USA) in the Arctic, where anthropogenic $\mathrm{NO_2}$ emission plumes led to the local

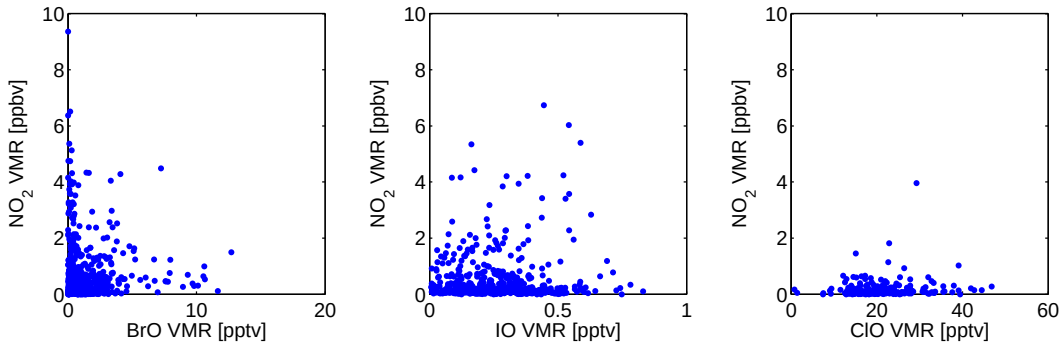

(a) BrO **(b)** IO **(c)** ClO

Figure 9.19.: Scott Base LP-DOAS: Halogen oxides vs. $\mathrm{NO_2}$ mixing ratios: Scatter plots of 1-hour averages for **(a)** BrO, **(b)** IO and **(c)** ClO.

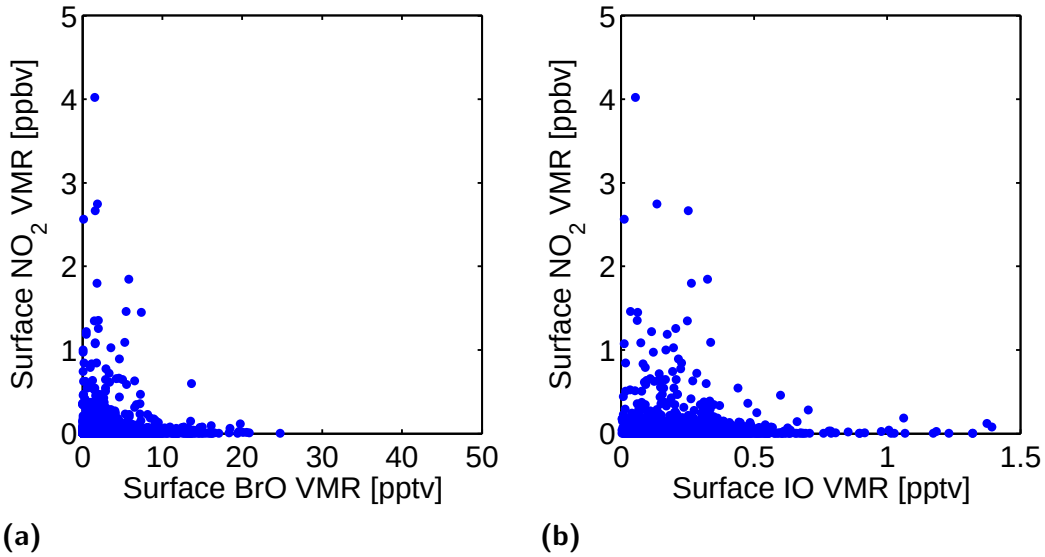

Figure 9.20.: Alert MAX-DOAS: Halogen oxides vs. NO_2 mixing ratios: Scatter plots of 1-hour averages for the year 2014 for **(a)** BrO and **(b)** IO.

decrease of BrO mixing ratios (Custard et al., 2015).

An analysis for the data of this work, in scatter plots of 1h averages, is given in fig. 9.19 for the Scott Base data for BrO, IO and ClO, and in fig. 9.20 for Alert for BrO and IO. The bulk of the measurements follows the expected behavior. The highest mixing ratios of halogen oxides are observed at low NO_2 concentrations, whereas at high NO_2 concentrations, levels of halogen oxides are typically low.

This is however not always the case, as for example seen in fig. 9.19b, where even at several ppbv of NO_2, IO seems to be not significantly diminished. An explanation for this is most likely the very localized sources of pollution at Scott Base, affecting only parts of the sampled air mass and leading to the impression of seeing both, halogen oxides and NO_2, simultaneously. This can not be excluded in the other cases as well, i.e. that only very localized NO_2 plumes traversed the light paths of the instruments and therefore also only affected the halogens within the plume region. The ones outside the plume in this case would be undisturbed by this.

10
Conclusions and Outlook

10.1 Conclusions

In the course of this work, studies were undertaken to improve the knowledge of reactive halogen species within the polar troposphere. To attain this goal, both methodological improvements, as well as field observations were successfully conducted.

Conclusions related to the applied DOAS methodologies

The two most important methodological advances attained within this work are:

- A CE-DOAS instrument was extensively modified, in order to withstand the polar environment and achieve detection limits for IO of approximately 1 pptv. The aim was to study potential local sources of IO, such as the snow pack, sea ice algae or penguin colonies. As a simplification for the deployment in the field, a novel system for the necessary wavelength-resolved determination of the length of the light path was developed and implemented. This was done by applying a tiltable interference filter as the wavelength-discriminating element and recoding ring-down curves with a photomultiplier tube. A comparison of the results from this technique, and the previously common method using different Rayleigh scatterers (air versus helium), shows a good agreement within measurement errors. This novel method can be easily automated and does not require compressed gas cylinders, which classify as dangerous goods and are therefore cumbersome at remote locations.
- Several MAX-DOAS observations were undertaken and evaluated within this work. The inversion algorithm applied on the measured SCDs, by

utilizing a radiative transfer model, in order to gain vertical profiles of aerosol extinction and trace gas mixing ratios was systematically characterized for the first time. This was done by simulating SCDs for four realistic profile shapes, which were then in turn input into the aerosol and trace gas inversion algorithm. The results not only show a generally good reproduction of the input profile shapes by the MAX-DOAS technique, but also the sensitivity of the involved input parameters. Of those, the most important ones for the trace gas inversion are the accuracy of the instrument's elevation angle and the set parameters of the a priori profile. Those are also important for the aerosol inversion, for which furthermore the surface albedo, the aerosol asymmetry parameter, the absolute magnitude of the O_4 absorption cross section and the dependence of the weighting functions on the current state need to be accurately considered.

Conclusions related to the halogen chemistry in the polar troposphere

Two extensive field studies were undertaken in the Antarctic during austral spring, each spanning several months, first at the New Zealand research station Scott Base in coastal Antarctica, and later aboard R/V Polarstern during expedition ANT-XXIX/7 in the Weddell Sea. Additionally, seven years of data from long-term MAX-DOAS measurements in the high Canadian Arctic at Alert were analyzed. The entirety of those measurements increases the amount of available data on halogens in the polar troposphere significantly. The most important results of those field studies are listed below:

- At Scott Base, ClO was observed in the Antarctic boundary layer for the first time. Only two previous observations of ClO in the boundary layer exist, one in the Arctic (Tuckermann et al., 1997) and one above a mid-latitude salt lake (Stutz et al., 2002). Moreover, BrO, IO and ClO were simultaneously measured for the first time anywhere on Earth. The ClO mixing ratios ranged up to 60 pptv, with values most commonly around 20 pptv. They also showed a strong diurnal cycle, with a maximum at solar noon and a minimum at highest solar zenith angles. These properties strongly suggest, that the release mechanism that was previously proposed to explain laboratory studies of ClO release from artificial snow doped with sea salt (Wren et al., 2013), has also been observed to occur in a natural environment. The release of ClO as a by-product of bromine chemistry, on the other hand, e.g. by the reaction of HOBr with Cl^- can be discounted, due to the missing correlation between BrO and ClO, as well as the significantly lower mixing ratios of BrO compared to ClO. BrO, in contrast, exhibited a maximum in the morning after sunrise, and a smaller secondary maximum before sunset, with lower values during the day. BrO was not detected during the night. IO showed less of a diurnal variation and can be observed even with the sun below the horizon at SZAs up to

100 °. This indicates that solar radiation is not the limiting factor of its daily mixing ratios. Its diurnal cycle though shows two distinct dips during sunrise and sunset, possibly due to the concurrent BrO maxima, with BrO pulling down IO levels to a lower steady-state because of inter-halogen reactions. Of the halogen dioxides, OClO, OBrO and OIO, none was positively identified, even during the darker periods in early spring, with respective detection limits of 0.7 pptv, 0.7 pptv and 0.8 pptv.

- The observations aboard R/V Polarstern reflect the results attained at Scott Base in terms of IO. Surprisingly, during both field studies, IO was not observed with the CE-DOAS instrument above its detection limit of 0.8 pptv - 3 pptv. Both locations, the Ross Sea and the Weddell Sea area were previously described as iodine chemistry hot spots, of which IO mixing ratios of 5 pptv - 10 pptv were reported (Saiz-Lopez et al., 2012). Measurements were undertaken at several sites, which were previously considered to be potential iodine sources. Those locations included coastal sites, sea ice, a chamber study in a pit in the snow pack, as well as a penguin colony.

- The LP-DOAS and MAX-DOAS observations at Scott Base however, found IO in the range of 0 pptv - 0.5 pptv, therefore below the CE-DOAS detection limit. A comparison of the surface values of both techniques, while sampling slightly different air masses, further showed a good agreement. The MAX-DOAS results from R/V Polarstern, in the range of 0 pptv - 0.5 pptv as well, and most commonly around 0.2 pptv, are highly similar. This indicates, together with the CE-DOAS upper limits, a homogeneous distribution of IO at the studied locations on a scale of the order of 10 km.

- The Alert dataset was evaluated for SCDs and mixing ratios of BrO, IO and NO_2. The results show the presence of IO in the Arctic with unprecedented accuracy. The derived mixing ratios exhibit a yearly cycle with a maximum in summer and, tentatively, a secondary one in autumn. The mixing ratios are highly similar to those seen at the two studied Antarctic sites with values most commonly around 0.2 pptv and a range of 0 pptv - 0.5 pptv. The supplementary data, from R/V Polarstern cruise ARK-XXV and the satellite instrument GOME-2a, reveal a consistent picture and show that the observed IO is indeed not a local effect, but in fact widespread over large areas of the Arctic in Baffin Bay and the Fram Strait and along the coast of Greenland. Comparing the monthly mean gas phase IO and BrO mixing ratios at Alert with previously published aerosol composition studies (Barrie and Barrie, 1990) shows a correlation between BrO and aerosol Br^- content, but an anti-correlation between IO and aerosol total iodine content.

- The strong discrepancy in (the few) previous studies of iodine levels between

the Arctic and Antarctic could not be observed. Contrarily, the highly similar IO mixing ratios at all three sites studied within this work hint at a similar source and less differences between the chemistry of iodine in both polar regions than previously thought. An estimate, based on previously published studies of iodine release from the ocean (Carpenter et al., 2013; Lampel, 2014), shows the compatibility of the observed mixing ratios with an inorganic, oceanic source of I_2 derived from sea water iodide.

- The observations of BrO within this work are comparable to previously published research and corroborate the notion that sea ice is an important factor in the release of bromine. At Scott Base and in the Weddell Sea, the air masses containing BrO were coming from sea ice-covered areas, whereas air masses from the continent or the open ocean were devoid of BrO.

Finally, the joint studies presented in this work (in detail in chapter 9) offer a more complete picture of the reactive halogen chemistry in both, the Arctic and the Antarctic, and reveal more similarities amongst the two regions than differences.

10.2 Outlook

While the above mentioned results of this work have answered several important questions, they also throw up further questions relating to the applied methodology and the chemistry of halogens in polar regions.

In terms of the MAX-DOAS inversion, the mentioned importance of the surface albedo could be addressed by retrieving this information from polarimetric MAX-DOAS measurements in the future (Udo Frieß, personal communication, 2015). Furthermore, 3D radiative transfer models could be used to study the effects of a very inhomogeneous albedo, such as over broken up sea ice.

In terms of ground instrumentation, several improvements would be necessary in further studies. For long-term LP-DOAS observations of ClO, a brighter, long-lasting light source in the ultraviolet would be necessary, of which currently unfortunately few, if any viable options are commercially available. Eger (2014) found that major improvements of the signal-to-noise ratio are also possible by using an altered configuration of the fiber setup of the LP-DOAS system. This modification should therefore be implemented in all future studies. Laboratory absorption cross sections of O_3 and O_2 with a high signal-to-noise ratio in the spectral range from 250 nm - 300 nm would help to evaluate ClO in this region, as well as other trace gases.

For the CE-DOAS instrument, with IO concentrations now known to be mostly more than an order of magnitude smaller than previously assumed, the detection limit would have to improve drastically from 1 pptv to at least 0.1 pptv in order to try to locate sources at those amounts. This can only be achieved by a combination of significantly longer light paths using resonator mirrors with

an even higher reflectivity, as well as utilizing spectrometers with a higher light throughput (f-number) and a more sensitive detector, e.g. a back-thinned CCD camera. Of course, the question is whether there are any local sources of iodine at all or whether the ocean or ice algae simply form a large, spread out, continuous source.

ClO was only observed during a ten day period. It is therefore uncertain how representative those measurements are. It is further unclear, whether this is a special local phenomenon, or happens all over the sea ice zone around the continent. Of special interest would be whether it is also present when the bromine chemistry is most active, starting with the first rays of light after polar night. In that case, it could contribute significantly to ozone destroying mechanisms. From the observations in this work, which show a strong dependence on the solar irradiation, this seems to be unlikely, though has to be shown in further studies.

The observed IO mixing ratios are highly similar at all three measurement locations studied within this work, but further (long-term) studies at the same locations where the previously reported high concentrations were found could show if those are only local effects and not representative.

The feasibility of retrieving IO VCDs using the GOME-2 instrument was shown in a first case study. Since the only instrument with which IO satellite maps have been created in the past (Schönhardt et al., 2008, 2012), SCIAMACHY, went out in April 2012, this could pave the way for further global maps spanning several more years.

Lastly, to determine the impact of the simultaneous presence of BrO, IO and ClO, as well as their actual interaction and sink mechanisms, chemical modeling is needed. For this to be realistic, it is necessary that several reaction rate coefficients, branching ratios and photolysis quantum yields are accurately determined in laboratory studies. This is especially the case for iodine chemistry, and here in particular for the fate of OIO, which plays a crucial role for the mechanisms involving iodine and is still a major unknown.

Bibliography

Abbatt, J. P. D., Thomas, J. L., Abrahamsson, K., Boxe, C., Granfors, A., Jones, A. E., King, M. D., Saiz-Lopez, A., Shepson, P. B., Sodeau, J., Toohey, D. W., Toubin, C., von Glasow, R., Wren, S. N., and Yang, X.: Halogen activation via interactions with environmental ice and snow in the polar lower troposphere and other regions, Atmospheric Chemistry and Physics, 12, 6237–6271, doi:10.5194/acp-12-6237-2012, 2012.

Adams, J. W., Holmes, N. S., and Crowley, J. N.: Uptake and reaction of HOBr on frozen and dry NaCl/NaBr surfaces between 253 and 233 K, Atmospheric Chemistry and Physics, 2, 79–91, doi:10.5194/acp-2-79-2002, 2002.

Ainley, D.: The Adélie Penguin: Bellwether of Climate Change, Columbia University Press, New York, 2002.

Alicke, B., Hebestreit, K., Stutz, J., and Platt, U.: Iodine oxide in the marine boundary layer, Nature, 397, 572–573, doi:10.1038/17508, 1999.

AMAP: AMAP Assessment 2009: Human Health in the Arctic, Arctic Monitoring and Assessment Programme (AMAP), Oslo, Norway, 2009.

AMAP: AMAP Assessment 2011: Mercury in the Arctic, Arctic Monitoring and Assessment Programme (AMAP), Oslo, Norway, 2011.

Ammann, M., Cox, R. A., Crowley, J. N., Jenkin, M. E., Mellouki, A., Rossi, M. J., Troe, J., and Wallington, T. J.: Evaluated kinetic and photochemical data for atmospheric chemistry: Volume VI - heterogeneous reactions with liquid substrates, Atmospheric Chemistry and Physics, 13, 8045–8228, doi:10.5194/acp-13-8045-2013, 2013.

Anderson, P. S. and Neff, W. D.: Boundary layer physics over snow and ice, Atmospheric Chemistry and Physics, 8, 3563–3582, doi:10.5194/acp-8-3563-2008, 2008.

Ångström, A.: On the Atmospheric Transmission of Sun Radiation and on Dust in the Air, Geografiska Annaler, 11, 156–166, 1929.

Anthofer, M. S.: Cavity Enhanced DOAS Measurements of Iodine Oxide, Diplomarbeit, Diplomarbeit, Institute of Environmental Physics, University of Heidelberg, Germany, 2013.

Ashworth, S. H., Allan, B. J., and Plane, J. M. C.: High resolution spectroscopy of the OIO radical: Implications for the ozone-depleting potential of iodine, Geophysical Research Letters, 29, 95–1–95–4, doi:10.1029/2001GL013851, 2002.

Atkinson, H. M., Huang, R.-J., Chance, R., Roscoe, H. K., Hughes, C., Davison, B., Schönhardt, A., Mahajan, A. S., Saiz-Lopez, A., Hoffmann, T., and Liss, P. S.: Iodine emissions from the sea ice of the Weddell Sea, Atmospheric Chemistry and Physics, 12, 11 229–11 244, doi:10.5194/acp-12-11229-2012, 2012.

Atkinson, R., Baulch, D. L., Cox, R. A., Crowley, J. N., Hampson, R. F., Hynes, R. G., Jenkin, M. E., Rossi, M. J., and Troe, J.: Evaluated kinetic and photochemical data for atmospheric chemistry: Volume III - gas phase reactions of inorganic halogens, Atmospheric Chemistry and Physics, 7, 981–1191, doi:10.5194/acp-7-981-2007, 2007.

Barber, R. J., Tennyson, J., Harris, G. J., and Tolchenov, R. N.: A high-accuracy computed water line list, Monthly Notices of the Royal Astronomical Society, 368, 1087–1094, doi:10.1111/j.1365-2966.2006.10184.x, 2006.

Barnes, I., Hjorth, J., and Mihalopoulos, N.: Dimethyl Sulfide and Dimethyl Sulfoxide and Their Oxidation in the Atmosphere, Chemical Reviews, 106, 940–975, doi:10.1021/cr020529+, 2006.

Barrie, L. and Barrie, M.: Chemical components of lower tropospheric aerosols in the high arctic: Six years of observations, Journal of Atmospheric Chemistry, 11, 211–226, doi:10.1007/BF00118349, 1990.

Barrie, L. and Platt, U.: Arctic tropospheric chemistry: an overview, Tellus B, 49, 450–454, doi:10.1034/j.1600-0889.49.issue5.2.x, 1997.

Barrie, L. A., Bottenheim, J. W., Schnell, R. C., Crutzen, P. J., and Rasmussen, R. A.: Ozone destruction and photochemical reactions at polar sunrise in the lower Arctic atmosphere, Nature, 334, 138–141, 1988.

Bedjanian, Y., Le Bras, G., and Poulet, G.: Kinetics and Mechanism of the IO + BrO Reaction, The Journal of Physical Chemistry A, 102, 10 501–10 511, doi:10.1021/jp982972n, 1998.

Berg, W. W., Sperry, P. D., Rahn, K. A., and Gladney, E. S.: Atmospheric bromine in the Arctic, Journal of Geophysical Research: Oceans, 88, 6719–6736, doi:10.1029/JC088iC11p06719, 1983.

Birks, J. W., Shoemaker, B., Leck, T. J., Borders, R. A., and Hart, L. J.: Studies of reactions of importance in the stratosphere. II. Reactions involving chlorine nitrate and chlorine dioxide, The Journal of Chemical Physics, 66, 4591–4599, doi:10.1063/1.433716, 1977.

Bobrowski, N., Honninger, G., Galle, B., and Platt, U.: Detection of bromine monoxide in a volcanic plume, Nature, 423, 273–276, doi:10.1038/nature01625, 2003.

Bogumil, K., Orphal, J., Homann, T., Voigt, S., Spietz, P., Fleischmann, O., Vogel, A., Hartmann, M., Kromminga, H., Bovensmann, H., Frerick, J., and Burrows, J.: Measurements of molecular absorption spectra with the SCIAMACHY pre-flight model: instrument characterization and reference data for atmospheric remote-sensing in the 230 - 2380 nm region, Journal of Photochemistry and Photobiology A: Chemistry, 157, 167 – 184, doi:10.1016/S1010-6030(03)00062-5, 2003.

Bottenheim, J. W., Gallant, A. G., and Brice, K. A.: Measurements of NOy species and O3 at 82 degree N latitude, Geophysical Research Letters, 13, 113–116, doi:10.1029/GL013i002p00113, 1986.

Bryukov, M. G., Slagle, I. R., and Knyazev, V. D.: Kinetics of Reactions of Cl Atoms with Methane and Chlorinated Methanes, The Journal of Physical Chemistry A, 106, 10 532–10 542, doi:10.1021/jp0257909, 2002.

Burrows, J., Richter, A., Dehn, A., Deters, B., Himmelmann, S., Voigt, S., and Orphal, J.: Atmospheric remote-sensing reference data from GOME-2. Temperature-dependent absorption cross sections of O3 in the 231 - 794 nm range, Journal of Quantitative Spectroscopy and Radiative Transfer, 61, 509 – 517, doi:10.1016/S0022-4073(98)00037-5, 1999.

Butkovskaya, N., Morozov, I., Tal'rose, V., and Vasiliev, E.: Kinetic studies of the bromine-oxygen system: A new paramagnetic particle, BrO2, Chemical Physics, 79, 21 – 30, doi:10.1016/0301-0104(83)85135-0, 1983.

Buxmann, J.: 'Bromine and chlorine explosion' in a simulated atmosphere, Ph.D. thesis, Heidelberg, Univ., Diss., 2012, URL `http://archiv.ub.uni-heidelberg.de/volltextserver/volltexte/2012/13655`, 2012.

Buys, Z., Brough, N., Huey, L. G., Tanner, D. J., von Glasow, R., and Jones, A. E.: High temporal resolution Br2, BrCl and BrO observations in coastal Antarctica, Atmospheric Chemistry and Physics, 13, 1329–1343, doi:10.5194/acp-13-1329-2013, 2013.

Calvert, J. G. and Lindberg, S. E.: Potential influence of iodine-containing compounds on the chemistry of the troposphere in the polar spring. I. Ozone

depletion, Atmospheric Environment, 38, 5087 – 5104, doi:10.1016/j.atmosenv.2004.05.049, 2004.

Cao, L., Sihler, H., Platt, U., and Gutheil, E.: Numerical analysis of the chemical kinetic mechanisms of ozone depletion and halogen release in the polar troposphere, Atmospheric Chemistry and Physics, 14, 3771–3787, doi:10.5194/acp-14-3771-2014, 2014.

Carpenter, L. J., MacDonald, S. M., Shaw, M. D., Kumar, R., Saunders, R. W., Parthipan, R., Wilson, J., and Plane, J. M. C.: Atmospheric iodine levels influenced by sea surface emissions of inorganic iodine, Nature Geosci, 6, 108–111, doi:10.1038/ngeo1687, 2013.

Chameides, W. L. and Davis, D. D.: Iodine: Its possible role in tropospheric photochemistry, Journal of Geophysical Research: Oceans, 85, 7383–7398, doi:10.1029/JC085iC12p07383, 1980.

Chance, K. and Kurucz, R.: An improved high-resolution solar reference spectrum for earth's atmosphere measurements in the ultraviolet, visible, and near infrared, Journal of Quantitative Spectroscopy and Radiative Transfer, 111, 1289 – 1295, doi:10.1016/j.jqsrt.2010.01.036, 2010.

Chance, K. V. and Spurr, R. J. D.: Ring effect studies: Rayleigh scattering, including molecular parameters for rotational Raman scattering, and the Fraunhofer spectrum, Appl. Opt., 36, 5224–5230, doi:10.1364/AO.36.005224, 1997.

Chance, R., Baker, A. R., Carpenter, L., and Jickells, T. D.: The distribution of iodide at the sea surface, Environ. Sci.: Processes Impacts, 16, 1841–1859, doi:10.1039/C4EM00139G, 2014.

Charlson, R. J., Lovelock, J. E., Andreae, M. O., and Warren, S. G.: Oceanic phytoplankton, atmospheric sulphur, cloud albedo and climate, Nature, 326, 655–661, doi:10.1038/326655a0, 1987.

Chipperfield, M. P., Glassup, T., Pundt, I., and Rattigan, O. V.: Model calculations of stratospheric OBrO indicating very small abundances, Geophysical Research Letters, 25, 3575–3578, doi:10.1029/98GL02759, 1998.

Clémer, K., Van Roozendael, M., Fayt, C., Hendrick, F., Hermans, C., Pinardi, G., Spurr, R., Wang, P., and De Mazière, M.: Multiple wavelength retrieval of tropospheric aerosol optical properties from MAXDOAS measurements in Beijing, Atmospheric Measurement Techniques, 3, 863–878, doi:10.5194/amt-3-863-2010, 2010.

Custard, K. D., Thompson, C. R., Pratt, K. A., Shepson, P. B., Liao, J., Huey, L. G., Orlando, J. J., Weinheimer, A. J., Apel, E., Hall, S. R., Flocke, F.,

Mauldin, L., Hornbrook, R. S., Pöhler, D., General, S., Zielcke, J., Simpson, W. R., Platt, U., Fried, A., Weibring, P., Sive, B. C., Ullmann, K., Cantrell, C., Knapp, D. J., and Montzka, D. D.: The NO_x dependence of bromine chemistry in the Arctic atmospheric boundary layer, Atmospheric Chemistry and Physics Discussions, 15, 8329–8360, doi:10.5194/acpd-15-8329-2015, 2015.

DeFelice, T.: Chemical composition of fresh snowfalls at Palmer Station, Antarctica, Atmospheric Environment, 33, 155 – 161, doi:10.1016/S1352-2310(98)80003-4, 1998.

Deutschmann, T., Beirle, S., Friess, U., Grzegorski, M., Kern, C., Kritten, L., Platt, U., Prados-Roman, C., Pukite, J., Wagner, T., Werner, B., and Pfeilsticker, K.: The Monte Carlo atmospheric radiative transfer model McArtim: Introduction and validation of Jacobians and 3D features, Journal of Quantitative Spectroscopy and Radiative Transfer, 112, 1119 – 1137, doi:10.1016/j.jqsrt.2010.12.009, 2011.

Dixneuf, S., Ruth, A. A., Vaughan, S., Varma, R. M., and Orphal, J.: The time dependence of molecular iodine emission from Laminaria digitata, Atmospheric Chemistry and Physics, 9, 823–829, doi:10.5194/acp-9-823-2009, 2009.

Domine, F., Sparapani, R., Ianniello, A., and Beine, H. J.: The origin of sea salt in snow on Arctic sea ice and in coastal regions, Atmospheric Chemistry and Physics, 4, 2259–2271, doi:10.5194/acp-4-2259-2004, 2004.

Eger, P.: Improving Long-Path DOAS measurements with a Laser Driven Light Source and a new fibre configuration, Master's thesis, Institute of Environmental Physics, University of Heidelberg, Germany, 2014.

Emison, W. B.: Antarctic Bird Studies, chap. Feeding Preferences of the Adélie Penguin at Cape Crozier, Ross Island, in Antarctic Bird Studies (ed O. L. Austin), pp. 191–212, American Geophysical Union, doi:10.1029/AR012p0191, 1968.

Erle, F., Platt, U., and Pfeilsticker, K.: Measurement of OBrO upper limits in the nighttime stratosphere, Geophysical Research Letters, 27, 2217–2220, doi:10.1029/2000GL011532, 2000.

Fan, S.-M. and Jacob, D. J.: Surface ozone depletion in Arctic spring sustained by bromine reactions on aerosols, Nature, 359, 522–524, doi:10.1038/359522a0, 1992.

Farman, J. C., Gardiner, B. G., and Shanklin, J. D.: Large losses of total ozone in Antarctica reveal seasonal ClOx/NOx interaction, Nature, 315, 207–210, doi:10.1038/315207a0, 1985.

Fickert, S., Adams, J. W., and Crowley, J. N.: Activation of Br2 and BrCl via uptake of HOBr onto aqueous salt solutions, Journal of Geophysical Research: Atmospheres, 104, 23 719–23 727, doi:10.1029/1999JD900359, 1999.

Fiedler, S. E.: Incoherent Broad-Band Cavity-Enhanced Absorption Spectroscopy, Ph.D. thesis, Technische Universität Berlin, 2005.

Fleischmann, O. C. and Burrows, J. P.: OBrO absorption measurements using a Fourier transform spectrometer, spectral resolution 10 cm-1 (vacuum wavelengths), unpublished results, data from http://www.iup.physik.uni-bremen.de/gruppen/molspec/index.html, University of Bremen, Germany, URL `http://www.iup.physik.uni-bremen.de/gruppen/molspec/index.html`, 2002.

Fleischmann, O. C., Hartmann, M., Burrows, J. P., and Orphal, J.: New ultraviolet absorption cross-sections of BrO at atmospheric temperatures measured by time-windowing Fourier transform spectroscopy, Journal of Photochemistry and Photobiology A: Chemistry, 168, 117 – 132, doi:10.1016/j.jphotochem.2004.03.026, 2004.

Fogelqvist, E. and Tanhua, T.: Iodinated C1-C4 hydrocarbons released from ice algae in Antarctica, in: Naturally-Produced Organohalogens, edited by Grimvall, A. and de Leer, E., vol. 1 of *Environment & Chemistry*, pp. 295–305, Springer Netherlands, doi:10.1007/978-94-011-0061-8_27, 1995.

Foster, K. L., Plastridge, R. A., Bottenheim, J. W., Shepson, P. B., Finlayson-Pitts, B. J., and Spicer, C. W.: The Role of Br2 and BrCl in Surface Ozone Destruction at Polar Sunrise, Science, 291, 471–474, doi:10.1126/science.291.5503.471, 2001.

Friess, U., Wagner, T., Pundt, I., Pfeilsticker, K., and Platt, U.: Spectroscopic measurements of tropospheric iodine oxide at Neumayer Station, Antarctica, Geophysical Research Letters, 28, 1941–1944, doi:10.1029/2000GL012784, 2001.

Friess, U., Hollwedel, J., Koenig-Langlo, G., Wagner, T., and Platt, U.: Dynamics and chemistry of tropospheric bromine explosion events in the Antarctic coastal region, Journal of Geophysical Research: Atmospheres, 109, doi:10.1029/2003JD004133, 2004.

Friess, U., Deutschmann, T., Gilfedder, B. S., Weller, R., and Platt, U.: Iodine monoxide in the Antarctic snowpack, Atmospheric Chemistry and Physics, 10, 2439–2456, doi:10.5194/acp-10-2439-2010, 2010.

Friess, U., Sihler, H., Sander, R., Poehler, D., Yilmaz, S., and Platt, U.: The vertical distribution of BrO and aerosols in the Arctic: Measurements by active

and passive differential optical absorption spectroscopy, Journal of Geophysical Research: Atmospheres, 116, doi:10.1029/2011JD015938, 2011.

Fussen, D., Vanhellemont, F., Dodion, J., Bingen, C., Mateshvili, N., Daerden, F., Fonteyn, D., Errera, Q., Chabrillat, S., Kyrölä, E., Tamminen, J., Sofieva, V., Hauchecorne, A., Dalaudier, F., Bertaux, J.-L., Renard, J.-B., Fraisse, R., d'Andon, O. F., Barrot, G., Guirlet, M., Mangin, A., Fehr, T., Snoeij, P., and Saavedra, L.: A global OClO stratospheric layer discovered in GOMOS stellar occultation measurements, Geophysical Research Letters, 33, doi:10.1029/2006GL026406, 2006.

Gilles, M. K., Turnipseed, A. A., , Ravishankara, A. R., and Solomon, S.: Kinetics of the IO Radical. 2. Reaction of IO with BrO, The Journal of Physical Chemistry A, 101, 5526–5534, doi:10.1021/jp9709159, 1997.

Grainger, J. F. and Ring, J.: Anomalous Fraunhofer Line Profiles, Nature, 193, 762–762, doi:10.1038/193762a0, 1962.

Granfors, A., Andersson, M., Chierici, M., Fransson, A., Gardfeldt, K., Torstensson, A., Wulff, A., and Abrahamsson, K.: Biogenic halocarbons in young Arctic sea ice and frost flowers, Marine Chemistry, 155, 124 – 134, doi:10.1016/j.marchem.2013.06.002, 2013.

Grannas, A. M., Jones, A. E., Dibb, J., Ammann, M., Anastasio, C., Beine, H. J., Bergin, M., Bottenheim, J., Boxe, C. S., Carver, G., Chen, G., Crawford, J. H., Dominé, F., Frey, M. M., Guzmán, M. I., Heard, D. E., Helmig, D., Hoffmann, M. R., Honrath, R. E., Huey, L. G., Hutterli, M., Jacobi, H. W., Klán, P., Lefer, B., McConnell, J., Plane, J., Sander, R., Savarino, J., Shepson, P. B., Simpson, W. R., Sodeau, J. R., von Glasow, R., Weller, R., Wolff, E. W., and Zhu, T.: An overview of snow photochemistry: evidence, mechanisms and impacts, Atmospheric Chemistry and Physics, 7, 4329–4373, doi:10.5194/acp-7-4329-2007, 2007.

Greenblatt, G. D., Orlando, J. J., Burkholder, J. B., and Ravishankara, A. R.: Absorption measurements of oxygen between 330 and 1140 nm, Journal of Geophysical Research: Atmospheres, 95, 18 577–18 582, doi:10.1029/JD095iD11p18577, 1990.

Großmann, K., Friess, U., Peters, E., Wittrock, F., Lampel, J., Yilmaz, S., Tschritter, J., Sommariva, R., von Glasow, R., Quack, B., Krüger, K., Pfeilsticker, K., and Platt, U.: Iodine monoxide in the Western Pacific marine boundary layer, Atmospheric Chemistry and Physics, 13, 3363–3378, doi:10.5194/acp-13-3363-2013, 2013.

Hara, K., Osada, K., Yabuki, M., and Yamanouchi, T.: Seasonal variation of fractionated sea-salt particles on the Antarctic coast, Geophysical Research Letters, 39, doi:10.1029/2012GL052761, 2012.

Harwood, M. H., Burkholder, J. B., Hunter, M., Fox, R. W., and Ravishankara, A. R.: Absorption Cross Sections and Self-Reaction Kinetics of the IO Radical, The Journal of Physical Chemistry A, 101, 853–863, doi:10.1021/jp962429b, 1997.

Hausmann, M. and Platt, U.: Spectroscopic measurement of bromine oxide and ozone in the high Arctic during Polar Sunrise Experiment 1992, Journal of Geophysical Research: Atmospheres, 99, 25 399–25 413, doi:10.1029/94JD01314, 1994.

Hebestreit, K., Stutz, J., Rosen, D., Matveiv, V., Peleg, M., Luria, M., and Platt, U.: DOAS Measurements of Tropospheric Bromine Oxide in Mid-Latitudes, Science, 283, 55–57, doi:10.1126/science.283.5398.55, 1999.

Helmschmidt, J.: Spektroskopische Messung von Spurengasen in der arktischen Atmosphäre, Master's thesis, Diplomarbeit, Institute of Environmental Physics, University of Heidelberg, Germany, zsfassung in engl. Sprache, 2008.

Henyey, L.-G. and Greenstein, J.-L.: Diffuse radiation in the Galaxy, Astrophysical Journal, 93, 70–83, doi:10.1086/144246, 1941.

Hermans, C., Vandaele, A., Fally, S., Carleer, M., Colin, R., Coquart, B., Jenouvrier, A., and Merienne, M.-F.: Absorption Cross-section of the Collision-Induced Bands of Oxygen from the UV to the NIR, in: Weakly Interacting Molecular Pairs: Unconventional Absorbers of Radiation in the Atmosphere, edited by Camy-Peyret, C. and Vigasin, A., vol. 27 of *NATO Science Series*, pp. 193–202, Springer Netherlands, doi:10.1007/978-94-010-0025-3_16, 2003.

Heumann, K., Gall, M., and H., W.: Geochemical investigations to explain iodine-overabundances in Antarctic meteorites, Geochimica et Cosmochimica Acta, 51, 2541 – 2547, doi:10.1016/0016-7037(87)90304-8, 1987.

Heumann, K., Neubauer, J., and Reifenhäuser, W.: Iodine overabundances measured in the surface layers of an antarctic stony and iron meteorite, Geochimica et Cosmochimica Acta, 54, 2503 – 2506, doi:10.1016/0016-7037(90)90236-E, 1990.

Heumann, K. G.: Determination of inorganic and organic traces in the clean room compartment of Antarctica, Analytica Chimica Acta, 283, 230 – 245, doi:10.1016/0003-2670(93)85227-B, 1993.

Holla, R.: Reactive halogen species above salt lakes and salt pans, Ph.D. thesis, Institute of Environmental Physics, University of Heidelberg, Germany, URL `http://archiv.ub.uni-heidelberg.de/volltextserver/14636/`, 2013.

Holleman, A. F.: Lehrbuch der anorganischen Chemie, Walter de Gruyter, 1995.

Hollwedel, J., Wenig, M., Beirle, S., Kraus, S., Kühl, S., Wilms-Grabe, W., Platt, U., and Wagner, T.: Year-to-year variations of spring time polar tropospheric BrO as seen by GOME, Advances in Space Research, 34, 804 – 808, doi: 10.1016/j.asr.2003.08.060, 2004.

Hönninger, G., Bobrowski, N., Palenque, E. R., Torrez, R., and Platt, U.: Reactive bromine and sulfur emissions at Salar de Uyuni, Bolivia, Geophysical Research Letters, 31, doi:10.1029/2003GL018818, 2004a.

Hönninger, G., Leser, H., Sebastian, O., and Platt, U.: Ground-based measurements of halogen oxides at the Hudson Bay by active longpath DOAS and passive MAX-DOAS, Geophysical Research Letters, 31, doi: 10.1029/2003GL018982, 2004b.

Honrath, R. E., Peterson, M. C., Guo, S., Dibb, J. E., Shepson, P. B., and Campbell, B.: Evidence of NOx production within or upon ice particles in the Greenland snowpack, Geophysical Research Letters, 26, 695–698, doi: 10.1029/1999GL900077, 1999.

Horbanski, M.: A Compact Resonator Based Instrument for DOAS Measurements of Ambient Nitrogen Dioxide, Master's thesis, Diplomarbeit, Institute of Environmental Physics, University of Heidelberg, Germany, zsfassung in engl. Sprache, 2010.

Ingham, T., Cameron, M., and Crowley, J. N.: Photodissociation of IO (355 nm) and OIO (532 nm): Quantum Yields for O(3P) and I(2PJ) Production, The Journal of Physical Chemistry A, 104, 8001–8010, doi:10.1021/jp001166p, 2000.

IPCC: Climate Change 2013: The Physical Science Basis. Contribution of Working Group I to the Fifth Assessment Report of the Intergovernmental Panel on Climate Change, Cambridge University Press, Cambridge, United Kingdom and New York, NY, USA, 2013.

Jacobi, H.-W., Morin, S., and Bottenheim, J. W.: Observation of widespread depletion of ozone in the springtime boundary layer of the central Arctic linked to mesoscale synoptic conditions, Journal of Geophysical Research: Atmospheres, 115, doi:10.1029/2010JD013940, 2010.

Jobson, B. T., Niki, H., Yokouchi, Y., Bottenheim, J., Hopper, F., and Leaitch, R.: Measurements of C2-C6 hydrocarbons during the Polar Sunrise 1992 Experiment: Evidence for Cl atom and Br atom chemistry, Journal of Geophysical Research: Atmospheres, 99, 25 355–25 368, doi:10.1029/94JD01243, 1994.

Jones, A. E., Anderson, P. S., Wolff, E. W., Turner, J., Rankin, A. M., and Colwell, S. R.: A role for newly forming sea ice in springtime polar tropospheric

ozone loss? Observational evidence from Halley station, Antarctica, Journal of Geophysical Research: Atmospheres, 111, doi:10.1029/2005JD006566, 2006.

Jones, A. E., Wolff, E. W., Brough, N., Bauguitte, S. J.-B., Weller, R., Yela, M., Navarro-Comas, M., Ochoa, H. A., and Theys, N.: The spatial scale of ozone depletion events derived from an autonomous surface ozone network in coastal Antarctica, Atmospheric Chemistry and Physics, 13, 1457–1467, doi:10.5194/acp-13-1457-2013, 2013.

Kalnajs, L. E. and Avallone, L. M.: Frost flower influence on springtime boundary-layer ozone depletion events and atmospheric bromine levels, Geophysical Research Letters, 33, doi:10.1029/2006GL025809, 2006.

Kaltsoyannis, N. and Plane, J. M. C.: Quantum chemical calculations on a selection of iodine-containing species (IO, OIO, INO3, (IO)2, I2O3, I2O4 and I2O5) of importance in the atmosphere, Physical Chemistry Chemical Physics, 10, 1723–1733, doi:10.1039/b715687c, 2008.

Keene, W. C., Maben, J. R., Pszenny, A. A. P., and Galloway, J. N.: Measurement technique for inorganic chlorine gases in the marine boundary layer, Environmental Science & Technology, 27, 866–874, doi:10.1021/es00042a008, 1993.

Keil, A. D. and Shepson, P. B.: Chlorine and bromine atom ratios in the springtime Arctic troposphere as determined from measurements of halogenated volatile organic compounds, Journal of Geophysical Research: Atmospheres, 111, doi:10.1029/2006JD007119, 2006.

Kern, C., Trick, S., Rippel, B., and Platt, U.: Applicability of light-emitting diodes as light sources for active differential optical absorption spectroscopy measurements, Appl. Opt., 45, 2077–2088, doi:10.1364/AO.45.002077, 2006.

Kieser, B., Bottenheim, J., Sideris, T., and Niki, H.: Spring 1989 observations of lower tropospheric chemistry in the Canadian high arctic, Atmospheric Environment. Part A. General Topics, 27, 2979 – 2988, doi:10.1016/0960-1686(93)90330-2, 1993.

Koop, T., Kapilashrami, A., Molina, L. T., and Molina, M. J.: Phase transitions of sea-salt/water mixtures at low temperatures: Implications for ozone chemistry in the polar marine boundary layer, Journal of Geophysical Research: Atmospheres, 105, 26 393–26 402, doi:10.1029/2000JD900413, 2000.

Kraus, S.: DOASIS: A framework design for DOAS, Ph.D. thesis, University of Mannheim, 2005.

Kromminga, H., Orphal, J., Spietz, P., Voigt, S., and Burrows, J.: New measurements of OClO absorption cross-sections in the 325 - 435 nm region and their temperature dependence between 213 and 293 K, Journal of Photochemistry and Photobiology A: Chemistry, 157, 149 – 160, doi: 10.1016/S1010-6030(03)00071-6, 2003.

Lampel, J.: Ship-borne MAX-DOAS Measurements of Tropospheric Halogen Oxides on Atlantic Transects, Master's thesis, Diplomarbeit, Institute of Environmental Physics, University of Heidelberg, Germany, 2010.

Lampel, J.: Measurements of reactive trace gases in the marine boundary layer using novel DOAS methods, Ph.D. thesis, Institute of Environmental Physics, University of Heidelberg, Germany, URL `http://archiv.ub.uni-heidelberg.de/volltextserver/17394/`, 2014.

Lampel, J., Frieß, U., and Platt, U.: The impact of vibrational Raman scattering of air on DOAS measurements of atmospheric trace gases, Atmospheric Measurement Techniques Discussions, 8, 3423–3469, doi:10.5194/amtd-8-3423-2015, 2015.

Langhoff, S. R., Jaffe, R. L., and Arnold, J. O.: Effective cross sections and rate constants for predissociation of ClO in the earth's atmosphere, Journal of Quantitative Spectroscopy and Radiative Transfer, 18, 227 – 235, doi: 10.1016/0022-4073(77)90008-5, 1977.

Laxon, S. W., Giles, K. A., Ridout, A. L., Wingham, D. J., Willatt, R., Cullen, R., Kwok, R., Schweiger, A., Zhang, J., Haas, C., and et al.: CryoSat-2 estimates of Arctic sea ice thickness and volume, Geophysical Research Letters, 40, 732–737, doi:10.1002/grl.50193, 2013.

Le Bras, G. and Platt, U.: A possible mechanism for combined chlorine and bromine catalyzed destruction of tropospheric ozone in the Arctic, Geophysical Research Letters, 22, 599–602, doi:10.1029/94GL03334, 1995.

Legrand, M., Gros, V., Preunkert, S., Sarda-Esteve, R., Thierry, A.-M., Pepy, G., and Jourdain, B.: A reassessment of the budget of formic and acetic acids in the boundary layer at Dumont d'Urville (coastal Antarctica): The role of penguin emissions on the budget of several oxygenated volatile organic compounds, Journal of Geophysical Research: Atmospheres, 117, n/a–n/a, doi:10.1029/2011JD017102, 2012.

Lehrer, E., Wagenbach, D., and Platt, U.: Aerosol chemical composition during tropospheric ozone depletion at Ny Alesund/Svalbard, Tellus B, 49, 486–495, doi:10.1034/j.1600-0889.49.issue5.5.x, 1997.

Lehrer, E., Hönninger, G., and Platt, U.: A one dimensional model study of the mechanism of halogen liberation and vertical transport in the polar

troposphere, Atmospheric Chemistry and Physics, 4, 2427–2440, doi:10.5194/acp-4-2427-2004, 2004.

Levenberg, K.: A method for the solution of certain problems in least squares, Quarterly of applied mathematics, 2, 164–168, 1944.

Liao, J., Sihler, H., Huey, L. G., Neuman, J. A., Tanner, D. J., Friess, U., Platt, U., Flocke, F. M., Orlando, J. J., Shepson, P. B., Beine, H. J., Weinheimer, A. J., Sjostedt, S. J., Nowak, J. B., Knapp, D. J., Staebler, R. M., Zheng, W., Sander, R., Hall, S. R., and Ullmann, K.: A comparison of Arctic BrO measurements by chemical ionization mass spectrometry and long path-differential optical absorption spectroscopy, Journal of Geophysical Research: Atmospheres, 116, n/a–n/a, doi:10.1029/2010JD014788, 2011.

Liao, J., Huey, L. G., Liu, Z., Tanner, D. J., Cantrell, C. A., Orlando, J. J., Flocke, F. M., Shepson, P. B., Weinheimer, A. J., Hall, S. R., Ullmann, K., Beine, H. J., Wang, Y., Ingall, E. D., Stephens, C. R., Hornbrook, R. S., Apel, E. C., Riemer, D., Fried, A., Mauldin III, R. L., Smith, J. N., Staebler, R. M., Neuman, J. A., and Nowak, J. B.: High levels of molecular chlorine in the Arctic atmosphere, Nature Geoscience, 7, 91–94, doi:10.1038/ngeo2046, 2014.

Lindberg, S., Bullock, R., Ebinghaus, R., Engstrom, D., Feng, X., Fitzgerald, W., Pirrone, N., Prestbo, E., and Seigneur, C.: A Synthesis of Progress and Uncertainties in Attributing the Sources of Mercury in Deposition, AMBIO: A Journal of the Human Environment, 36, 19–33, doi:10.1579/0044-7447(2007)36[19:ASOPAU]2.0.CO;2, 2007.

Lu, J. Y., Schroeder, W. H., Barrie, L. A., Steffen, A., Welch, H. E., Martin, K., Lockhart, L., Hunt, R. V., Boila, G., and Richter, A.: Magnification of atmospheric mercury deposition to polar regions in springtime: The link to tropospheric ozone depletion chemistry, Geophysical Research Letters, 28, 3219–3222, doi:10.1029/2000GL012603, 2001.

Mahajan, A. S., Shaw, M., Oetjen, H., Hornsby, K. E., Carpenter, L. J., Kaleschke, L., Tian-Kunze, X., Lee, J. D., Moller, S. J., Edwards, P., Commane, R., Ingham, T., Heard, D. E., and Plane, J. M. C.: Evidence of reactive iodine chemistry in the Arctic boundary layer, Journal of Geophysical Research: Atmospheres, 115, doi:10.1029/2009JD013665, 2010.

Marquardt, D. W.: An algorithm for least-squares estimation of nonlinear parameters, Journal of the Society for Industrial & Applied Mathematics, 11, 431–441, 1963.

McElroy, C., McLinden, C., and McConnell, J.: Evidence for bromine monoxide in the free troposphere during the Arctic polar sunrise, Nature, 397, 338–341, 1999.

Meller, R. and Moortgat, G. K.: Temperature dependence of the absorption cross sections of formaldehyde between 223 and 323 K in the wavelength range 225 - 375 nm, Journal of Geophysical Research: Atmospheres, 105, 7089–7101, doi:10.1029/1999JD901074, 2000.

Merten, A.: New Design of Longpath-DOAS instruments based on fibre optics and applications in the study of the urban atmosphere, Ph.D. thesis, Institute of Environmental Physics, University of Heidelberg, Germany, 2008.

Meyer, B. and Auerswald, L.: The expedition of the research vessel "Polarstern" to the Antarctic in 2013 (ANT-XXIX/7), URL `http://hdl.handle.net/10013/epic.43441.d001`, 2014.

Mie, G.: Beiträge zur Optik trüber Medien, speziell kolloidaler Metalllösungen, Annalen der Physik, 330, 377–445, doi:10.1002/andp.19083300302, 1908.

Miller, G. H., Lehman, S. J., Refsnider, K. A., Southon, J. R., and Zhong, Y.: Unprecedented recent summer warmth in Arctic Canada, Geophysical Research Letters, 40, 5745–5751, doi:10.1002/2013GL057188, 2013.

Molina, M. J. and Rowland, F. S.: Stratospheric sink for chlorofluoromethanes: chlorine atom-catalysed destruction of ozone, Nature, 249, 810–812, doi:10.1038/249810a0, 1974.

Morin, S., Marion, G. M., von Glasow, R., Voisin, D., Bouchez, J., and Savarino, J.: Precipitation of salts in freezing seawater and ozone depletion events: a status report, Atmospheric Chemistry and Physics, 8, 7317–7324, doi:10.5194/acp-8-7317-2008, 2008.

Nakano, Y., Goto, M., Hashimoto, S., Kawasaki, M., and Wallington, T. J.: Cavity Ring-Down Spectroscopic Study of the Reactions of Br Atoms and BrO Radicals with Dimethyl sulfide, The Journal of Physical Chemistry A, 105, 11 045–11 050, doi:10.1021/jp012326f, 2001.

Nakano, Y., Enami, S., Nakamichi, S., Aloisio, S., Hashimoto, S., and Kawasaki, M.: Temperature and Pressure Dependence Study of the Reaction of IO Radicals with Dimethyl Sulfide by Cavity Ring-Down Laser Spectroscopy, The Journal of Physical Chemistry A, 107, 6381–6387, doi:10.1021/jp0345147, 2003.

Nasse, J.-M.: Retrieval of aerosol and trace gas vertical profiles in the Antarctic troposphere using helicopter- and ship-borne MAX-DOAS measurements, Master's thesis, Institute of Environmental Physics, University of Heidelberg, Germany, 2014.

Nickolaisen, S. L., Friedl, R. R., and Sander, S. P.: Kinetics and mechanism of the chlorine oxide ClO + ClO reaction: pressure and temperature dependences

of the bimolecular and termolecular channels and thermal decomposition of chlorine peroxide, The Journal of Physical Chemistry, 98, 155–169, doi: 10.1021/j100052a027, 1994.

O'Dowd, C. D. and Hoffmann, T.: Coastal New Particle Formation: A Review of the Current State-Of-The-Art, Environ. Chem., 2, 245–255, doi:10.1071/EN05077, 2005.

O'Keefe, A. and Deacon, D. A. G.: Cavity ring-down optical spectrometer for absorption measurements using pulsed laser sources, Review of Scientific Instruments, 59, 2544–2551, doi:10.1063/1.1139895, 1988.

Oltmans, S., Schnell, R., Sheridan, P., Peterson, R., Li, S.-M., Winchester, J., Tans, P., Sturges, W., Kahl, J., and Barrie, L.: Seasonal surface ozone and filterable bromine relationship in the high Arctic, Atmospheric Environment (1967), 23, 2431 – 2441, doi:10.1016/0004-6981(89)90254-0, 1989.

Oltmans, S. J.: Surface ozone measurements in clean air, Journal of Geophysical Research: Oceans, 86, 1174–1180, doi:10.1029/JC086iC02p01174, 1981.

Oltmans, S. J. and Komhyr, W. D.: Surface ozone distributions and variations from 1973 - 1984: Measurements at the NOAA Geophysical Monitoring for Climatic Change Baseline Observatories, Journal of Geophysical Research: Atmospheres, 91, 5229–5236, doi:10.1029/JD091iD04p05229, 1986.

Oltmans, S. J. and Levy, H.: Surface ozone measurements from a global network, Atmospheric Environment, 28, 9 – 24, doi:10.1016/1352-2310(94)90019-1, 1994.

Oum, K. W., Lakin, M. J., DeHaan, D. O., Brauers, T., and Finlayson-Pitts, B. J.: Formation of Molecular Chlorine from the Photolysis of Ozone and Aqueous Sea-Salt Particles, Science, 279, 74–76, doi:10.1126/science.279.5347.74, 1998.

Overland, J. E. and Wang, M.: When will the summer Arctic be nearly sea ice free?, Geophysical Research Letters, 40, 2097–2101, doi:10.1002/grl.50316, 2013.

Papayannis, D., Kosmas, A. M., and Melissas, V. S.: Ab initio calculations for (BrO)2 system and quasiclassical dynamics study of BrO self-reaction, Chemical Physics, 243, 249 – 262, doi:10.1016/S0301-0104(99)00070-1, 1999.

Park, K.-T., Lee, K., Yoon, Y.-J., Lee, H.-W., Kim, H.-C., Lee, B.-Y., Hermansen, O., Kim, T.-W., and Holmen, K.: Linking atmospheric dimethyl sulfide and the Arctic Ocean spring bloom, Geophysical Research Letters, 40, 155–160, doi:10.1029/2012GL054560, 2013.

Perner, D., Arnold, T., Crowley, J., Kluepfel, T., Martinez, M., and Seuwen, R.: The Measurement of Active Chlorine in the Atmosphere by Chemical Amplification, Journal of Atmospheric Chemistry, 34, 9–20, doi:10.1023/A:1006208828324, 1999.

Perovich, D.: Physics of ice-covered seas, Volume 1, chap. Optical properies of sea ice, pp. 195 – 230, University of Helsinki, 1998.

Peterson, P. K., Simpson, W. R., Pratt, K. A., Shepson, P. B., Frieß, U., Zielcke, J., Platt, U., Walsh, S. J., and Nghiem, S. V.: Dependence of the vertical distribution of bromine monoxide in the lower troposphere on meteorological factors such as wind speed and stability, Atmospheric Chemistry and Physics, 15, 2119–2137, doi:10.5194/acp-15-2119-2015, 2015.

Piot, M. and von Glasow, R.: The potential importance of frost flowers, recycling on snow, and open leads for ozone depletion events, Atmospheric Chemistry and Physics, 8, 2437–2467, doi:10.5194/acp-8-2437-2008, 2008.

Platt, U. and Hönninger, G.: The role of halogen species in the troposphere, Chemosphere, 52, 325 – 338, doi:10.1016/S0045-6535(03)00216-9, 2003.

Platt, U. and Janssen, C.: Observation and role of the free radicals NO3, ClO, BrO and IO in the troposphere, Faraday Discuss., 100, 175–198, doi:10.1039/FD9950000175, 1995.

Platt, U. and Lehrer, E.: ARCTOC, Final Report of the EU-Project No. EV5V-CT93-0318, University of Heidelberg, 1997.

Platt, U. and Stutz, J.: Differential Optical Absorption Spectroscopy - Principles and Applications, Springer Berlin Heidelberg, doi:10.1007/978-3-540-75776-4_6, 2008.

Platt, U., Perner, D., and Pätz, H. W.: Simultaneous measurement of atmospheric CH2O, O3, and NO2 by differential optical absorption, Journal of Geophysical Research: Oceans, 84, 6329–6335, doi:10.1029/JC084iC10p06329, 1979.

Platt, U., Allan, W., and Lowe, D.: Hemispheric average Cl atom concentration from $^{13}C/^{12}C$ ratios in atmospheric methane, Atmospheric Chemistry and Physics, 4, 2393–2399, doi:10.5194/acp-4-2393-2004, 2004.

Platt, U., Meinen, J., Pöhler, D., and Leisner, T.: Broadband Cavity Enhanced Differential Optical Absorption Spectroscopy (CE-DOAS) - applicability and corrections, Atmospheric Measurement Techniques, 2, 713–723, doi:10.5194/amt-2-713-2009, 2009.

Pöhler, D., Vogel, L., Friess, U., and Platt, U.: Observation of halogen species in the Amundsen Gulf, Arctic, by active long-path differential optical absorption

spectroscopy, Proceedings of the National Academy of Sciences, 107, 6582–6587, doi:10.1073pnas.0912231107, 2010.

Pollack, S. A.: Angular Dependence of Transmission Characteristics of Interference Filters and Application to a Tunable Fluorometer, Appl. Opt., 5, 1749–1756, doi:10.1364/AO.5.001749, 1966.

Pratt, K. A., Custard, K. D., Shepson, P. B., Douglas, T. A., Pohler, D., General, S., Zielcke, J., Simpson, W. R., Platt, U., Tanner, D. J., Gregory Huey, L., Carlsen, M., and Stirm, B. H.: Photochemical production of molecular bromine in Arctic surface snowpacks, Nature Geoscience, 6, 351–356, doi:10.1038/ngeo1779, 2013.

Rasmussen, R. A., Khalil, M. A. K., Gunawardena, R., and Hoyt, S. D.: Atmospheric methyl iodide (CH3I), Journal of Geophysical Research: Oceans, 87, 3086–3090, doi:10.1029/JC087iC04p03086, 1982.

Rattigan, O. V., Cox, R. A., and Jones, R. L.: Br2-sensitised decomposition of ozone: kinetics of the reaction BrO + O3[rightward arrow] products, J. Chem. Soc., Faraday Trans., 91, 4189–4197, doi:10.1039/FT9959104189, 1995.

Reifenhäuser, W. and Heumann, K. G.: Determinations of methyl iodide in the Antarctic atmosphere and the south polar sea, Atmospheric Environment. Part A. General Topics, 26, 2905 – 2912, doi:10.1016/0960-1686(92)90282-P, 1992.

Renard, J.-B., Pirre, M., Robert, C., and Huguenin, D.: The possible detection of OBrO in the stratosphere, Journal of Geophysical Research: Atmospheres, 103, 25 383–25 395, doi:10.1029/98JD01805, 1998.

Rodgers, C. D.: Inverse methods for atmospheric sounding: Theory and practice, World Scientific Singapore, 2000.

Roedel, W. and Wagner, T.: Physik unserer Umwelt: Die Atmosphäre, SpringerLink : Bücher, Springer Berlin Heidelberg, Berlin, Heidelberg, doi:10.1007/978-3-642-15729-5, 2011.

Rozanov, A., Rozanov, V., Buchwitz, M., Kokhanovsky, A., and Burrows, J.: SCIATRAN 2.0 A new radiative transfer model for geophysical applications in the 175 - 2400nm spectral region, Advances in Space Research, 36, 1015 – 1019, doi:10.1016/j.asr.2005.03.012, 2005.

Rozanov, V., Buchwitz, M., Eichmann, K.-U., de Beek, R., and Burrows, J.: Sciatran - a new radiative transfer model for geophysical applications in the 240 - 2400nm spectral region: the pseudo-spherical version, Advances in Space Research, 29, 1831 – 1835, doi:10.1016/S0273-1177(02)00095-9, 2002.

Saiz-Lopez, A. and von Glasow, R.: Reactive halogen chemistry in the troposphere, Chem. Soc. Rev., 41, 6448–6472, doi:10.1039/C2CS35208G, 2012.

Saiz-Lopez, A., Saunders, R. W., Joseph, D. M., Ashworth, S. H., and Plane, J. M. C.: Absolute absorption cross-section and photolysis rate of I_2, Atmospheric Chemistry and Physics, 4, 1443–1450, doi:10.5194/acp-4-1443-2004, 2004.

Saiz-Lopez, A., Mahajan, A. S., Salmon, R. A., Bauguitte, S. J.-B., Jones, A. E., Roscoe, H. K., and Plane, J. M. C.: Boundary Layer Halogens in Coastal Antarctica, Science, 317, 348–351, doi:10.1126/science.1141408, 2007.

Saiz-Lopez, A., Plane, J. M. C., Baker, A. R., Carpenter, L. J., von Glasow, R., Gomez Martin, J. C., McFiggans, G., and Saunders, R. W.: Atmospheric Chemistry of Iodine, Chemical Reviews, 112, 1773–1804, doi:10.1021/cr200029u, 2012.

Sander, R., Vogt, R., Harris, G. W., and Crutzen, P. J.: Modelling the chemistry of ozone, halogen compounds, and hydrocarbons in the arctic troposphere during spring, Tellus B, 49, 522–532, doi:10.1034/j.1600-0889.49.issue5.8.x, 1997.

Sander, R., Burrows, J., and Kaleschke, L.: Carbonate precipitation in brine - a potential trigger for tropospheric ozone depletion events, Atmospheric Chemistry and Physics, 6, 4653–4658, doi:10.5194/acp-6-4653-2006, 2006.

Sander, S. P. and Friedl, R. R.: Kinetics and product studies of the reaction chlorine monoxide + bromine monoxide using flash photolysis-ultraviolet absorption, The Journal of Physical Chemistry, 93, 4764–4771, doi:10.1021/j100349a017, 1989.

Sander, S. P., Friedl, R. R., Barker, J. R., Golden, D. M., Kurylo, M. J., Wine, P. H., Abatt, J. P. D., Burkholder, J. B., Kolb, C. E., Moortgat, G. K., Huie, R. E., and Orkin, V. L.: Chemical kinetics and photochemical data for use in Atmospheric Studies Evaluation Number 17, Pasadena, CA : Jet Propulsion Laboratory, National Aeronautics and Space Administration, JPL Publication 10-6, http://hdl.handle.net/2014/41648, 2011.

Schönhardt, A., Richter, A., Wittrock, F., Kirk, H., Oetjen, H., Roscoe, H. K., and Burrows, J. P.: Observations of iodine monoxide columns from satellite, Atmospheric Chemistry and Physics, 8, 637–653, doi:10.5194/acp-8-637-2008, 2008.

Schönhardt, A., Begoin, M., Richter, A., Wittrock, F., Kaleschke, L., Gómez Martín, J. C., and Burrows, J. P.: Simultaneous satellite observations of IO and BrO over Antarctica, Atmospheric Chemistry and Physics, 12, 6565–6580, doi:10.5194/acp-12-6565-2012, 2012.

Schroeder, W. H. and Munthe, J.: Atmospheric mercury - An overview, Atmospheric Environment, 32, 809 – 822, doi:10.1016/S1352-2310(97)00293-8, 1998.

Schroeder, W. H., Anlauf, K. G., Barrie, L. A., Lu, J. Y., Steffen, A., Schneeberger, D. R., and Berg, T.: Arctic springtime depletion of mercury, Nature, 394, 331–332, doi:10.1038/28530, 1998.

Serdyuchenko, A., Gorshelev, V., Weber, M., Chehade, W., and Burrows, J. P.: High spectral resolution ozone absorption cross-sections - Part 2: Temperature dependence, Atmospheric Measurement Techniques, 7, 625–636, doi:10.5194/amt-7-625-2014, 2014.

Sessler, J., Chipperfield, M. P., Pyle, J. A., and Toumi, R.: Stratospheric OClO measurements as a poor quantitative indicator of chlorine activation, Geophysical Research Letters, 22, 687–690, doi:10.1029/95GL00202, 1995.

Shaw, G. E.: The Arctic Haze Phenomenon, Bull. Amer. Meteor. Soc., 76, 2403–2413, doi:10.1175/1520-0477(1995)076<2403:TAHP>2.0.CO;2, 1995.

Sihler, H.: Light-Emitting Diodes as Light Sources in Spectroscopic Measurements of Atmospheric Trace Gases, Master's thesis, Diplomarbeit, Universität Jena, Germany, 2007.

Sihler, H.: Halogen activation in the polar troposphere, Ph.D. thesis, Institute of Environmental Physics, University of Heidelberg, Germany, URL `http://archiv.ub.uni-heidelberg.de/volltextserver/volltexte/2012/13663`, 2012.

Sihler, H., Kern, C., Pöhler, D., and Platt, U.: Applying light-emitting diodes with narrowband emission features in differential spectroscopy, Opt. Lett., 34, 3716–3718, doi:10.1364/OL.34.003716, 2009.

Simon, F., Schneider, W., Moortgat, G., and Burrows, J.: A study of the ClO absorption cross-section between 240 and 310 nm and the kinetics of the self-reaction at 300 K, Journal of Photochemistry and Photobiology A: Chemistry, 55, 1 – 23, doi:10.1016/1010-6030(90)80014-O, 1990.

Simpson, W. R., Alvarez-Aviles, L., Douglas, T. A., Sturm, M., and Domine, F.: Halogens in the coastal snow pack near Barrow, Alaska: Evidence for active bromine air-snow chemistry during springtime, Geophysical Research Letters, 32, n/a–n/a, doi:10.1029/2004GL021748, 2005.

Simpson, W. R., Carlson, D., Hönninger, G., Douglas, T. A., Sturm, M., Perovich, D., and Platt, U.: First-year sea-ice contact predicts bromine monoxide (BrO) levels at Barrow, Alaska better than potential frost flower contact, Atmospheric Chemistry and Physics, 7, 621–627, doi:10.5194/acp-7-621-2007, 2007a.

Simpson, W. R., von Glasow, R., Riedel, K., Anderson, P., Ariya, P., Bottenheim, J., Burrows, J., Carpenter, L. J., Frieß, U., Goodsite, M. E., Heard, D., Hutterli, M., Jacobi, H.-W., Kaleschke, L., Neff, B., Plane, J., Platt, U., Richter, A., Roscoe, H., Sander, R., Shepson, P., Sodeau, J., Steffen, A., Wagner, T., and Wolff, E.: Halogens and their role in polar boundary-layer ozone depletion, Atmospheric Chemistry and Physics, 7, 4375–4418, doi: 10.5194/acp-7-4375-2007, 2007b.

Simpson, W. R., Brown, S. S., Saiz-Lopez, A., Thornton, J. A., and Glasow, R. v.: Tropospheric Halogen Chemistry: Sources, Cycling, and Impacts, Chemical Reviews, doi:10.1021/cr5006638, 2015.

Skov, H., Christensen, J. H., Goodsite, M. E., Heidam, N. Z., Jensen, B., Wahlin, P., and Geernaert, G.: Fate of Elemental Mercury in the Arctic during Atmospheric Mercury Depletion Episodes and the Load of Atmospheric Mercury to the Arctic, Environmental Science & Technology, 38, 2373–2382, doi:10.1021/es030080h, 2004.

Solomon, S., Garcia, R. R., and Ravishankara, A. R.: On the role of iodine in ozone depletion, Journal of Geophysical Research: Atmospheres, 99, 20 491–20 499, doi:10.1029/94JD02028, 1994.

Spicer, C. W., Chapman, E. G., Finlayson-Pitts, B. J., Plastridge, R. A., Hubbe, J. M., Fast, J. D., and Berkowitz, C. M.: Unexpectedly high concentrations of molecular chlorine in coastal air, Nature, 394, 353–356, doi:10.1038/28584, 1998.

Spicer, C. W., Plastridge, R. A., Foster, K. L., Finlayson-Pitts, B. J., Bottenheim, J. W., Grannas, A. M., and Shepson, P. B.: Molecular halogens before and during ozone depletion events in the Arctic at polar sunrise: concentrations and sources, Atmospheric Environment, 36, 2721 – 2731, doi: 10.1016/S1352-2310(02)00125-5, 2002.

Spietz, P., Martin, J. C. G., and Burrows, J. P.: Spectroscopic studies of the I2/O3 photochemistry: Part 2. Improved spectra of iodine oxides and analysis of the {IO} absorption spectrum, Journal of Photochemistry and Photobiology A: Chemistry, 176, 50 – 67, doi:10.1016/j.jphotochem.2005.08.023, 2005.

Spietz, P., Gómez Martín, J., and Burrows, J. P.: Effects of column density on I2 spectroscopy and a determination of I2 absorption cross section at 500 nm, Atmospheric Chemistry and Physics, 6, 2177–2191, doi:10.5194/acp-6-2177-2006, 2006.

Stolarski, R. S. and Cicerone, R. J.: Stratospheric Chlorine: a Possible Sink for Ozone, Canadian Journal of Chemistry, 52, 1610–1615, doi:10.1139/v74-233, 1974.

Stull, R. B.: An introduction to boundary layer meteorology, vol. 13, Springer Science & Business Media, 1988.

Sturges, W. and Barrie, L.: Chlorine, Bromine and Iodine in arctic aerosols, Atmospheric Environment (1967), 22, 1179 – 1194, doi:10.1016/0004-6981(88)90349-6, 1988.

Sturges, W. T.: Excess particulate and gaseous bromine at a remote coastal location, Atmospheric Environment. Part A. General Topics, 24, 167 – 171, doi:10.1016/0960-1686(90)90452-S, 1990.

Sturges, W. T., Cota, G. F., and Buckley, P. T.: Bromoform emission from Arctic ice algae, Nature, 358, 660–662, doi:10.1038/358660a0, 1992.

Stutz, J. and Platt, U.: Numerical analysis and estimation of the statistical error of differential optical absorption spectroscopy measurements with least-squares methods, Appl. Opt., 35, 6041–6053, doi:10.1364/AO.35.006041, 1996.

Stutz, J., Kim, E. S., Platt, U., Bruno, P., Perrino, C., and Febo, A.: UV-visible absorption cross sections of nitrous acid, Journal of Geophysical Research: Atmospheres, 105, 14 585–14 592, doi:10.1029/2000JD900003, 2000.

Stutz, J., Ackermann, R., Fast, J. D., and Barrie, L.: Atmospheric reactive chlorine and bromine at the Great Salt Lake, Utah, Geophysical Research Letters, 29, 18–1–18–4, doi:10.1029/2002GL014812, 2002.

Stutz, J., Thomas, J. L., Hurlock, S. C., Schneider, M., von Glasow, R., Piot, M., Gorham, K., Burkhart, J. F., Ziemba, L., Dibb, J. E., and Lefer, B. L.: Longpath DOAS observations of surface BrO at Summit, Greenland, Atmospheric Chemistry and Physics, 11, 9899–9910, doi:10.5194/acp-11-9899-2011, 2011.

Takemura, T., Nakajima, T., Dubovik, O., Holben, B. N., and Kinne, S.: Single-Scattering Albedo and Radiative Forcing of Various Aerosol Species with a Global Three-Dimensional Model, J. Climate, 15, 333–352, doi:10.1175/1520-0442(2002)015<0333:SSAARF>2.0.CO;2, 2002.

Tarasick, D. W. and Bottenheim, J. W.: Surface ozone depletion episodes in the Arctic and Antarctic from historical ozonesonde records, Atmospheric Chemistry and Physics, 2, 197–205, doi:10.5194/acp-2-197-2002, 2002.

Thomas, D. N. and Dieckmann, G. S.: Sea ice, John Wiley & Sons, 2nd edn., 2009.

Tschritter, J.: Untersuchung mariner Halogenemissionen im tropischen Atlantik, Ph.D. thesis, Institute of Environmental Physics, University of Heidelberg, Germany, URL http://archiv.ub.uni-heidelberg.de/volltextserver/15312/, 2013.

Tucceri, M. E., Holscher, D., Rodriguez, A., Dillon, T. J., and Crowley, J. N.: Absorption cross section and photolysis of OIO, Phys. Chem. Chem. Phys., 8, 834–846, doi:10.1039/B512702E, 2006.

Tuckermann, M., Ackermann, R., Goelz, C., Lorenzen-Schmidt, H., Senne, T., Stutz, J., Trost, B., Unold, W., and Platt, U.: DOAS-observation of halogen radical-catalysed arctic boundary layer ozone destruction during the ARCTOC-campaigns 1995 and 1996 in Ny-Alesund, Spitsbergen, Tellus B, 49, 533–555, doi:10.1034/j.1600-0889.49.issue5.9.x, 1997.

Turnipseed, A. A., Birks, J. W., and Calvert, J. G.: Kinetics and temperature dependence of the bromine monoxide + chlorine monoxide reaction, The Journal of Physical Chemistry, 95, 4356–4364, doi:10.1021/j100164a035, 1991.

van de Hulst, H. C.: Light scattering by small particles, Courier Dover Publications, 1957.

Vandaele, A. C., Hermans, C., Fally, S., Carleer, M., Colin, R., Merienne, M.-F., Jenouvrier, A., and Coquart, B.: High-resolution Fourier transform measurement of the NO2 visible and near-infrared absorption cross sections: Temperature and pressure effects, Journal of Geophysical Research: Atmospheres, 107, ACH 3–1–ACH 3–12, doi:10.1029/2001JD000971, 2002.

Vetter, R.: Photodissociation of {OBrO} through the excited 22A(12A2) electronic state: Theoretical prediction of the absorption cross-section, Chemical Physics, 343, 303 – 310, doi:10.1016/j.chemphys.2007.06.034, 2008.

Vogt, R., Sander, R., von Glasow, R., and Crutzen, P. J.: Iodine Chemistry and its Role in Halogen Activation and Ozone Loss in the Marine Boundary Layer: A Model Study, Journal of Atmospheric Chemistry, 32, 375–395, doi:10.1023/A:1006179901037, 1999.

Voigt, S., Orphal, J., Bogumil, K., and Burrows, J.: The temperature dependence (203 - 293 K) of the absorption cross sections of O3 in the 230 - 850 nm region measured by Fourier-transform spectroscopy, Journal of Photochemistry and Photobiology A: Chemistry, 143, 1 – 9, doi:10.1016/S1010-6030(01)00480-4, 2001.

Voigt, S., Orphal, J., and Burrows, J.: The temperature and pressure dependence of the absorption cross-sections of {NO2} in the 250 - 800 nm region measured by Fourier-transform spectroscopy, Journal of Photochemistry and Photobiology A: Chemistry, 149, 1 – 7, doi:10.1016/S1010-6030(01)00650-5, 2002.

Volkamer, R., Spietz, P., Burrows, J., and Platt, U.: High-resolution absorption cross-section of glyoxal in the UV-vis and {IR} spectral ranges, Journal of

Photochemistry and Photobiology A: Chemistry, 172, 35 – 46, doi:10.1016/j.jphotochem.2004.11.011, 2005.

von Clarmann, T.: Smoothing error pitfalls, Atmospheric Measurement Techniques, 7, 3023–3034, doi:10.5194/amt-7-3023-2014, 2014.

von Glasow, R. and Crutzen, P. J.: Model study of multiphase DMS oxidation with a focus on halogens, Atmospheric Chemistry and Physics, 4, 589–608, doi:10.5194/acp-4-589-2004, 2004.

von Glasow, R., Sander, R., Bott, A., and Crutzen, P. J.: Modeling halogen chemistry in the marine boundary layer 1. Cloud-free MBL, Journal of Geophysical Research: Atmospheres, 107, ACH 9–1–ACH 9–16, doi:10.1029/2001JD000942, 2002.

Wagner, T. and Platt, U.: Satellite mapping of enhanced BrO concentrations in the troposphere, Nature, 395, 486–490, 1998.

Wagner, T., Leue, C., Wenig, M., Pfeilsticker, K., and Platt, U.: Spatial and temporal distribution of enhanced boundary layer BrO concentrations measured by the GOME instrument aboard ERS-2, Journal of Geophysical Research: Atmospheres, 106, 24 225–24 235, doi:10.1029/2000JD000201, 2001.

Wagner, T., Ibrahim, O., Sinreich, R., Friess, U., von Glasow, R., and Platt, U.: Enhanced tropospheric BrO over Antarctic sea ice in mid winter observed by MAX-DOAS on board the research vessel Polarstern, Atmospheric Chemistry and Physics, 7, 3129–3142, doi:10.5194/acp-7-3129-2007, 2007.

Wagner, T., Beirle, S., and Deutschmann, T.: Three-dimensional simulation of the Ring effect in observations of scattered sun light using Monte Carlo radiative transfer models, Atmospheric Measurement Techniques, 2, 113–124, doi:10.5194/amt-2-113-2009, 2009.

Washenfelder, R. A., Langford, A. O., Fuchs, H., and Brown, S. S.: Measurement of glyoxal using an incoherent broadband cavity enhanced absorption spectrometer, Atmospheric Chemistry and Physics, 8, 7779–7793, doi:10.5194/acp-8-7779-2008, 2008.

Watanabe, K., Nojiri, Y., and Kariya, S.: Measurements of ozone concentrations on a commercial vessel in the marine boundary layer over the northern North Pacific Ocean, Journal of Geophysical Research: Atmospheres, 110, doi:10.1029/2004JD005514, 2005.

Wennberg, P.: Atmospheric chemistry: Bromine explosion, Nature, 397, 299–301, doi:10.1038/16805, 1999.

Wittrock, F., Müller, R., Richter, A., Bovensmann, H., and Burrows, J. P.: Measurements of iodine monoxide (IO) above Spitsbergen, Geophysical Research Letters, 27, 1471–1474, doi:10.1029/1999GL011146, 2000.

Wongdontri-Stuper, W., Jayanty, R., Simonaitis, R., and Heicklen, J.: The Cl2 photosensitized decomposition of O3: the reactions of ClO and OClO with O3, Journal of Photochemistry, 10, 163 – 186, doi:10.1016/0047-2670(79)80004-0, 1979.

Wren, S. N., Donaldson, D. J., and Abbatt, J. P. D.: Photochemical chlorine and bromine activation from artificial saline snow, Atmospheric Chemistry and Physics, 13, 9789–9800, doi:10.5194/acp-13-9789-2013, 2013.

Yang, X., Pyle, J. A., Cox, R. A., Theys, N., and Van Roozendael, M.: Snow-sourced bromine and its implications for polar tropospheric ozone, Atmospheric Chemistry and Physics, 10, 7763–7773, doi:10.5194/acp-10-7763-2010, 2010.

Yilmaz, S.: Retrieval of atmospheric aerosol and trace gas vertical profiles using multi-axis differential optical absorption spectroscopy, Ph.D. thesis, Institute of Environmental Physics, University of Heidelberg, Germany, URL `http://archiv.ub.uni-heidelberg.de/volltextserver/volltexte/2012/13128`, 2012.

Yokelson, R. J., Burkholder, J. B., Fox, R. W., Talukdar, R. K., and Ravishankara, A. R.: Temperature Dependence of the NO3 Absorption Spectrum, The Journal of Physical Chemistry, 98, 13 144–13 150, doi:10.1021/j100101a009, 1994.

Yung, Y. L., Pinto, J. P., Watson, R. T., and Sander, S. P.: Atmospheric Bromine and Ozone Perturbations in the Lower Stratosphere, J. Atmos. Sci., 37, 339–353, doi:10.1175/1520-0469(1980)037<0339:ABAOPI>2.0.CO;2, 1980.

Zeng, T., Wang, Y., Chance, K., Browell, E. V., Ridley, B. A., and Atlas, E. L.: Widespread persistent near-surface ozone depletion at northern high latitudes in spring, Geophysical Research Letters, 30, doi:10.1029/2003GL018587, 2003.

Zielcke, J.: Direct moonlight studies of volcanic plumes using differential optical absorption spectroscopy, Master's thesis, Diplomarbeit, Institute of Environmental Physics, University of Heidelberg, Germany, zsfassung in dt. und engl. Sprache, 2010.

Zielcke, J., Horbanski, M., Pöhler, D., Friess, U., and Platt, U.: A new calibration system for lightweight, compact and mobile Cavity-Enhanced Differential Optical Absorption Spectroscopy instruments, in: EGU General Assembly Conference Abstracts, vol. 15 of *EGU General Assembly Conference Abstracts*, p. 10134, 2013.

A

Appendix

A.1 MAX-DOAS inversion sensitivity studies: Aerosol

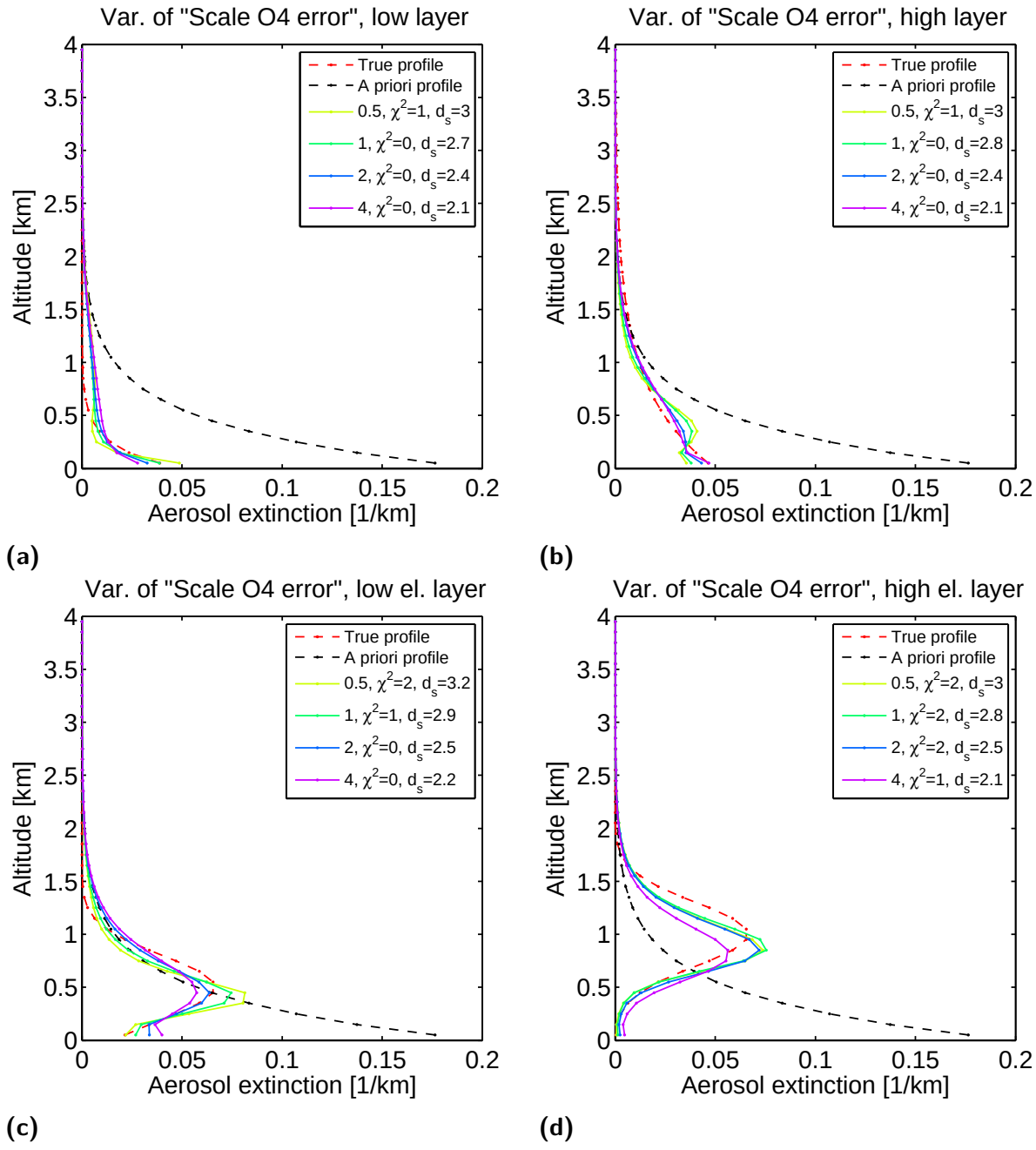

Figure A.1.: Case 1 - Low aerosol extinction scenarios: Analysis of the effect of scaling the error on the measurement SCDs before the inversion with values from 0.5 to 4. The effect is exactly equivalent to a scaling of the a priori profile error with the inverse. For details of the method see section 5.1.

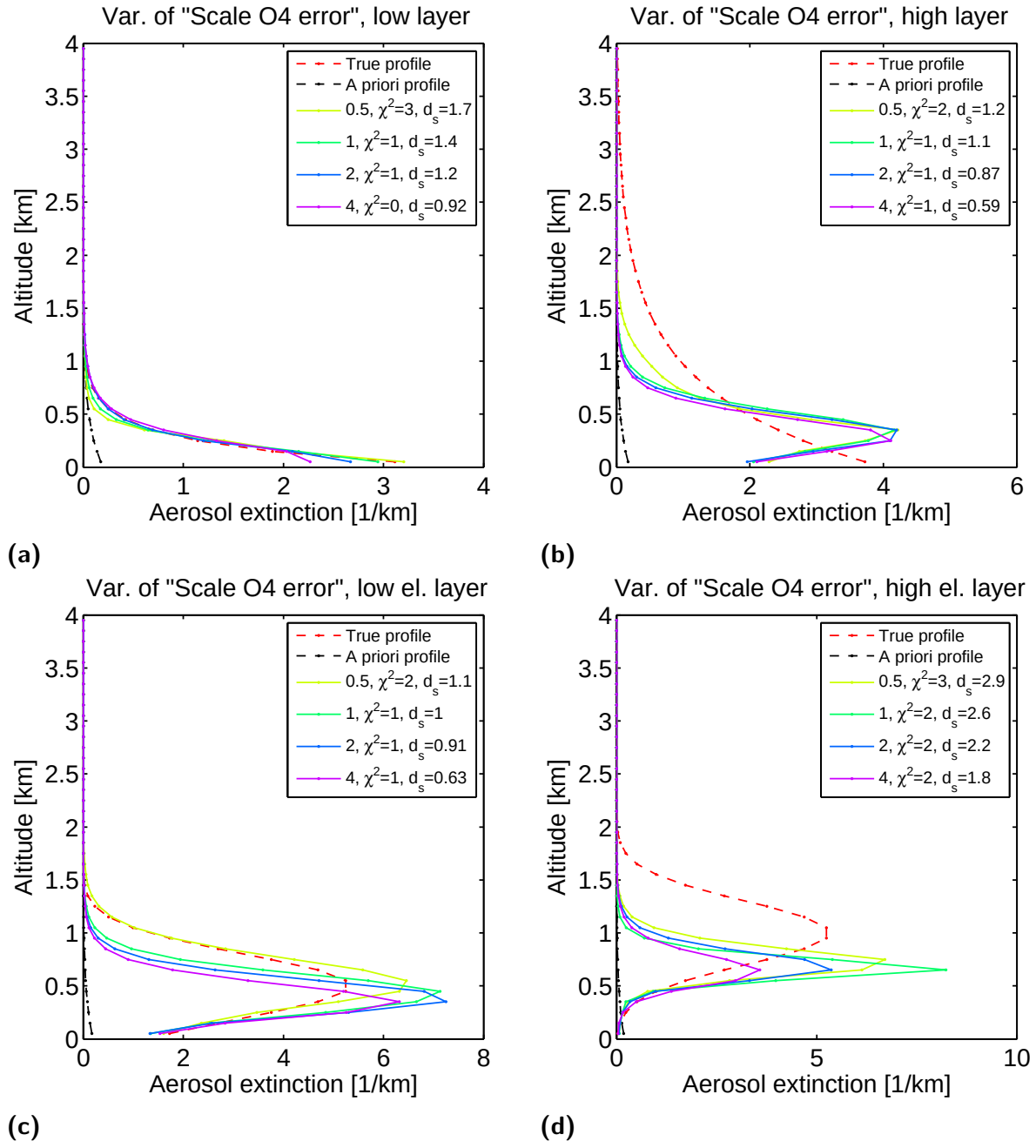

Figure A.2.: Case 2 - Medium aerosol extinction scenarios: Analysis of the effect of scaling the error on the measurement SCDs before the inversion with values from 0.5 to 4. The effect is exactly equivalent to a scaling of the a priori profile error with the inverse. For details of the method see section 5.1.

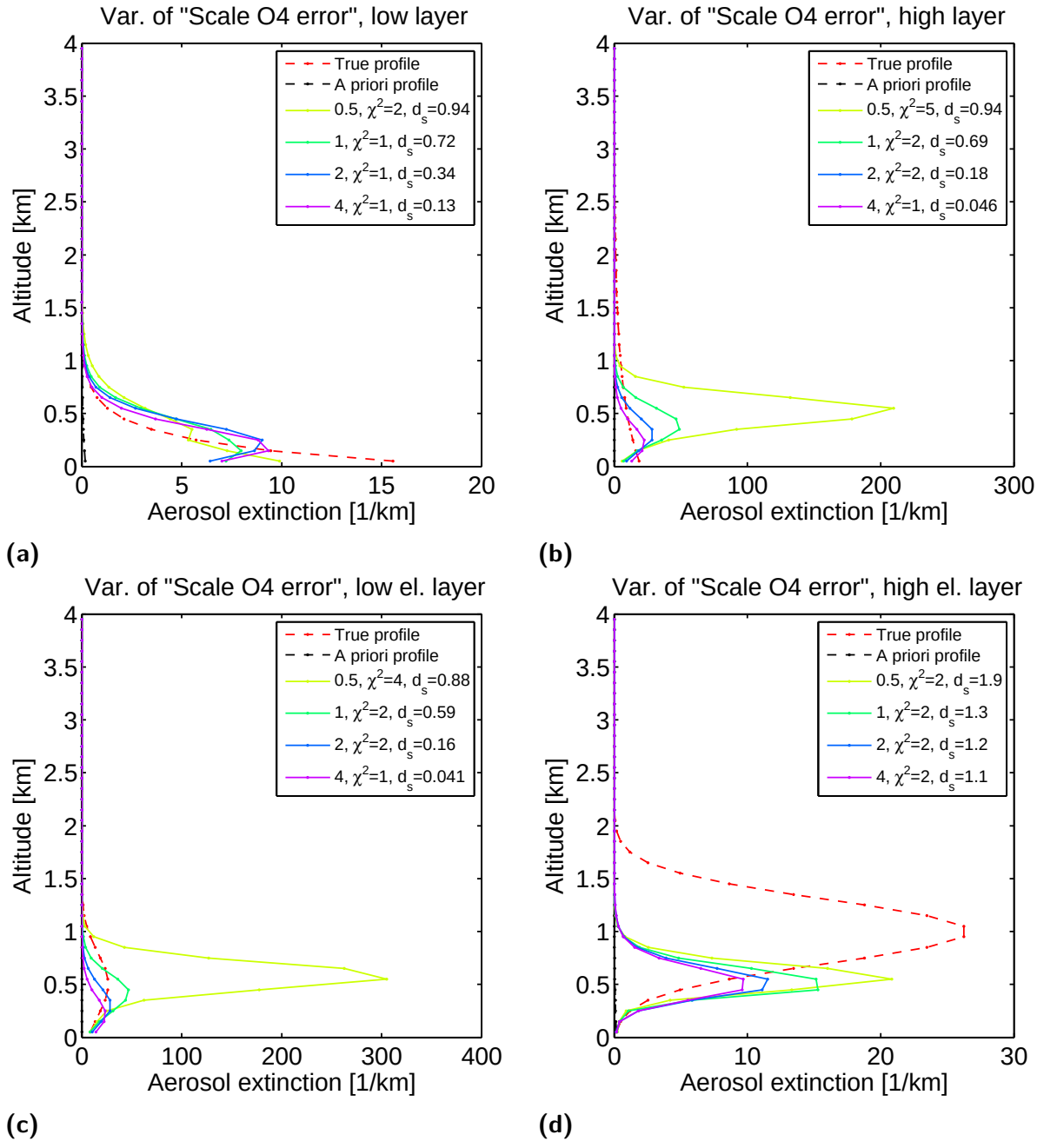

Figure A.3.: Case 3 - High aerosol extinction scenarios: Analysis of the effect of scaling the error on the measurement SCDs before the inversion with values from 0.5 to 4. The effect is exactly equivalent to a scaling of the a priori profile error with the inverse. For details of the method see section 5.1.

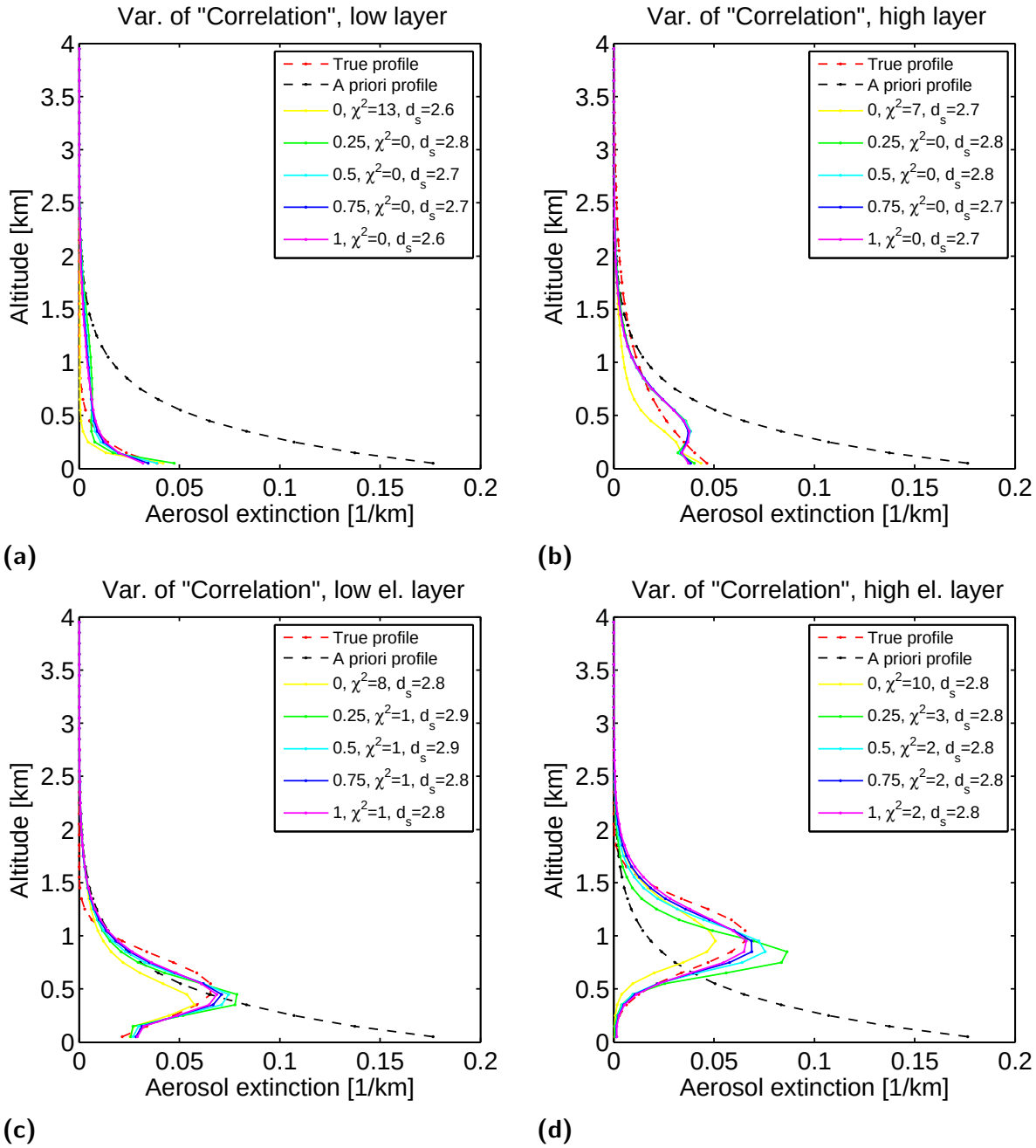

Figure A.4.: Case 1 - Low aerosol extinction scenarios: Analysis of the effect of a change of the correlation length, given in km, from 0 km to 1 km. The correlation length determines the coupling of different grid boxes through the covariance matrix of the a priori profile. For details of the method see section 5.1.

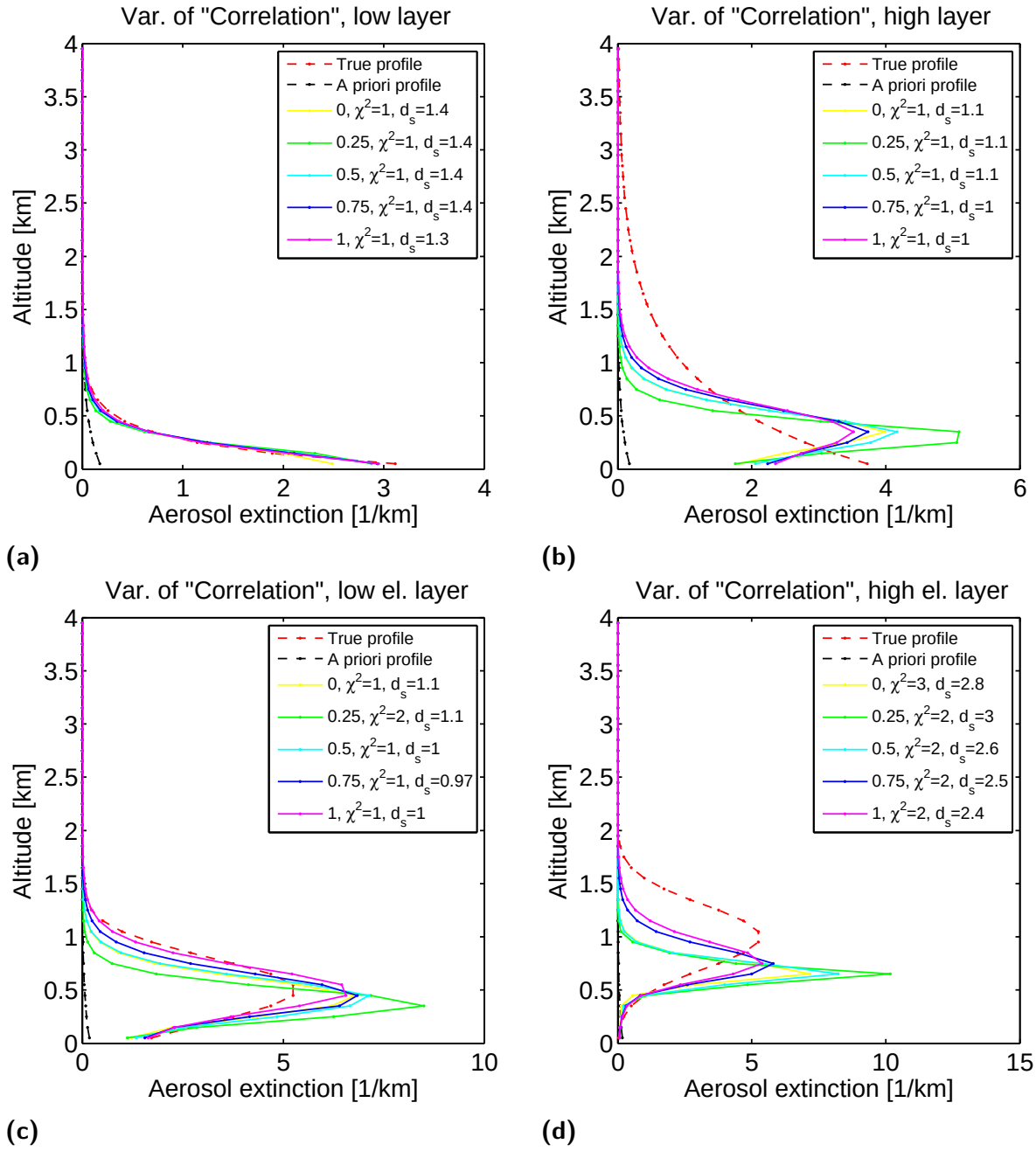

Figure A.5.: Case 2 - Medium aerosol extinction scenarios: Analysis of the effect of a change of the correlation length, given in km, from 0 km to 1 km. The correlation length determines the coupling of different grid boxes through the covariance matrix of the a priori profile. For details of the method see section 5.1.

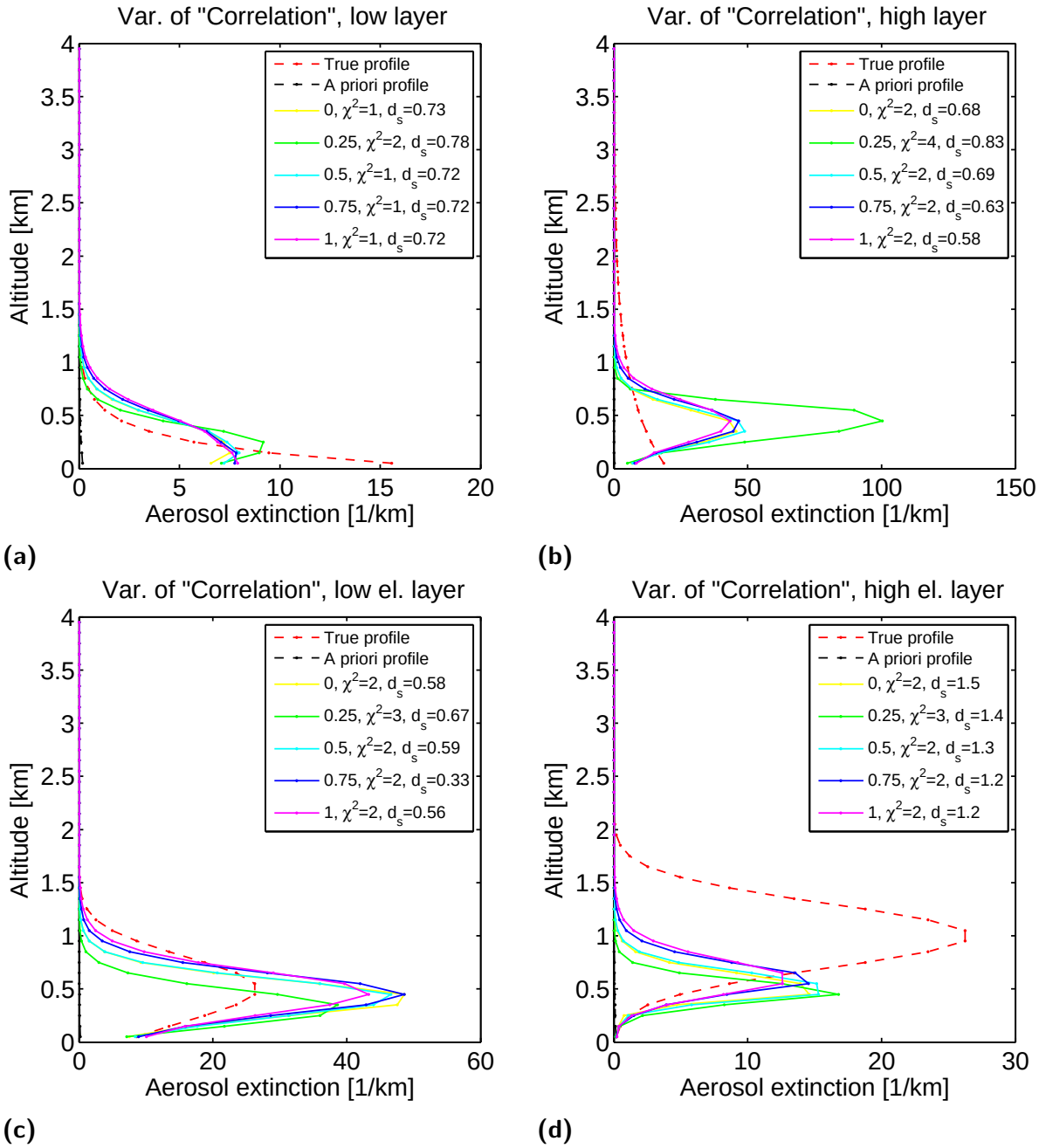

Figure A.6.: Case 3 - High aerosol extinction scenarios: Analysis of the effect of a change of the correlation length, given in km, from 0 km to 1 km. The correlation length determines the coupling of different grid boxes through the covariance matrix of the a priori profile. For details of the method see section 5.1.

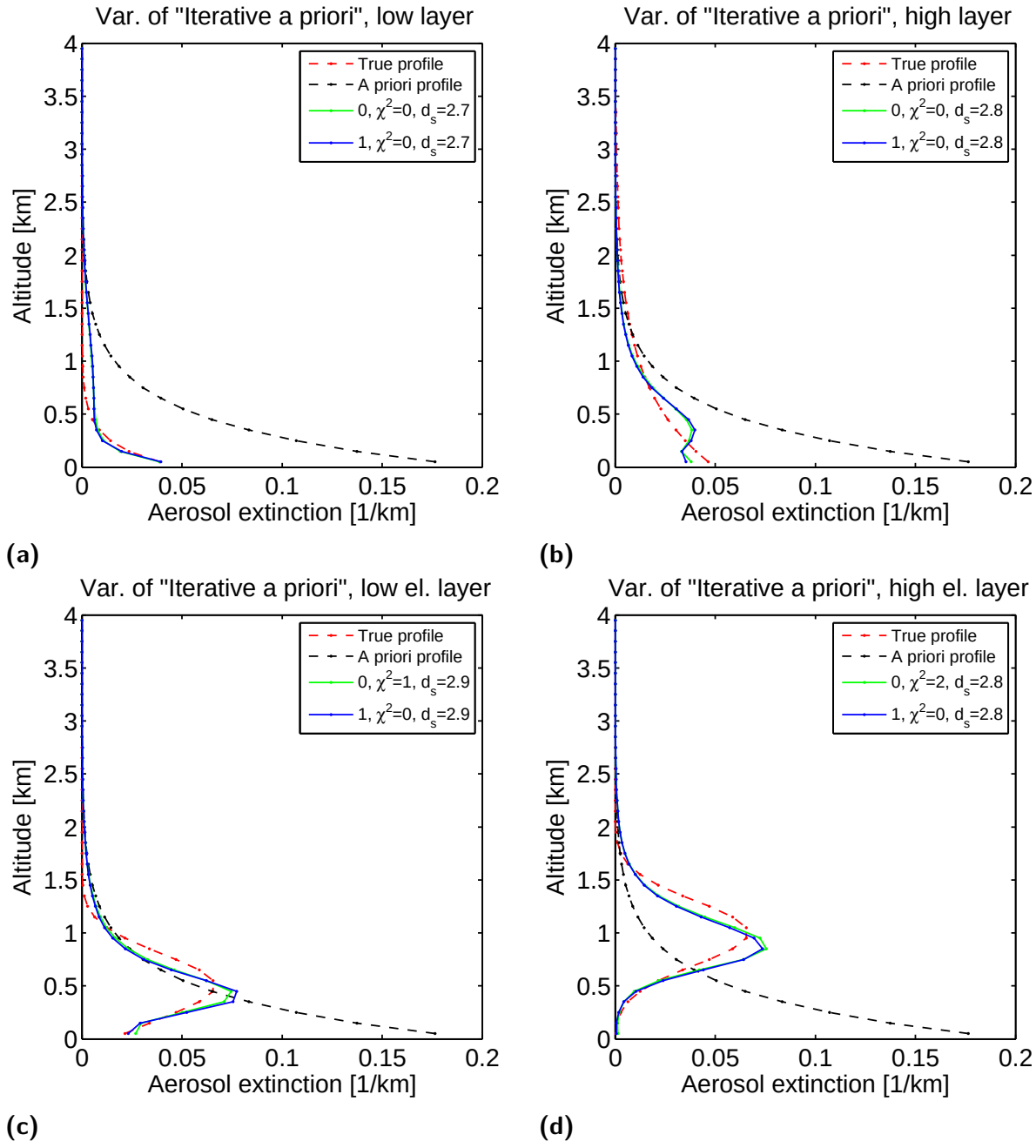

Figure A.7.: Case 1 - Low aerosol extinction scenarios: Analysis of the effect of whether to use an iterative a priori profile (1), where the profile resulting from the last iteration is taken as a priori profile for the next iteration, or to use the classic approach (0). For details of the method see section 5.1.

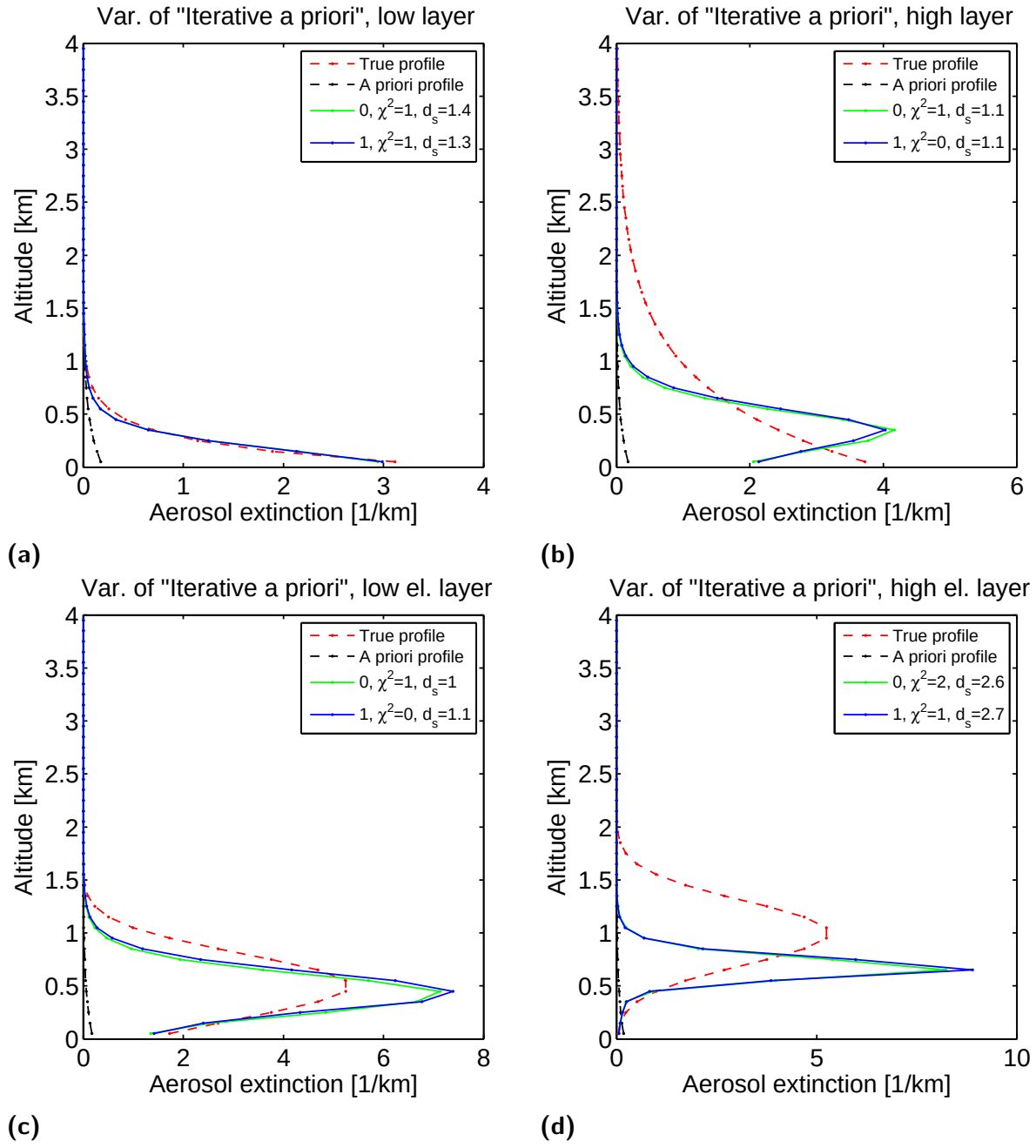

Figure A.8.: Case 2 - Medium aerosol extinction scenarios: Analysis of the effect of whether to use an iterative a priori profile (1), where the profile resulting from the last iteration is taken as a priori profile for the next iteration, or to use the classic approach (0). For details of the method see section 5.1.

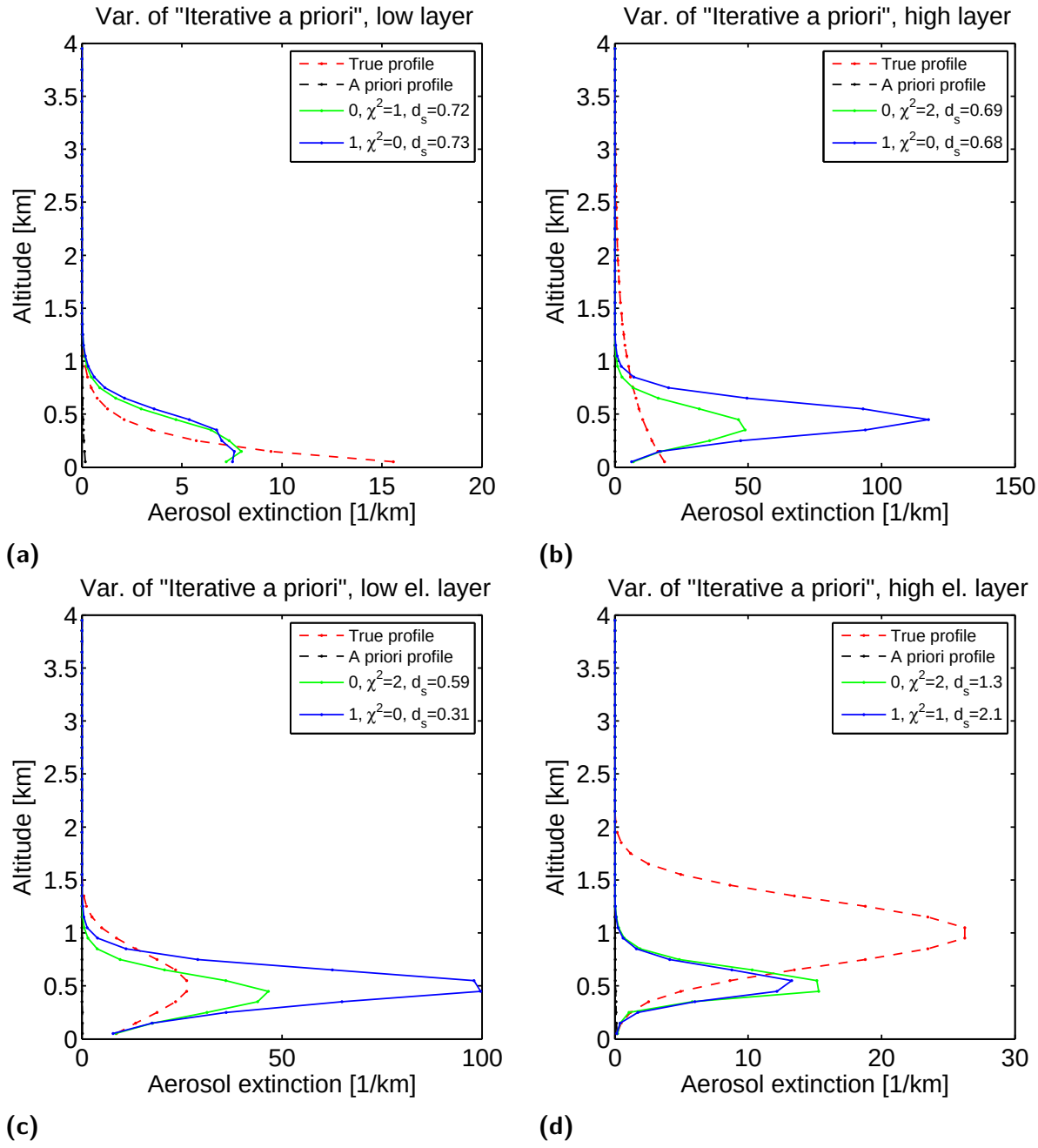

Figure A.9.: Case 3 - High aerosol extinction scenarios: Analysis of the effect of whether to use an iterative a priori profile (1), where the profile resulting from the last iteration is taken as a priori profile for the next iteration, or to use the classic approach (0). For details of the method see section 5.1.

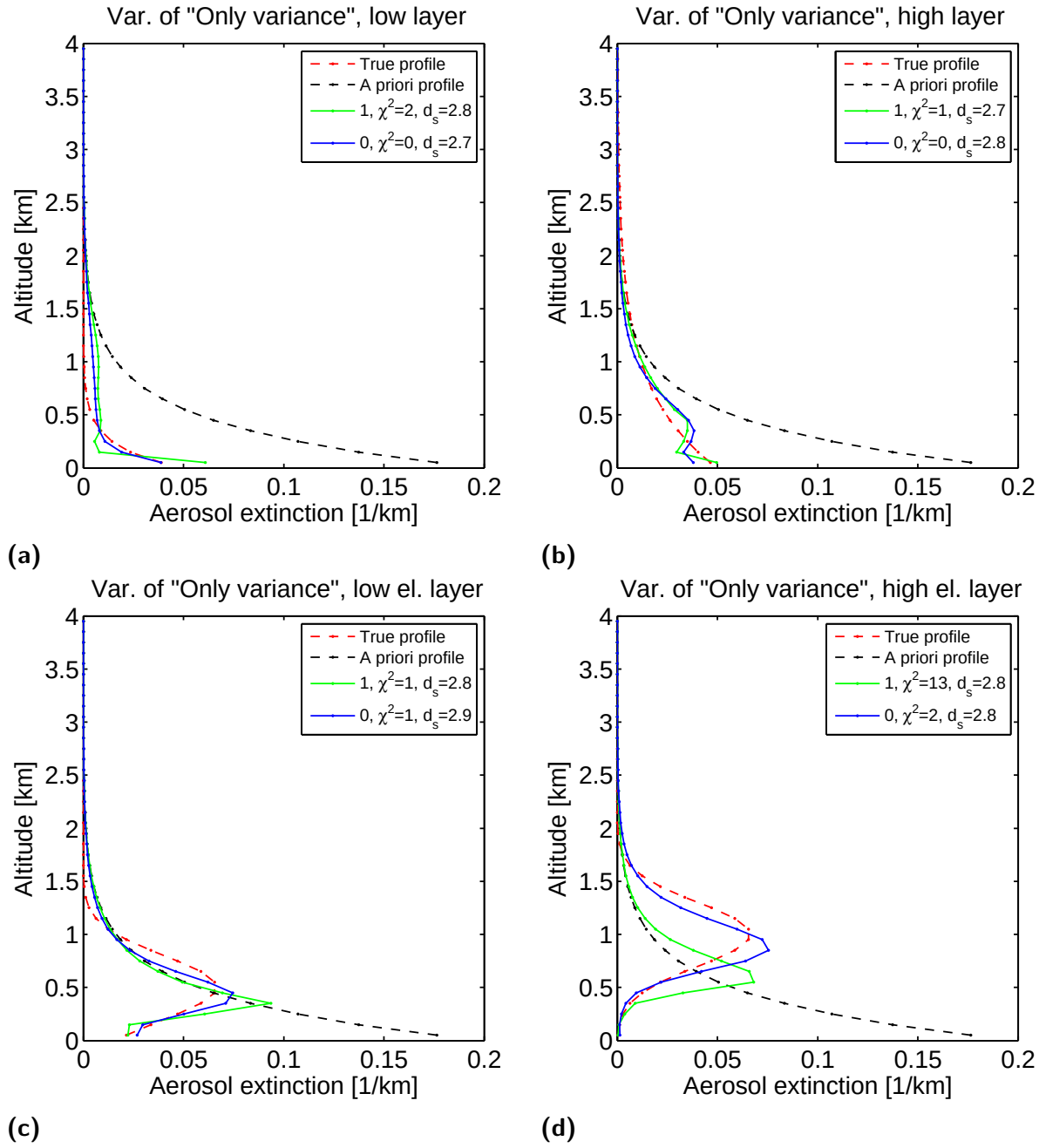

Figure A.10.: Case 1 - Low aerosol extinction scenarios: Analysis of the effect of whether the used a priori covariance matrix contains off-axis elements (0), whose value is determined by the correlation length, or only diagonal values (1). In the last case, neighboring grid boxes are independent of each other. For details of the method see section 5.1.

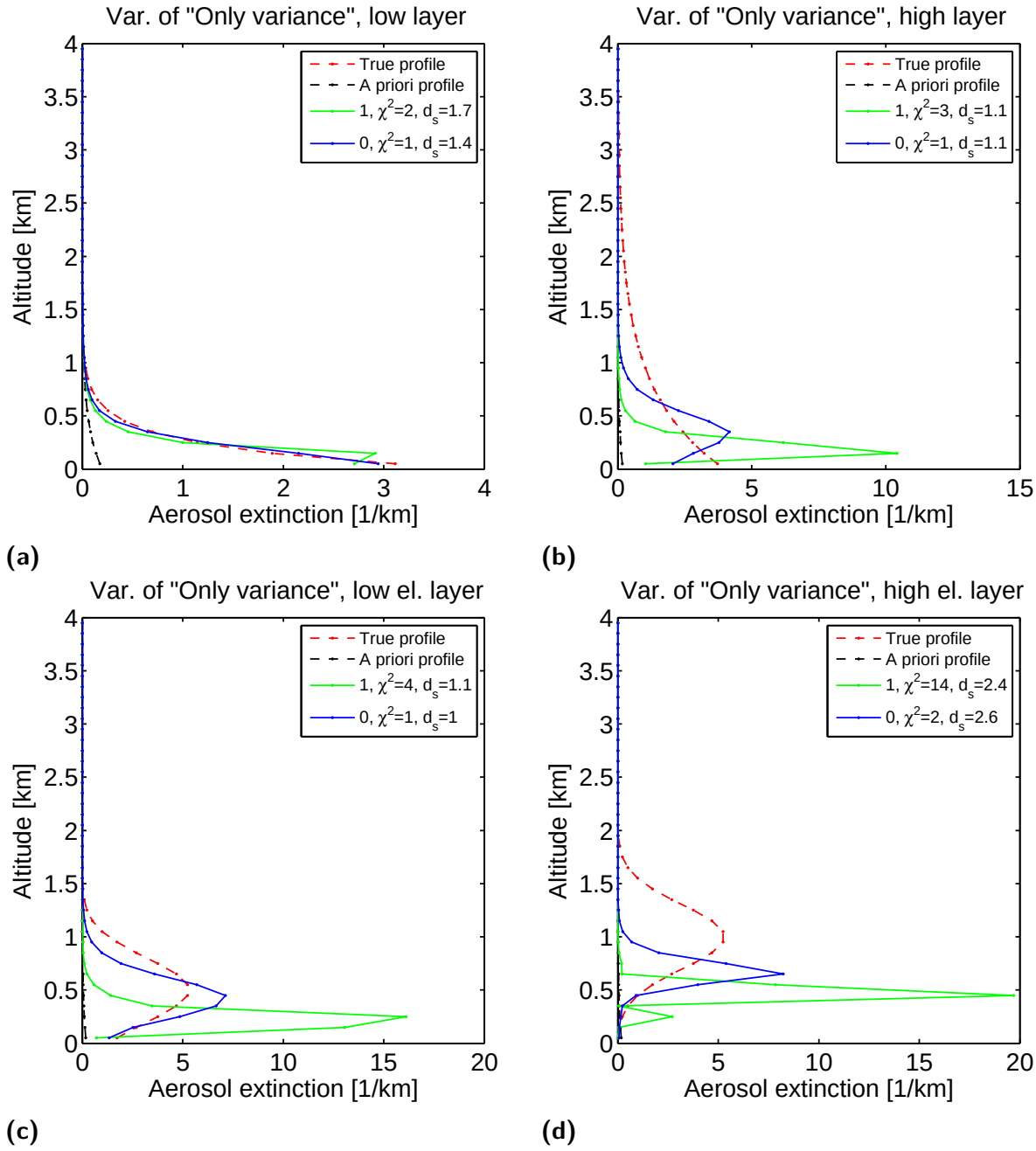

Figure A.11.: Case 2 - Medium aerosol extinction scenarios: Analysis of the effect of whether the used a priori covariance matrix contains off-axis elements (0), whose value is determined by the correlation length, or only diagonal values (1). In the last case, neighboring grid boxes are independent of each other. For details of the method see section 5.1.

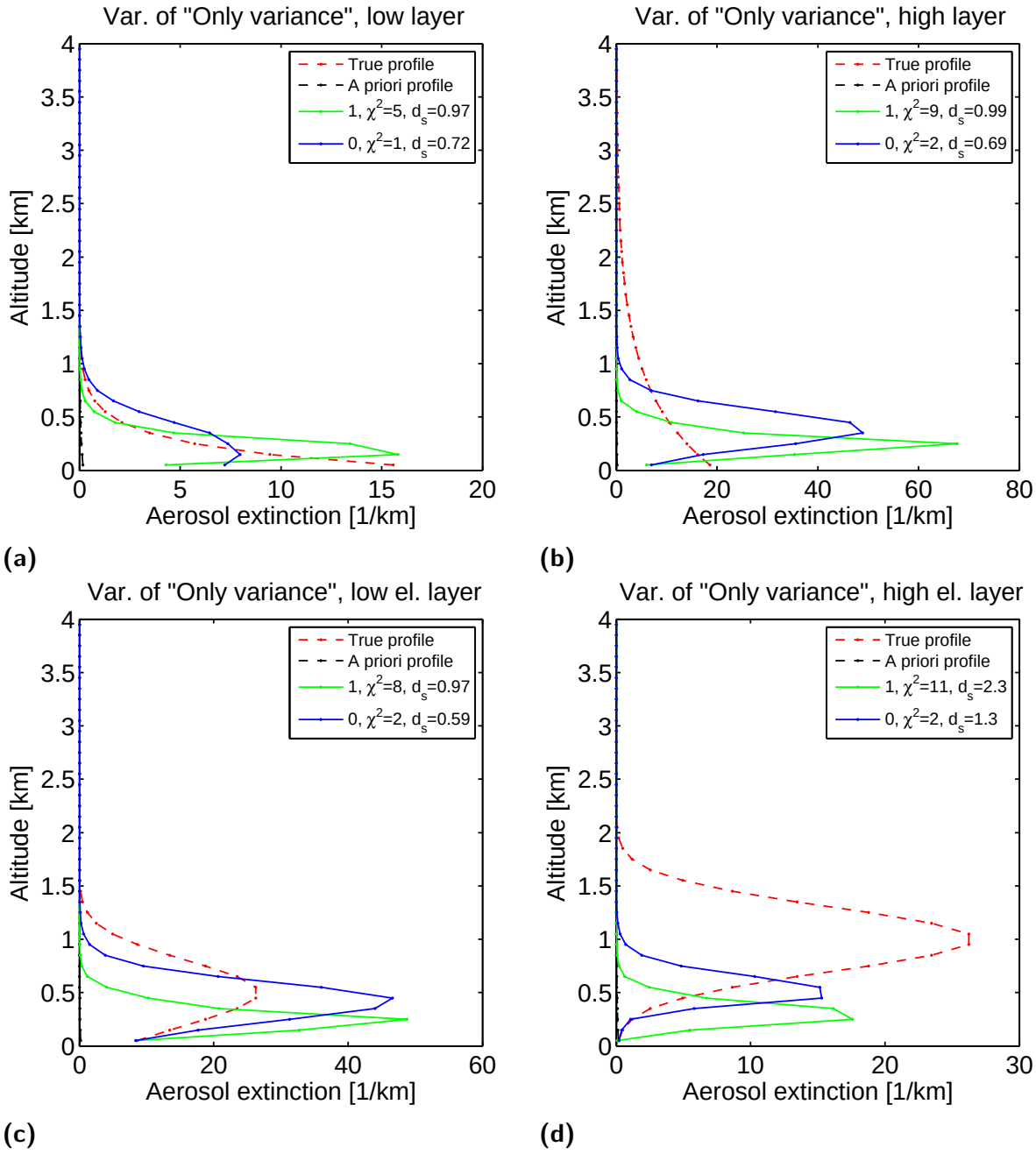

Figure A.12.: Case 3 - High aerosol extinction scenarios: Analysis of the effect of whether the used a priori covariance matrix contains off-axis elements (0), whose value is determined by the correlation length, or only diagonal values (1). In the last case, neighboring grid boxes are independent of each other. For details of the method see section 5.1.

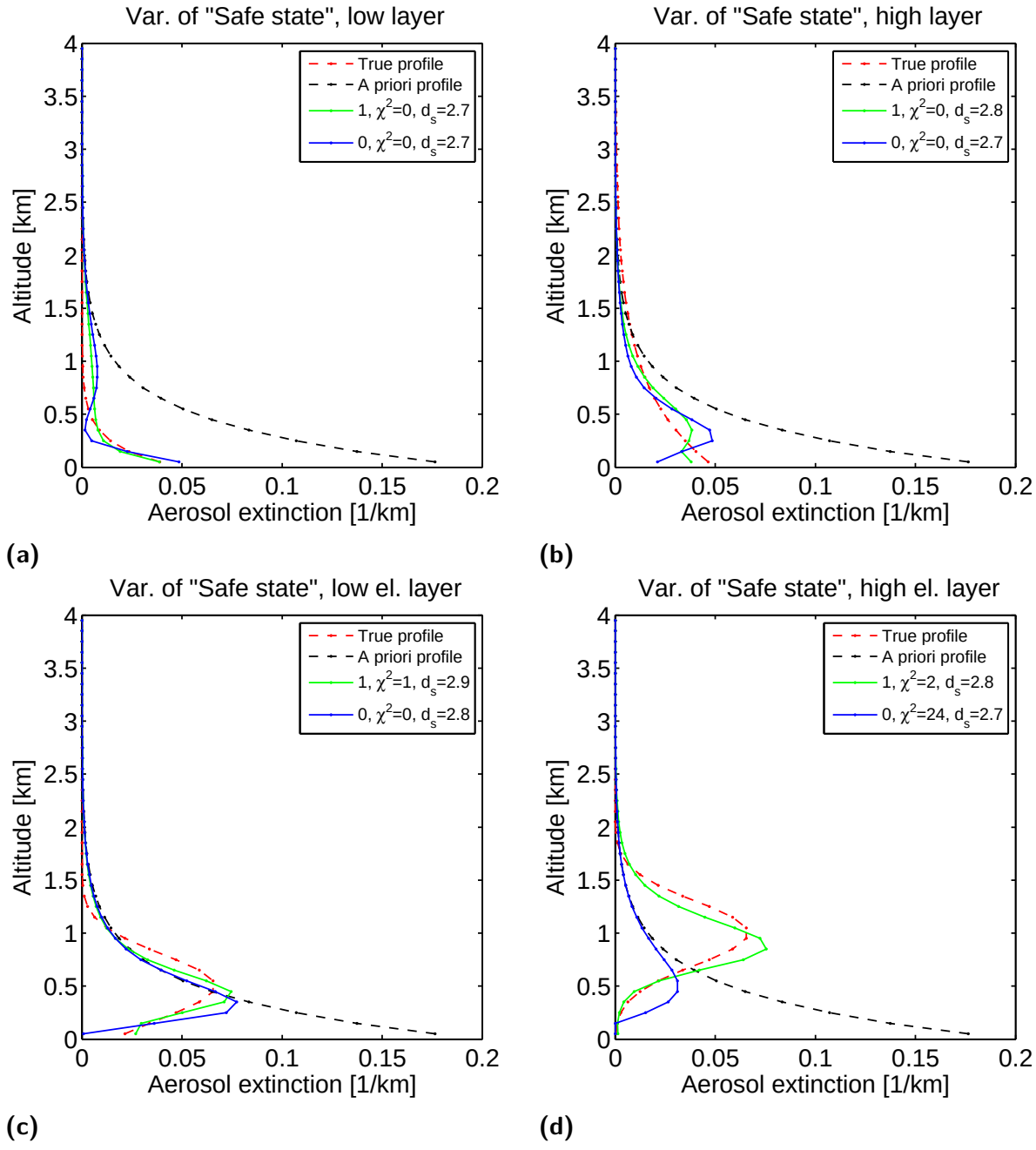

Figure A.13.: Case 1 - Low aerosol extinction scenarios: Analysis of the effect of whether a transformation into the safe state is done before the inversion (1) or not (0). For details of the method see section 5.1.

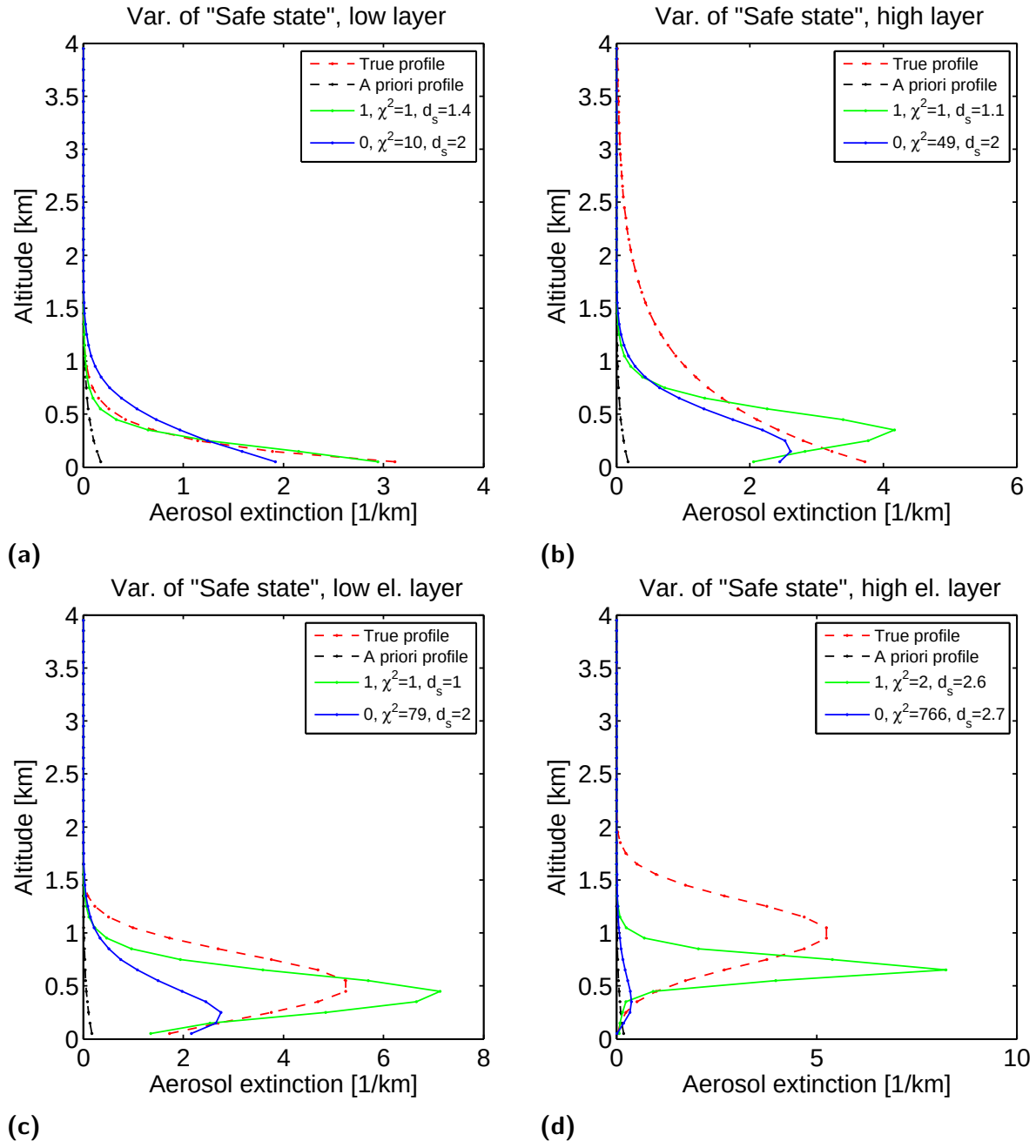

Figure A.14.: Case 2 - Medium aerosol extinction scenarios: Analysis of the effect of whether a transformation into the safe state is done before the inversion (1) or not (0). For details of the method see section 5.1.

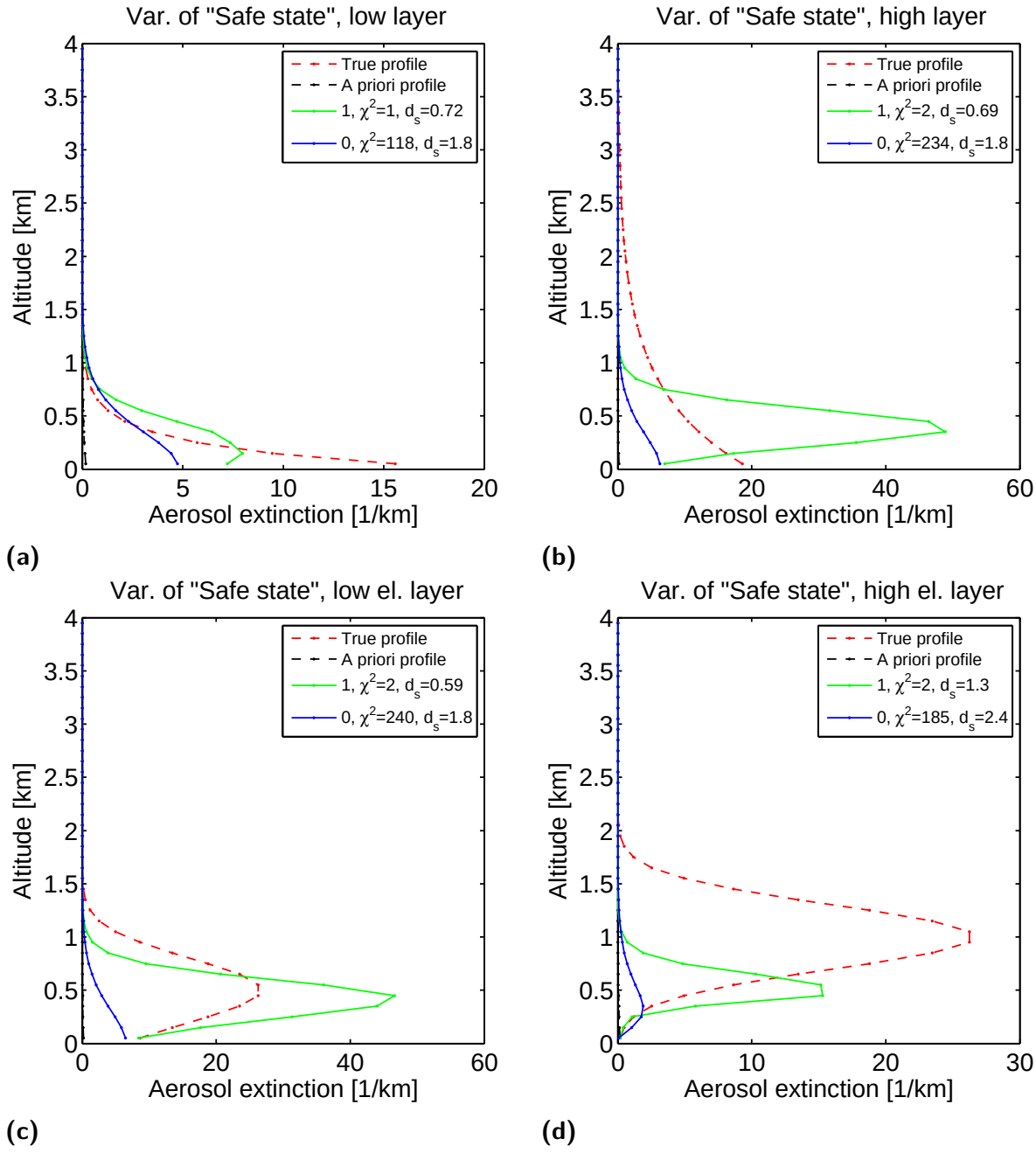

Figure A.15.: Case 3 - High aerosol extinction scenarios: Analysis of the effect of whether a transformation into the safe state is done before the inversion (1) or not (0). For details of the method see section 5.1.

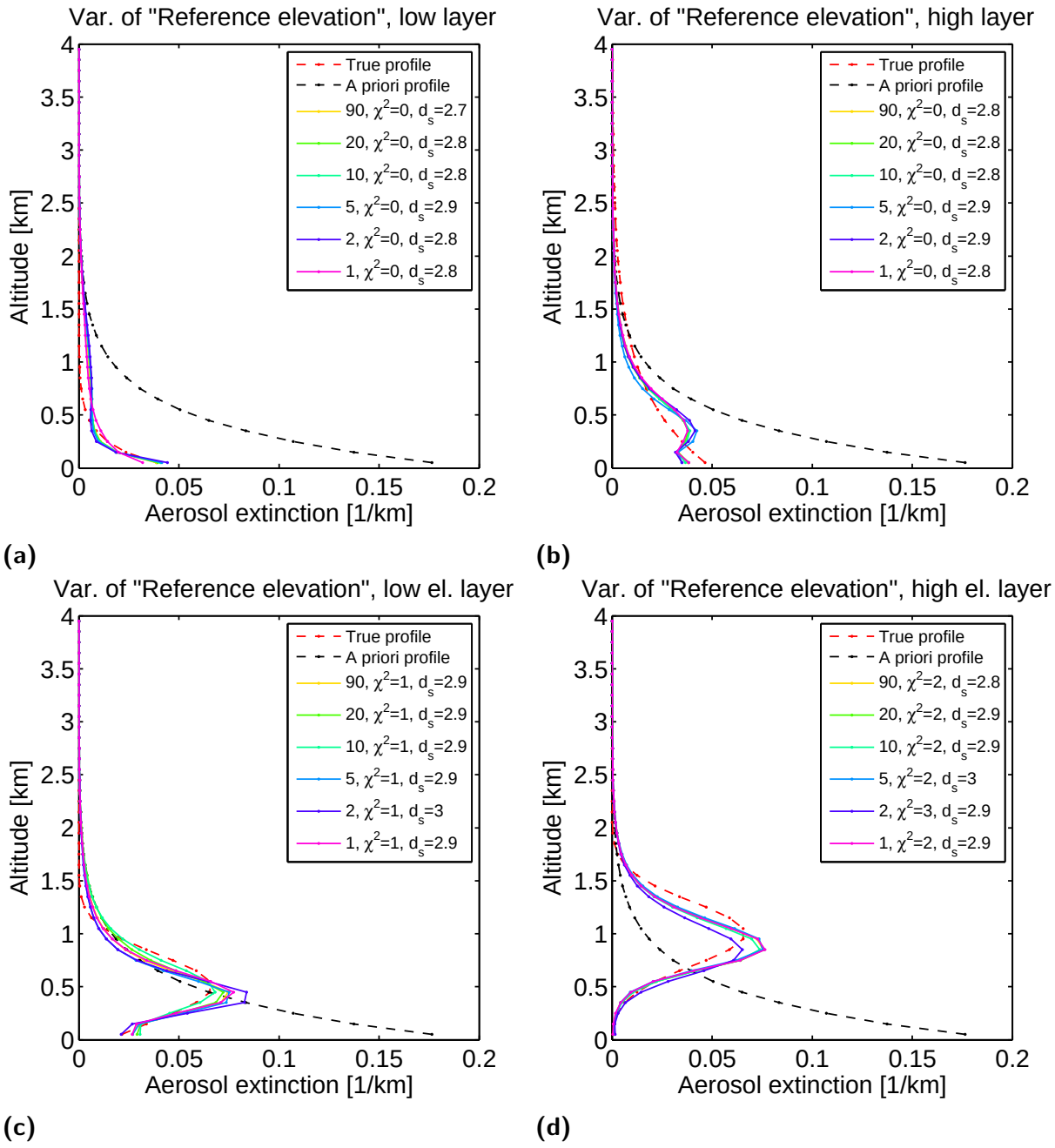

Figure A.16.: Case 1 - Low aerosol extinction scenarios: Analysis of the effect of which elevation angle is used as the reference angle. For details of the method see section 5.1.

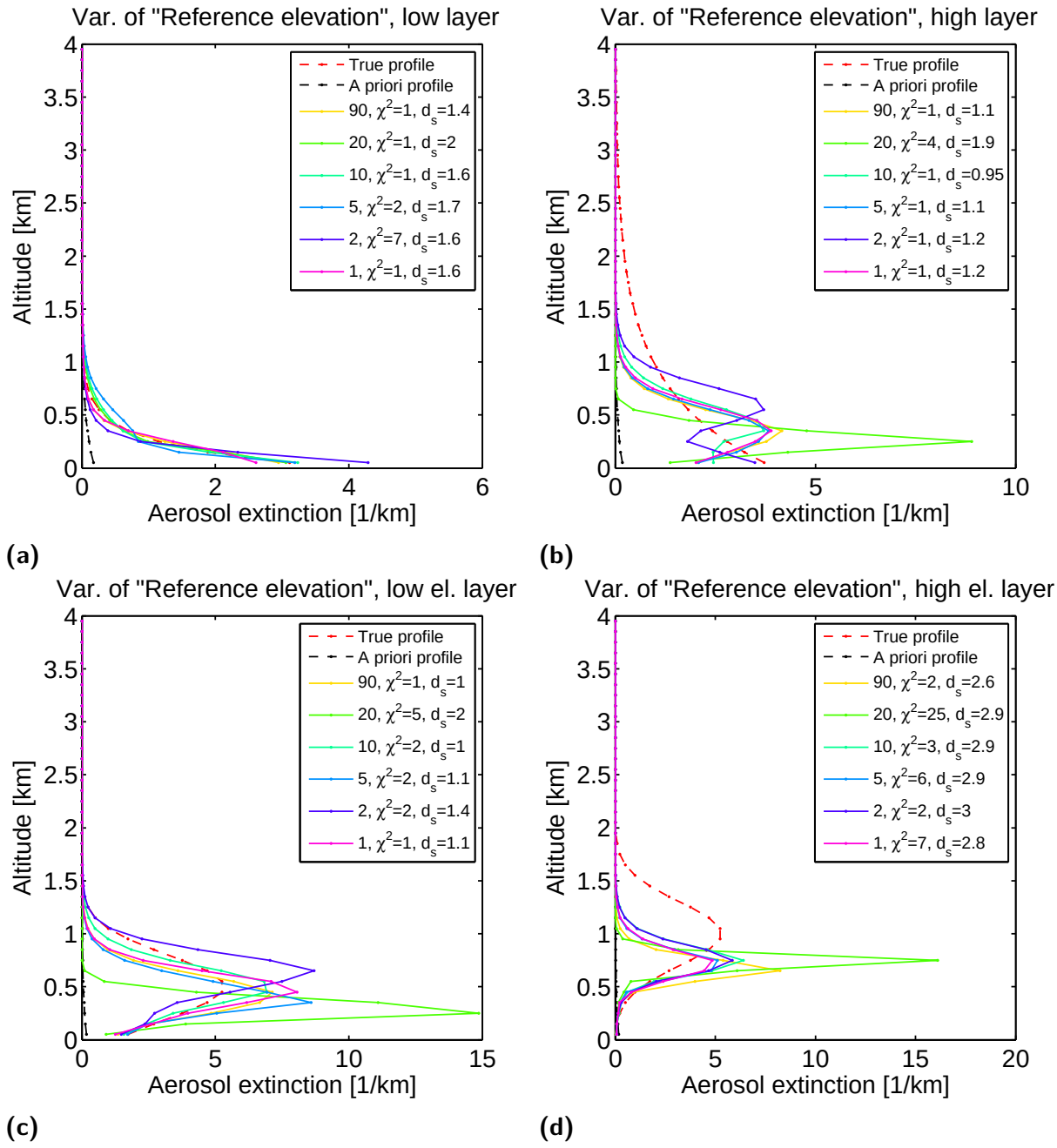

Figure A.17.: Case 2 - Medium aerosol extinction scenarios: Analysis of the effect of which elevation angle is used as the reference angle. For details of the method see section 5.1.

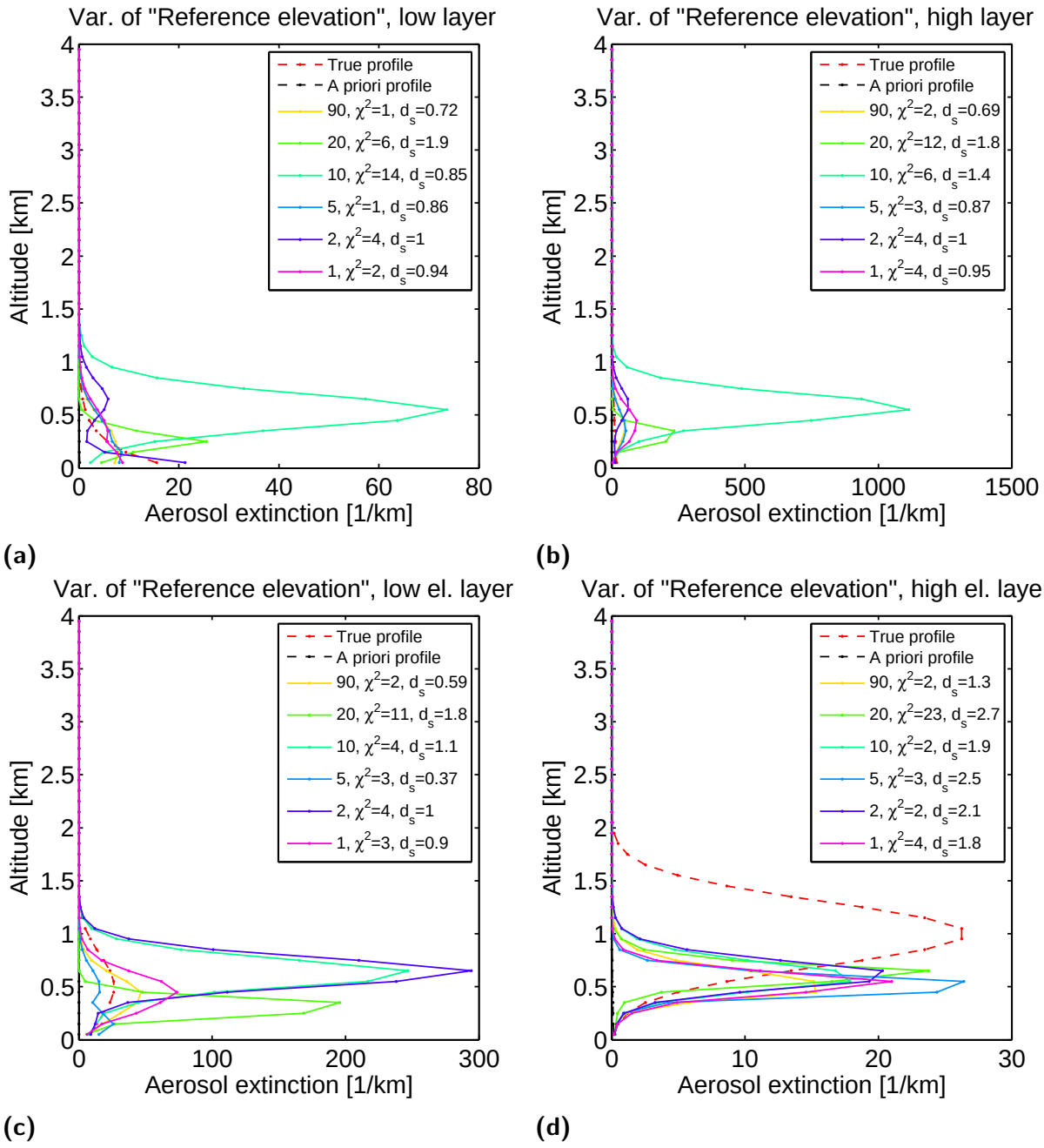

Figure A.18.: Case 3 - High aerosol extinction scenarios: Analysis of the effect of which elevation angle is used as the reference angle. For details of the method see section 5.1.

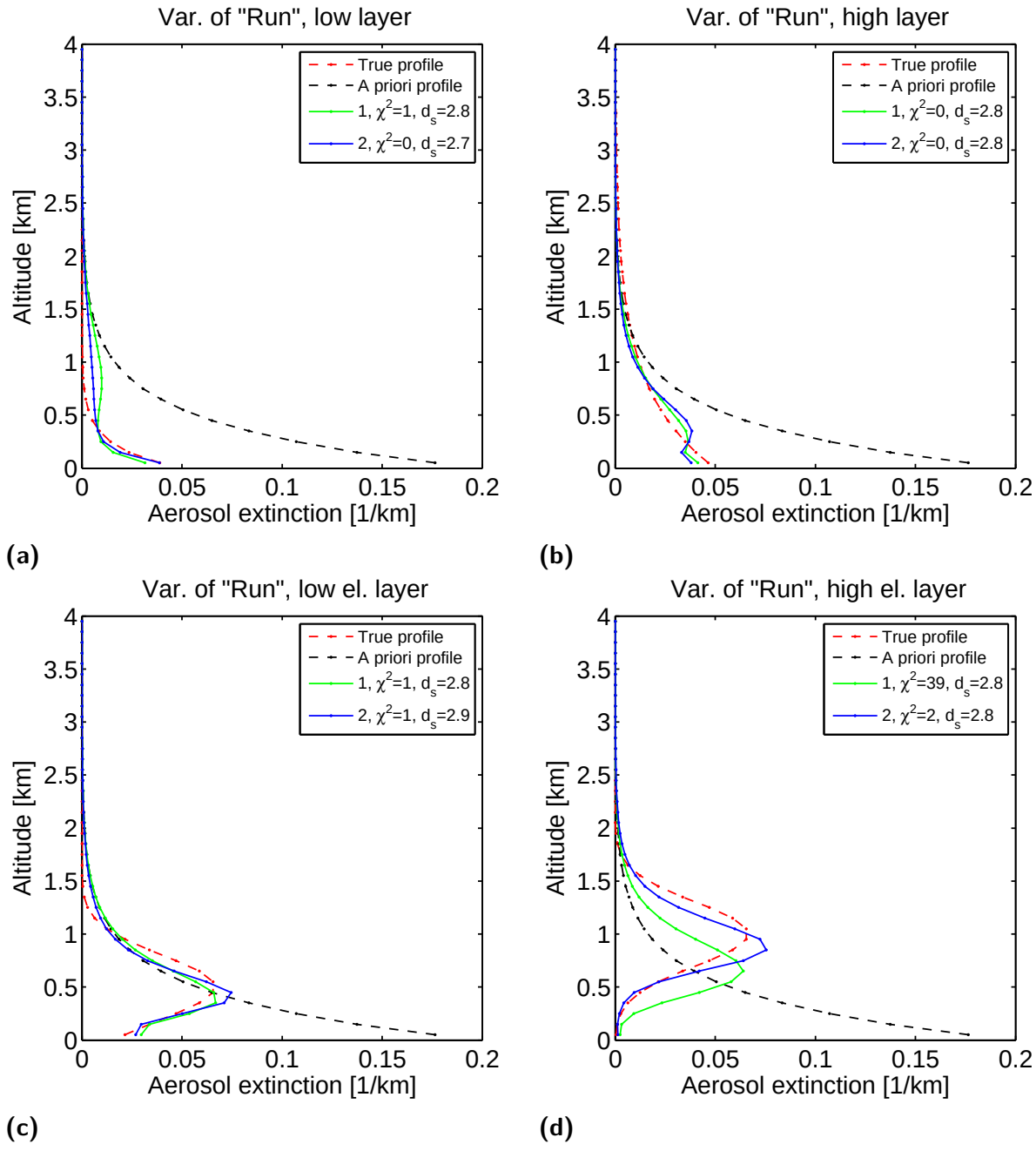

Figure A.19.: Case 1 - Low aerosol extinction scenarios: Analysis of the effect of using one (1) or two (2) runs. For details of the method see section 5.1.

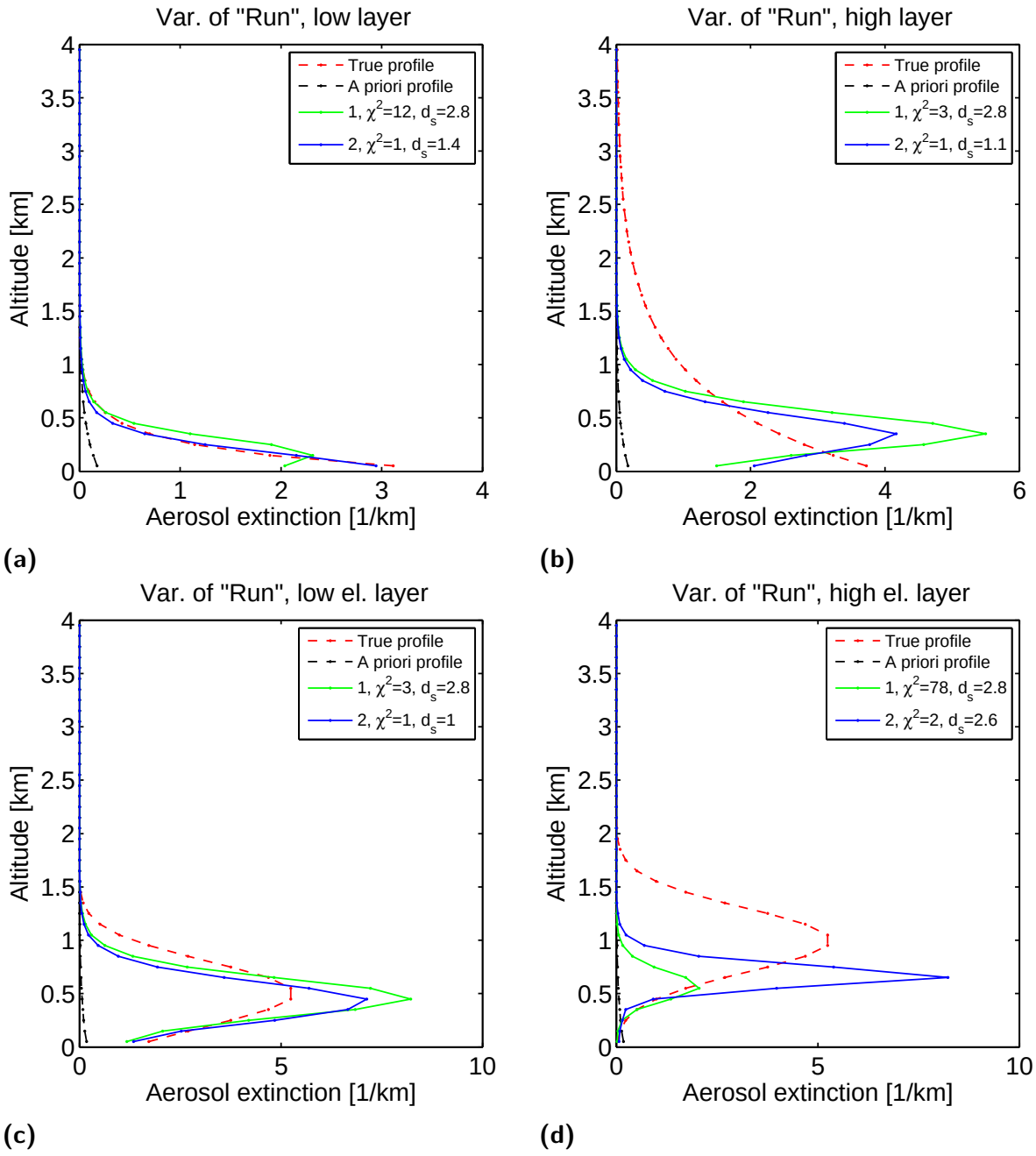

Figure A.20.: Case 2 - Medium aerosol extinction scenarios: Analysis of the effect of using one (1) or two (2) runs. For details of the method see section 5.1.

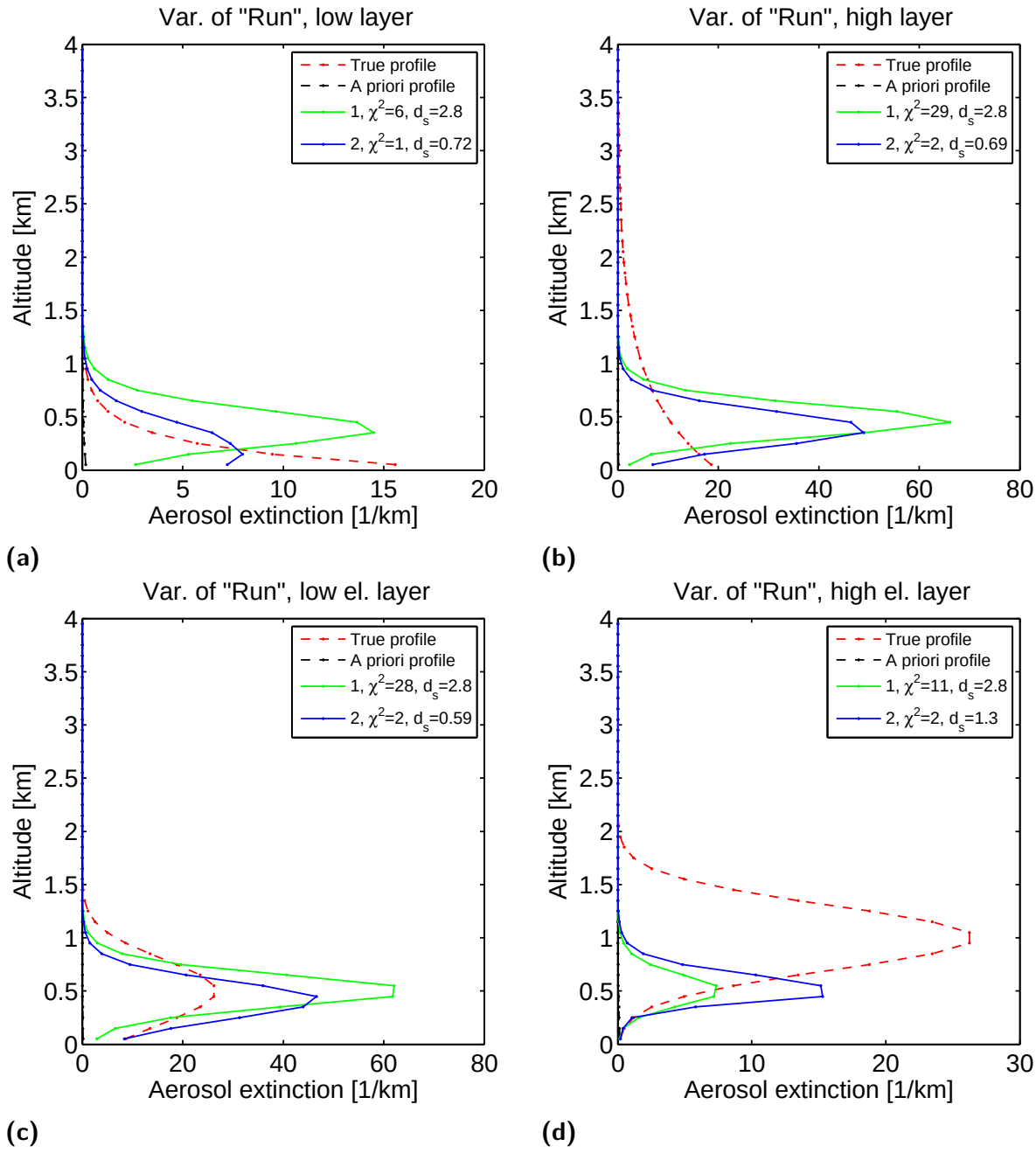

Figure A.21.: Case 3 - High aerosol extinction scenarios: Analysis of the effect of using one (1) or two (2) runs. For details of the method see section 5.1.

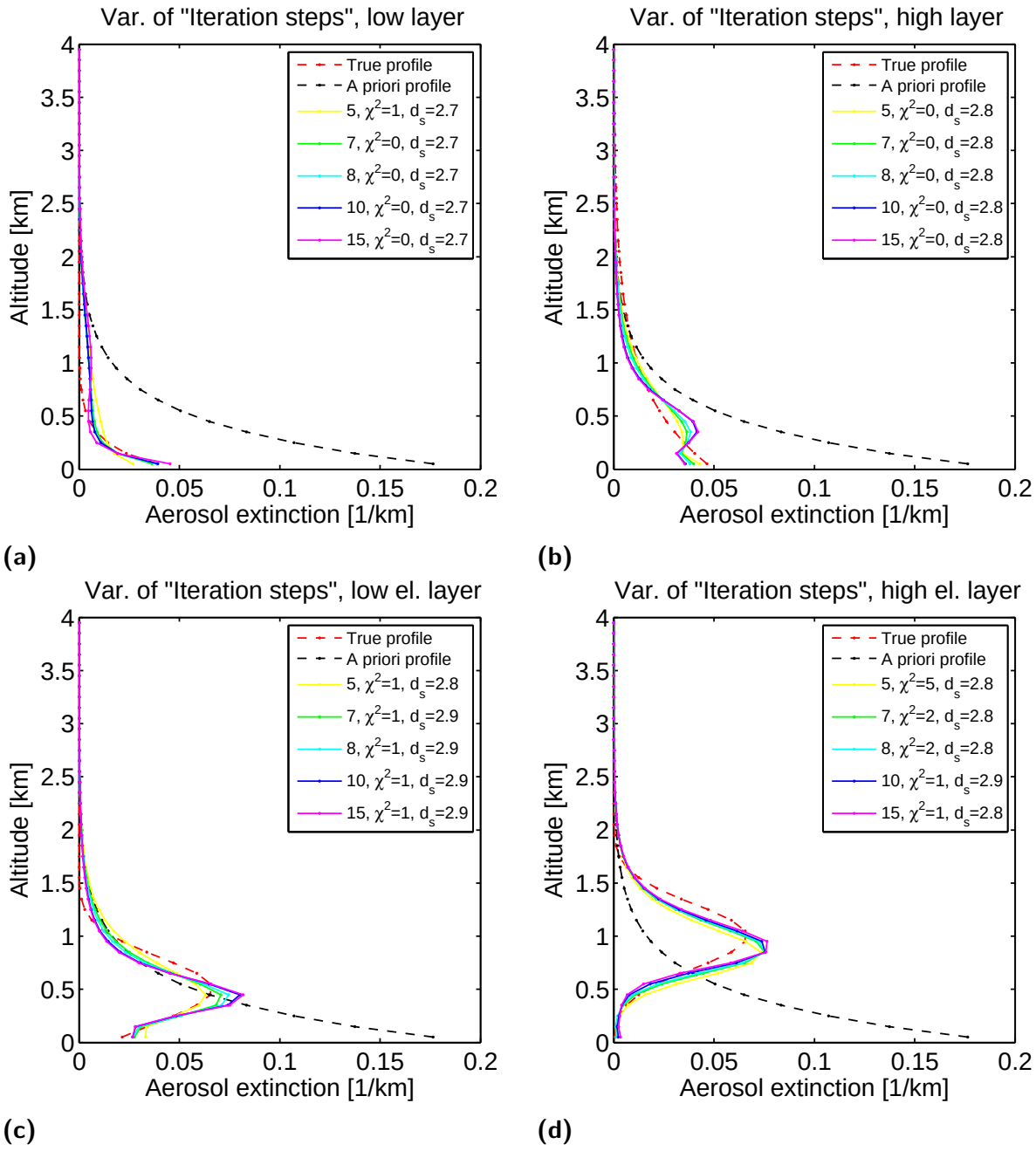

Figure A.22.: Case 1 - Low aerosol extinction scenarios: Analysis of the effect of how many iteration steps (5 to 15) are maximally performed per inversion. For details of the method see section 5.1.

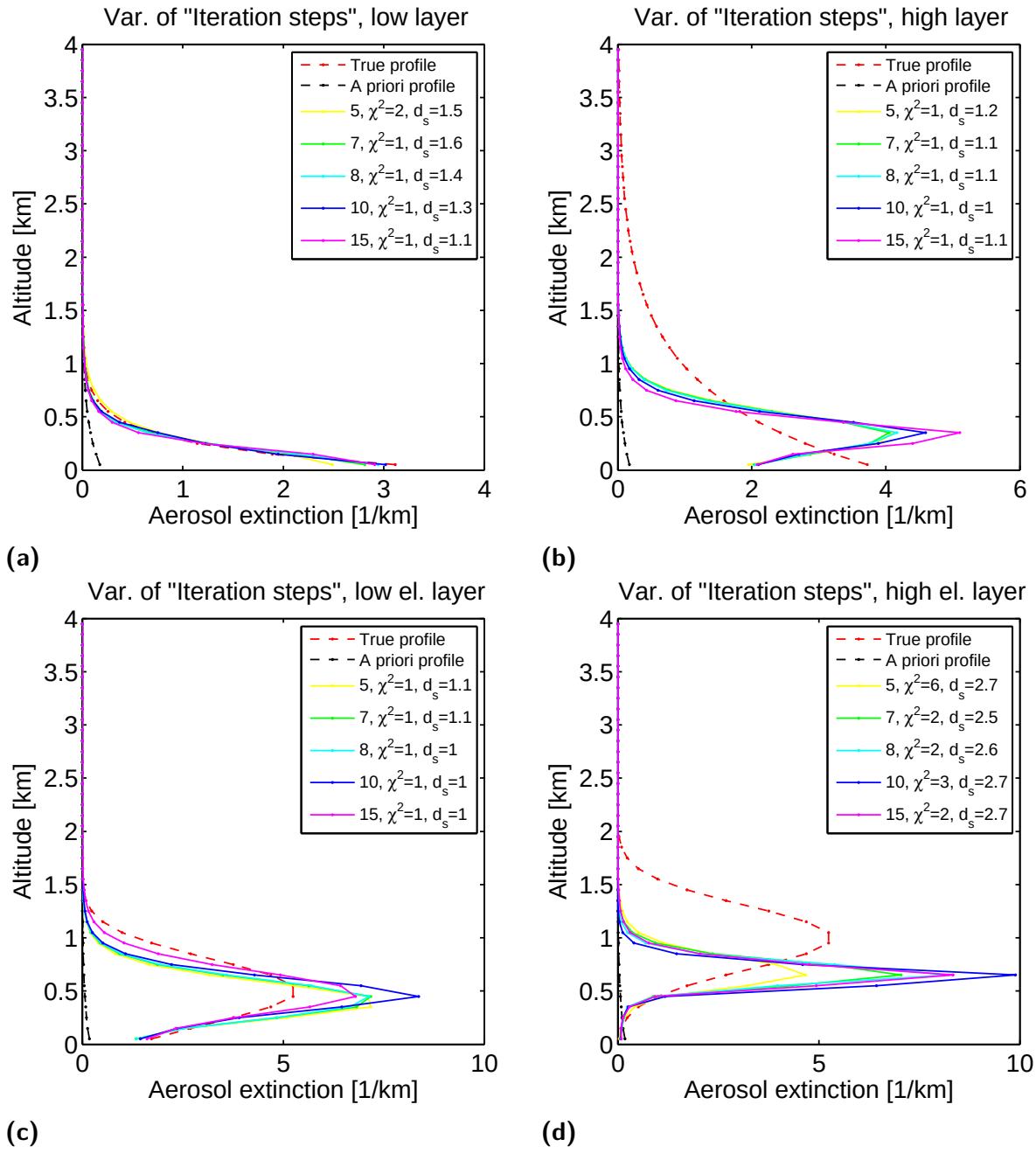

Figure A.23.: Case 2 - Medium aerosol extinction scenarios: Analysis of the effect of how many iteration steps (5 to 15) are maximally performed per inversion. For details of the method see section 5.1.

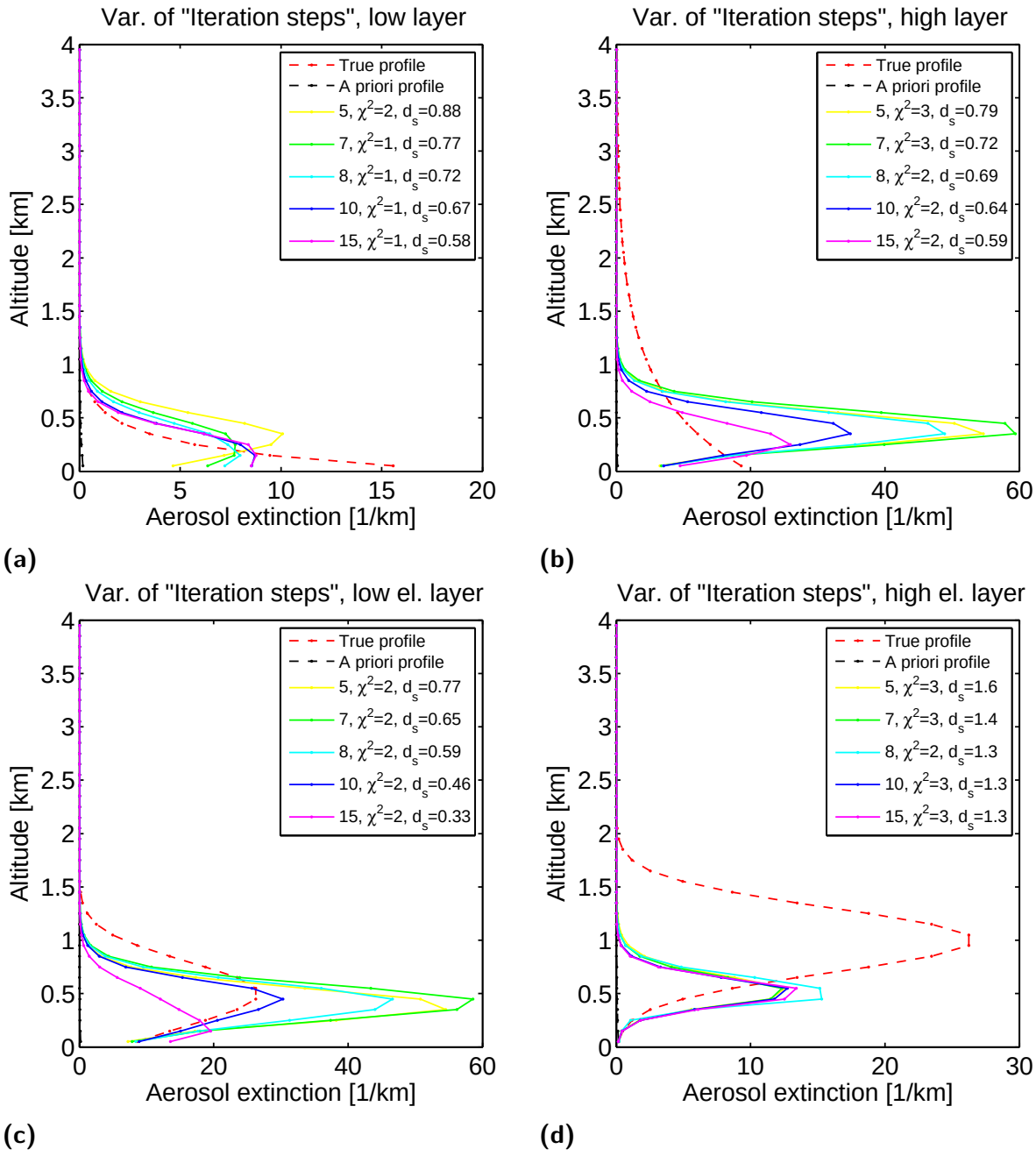

Figure A.24.: Case 3 - High aerosol extinction scenarios: Analysis of the effect of how many iteration steps (5 to 15) are maximally performed per inversion. For details of the method see section 5.1.

A.2 MAX-DOAS inversion sensitivity studies: Trace gas

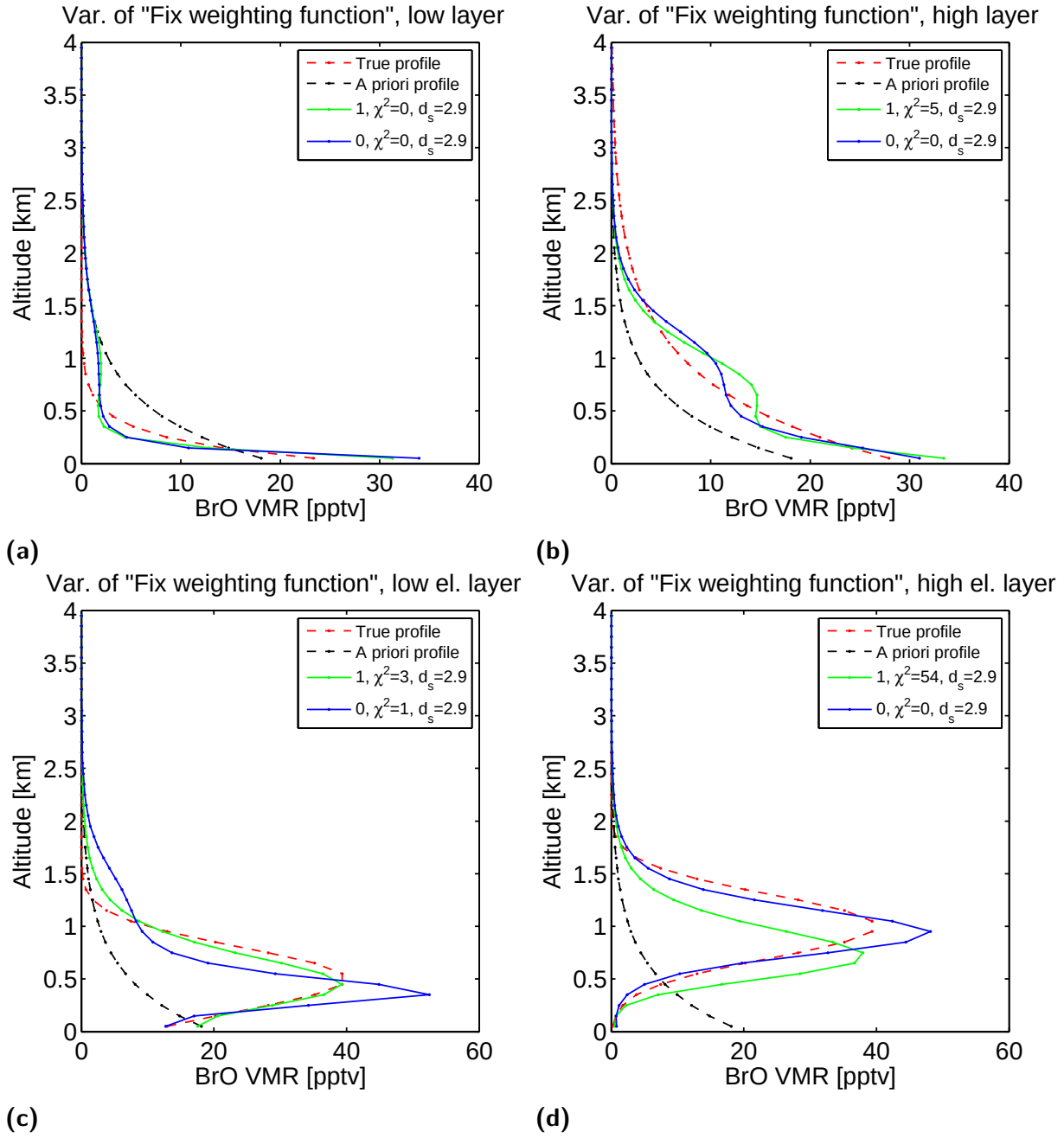

Figure A.25.: Case 1 - High BrO mixing ratios: Analysis of the effect of the recalculation of the weighting functions with every single iteration. Two settings are possible: True (1) and false (0). For details of the method see section 5.2.

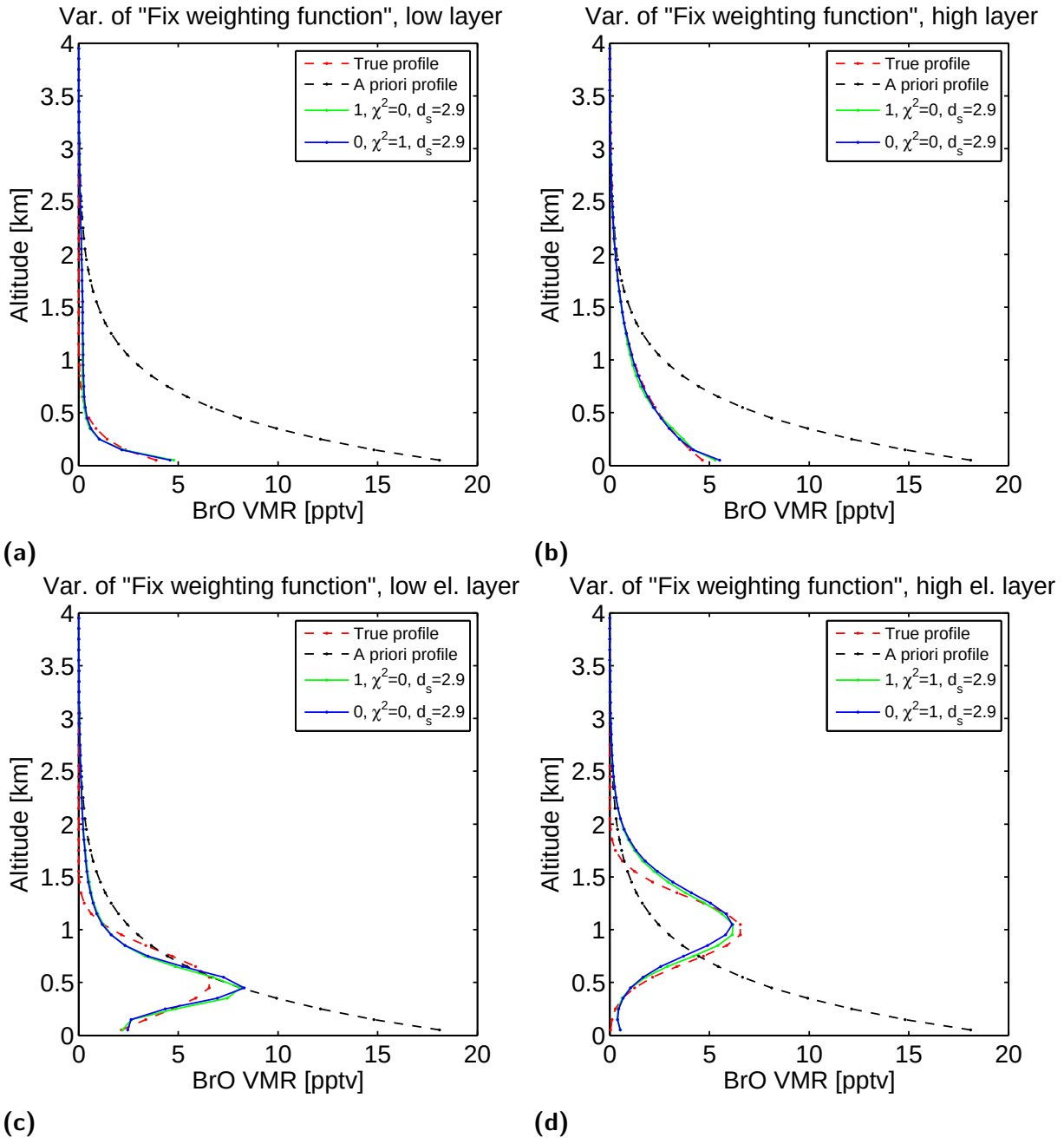

Figure A.26.: Case 2 - Low BrO mixing ratios: Analysis of the effect of the recalculation of the weighting functions with every single iteration. Two settings are possible: True (1) and false (0). For details of the method see section 5.2.

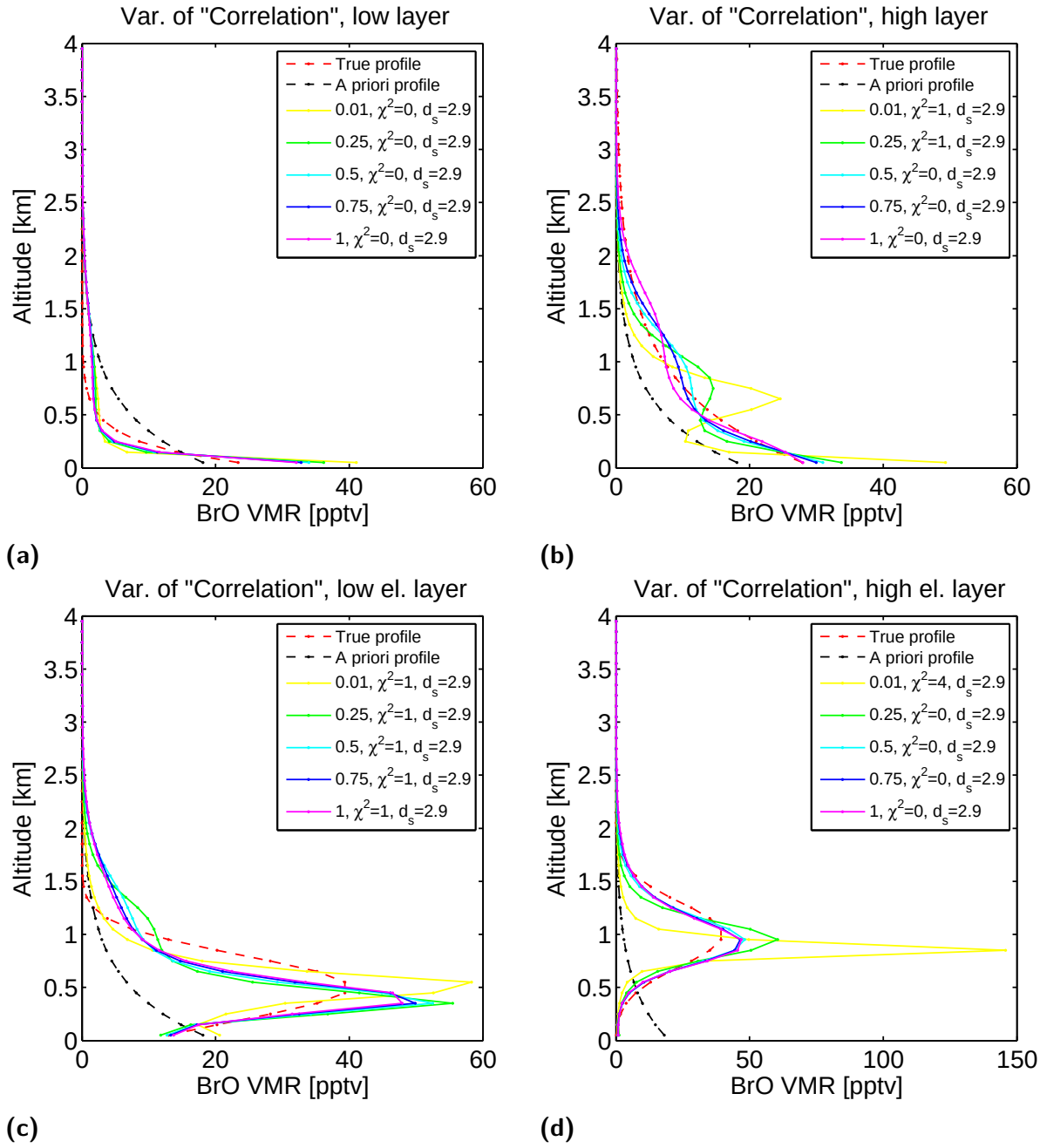

Figure A.27.: Case 1 - High BrO mixing ratios: Analysis of the effect of a change of the correlation length, given in km, from 0.01 km to 1 km. The correlation length determines the coupling of different grid boxes through the covariance matrix of the a priori profile. For details of the method see section 5.2.

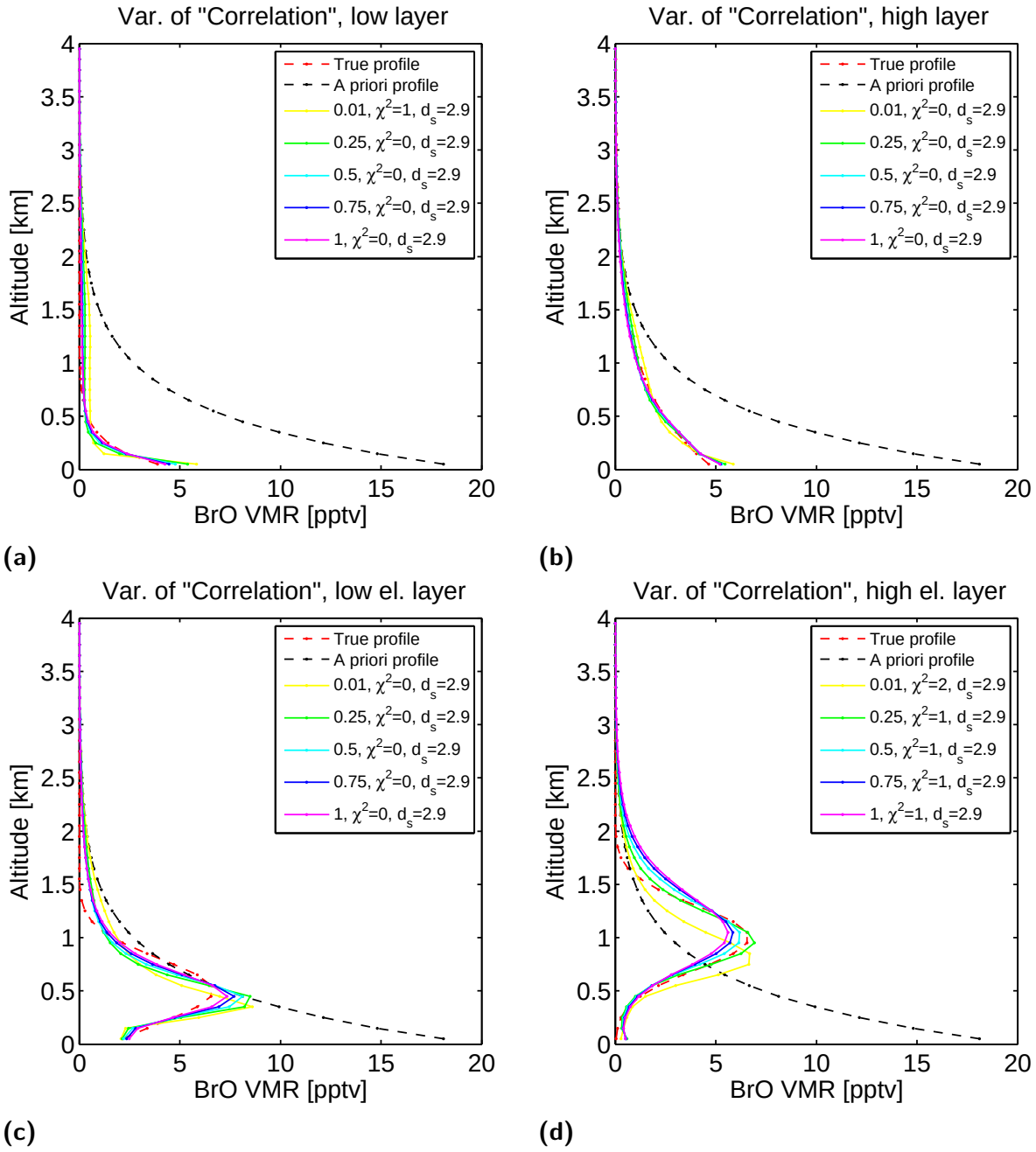

Figure A.28.: Case 2 - Low BrO mixing ratios: Analysis of the effect of a change of the correlation length, given in km, from 0.01 km to 1 km. The correlation length determines the coupling of different grid boxes through the covariance matrix of the a priori profile. For details of the method see section 5.2.

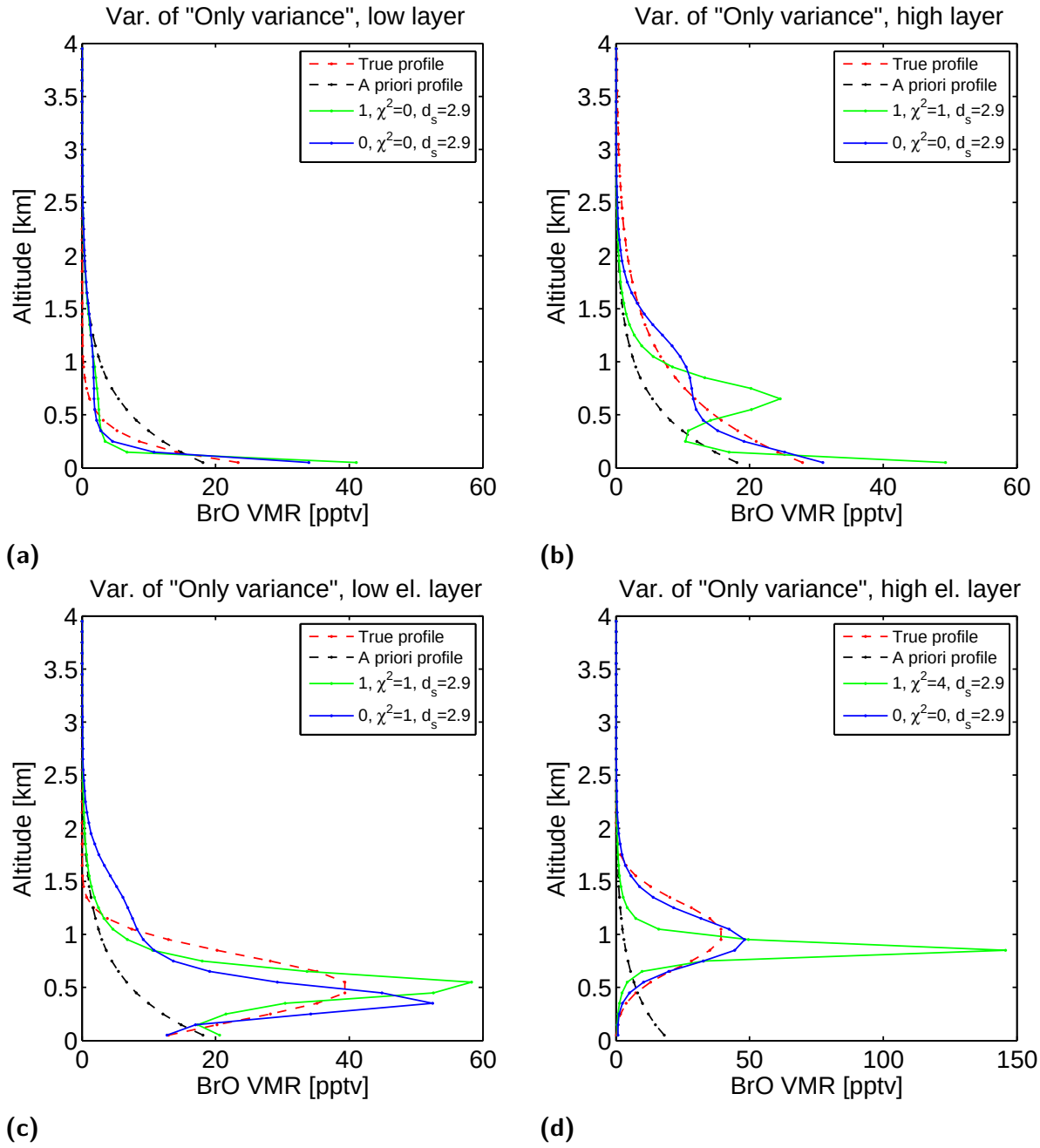

Figure A.29.: Case 1 - High BrO mixing ratios: Analysis of the effect of whether the used a priori covariance matrix contains off-axis elements (0), whose value is determined by the correlation length, or only diagonal values (1). In the last case, neighboring grid boxes are independent of each other. For details of the method see section 5.2.

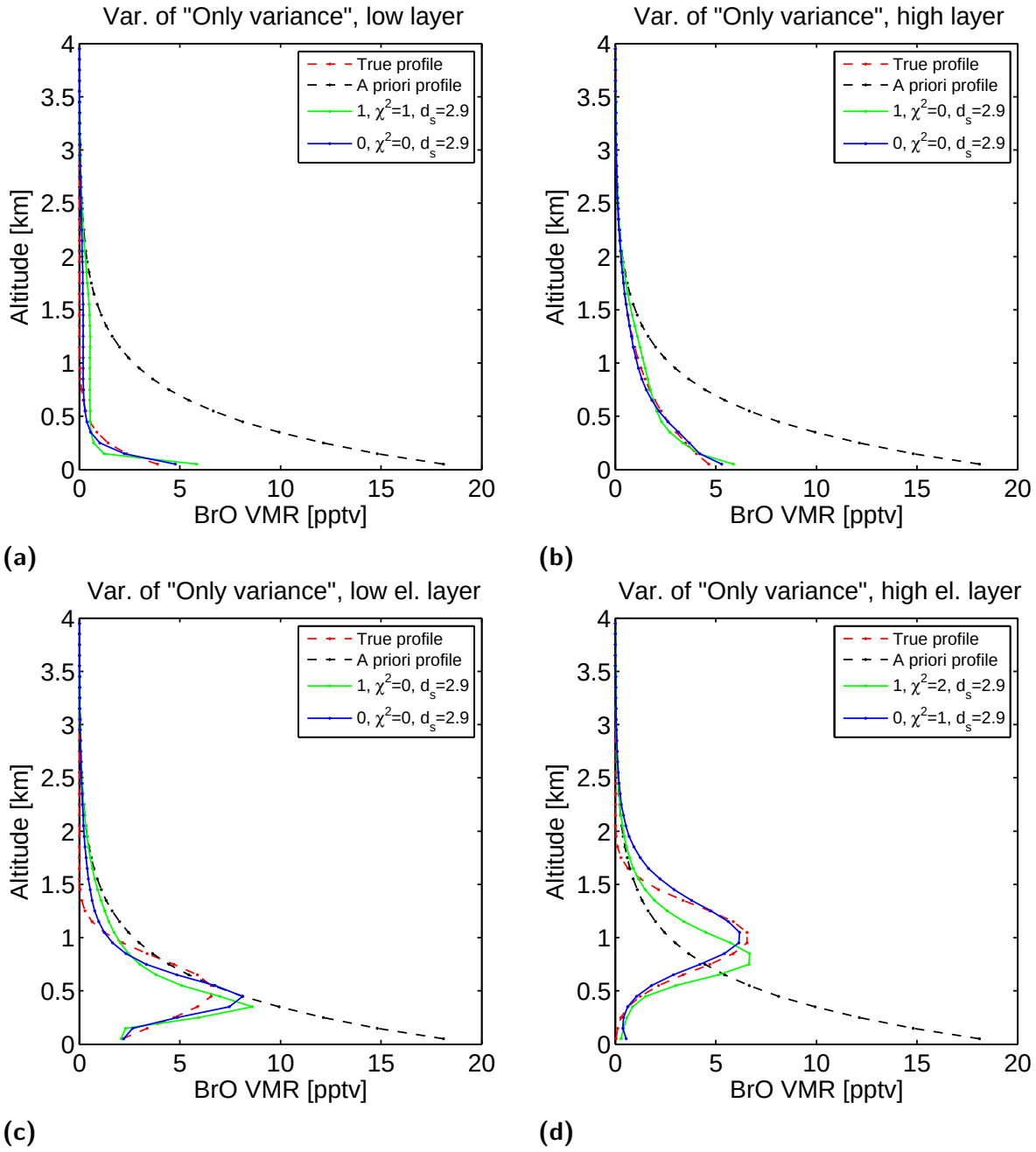

Figure A.30.: Case 2 - Low BrO mixing ratios: Analysis of the effect of whether the used a priori covariance matrix contains off-axis elements (0), whose value is determined by the correlation length, or only diagonal values (1). In the last case, neighboring grid boxes are independent of each other. For details of the method see section 5.2.

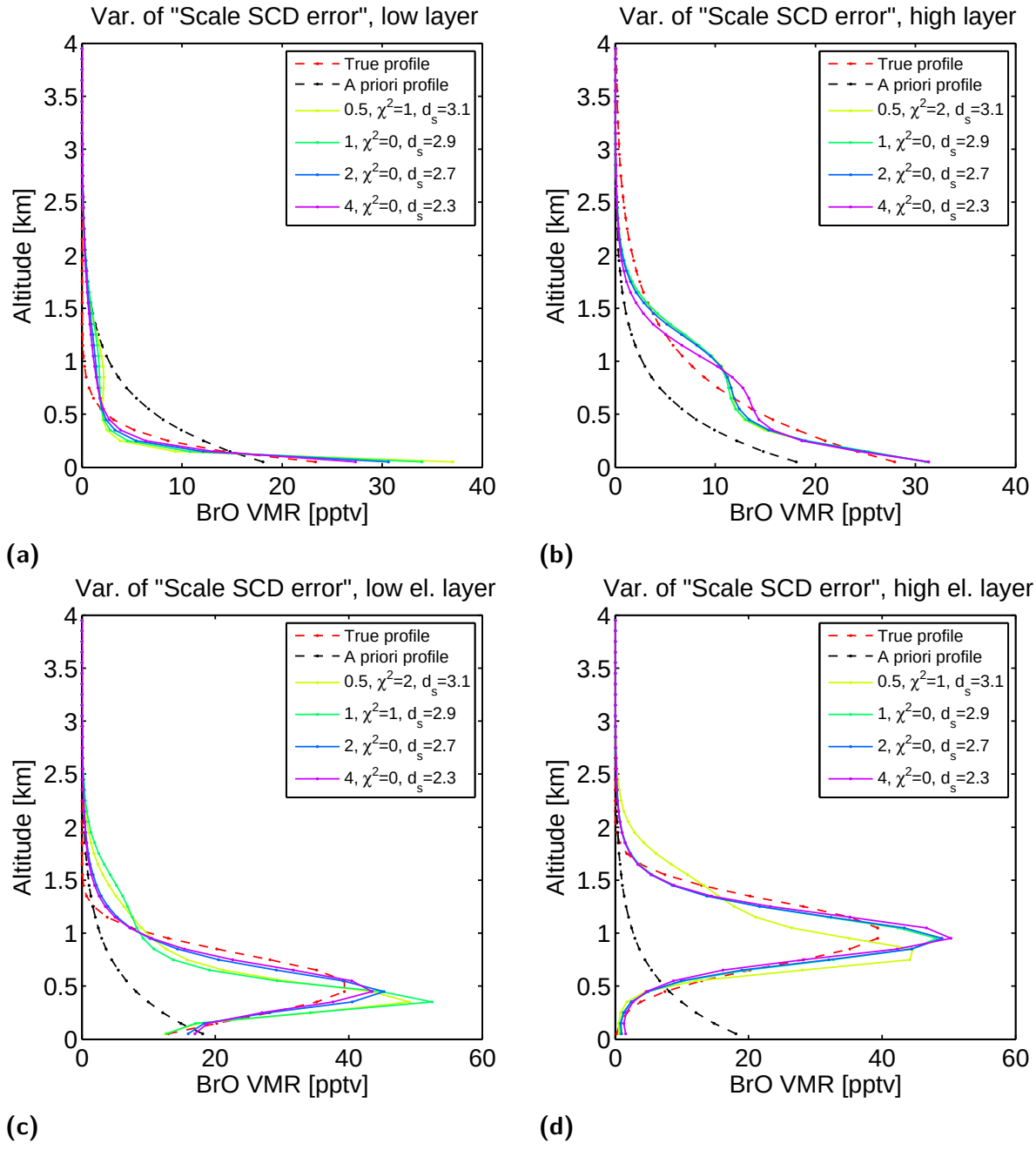

Figure A.31.: Case 1 - High BrO mixing ratios: Analysis of the effect of scaling the error on the measurement SCDs before the inversion with values from 0.5 to 4. The effect is exactly equivalent to a scaling of the a priori profile error with the inverse. For details of the method see section 5.2.

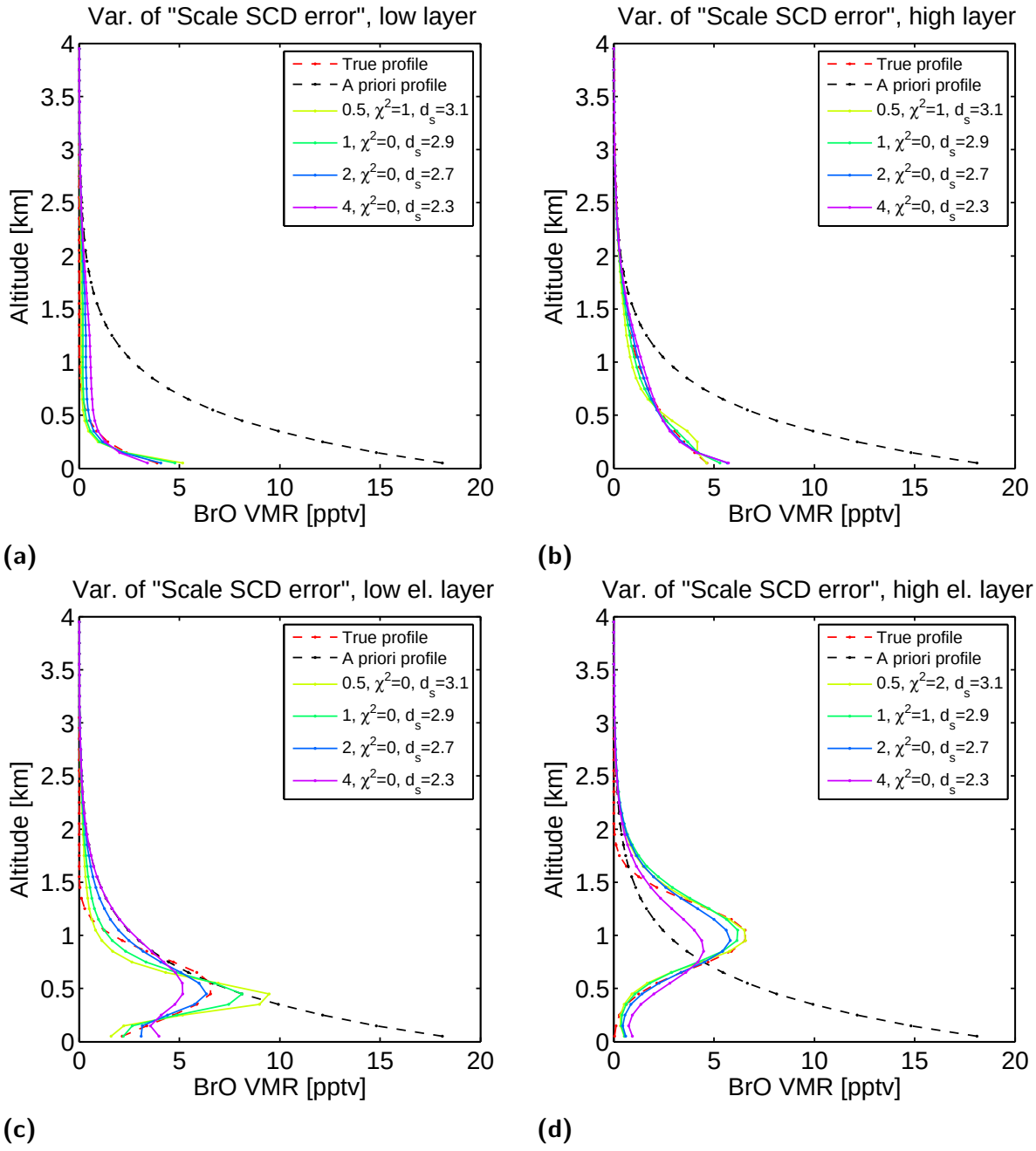

Figure A.32.: Case 2 - Low BrO mixing ratios: Analysis of the effect of scaling the error on the measurement SCDs before the inversion with values from 0.5 to 4. The effect is exactly equivalent to a scaling of the a priori profile error with the inverse. For details of the method see section 5.2.

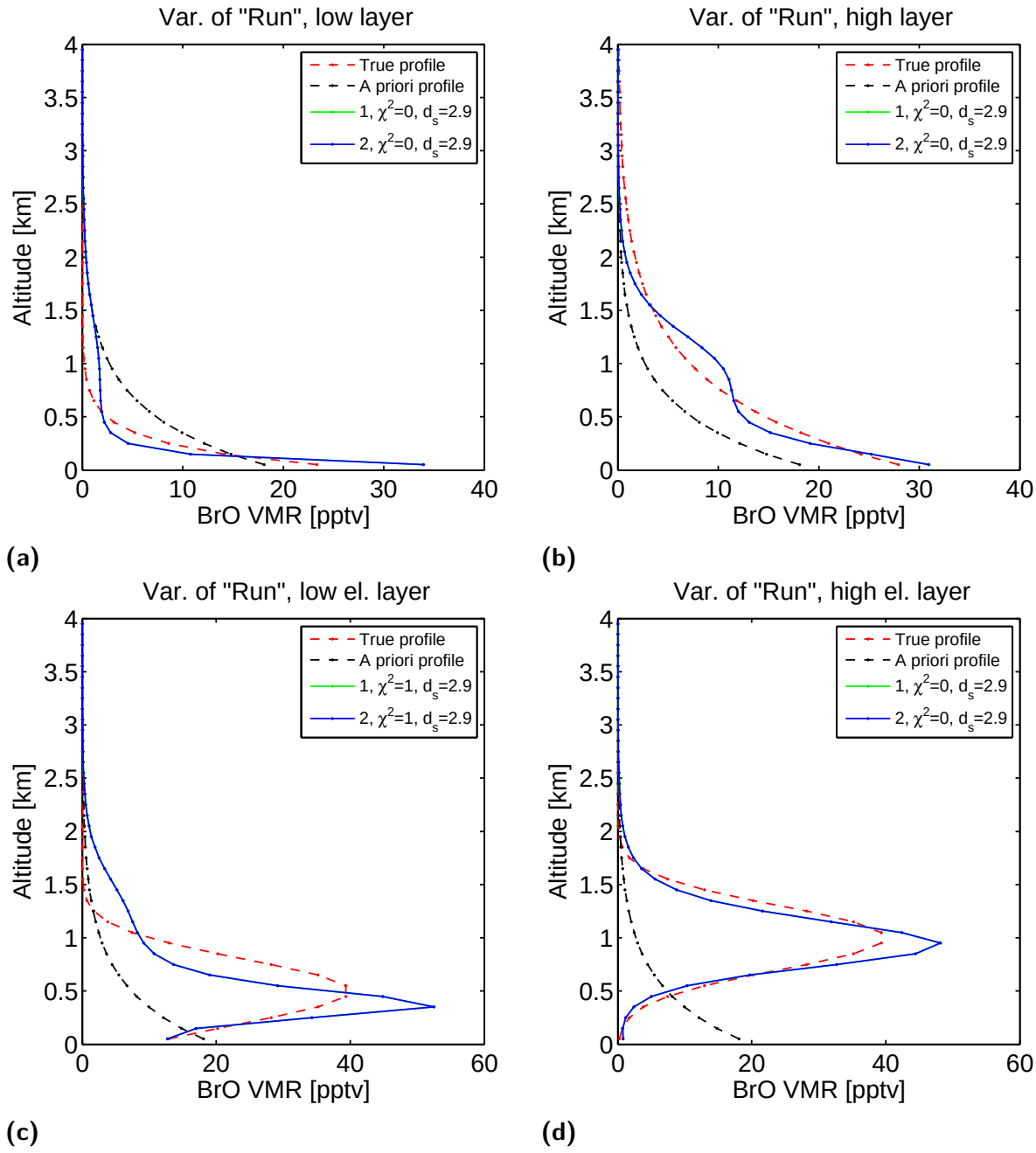

Figure A.33.: Case 1 - High BrO mixing ratios: Analysis of the effect of using one (1) or two (2) runs. For details of the method see section 5.2.

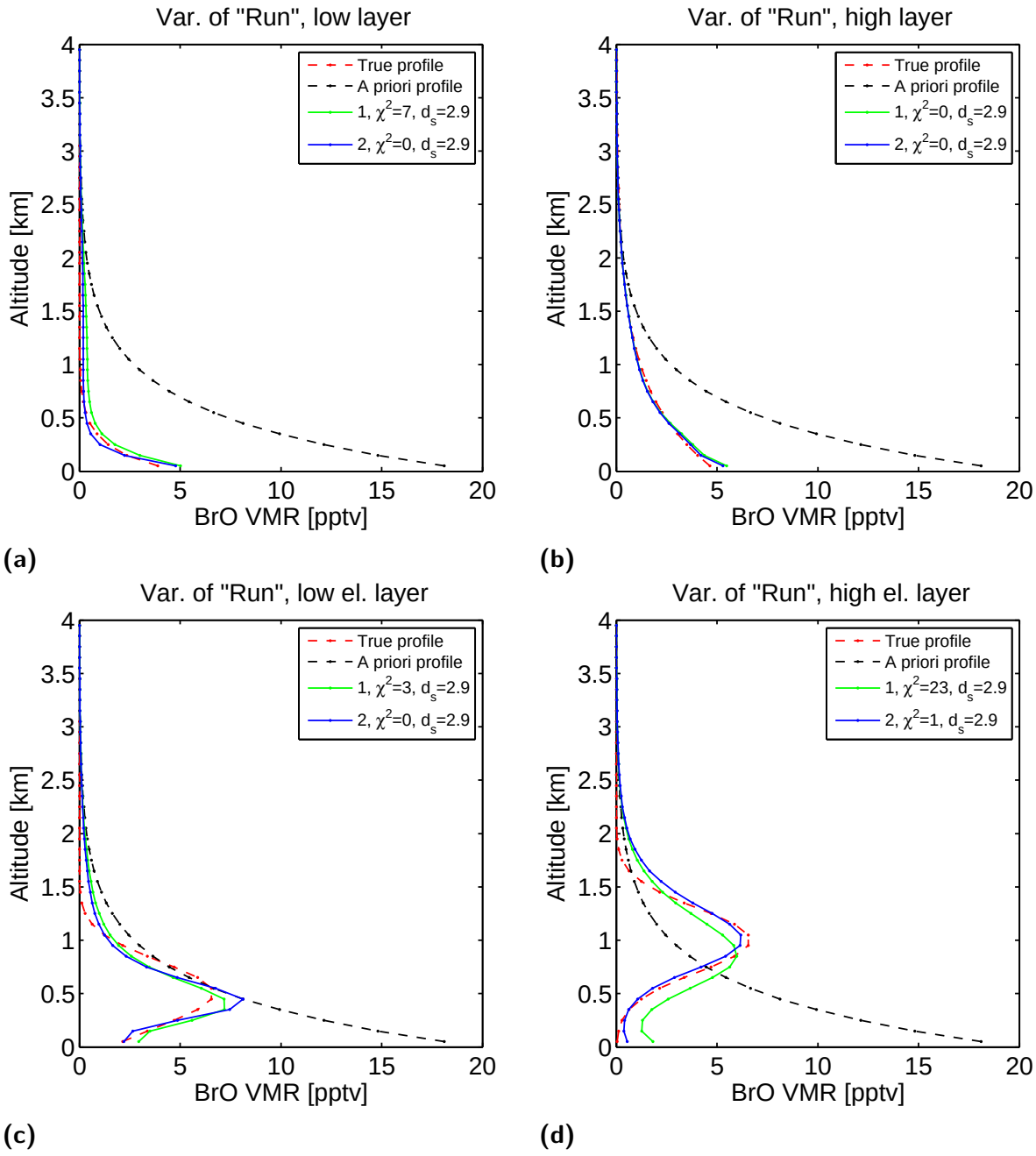

Figure A.34.: Case 2 - Low BrO mixing ratios: Analysis of the effect of using one (1) or two (2) runs. For details of the method see section 5.2.

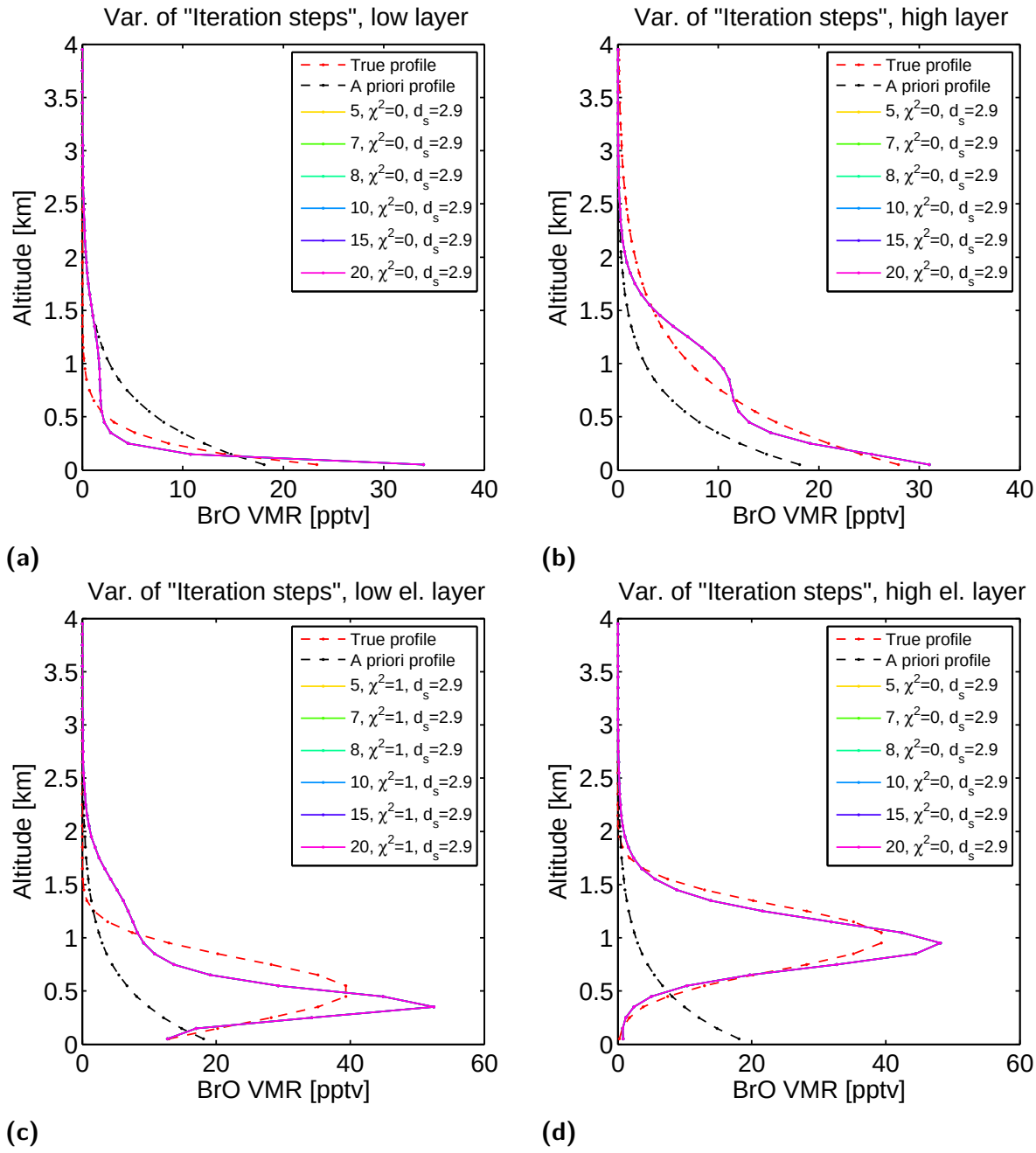

Figure A.35.: Case 1 - High BrO mixing ratios: Analysis of the effect of how many iteration steps (5 to 20) are maximally performed per inversion. For details of the method see section 5.2.

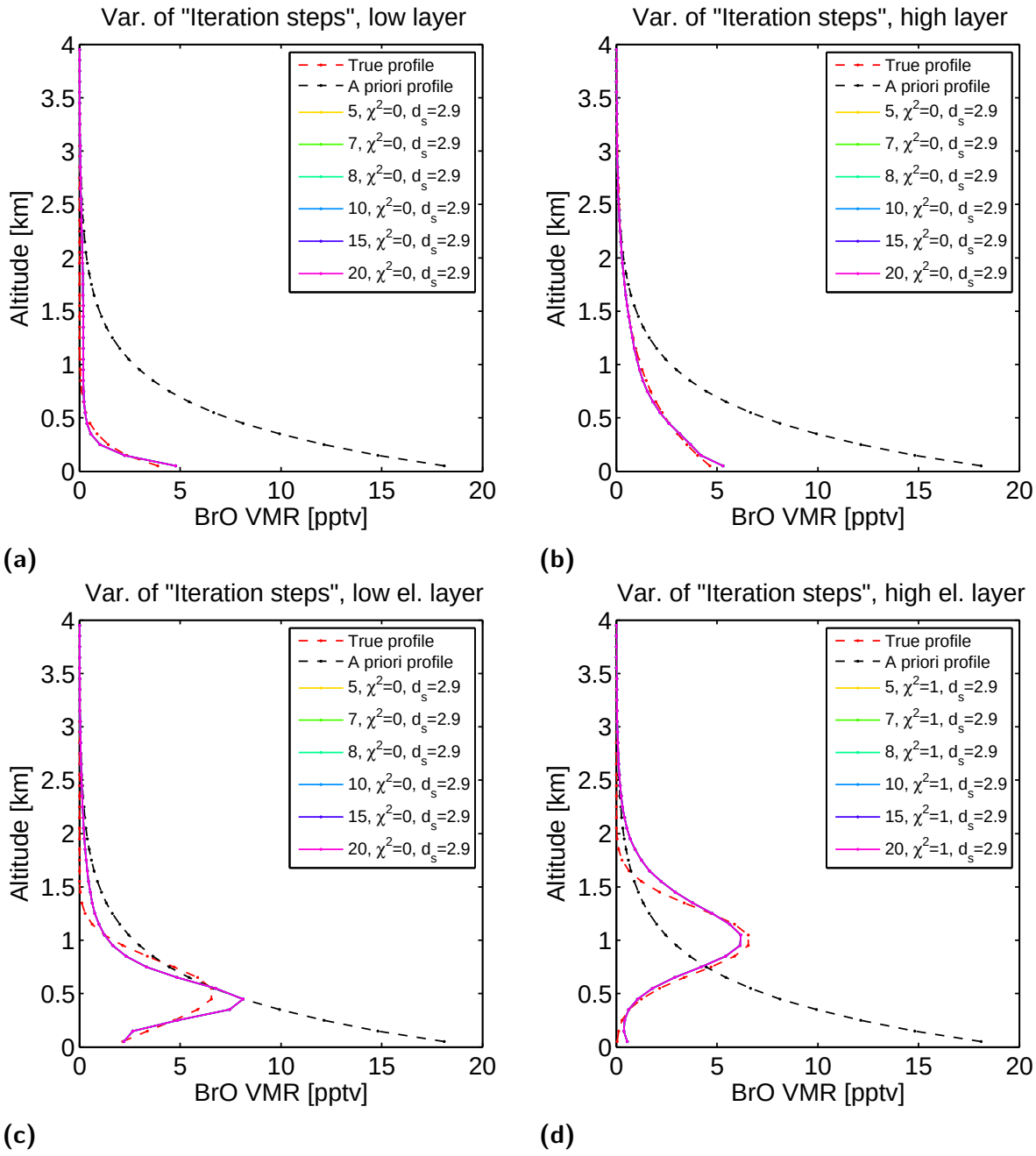

Figure A.36.: Case 2 - Low BrO mixing ratios: Analysis of the effect of how many iteration steps (5 to 20) are maximally performed per inversion. For details of the method see section 5.2.

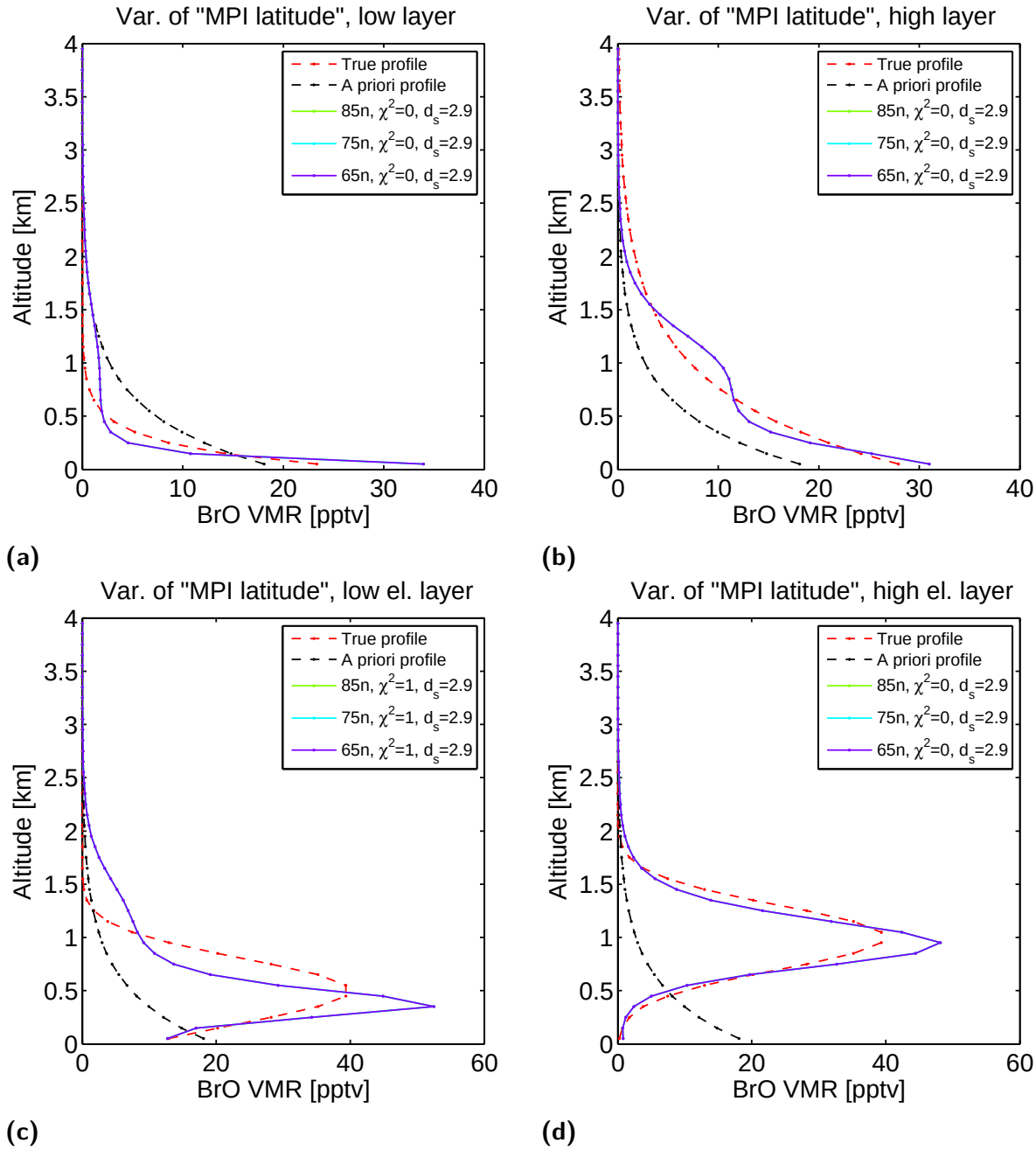

Figure A.37.: Case 1 - High BrO mixing ratios: Analysis of the effect of using different atmospheric temperature and pressure profiles included in the algorithm for 65 °N, 75 °N and 85 °N (true state). The provided profiles are monthly averages and given in steps of 10 ° latitude. For details of the method see section 5.2.

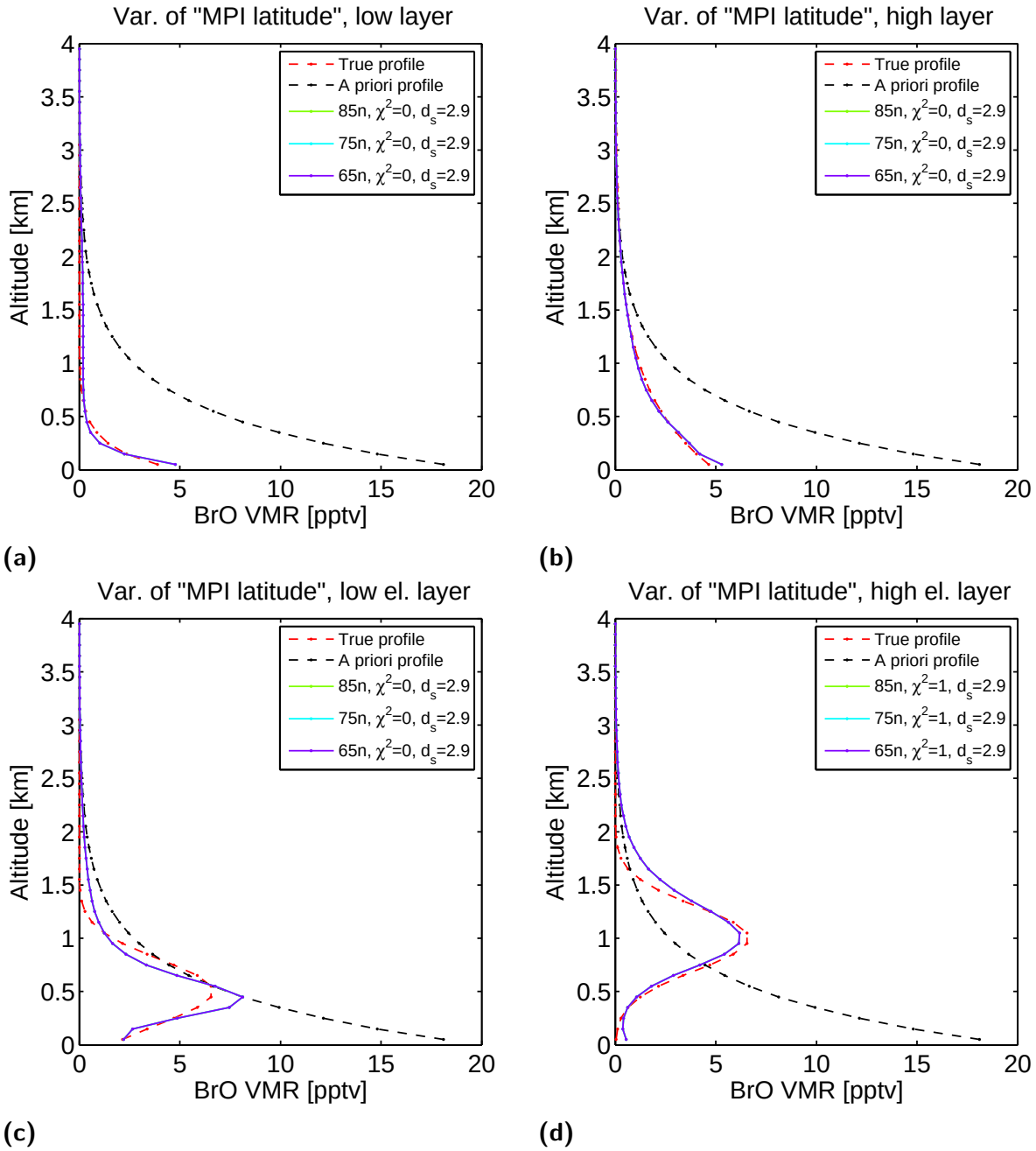

Figure A.38.: Case 2 - Low BrO mixing ratios: Analysis of the effect of using different atmospheric temperature and pressure profiles included in the algorithm for 65 °N, 75 °N and 85 °N (true state). The provided profiles are monthly averages and given in steps of 10 ° latitude. For details of the method see section 5.2.

A.3 DOAS evaluation: Chosen laboratory absorption cross sections

Absorber	**Laboratory reference cross section used in this work**
BrO	Fleischmann et al. (2004)
IO	Spietz et al. (2005)
ClO	Simon et al. (1990)
O_4	for BrO: Greenblatt et al. (1990), otherwise: Hermans et al. (2003)
H_2O	Barber et al. (2006)
NO_2	UV: Voigt et al. (2002), VIS: Vandaele et al. (2002)
NO_3	Yokelson et al. (1994)
SO_2	Bogumil et al. (2003)
O_3	for ClO: Voigt et al. (2001), otherwise: Serdyuchenko et al. (2014)
OClO	Kromminga et al. (2003)
OBrO	Fleischmann and Burrows (2002)
OIO	Spietz et al. (2005)
I_2	Spietz et al. (2006)
CHOCHO	Volkamer et al. (2005)
HCHO	Meller and Moortgat (2000)
HONO	Stutz et al. (2000)

Table A.1.: List of the used high resolution laboratory cross sections for the DOAS analysis for all absorbers considered in this work. Unless specifically noted, the cross sections listed here were used in all evaluations.

A.4 Scott Base: Additional CE-DOAS measurements

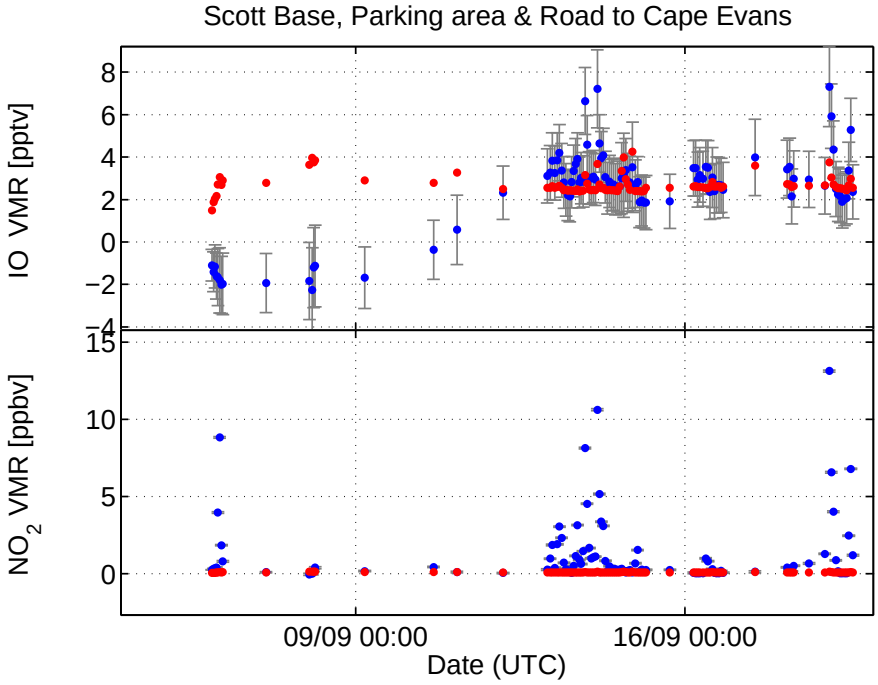

Figure A.39.: Scott Base CE-DOAS: Derived mixing ratios for IO and NO_2. The detection limit is given as 4 times the fit error. However at levels of more than 1 ppbv of NO_2, the DL for IO is already over 10 pptv due to strong remaining residual structures. Measurements are marked blue, the respective detection limit red.

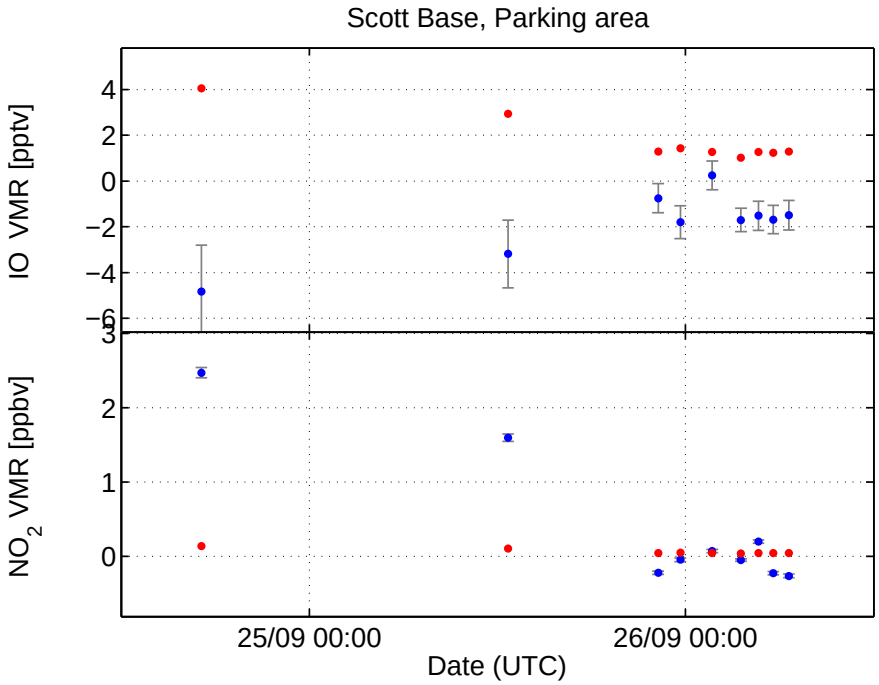

Figure A.40.: Scott Base CE-DOAS: Derived mixing ratios for IO and NO_2. Measurements are marked blue, the respective detection limit red.

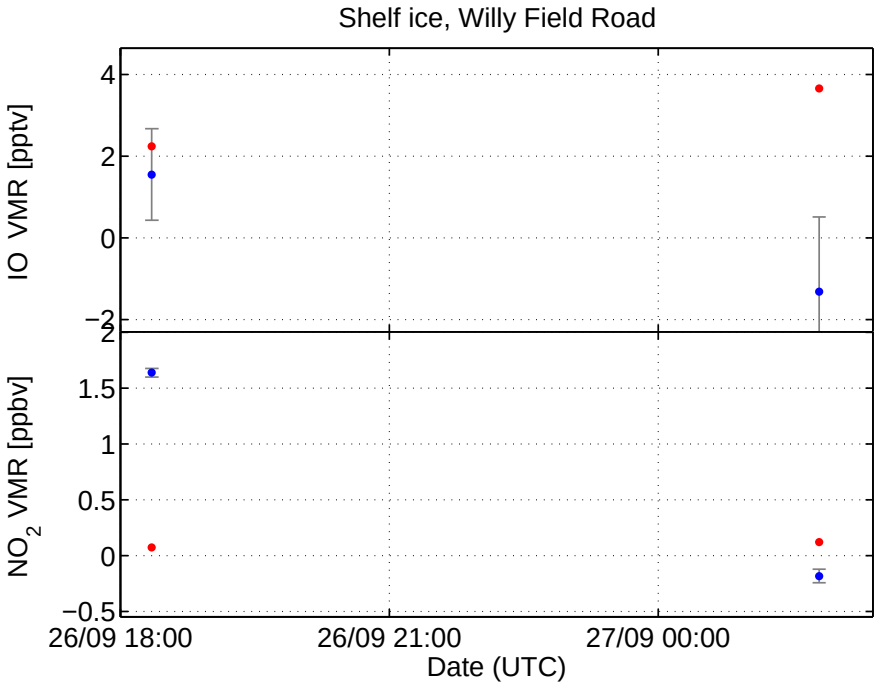

Figure A.41.: Scott Base CE-DOAS: Derived mixing ratios for IO and NO_2. The detection limit is given as 4 times the fit error. However at levels of more than 1 ppbv of NO_2, the DL for IO is already over 10 pptv due to strong remaining residual structures. Measurements are marked blue, the respective detection limit red.

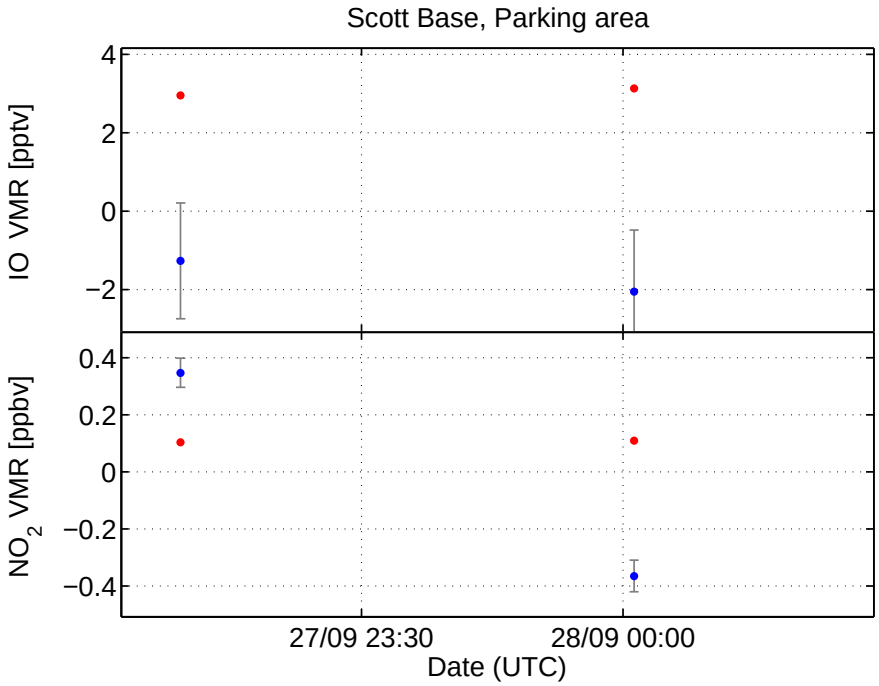

Figure A.42.: Scott Base CE-DOAS: Derived mixing ratios for IO and NO_2. Measurements are marked blue, the respective detection limit red.

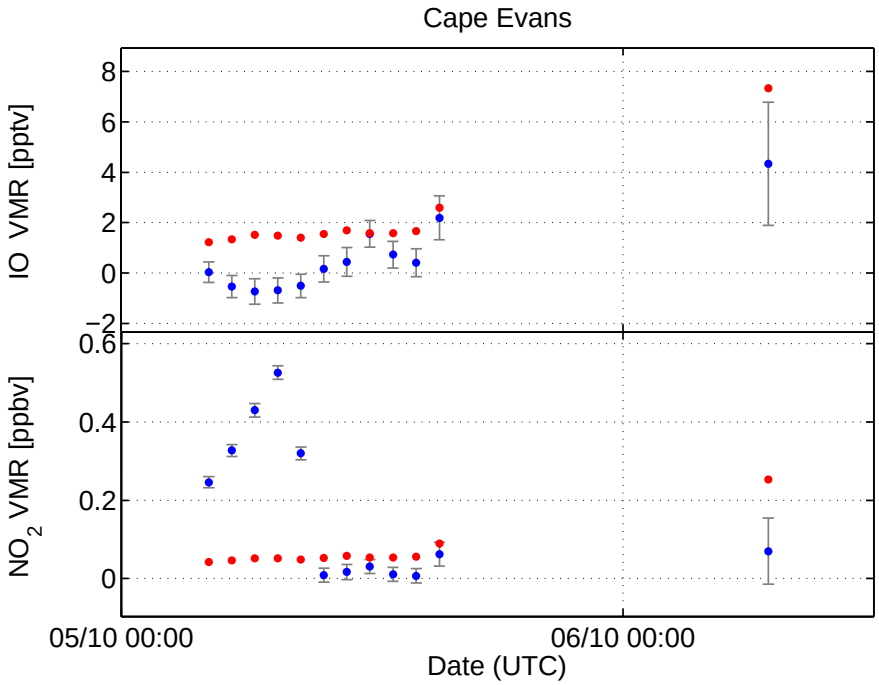

Figure A.43.: Scott Base CE-DOAS: Derived mixing ratios for IO and NO_2. Measurements are marked blue, the respective detection limit red.

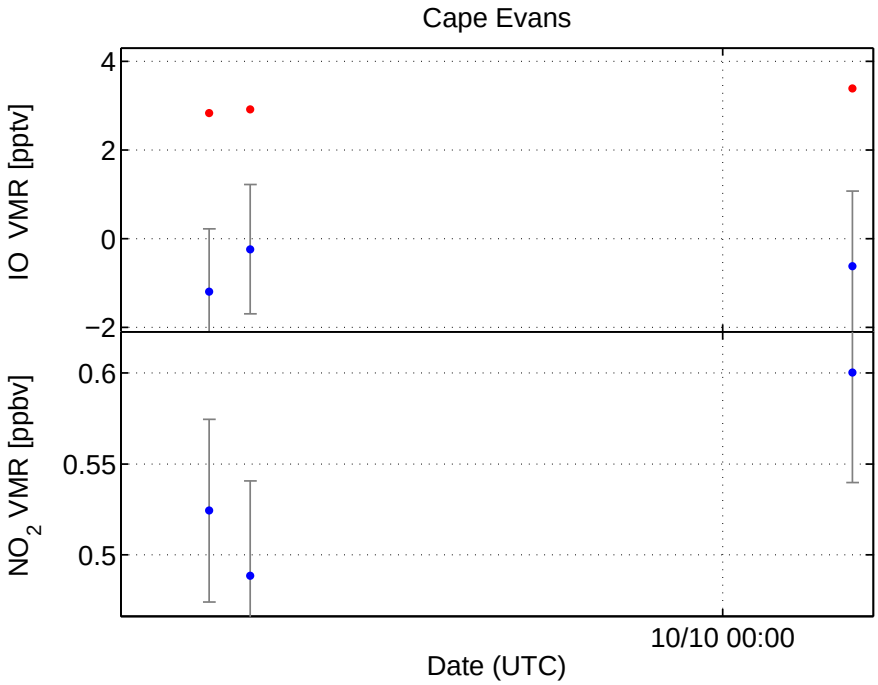

Figure A.44.: Scott Base CE-DOAS: Derived mixing ratios for IO and NO_2. Measurements are marked blue, the respective detection limit red.

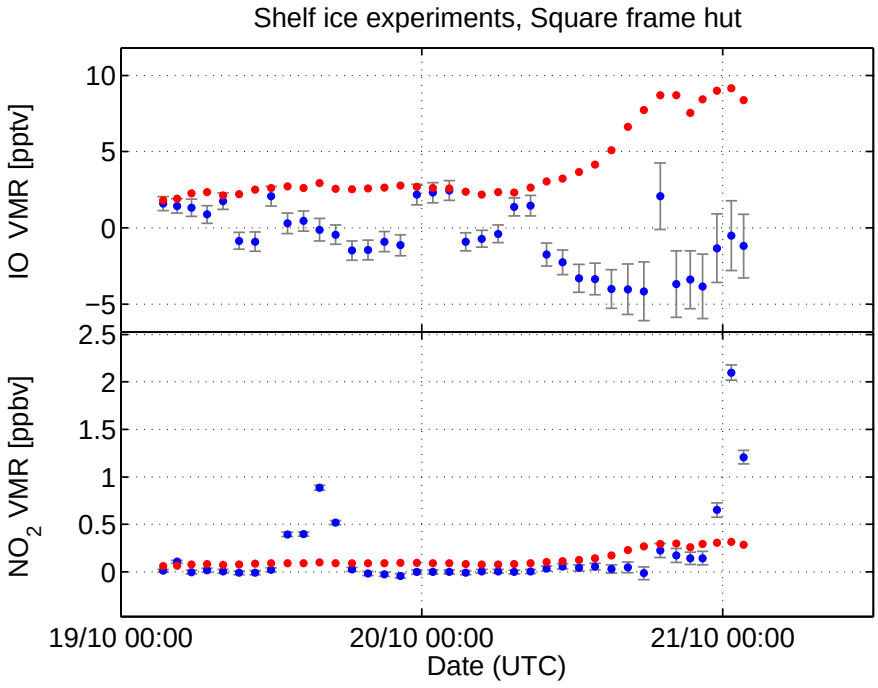

Figure A.45.: Scott Base CE-DOAS: Derived mixing ratios for IO and NO_2. Measurements are marked blue, the respective detection limit red.

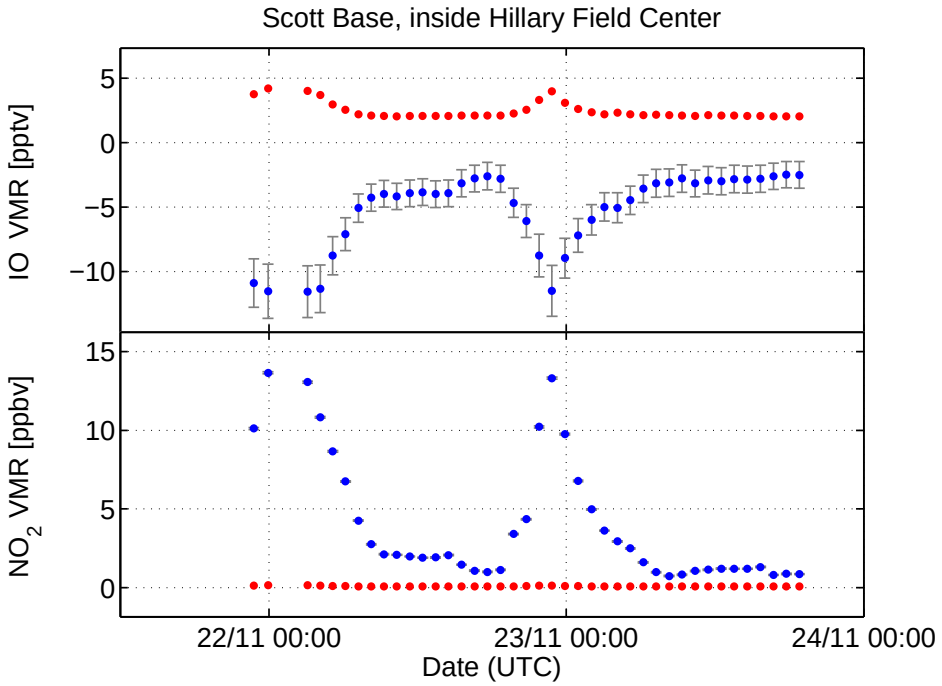

Figure A.46.: Scott Base CE-DOAS: Derived mixing ratios for IO and NO_2. The detection limit is given as 4 times the fit error. However at levels of more than 1 ppbv of NO_2, the DL for IO is already over 10 pptv due to strong remaining residual structures. Measurements are marked blue, the respective detection limit red.

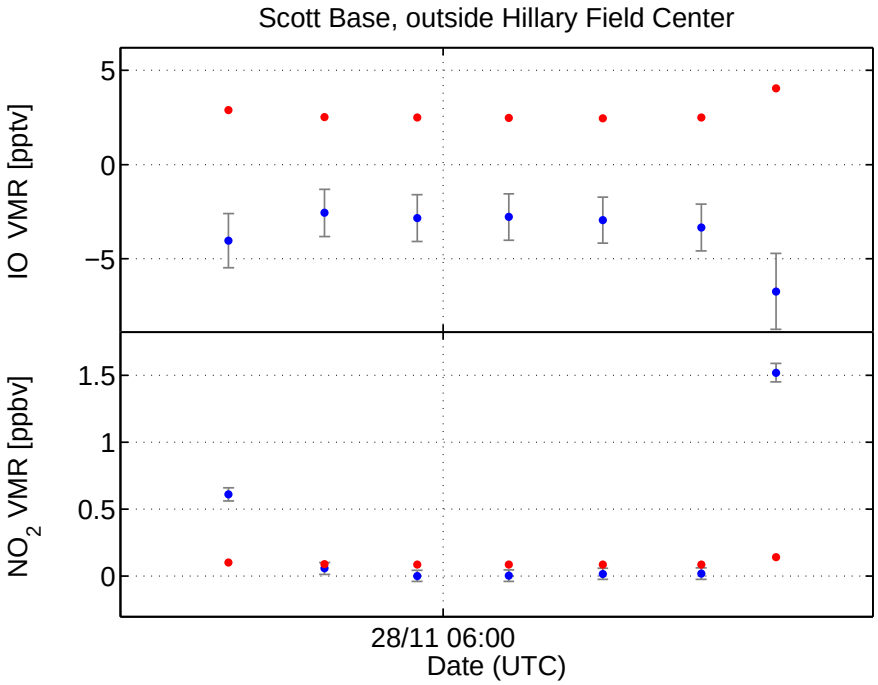

Figure A.47.: Scott Base CE-DOAS: Derived mixing ratios for IO and NO_2. Measurements are marked blue, the respective detection limit red.

A.5 Alert: MAX-DOAS evaluation

Year	Hg emission line spectrum	Offset spectrum	Dark current spectrum
2007	A0009462	A0014557	A0014560
2008	A0000555	A0000549	A0000551
2009	A0032495	A0032496	A0032499
2011	A0086529	A0086532	A0086533
2012	A0110026	A0109927	A0109797
2013	A0169681	A0159146	A0159153
2014	A0085192	A0085180	A0085181

Table A.2.: List of the numbers of the used Hg emission line, offset and dark current spectra in the DOAS evaluation of the Alert measurement data.

A.6 Alert: MAX-DOAS SCD time series

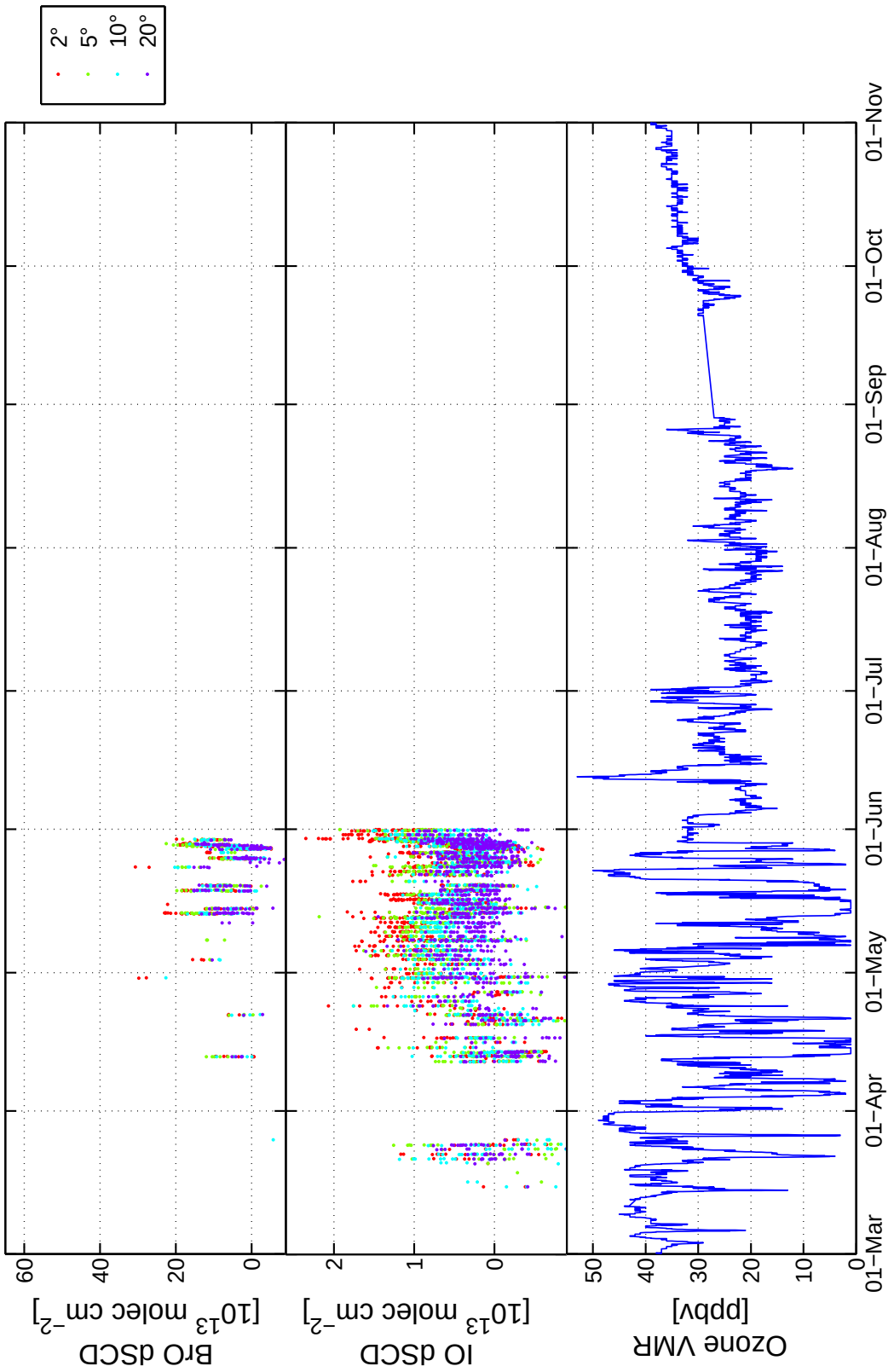

Figure A.48.: 2011: The derived BrO and IO column densities of the Alert MAX-DOAS measurements. The elevation angle is color-coded and values are selected to have a DOAS fit residual RMS of less than $1 \cdot 10^{-3}$ for BrO and $5 \cdot 10^{-4}$ for IO. Also shown are the local ozone mixing ratios, which were provided by Environment Canada.

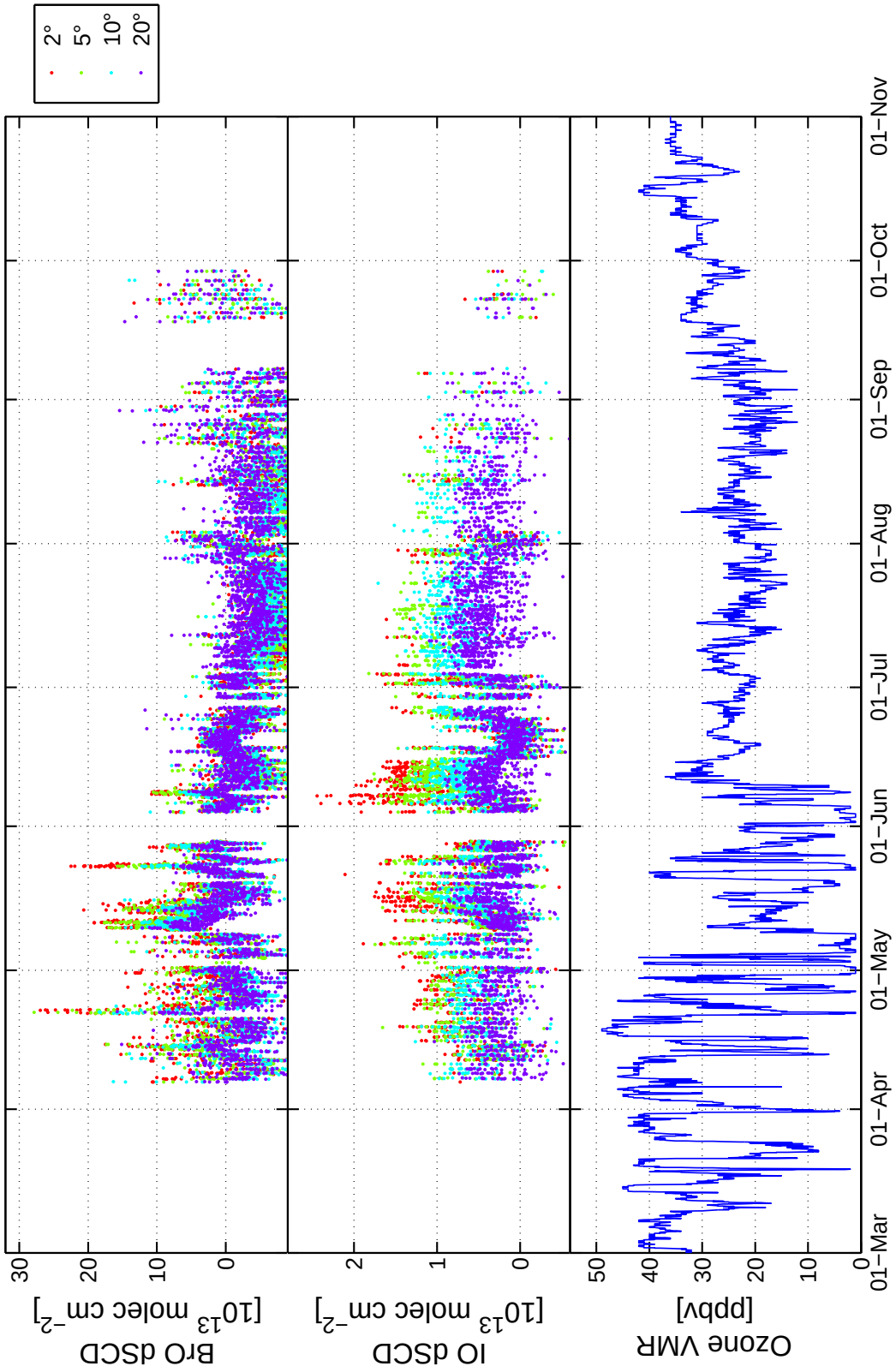

Figure A.49.: 2009: The derived BrO and IO column densities of the Alert MAX-DOAS measurements. The elevation angle is color-coded and values are selected to have a DOAS fit residual RMS of less than $1 \cdot 10^{-3}$ for BrO and $1.5 \cdot 10^{-4}$ for IO. Also shown are the local ozone mixing ratios, which were provided by Environment Canada.

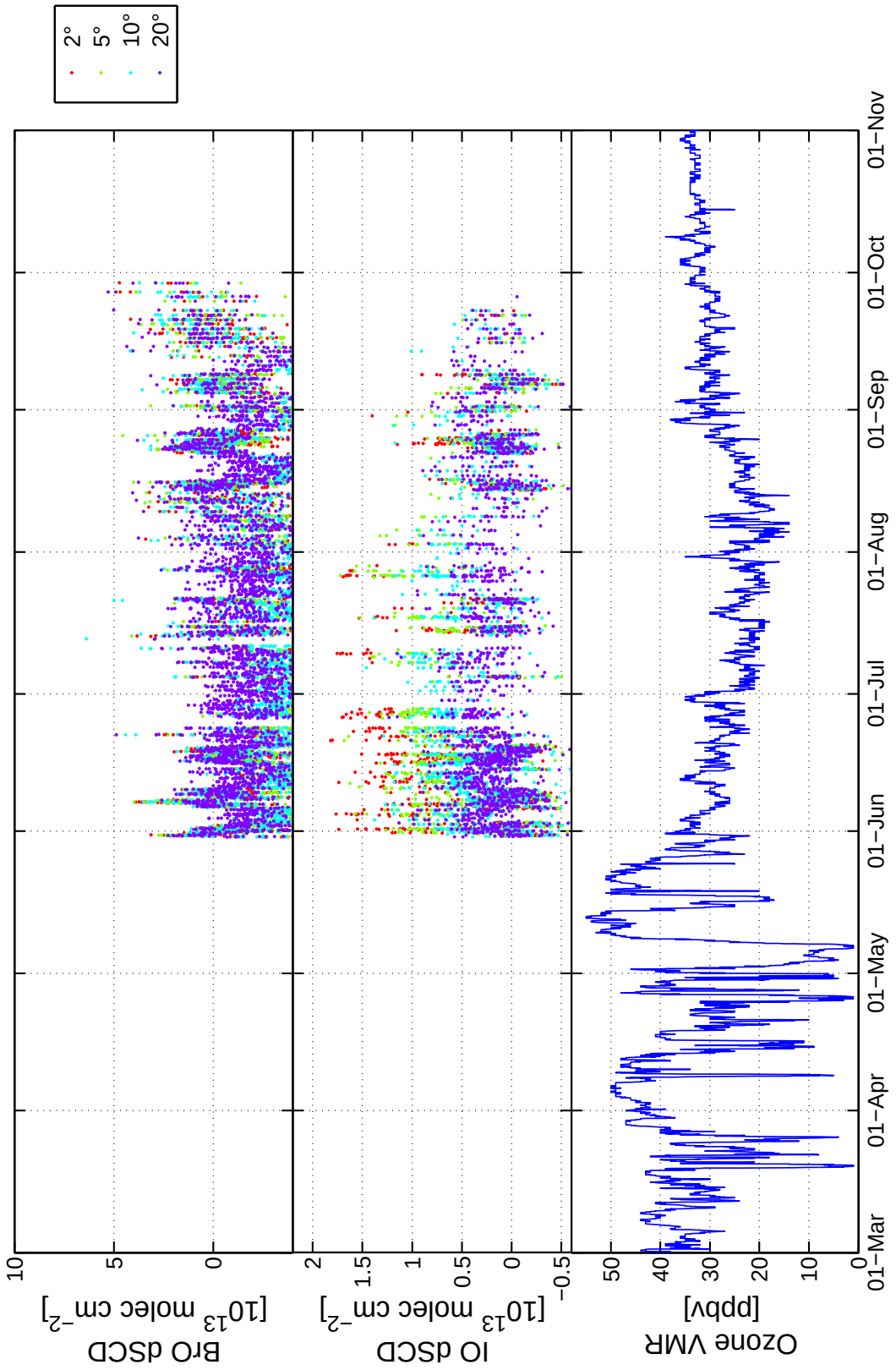

Figure A.50.: 2008: The derived BrO and IO column densities of the Alert MAX-DOAS measurements. The elevation angle is color-coded and values are selected to have a DOAS fit residual RMS of less than $5 \cdot 10^{-4}$ for BrO and $1.5 \cdot 10^{-4}$ for IO. Also shown are the local ozone mixing ratios, which were provided by Environment Canada.

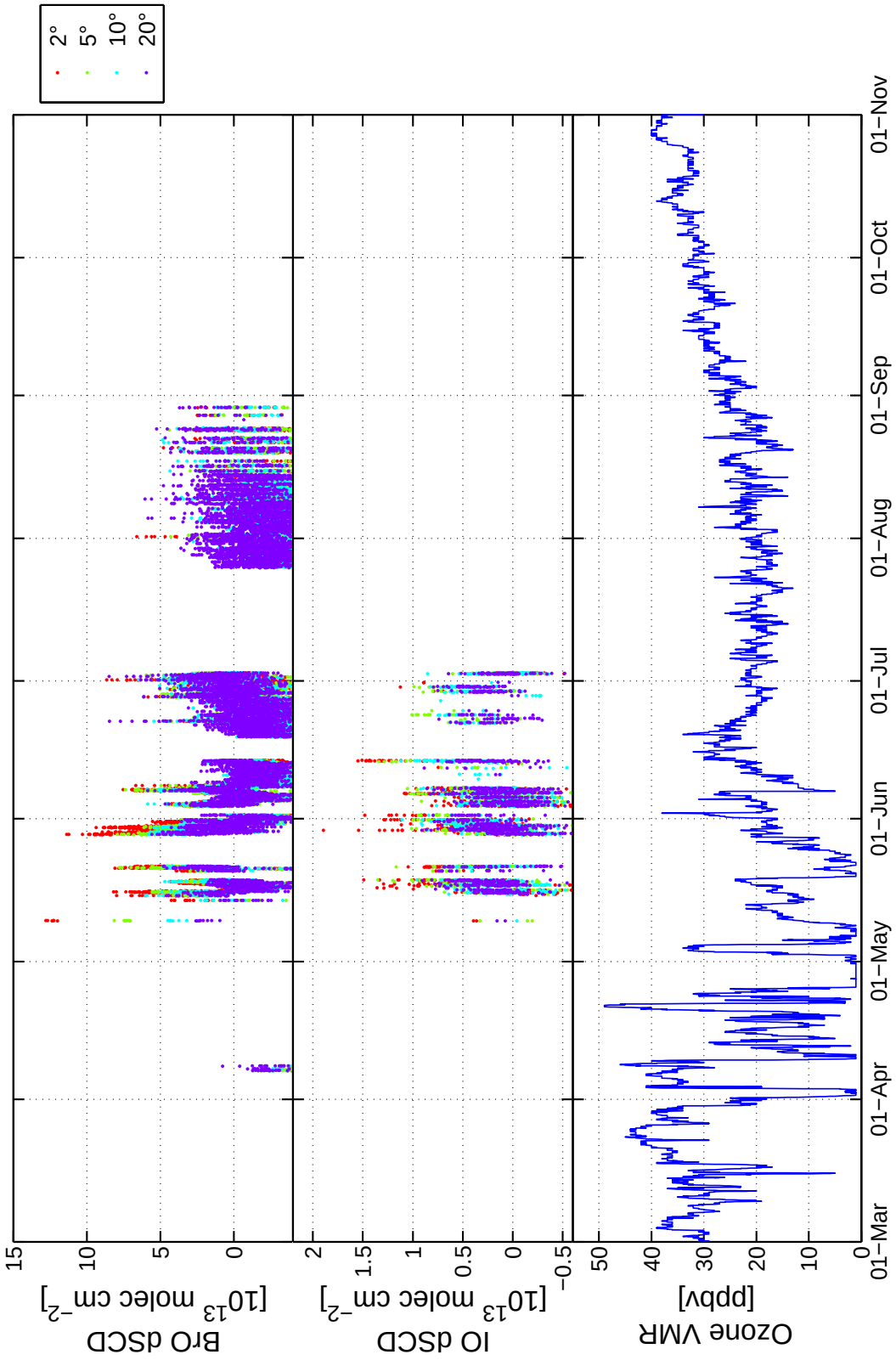

Figure A.51.: 2007: The derived BrO and IO column densities of the Alert MAX-DOAS measurements. The elevation angle is color-coded and values are selected to have a DOAS fit residual RMS of less than $5 \cdot 10^{-4}$ for BrO and $1.5 \cdot 10^{-4}$ for IO. Also shown are the local ozone mixing ratios, which were provided by Environment Canada.

A.7 Alert: MAX-DOAS mixing ratio time series

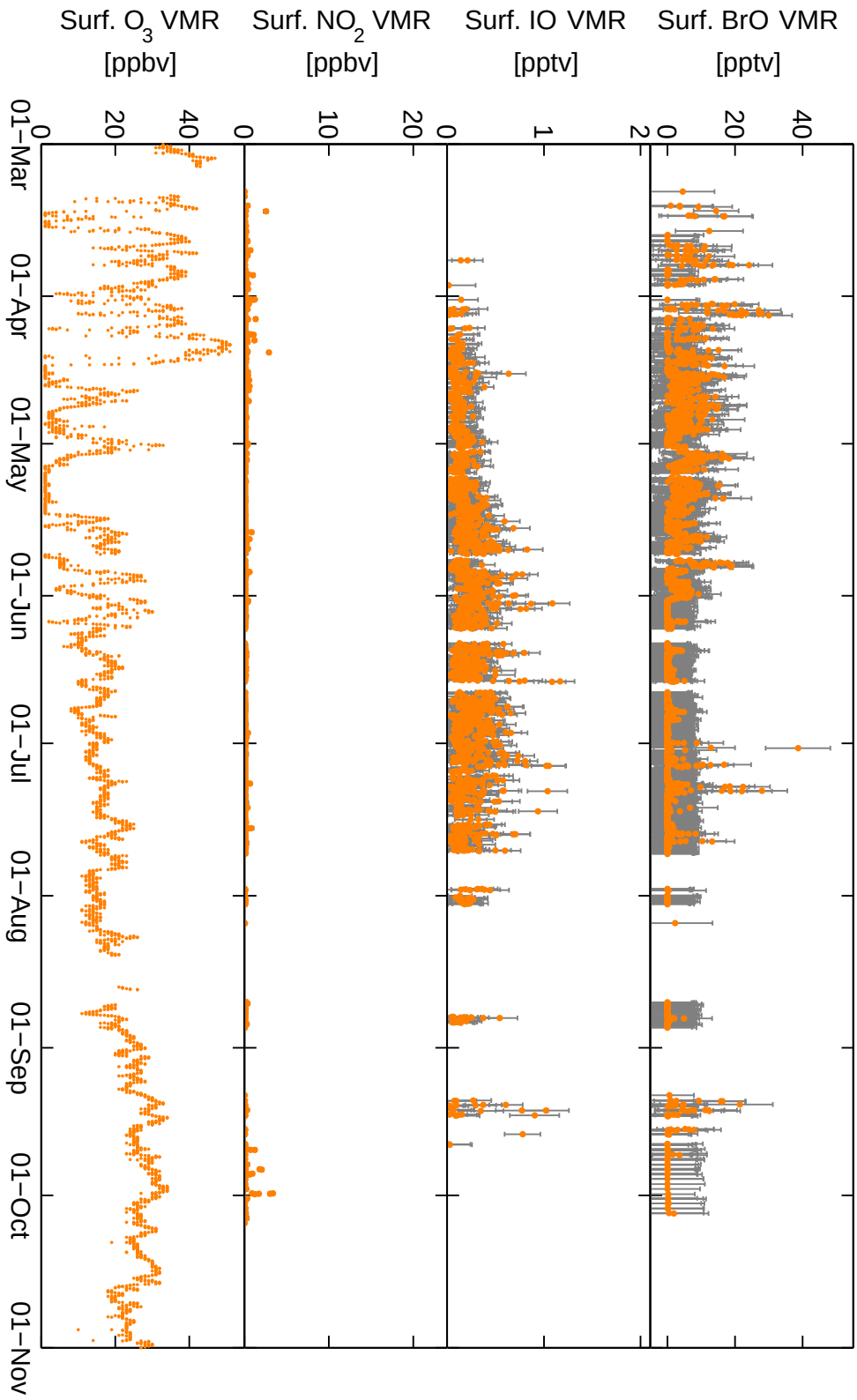

Figure A.52.: 2013: Time series of retrieved surface mixing ratios of BrO, IO and NO_2. The results are filtered to have at least 1 degree of freedom for signal. Also shown are the local ozone mixing ratios, which were provided by Environment Canada.

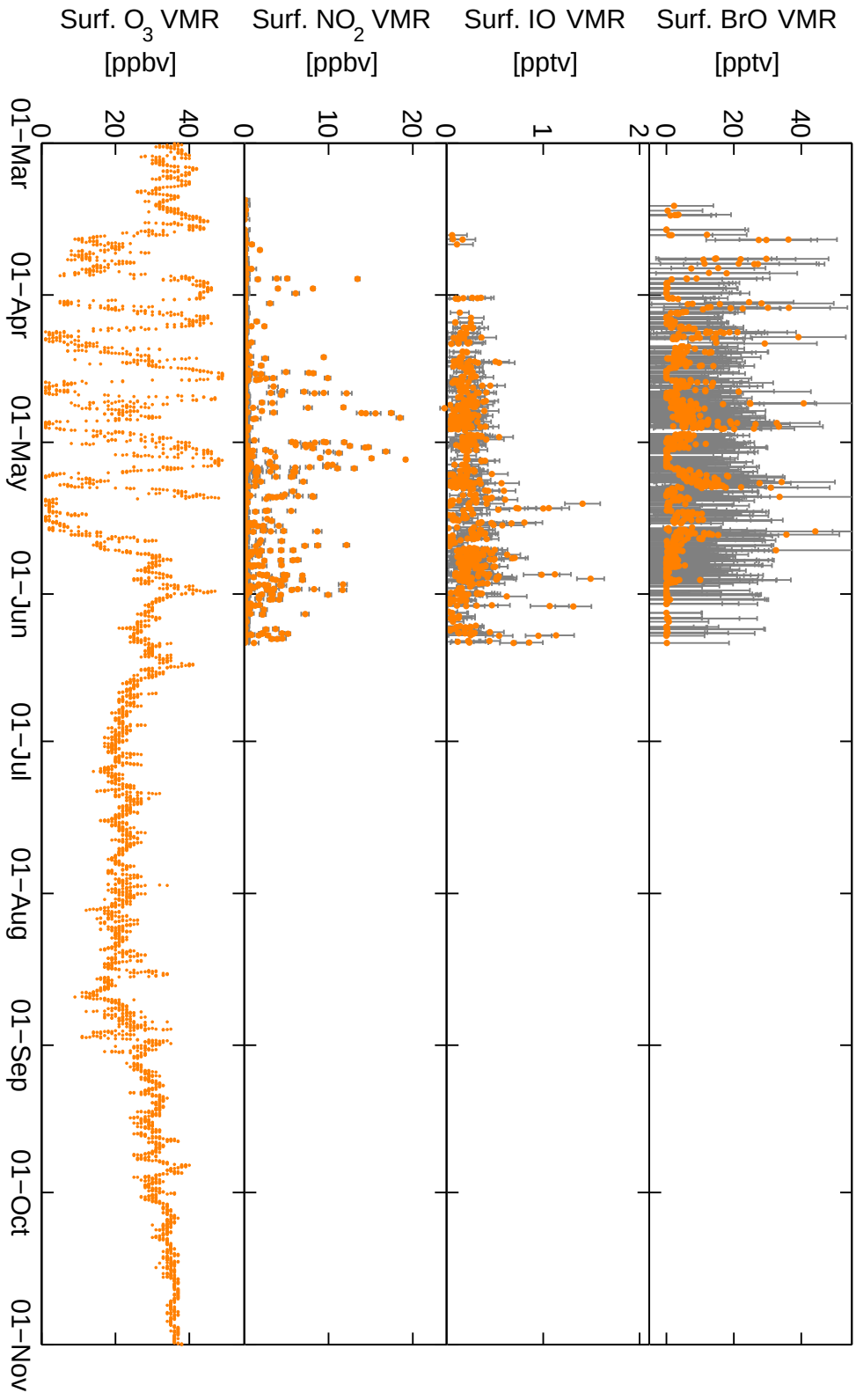

Figure A.53.: 2012: Time series of retrieved surface mixing ratios of BrO, IO and NO_2. The results are filtered to have at least 1 degree of freedom for signal. Also shown are the local ozone mixing ratios, which were provided by Environment Canada.

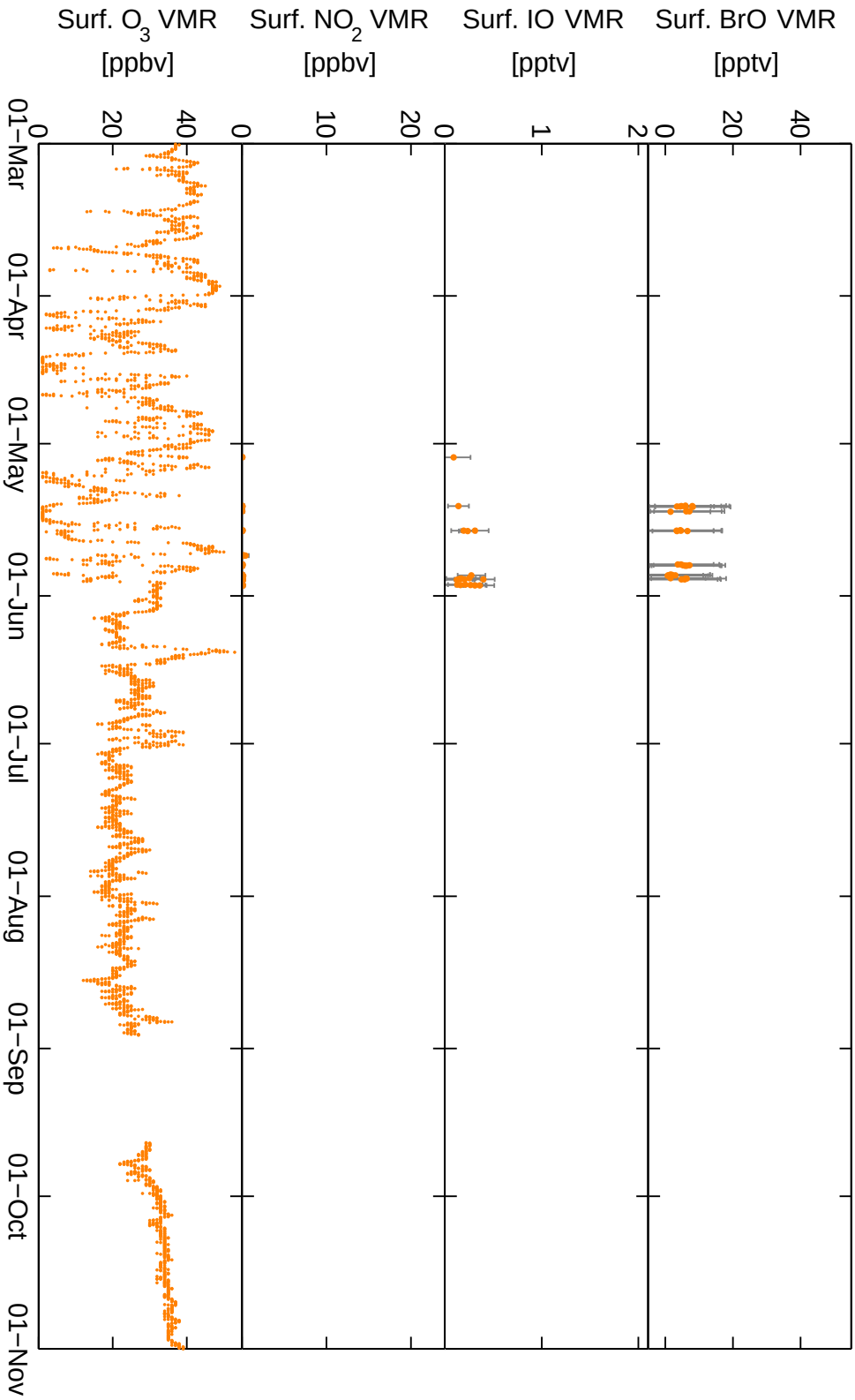

Figure A.54.: 2011: Time series of retrieved surface mixing ratios of BrO, IO and NO_2. The results are filtered to have at least 1 degree of freedom for signal. Also shown are the local ozone mixing ratios, which were provided by Environment Canada.

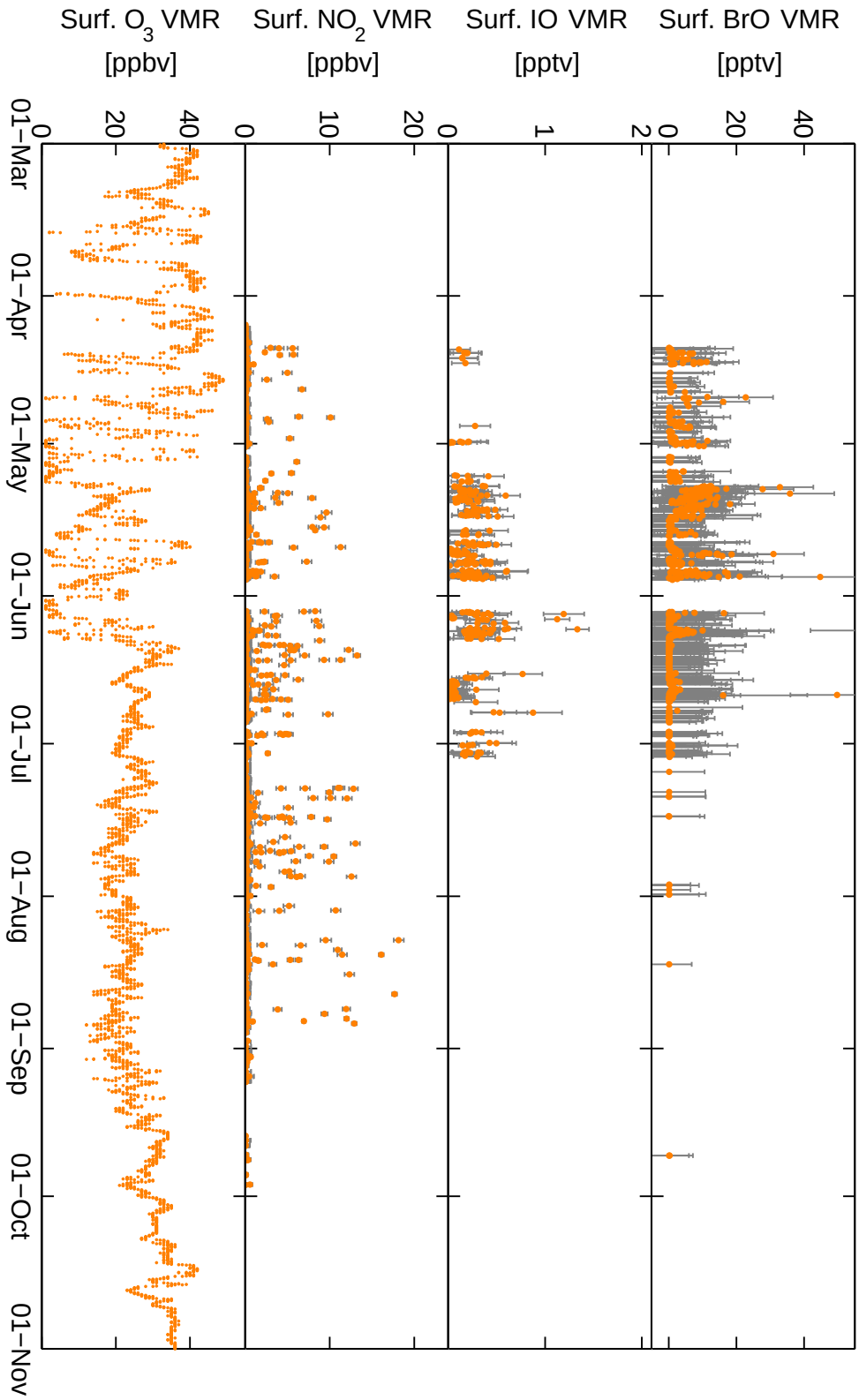

Figure A.55.: 2009: Time series of retrieved surface mixing ratios of BrO, IO and NO_2. The results are filtered to have at least 1 degree of freedom for signal. Also shown are the local ozone mixing ratios, which were provided by Environment Canada.

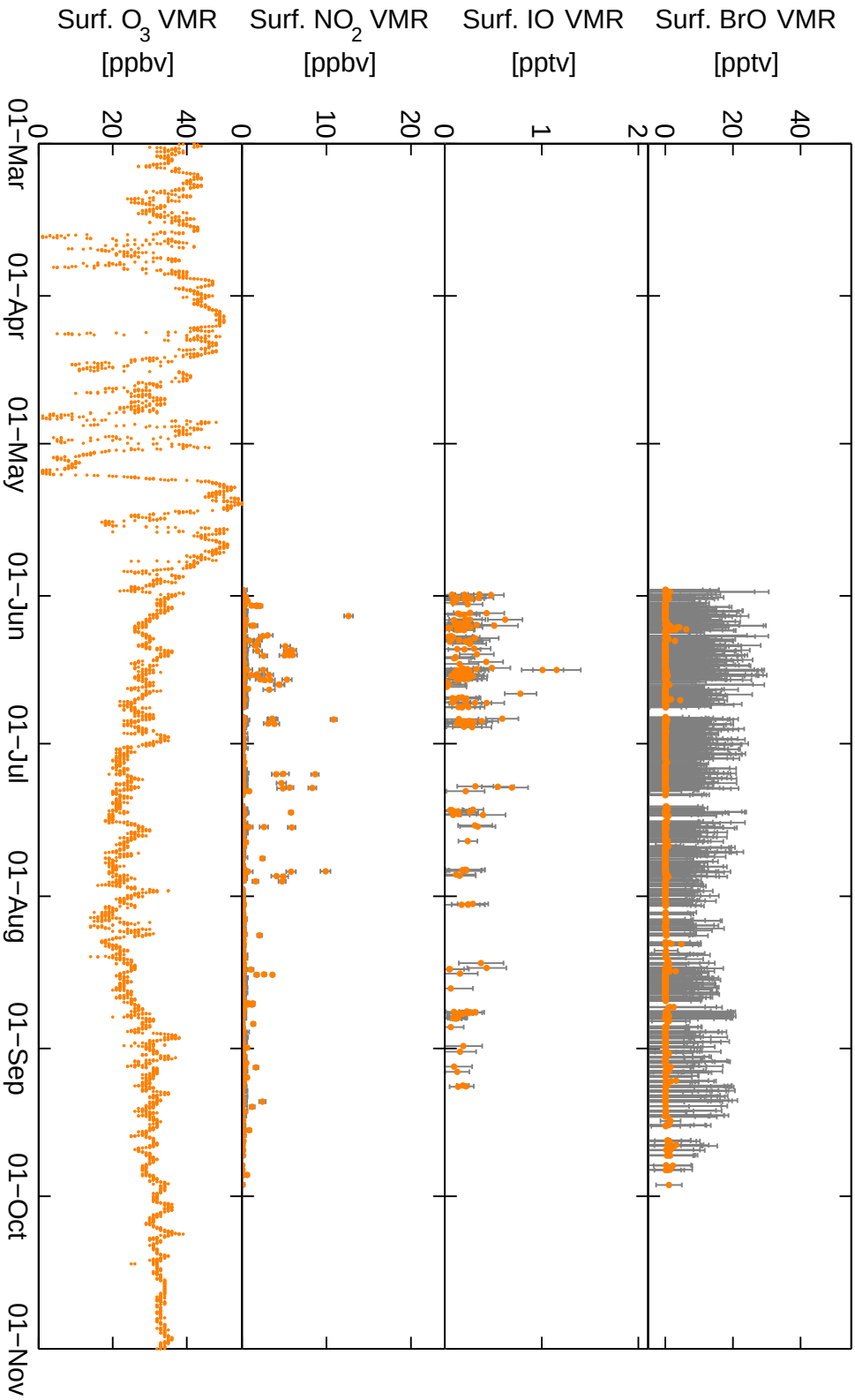

Figure A.56.: 2008: Time series of retrieved surface mixing ratios of BrO, IO and NO_2. The results are filtered to have at least 1 degree of freedom for signal. Also shown are the local ozone mixing ratios, which were provided by Environment Canada.

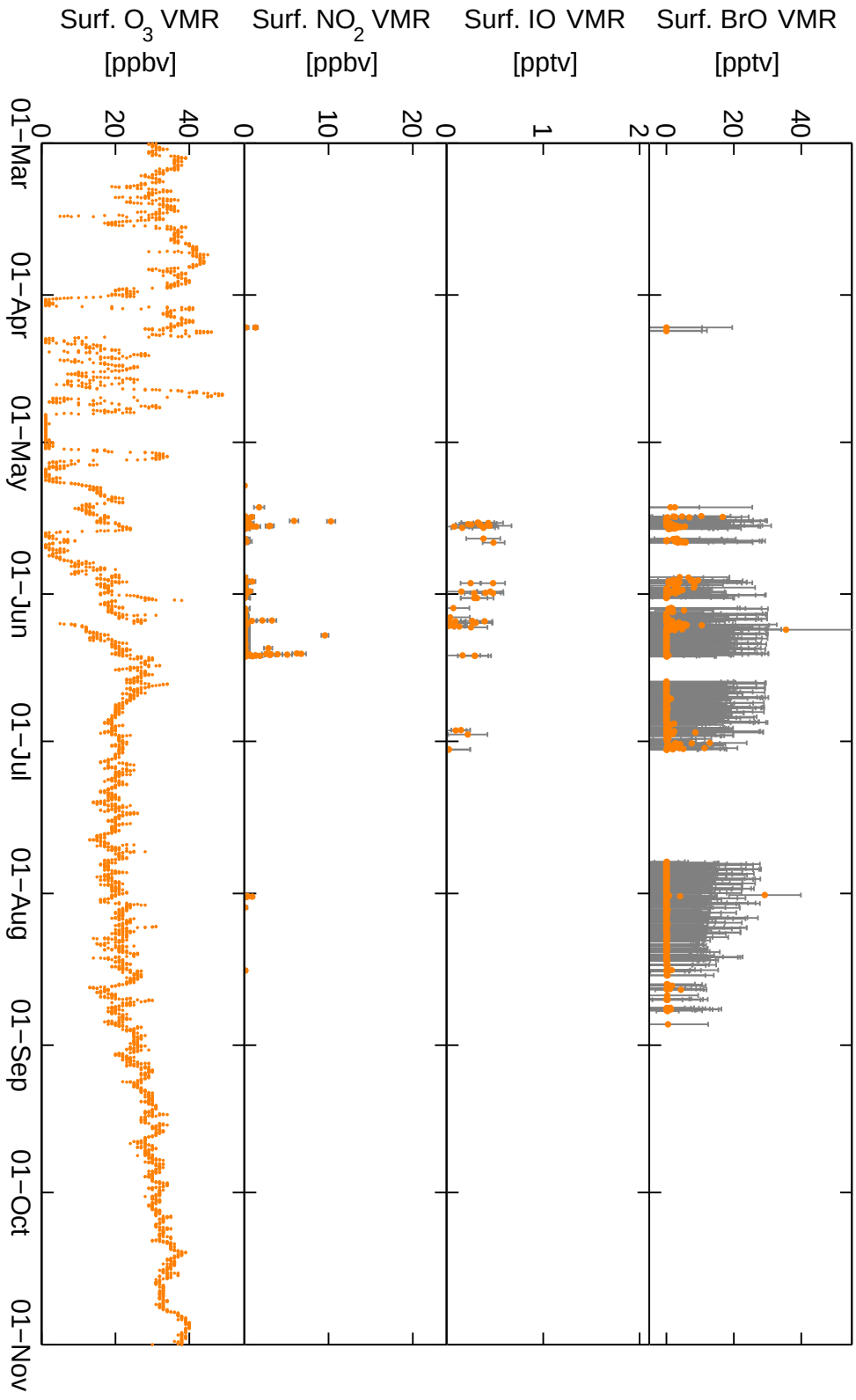

Figure A.57.: 2007: Time series of retrieved surface mixing ratios of BrO, IO and NO_2. The results are filtered to have at least 1 degree of freedom for signal. Also shown are the local ozone mixing ratios, which were provided by Environment Canada.

Acknowledgements

This thesis would not have been possible without all the people who helped me over the years, and there were a lot of them. Therefore i want to express my gratitude to / Daher möchte ich meine Dankbarkeit ausdrücken gegenüber

- Prof. Ulrich Platt, mir diese Arbeit überhaupt erst zu ermöglichen, die vielen Tips über die Jahre, vor allem zur Reaktionskinetik und praktischen Mess- und Alltagsproblemen und die vielen ermöglichten Messkampagnen und Konferenzteilnahmen.

- Prof. Bernd Jähne, für die spontane Übernahme des Zweitgutachtens.

- Udo, dafür genug Vertrauen in mich zu haben, mich an diesem Projekt arbeiten zu lassen, die ganzen Tips bezüglich der Inversionen und die Mitnahme auf IPY und auf Kampagnen.

- Am Institut der gesamten Verwaltung sowie der Werkstatt, die ich vor allem am Anfang der Arbeit mit unzähligen Abrechnungs-, Vertrags-, Zoll- und Dienstreiseformularen sowie mechanischen Problemen, die kurzfristigst und unbedingt sofort gelöst werden mussten, genervt habe.

- Der gesamten Luftchemiegruppe, für die tolle Arbeitsatmosphäre, vor allem auch Stefan und Peter für die ganzen Diskussionen und Kaffee.

- Denis, für die super produktive Zusammenarbeit in der Arktis und Antarktis und die vielen Tips und Diskussionen bei allerlei technischen Problemen.

- Nicole, für die aufmunternden Worte wenn immer mal etwas (fachlich oder menschlich) schief gelaufen ist.

- Johannes, für den geteilten Glauben daran, dass auch aus Messdaten die auf den ersten Blick nichtssagend oder schlecht aussehen, noch etwas rauszuholen ist.

- Martin, für den gemeinsamen Sommer im Institutskeller um die beiden Cavities kampagnenbereit zu machen und das gemeinsame Gefluche.

- Meinen Bürokollegen über die Jahre, Cora, Leila, Leif, Jenny und Christiane, für die ganzen Unterhaltungen, Kuchen und Kekse.

- Everyone involved in the BROMEX campaign in Barrow for the great atmosphere, Paul Shepson, Kerri Pratt, Kyle Custard, the Fairbanks people, Tom Douglas for mailing two mission critical sampling bottles of single malt whisky, Son Nghiem, Ross Lieb-Lappen and the team at NARL.

- Bill Simpson, Chris Iceman, Peter Peterson, Steve Walsh and Erin Gleason for the overwhelming hospitality during my stay in Fairbanks.

- Stoyka Netcheva for the hospitality in Canada, taking us to Alert, and for taking care of the instrument together with the local operators.

- All the folks i met during my stay at Scott Base/McMurdo, Tim Hay (the sampling of "Antarctic Culture", going mountain-biking, the Yacht Club barbecue, Lars Kalnajs, Ross Lieb-Lappen, Tom, the Belgians, Speights training beer, the cooks, the field support team, mechanical workshop and carpenter, and also the random person i met going for a run on Observation Hill for giving me a high five, showing me i'm not the only one crazy enough to go running in Antarctica.

- Auch denen die an der teils frustrierenden Polarsternfahrt beteiligt waren, das beste daraus zu machen, Jan, den Piloten und Helitechnikern, den Matrosen, den Schiffsmechanikern und vor allem auch der Küche.

- Den Korrekturlesern dieser Arbeit, Stefan, Katja, Jonas, Holger, Johannes, Udo, Nicole und Jan.

- Jonas, für die hunderte von gemeinsamen, motivierenden Laufkilometer und Höhenmeter während der letzten Monate bei Schnee, Eis, Regen, Wind und Sonne.

- Meinen Eltern, für die Unterstützung wenn immer möglich während der letzten 30 Jahre.

- Ellen, für die andauernde Motivation und Unterstützung, und das Verständnis für die vielen durchgearbeiteten Wochenenden und langen Abende.